

**DESIGN, SYNTHESIS AND EVALUATION OF
BIOREDUCTIVELY-ACTIVATED
FLUOROQUINOLONE PRODRUGS**

A THESIS
SUBMITTED IN PARTIAL FULFILLMENT OF THE
REQUIREMENTS
OF THE DEGREE OF

DOCTOR OF PHILOSOPHY

BY

T. ANAND KUMAR

20163463



**INDIAN INSTITUTE OF SCIENCE EDUCATION
AND RESEARCH, PUNE – 411 008**

2022

भारतीय विज्ञान शिक्षा एवं अनुसंधान संस्थान पुणे

INDIAN INSTITUTE OF SCIENCE EDUCATION AND RESEARCH PUNE

डॉ. होमी भाभा मार्ग, पुणे 411008, महाराष्ट्र, भारत | Dr. Homi Bhabha Road, Pune 411008, Maharashtra, India
T +91 20 2590 8001 W www.iiserpune.ac.in



CERTIFICATE

Certified that the work incorporated in the thesis entitled, "*Design, Synthesis and Evaluation of Bioreductively-Activated Fluoroquinolone Prodrugs*" submitted by *T. Anand Kumar* was carried out by the candidate, under my supervision. The work presented here or any part of it has not been included in any other thesis submitted previously for the award of any degree or diploma from any other University or institution.

Date: DEC 19, 2022

Pune (MH), India

C. Harinath

Prof. Harinath Chakrapani

DECLARATION

I declare that this written submission represents my ideas in my own words and where others' ideas have been included, I have adequately cited and referenced the original sources. I also declare that I have adhered to all principles of academic honesty and integrity and have not misrepresented or fabricated or falsified any idea/data/fact/source in my submission. I understand that violation of the above will be cause for disciplinary action by the Institute and can also evoke penal action from the sources which have thus not been properly cited or from whom proper permission has not been taken when needed.

Date: 20/12/2022

Pune (MH), India

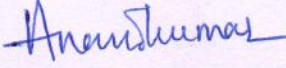

T. Anand Kumar
20163463

Table of Contents

| | |
|------------------------------|-------------|
| Table of Contents | I |
| General Remarks | V |
| List of Abbreviations | VII |
| Acknowledgements | XI |
| Abstract | XIII |

Chapter 1. Introduction

| | |
|---|----|
| 1.1. Tuberculosis | 1 |
| 1.2. Persisters | 1 |
| 1.3. Characteristics of persisters | 3 |
| 1.4. Therapeutic strategies to eliminate persisters | 5 |
| 1.4.1. Antitubercular prodrugs containing nitro group | 6 |
| 1.4.2. Fluoroquinolones (FQs) | 8 |
| 1.4.2.1. Discovery, development and use of FQs | 8 |
| 1.4.2.1.A. First generation FQs | 9 |
| 1.4.2.1.B. Second generation FQs | 10 |
| 1.4.2.1.C. Third generation FQs | 10 |
| 1.4.2.1.D. Fourth generation FQs | 10 |
| 1.4.2.2. Mechanism of action | 11 |
| 1.4.2.3. Adverse effects | 12 |
| 1.4.2.4. Fluoroquinolone prodrugs | 13 |
| 1.4.2.4.A. Light activated FQ prodrugs | 13 |
| 1.4.2.4.B. Thiol activated FQ prodrugs | 16 |
| 1.4.2.4.C. Enzyme activated FQ prodrugs. | 17 |
| 1.5. Fluoroquinolones in TB | 21 |
| 1.5.1. Moxifloxacin (MXF) in TB | 22 |
| 1.5.2. Reduced efficacy of MXF in <i>Mtb</i> persisters | 24 |
| 1.6. Motivation and outline of the thesis | 25 |
| 1.7. References | 27 |

Chapter 2. Design, Synthesis and Evaluation of Nitroheterocyclic Prodrugs of Moxifloxacin (MXF)

| | |
|--|-----|
| 2.1. Introduction | 45 |
| 2.2. Design of nitroreductase (NTR)-activated FQ prodrug | 45 |
| 2.3. Results and discussion | 46 |
| 2.3.1. Synthesis | 46 |
| 2.3.2. Physicochemical properties | 57 |
| 2.3.3. Electrochemistry | 58 |
| 2.3.4. Photophysical properties | 61 |
| 2.3.5. Chemoreduction | 62 |
| 2.4. Conclusion | 66 |
| 2.5. Experimental and Characterization data | 68 |
| 2.6. NMR spectral data | 94 |
| 2.7. HRMS spectra of final compounds | 139 |
| 2.8. References | 144 |

Chapter 3. Nitroreductase (NTR) mediated Bioreductive Activation of Moxifloxacin (MXF) Prodrugs

| | |
|--|-----|
| 3.1. Introduction | 147 |
| 3.2. Results and discussion | 148 |
| 3.2.1. Enzymatic nitroreduction of prodrugs and evaluation of release of MXF | 148 |
| 3.2.2. Kinetics of <i>E. coli</i> NTR dependent reductive activation of MXF prodrugs | 149 |
| 3.2.3. Assessment of bioreduction of prodrugs | 155 |
| 3.2.4. Mechanism | 159 |
| 3.2.5. Computational studies | 160 |
| 3.2.5.1. Docking analysis | 160 |
| 3.2.5.2. Molecular dynamics simulations | 166 |
| 3.2.6. Selectivity of 38 towards NTR | 169 |
| 3.2.7. <i>E. coli</i> mediated bioreductive activation of prodrugs | 169 |
| 3.2.8. <i>In silico</i> modeling of the interaction of prodrug with Mycobacterial NTRs | 170 |
| 3.2.9. Bioreductive transformation of 38 in mycobacterial lysates | 173 |
| 3.2.10. Stability of 38 in mammalian lysate | 175 |

| | |
|-----------------------------|-----|
| 3.3. Conclusion | 176 |
| 3.4. Experimental protocols | 177 |
| 3.5. References | 184 |

Chapter 4. Evaluation of Antibacterial and Antimycobacterial activity of NTR-MXF

Prodrugs

| | |
|--|-----|
| 4.1. Introduction | 194 |
| 4.2. Results and discussion | 194 |
| 4.2.1. <i>In vitro</i> antibacterial activity | 194 |
| 4.2.2. <i>In vitro</i> antimycobacterial activity | 195 |
| 4.2.2.1. Against <i>M. smegmatis</i> mc ² 155 | 195 |
| 4.2.2.2. Against <i>M. tuberculosis</i> H37Rv | 198 |
| 4.2.3. Plausible mechanism behind the enhanced efficacy of 38 | 202 |
| 4.2.4. Accumulation studies | 203 |
| 4.2.4.1. Fluorescence based accumulation studies | 203 |
| 4.2.4.2. LC-MS/MS based accumulation studies | 205 |
| 4.2.4.2.A. Drug uptake studies in <i>E. coli</i> ATCC 25922 | 205 |
| 4.2.4.2.B. Drug uptake studies in <i>Mtb</i> H37Rv | 210 |
| 4.3. Conclusion | 215 |
| 4.4. Experimental protocols | 216 |
| 4.5. References | 220 |

Chapter 5.1. Design, Synthesis and Evaluation of Nitroreductase (NTR) activated Prodrugs of Ciprofloxacin (CIP)

| | |
|---|-----|
| 5.1.1. Introduction | 222 |
| 5.1.2. Results and discussion | 223 |
| 5.1.2.1. Synthesis | 223 |
| 5.1.2.2. <i>E. coli</i> NTR mediated nitroreduction of prodrugs | 224 |
| 5.1.2.3. Bioreductive activation of prodrugs | 225 |
| 5.1.2.4. Antibacterial activity | 226 |
| 5.1.3. Conclusion | 226 |
| 5.1.4. Experimental and characterization data | 228 |
| 5.1.5. NMR spectral data | 232 |
| 5.1.6. HRMS spectra of final compounds | 239 |

| | |
|-------------------|-----|
| 5.1.7. References | 240 |
|-------------------|-----|

Chapter 5.2. Design and Development of Nitroreductase (NTR) Responsive Dual Colorimetric Fluorescence “Turn OFF-ON” Probes

| | |
|--|-----|
| 5.2.1. Introduction | 241 |
| 5.2.2. Design of Nitroreductase (NTR)-responsive dual colorimetric fluorescent probe | 242 |
| 5.2.3. Results and discussion | 242 |
| 5.2.3.1. Synthesis | 242 |
| 5.2.3.2. Photophysical properties | 244 |
| 5.2.3.3. <i>E. coli</i> NTR mediated activation of latent fluorophores | 245 |
| 5.2.3.4. <i>E. coli</i> dependent colorimetric and fluorescence “turn OFF-ON” response | 246 |
| 5.2.3.5. Selectivity and sensitivity of 61 towards <i>E. coli</i> NTR | 247 |
| 5.2.3.6. Cell viability | 251 |
| 5.2.3.7. Real-time detection of bacteria by confocal microscopy | 252 |
| 5.2.4. Conclusion | 253 |
| 5.2.5. Experimental and characterization data | 254 |
| 5.2.6. NMR spectral data | 261 |
| 5.2.7. HRMS spectra of final compounds | 269 |
| 5.2.8. References | 270 |

| | |
|--|-----|
| Appendix-I: Synopsis | 274 |
| Appendix-II: List of Figures | 293 |
| Appendix-III: List of Schemes | 307 |
| Appendix-IV: List of Tables | 309 |
| Appendix-V: Copyright permits | 310 |
| Appendix-VI: List of Patents and Publications | 311 |

- Thin-layer chromatography (TLC) was performed using silica gel 60 GF₂₅₄ precoated aluminium backed plates (0.25 mm thickness) and visualization was accomplished by irradiation with short and long UV light at 254 and 365 nm respectively or by staining with bromocresol green or phosphomolybdic acid (PMA) for the identification of carboxylic acid or alcohols respectively.
- ¹⁹F spectra were recorded on a JEOL (376 MHz) using an external reference (α, α, α -trifluorotoluene, $\delta_F = -63.72$ ppm).
- ¹H and ¹³C spectra were recorded on JEOL or Bruker 400 MHz (or 100 MHz for ¹³C) spectrometers using tetramethylsilane (TMS) as an internal standard.
- Chemical shifts (δ) are reported in ppm downfield from CDCl₃ ($\delta = 7.26$ and 77.2 ppm) or DMSO-*d*₆ ($\delta = 2.50$ and 39.5 ppm) for ¹H and ¹³C-NMR respectively as an internal reference. The coupling constants (*J*) are given in Hz. Multiplicities are indicated using the following abbreviations: br (broad), m (multiplet), s (singlet), d (doublet), t (triplet), q (quartet), h (heptet), ddd (doublet of doublet of doublet), dd (doublet of doublet), dt (doublet of triplet), dq (doublet of quartet), and td (triplet of doublet). The nature of the carbons (C, CH, CH₂ or CH₃) was determined by recording the DEPT-135 spectra, and is given in parentheses.
- Column chromatography was performed using Rankem silica gel (60-120 mesh) eluting with petroleum ether and ethyl acetate (EtOAc).
- Preparative High Performance Liquid Chromatography (Prep HPLC) was carried out on a Combiflash EZ Prep UV equipped with a Kromasil[®]C-18 preparative column (21.5 mm x 250 mm, 10 μ m) at a flow rate of 12 mL/min.
- High-resolution mass spectra were obtained from HRMS-ESI-QTOF (quadrupole time-of flight).
- FT-IR spectra were recorded using Bruker ALPHA FT-IR spectrometer and reported in cm⁻¹.
- Melting point was measured using a BÜCHI M-560 melting point apparatus. All melting points were measured in an open glass capillary, and the values are uncorrected.
- LC-MS experiments were performed either on a Sciex X500R QTOF mass spectrometer fitted with an Exion UHPLC system or on a Bruker Daltonics ESI-QTOF (Maxis Impact) mass spectrometer connected to a Thermo Dionex (Ultimate 3000) micro-LC system in a positive ion mode using high resolution multiple reaction monitoring (MRM-HR) method.

- Fluorescence measurement corresponding to MXF was carried out using a Horiba Jobin Yvon Fluorolog Fluorescence Spectrophotometer or an EnSight Multimode Plate Reader (PerkinElmer) in a 96-well plate format.
- Cyclic voltammetry studies were conducted using a standard three-electrode setup connected to a CHI760E electrochemical workstation. Glassy carbon and platinum wire were used as the working electrode and counter electrode respectively. Ag/AgCl was used as a reference electrode. These experiments were conducted under an atmosphere of argon in anhydrous ACN with tetra-butyl ammonium hexafluorophosphate (TBAP; 0.1 M) as supporting electrolyte.

Abbreviations

AF = Ammonium formate

ARG = antibiotic-resistant genes

AUC_{tot} = Total area under the curve

ALP = Alkaline phosphatase

BDP = BODIPY

BTZs = Benzothiazinones

casMBC₉₀ = Caseum minimum bactericidal concentration

CFU = Colony forming unit

CIP = Ciprofloxacin

CYP1A2 = Cytochrome P450 1A2

COPD = Chronic obstructive pulmonary disease (COPD)

CV = Cyclic voltammograms

CHCl₃ = Chloroform

DCOM = Dicoumarol

DNBs = Dinitrobenzamides

DMSO = Dimethyl sulfoxide

Ddn = Deazaflavin dependent nitroreductase

DOT = Directly observed therapy

EIC = Extracted ion chromatogram

E. coli = *Escherichia coli*

EBA = Early bactericidal activity

Fc/Fc⁺ = Ferrocene/Ferrocenium

FMN = Flavin mononucleotide

FQ = Fluoroquinolone

FDA = Food and Drug Administration

GFX = Gatifloxacin

GSH = Glutathione

GDEPT = Gene directed enzyme prodrug therapy

hPON1 = Human paraoxonase

HAPs = Hypoxia-activated prodrugs

HRZE regimen = Regimen containing Isoniazid (H), rifampicin (R), pyrazinamide (Z) and ethambutol (E)

hERG = human ether-a-go-go-related gene

HPLC = High performance liquid chromatography

HT = Hydride transfer

HyRRA = Hypoxia resazurin reduction assay

ICI = Imperial Chemical Industries

INH = Isoniazid

K_m = Michaelis-Menten constant

k_{cat}/K_m = Catalytic efficiency

KG = 2-ketoglutarate

K_2CO_3 = Potassium carbonate

KSCN = Potassium thiocyanate

logP = Partition coefficient

LSD1 = Lysine-specific demethylase 1

LC-MS/MS = Liquid chromatography (LC) tandem mass spectrometry (MS/MS)

LVX = Levofloxacin

MXF = Moxifloxacin

MR = Molar refractivity

MeOH = Methanol

MIC = Minimum inhibitory concentration

MDR = Multidrug-resistant

MPC = Mutant prevention concentration

Msm = *Mycobacterium smegmatis*

Δ mshA = MshA

MSH = Mycothiol

Mrx2 = Mycothiol-dependent NTR

Mtb = *Mycobacterium tuberculosis*

MZ = Metronidazole

NA = Nalidixic acid

NADH = Reduced form of Nicotinamide adenine dinucleotide (NAD)

NADPH = Reduced form of Nicotinamide adenine dinucleotide phosphate (NADP)

NIR = Near-infrared

NFCs = Nitrofuranylcalanolides

NO = Nitric oxide

NRP = Non-replicating persistent

NTRs = Nitroreductases

OFX = Ofloxacin

P. aeruginosa = *Pseudomonas aeruginosa*

PDB = Protein data bank

PB = Phosphate buffer

PBS = Phosphate buffer saline

PT = Proton transfer

QTOF = Quadrupole time-of flight

REMA = Resazurin reduction microplate assay

ROS = Reactive oxygen species

S. aureus = *Staphylococcus aureus*

SI = Selective index

SwissADME = Swiss Absorption, distribution, metabolism and excretion based webtool

NaNO₂ = Sodium nitrite

TB = Tuberculosis

TDR = Totally drug-resistant

TVX = Trovafloxacin

Topo-IV = Topoisomerase-IV

TFA = Trifluoroacetic acid

TBAP = tetra-butyl ammonium hexafluorophosphate

TPSA = Topological polar surface area

TLC = Thin layer chromatography

TsN₃ = Tosyl azide

THF = Tetrahydrofuran

UV = Ultraviolet light

Umb = Umbelliferone

UTIs = Urinary tract infections

V_{\max} = Maximum reaction velocity

WT = Wild-type

WHO = World Health Organization

XDR = Extensively drug-resistant

Acknowledgements

First and foremost, I want to express my sincere gratitude to Prof. Harinath Chakrapani, my supervisor and guru for his invaluable guidance, support and encouragement he provided me throughout my doctoral studies. His continuous commitment and enthusiasm have helped my work advance and come to fruition. His scholarly insightful discussions about many topics in science as well as in life has made an inspiring experience for me in IISER. I have learnt a lot of new things under his tutelage which encouraged me further to push my limits and do better quality research. I also appreciate his continuous support in allowing me to work as a teaching assistant (TA) for the past four years in the NPTEL-Medical Chemistry course, which eventually helped me to gain a lot of teaching experience.

I am extremely grateful to our collaborators for their continued support that has helped me to make significant progress in the project and complete my PhD dissertation on time. I am particularly thankful to Prof. Amit Singh (IISc Bangalore) and his group members, Dr. Piyali Mukherjee, Ms. Shalini Birua and Dr. Samsher Singh for Mycobacterium tuberculosis (Mtb) related studies. I must also thank Prof. Jennifer Hirschi (University of Binghamton, USA) and her group member, Dr. SharathChandra M. for their assistance and guidance related to computational studies. I would like to thank our collaborator, Dr. Sidharth Chopra (CSIR-CDRI, Lucknow) for his assistance with antibacterial studies and for providing results quickly. I also thank our new collaborator, Dr. Rachit Agarwal and his group members (IISc, Bangalore) for their support on another ongoing project. I am also thankful to Dr. Ruma Banerjee (Prof. Jayakannan M. Lab) for her help in confocal imaging studies. I would also like to thank Dr. Amrita Hazra and her lab members (Dr. Roopali, Dr. Yamini and Aniket) for their helpful discussions on some of the bacterial experiments. Finally, I would especially like to thank PerkinElmer-IISER Pune Center of excellence for providing access to EnSight microplate reader that helped me to meet majority of the research needs related to my thesis work.

I want to convey my sincere thanks to my RAC committee members, Prof. Pinaki Talukdar (IISER-Pune) and Dr. C. V. Ramana (CSIR NCL-Pune) for their insightful suggestions and criticisms that motivated me to broaden my research. I want to thank Prof. Jayant B. Udgoankar (Director of IISER-Pune), Prof. K. N. Ganesh (former Director of IISER-Pune), Prof. H.N. Gopi and Prof. Nirmalya Ballav (former and present chair of the chemistry

department) for providing top-notch research lab facilities. I gratefully acknowledge the funding agency (DST) for providing me with the INSPIRE fellowship.

I have been fortunate enough to work with an incredible group of people. Their unparalleled support, guidance and motivation made my 6-year long journey smooth. I would like to thank to all of my former lab members Dr. Vinayak, Dr. Kundan, Dr. Ravi, Dr. Ajay, Dr. Preeti, Dr. Amogh, Dr. Prerona, Dr. Pooja, Dr. Amol and Dr. Minhaj for their good wishes, timely help and unstinted support. I must sincerely thank Dr. Kavita, Laxman, Suman, Gaurav, Harshit, Bharat, Utsav, Simran and Pooja for their unwavering support and constant help in navigating me through the challenges faced after COVID and a major fire break at IISER. Especially, I am thankful to Dr. Ajay, Dr. Preeti, Dr. Amogh, Dr. Ravi, Dr. Prerona, Dr. Pooja, Suman, Laxman, Gaurav and Harshit for their stimulating discussions and endless conversations on any random topics during tea-breaks. I want to extend my thanks to the current new members of our lab Abhishek, Hariprasad and Arnab. I also thank all BS-MS students worked in our lab, Farhan, Sushma, Swetha, Aswin, Harsha, Mrutyunjay, Amal, Suraj, Bhakti, Manjima, Jishnu, Shayandeep, and Utkarsh. I have been fortunate enough to make close friends at IISER and I am thankful to Ankit, Puneeth, Abdul, Saddam, Prakash, Dr. Ruma, Rashmi, Sandhya, Avisikta, Abhsihek Mondal, Naveen, Dr. Deepak Sharma, Dr. Saptashwa and Dr. Yogesh. I am also grateful to friends from NIPER-Hyderabad, CSIR-IICT and Acharya & B.M. Reddy college of Pharmacy for their constant encouragement and support.

I am particularly grateful to Dr. Siddhesh Kamat (IISER Pune) and his group members (Arnab Chakraborty, Dr. Shubham Singh and Akash) and Mrs. Sunita Prakash (LC-MS facility, IISc Bangalore), who assisted me in performing LC-MS based drug accumulation assays in bacteria (*E. coli* and *Mtb*). I also thank instrument operators (NMR, and HRMS), non-teaching staff, and administrative staff for their timely help.

I would not miss this opportunity to express my deep gratitude to my parents and family members (Dad, Mom, Usha, Ravi and Srikant) for their support, encouragement and sacrifice in completing this piece of work. I am also grateful to Prashant and Bhumika for their continuous support and motivation during few ups and especially in several downs of my Ph.D. journey. Finally, I would like to thank everybody who was important to the successful realization of this thesis.

Abstract

During tuberculosis (TB) infection caused by *Mycobacterium tuberculosis* (*Mtb*), a sub-population of mycobacteria enter into a metabolically inactive, non-replicating persistent state that are not susceptible to most frontline TB drugs. Persisters become a reservoir with conditions favouring the emergence of drug-resistant mutants and also contribute to extended duration of TB therapy. Recent clinical trial data indicated that inclusion of Moxifloxacin (MXF) led to a shortening of TB treatment from 6-months to 4-months. Although MXF demonstrated lethality against actively replicating *Mtb*, it has limited efficacy against mycobacterial persisters. One important reason for the lack of activity of MXF against non-replicating *Mtb* is its poor accumulation within bacteria. Non-replicating *Mtb* is known to have a thick lipid-rich cell wall and being relatively hydrophilic (clogP = -0.49), the permeability of MXF may be limited.

To address this problem, we utilized a prodrug approach to enhance the efficacy of MXF by increasing its permeation in non-replicating *Mtb*. Prodrugs are normally activated by enzymes and/or related metabolic conditions within the target cells. Non-replicating *Mtb* are associated with a reductive environment (hypoxia) and induce the expression of reductive enzymes such as nitroreductases (NTRs). Since NTRs are prevalent in both replicating and non-replicating *Mtb*, we propose that a MXF prodrug can be cleaved by NTR to generate MXF and as a consequence may exhibit potent inhibitory activity against exponentially growing as well as dormant bacilli.

Herein, we designed and developed a focussed library of nitroaryl and nitroheteroaryl conjugates of MXF with varying reduction potentials to modulate the propensity to undergo reduction, rate and efficiency of drug release. A systematic screening was then conducted to identify the optimal prodrug to generate MXF under reductive conditions, in the presence of NTRs as well as in bacterial lysates. Our data revealed that the 2-nitrothiazole-based prodrug was rapidly and efficiently cleaved under both chemo- and bio-reductive conditions to produce MXF. Notably, this prodrug was equipotent in its inhibitory activity in both cellular models and animal models, and had superior inhibitory activity against non-replicating *Mtb* when compared with MXF. LC-MS based studies further supported that the increased intracellular accumulation of MXF from the prodrug as compared to MXF alone, could contribute to enhanced potency in the non-replicating *Mtb* model. Hence, the newly developed 2-nitrothiazole-prodrug is rapidly, efficiently and selectively cleaved under reductive conditions to produce the active drug. Inspired by these differences in the sensitivity and specificity of 2-

nitrothiazolyl group towards NTR, a dual colorimetric fluorescent probe sensitive to bacterial NTR was constructed. The probe exhibited high selectivity and sensitivity with an excellent ability for non-invasive real time detection of bacteria. The results outlined in this thesis lay the foundation for new prodrug approaches to developing interventions that are effective against both replicating as well as non-replicating *Mtb* and may have applications in imaging and diagnostics.

Chapter 1: Introduction

1.1. Tuberculosis

Tuberculosis is one of the world's oldest and deadliest infectious diseases caused by facultative intracellular bacterium *Mycobacterium tuberculosis* (*Mtb*). Over the past twenty centuries, many people have died from tuberculosis (TB) than from any other infectious disease.^{1,2} According to World Health Organization (WHO), in 2021, a total of 1.6 million people died from TB worldwide, making it the leading cause of mortality, surpassing COVID-19 and HIV.³ The recommended standard treatment for drug-susceptible TB has a cure rate of >95% when provided under directly observed therapy (DOT).^{4,5} The 6-month regimen consists of two phases: an initial induction phase of 2 months consisting of a combination of four front-line TB drugs (isoniazid, rifampicin, pyrazinamide, and ethambutol) followed by a 4-month continuation phase consisting of isoniazid and rifampicin. This regimen is currently used in the treatment of pulmonary TB as well as most forms of extrapulmonary TB.⁶ The duration of this drug regimen is notably longer than that of other bacterial infectious diseases. It therefore leads to poor patient adherence to therapy, which in conjunction with inadequate control and management of TB led to emergence of multidrug-resistant (MDR), extensively drug-resistant (XDR) and totally drug-resistant (TDR) TB.^{4,7-10} The prolonged cumbersome treatment for TB is partly due to the coexistence of drug-sensitive replicating and drug-tolerant non-replicating bacteria.

1.2. Persisters

During the first two months of effective intensive treatment, a distinctive biphasic kill curve for viable bacteria is observed in patient sputum samples (Figure 1.1). This suggests that there are at least two bacterial subpopulations, one of which responds to TB drugs faster than the other. The majority of the susceptible replicating bacterial subpopulation is rapidly and effectively killed by front-line TB drugs. A smaller subpopulation of slowly growing non-replicating bacteria, also known as persisters, survives for a longer time.⁷

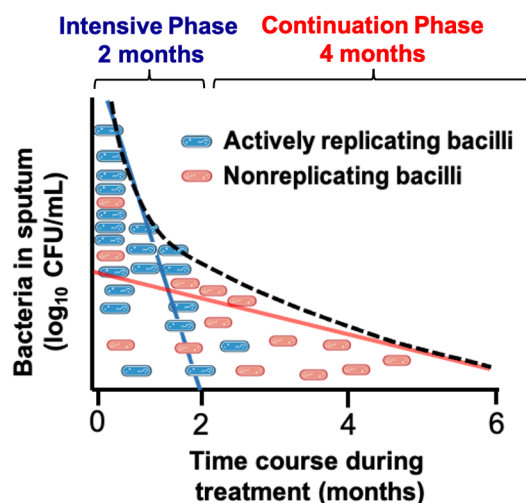


Figure 1.1. Heterogeneity in the intrinsic drug susceptibility in the bacterial subpopulations of *Mtb*. A rapid rate of decline was seen with the replicating bacilli (blue line), but the number of non-replicating bacilli declined at a slower rate (red line). Adapted from Horsburgh, C. R et al. *New Eng. J. Med.* **2015**.⁷

In 1942, Hobby observed that exposure of *Staphylococcus aureus* culture to penicillin (β -lactam antibiotic) killed only 99% of cells.¹¹ The surviving 1% bacterial subpopulation was later termed as “Persisters” by Bigger.¹² Persisters are genetically identical to the original susceptible population but are slow growing, and enter into a metabolically inactive phase, which makes them transiently resistant to antibiotics. Unlike resistant mutants, persisters, when re-established, retain their drug susceptibility as the original population. Persisters reside frequently in hostile microenvironments, such as in macrophages or granulomatous lesions.¹³ However, they have also been discovered in adipose tissues, sputum, and biofilms.^{14–19}

During the course of infection, several unfavourable conditions such as acidic pH, hypoxia, nitrosative stress, nutrient starvation, and iron deprivation encountered within the granuloma trigger the metabolic downshift of *Mtb* into a viable dormant state.^{20–24} Recent findings have shown that persisters are present in exponentially growing and stationary phase cultures.²⁵ This suggests that the formation of persister cells is driven by both stochastic and deterministic events.^{25,26} These persisters provide an evolutionary reservoir that favours the emergence of drug-resistant mutants and also contribute to the protracted regimen required for TB treatment.^{27,28} These non-replicating population can switch to active growth at any point resulting in the recalcitrance and relapse of TB infection.^{20,29} Hence, their existence often contributes to the development of latent infections which pose a significant problem for those with a weak or compromised immune system. Although the proportion of dormant and

replicating bacilli may differ, the equilibrium between them serves as a defining characteristic between latent and active infection.^{30,31} The proportion of non-replicating to replicating bacilli during latent infection is believed to be comparatively higher than during active disease.^{13,20} Recently, a comprehensive study by Colangeli et al. suggested that *Mtb* exists in a replicating state during the early latency and later transitions into a non-replicating state during prolonged latency and plays a significant role in relapse and recalcitrance of TB.³²

1.3. Characteristics of persisters

Numerous *in vitro* dormancy models, including the Loebel nutrient starvation model, Wayne hypoxic model, and the multiple stress model have elucidated the mechanisms underlying the transition of bacterium into a non-replicating persistent (NRP) state.²³ In the Wayne hypoxic model, depletion of oxygen (hypoxia) induces a shift of replicating *Mtb* tubercle to a non-replicating state through two characteristic stages: non-replicating persistence stage I and II (NRP-I and II). While microaerophilic NRP-I is achieved after oxygen levels are depleted to 1%, anaerobic NRP-II is reached when oxygen levels are less than 0.06% (Figure 1.2).³³

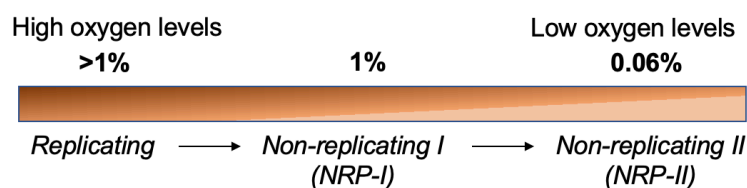


Figure 1.2. Hypoxia induced progressive transition of replicating into non-replicating persistent states in wayne model

The adaptation into a drug-tolerant NRP-II state is associated with following metabolic and morphological changes -

(a) Metabolic downshift:

High-throughput RNA sequencing (RNA-seq) studies of hypoxic *Mtb* cultures have demonstrated that lipid/energy metabolism, gluconeogenesis, protein synthesis, DNA replication and repair machinery pathways are down-regulated.³⁴ This is accompanied by an induction of the DevR/DosR dormancy regulon, a collection of about 50 genes essential for the survival of bacteria during latent infection.³⁵ Furthermore, a plethora of genes associated with metabolism of carbohydrates, amino acids, sulfur, nucleotide and peptidoglycan biosynthesis are also upregulated.^{34,36} Global phosphoproteomic profiling revealed that several proteins associated with peptidoglycan and mycolic acid synthesis are differentially

phosphorylated in the non-replicating state.^{37–39} These post-translational modifications mediate cell-wall remodelling in non-replicating *Mtb*.³⁹

(b) Morphological changes:

Non-replicating *Mtb* have also been found to undergo numerous morphological changes including altered outer surface, increased cell length, and thickened cell wall. Non-replicating *Mtb* cells are much larger than replicating cells, and possess a rough and unevenly wrinkled surface. An increase in the net negative charge on the cell surface is also observed as the cells progressed into NRP-I and NRP-II, as a result of an accumulation of negatively charged polysaccharides on the outer layer of the cell wall. Compared to rapidly dividing mid-log phase bacteria (~15.1 nm), non-replicating bacilli (NRP-I = 52.5 nm; NRP-II = 51.1 nm) exhibited increased thickening of lipid-rich cell walls, as a result of the extensive accumulation of free mycolates and lipoarabinomannans under hypoxic conditions.⁴⁰ This also contributes to the loss of acid-fastness in Ziehl-Neelsen stained lung sections of mice and human patients.⁴¹ Metabolomic and lipidomic analysis demonstrated that NRP bacteria accumulate mycolate wax esters and long-chain triacylglycerol esters along with an increase in the ratio of lipoarabinomannan to lipomannan.^{42,43} This distinct feature is a characteristic phenotype of non-replicating tubercle bacilli and contributes to hindering the penetration and accumulation of antibiotics to reach their periplasmic or intracellular targets.⁴⁴ LC-MS/MS analysis demonstrated that the intracellular accumulation of different TB drugs is affected to varying degrees in the non-replicating state. The permeability of many anti-TB drugs is significantly impaired and this account for the phenotypic drug resistance in non-replicating *Mtb*.⁴⁵

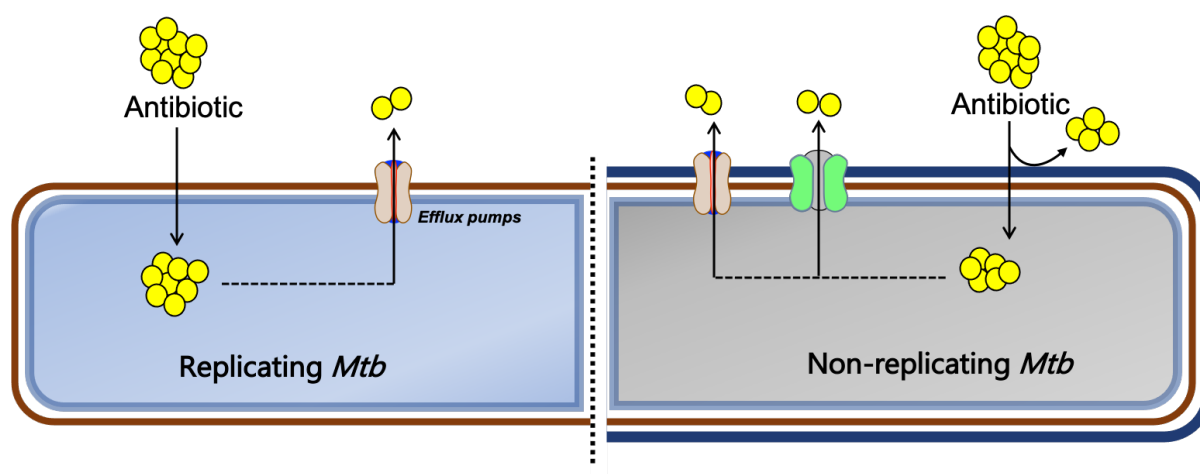


Figure 1.3. Schematic representation of distinct morphological differences observed in replicating and non-replicating *Mtb*

(c) Overexpression of nitroreductases (NTRs):

NTRs are widespread among bacteria and are well known to catalyze the reduction of nitro groups using diverse mechanisms on a broad repertoire of substrates.^{46–48} Based on the sensitivities to molecular oxygen, the bacterial NTRs can be categorized into type I and type II NTRs.⁴⁹ The type I or oxygen-insensitive NTR performs a stepwise two electron reduction of the nitro group while type II or oxygen-sensitive NTR carries out an one electron reduction of nitroaromatic moiety using a ping-pong bi-bi catalytic mechanism (Figure 1.4). In *E. coli*, oxygen-insensitive NTRs are either dependent on NADPH (major NTR; NfsA) or employ NADH and NADPH as electron donors (minor NTR; NfsB).^{48–52}

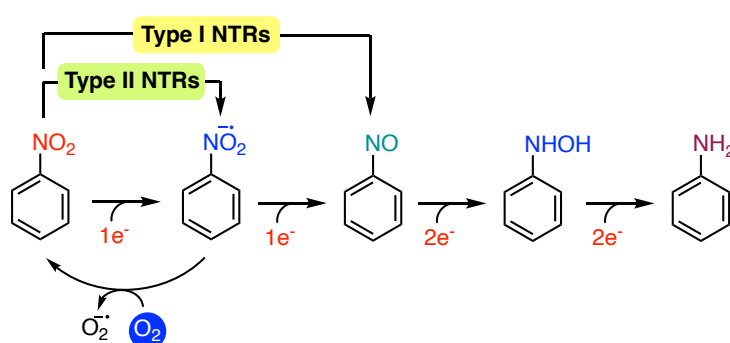


Figure 1.4. Proposed mechanisms of activation by Type I and II NTRs

Non-replicating mycobacteria reside in the hypoxic regions of granulomas. Under these conditions, non-replicating bacteria strongly induce DevR regulon-controlled genes encoding several nitroreductases (NTRs) such as Rv2032, Rv3131, and Rv3127.^{53–55} Although several NTRs have been recognised in *Mtb*, their precise role in *Mtb* pathogenesis remains unclear. These NTRs probably contribute to combat nitrosative and oxidative stress encountered by *Mtb* inside host macrophage to survive and establish infection.^{56,57}

1.4. Therapeutic strategies to eliminate persisters

The current objective of achieving effective and complete sterilisation with the recommended 6-month therapy is rather difficult due to the presence of a persister subpopulation. Although targeting persisters is a very promising therapeutic strategy, it is not straightforward as multiple genes, pathways, or mechanisms are involved. Limited efforts have been devoted to the development of innovative therapies targeting both replicating and dormant bacilli. This necessitate the requirement of multiple strategies such as (a) combination treatment with other drugs or adjuvants, (b) enhancement of host immune defence through the use of

immunomodulators, (c) the development of novel molecules to specifically target persisters, and (d) resensitization of the persisters by prodrugs using existing antibiotics.

Although the development of new molecules with novel mechanism and targets is a promising strategy, the discovery and subsequent introduction of new antibiotics into the global market is a slow, expensive and cumbersome process.^{58,59} Therefore, the clinical need for new alternative approaches that would enhance the efficacy of existing antibiotics is urgent. The prodrug approach is a highly desirable strategy for the revival of drugs associated with suboptimal pharmacokinetic properties or host toxicity, to enhance therapeutic efficacy, and to selectively target drug-resistant clinical strains of *E. coli*. Prodrugs were also found to be lethal against antibiotic-tolerant persisters enriched in stationary phase cultures and biofilms of *E. coli*.⁶⁰ Moreover, this approach has been widely employed to enhance the permeability of many hydrophilic drugs by increasing lipophilicity and allowing the targeted delivery of drugs *via* the activation of prodrug by mycobacteria-specific enzymes.⁶¹⁻⁶⁹ This strategy is promising considering the fact that many anti-tubercular drugs share the common characteristic trait of being more hydrophobic, unlike many conventional antibiotics.⁷⁰⁻⁷³

1.4.1. Antitubercular prodrugs containing nitro group

Interestingly, several antitubercular drugs containing nitro groups have potent mycobactericidal activity against replicating as well as non-replicating *Mtb*. Bicyclic nitroimidazole prodrugs, such as delamanid (earlier known as OPC-67683), pretomanid (also known as PA-824), and TBA-354, have been approved as anti-tubercular agents. These prodrugs require specific activation by *Mtb* specific deazaflavin dependent nitroreductase (Ddn or Rv3547) to release nitric oxide (NO), crucial to kill both replicating and non-replicating tubercle bacilli by respiratory poisoning (Figure 1.5).^{64,74-76}

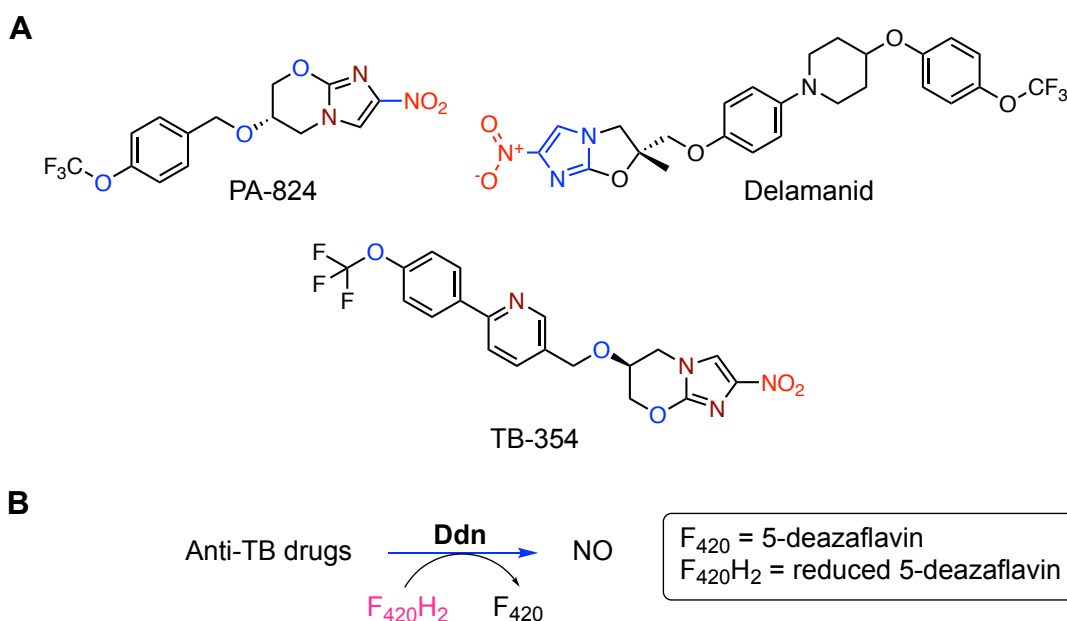


Figure 1.5. (A) Structures of bicyclic nitroimidazole anti-tubercular prodrugs and their (B) proposed mechanism of activation by deazaflavin dependent nitroreductase (Ddn)

Recently, a novel class of potent anti-TB compounds such as nitrothienopyrimidine analogue (TP-053) and nitrofuranylcalanolides (NFCs) were identified as prodrugs that require activation by a reduced form of unusual mycothiol-dependent NTR (Mrx2; also known as Rv2466c) (Figure 1.6.A).⁷⁷⁻⁷⁹ Although reductive activation by Mrx2 was central to the mechanism of action of NFC and TP053, the mycobactericidal metabolites generated from these prodrugs are entirely different. For instance, activation of TP053 by Mrx2 resulted in NO release similar to pretomanid activated by Ddn.⁷⁷ In addition, Mrx2-mediated biotransformation of TP053 resulted in the generation of a highly reactive thiol intermediate that appears to be responsible for pleiotropic effects on *Mtb* growth that inhibit lipid biosynthesis, transcription and protein synthesis.⁷⁸ In contrast, elegant studies by Negri et al. demonstrated that the mycobactericidal activity of nitrofuranyl calanolide (NFC) derivative relies on Mrx2-dependent reduction of the nitro group to an amine form using mycothiol (MSH) as a cofactor (Figure 1.6.B).⁷⁹

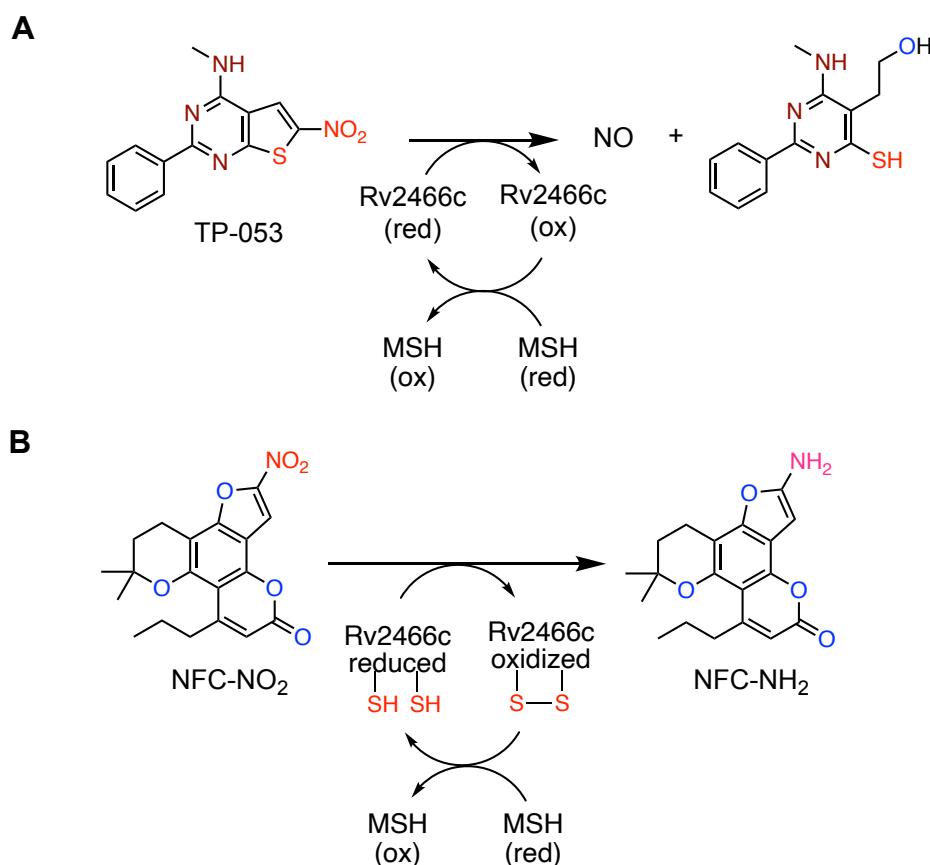


Figure 1.6. Proposed mechanism of activation of (A) nitrothienopyrimidine analogue (TP-053) and (B) nitrofuranylcalanolides (NFCs) by mycothiol dependent NTR

1.4.2. Fluoroquinolones (FQs)

Fluoroquinolone (FQ) antibiotics have been a cornerstone of antimicrobial therapy for more than three decades. These are widely prescribed class of potent, broad-spectrum bactericidal agents commonly used in the treatment of bacterial infections. Among several classes of antimicrobial agents, FQs exhibited bactericidal activity against dormant as well as growing cultures of *E. coli*.^{26,80} Considering the fact that slow or non-growing populations may be transcriptionally active, it is not surprising that FQs retained lethality against these cells by inhibiting DNA gyrases.^{81,82}

1.4.2.1. Discovery, development and use of FQs

The synthetic quinolones **1** and **2**, reported in 1949, were first prepared by oxidation of the Australian *Melicope* alkaloids (Figure 1.7).^{83–85} However, the specific antibacterial property of 3-carboxy substituted quinolones, including **3** and **4**, was publicly unveiled in the patents published by Imperial Chemical Industries (ICI) in the early 1960s (Figure 1.7).⁸⁶ Contemporaneously, during the discovery of “quinolone-core” based scaffolds, Lesher and his

colleagues at Sterling Drug stumbled upon compound **4**, serendipitously discovered as a by-product in the synthesis of antimalarial therapeutic chloroquine, which was later found to exhibit modest *in vitro* antibacterial activity.⁸⁷ ICI's intellectual property constraints certainly impelled Sterling Drug to launch the first clinically used antibiotic possessing "1,8-naphthyridone-core", Nalidixic acid with an improved activity restricted to gram-negative aerobes.⁸⁸⁻⁹⁰ Since then, several structural modifications were attempted in the basic core, which then ushered in a new era in the development of quinolones (Figure 1.8).⁹¹

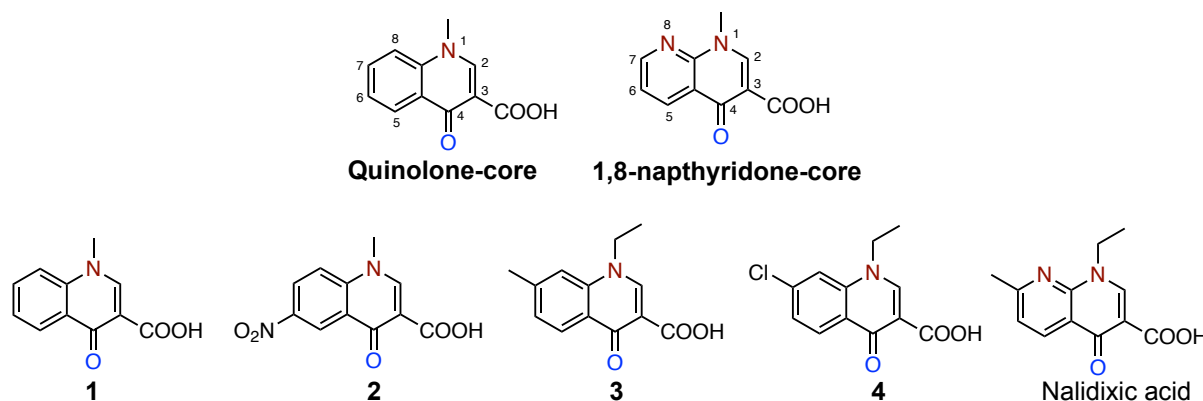


Figure 1.7. Origin of Quinolone's pharmacophore

1.4.2.1.A. First generation FQs

In 1967, Nalidixic acid (NA) was introduced into clinical practice for the treatment of complicated urinary tract infections (UTIs) caused by gram-negative enterobacteriaceae except *P. aeruginosa*. Over the next few years, compounds such as oxolinic acid, piromidic acid, and cinoxacin were developed and offered a marginal improvement in antibacterial activity relative to NA. However, due to the lack of a broad spectrum activity and poor pharmacokinetic profile, its use was still limited to the treatment of UTIs. The introduction of fluoro group at the C-6 position onto the quinolone nucleus augmented the spectrum of activity. This outstanding breakthrough led to the development of the first-generation fluoroquinolone (FQ) called Flumequine, which interestingly retained antibacterial activity against NA-resistant strains. Further structural modifications have led to the development of newer generation fluoroquinolones with improved pharmacological profile and antimicrobial properties.

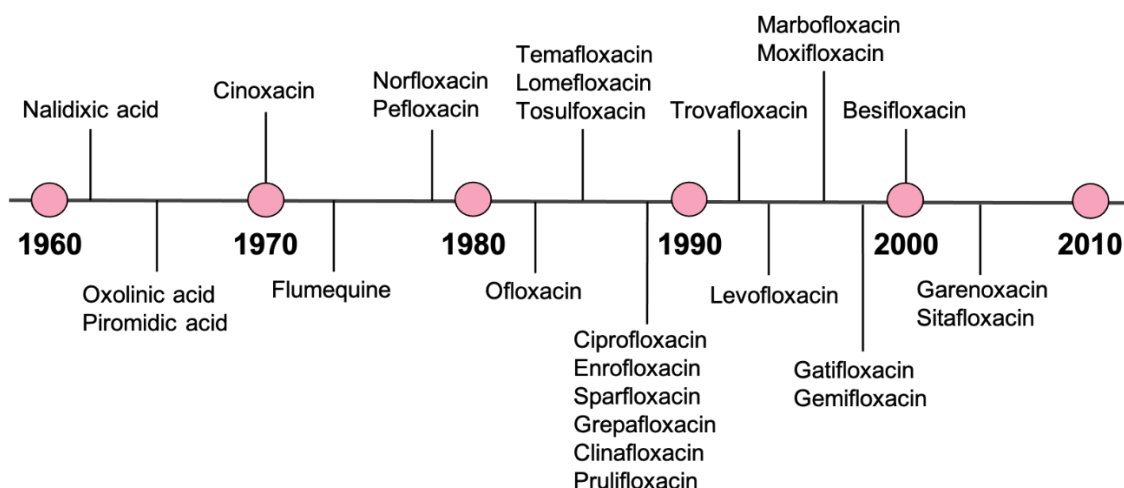


Figure 1.8. Discovery and development of FQs

1.4.2.1.B. Second generation FQs

Subsequently, both fluorination at position C-6 and substitution of piperazine/methyl-piperazine at position C-7 spawned an array of newer agents (including Norfloxacin, Ofloxacin, Pefloxacin, Lomefloxacin, Temafloxacin, Tosulfoxacin and Ciprofloxacin) acting on a wide range of gram-positive and gram-negative bacteria, mycobacteria, mycoplasma, and legionella spp. Ciprofloxacin (CIP) is one of the most successful and commonly prescribed antibiotic of this class used to treat a variety of gram-negative infections, including UTIs, prostatitis, enteric infections, biliary tract infections, sexually transmitted diseases (STDs) and gram-positive infections to a lesser extent.

1.4.2.1.C. Third generation FQs

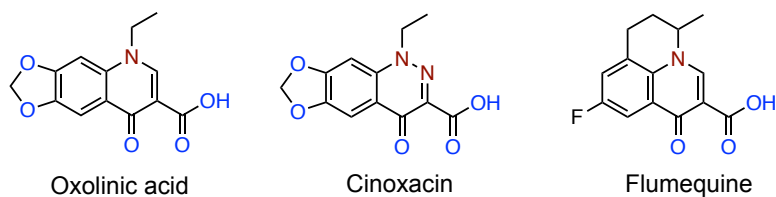
The advent of third-generation FQs epitomized by Enrofloxacin, Levofloxacin (*L*-enantiomer of Ofloxacin), Sparfloxacin, Grepafloxacin, Clinafloxacin, Marbofloxacin and Gatifloxacin has expanded the spectrum of activity to include anaerobes, *S. pneumoniae* resistant gram-positive cocci and ciprofloxacin resistant gram-negative bacilli. Despite the favourable pharmacokinetic profile and better patient tolerance, the use of these fluoroquinolones has been restricted due to major adverse effects.

1.4.2.1.D. Fourth generation FQs

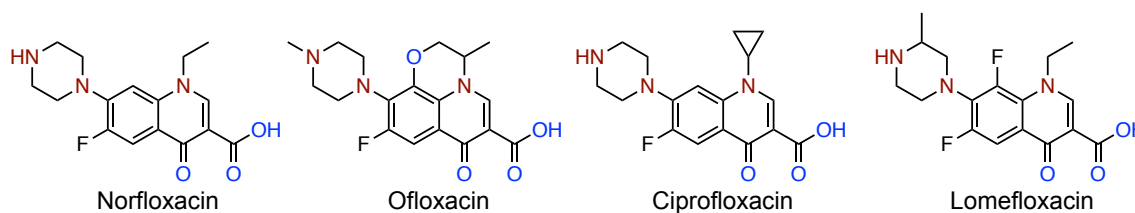
The clinical success of Ciprofloxacin (CIP) and Levofloxacin (LVX) has fuelled the emergence of next generation fluoroquinolones exemplified by Moxifloxacin (MXF), Trovafloxacin (TVX), Besifloxacin, Prulifloxacin, Garenoxacin, and Sitafoxacin. These antibiotics displayed

significantly greater bactericidal activity against anaerobes and atypical organisms than their predecessors, while retaining their broad-spectrum efficacy.

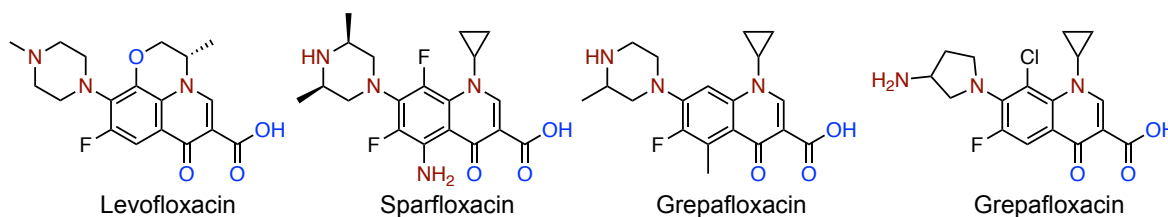
1) First-generation fluoroquinolones



2) Second-generation fluoroquinolones



3) Third-generation fluoroquinolones



4) Fourth-generation fluoroquinolones

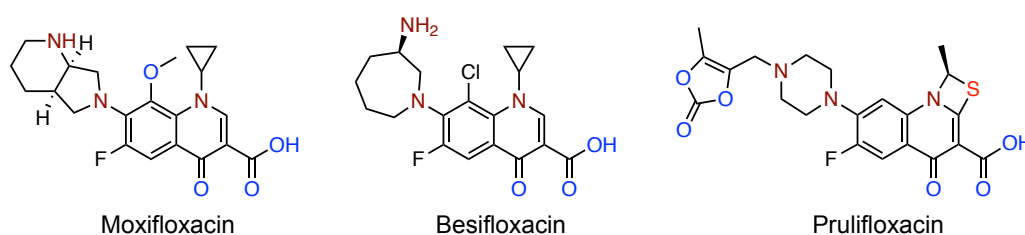


Figure 1.9. Structures of widely prescribed clinically imperative FQs

1.4.2.2. Mechanism of action

The antibiotic activity of the FQs is attributed to the inhibition of bacterial type II topoisomerase enzymes (DNA gyrase and Topo-IV), crucial for DNA replication and transcription. Although the Type II topoisomerases share a common trait of cleaving and resealing double stranded DNA, they exhibit substantial differences in topoisomerization activities.⁹² Primarily, DNA gyrase induces negative supercoiling whereas topoisomerase-IV (Topo-IV) is responsible for decatenating DNA.⁹³ The susceptibility of these targets to FQs

varies across bacterial species. For instance, DNA gyrase is the primary target in gram-negative bacteria, while Topo-IV is preferentially targeted in gram-positive organisms. The FQs reversibly binds to the complexes formed between DNA and gyrase or Topo-IV at the interface in the DNA cleavage/ligation active site resulting in the formation of quinolone-enzyme-DNA complex, which is later processed into a ternary cleavage complex. At subinhibitory concentrations of FQs, the cleavage complex reversibly inhibits DNA synthesis culminating in impaired cell growth and eventually leading to slow cell death. This is thought to be predominantly responsible for bacteriostatic effect of FQs. At lethal concentrations (minimum inhibitory concentration; MIC and minimum bactericidal concentration; MBC), FQs are bactericidal and promote rapid cell death by converting transient cleavage complexes into permanent double-stranded breaks (DSBs), thereby inducing chromosomal fragmentation and, in turn, the SOS response.^{94–97} However, if quinolone-mediated primary DNA damage is insufficient to kill cells, FQs stimulates accumulation of intracellular reactive oxygen species (ROS) such as superoxide anion (O_2^-), hydrogen peroxide (H_2O_2) and hydroxyl radical ($\dot{O}H$) by unknown mechanisms. FQ-induced ROS surge causes irreversible oxidative damage of macromolecules, and ultimately cell death.

1.4.2.3. Adverse effects

The most frequent side effects of FQs are gastrointestinal effects (including nausea, vomiting, and diarrhea) and CNS effects (such as headache and dizziness). Although FQs have been a cornerstone of antimicrobial therapy for more than three decades, serious side effects associated with long-term usage of FQs have prompted the Food and Drug Administration (FDA) to issue black box warnings and restrict the use to “drugs of last resort” for complicated life threatening infections. In fact, many FDA approved FQs (temafloxacin, sparfloxacin, grepafloxacin and trovafloxacin) were swiftly withdrawn from the market soon after clinical introduction owing to rare, devastating and irreversible adverse effects, often referred to as “floxing” or “being floxed” by patients. FQs have been found to prolong QT interval by blocking voltage gated hERG K^+ channels, ultimately resulting in Torsades de Pointes, a potentially fatal polymorphic ventricular tachyarrhythmia. A study based on the analysis of FAERS database also reported that many patients treated with FQs were plagued with chondrotoxicity and tendinopathies.⁹⁸ Badal and co-workers laid the molecular basis for these unusual obscure side effects and suggested that the strong iron chelating property of FQs presumably accounts for the inhibition of Fe^{+2} dependent 2-ketoglutarate (KG) dioxygenases,

a class of enzymes crucial in collagen biosynthesis and maturation.⁹⁹ Therapy with FQs was also accompanied by a greater risk of acute kidney and liver injury.

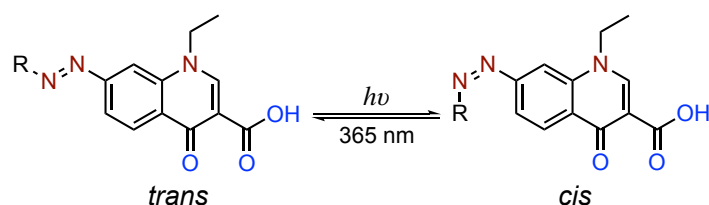
Despite significant toxicity concerns, the rampant overuse of FQs dramatically escalated the consumption of these broad-spectrum antibiotics that has been linked to affect the host health by perturbing the composition and functional diversity of the human microbiome, particularly in terms of emergence of resistance.^{100,101} Numerous studies have illuminated that the administration of FQs eventuated in selective depletion of oral and intestinal microflora,^{102–105} insurgence of FQ-resistant strains and accumulation of antibiotic-resistant genes (ARGs) in the gut microbiota.^{106–109} To mitigate FQ induced host toxicity and reduce their tremendous impact on host microbial symbiosis, prodrug strategies have been considered to minimize the unintended systemic exposure of antibiotics to host cells and deliver them in a spatiotemporal manner for selective targeting of the bacterial pathogen at an infection site.

1.4.2.4. Fluoroquinolone prodrugs

Due to the presence of distinct functional groups (secondary amine and carboxylic acid) in FQs, several research groups have employed post-hoc approach to utilize these groups as a synthetic handle for the design of carbamate and ester based prodrugs triggered by light, thiol and enzymatic stimuli.

1.4.2.4.A. Light activated FQ prodrugs

Feringa and co-workers did ground-breaking work in the development of photoresponsive antibiotics by incorporating photochromic molecular switches into the quinolone core to control the antibacterial activity with light. The piperazinyl moiety at the C-7 position of the parent antibiotic was swapped for an aryldiazo photoswitchable group, which upon irradiation with UV-light undergoes *trans-to-cis* isomerization resulting in the selective photoactivation of the modified quinolone (Scheme 1.1). Over time, slow reconversion to the thermodynamically stable inactive *trans* isomer led to the auto-inactivation of the compound, thereby avoiding the emergence of bacterial resistance to antibiotics by limiting their accumulation in the environment.¹¹⁰



Scheme 1.1. UV-light mediated selective photoactivation

The authors later expanded this work by conjugating the secondary amine of ciprofloxacin (CIP) with an azobenzene or a spiropyran molecular switch that render the caged compounds with photoswitchable antibiotic activity (Figure 1.10).¹¹¹

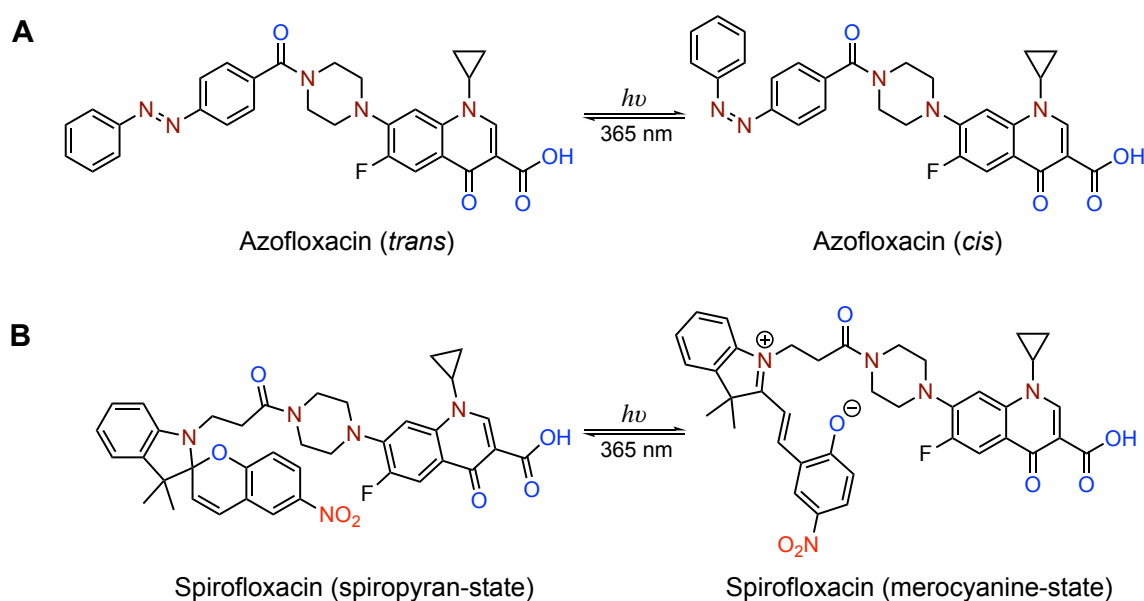


Figure 1.10. UV light triggered uncaging of CIP

However, to minimize the influence of covalently linked molecular switches on the drug's PK/PD profile, the same group relied on another noteworthy approach of caging the FQ with a photocleavable motif. Light triggered orthogonal release of FQ in its active form from the photolyzable ester (FQNC), which paved the way for the development of a unique methodology to selectively target a single bacterial strain in the complex populations (Figure 1.11).¹¹²

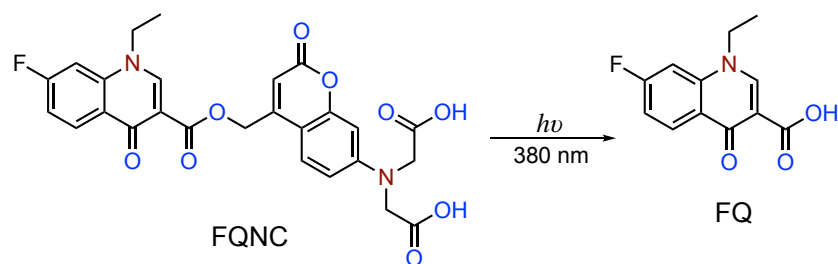


Figure 1.11. UV light triggered release of FQ from photolizable ester

Forsythe and colleagues examined the on-demand release of ciprofloxacin from a click cross-linked hydrogel triggered by UV light.¹¹³ The LPS-targeted dendrimer nanoconjugate was used to further extend the light controlled specific delivery of caged FQ to gram-negative bacteria.¹¹⁴ Similarly, Pang and co-workers reported that the controllable release of levofloxacin (LVX) from a photocleavable polyprodrug-loaded wound dressing resulted in UV light responsive antibacterial activity.¹¹⁵ Due to the potential photodamaging ability and limited tissue penetration depth, to date, the therapeutic application of UV light is extremely restricted. More recently, Chakrapani and co-workers addressed these undesirable shortcomings and showcased the visible light mediated tunable release of LVX from BDP-LVX (Figure 1.12).¹¹⁶

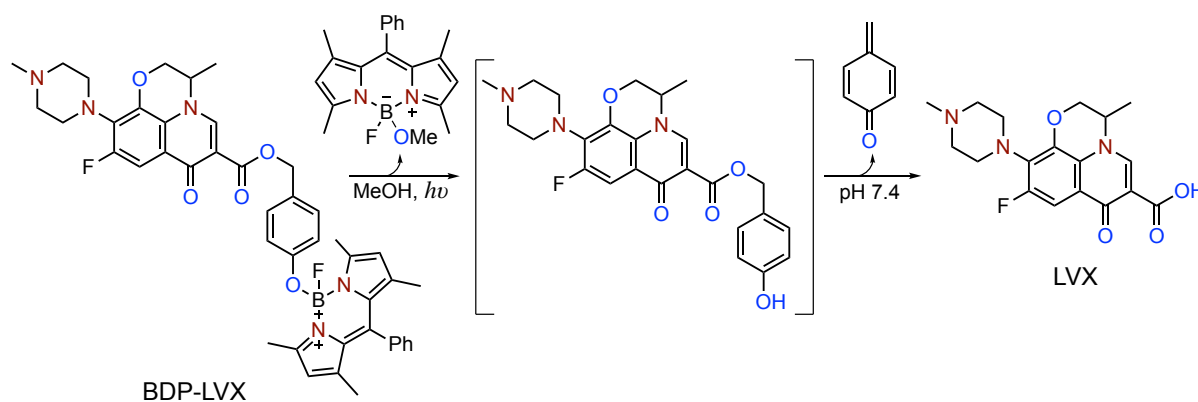


Figure 1.12. Visible light mediated release of LVX

Although the aforementioned prodrugs had excellent spatiotemporal precision, the use of phototriggered antibiotic poses major concerns, including light delivery at the site of irradiation, photodruggability, lack of selectivity of bacterial over mammalian cells and subdued activity compared to parent antibiotic.

1.4.2.4.B. Thiol activated FQ prodrugs

A different approach was proposed by Reddy and colleagues, who first demonstrated the directed controlled delivery of levofloxacin (LVX) to the infection site following glutathione (GSH) mediated disulphide bond cleavage of LSSTr prodrug (Figure 1.13).¹¹⁷ Recently, Nolan and co-workers employed a self-immolative disulphide linker for a siderophore-FQ conjugate and showed that the GSH mediated reductive cleavage of the disulphide bond facilitated the release of unmodified FQ, which afforded antibacterial activity against a few strains of *E.coli* (Figure 1.14).¹¹⁸ However, the selectivity of these prodrugs toward bacteria remains a major concern due to the ubiquitous nature of thiols.

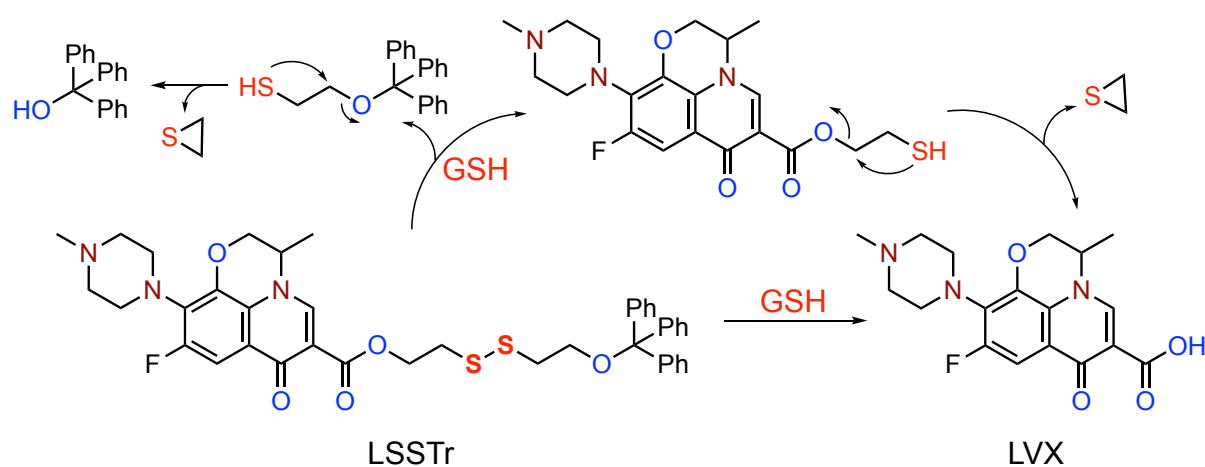


Figure 1.13. Glutathione (GSH) mediated release of LVX from prodrug

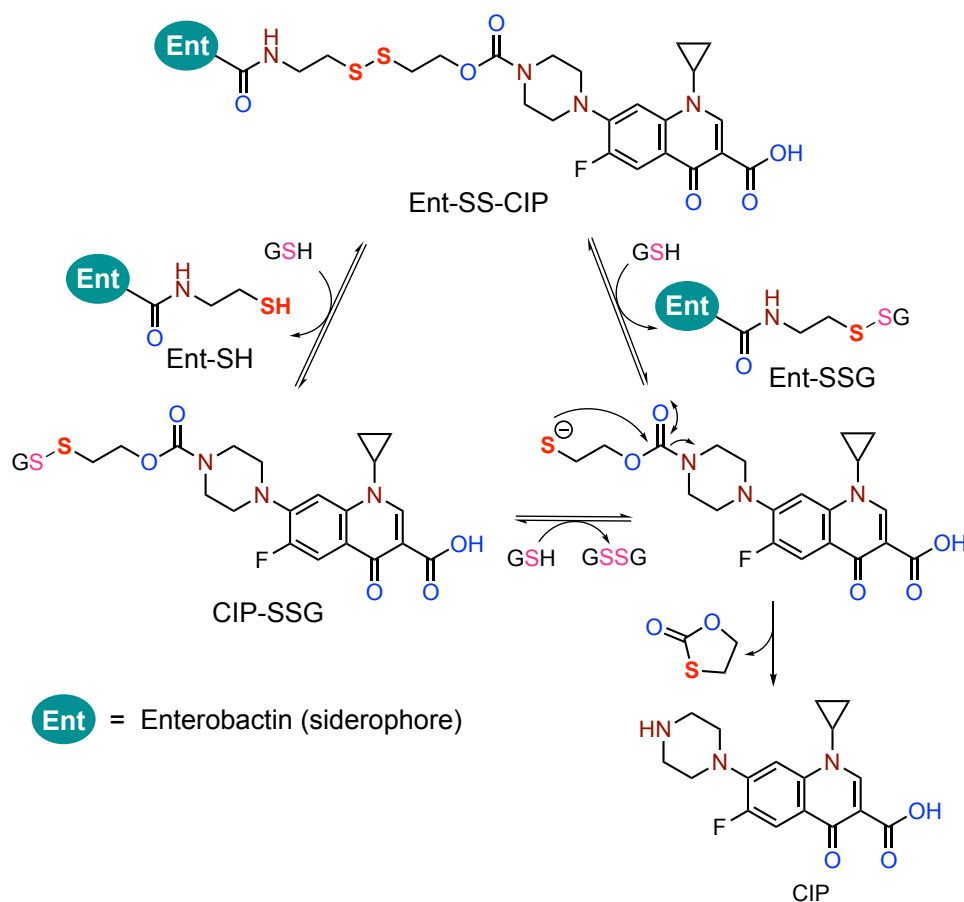


Figure 1.14. Glutathione (GSH) mediated reductive cleavage of siderophore-FQ conjugate

1.4.2.4.C. Enzyme activated FQ prodrugs

The selective enzyme mediated metabolic biotransformation of prodrug is one of the most promising strategies that provides an edge over the rest in the controlled and targeted delivery of antibiotics. Clinically, Prulifloxacin was developed as a new FQ lipophilic prodrug for the treatment of acute lower UTIs, bacterial prostatitis and chronic bronchitis. After absorption, human paraoxonase (hPON1) extensively hydrolyzes prulifloxacin to ulifloxacin, an active FQ (Figure 1.15.A).^{119,120} Baker and co-workers demonstrated the release of an active antibiotic (PA2789) from a water-soluble FQ prodrug, PA2808 by taking advantage of alkaline phosphatase (ALP), an enzyme known to be elevated in the lungs of patients with cystic fibrosis (Figure 1.15.B).¹²¹ Similarly, bisphosphonated FQ esters were designed as osteotropic prodrugs to enhance FQ delivery to bone in the treatment of osteomyelitis.¹²² Another enzyme based prodrug strategy focused on the localized delivery of parent antibiotic (CIP or MXF) from glucuronide prodrugs mediated by an engineered implantable biomaterial to effectively tackle biofilm formation in bacteria (Figure 1.15.C).¹²³

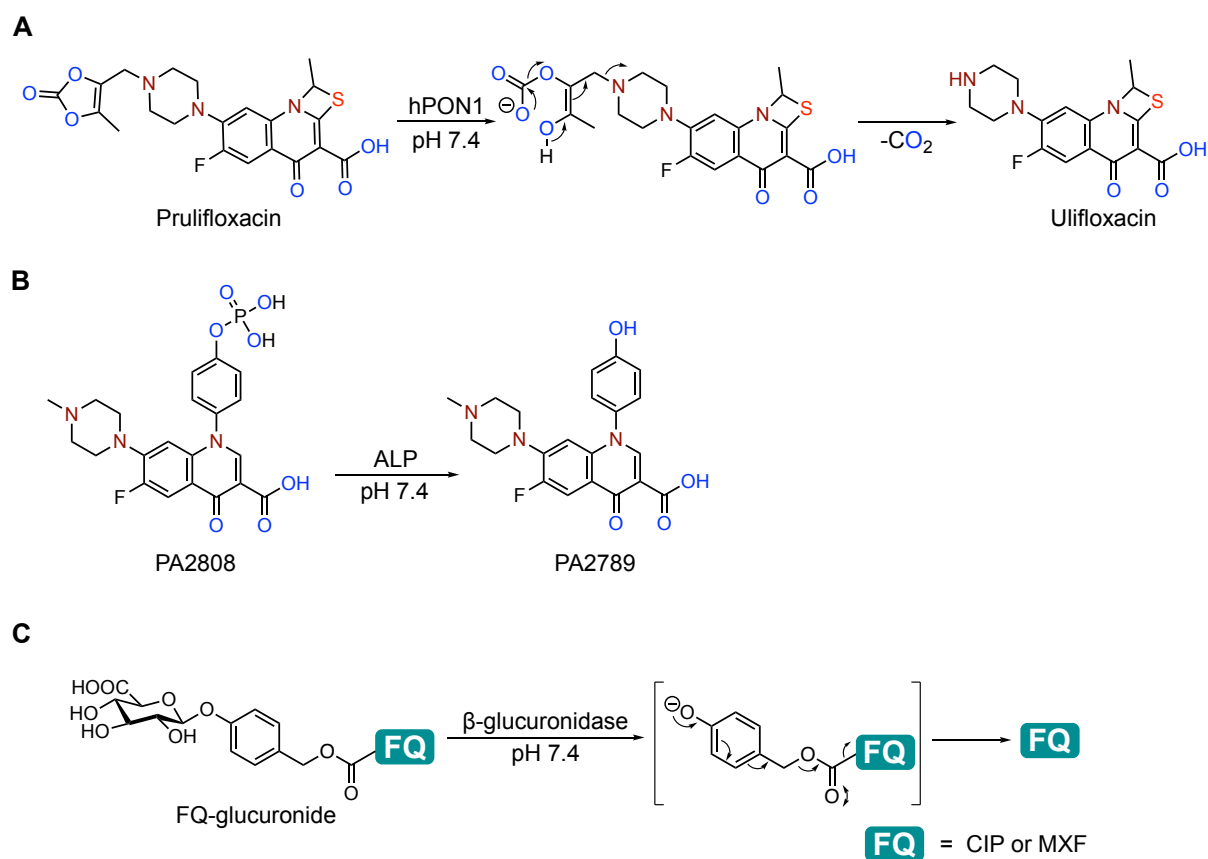


Figure 1.15. FQ prodrugs activated by enzymes such as (A) human paraoxonase (hPON1), (B) alkaline phosphatase (ALP) and (C) β -glucuronidase

Miller and co-workers reported several *N*-acylated CIP derivatives based on quinone-trimethyl lock, which were activated by bioreductive enzymes to release CIP (Figure 1.16).¹²⁴ The conjugate may exhibit dual action mechanism by serving as a covalent enzyme inhibitor. Despite notable success in localized delivery of FQ, these prodrugs suffered from lack of selectivity toward bacterial over mammalian cells owing to the wide distribution of the aforesaid enzymes.

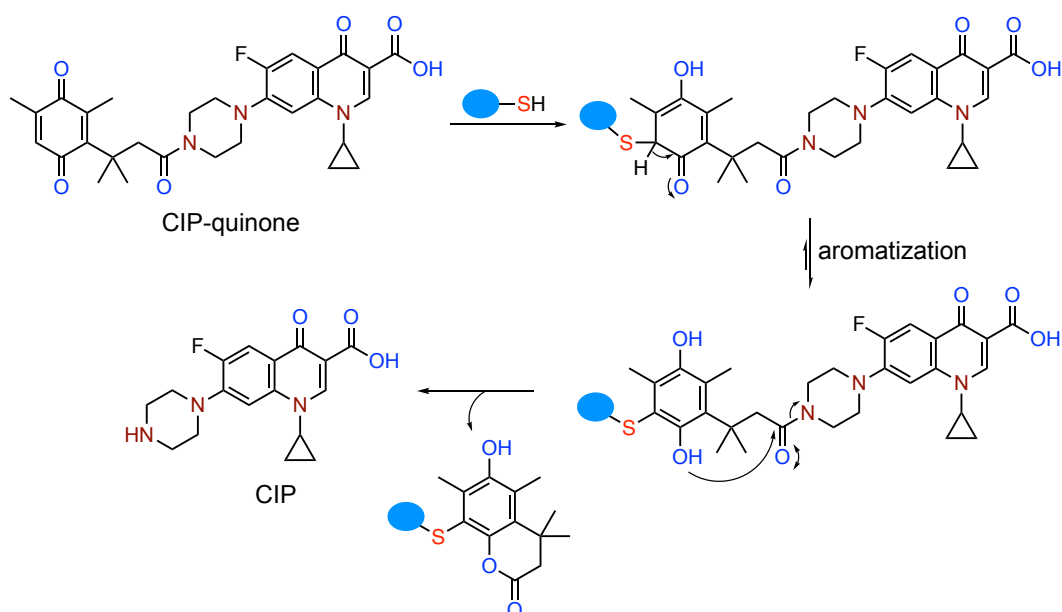


Figure 1.16. Proposed mechanism of release of CIP from dual-action FQ prodrug

Recently, Nolan and co-workers presented an elegant strategy to enhance the specific uptake of prodrugs into pathogenic bacteria by using a Ent-CIP siderophore conjugate. The prodrug was selectively transported into the cytoplasm by Ent uptake machinery and subsequent intracellular hydrolysis catalyzed by the salmochelin esterase IroD conferred targeted antibacterial activity against uropathogenic strains of *E. coli*.¹²⁵ In another pioneering work, Albrecht and co-workers recognised the utility of β -lactamase activated FQ prodrugs by leveraging the established use of cephalosporins as highly versatile substrates for β -lactamase (Figure 1.17.A).^{126–129} Evans and co-workers have pursued an analogous approach using a cephalosporin-ciprofloxacin prodrug, to exploit antibiotic resistance by delivering ciprofloxacin selectively to β -lactamase expressing uropathogenic strains of *E. coli* (Figure 1.17.B).¹³⁰

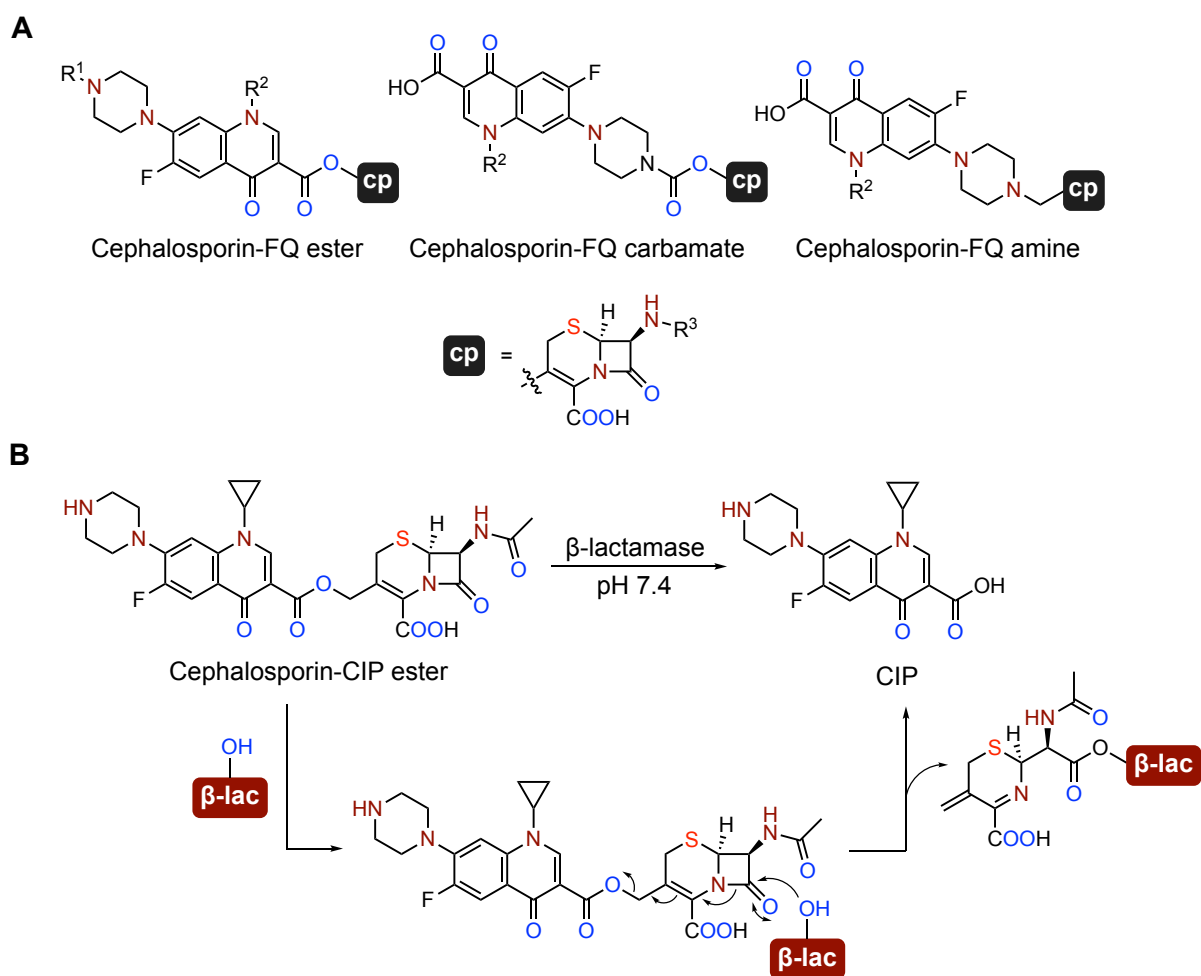


Figure 1.17. (A) β -lactamase activated ester, carbamate and amine based FQ prodrugs. (B) Proposed mechanism of activation of cephalosporin-CIP prodrug by β -lactamase

Although many fluoroquinolone prodrugs have been reported, but majority of them were not evaluated against *Mtb*. More recently, Chakrapani and co-workers has reported ciprofloxacin-fluorophore conjugate, NTR-Umb-CIP that was unmasked by *E. coli* NTR to deliver FQ along with concomitant release of fluorescence reporter (Figure 1.18). The conjugate exhibited significant, albeit subdued bactericidal effect against many bacterial strains, compared to CIP, likely as a result of marked differences in metabolism of nitroaromatic substrate and varied bacterial cell permeability.¹³¹ Unfortunately, this conjugate was found to be ineffective against *Mtb*.

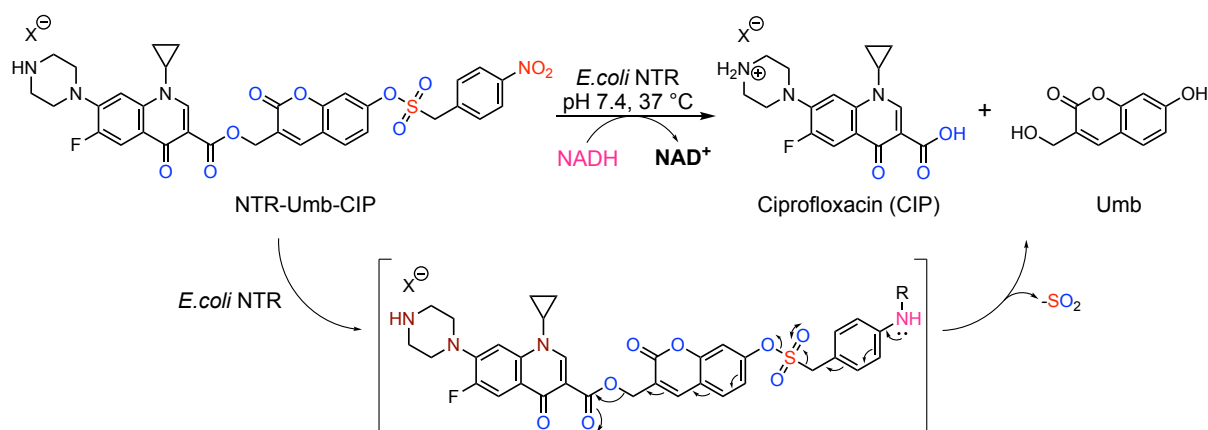


Figure 1.18. Nitroreductase catalyzed activation of prodrug to generate CIP and fluorescence reporter

Constantino and colleagues employed lipophilic prodrug approach to deliver FQs from medium to long-chain alkyl ester prodrugs upon hydrolysis by *Mtb* specific esterases (Figure 1.19). Despite being less potent than parent FQs, the prodrugs nonetheless showed antimycobacterial activity, albeit to a lesser extent against drug-susceptible as well as drug-resistant strains. This could be partly explained by the presence of a different mode of action, a lack of selectivity, or inherent resistance to hydrolysis.¹³²

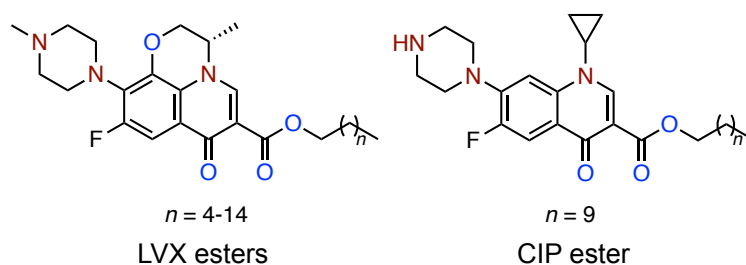


Figure 1.19. Lipophilic ester prodrugs of FQs

1.5. Fluoroquinolones in TB

Preclinical and clinical studies have shown that fluoroquinolones showcased excellent activity against *Mtb*. Many of them offer a favourable microbiological, pharmacokinetic and pharmacological profile with a well-tolerated safety profile. FQs such as Ciprofloxacin (CIP), Levofloxacin (LVX) and Moxifloxacin (MXF) are commonly used to combat TB. These are classified as Group A drugs by the WHO and are recommended in first-line therapy for multidrug-resistant tuberculosis (MDR-TB), to restrict the further development of XDR-TB and in patients unable to tolerate the standard HRZE regimen (WHO 2016).^{133,134}

1.5.1. Moxifloxacin (MXF) in TB

Fluoroquinolones have been extensively tested against TB, and the results have shown significant differences in their efficacy against *Mtb*. For example, Ciprofloxacin (CIP) is only moderately active and is no longer recommended in clinical settings. It has been substituted by newer-generation FQs such as ofloxacin (OFX) and levofloxacin (LVX). Currently, these two drugs have been found to be less effective and are replaced by fourth-generation FQs such as gatifloxacin (GFX) and moxifloxacin (MXF).^{135–138}

Moxifloxacin (MXF), patented by Bayer A. G. in 1991, is a fluorinated fourth-generation broad-spectrum quinolone antibiotic with C-7 azabicyclo and 8-methoxy substituents (Figure 1.20).

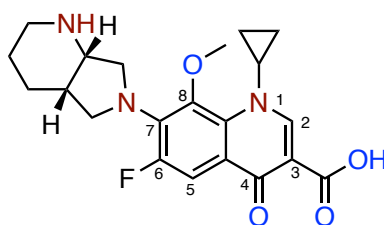


Figure 1.20. Structure of moxifloxacin (MXF)

As a result of the structural innovations, MXF showed an impressive clinical and bacteriological outcomes for patients with TB. Besides, MXF has following distinct pharmacological features that makes it a special candidate among other FQs.

- (a) **Efficacy against drug-susceptible *Mtb*:** Linderman and co-workers used a systems pharmacology approach to compare the efficacy of three fluoroquinolones in TB granuloma and concluded that MXF has a potential clinical significant advantage over LVX and GFX in terms of total bacterial load, early bactericidal activity (EBA) efficacy.^{139,140} This in turn translated into superiority of MXF over other FQs in reducing bacterial burden in both mice and rabbit models.^{141,142}
- (b) **Enhanced DNA gyrase inhibitory activity:** Comparative structural and *in vitro* biochemical analyses indicated that MXF fostered the highest level of antibiotic-induced cleaved-complex formation and inhibition of *Mtb* gyrase-mediated supercoiling over other FQs. Furthermore, this correlates more closely with the superior *in vitro* and *in vivo* efficacy of MXF.^{143,144}
- (c) **Emergence of resistance:** The bulkiness at the C-7 substituent in MXF may contribute to the reduction of active drug efflux by *Mtb* and thus lowered the risk of the development of

bacterial resistance mediated by efflux mechanisms as compared to the earlier generation FQs.¹⁴⁵ A population-based survey showed that resistance to MXF was much lower in many countries.¹⁴⁶ A multitude of *in vitro* studies further showcased that FQs harbouring 8-methoxy substituent, such as MXF, displayed lower MPC (mutant prevention concentration is the concentration that prevents the emergence of mutants from the drug-susceptible population) than the earlier FQs.^{147,148}

- (d) **Drug interactions:** The FQ-theophylline drug interaction is primarily controlled by the C-7 substituent primarily and to a lesser extent by the C-8 substituent. Due to the presence of a bulky C-7 moiety and a C-8 methoxy substituent, MXF does not interact pharmacokinetically with xanthine derivatives, including theophylline that is metabolized by CYP1A2. In contrast to older FQs, no clinically significant drug interactions with probenecid, digoxin, and warfarin have been reported yet.^{149,150}
- (e) **PK/PD profile:** Since FQs have concentration dependent bactericidal activity, AUC_{tot}/MPC (total area under the curve/mutant prevention concentration) is often used as a practical predictor of their clinical and microbiological efficacy. Despite substantial inter-patient pharmacokinetic and pathogen-specific variability, several studies have reflected that a higher AUC_{tot}/MPC of MXF resulted in the superior pharmacokinetic and pharmacodynamic properties that encouraged its extensive use as a promising surrogate for older FQs against *Mtb*.^{151–155} Furthermore, the structural modifications extended the elimination half-life and permitted once-daily dosing as compared to its predecessors.¹⁵⁶
- (f) **Safety profile:** The overall incidence of phototoxicity, hepatotoxicity and CNS adverse effects were infrequent than with other FQs. Moreover, the risk of tendon rupture, a class effect of FQ, was rare with MXF, even in elderly patients with chronic obstructive pulmonary disease (COPD).¹⁵⁷
- (g) **Shortening of TB treatment:** The effective sterilizing activity of MXF in preclinical and clinical studies raised the hope about its potential to shorten the duration of therapy when given in combination with standard frontline anti-TB agents. Numerous clinical trials were performed to evaluate the effectiveness of MXF-containing regimens in the treatment of drug-susceptible TB. Recent clinical trial on MXF (RPT-MOXTB, 2020) have led to a shortening of TB treatment to 4-months from standard 6-months (Figure 1.21).^{134,158,159}

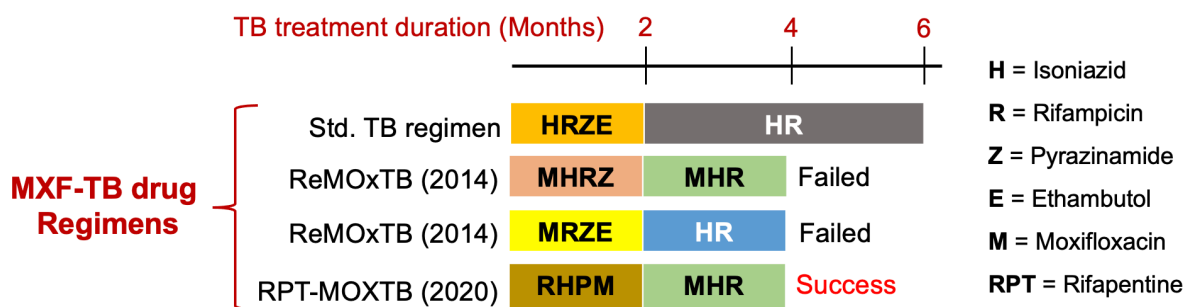


Figure 1.21. MXF containing TB-drug regimens

1.5.2. Reduced efficacy of MXF in *Mtb* persisters

The elevated rate of successful clinical outcomes in MXF-containing regimens could be explained in part by its favourable intralesional partitioning and superior efficacy in reducing *Mtb* burden in cellular and necrotic lesions in a rabbit model.^{160,161} Although MXF demonstrated effective sterilization activity ($\text{casMBC}_{90} = 2 \mu\text{M}$), it displayed heterogeneous partitioning across the granuloma, with moderate to poor diffusion into the lipid-rich areas of caseous necrotic regions in the lungs of TB patients.^{140,160–163} Several confounding factors such as poor vascularization, decreased oxygen levels, and high hydrophilicity of MXF ($\text{clogP} = -0.49$) might contribute to the differential spatial distribution and accumulation of MXF in necrotic lesions. The requirement that MXF permeate *Mtb* infected macrophages complicates the matters further. Following the penetration and accumulation in bacilli, MXF must finally reach to its molecular target to exhibit antimycobacterial activity.¹⁶⁴

Mass spectrometric studies revealed that the intracellular accumulation of many fluoroquinolones, including MXF is impaired to a significant extent in nutrient starved non-replicating *Mtb*. This probably contributes to the marked reduction in bactericidal efficacy of MXF by more than 100-fold in non-replicating bacteria compared to replicating *Mtb*.⁴⁵ Similarly, MXF was found to be less effective against hypoxic non-replicating *Mtb*.¹⁴⁸ As mentioned earlier, the presence of thickened cell envelope makes the non-replicating bacilli even more impermeable than replicating *Mtb* contributing to the reduced uptake of MXF in quiescent populations.

To increase the efficacy of MXF against non-replicating bacilli while retaining its activity against replicating bacilli, lipophilic prodrugs activated by mycobacteria specific enzymes such as NTRs can be a potential approach.

1.6. Motivation and outline of the thesis

The presence of a lipid rich thickened cell wall in non-replicating *Mtb* imposes a formidable barrier that reduce the uptake of many hydrophilic antibiotics, including MXF (clogP = -0.49). This is one of the important reason for the lack of activity of MXF against persisters.

To address this problem, we explored the possibility of utilizing a prodrug approach to enhance the efficacy of MXF by increasing its permeability in non-replicating *Mtb*. Since bacterial NTRs are prevalent in both replicating and non-replicating *Mtb*, we propose that a MXF prodrug may be cleaved by NTR to generate MXF. Hence, these prodrugs should retain their potency against both exponentially growing cells and persisters of *Mtb* (Figure 1.22). Additionally, the prodrug should have the following characteristics:

- Entry inside mycobacteria;
- Rapid and efficient cleavage to release MXF;
- Bacterial selective;
- Equipotent like MXF against replicating *Mtb*;
- Enhanced lethality in non-replicating *Mtb*.

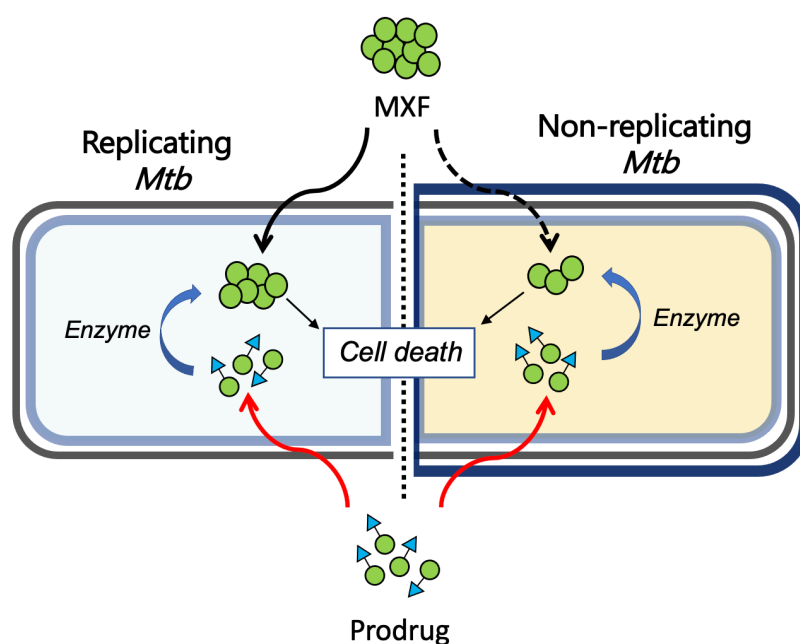


Figure 1.22. Proposed prodrug strategy to enhance accumulation and efficacy of MXF in non-replicating *Mtb*

Non-replicating *Mtb* are associated with a reductive environment (hypoxia) and induce the expression of reductive enzymes such as nitroreductases (NTRs). In **Chapter 2**, we designed

and developed a focussed library of nitroaryl and nitroheteroaryl conjugates of MXF. Two principles were used in the enzyme-prodrug design: first, to use NTR as an enzyme to activate a prodrug to produce MXF with both rate and efficiency serving as optimization criteria; and second, to increase lipophilicity of the ensuing prodrug in order to improve permeability.

In **Chapter 3**, a detailed computational and biochemical analysis was conducted to understand the reactivity of substrates toward *E.coli* NTR and identify an optimal substrate. The ability of prodrugs to generate MXF in a variety of bacterial lysates and their stability in mammalian lysates were also tested. Among the tested prodrugs, 2-nitrothiazole-based prodrug was found to undergo rapid and efficient cleavage under both chemo- and bio-reductive conditions to release MXF.

In **Chapter 4**, the prodrugs were evaluated for antimycobacterial activity against replicating and non-replicating *Mtb*. Again, 2-nitrothiazole MXF prodrug demonstrated equipotent antimycobacterial activity against replicating *Mtb* and superior inhibitory activity against non-replicating *Mtb* compared to MXF. LC-MS/MS analysis was conducted to correlate the enhanced efficacy of the prodrug with the intracellular accumulation of MXF in non-replicating *Mtb*.

The prodrug strategy was further exploited to enhance the antibacterial activity of another fluoroquinolone antibiotic, ciprofloxacin (CIP) in **Chapter 5.1**. Since detection of *Mtb* is challenging and in order to work towards rapid and real detection of *Mtb*, we next proposed to utilize the newly identified NTR sensitive 2-nitrothiazole moiety to develop NTR responsive dual colorimetric fluorescence “turn OFF-ON” NIR probe in **Chapter 5.2**.

1.7. References

- (1) Daniel, T. M. The History of Tuberculosis. *Respir. Med.* **2006**, *100* (11), 1862–1870.
- (2) Barberis, I.; Bragazzi, N. L.; Galluzzo, L.; Martini, M. The History of Tuberculosis: From the First Historical Records to the Isolation of Koch's Bacillus. *J. Prev. Med. Hyg.* **2017**, *58* (1), E9-E12.
- (3) World Health Organization. *Global Tuberculosis Report 2021*; WHO: Geneva, **2021**, 1–27.
- (4) Zumla, A.; Nahid, P.; Cole, S. T. Advances in the Development of New Tuberculosis Drugs and Treatment Regimens. *Nat. Rev. Drug Discov.* **2013**, *12*, 388–404.
- (5) Hopewell, P. C.; Pai, M.; Maher, D.; Uplekar, M.; Raviglione, M. C. International standards for tuberculosis care. *Lancet Infect. Dis.* **2006**, *6* (11), 710-25.
- (6) Tiemersma, E. W.; van der Werf, M. J.; Borgdorff, M. W.; Williams, B. G.; Nagelkerke, N. J. D. Natural History of Tuberculosis: Duration and Fatality of Untreated Pulmonary Tuberculosis in HIV Negative Patients: A Systematic Review. *PLoS One.* **2011**, *6* (4), e17601
- (7) Horsburgh, C. R.; Barry, C. E.; Lange, C. Treatment of Tuberculosis. *New Eng. J. Med.* **2015**, *373* (22), 2149–2160.
- (8) Gandhi, N. R.; Moll, A.; Sturm, W.; Pawinski, R.; Govender, T.; Lalloo, U.; Zeller, K.; Andrews, J.; Friedland, G. Extensively Drug-Resistant Tuberculosis as a Cause of Death in Patients Co-Infected with Tuberculosis and HIV in a Rural Area of South Africa. *Lancet*, **2006**, *368* (9547), 1575-80.
- (9) Dooley, K. E.; Mitnick, C. D.; DeGroote, M. A.; Obuku, E.; Belitsky, V.; Hamilton, C. D.; Makhene, M.; Shah, S.; Brust, J. C. M.; Durakovic, N.; Nuermberger, E. Old Drugs, New Purpose: Retooling Existing Drugs for Optimized Treatment of Resistant Tuberculosis. *Clin. Infect. Dis.* **2012**, *55* (4), 572-81.
- (10) Udhwadia, Z. F.; Amale, R. A.; Ajbani, K. K.; Rodrigues, C. Totally Drug-Resistant Tuberculosis in India. *Clin. Infect. Dis.* **2012**, *54* (4), 579-81
- (11) Hobby, G. L.; Meyer, K.; Chaffee, E. 3773 Observations on the Mechanism of Action of Penicillin. *Proc. Soc. Exp. Biol. Med.* **1942**, *50* (2), 281-285.

-
- (12) Bigger J. Treatment of Staphylococcal Infections with Penicillin by Intermittent Sterilisation. *The Lancet* **1944**, *244*, 497–500.
- (13) Mandal, S.; Njikan, S.; Kumar, A.; Early, J. v.; Parish, T. The Relevance of Persisters in Tuberculosis Drug Discovery. *Microbiology (United Kingdom)*. **2019**, *165* (5), 492–499.
- (14) Conlon, B. P.; Nakayasu, E. S.; Fleck, L. E.; Lafleur, M. D.; Isabella, V. M.; Coleman, K.; Leonard, S. N.; Smith, R. D.; Adkins, J. N.; Lewis, K. Activated ClpP Kills Persisters and Eradicates a Chronic Biofilm Infection. *Nature* **2013**, *503* (7476), 365–370.
- (15) Garton, N. J.; Waddell, S. J.; Sherratt, A. L.; Lee, S. M.; Smith, R. J.; Senner, C.; Hinds, J.; Rajakumar, K.; Adegbola, R. A.; Besra, G. S.; Butcher, P. D.; Barer, M. R. Cytological and Transcript Analyses Reveal Fat and Lazy Persister-like Bacilli in Tuberculous Sputum. *PLoS Med.* **2008**, *5* (4), 0634–0645.
- (16) Dhillon, J.; Fourie, P. B.; Mitchison, D. A. Persister Populations of Mycobacterium Tuberculosis in Sputum That Grow in Liquid but Not on Solid Culture Media. *J. Antimicrob. Chemother.* **2014**, *69* (2), 437–440.
- (17) Neyrolles, O.; Hernández-Pando, R.; Pietri-Rouxel, F.; Fornès, P.; Tailleux, L.; Payán, J. A. B.; Pivert, E.; Bordat, Y.; Aguilar, D.; Prévost, M. C.; Petit, C.; Gicquel, B. Is Adipose Tissue a Place for Mycobacterium Tuberculosis Persistence? *PLoS One*. **2006**, *1* (1), e43.
- (18) Agarwal, P.; Khan, S. R.; Verma, S. C.; Beg, M.; Singh, K.; Mitra, K.; Gaikwad, A. N.; Akhtar, M. S.; Krishnan, M. Y. Mycobacterium Tuberculosis Persistence in Various Adipose Depots of Infected Mice and the Effect of Anti-Tubercular Therapy. *Microbes Infect.* **2014**, *16* (7), 571–580.
- (19) Agarwal, P.; Pandey, P.; Sarkar, J.; Krishnan, M. Y. Mycobacterium Tuberculosis Can Gain Access to Adipose Depots of Mice Infected via the Intra-Nasal Route and to Lungs of Mice with an Infected Subcutaneous Fat Implant. *Microb. Pathog.* **2016**, *93*, 32–37.
- (20) Zhang, Y.; Yew, W. W.; Barer, M. R. Targeting Persisters for Tuberculosis Control. *Antimicrob. Agents Chemother.* **2012**, *56* (5), 2223–30.

-
- (21) Gomez, J. E.; McKinney, J. D. M. Tuberculosis Persistence, Latency, and Drug Tolerance. *Tuberculosis (Edinb)*. **2004**, *84* (1-2), 29-44.
- (22) Monack, D. M.; Mueller, A.; Falkow, S. Persistent Bacterial Infections: The Interface of the Pathogen and the Host Immune System. *Nat. Rev. Microbiol.* **2004**, *2* (9), 747-65.
- (23) Lipworth, S.; Hammond, R. J. H.; Baron, V. O.; Hu, Y.; Coates, A.; Gillespie, S. H. Defining Dormancy in Mycobacterial Disease. *Tuberculosis (Edinb)*. **2016**, *99*, 131-142.
- (24) Shleeva, M. O.; Kudykina, Y. K.; Vostroknutova, G. N.; Suzina, N. E.; Mulyukin, A. L.; Kaprelyants, A. S. Dormant Ovoid Cells of Mycobacterium Tuberculosis Are Formed in Response to Gradual External Acidification. *Tuberculosis (Edinb)*. **2011**, *91* (2), 146–154.
- (25) Keren, I.; Minami, S.; Rubin, E.; Lewis, K. Characterization and Transcriptome Analysis of Mycobacterium Tuberculosis Persisters. *mBio*. **2011**, *2* (3), e00100-11.
- (26) Keren, I.; Kaldalu, N.; Spoering, A.; Wang, Y.; Lewis, K. Persister Cells and Tolerance to Antimicrobials. *FEMS Microbiol. Lett.* **2004**, *230* (1), 13–18.
- (27) Cohen, N. R.; Lobritz, M. A.; Collins, J. J. Microbial Persistence and the Road to Drug Resistance. *Cell Host Microbe*. **2013**, *13* (6), 632-42.
- (28) Sebastian, J.; Swaminath, S.; Nair, R. R.; Jakkala, K.; Pradhan, A.; Ajitkumar, P. De Novo Emergence of Genetically Resistant Mutants of Mycobacterium Tuberculosis from the Persistence Phase Cells Formed against Antituberculosis Drugs in Vitro. *Antimicrob. Agents Chemother.* **2017**, *61* (2), e01343-16.
- (29) Zhang, Y. Persisters, Persistent Infections and the Yin-Yang Model. *Emerg. Microbes Infect.* **2014**, *3* (1), e3.
- (30) Dhar, N.; Mckinney, J.; Manina, G. Phenotypic Heterogeneity in Mycobacterium Tuberculosis. *Microbiol Spectr.* **2016**, *4* (6), 1-27.
- (31) Esmail, H.; Barry, C. E.; Young, D. B.; Wilkinson, R. J. The Ongoing Challenge of Latent Tuberculosis. *Philos. Trans. R. Soc. Lond. B. Biol. Sci.* **2014**, *369* (1645). 1-14.

-
- (32) Colangeli, R.; Gupta, A.; Vinhas, S. A.; Chippada Venkata, U. D.; Kim, S.; Grady, C.; Jones-López, E. C.; Soteropoulos, P.; Palaci, M.; Marques-Rodrigues, P.; Salgame, P.; Ellner, J. J.; Dietze, R.; Alland, D. Mycobacterium Tuberculosis Progresses through Two Phases of Latent Infection in Humans. *Nat. Commun.* **2020**, *11* (1), 1-10.
- (33) Wayne, L. G.; Hayes, L. G. An In Vitro Model for Sequential Study of Shiftdown of Mycobacterium Tuberculosis through Two Stages of Nonreplicating Persistence. *Infect. Immun.* **1996**, *64*, (6), 2062-9.
- (34) Vilchèze, C.; Yan, B.; Casey, R.; Hingley-Wilson, S.; Ettwiller, L.; Jacobs, W. R. Commonalities of Mycobacterium Tuberculosis Transcriptomes in Response to Defined Persisting Macrophage Stresses. *Front. Immunol.* **2022**, *13* (909904), 1-18.
- (35) Rustad, T. R.; Harrell, M. I.; Liao, R.; Sherman, D. R. The Enduring Hypoxic Response of Mycobacterium Tuberculosis. *PLoS One.* **2008**, *3* (1), e1502.
- (36) Gopinath, V.; Raghunandan, S.; Gomez, R. L.; Jose, L.; Surendran, A.; Ramachandran, R.; Pushparajan, A. R.; Mundayoor, S.; Jaleel, A.; Kumar, R. A. Profiling the Proteome of Mycobacterium Tuberculosis during Dormancy and Reactivation. *Mol. Cell. Proteom.* **2015**, *14* (8), 2160–2176.
- (37) Ortega, C.; Liao, R.; Anderson, L. N.; Rustad, T.; Ollodart, A. R.; Wright, A. T.; Sherman, D. R.; Grundner, C. Mycobacterium Tuberculosis Ser/Thr Protein Kinase B Mediates an Oxygen-Dependent Replication Switch. *PLoS Biol.* **2014**, *12* (1), e1001746.
- (38) Zeng, J.; Platig, J.; Cheng, T. Y.; Ahmed, S.; Skaf, Y.; Potluri, L. P.; Schwartz, D.; Steen, H.; Branch Moody, D.; Husson, R. N. Protein Kinases PknA and PknB Independently and Coordinately Regulate Essential Mycobacterium Tuberculosis Physiologies and Antimicrobial Susceptibility. *PLoS Pathog.* **2020**, *16* (4), e1008452.
- (39) Stokas, H.; Rhodes, H. L.; Purdy, G. E. Modulation of the M. Tuberculosis Cell Envelope between Replicating and Non-Replicating Persistent Bacteria. *Tuberculosis (Edinb).* **2020**, *125*, 102007.
- (40) Jakkala, K.; Ajitkumar, P. Hypoxic Non-Replicating Persistent Mycobacterium Tuberculosis Develops Thickened Outer Layer That Helps in Restricting Rifampicin Entry. *Front. Microbiol.* **2019**, *10*, 2339.

-
- (41) Seiler, P.; Ulrichs, T.; Bandermann, S.; Pradl, L.; Jörg, S.; Krenn, V.; Morawietz, L.; Kaufmann, S. H. E.; Aichele, P.; Kaufmann, S. H. E. Cell-Wall Alterations as an Attribute of Mycobacterium Tuberculosis in Latent Infection. *J. Infect. Dis.* **2003**, *188* (9), 1326-31.
- (42) Wright, C. C.; Hsu, F. F.; Arnett, E.; Dunaj, J. L.; Davidson, P. M.; Pacheco, S. A.; Harriff, M. J.; Lewinsohn, D. M.; Schlesinger, L. S.; Purdy, G. E. The Mycobacterium Tuberculosis MmpL11 Cell Wall Lipid Transporter Is Important for Biofilm Formation, Intracellular Growth, and Nonreplicating Persistence. *Infect. Immun.* **2017**, *85* (8), e00131-17.
- (43) Bacon, J.; Alderwick, L. J.; Allnut, J. A.; Gabasova, E.; Watson, R.; Hatch, K. A.; Clark, S. O.; Jeeves, R. E.; Marriott, A.; Rayner, E.; Tolley, H.; Pearson, G.; Hall, G.; Besra, G. S.; Wernisch, L.; Williams, A.; Marsh, P. D. Non-Replicating Mycobacterium Tuberculosis Elicits a Reduced Infectivity Profile with Corresponding Modifications to the Cell Wall and Extracellular Matrix. *PLoS One.* **2014**, *9* (2), e87329.
- (44) Cunningham, A. F.; Spreadbury, C. L. Mycobacterial Stationary Phase Induced by Low Oxygen Tension: Cell Wall Thickening and Localization of the 16-Kilodalton-Crystallin Homolog. *J. Bacteriol.* **1998**, *180* (4), 801-8.
- (45) Sarathy, J.; Dartois, V.; Dick, T.; Gengenbacher, M. Reduced Drug Uptake in Phenotypically Resistant Nutrient-Starved Nonreplicating Mycobacterium Tuberculosis. *Antimicrob. Agents Chemother.* **2013**, *57* (4), 1648–1653.
- (46) Akiva, E.; Copp, J. N.; Tokuriki, N.; Babbitt, P. C. Evolutionary and Molecular Foundations of Multiple Contemporary Functions of the Nitroreductase Superfamily. *Proc. Natl. Acad. Sci. U. S. A.* **2017**, *114* (45), E9549–E9558.
- (47) Valiauga, B.; Williams, E. M.; Ackerley, D. F.; Čėnas, N. Reduction of Quinones and Nitroaromatic Compounds by Escherichia Coli Nitroreductase A (NfsA): Characterization of Kinetics and Substrate Specificity. *Arch. Biochem. Biophys.* **2017**, *614*, 14–22.
- (48) Roldán, M. D.; Pérez-Reinado, E.; Castillo, F.; Moreno-Vivián, C. Reduction of Polynitroaromatic Compounds: The Bacterial Nitroreductases. *FEMS Microbiol. Rev.* **2008**, *32* (3), 474-500.

-
- (49) Peterson, F. J.; Mason, R. P.; Hovsepian, J.; Holtzman, J. L. Oxygen-Sensitive and -Insensitive Nitroreduction by *Escherichia Coli* and Rat Hepatic Microsomes. *J. Biol. Chem.* **1979**, *254*, (10), 4009-14.
- (50) Bryant, D. W.; McCalla, D. R.; Leeksa, M.; Laneuville, P. Type I Nitroreductases of *Escherichia Coli*. *Can. J. Microbiol.* **1981**, *27* (1), 81–86.
- (51) Koder, R. L.; Haynes, C. A.; Rodgers, M. E.; Rodgers, D. W.; Miller, A. F. Flavin Thermodynamics Explain the Oxygen Insensitivity of Enteric Nitroreductases. *Biochemistry* **2002**, *41* (48), 14197–14205.
- (52) Race, P. R.; Lovering, A. L.; Green, R. M.; Ossor, A.; White, S. A.; Searle, P. F.; Wrighton, C. J.; Hyde, E. I. Structural and Mechanistic Studies of *Escherichia Coli* Nitroreductase with the Antibiotic Nitrofurazone: Reversed Binding Orientations in Different Redox States of the Enzyme. *J. Biol. Chem.* **2005**, *280* (14), 13256-64.
- (53) Chauhan, S.; Sharma, D.; Singh, A.; Surolia, A.; Tyagi, J. S. Comprehensive Insights into *Mycobacterium Tuberculosis* DevR (DosR) Regulon Activation Switch. *Nucleic Acids Res.* **2011**, *39* (17), 7400–7414.
- (54) Dong, W.; Shi, J.; Chu, P.; Liu, R.; Wen, S.; Zhang, T.; Pang, Y.; Lu, J. Rv3131, a Gene Encoding Nitroreductase, is Essential for Metronidazole Activation in *Mycobacterium Tuberculosis* under Hypoxic Condition. *Res. Sq.* **2020**.
- (55) Sherman, D. R.; Voskuil, M.; Schnappinger, D.; Liao, R.; Harrell, M. I.; Schoolnik, G. K. Regulation of the *Mycobacterium Tuberculosis* Hypoxic Response Gene Encoding-Crystallin. *Proc. Natl. Acad. Sci. U. S. A.* **2001**, *98* (13), 7534-9.
- (56) Peddireddy, V.; Doddam, S. N.; Qureshi, I. A.; Yerra, P.; Ahmed, N. A Putative Nitroreductase from the DosR Regulon of *Mycobacterium Tuberculosis* Induces Pro-Inflammatory Cytokine Expression via TLR2 Signaling Pathway. *Sci. Rep.* **2016**, *6* (24535), 1–9.
- (57) Hu, Y.; Coates, A. R. M. *Mycobacterium Tuberculosis* Acg Gene Is Required for Growth and Virulence in Vivo. *PLoS One.* **2011**, *6* (6), e20958.
- (58) Hughes, J. P.; Rees, S.; Kalindjian, S. B.; Philpott, K. L. Principles of Early Drug Discovery. *Br. J. Pharmacol.* **2011**, *162* (6), 1239–1249.

- (59) Yuan, T.; Sampson, N. S. Hit Generation in TB Drug Discovery: From Genome to Granuloma. *Chem. Rev.* **2018**, *118* (4), 1887–1916.
- (60) Fleck, L. E.; North, E. J.; Lee, R. E.; Mulcahy, L. R.; Casadei, G.; Lewis, K. A Screen for and Validation of Prodrug Antimicrobials. *Antimicrob. Agents Chemother.* **2014**, *58* (3), 1410–1419.
- (61) Laborde, J.; Deraeve, C.; Bernardes-Génisson, V. Update of Antitubercular Prodrugs from a Molecular Perspective: Mechanisms of Action, Bioactivation Pathways, and Associated Resistance. *ChemMedChem.* **2017**, *12* (20), 1657-1676.
- (62) Vannelli, T. A.; Dykman, A.; Ortiz De Montellano, P. R. The Antituberculosis Drug Ethionamide Is Activated by a Flavoprotein Monooxygenase. *J. Biol. Chem.* **2002**, *277* (15), 12824–12829.
- (63) Locher, C. P.; Jones, S. M.; Hanzelka, B. L.; Perola, E.; Shoen, C. M.; Cynamon, M. H.; Ngwane, A. H.; Wiid, I. J.; van Helden, P. D.; Betoudji, F.; Nuernberger, E. L.; Thomson, J. A. A Novel Inhibitor of Gyrase B Is a Potent Drug Candidate for Treatment of Tuberculosis and Nontuberculosis Mycobacterial Infections. *Antimicrob. Agents Chemother.* **2015**, *59* (3), 1455–1465.
- (64) Singh, R.; Manjunatha, U.; Boshoff, H. I. M.; Young, H. H.; Niyomrattanakit, P.; Ledwidge, R.; Dowd, C. S.; Ill, Y. L.; Kim, P.; Zhang, L.; Kang, S.; Keller, T. H.; Jiricek, J.; Barry, C. E. PA-824 Kills Nonreplicating Mycobacterium Tuberculosis by Intracellular NO Release. *Science.* **2008**, *322* (5906), 1392–1395.
- (65) Rybniker, J.; Vocat, A.; Sala, C.; Busso, P.; Pojer, F.; Benjak, A.; Cole, S. T. Lansoprazole Is an Antituberculous Prodrug Targeting Cytochrome Bc 1. *Nat. Commun.* **2015**, *6* (7659), 1-8.
- (66) Mori, G.; Chiarelli, L. R.; Esposito, M.; Makarov, V.; Bellinzoni, M.; Hartkoorn, R. C.; Degiacomi, G.; Boldrin, F.; Ekins, S.; de Jesus Lopes Ribeiro, A. L.; Marino, L. B.; Centárová, I.; Svetlíková, Z.; Blaško, J.; Kazakova, E.; Lepioshkin, A.; Barilone, N.; Zanoni, G.; Porta, A.; Fondi, M.; Fani, R.; Baulard, A. R.; Mikušová, K.; Alzari, P. M.; Manganelli, R.; de carvalho, L. P. S.; Riccardi, G.; Cole, S. T.; Pasca, M. R. Thiophenecarboxamide Derivatives Activated by EthA Kill Mycobacterium Tuberculosis by Inhibiting the CTP Synthetase PyrG. *Chem. Biol.* **2015**, *22* (7), 917–927.

-
- (67) Chakraborty, S.; Gruber, T.; Barry, C. E.; Boshoff, H. I.; Rhee, K. Y. Para-Aminosalicylic Acid Acts as an Alternative Substrate of Folate Metabolism in Mycobacterium Tuberculosis. *Science*. **2013**, *339* (6115), 88–91.
- (68) Mori, G.; Chiarelli, L. R.; Riccardi, G.; Pasca, M. R. New Prodrugs against Tuberculosis. *Drug Discov. Today*. **2017**, *22* (3), 519-525.
- (69) Zhang, Y.; Shi, W.; Zhang, W.; Mitchison, D. Mechanisms of Pyrazinamide Action and Resistance. *Microbiol. Spectr*. **2014**, *2* (4) 1-12.
- (70) Lakshminarayana, S. B.; Huat, T. B.; Ho, P. C.; Manjunatha, U. H.; Dartois, V.; Dick, T.; Rao, S. P. S. Comprehensive Physicochemical, Pharmacokinetic and Activity Profiling of Anti-TB Agents. *J. Antimicrob. Chemother*. **2015**, *70* (3), 857–867.
- (71) Goldman, R. C. Why Are Membrane Targets Discovered by Phenotypic Screens and Genome Sequencing in Mycobacterium Tuberculosis? *Tuberculosis (Edinb)*. **2013**, *93* (6), 569-88.
- (72) Piccaro, G.; Poce, G.; Biava, M.; Giannoni, F.; Fattorini, L. Activity of Lipophilic and Hydrophilic Drugs against Dormant and Replicating Mycobacterium Tuberculosis. *J. Antibiot*. **2015**, *68* (11), 711–714.
- (73) Machado, D.; Girardini, M.; Viveiros, M.; Pieroni, M. Challenging the Drug-Likeness Dogma for New Drug Discovery in Tuberculosis. *Front. Microbiol*. **2018**, *9* (1367), 1-23.
- (74) Manjunatha, U. H.; Boshoff, H.; Dowd, C. S.; Zhang, L.; Albert, T. J.; Norton, J. E.; Daniels, L.; Dick, T.; Pang, S. S.; Barry, C. E. Identification of a Nitroimidazo-Oxazine-Specific Protein Involved in PA-824 Resistance in Mycobacterium Tuberculosis. *Proc. Natl. Acad. Sci. U. S. A*. **2006**, *103* (2), 431–436.
- (75) Matsumoto, M.; Hashizume, H.; Tomishige, T.; Kawasaki, M.; Tsubouchi, H.; Sasaki, H.; Shimokawa, Y.; Komatsu, M. OPC-67683, a Nitro-Dihydro-Imidazooxazole Derivative with Promising Action against Tuberculosis in Vitro and in Mice. *PLoS Med*. **2006**, *3* (11), 2131–2144.
- (76) Upton, A. M.; Cho, S.; Yang, T. J.; Kim, A. Y.; Wang, Y.; Lu, Y.; Wang, B.; Xu, J.; Mdluli, K.; Ma, Z.; Franzblaub, S. G. In Vitro and in Vivo Activities of the

- Nitroimidazole TBA-354 against Mycobacterium Tuberculosis. *Antimicrob. Agents Chemother.* **2015**, *59* (1), 136–144.
- (77) Albesa-Jové, D.; Chiarelli, L. R.; Makarov, V.; Pasca, M. R.; Urresti, S.; Mori, G.; Salina, E.; Vocat, A.; Comino, N.; Mohorko, E.; Ryabova, S.; Pfeiffer, B.; Lopes Ribeiro, A. L. D. J.; Rodrigo-Unzueta, A.; Tera, M.; Zanoni, G.; Buroni, S.; Altmann, K. H.; Hartkoorn, R. C.; Glockshuber, R.; Cole, S. T.; Riccardi, G.; Guerin, M. E. Rv2466c Mediates the Activation of TP053 to Kill Replicating and Non-Replicating Mycobacterium Tuberculosis. *ACS Chem. Biol.* **2014**, *9* (7), 1567–1575.
- (78) Chiarelli, L. R.; Salina, E. G.; Mori, G.; Azhikina, T.; Riabova, O.; Lepioshkin, A.; Grigorov, A.; Forbak, M.; Madacki, J.; Orena, B. S.; Manfredi, M.; Gosetti, F.; Buzzi, A.; Degiacomi, G.; Sammartino, J. C.; Marengo, E.; Korduláková, J.; Riccardi, G.; Mikušová, K.; Makarov, V.; Pasca, M. R. New Insights into the Mechanism of Action of the Thienopyrimidine Antitubercular Prodrug TP053. *ACS Infect. Dis.* **2020**, *6* (2), 313–323.
- (79) Negri, A.; Javidnia, P.; Mu, R.; Zhang, X.; Vendome, J.; Gold, B.; Roberts, J.; Barman, D.; Ioerger, T.; Sacchettini, J. C.; Jiang, X.; Burns-Huang, K.; Warriar, T.; Ling, Y.; Warren, J. D.; Oren, D. A.; Beuming, T.; Wang, H.; Wu, J.; Li, H.; Rhee, K. Y.; Nathan, C. F.; Liu, G.; Somersan-Karakaya, S. Identification of a Mycothiol-Dependent Nitroreductase from Mycobacterium Tuberculosis. *ACS Infect. Dis.* **2018**, *4* (5), 771–787.
- (80) Eng, R. H. K.; Padberg, F. T.; Smith, S. M.; Tan, E. N.; Cherubin, C. E. Bactericidal Effects of Antibiotics on Slowly Growing and Nongrowing Bacteria. *Antimicrob. Agents Chemother.* **1991**, *35* (9), 1824–8.
- (81) Bergkessel, M.; Basta, D. W.; Newman, D. K. The Physiology of Growth Arrest: Uniting Molecular and Environmental Microbiology. *Nat. Rev. Microbiol.* **2016**, *14*, 549–562.
- (82) Gefen, O.; Fridman, O.; Ronin, I.; Balaban, N. Q. Direct Observation of Single Stationary-Phase Bacteria Reveals a Surprisingly Long Period of Constant Protein Production Activity. *Proc. Natl. Acad. Sci. U. S. A.* **2014**, *111* (1), 556–561.
- (83) Drummond, L. J.; Lahey, F. N. Alkaloids of the Australian Rutaceae: Acronychia Baueri. III. The Structure of Acronycine. *Aust. J. Sci. Res., Ser. B.* **1949**, *2*, 631–637.

-
- (84) Price, J. R. Alkaloids of the Australian Rutaceae: Melicope Fareana. IV. Some Reactions of 1-Methyl-4-Quinolone-3-Carboxylic Acid, a Degradation Product of the Alkaloids. *Aust. J. Sci. Res., Ser. B.* **1949**, 2 (2), 272–281.
- (85) Crow, W. D.; Price, J. R. Alkaloids of the Australian Rutaceae: Melicope Fareana. V. *Aust. J. Sci. Res., Ser. B.* **1949**, 2 (2), 82–306.
- (86) Barton, N.; Crowther, A. F.; Hepworth, W.; Richardson, N. D.; Driver, G. W. New Quinolones and Therapeutic Compositions Containing Them. U.K. Patent GB830832, March 23, **1960**.
- (87) Leshner, G. Y. Presented. In *Presented in International Symposium on Quinolone Antibiotics*; Chicago, IL, **1986**.
- (88) Leshner, G. Y.; Froelich, E. J.; Gruett, M. D.; Bailey, J. H.; Brundage, R. P. 1,8-Naphthyridine Derivatives. A New Class of Chemotherapeutic Agents. *J. Med. Pharm. Chem.* **1962**, 5 (5), 1063–1065.
- (89) Leshner, G. Y. Nalidixic Acid, 1-Ethyl-1,4-Dihydro-7-Methyl-4-Oxo- 1,8-Naphthyridine-3-Carboxylic Acid. A New Antibacterial Agent. *Int. Congr. Chemother., Proc.* **1964**, 2, 1367–1369.
- (90) Bisacchi, G. S. Origins of the Quinolone Class of Antibacterials: An Expanded “Discovery Story.” *J. Med. Chem.* **2015**, 58 (12), 4874–82.
- (91) Walker, R. C. The Fluoroquinolones. *Mayo Clin. Proc.* **1999**, 74 (10), 1030–1037.
- (92) Drlica, K.; Zhao, X. DNA Gyrase, Topoisomerase IV, and the 4-Quinolones. *Microbiol. Mol. Biol. Rev.* **1997**, 61 (3), 377–392.
- (93) Hooper, D. C. Mechanisms of Action and Resistance of Older and Newer Fluoroquinolones. *Clin. Infect. Dis.* **2000**, 31 (2), S24–8.
- (94) Heisig, P. Type II Topoisomerases - Inhibitors, Repair Mechanisms and Mutations. *Mutagenesis* **2009**, 24 (6), 465–469.
- (95) Mustaev, A.; Malik, M.; Zhao, X.; Kurepina, N.; Luan, G.; Oppegard, L. M.; Hiasa, H.; Marks, K. R.; Kerns, R. J.; Berger, J. M.; Drlica, K. Fluoroquinolone-Gyrase-DNA Complexes Two Modes of Drug Binding. *J. Biol. Chem.* **2014**, 289 (18), 12300–12312.

-
- (96) Aldred, K. J.; Kerns, R. J.; Osheroff, N. Mechanism of Quinolone Action and Resistance. *Biochemistry* **2014**, *53*, 1565–1574.
- (97) Zhao, X.; Hong, Y.; Drlica, K. Moving Forward with Reactive Oxygen Species Involvement in Antimicrobial Lethality. *J. Antimicrob. Chemother.* **2015**, *70* (3), 639–642.
- (98) Arabyat, R. M.; Raisch, D. W.; McKoy, J. M.; Bennett, C. L. Fluoroquinolone-Associated Tendon-Rupture: A Summary of Reports in the Food and Drug Administration’s Adverse Event Reporting System. *Expert Opin. Drug Saf.* **2015**, *14* (11), 1653–1660.
- (99) Badal, S.; Her, Y. F.; Maher, L. J. Nonantibiotic Effects of Fluoroquinolones in Mammalian Cells. *J. Biol. Chem.* **2015**, *290* (36), 22287–22297.
- (100) Van Boeckel, T. P.; Gandra, S.; Ashok, A.; Caudron, Q.; Grenfell, B. T.; Levin, S. A.; Laxminarayan, R. Global Antibiotic Consumption 2000 to 2010: An Analysis of National Pharmaceutical Sales Data. *Lancet Infect. Dis.* **2014**, *14* (8), 742–750.
- (101) de Lastours, V. Impact of Fluoroquinolones on Human Microbiota. *J. des Anti-Infectieux.* **2016**, *18* (1), 1–4.
- (102) Borzio, M.; Salerno, F.; Saudelli, M.; Galvagno, D.; Piantoni, L.; Fragiaco, L. Efficacy of Oral Ciprofloxacin as Selective Intestinal Decontaminant in Cirrhosis. *Ital. J. Gastroenterol. Hepatol.* **1997**, *29*, 262–266.
- (103) Inagaki, Y.; Nakaya, R.; Chida, T.; Hashimoto, S. The Effect of Levofloxacin, an Optically-Active Isomer of Ofloxacin, on Fecal Microflora in Human Volunteers. *Jpn. J. Antibiot.* **1992**, *45* (3), 241–252.
- (104) Edlund, C.; Beyer, G.; Hiemer-Bau, M.; Ziege, S.; Lode, H.; Nord, C. E. Comparative Effects of Moxifloxacin and Clarithromycin on the Normal Intestinal Microflora. *Scand. J. Infect. Dis.* **2000**, *32*, 81–85.
- (105) Edlund, C.; Sjöstedt, S.; Nord, C. E. Comparative Effects of Levofloxacin and Ofloxacin on the Normal Oral and Intestinal Microflora. *Scand. J. Infect. Dis.* **1997**, *29* (4), 383–386.

-
- (106) Huse, S. M.; Dethlefsen, L.; Huber, J. A.; Welch, D. M.; Relman, D. A.; Sogin, M. L. Exploring Microbial Diversity and Taxonomy Using SSU rRNA Hypervariable Tag Sequencing. *PLoS Genet.* **2008**, *4* (11), e1000255.
- (107) Stewardson, A. J.; Gaïa, N.; François, P.; Malhotra-Kumar, S.; Delémont, C.; Martinez de Tejada, B.; Schrenzel, J.; Harbarth, S.; Lazarevic, V.; Vervoort, J.; Lammens, C.; Adriaenssens, N.; Coenen, S.; Goossens, H.; Kowalczyk, A.; Godycki-Cwirko, M.; Brossier, C.; Huttner, B. Collateral Damage from Oral Ciprofloxacin versus Nitrofurantoin in Outpatients with Urinary Tract Infections: A Culture-Free Analysis of Gut Microbiota. *Clin. Microbiol. Infect.* **2015**, *21* (4), 344.e1-11.
- (108) Willmann, M.; El-Hadidi, M.; Huson, D. H.; Schütz, M.; Weidenmaier, C.; Autenrieth, I. B.; Peter, S. Antibiotic Selection Pressure Determination through Sequence-Based Metagenomics. *Antimicrob. Agents Chemother.* **2015**, *59* (12), 7335–7345.
- (109) Dubinsky, V.; Reshef, L.; Bar, N.; Keizer, D.; Golan, N.; Rabinowitz, K.; Godny, L.; Yadgar, K.; Zonensain, K.; Tulchinsky, H.; Gophna, U.; Dotan, I. Prolonged Antibiotic Treatment Generates a Fluoroquinolone Resistant Gut Microbiome and Collateral Multi-Drug Resistance. *Gastroenterology.* **2020**, *158* (3), e13-610-624..
- (110) Velema, W. A.; van der Berg, J. P.; Hansen, M. J.; Szymanski, W.; Driessen, A. J. M.; Feringa, B. L. Optical Control of Antibacterial Activity. *Nat. Chem.* **2013**, *5*, 924-928.
- (111) Velema, W. A.; Hansen, M. J.; Lerch, M. M.; Driessen, A. J. M.; Szymanski, W.; Feringa, B. L. Ciprofloxacin-Photoswitch Conjugates: A Facile Strategy for Photopharmacology. *Bioconjug. Chem.* **2015**, *26* (12), 2592–2597.
- (112) Velema, W. A.; Van Der Berg, J. P.; Szymanski, W.; Driessen, A. J. M.; Feringa, B. L. Orthogonal Control of Antibacterial Activity with Light. *ACS Chem. Biol.* **2014**, *9* (9), 1969–1974.
- (113) Shi, Y.; Truong, V. X.; Kulkarni, K.; Qu, Y.; Simon, G. P.; Boyd, R. L.; Perlmutter, P.; Lithgow, T.; Forsythe, J. S. Light-Triggered Release of Ciprofloxacin from an in Situ Forming Click Hydrogel for Antibacterial Wound Dressings. *J. Mater. Chem. B* **2015**, *3* (45), 8771–8774.
- (114) Wong, P. T.; Tang, S.; Mukherjee, J.; Tang, K.; Gam, K.; Isham, D.; Murat, C.; Sun, R.; Baker, J. R.; Choi, S. K. Light-Controlled Active Release of Photocaged

- Ciprofloxacin for Lipopolysaccharide-Targeted Drug Delivery Using Dendrimer Conjugates. *Chem. Comm.* **2016**, 52 (68), 10357–10360.
- (115) Pang, Q.; Zheng, X.; Luo, Y.; Ma, L.; Gao, C. A Photo-Cleavable Polyprodrug-Loaded Wound Dressing with UV-Responsive Antibacterial Property. *J. Mater. Chem. B.* **2017**, 5 (45), 8975–8982.
- (116) Kumari, P.; Kulkarni, A.; Sharma, A. K.; Chakrapani, H. Visible-Light Controlled Release of a Fluoroquinolone Antibiotic for Antimicrobial Photopharmacology. *ACS Omega.* **2018**, 3 (2), 2155–2160.
- (117) Pal, S.; Ramu, V.; Taye, N.; Mogare, D. G.; Yeware, A. M.; Sarkar, D.; Reddy, D. S.; Chattopadhyay, S.; Das, A. GSH Induced Controlled Release of Levofloxacin from a Purpose-Built Prodrug: Luminescence Response for Probing the Drug Release in Escherichia Coli and Staphylococcus Aureus. *Bioconjug. Chem.* **2016**, 27 (9), 2062–2070.
- (118) Neumann, W.; Nolan, E. M. Evaluation of a Reducible Disulfide Linker for Siderophore-Mediated Delivery of Antibiotics. *J. Biol. Inorg. Chem.* **2018**, 23 (7), 1025-1036.
- (119) Tougou, K.; Nakamura, A.; Watanabe, S.; Okuyama, Y.; Morino, A. Paraoxonase Has a Major Role in the Hydrolysis of Prulifloxacin (NM441), a Prodrug of a New Antibacterial Agent. *Drug Metab. Dispos.* **1998**, 26 (4), 355-359.
- (120) Prats, G.; Rossi, V.; Salvatori, E.; Mirelis, B. Prulifloxacin: A New Antibacterial Fluoroquinolone. *Expert Rev. Anti. Infect. Ther.* **2006**, 4 (1), 27–41.
- (121) Baker, W. R.; Cai, S.; Dimitroff, M.; Fang, L.; Huh, K. K.; Ryckman, D. R.; Shang, X.; Shawar, R. M.; Therrien, J. H. A Prodrug Approach toward the Development of Water Soluble Fluoroquinolones and Structure-Activity Relationships of Quinoline-3-Carboxylic Acids. *J. Med. Chem.* **2004**, 47 (19), 4693–4709.
- (122) Tanaka, K. S. E.; Houghton, T. J.; Kang, T.; Dietrich, E.; Delorme, D.; Ferreira, S. S.; Caron, L.; Viens, F.; Arhin, F. F.; Sarmiento, I.; Lehoux, D.; Fadhil, I.; Laquerre, K.; Liu, J.; Ostiguy, V.; Poirier, H.; Moeck, G.; Parr, T. R.; Rafai Far, A. Bisphosphonated Fluoroquinolone Esters as Osteotropic Prodrugs for the Prevention of Osteomyelitis. *Bioorg. Med. Chem.* **2008**, 16 (20), 9217–9229.

- (123) Walther, R.; Nielsen, S. M.; Christiansen, R.; Meyer, R. L.; Zelikin, A. N. Combatting Implant-Associated Biofilms through Localized Drug Synthesis. *J. Control. Release.* **2018**, *287*, 94–102.
- (124) Ji, C.; Miller, P. A.; Miller, M. J. Syntheses and Antibacterial Activity of N-Acylated Ciprofloxacin Derivatives Based on the Trimethyl Lock. *ACS Med. Chem. Lett.* **2015**, *6* (6), 707–710.
- (125) Neumann, W.; Sassone-Corsi, M.; Raffatellu, M.; Nolan, E. M. Esterase-Catalyzed Siderophore Hydrolysis Activates an Enterobactin-Ciprofloxacin Conjugate and Confers Targeted Antibacterial Activity. *J. Am. Chem. Soc.* **2018**, *140* (15), 5193–5201.
- (126) Georgopapadakou, N. H.; Bertasso, A. Mechanisms of Action of Cephalosporin 3'-Quinolone Esters, Carbamates, and Tertiary Amines in Escherichia Coli. *Antimicrob. Agents Chemother.* **1993**, *37* (3), 559–565.
- (127) Albrecht, H. A.; Beskid, G.; Chan, K. K.; Christenson, J. G.; Cleeland, R.; Deitcher, K. H.; Georgopapadakou, N. H.; Keith, D. D.; Pruess, D. L.; Sepinwall, J. Cephalosporin 3'-Quinolone Esters with a Dual Mode of Action. *J. Med. Chem.* **1990**, *33* (1), 77–86.
- (128) Albrecht, H. A.; Beskid, G.; Christenson, J. G.; Durkin, J. W.; Fallat, V.; Georgopapadakou, N. H.; Keith, D. D.; Konzelmann, F. M.; Lipschitz, E. R.; McGarry, D. H. Dual-Action Cephalosporins: Cephalosporin 3'-Quaternary Ammonium Quinolones. *J. Med. Chem.* **1991**, *34* (2), 669–675.
- (129) Albrecht, H. A.; Beskid, G.; Christenson, J. G.; Georgopapadakou, N. H.; Keith, D. D.; Konzelmann, F. M.; Pruess, D. L.; Rossman, P. L.; Wei, C. C. Dual-Action Cephalosporins: Cephalosporin 3'-Quinolone Carbamates. *J. Med. Chem.* **1991**, *34* (9), 2857–2864.
- (130) Evans, L. E.; Krishna, A.; Ma, Y.; Webb, T. E.; Marshall, D. C.; Tooke, C. L.; Spencer, J.; Clarke, T. B.; Armstrong, A.; Edwards, A. M. Exploitation of Antibiotic Resistance as a Novel Drug Target: Development of a β -Lactamase-Activated Antibacterial Prodrug. *J. Med. Chem.* **2019**, *62* (9), 4411–4425.
- (131) Pardeshi, K. A.; Kumar, T. A.; Ravikumar, G.; Shukla, M.; Kaul, G.; Chopra, S.; Chakrapani, H. Targeted Antibacterial Activity Guided by Bacteria-Specific Nitroreductase Catalytic Activation to Produce Ciprofloxacin. *Bioconjug. Chem.* **2019**, *30* (3), 751–759.

-
- (132) Pais, J. P.; Policarpo, M.; Pires, D.; Francisco, A. P.; Madureira, A. M.; Testa, B.; Anes, E.; Constantino, L. Fluoroquinolone Derivatives in the Treatment of Mycobacterium Tuberculosis Infection. *Pharmaceuticals* (Basel). **2022**, *15* (10), 1213.
- (133) Pletz, M. W. R.; de Roux, A.; Roth, A.; Neumann, K. H.; Mauch, H.; Lode, H. Early Bactericidal Activity of Moxifloxacin in Treatment of Pulmonary Tuberculosis: A Prospective, Randomized Study. *Antimicrob. Agents Chemother.* **2004**, *48* (3), 780–782.
- (134) Dorman, S. E.; Nahid, P.; Kurbatova, E. v.; Phillips, P. P. J.; Bryant, K.; Dooley, K. E.; Engle, M.; Goldberg, S. v.; Phan, H. T. T.; Hakim, J.; Johnson, J. L.; Lourens, M.; Martinson, N. A.; Muzanyi, G.; Narunsky, K.; Nerette, S.; Nguyen, N. v.; Pham, T. H.; Pierre, S.; Purfield, A. E.; Samaneka, W.; Savic, R. M.; Sanne, I.; Scott, N. A.; Shenje, J.; Sizemore, E.; Vernon, A.; Waja, Z.; Weiner, M.; Swindells, S.; Chaisson, R. E. Four-Month Rifapentine Regimens with or without Moxifloxacin for Tuberculosis. *New Eng. J. Med.* **2021**, *384* (18), 1705–1718.
- (135) Berning, S. E. The Role of Fluoroquinolones in Tuberculosis Today. *Drugs.* **2001**, *61* (1), 9-18.
- (136) Gillespie, S. H. The Role of Moxifloxacin in Tuberculosis Therapy. *Eur. Respir. Rev.* **2016**, *25* (139), 19-28.
- (137) Saravolatz, L. D.; Leggett, J. Gatifloxacin, Gemifloxacin, and Moxifloxacin: The Role of 3 Newer Fluoroquinolones. *Clin. Infect. Dis.* **2003**, *37* (9), 1210–1215.
- (138) Pranger, A. D.; van der Werf, T. S.; Kosterink, J. G. W.; Alffenaar, J. W. C. The Role of Fluoroquinolones in the Treatment of Tuberculosis in 2019. *Drugs* **2019**, *79* (2), 161–171.
- (139) Pienaar, E.; Sarathy, J.; Prideaux, B.; Dietzold, J.; Dartois, V.; Kirschner, D. E.; Linderman, J. J. Comparing Efficacies of Moxifloxacin, Levofloxacin and Gatifloxacin in Tuberculosis Granulomas Using a Multi-Scale Systems Pharmacology Approach. *PLoS Comput. Biol.* **2017**, *13* (8), e1005650.
- (140) Prideaux, B.; Via, L. E.; Zimmerman, M. D.; Eum, S.; Sarathy, J.; O'Brien, P.; Chen, C.; Kaya, F.; Weiner, D. M.; Chen, P.-Y.; Song, T.; Lee, M.; Shim, T. S.; Cho, J. S.; Kim, W.; Cho, S. N.; Olivier, K. N.; Barry III, C. E.; Dartois, V. The Association

- between Sterilizing Activity and Drug Distribution into Tuberculosis Lesions. *Nat. Med.* **2015**, *21*, 1223.
- (141) Maitre, T.; Petitjean, G.; Chauffour, A.; Bernard, C.; el Helali, N.; Jarlier, V.; Reibel, F.; Chavanet, P.; Aubry, A.; Veziris, N. Are Moxifloxacin and Levofloxacin Equally Effective to Treat XDR Tuberculosis? *J. Antimicrob. Chemother.* **2017**, *72* (8), 2326–2333.
- (142) Sarathy, J.; Blanc, L.; Alvarez-Cabrera, N.; O'Brien, P.; Dias-Freedman, I.; Mina, M.; Zimmerman, M.; Kaya, F.; Liang, H. P. H.; Prideaux, B.; Dietzold, J.; Salgame, P.; Savic, R. M.; Linderman, J.; Kirschner, D.; Pienaar, E.; Dartois, V. Fluoroquinolone Efficacy against Tuberculosis Is Driven by Penetration into Lesions and Activity against Resident Bacterial Populations. *Antimicrob. Agents Chemother.* **2019**, *63* (5), e02516-18.
- (143) Aldred, K. J.; Blower, T. R.; Kerns, R. J.; Berger, J. M.; Osheroff, N. Fluoroquinolone Interactions with Mycobacterium Tuberculosis Gyrase: Enhancing Drug Activity against Wild-Type and Resistant Gyrase. *Proc. Natl. Acad. Sci. U. S. A.* **2016**, *113* (7), E839–E846.
- (144) Blower, T. R.; Williamson, B. H.; Kerns, R. J.; Berger, J. M. Crystal Structure and Stability of Gyrase-Fluoroquinolone Cleaved Complexes from Mycobacterium Tuberculosis. *Proc. Natl. Acad. Sci. U. S. A.* **2016**, *113* (7), 1706–1713.
- (145) Sirgel, F. A.; Warren, R. M.; Streicher, E. M.; Victor, T. C.; Van helden, P. D.; Böttger, E. C. GyrA Mutations and Phenotypic Susceptibility Levels to Ofloxacin and Moxifloxacin in Clinical Isolates of Mycobacterium Tuberculosis. *J. Antimicrob. Chemother.* **2012**, *67* (5), 1088–1093.
- (146) Zignol, M.; Dean, A. S.; Alikhanova, N.; Andres, S.; Cabibbe, A. M.; Cirillo, D. M.; Dadu, A.; Dreyer, A.; Driesen, M.; Gilpin, C.; Hasan, R.; Hasan, Z.; Hoffner, S.; Husain, A.; Hussain, A.; Ismail, N.; Kamal, M.; Mansjö, M.; Mvusi, L.; Niemann, S.; Omar, S. v.; Qadeer, E.; Rigouts, L.; Ruesch-Gerdes, S.; Schito, M.; Seyfaddinova, M.; Skrahina, A.; Tahseen, S.; Wells, W. A.; Mukadi, Y. D.; Kimerling, M.; Floyd, K.; Weyer, K.; Raviglione, M. C. Population-Based Resistance of Mycobacterium Tuberculosis Isolates to Pyrazinamide and Fluoroquinolones: Results from a Multicountry Surveillance Project. *Lancet Infect. Dis.* **2016**, *16* (10), 1185–1192.

- (147) Dong, Y.; Zhao, X.; Kreiswirth, B. N.; Drlica, K. Mutant Prevention Concentration as a Measure of Antibiotic Potency: Studies with Clinical Isolates of Mycobacterium Tuberculosis, *Antimicrob. Agents Chemother.* **2000**, *44* (9), 2581-4.
- (148) Somnath, S.; Samsher, S.; Ashutosh, T.; Chandrani, T.; Anand, K. T.; Mayashree, D.; Vikas, Y.; Sakshi, K.; S, R. R.; Nagasuma, C.; Harinath, C.; Karl, D.; Amit, S. Moxifloxacin-Mediated Killing of Mycobacterium Tuberculosis Involves Respiratory Downshift, Reductive Stress, and Accumulation of Reactive Oxygen Species. *Antimicrob. Agents Chemother.* **2022**, *66* (9), e00592-22.
- (149) Stass, H.; Kubitzka, D. Lack of Pharmacokinetic Interaction between Moxifloxacin, a Novel 8-Methoxyfluoroquinolone, and Theophylline. *Clin. Pharmacokinet.* **2001**, *40*, 63–70.
- (150) Fish, D. N. Fluoroquinolone Adverse Effects and Drug Interactions. *Pharmacotherapy* **2001**, *21* (10 Pt 2), 253S-272S.
- (151) Rodríguez, J. C.; Cebrián, L.; López, M.; Ruiz, M.; Jiménez, I.; Royo, G. Mutant Prevention Concentration: Comparison of Fluoroquinolones and Linezolid with Mycobacterium Tuberculosis. *J. Antimicrob. Chemother.* **2004**, *53* (3), 441–444.
- (152) Birmingham, M. C.; Guarino, R.; Heller, A.; Wilton, J. H.; Shah, A. Hejmanowski, L.; Nix, D. E.; Schentag, J. J. Ciprofloxacin concentrations in lung tissue following a single 400 mg intravenous dose. *J. Antimicrob. Chemother.* **1999**, *43*, (Suppl A), 43-8.
- (153) Soman, A.; Honeybourne, D.; Andrews, J.; Jevons, G.; Wise, R. Concentrations of moxifloxacin in serum and pulmonary compartments following a single 400 mg oral dose in patients undergoing fibre-optic bronchoscopy. *J. Antimicrob. Chemother.* **1999**, *44* (6), 835-8.
- (154) Lutsar, I.; Friedland, I. R.; Wubbel, L.; Mccoig, C. C.; Jafri, H. S.; Ng, W.; Ghaffar, F.; Mccracken, G. H. Pharmacodynamics of Gatifloxacin in Cerebrospinal Fluid in Experimental Cephalosporin-Resistant Pneumococcal Meningitis. *Antimicrob. Agents Chemother.* **1998**, *42* (10), 2650-5.
- (155) Firsov, A. A.; Vostrov, S. N.; Lubenko, I. Y.; Drlica, K.; Portnoy, Y. A.; Zinner, S. H. In Vitro Pharmacodynamic Evaluation of the Mutant Selection Window Hypothesis Using Four Fluoroquinolones against Staphylococcus Aureus. *Antimicrob. Agents Chemother.* **2003**, *47* (5), 1604–1613.

-
- (156) Zhanel, G. G.; Walkty, A.; Vercaigne, L.; Karlowsky, J. A.; Embil, J.; Gin, A. S.; Hoban, D. J. The New Fluoroquinolones: A Critical Review. *Can. J. Infect. Dis.* **1999**, *10* (3), 207–238.
- (157) Van Bambeke, F.; Tulkens, P. M. Safety Profile of the Respiratory Fluoroquinolone Moxifloxacin: Comparison with Other Fluoroquinolones and Other Antibacterial Classes. *Drug Saf.* **2009**, *32* (5), 359–378.
- (158) Silva, D. R.; Mello, F. C. de Q.; Migliori, G. B. Shortened Tuberculosis Treatment Regimens: What Is New? *J. Bras. Pneumol.* **2020**, *46* (2), 1–8.
- (159) Gillespie, S. H.; Crook, A. M.; McHugh, T. D.; Mendel, C. M.; Meredith, S. K.; Murray, S. R.; Pappas, F.; Phillips, P. P. J.; Nunn, A. J. Four-Month Moxifloxacin-Based Regimens for Drug-Sensitive Tuberculosis. *New Engl. J. Med.* **2014**, *371* (17), 1577–1587.
- (160) Sarathy, J. P.; Via, L. E.; Weiner, D.; Blanc, L.; Boshoff, H.; Eugenin, E. A.; Barry, C. E.; Dartois, V. A. Extreme Drug Tolerance of Mycobacterium Tuberculosis in Caseum. *Antimicrob. Agents Chemother.* **2018**, *62* (2), e02266-17.
- (161) Blanc, L.; Daudelin, I. B.; Podell, B. K.; Chen, P. Y.; Zimmerman, M.; Martinot, A. J.; Savic, R. M.; Prideaux, B.; Dartois, V. High-Resolution Mapping of Fluoroquinolones in TB Rabbit Lesions Reveals Specific Distribution in Immune Cell Types. *Elife*. **2018**, *7*, 1–21.
- (162) Prideaux, B.; Dartois, V.; Staab, D.; Weiner, D. M.; Goh, A.; Via, L. E.; Barry, C. E. 3rd; Stoeckli, M. High-Sensitivity MALDI-MRM-MS Imaging of Moxifloxacin Distribution in Tuberculosis-Infected Rabbit Lungs and Granulomatous Lesions. *Anal. Chem.* **2011**, *83* (6), 2112–2118.
- (163) Dartois, V. The Path of Anti-Tuberculosis Drugs: From Blood to Lesions to Mycobacterial Cells. *Nat. Rev. Microbiol.* **2014**, *12* (3), 159–167.

Chapter 2. Design, Synthesis, and Evaluation of Nitroheterocyclic prodrugs of Moxifloxacin (MXF)

2.1. Introduction

As mentioned in Chapter 1, the adaptation of *M. tuberculosis* (*Mtb*) into a drug-tolerant persistent state during latent infection has been implicated in the failure of TB therapy, emergence of resistance, relapse, and recalcitrance of infection. This characteristic phenotype contributes to the reduced permeability of MXF conferring phenotypic drug resistance in non-replicating *Mtb*.¹⁻³ Therefore, we sought to enhance permeation and efficacy of MXF by developing lipophilic bioreductive prodrugs, which upon activation under conditions associated with both replicating and non-replicating bacteria could liberate MXF.

2.2. Design of nitroreductase (NTR)-activated FQ prodrug

MXF contains two functional groups that can be modified into a prodrug form (Figure 2.1). The carboxylic acid can be converted to a nitroaryl ester, and the amine on the piperidine ring can be derivatized as a nitroaryl carbamate.

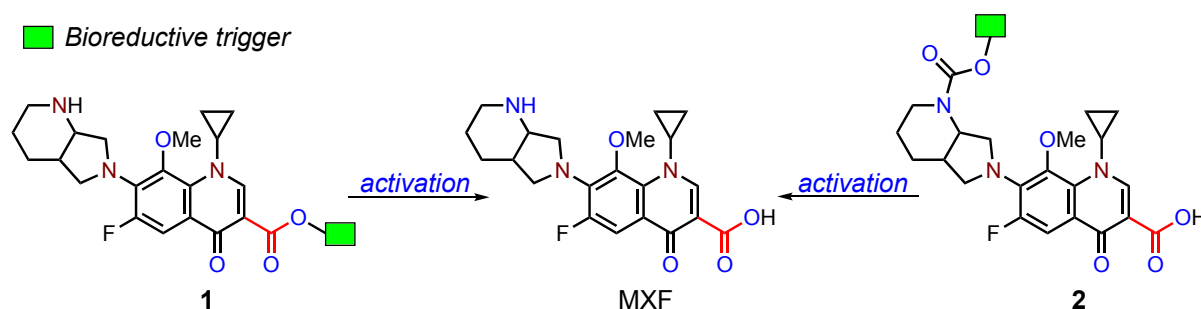


Figure 2.1. Proposed strategy for the generation of MXF from ester and carbamate prodrugs

The activation of bioreductive prodrugs involves sequential one- or two-electron reductions of the nitroaryl ring to form a hydroxylamino intermediate, which then rearranges to liberate the drug (Figure 2.2). The propensity to undergo reduction will likely determine the efficiency of the formation of the key intermediate whereas the rate of self-immolation will influence the rate of drug release. Lastly, the efficiency of release also depends on the cell permeability of the prodrug and its subsequent enzymatic turnover by mycobacterial NTRs. We considered a series of heterocycles with varying reduction potentials as possible structures wherein the above parameters could be modulated. Hence, we sought to rationally design MXF prodrugs that could be activated in reductive environments prevalent in replicating and non-replicating

Mtb (Figure 2.2). Our strategy involved exploiting the expressed NTRs as an enzyme trigger to activate the prodrug to produce MXF with both rate and efficiency as parameters for optimization; and to increase the lipophilicity of the ensuing prodrug to improve permeability. This strategy may shorten the duration of TB treatment and reduce the relapse rate. Additionally, the prodrug strategy can mitigate FQ-induced host toxicity and reduce its tremendous impact on the host microbial symbiosis by minimizing the unintended systemic exposure of MXF to host cells.

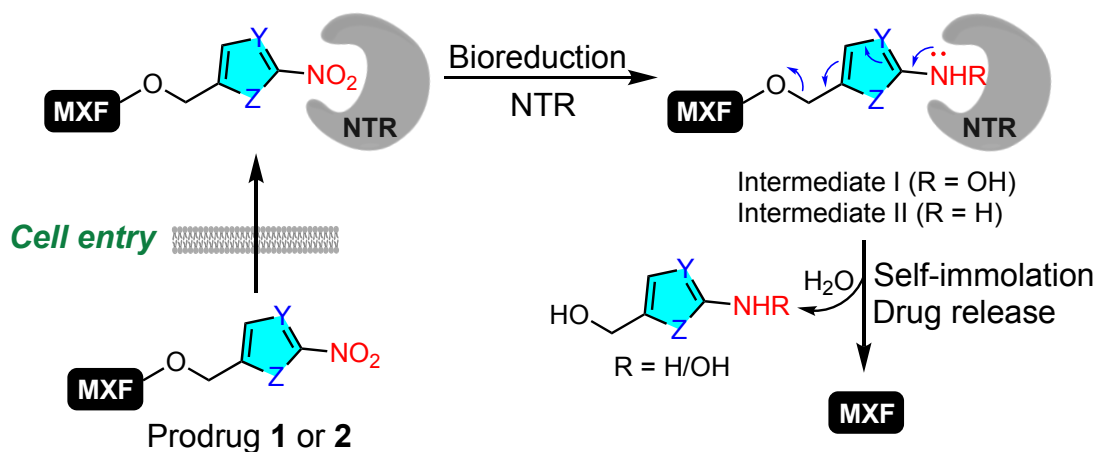


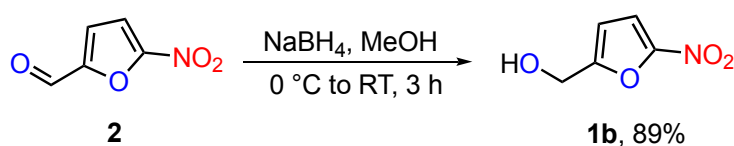
Figure 2.2. Design and mechanism of bioreductive activation of nitroheteroaryl prodrugs. Reduction of prodrug by NTR results in the formation of hydroxylamine or amine intermediate, which upon subsequent self-immolation releases MXF.

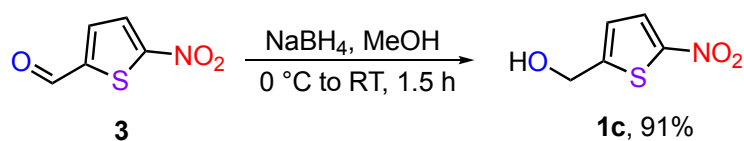
2.3. Results and discussion

2.3.1. Synthesis

The commercially available 4-nitrobenzyl alcohol **1a** was used without further purification. The synthesis of compounds **1b** and **1c** was achieved by reducing the corresponding aldehydes in the presence of sodium borohydride (NaBH₄) as outlined in Scheme 2.1 and 2.2.⁴

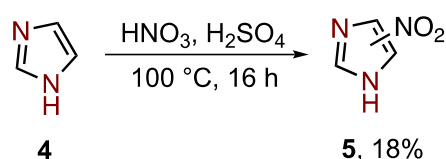
Scheme 2.1. Synthesis of **1b**



Scheme 2.2. Synthesis of **1c**

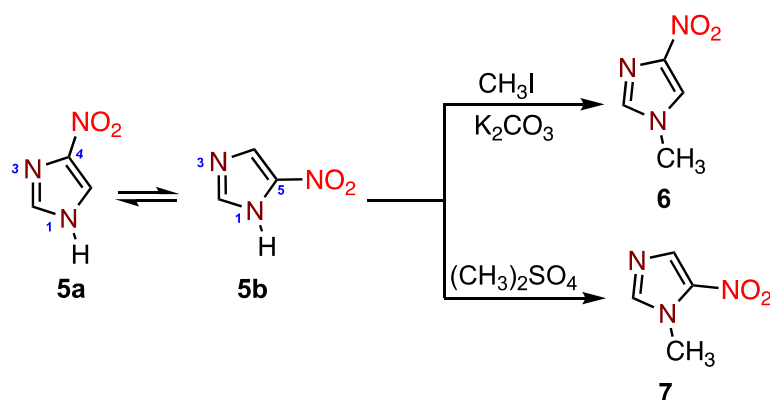
A previously published method was used for the synthesis of compound **1d**. Nitration of imidazole **4** with a nitrating mixture of nitric acid and sulphuric acid in water gave 4(5)-nitro-1*H*-imidazole **5** (Scheme 2.3).⁵

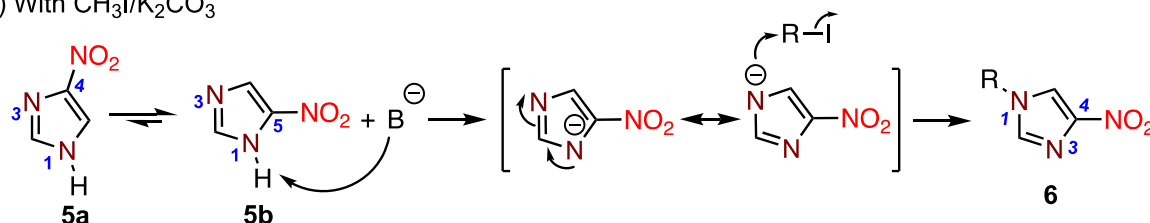
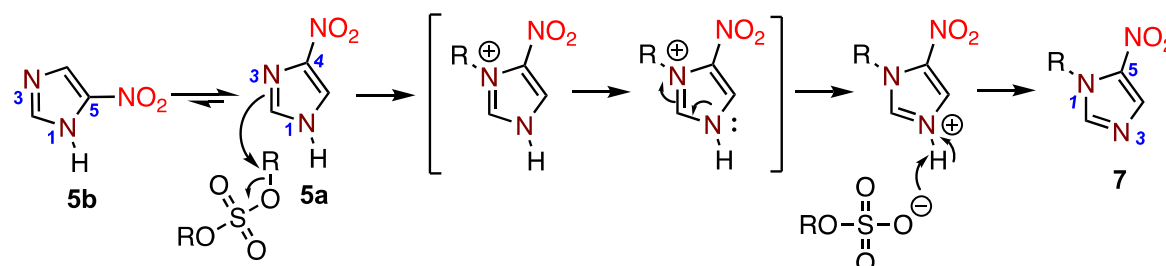
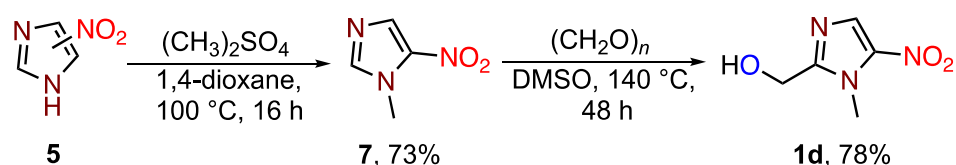
Scheme 2.3. Synthesis of 4(5)-nitroimidazole



The regioselective *N*-alkylation of **5** was found to be strongly influenced by several factors including the reaction conditions, orientation of the nitro substituent, and tautomeric nature of imidazole. Under alkaline conditions, the predominant tautomer **5b** was preferentially methylated on *N*-3 via an $\text{S}_{\text{E}}2_{\text{cB}}$ process to produce 1-methyl-4-nitroimidazole **6**. However, methylation of the major tautomeric form **5a** in the presence of dimethyl sulphate exclusively favoured the formation of 1-methyl-5-nitroimidazole **7** (Scheme 2.4 and 2.5).^{5,6}

Consistent with the above discussion and earlier findings, methylation of **5** with dimethyl sulfate in 1,4-dioxane yielded **7**.⁶ The hydroxymethylation of the latter compound was performed in a sealed tube with paraformaldehyde in DMSO to furnish **1d** in an overall 57% yield (Scheme 2.6).⁷

Scheme 2.4. Regioselective *N*-methylation of **5** with CH_3I and $(\text{CH}_3)_2\text{SO}_4$ 

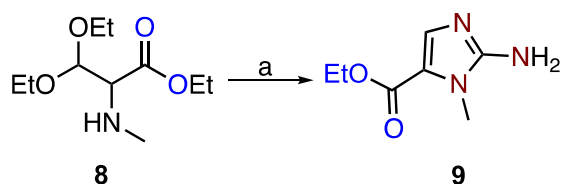
Scheme 2.5. Plausible mechanism for regioselective *N*-alkylation of **5**a) With $\text{CH}_3\text{I}/\text{K}_2\text{CO}_3$ b) With $(\text{CH}_3)_2\text{SO}_4$ Scheme 2.6. Synthesis of **1d**

Considering the wide popularity and significant clinical acceptance of 1-methyl-2-nitroimidazole groups in the development of bioreductive prodrugs and hypoxia-imaging agents,^{8–11} we next focused on the synthesis of **1e**. The landmark synthesis of **9** as a key intermediate for **1e** was initially disclosed by Cavalleri et al. (Scheme 2.7.A)¹² and later modified and patented by Matteucci et al. (Scheme 2.7.B).¹³

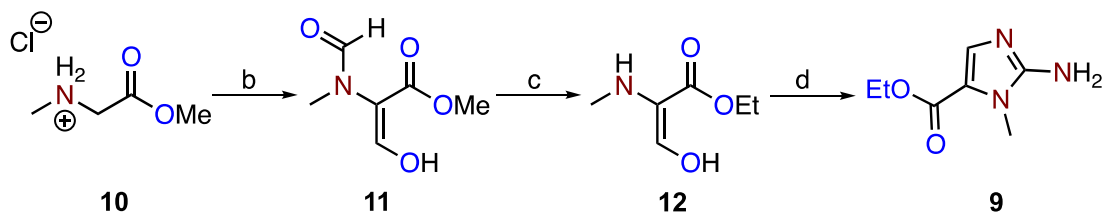
Despite its extensive use, synthesis of 1-methyl-2-nitroimidazole precursor, **9** from the hydrochloride salt of sarcosine methyl ester in high yields seems to be a challenging task and reinforces the need for scrupulous attention. Recently, O'Connor et al. reported an improved one-pot methodology for the synthesis of **9** in high yield (Scheme 2.7.C).^{10,14} This synthetic route was adopted to successfully isolate **16** by *N*-formylation of sarcosine ethyl ester **13** in the presence of ethyl formate and K_2CO_3 in THF (Scheme 2.8).^{10,15} However, the subsequent formation and isolation of enolate **14** proved futile. Further attempts aimed to obtain **15** directly without isolating enolate **14** from **13** were also unsuccessful, and consequently, an alternative route for the synthesis of **1e** from **17** was pursued.⁹

Scheme 2.7. Original and optimized synthetic routes for 2-aminoimidazole ester **9**

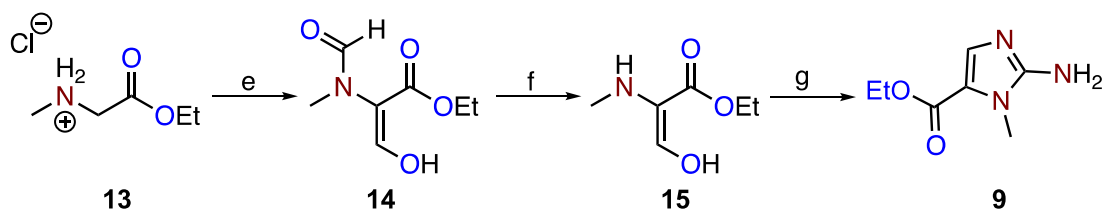
A. Original synthesis (Route 1)



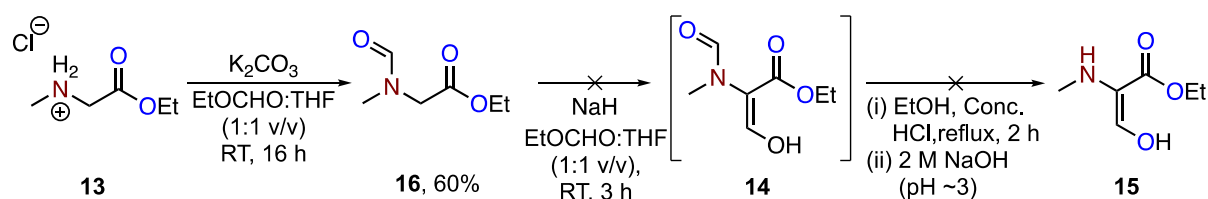
B. Revised synthesis (Route 2)



C. Improved synthesis (Route 3)



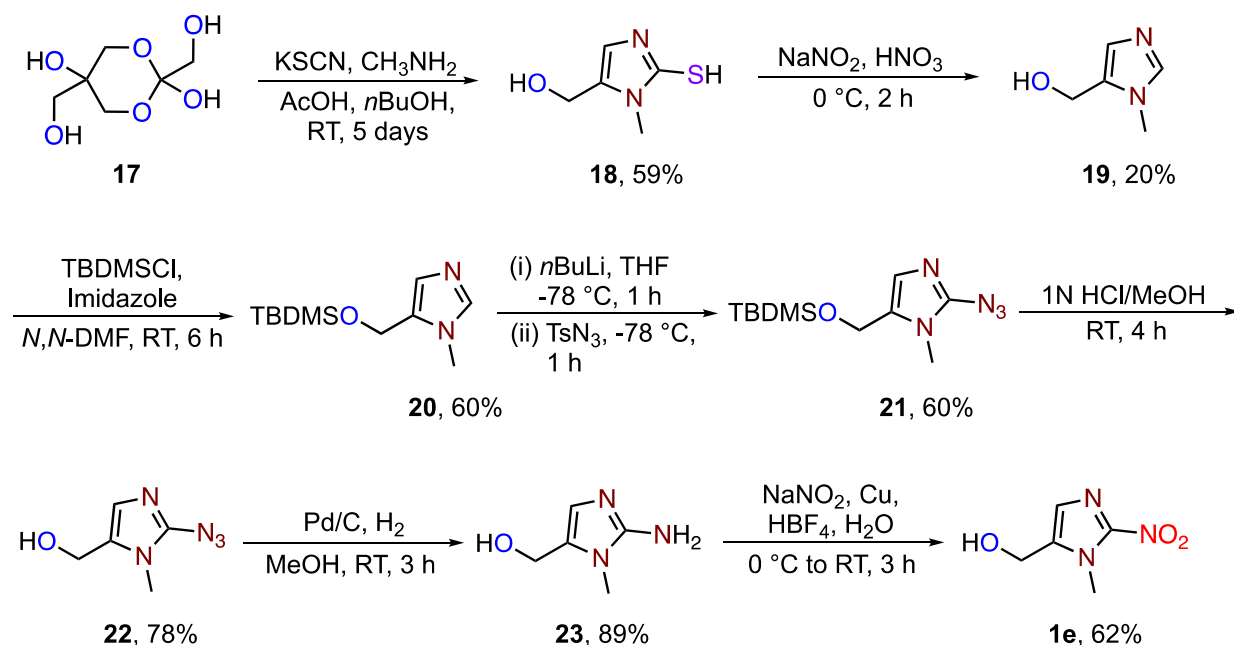
Reagents and conditions: (A) Route 1: (a) HCl, NH₂CN, 60 °C, 2 h. (B) Route 2: (b) EtOCHO, NaH, 16 h; (c) EtOH, conc. HCl, 90 °C, 2 h; (d) AcOH (aq.), NaOAc, NH₂CN, 100 °C, 1.5 h. (C) Route 3: (e) EtOCHO, THF, NaH, 3 h; (f) EtOH, conc. HCl, 90 °C, 2 h; (g) EtOH, H₂O, NH₂CN, pH 3, 100 °C, 1.5 h.

Scheme 2.8. Attempted synthesis of **15**

The route proceeds through Marckwald cyclization of dihydroxyacetone dimer **17** with KSCN and methylamine to generate **18** in 59% yield.^{16,17} Following a modified reported protocol, NaNO₂ mediated desulfurization of **18** under acidic conditions led to a lower yield (6%) of **19**.¹⁷ Further investigation of this step demonstrated that the slow addition of NaNO₂ to the reaction mixture over 30 min significantly improved the yield of **19**. The protection of the resultant alcohol **19** as silyl ether **20**,¹⁸ followed by selective lithiation at the C-2 position and

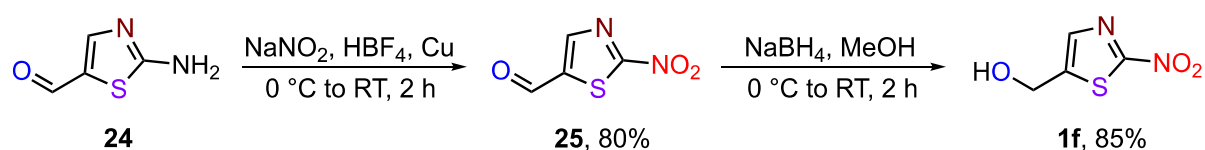
subsequent reaction with TsN_3 , eventually afforded **21**. This azide derivative was deprotected with HCl/MeOH to alcohol **22** and later hydrogenated with Pd/C to provide **23**. Finally, compound **1e** was obtained in 62% yield by diazotization of **23** (Scheme 2.9).⁹

Scheme 2.9. Synthesis of **1e**



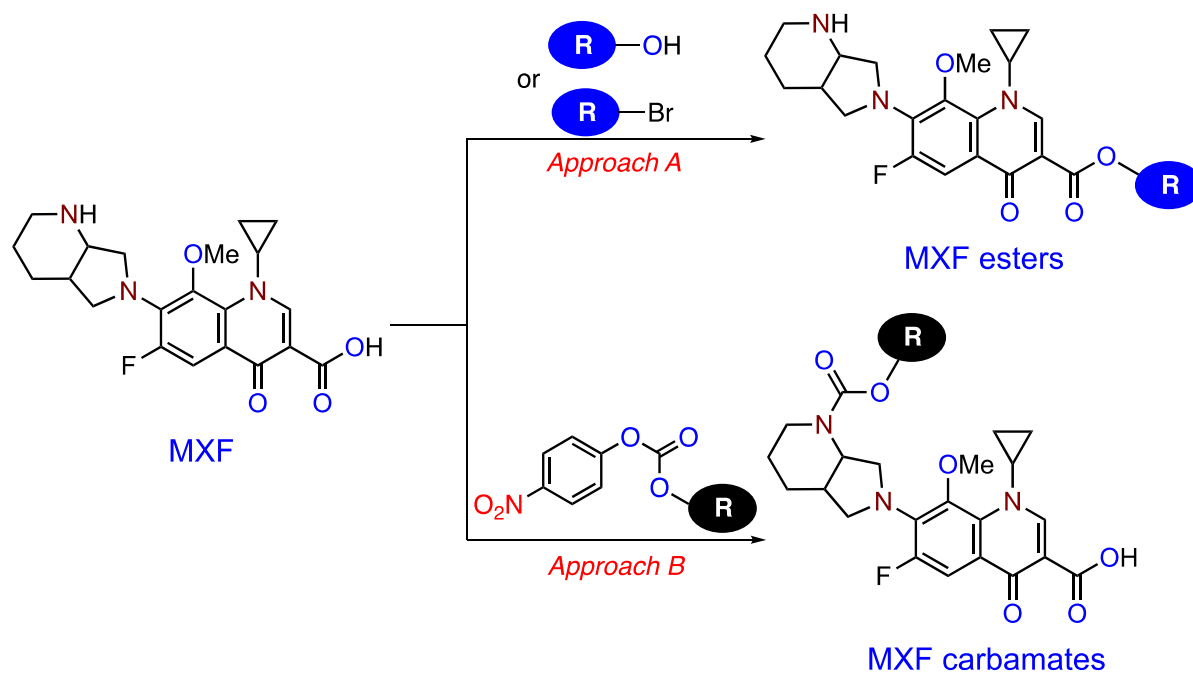
To explore the quest of utilizing 2-nitrothiazole group as a bioreductive trigger, we set out to synthesize **1f** as outlined in Scheme 2.10. The aromatic amine **24** was diazotized, and reacted with nitrite in the presence of catalytic amount of Cu to generate **25**, which was subsequently reduced by NaBH_4 to generate alcohol **1f** in an overall yield of 68%.^{19,20}

Scheme 2.10. Synthesis of **1f**

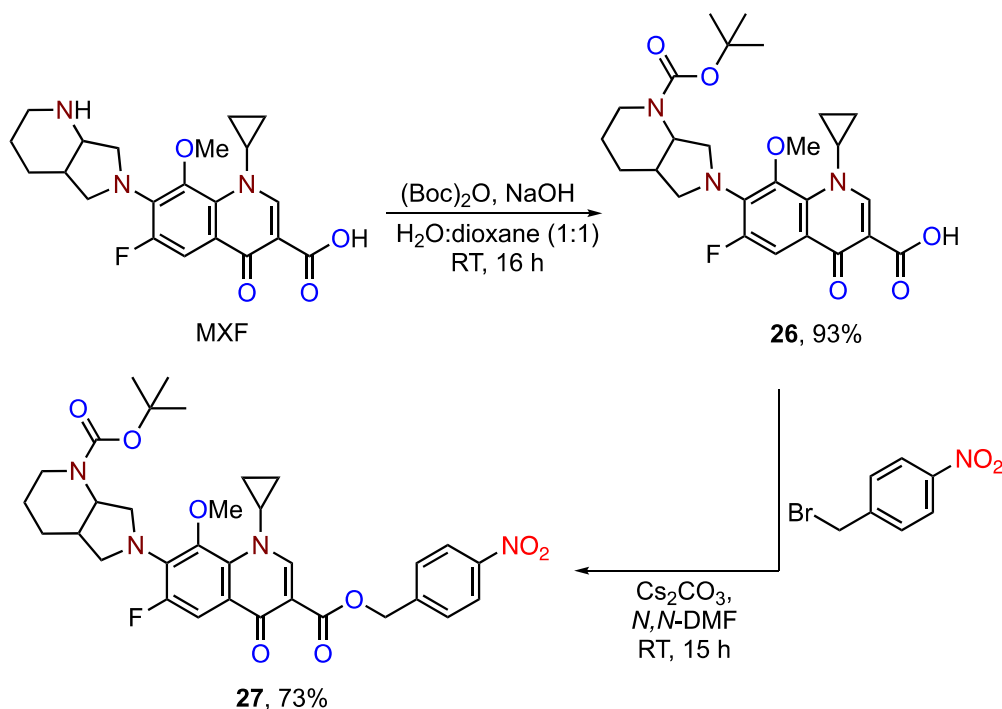


With various bioreductive building blocks in hand, two different approaches have been tried to synthesize MXF prodrugs. The first approach enables facile access to esters either by nucleophilic substitution of aryl bromides with reactive carboxylate or condensation of carboxylic acid with nitroaryl alcohols. The second approach entailed the construction of carbamate prodrugs through base-catalyzed coupling of MXF with requisite carbonates (Scheme 2.11).

Scheme 2.11. Synthetic approaches to generate ester and carbamate prodrugs of MXF



N-Boc protection of the secondary amine of MXF using $(\text{Boc})_2\text{O}$ delivered **26** with a readily modifiable carboxylate functionality.²¹ The conversion of the resulting intermediate *in situ* to a highly reactive cesium carboxylate²², followed by nucleophilic substitution with 4-nitrobenzyl bromide, furnished **27** in 73% yield (Scheme 2.12).

Scheme 2.12. Synthesis of **27**

Next, access to a series of esters **28-32** was gained through HBTU-mediated esterification of **26** with various alcohols **1b-1f** (Scheme 2.13 and Table 2.1).

Scheme 2.13. Synthesis of **28-32**

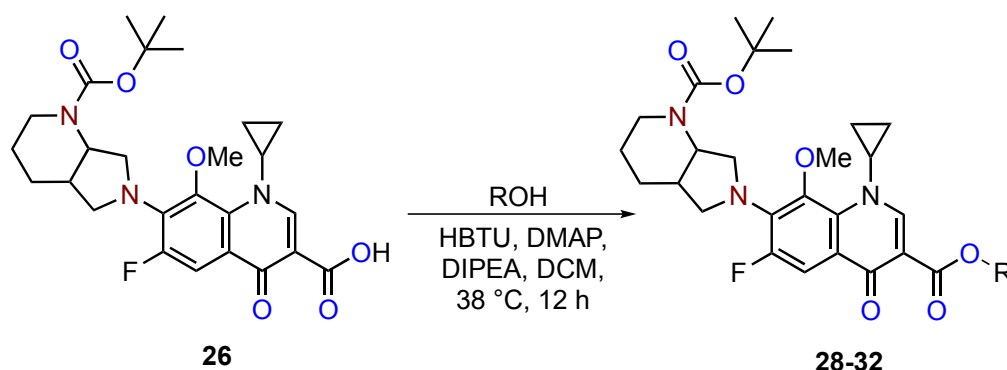
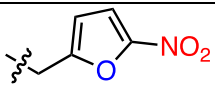
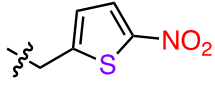
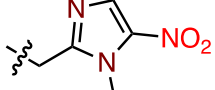
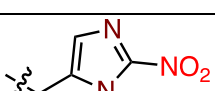
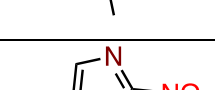


Table 2.1. Synthesis of *N*-boc protected nitroheterocyclic esters of MXF

| Entry | R | Alcohol | Ester | % Yield |
|-------|---|-----------|-----------|---------|
| 1 |  | 1b | 28 | 61 |
| 2 |  | 1c | 29 | 60 |
| 3 |  | 1d | 30 | 85 |
| 4 |  | 1e | 31 | 81 |
| 5 |  | 1f | 32 | 78 |

Chemoselective *N*-Boc deprotection was next attempted under acidic conditions using TFA. Given that the carboxylester group is also labile like *t*-butyl ester to acid-catalyzed hydrolysis, the optimal conditions were investigated, which favoured a maximal yield of compound accompanied by minimal non-specific hydrolysis. Initial screening for selective *N*-Boc deprotection was performed using **27** as a model compound, with varied equivalents of TFA. It was found that lower equivalents of TFA proved optimal for the quantitative formation of **33** (Scheme 2.14). Furthermore, TLC analysis revealed that *N*-Boc deprotection of **27** in the presence of 100 equivalents of TFA at 0 °C successfully delivered **33** in quantitative yield over

a period of 6 h (Figure 2.3). Utilizing the optimized conditions, the reactions of **27-32** with TFA proceeded smoothly to give desired products **33-38** in excellent yields (Figure 2.4).

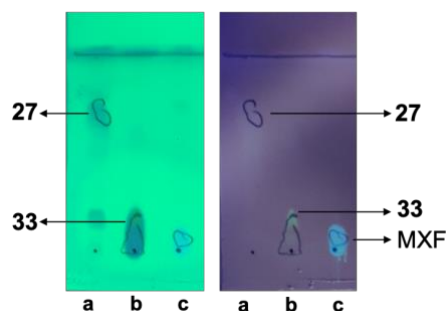
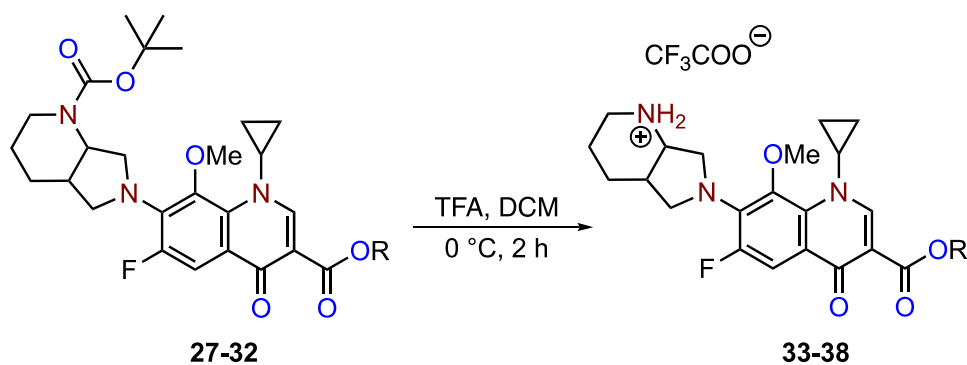


Figure 2.3. Monitoring the formation of **33** following *N*-Boc deprotection of **27** with TFA by TLC using a 1:9 MeOH:CHCl₃ solvent system. The TLC was visualized under a UV chamber (*left panel*: 250 nm and *right panel*: 365 nm) after 6 h with (a) authentic **27**, (b) **27** + TFA (100 eq.), and (c) authentic MXF.

Scheme 2.14. Synthesis of **33-38**



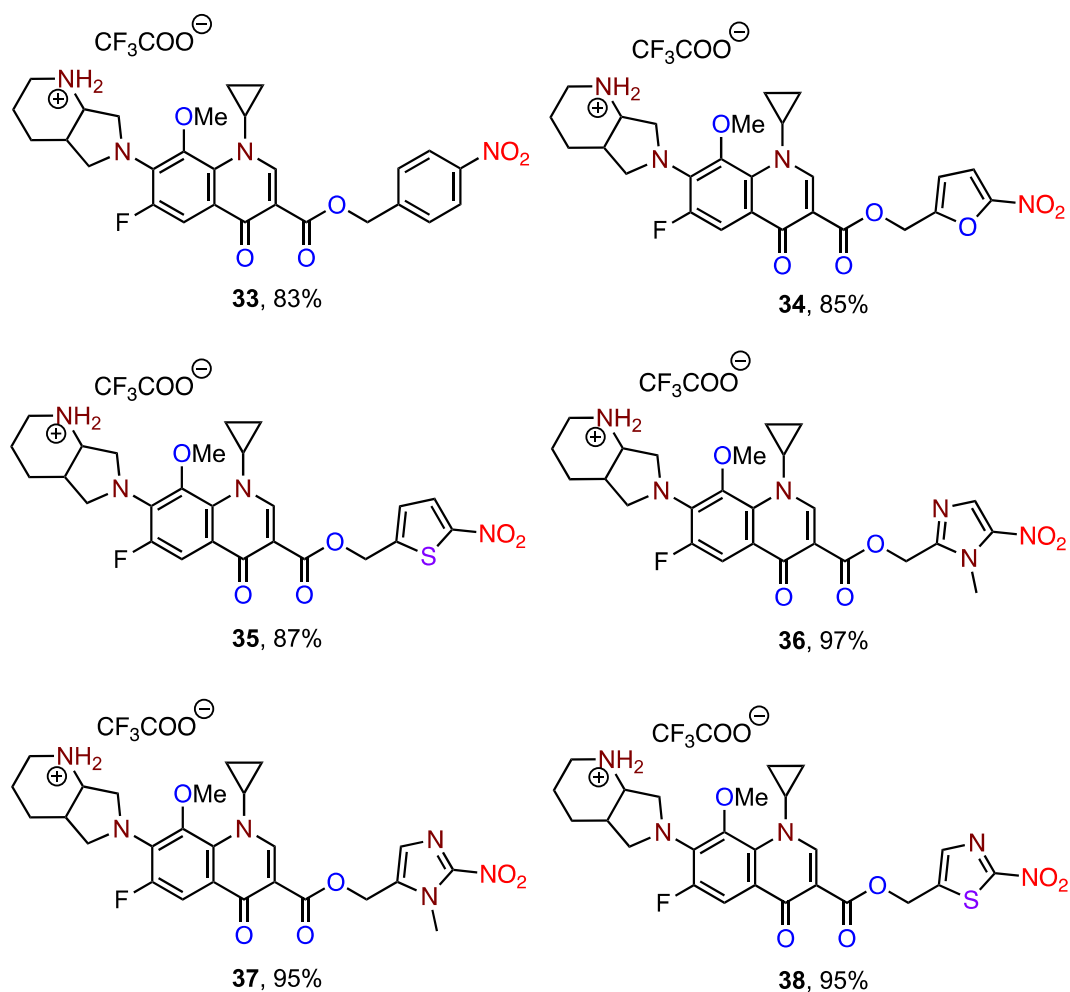


Figure 2.4. Structures of **33-38**

The two structurally closely related compounds lacking nitro groups, **41** and **42**, were synthesized and used as negative controls (Scheme 2.15). These analogues were obtained in a two-step protocol following the scheme outlined below through coupling of **26** with alcohols **1g** and **1h**, followed by subsequent *N*-*boc* deprotection with the resultant analogues with TFA (Table 2.2).

Scheme 2.15. Synthesis of negative control compounds

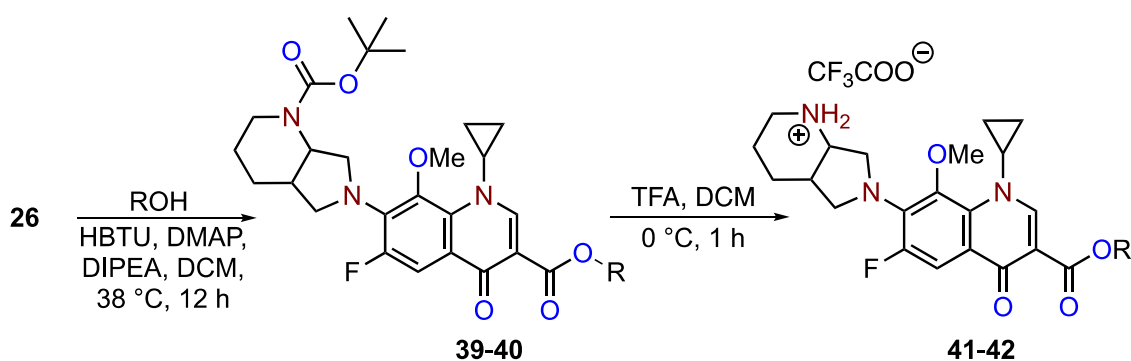
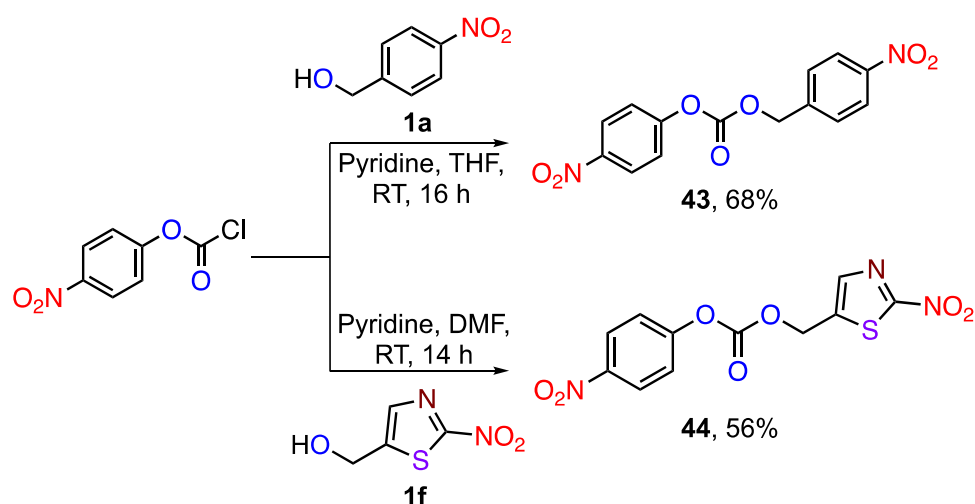


Table 2.2. Synthesis of negative control compounds

| Entry | R | Alcohol | Ester | % Yield | Ester | % Yield |
|-------|---|-----------|-----------|---------|-----------|---------|
| 1 | | 1g | 39 | 65 | 41 | 85 |
| 2 | | 1h | 40 | 55 | 42 | 83 |

As outlined in Scheme 2.16, base-promoted activation of alcohols **1a** and **1f** with 4-nitrophenyl chloroformate delivered carbonates **43**²³ and **44**, respectively, in moderate yields. The resulting mixed stable carbonates were isolated. The reaction of these carbonates with MXF in the presence of triethylamine provided **45** and **46** in good yields following the elimination of 4-nitrophenyl moiety (Scheme 2.17 and Table 2.3).

Scheme 2.16. Synthesis of 4-nitrophenyl mixed carbonates



Scheme 2.17. Synthesis of carbamate derivatives of MXF

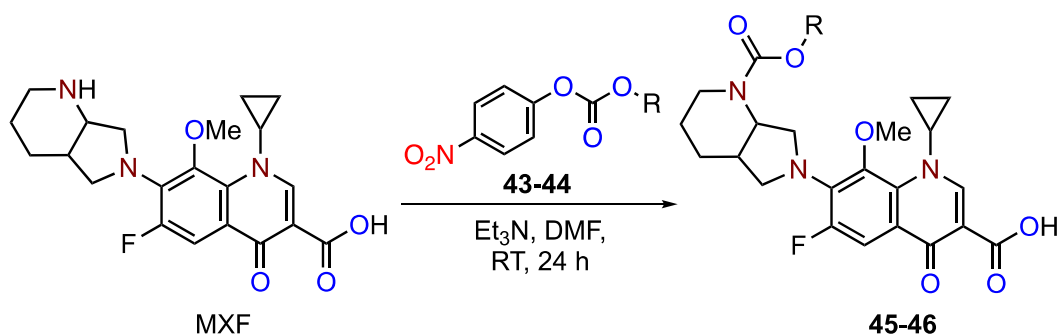


Table 2.3. Synthesis of nitro(hetero)cyclic carbamates of MXF

| Entry | R | Carbonates | Carbamates | % Yield |
|-------|---|------------|------------|---------|
| 1 | | 43 | 45 | 56 |
| 2 | | 44 | 46 | 62 |

The purity of the prodrugs **33-38**, **45** and **46** were found to be >95% pure, as determined by HPLC analysis. The retention times of the prodrugs are shown in Table 2.4 and HPLC traces are included in the experimental section 2.5.3.

Table 2.4. HPLC analysis

| Entry | Prodrug | Retention time, min |
|-------|-----------|---------------------|
| 1 | 33 | 3.0 |
| 2 | 34 | 3.0 |
| 3 | 35 | 3.0 |
| 4 | 36 | 3.0 |
| 5 | 37 | 2.9 |
| 6 | 38 | 3.0 |
| 7 | 45 | 11.4 |
| 8 | 46 | 10.8 |

2.3.2. Physicochemical properties

Inspired by the peculiar physicochemical space occupied by anti-tubercular drugs, we determined a variety of molecular descriptors using the SwissADME web tool²⁴ and compared their properties with those of MXF (Table 2.5). As anticipated, the molar refractivity (MR), topological polar surface area (TPSA) and partition coefficient (log P) increased with increasing molecular weight of the MXF derivatives (Figure 2.5).

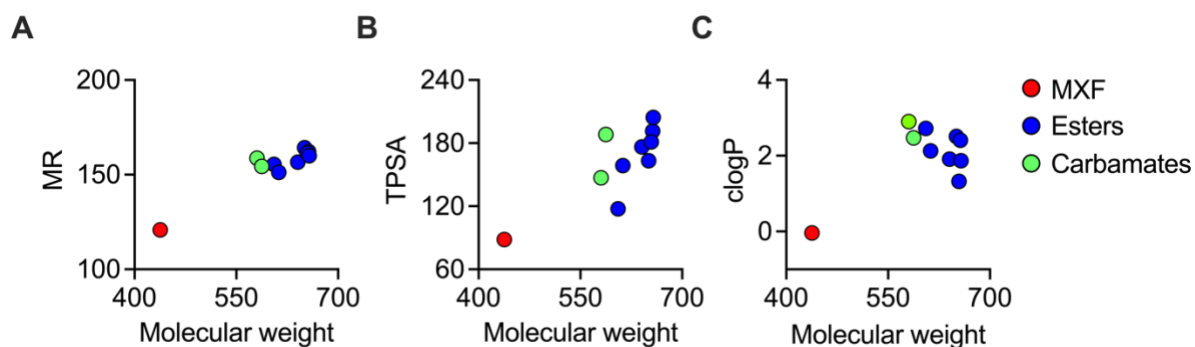


Figure 2.5. Plot of (A) MR vs molecular weight, (B) TPSA vs molecular weight and (C) clogP vs molecular weight of MXF and its prodrugs (esters and carbamates)

Table 2.5. Physicochemical descriptors of NTR-MXF prodrugs

| Entry | Cmpd /Drug | Mol. wt. | MR | TPSA | clogP | | | |
|-------|------------|----------|-------|-------|------------|-------|-----------|----------|
| | | | | | Silicos-IT | WLogP | Consensus | ChemDraw |
| 1 | MXF | 437.8 | 120.8 | 88.3 | 2.23 | -2.06 | -0.04 | -0.49 |
| 2 | 33 | 650.5 | 164.3 | 163.3 | 2.04 | 2.91 | 2.51 | 3.0 |
| 3 | 34 | 640.5 | 156.6 | 176.4 | 1.42 | 2.51 | 1.91 | 2.08 |
| 4 | 35 | 656.6 | 162.2 | 191.5 | 2.67 | 2.98 | 2.41 | 2.55 |
| 5 | 36 | 654.5 | 161.4 | 181.1 | 0.47 | 1.65 | 1.32 | 0.72 |
| 6 | 37 | 654.5 | 161.4 | 181.1 | 0.47 | 1.65 | 1.32 | 0.72 |
| 7 | 38 | 657.5 | 160.0 | 204.4 | 2.1 | 2.37 | 1.87 | 1.05 |
| 8 | 41 | 605.5 | 155.5 | 117.5 | 4.2 | 3.01 | 2.72 | 2.82 |
| 9 | 42 | 612.5 | 151.2 | 158.6 | 4.25 | 2.46 | 2.13 | 0.97 |
| 10 | 45 | 580.5 | 158.7 | 147.1 | 0.95 | 3.77 | 2.9 | 4.46 |
| 11 | 46 | 587.5 | 154.4 | 188.2 | 1.01 | 3.23 | 2.47 | 2.61 |

Mol. wt. = Molecular weight; MR = molar refractivity; TPSA = total polar surface area; clogP = calculated partition coefficient determined by (a) Silicos-IT = an hybrid method relying on 27 fragments and 7 topological descriptors to calculate logP; (b) WLogP = atomistic method based on the fragmental system of Wildman and Crippen; (c) Consensus = arithmetic mean of the values predicted by the five methods (XLogP3, WLogP, Silicos-IT, MLogP and iLogP)²⁴; and (d) using ChemDraw 19.1.

2.3.3. Electrochemistry

To measure the intrinsic potential required to reduce the nitroaromatic functionality of the prodrugs, their electrochemical behaviour was investigated using cyclic voltammetry (Figure 2.6). Experiments were performed under an inert atmosphere on a typical three-electrode cell with glassy carbon as the working electrode, platinum and Ag/AgCl as the counter and reference electrodes respectively. All the potentials were referenced to Ferrocene/Ferrocenium (Fc/Fc⁺) redox couple as an internal standard. The onset potentials were measured using 0.5 mM solutions of MXF derivatives in DMSO containing 0.1 M TBAP as a supporting electrolyte in anhydrous acetonitrile.

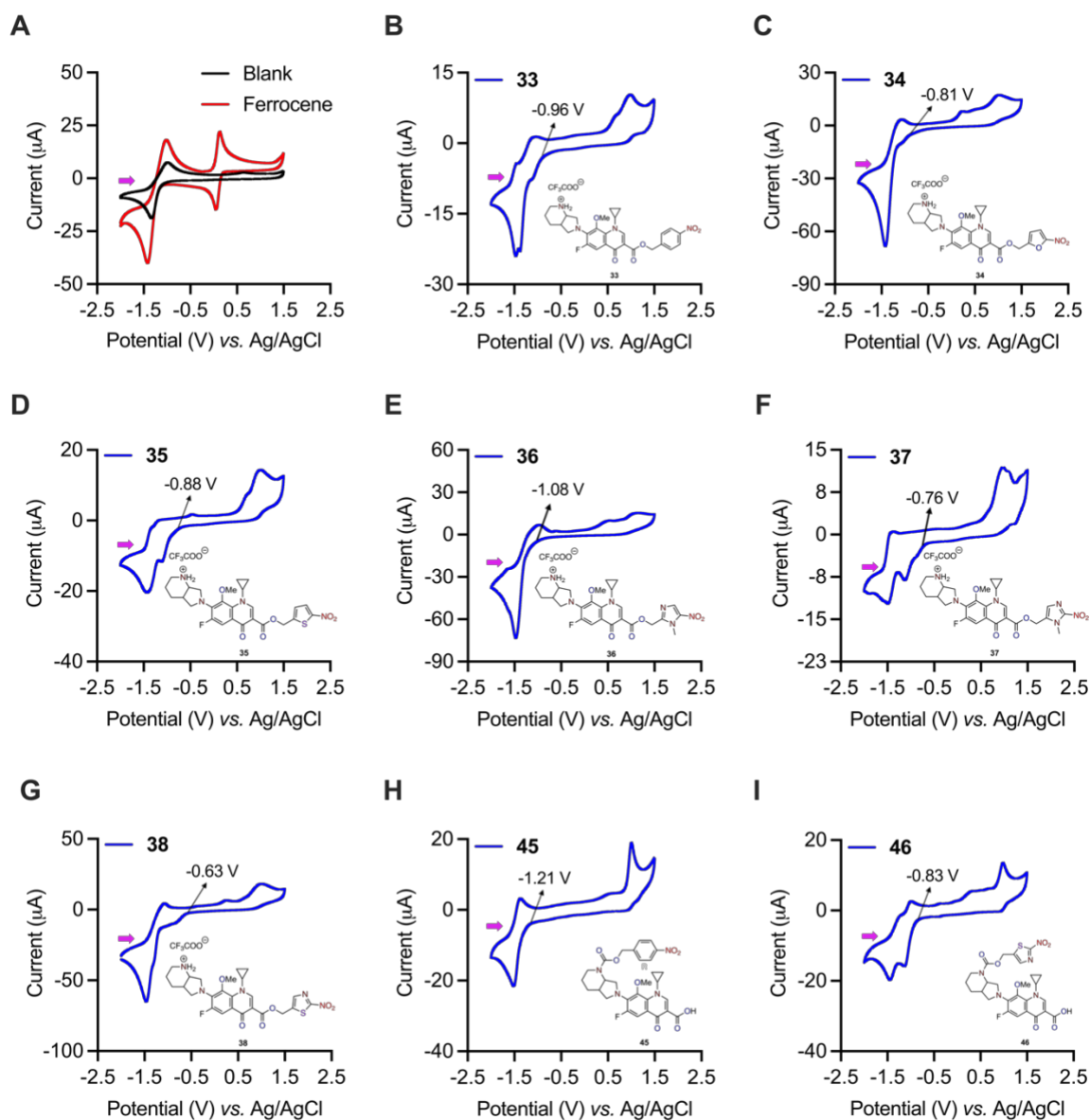
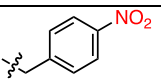
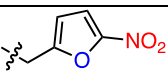
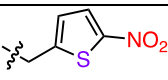
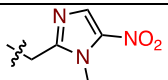
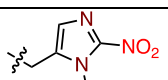
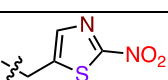
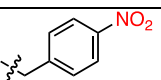
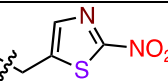


Figure 2.6. Cyclic voltammograms of (A) controls (blank electrolyte and ferrocene), (B) **33**, (C) **34**, (D) **35**, (E) **36**, (F) **37**, (G) **38**, (H) **45** and (I) **46** recorded in argon saturated 0.1 M TBAP solution in ACN with an initial positive scan (shown by a purple arrow) at a sweep rate of 100 mV/s, sample interval of 1 mV, quiet time of 2 s, and a sensitivity of 1×10^{-5} A/V. The final concentration of analytes was 0.5 mM. The onset reduction potentials are indicated by arrows in the voltammograms.

Owing to the reversibly redox active behaviour, Fc/Fc^+ exhibited a characteristic “duck-shaped” cyclic voltammogram showing cathodic and anodic peaks with a peak current ratio (i_{pa}/i_{pc}) close to unity (Figure 2.6.A).²⁵ On the contrary, a well-defined anodic peak was not observed, indicating an irreversible reduction of **33** at an onset potential of -0.96 V referenced against Fc/Fc^+ (Figure 2.6.B). A similar irreversible cyclic voltammetric response was observed for other prodrugs **34–38**, **45**, and **46** (Figure 2.6.C-I). The onset reduction potential

for prodrug **38** at -0.63 V was significantly lower (Table 2.7., entry 6) than other prodrugs tested (Table 2.7. entries 1-5, 7, and 8), supporting that the reduction of 2-nitrothiazole moiety is more thermodynamically favoured when compared with other similar nitroaryl groups. Furthermore, a moderately good linear correlation between the experimentally determined values and the computed reduction potentials was found (data provided by Dr. SharathChandra M., Prof. Jennifer Hirschi Lab, Department of Chemistry, Binghamton University, New York, U.S.A.) (Table 2.7. and Figure 2.7).

Table 2.7. Experimentally and computationally derived reduction potentials of prodrugs

| Entry | Prodrug | R | Onset potential (V) ^a | Computed E° (V) ^b |
|-------|-----------|---|----------------------------------|------------------------------|
| 1 | 33 |  | -0.96 | -1.02 |
| 2 | 34 |  | -0.81 | -0.89 |
| 3 | 35 |  | -0.88 | -0.86 |
| 4 | 36 |  | -1.20 | - |
| 5 | 37 |  | -0.95 | -0.99 |
| 6 | 38 |  | -0.63 | -0.53 |
| 7 | 45 |  | -1.21 | -1.02 |
| 8 | 46 |  | -0.83 | -0.53 |

^aOnset reduction potentials were measured using cyclic voltammetry and are reported in volts (V); ^bcomputed reduction potentials are reported in volts (V)

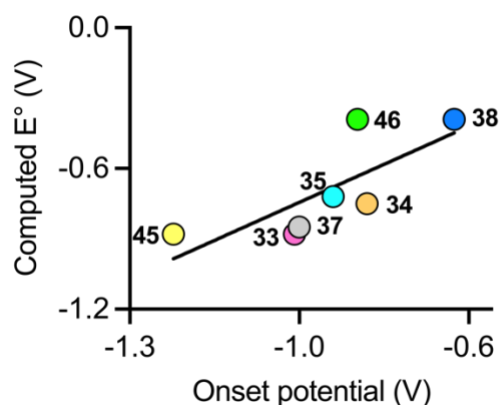


Figure 2.7. Comparison of the experimentally measured onset potentials with the computationally derived reduction potentials. A moderately good correlation ($R^2 = 0.58$) was observed between the experimental and computed reduction values.

2.3.4. Photophysical properties

The spectral properties of the ester and carbamate prodrugs were investigated to determine the release of MXF following the reductive activation of prodrugs. Consistent with prior findings, MXF a characteristic absorption band centered at 289 nm in buffer (Figure 2.8.A). Similarly, MXF exhibited a distinct fluorescence response, with emission maxima at 488 nm upon excitation at 289 nm (Figure 2.8.B).²⁶ In contrast, prodrugs were less fluorescent and displayed a weak emission band at 488 nm owing to the MXF fluorescence quenching effect by electron-withdrawing nitroaromatic functionality (Figure 2.8.C). Consistent with this model, control compounds **41** and **42** were more fluorescent than their nitro counterparts, likely due to the absence of the nitroaryl group. Hence, we performed further *in vitro* studies to inspect the release of MXF from prodrugs under chemoreductive conditions by monitoring fluorescence.

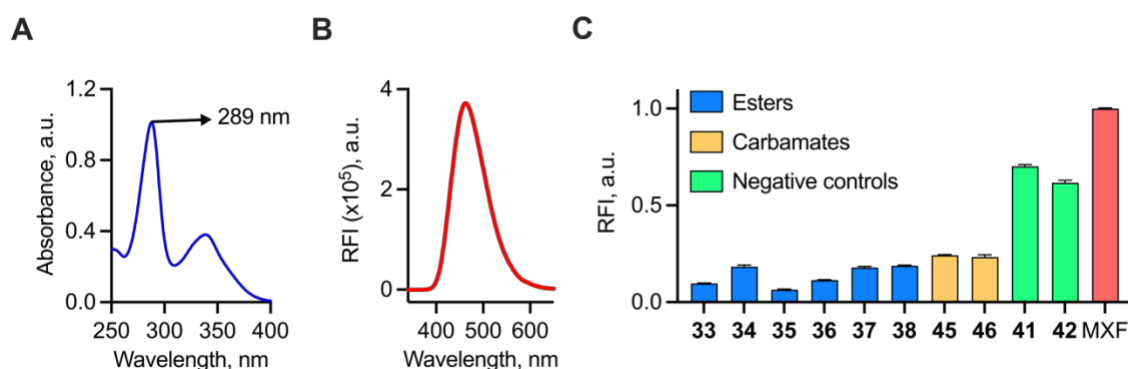


Figure 2.8. (A) Absorbance spectra and (B) Fluorescence emission spectra of MXF (10 μM , $\lambda_{\text{ex}} = 289$ nm) in phosphate buffer (pH 7.4, 10 mM) at 37 $^{\circ}\text{C}$. MXF exhibits a strong emission peak at 488 nm. (C) Fluorescence response of MXF prodrugs (10 μM , $\lambda_{\text{ex}} = 289$ nm; $\lambda_{\text{em}} = 488$ nm) in phosphate buffer (pH 7.4, 10 mM) at 37 $^{\circ}\text{C}$.

2.3.5. Chemoreduction

To evaluate the sensitivity to reduction of nitroaryl groups under milder and physiologically relevant bioreductive conditions, prodrugs were tested in the presence of sodium dithionite ($\text{Na}_2\text{S}_2\text{O}_4$)²⁷ and the fluorescence response was recorded after 15 min. The prodrug was mildly fluorescent in the absence of the reductant. However, the addition of a reducing agent led to a significant increase in the fluorescence signal ($\lambda_{\text{ex}} = 289 \text{ nm}$ and $\lambda_{\text{em}} = 488 \text{ nm}$) attributable to generation of MXF (Figure 2.9). This suggests that the chemical reduction and subsequent fragmentation of nitroaryl moieties, including 2-nitrothiazole moiety effectively triggers the release of MXF from the respective prodrugs. On the contrary, addition of the reducing agent did not elicit fluorescence in the negative control compounds, **41** and **42**. This is understandable as the elimination of MXF is not feasible in **41** and **42** due to the absence of a nitro group. Overall, these studies indicate that the nitro group is crucial for reductive activation of prodrugs to generate MXF.

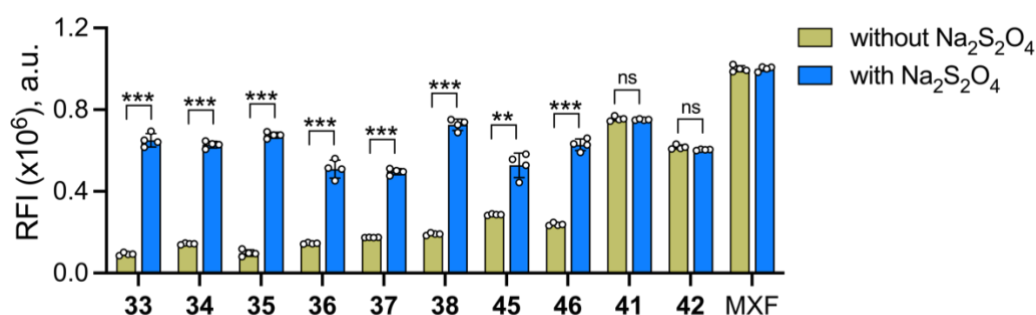


Figure 2.9. Screening and evaluation for release of MXF following sodium dithionite ($\text{Na}_2\text{S}_2\text{O}_4$) induced chemoreduction of compounds (10 μM) in $\text{H}_2\text{O}:\text{MeOH}$ (1:1) in a fluorescence-assay ($\lambda_{\text{ex}} = 289 \text{ nm}$; $\lambda_{\text{em}} = 488 \text{ nm}$). All the data represent mean \pm SD from quadruplicate experiments performed in triplicate. p values were determined by student's two-tailed unpaired parametric t -test relative to untreated control. (** $p \leq 0.01$, *** $p \leq 0.001$ and ns indicate not significant).

To determine the kinetics of MXF release from the prodrugs, fluorescence at $\lambda_{\text{em}} 488 \text{ nm}$ was monitored over time. Dithionite-induced reduction was rapid even with 250 eq. (2.5 mM), reaching a plateau in relative fluorescence intensity within 5 min. Compared to the other derivatives, prodrug **38** exhibited the highest fluorescence response (Figure 2.10). The 2-nitroimidazole analogue, which is widely utilised in hypoxia activated prodrugs, was found to be considerably less effective than the 2-nitrothiazole derivative (Figure 2.11.A) Next, experiments were conducted to evaluate the degree of sensitivity to dithionite at different concentrations. The 2-nitrothiazole prodrug **38** provided maximal fluorescence even at the

lowest concentration of dithionite (250 eq., 2.5 mM) (Figure 2.11.B). Overall, these results clearly suggest that 2-nitrothiazole tethered MXF prodrug with the lowest reduction potential demonstrated superior sensitivity and enhanced response in an unprecedented fashion towards milder reducing agents such as dithionite.

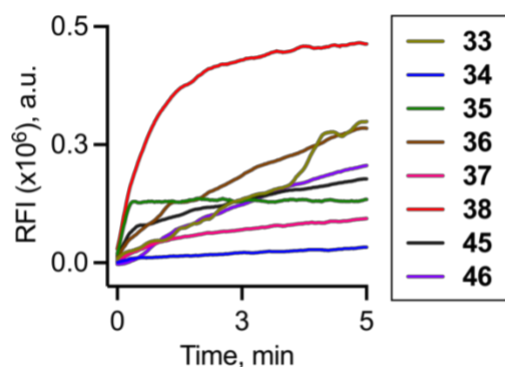


Figure 2.10. Kinetics of dithionite-dependent reduction of NTR-MXF prodrugs (10 μ M) in H₂O:MeOH (1:1) by measuring fluorescence attributable to MXF ($\lambda_{\text{ex}} = 289$ nm; $\lambda_{\text{em}} = 488$ nm) at a time interval of 1 s. The data was smoothed with second order function in GraphPad Prism 9.0 and the representative traces are shown.

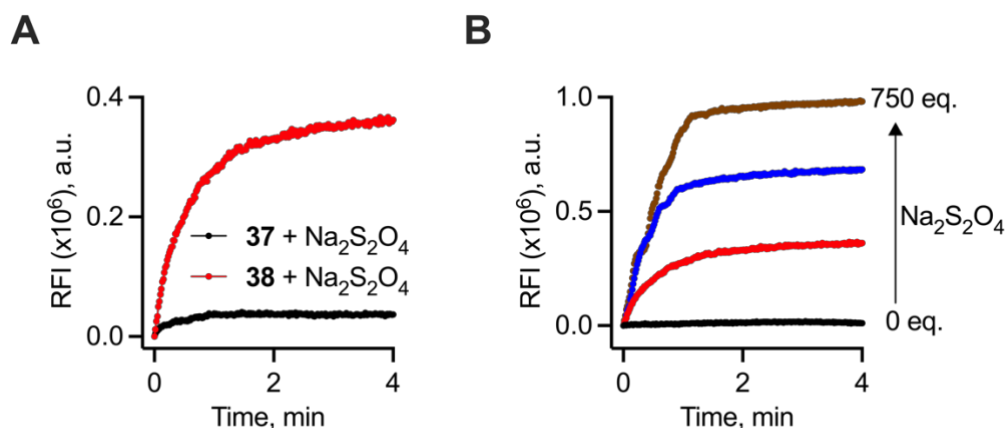


Figure 2.11. Monitoring time-dependent release kinetics of MXF following (A) chemical reduction with 250 eq. (2.5 mM) of sodium dithionite ($\text{Na}_2\text{S}_2\text{O}_4$) from **37** and **38** and (B) with **38** and various equivalents (0, 250, 500 and 750 eq.; 0, 2.5, 5 and 7.5 mM) of sodium dithionite.

To ascertain the reductive activation of prodrugs and subsequent release of MXF, a fluorescence-based experiment was next carried out on **33** in the presence of Zn dust and ammonium formate ($\text{Zn}/\text{HCOONH}_4$) in H₂O:MeOH (1:1) as the reductant system.²⁸ Under these conditions, cleavage of prodrugs provided MXF in considerably higher yields than dithionite-induced chemoreduction (Figure 2.12.A). Concurrent with these results, a time-

dependent increase in fluorescence signal corresponding to the formation of MXF from **33** was observed under these conditions over a period of 90 min (Figure 2.12.B). In agreement with the former findings, the addition of the reducing agent did not elicit fluorescence in the negative control, **41**.

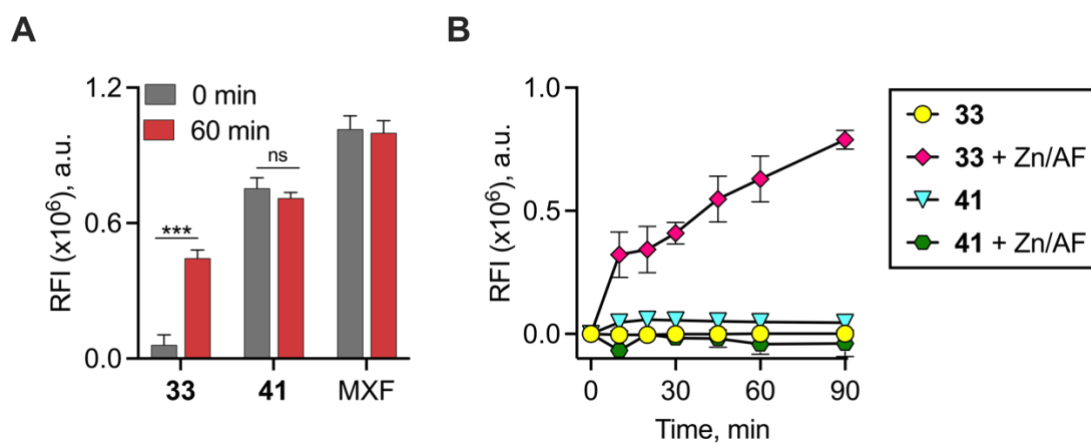


Figure 2.12. (A) Evaluating the release of MXF from **33** and **41** following Zn/HCOONH₄ mediated chemoreduction of compounds (10 μ M) in H₂O:MeOH (1:1) by monitoring fluorescence ($\lambda_{\text{ex}} = 289$ nm; $\lambda_{\text{em}} = 488$ nm). Data represent mean \pm SD from quadruplicate experiments performed in triplicate. *p* values were determined by student's two-tailed unpaired parametric *t*-test relative to *t* = 0 min. (***) *p* \leq 0.001 and ns indicate not significant). (B) Investigating the time-dependent release of MXF from **33** following chemical reduction with Zinc/ammonium formate (Zn/HCOONH₄).

Following this assessment, reduction products of **33** were analysed using HPLC. As shown in Figure 2.13, the peak corresponding to **33** decreased over time. This was accompanied by the appearance of a new peak at 3.7 min corresponding to MXF after 2 h of incubation. As expected, HPLC analysis revealed that benzyl substituted analogue **41** was barely consumed without MXF formation during the reaction. Collectively, these findings are consistent with the proposed mechanism of reduction of electron-withdrawing nitro group to corresponding electron-rich hydroxylamine or amine intermediate, which subsequently undergoes fragmentation *via* 1,6-elimination to release MXF (Scheme 2.18).

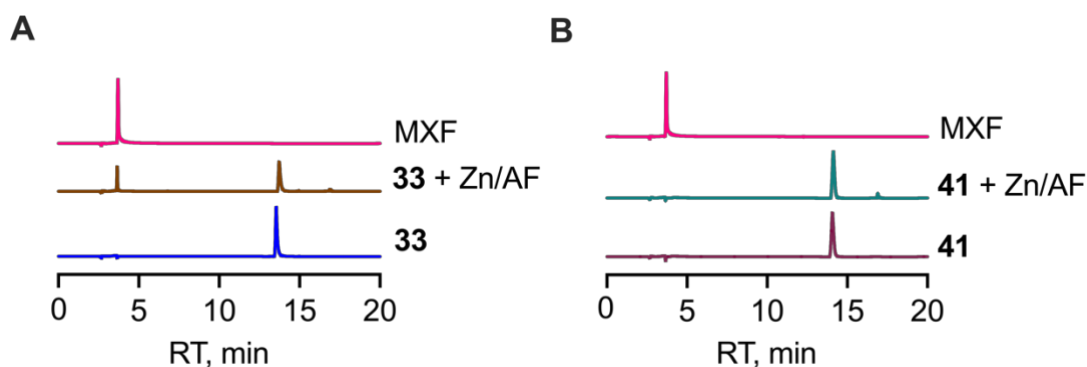
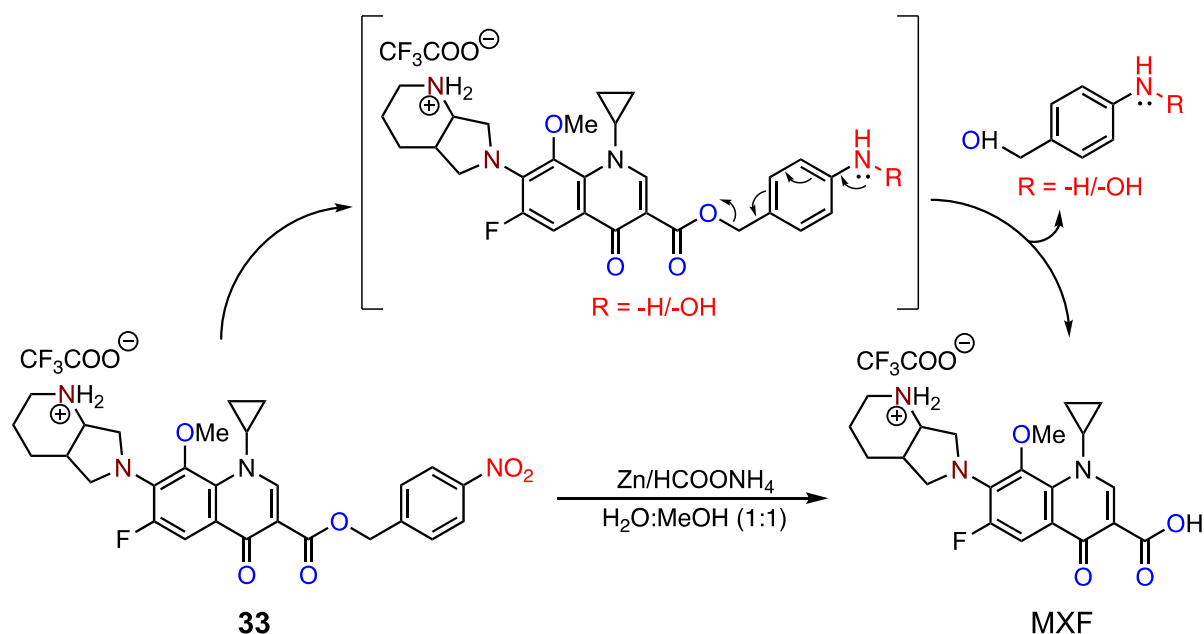


Figure 2.13. HPLC traces of chemoreduction of compounds (A) **33** and (B) **41** (10 μ M) in the absence and presence of Zn dust and ammonium formate in H₂O:MeOH (1:1). MXF (10 μ M) was used as a positive control. The signal was detected using the UV detector set at 280 nm.

Scheme 2.18. Mechanism of Zn-dependent chemoreduction of **33** to release MXF



Next, the propensity of prodrugs **34-38**, **45**, and **46** to undergo reduction and release of MXF was tested by measuring fluorescence after the addition of reducing agent. It was found that **37**, **38**, and **46** exhibited a significant fluorescence enhancement relative to the other prodrugs (Figure 2.14). This suggests that chemical reduction and subsequent fragmentation of 2-nitroimidazole and 2-nitrothiazole moiety efficiently triggers the release of MXF from these prodrugs.

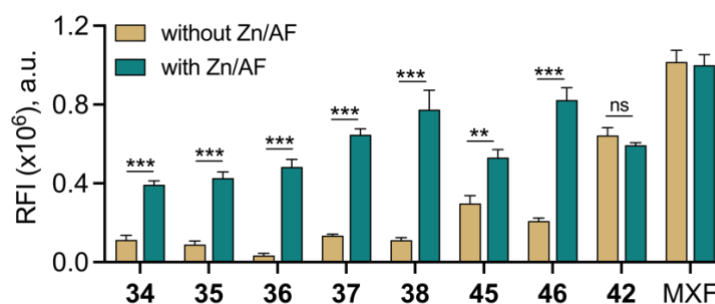


Figure 2.14. Screening and evaluation for release of MXF following Zinc/ammonium formate ($\text{Zn}/\text{HCOONH}_4$) based mediated chemoreduction of compounds ($10 \mu\text{M}$) in $\text{H}_2\text{O}:\text{MeOH}$ (1:1) in a fluorescence-assay. All the data represent mean \pm SD from quadruplicate experiments performed in triplicate. p values were determined by student's two-tailed unpaired parametric t -test relative to untreated control. (** $p \leq 0.01$, *** $p \leq 0.001$ and ns indicate not significant).

To identify the optimal nitroheteroaryl substrate, a comparative MXF release profile from **37** and **38** was studied. Interestingly, the 2-nitrothiazole ester prodrug displayed identical behaviour to **37** in Zn-mediated chemoreductive condition (Figure 2.15). Altogether, these results establish that 2-nitrothiazole tethered MXF prodrug undergoes chemoreduction similar to the 2-nitroimidazole based prodrug to release active antibiotic.

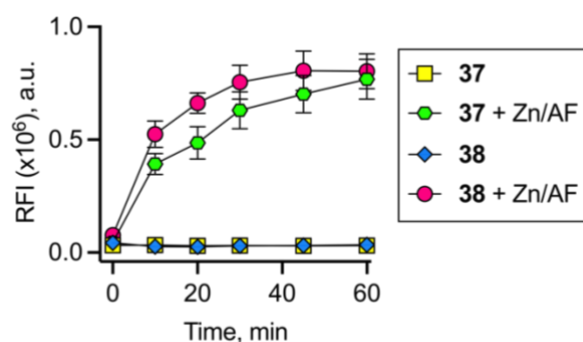


Figure 2.15. Monitoring time-dependent release of MXF from **37** and **38** following chemical reduction with Zinc/ammonium formate ($\text{Zn}/\text{HCOONH}_4$) by a fluorescence-based assay

Overall, these results clearly suggest that 2-nitrothiazole tethered MXF prodrug with the lowest reduction potential demonstrated superior sensitivity and enhanced response towards different reducing agents in an unprecedented fashion.

2.4. Conclusion

In summary, we have designed enzyme-activated Moxifloxacin (MXF) prodrugs. Two principles were used in the enzyme-prodrug design: first, to use NTR as an enzyme to activate a prodrug to produce MXF with both rate and efficiency as parameters for optimization; and

second, to increase lipophilicity of the ensuing prodrug in order to improve permeability. To this end, we synthesized a focussed library of nitro-heterocyclic esters and carbamates of MXF with a wide range of reduction potentials. The prodrugs were evaluated for physicochemical descriptors commonly observed with many anti-tubercular drugs. The prodrugs have shown significantly higher polar surface area and lipophilicity compared to MXF. Encouraged by the fact that lipophilic compounds have increased availability in areas of lipid-rich necrotic regions of lungs of TB patients and enhanced intracellular accumulation inside non-replicating *Mtb*, the prodrugs would presumably have higher accumulation than hydrophilic antibiotic, MXF. A systematic investigation was conducted to identify the optimal nitroaryl prodrug to generate MXF in the presence of mild and strong reducing agents. Despite the wide popularity of 2-nitroimidazolyl group in the development of hypoxia-activated prodrugs, the synthesis of 1-methyl-2-nitroimidazole precursor is quite lengthy and reinforces the need for rigorous attention. To circumvent these problems, the identification of a reliable, time-efficient, high yielding, and more sensitive bioreductive trigger appears to be a more logical and promising approach. Our synthetic endeavour culminated in the utilization of 2-nitrothiazole functionality to design ester and carbamate prodrugs of MXF. Interestingly, the 2-nitrothiazole prodrug demonstrated superior sensitivity and enhanced response towards milder reducing agents than prodrug tethered with extensively employed 2-nitroimidazole moiety. Moreover, the 2-nitrothiazole ester prodrug follows a chemoreduction profile similar to the 2-nitroimidazole based prodrug in the presence of strong reducing agents.

2.5. Experimental and Characterization data

2.5.1 General methods

All the reagents were purchased from commercial sources and used as received unless stated otherwise. Tetrahydrofuran (THF) was dried and distilled over benzophenone/sodium under nitrogen and stored over activated 4 Å molecular sieves. All solvents were freshly distilled according to standard procedures prior to use. Unless otherwise noted, all reactions were performed with dried solvents using oven-dried glassware under nitrogen atmosphere. Thin-layer chromatography (TLC) was performed using silica gel 60 GF₂₅₄ precoated aluminium backed plates (0.25 mm thickness) and visualization was accomplished by irradiation with short and long UV light at 254 and 365 nm respectively or by staining with bromocresol green or phosphomolybdic acid (PMA) for the identification of carboxylic acid or alcohols respectively. The column chromatography was performed using Rankem silica gel (60-120 mesh) eluting with petroleum ether and ethyl acetate (EtOAc). Preparative High Performance Liquid Chromatography (Prep HPLC) was carried out on a Combiflash EZ Prep UV equipped with a Kromasil[®]C-18 preparative column (21.5 mm x 250 mm, 10 µm) at a flow rate of 12 mL/min. ¹⁹F spectra were recorded on a JEOL (376 MHz) using an external reference (α, α, α -trifluorotoluene, $\delta_F = -63.72$ ppm). ¹H and ¹³C spectra were recorded on JEOL or Bruker 400 MHz (or 100 MHz for ¹³C) spectrometers using tetramethylsilane (TMS) as an internal standard. Chemical shifts (δ) are reported in ppm downfield from CDCl₃ ($\delta = 7.26$ and 77.2 ppm) or DMSO-*d*₆ ($\delta = 2.50$ and 39.5 ppm) for ¹H and ¹³C-NMR respectively as an internal reference. The coupling constants (*J*) are given in Hz. Multiplicities are indicated using the following abbreviations: br (broad), m (multiplet), s (singlet), d (doublet), t (triplet), q (quartet), h (heptet), ddd (doublet of doublet of doublet), dd (doublet of doublet), dt (doublet of triplet), dq (doublet of quartet), and td (triplet of doublet). The nature of the carbons (C, CH, CH₂ or CH₃) was determined by recording the DEPT-135 spectra, and is given in parentheses. High-resolution mass spectra were obtained from HRMS-ESI-QTOF (quadrupole time-of flight). FT-IR spectra were recorded using Bruker ALPHA FT-IR spectrometer and reported in cm⁻¹. Melting point was measured using a BÜCHI M-560 melting point apparatus. All melting points were measured in an open glass capillary, and the values are uncorrected. LC-MS experiments were performed on a Sciex X500R QTOF mass spectrometer fitted with an Exion UHPLC system in a positive ion mode using high resolution multiple reaction monitoring (MRM-HR) method. Fluorescence measurement corresponding to MXF was carried out using a Horiba

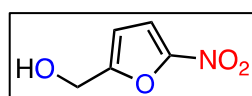
Jobin Yvon Fluorolog Fluorescence Spectrophotometer or an EnSight Multimode Plate Reader (PerkinElmer) in a 96-well plate format.

2.5.2 Synthesis and characterization

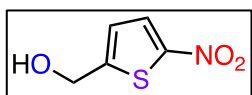
Compounds **1b**, **1c**, **1d**, **1e**, **1f**, **43**, **5**, **7**, **15**, **18-23** and **25** were synthesized following previously reported protocols and the analytical data for each compound was consistent with reported values.

2.5.2.A. Synthesis of heterocyclic alcohols (**1b-1f**)

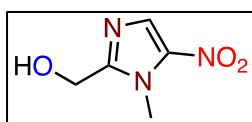
(5-nitrofuran-2-yl)methanol (1b):⁴ NaBH₄ (0.294 g, 7.80 mmol) was slowly added to a vigorously stirred one-neck round bottom flask charged with **2** (1 g, 7.09 mmol) in dry MeOH (15 mL) under nitrogen atmosphere at 0 °C. The reaction mixture was allowed to stir at RT for 3 h. After completion of the reaction (as monitored by TLC), ice cold water (20 mL) was added and the solution was acidified to pH 7.0 with 3 M HCl. The reaction mixture was extracted with EtOAc water (3 × 25 mL) and the combined organic extracts were dried over anhydrous Na₂SO₄, filtered and the filtrate was concentrated *in vacuo*. The residue was purified by silica gel (60-120 mesh) column chromatography using 20-25% EtOAc/hexane as an eluant to afford **1b** (0.890 g, 89%) as a yellow oil.



(5-nitrothiophen-2-yl)methanol (1c):⁴ To a stirred solution of **3** (1 g, 6.36 mmol) in dry MeOH (15 mL), NaBH₄ (0.265 g, 7.00 mmol) was added at 0 °C and the reaction mixture was allowed to stir at RT for 1.5 h. After completion of the reaction (as monitored by TLC), ice cold water (20 mL) was added and the solution was acidified to pH 7.0 with 3 M HCl. The reaction mixture was extracted with EtOAc water (3 × 25 mL) and the combined organic extracts were dried over anhydrous Na₂SO₄, filtered and the filtrate was concentrated *in vacuo*. The residue was purified by silica gel (60-120 mesh) column chromatography using 25-30% EtOAc/hexane as an eluant to afford **1c** (0.920 g, 91%) as a brown oil.

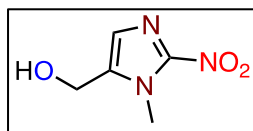


(1-methyl-5-nitro-1H-imidazol-2-yl)methanol (1d):⁷ To a stirred solution of **7** (0.5 g, 3.93 mmol) in DMSO (6 mL), paraformaldehyde (0.756 g, 9.83 mmol) was added. The reaction mixture was heated at 140 °C for 48 h. After



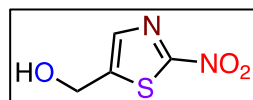
completion of the reaction (as monitored by TLC), the solution was cooled to RT, poured into brine solution (20 mL) and extracted with EtOAc (3 × 30 mL). The combined organic extracts were dried over Na₂SO₄, filtered, and the filtrate was concentrated *in vacuo*. The residue was purified by silica gel (60-120 mesh) column chromatography using 5% MeOH/DCM as an eluant to afford **1d** (0.392 g, 63%) as a white solid.

(1-methyl-2-nitro-1H-imidazol-5-yl)methanol (1e):⁹ Compound **23** (0.160 g, 1.26 mmol)



was dissolved in fluoroboric acid (48% w/v, 986 μL) and the resulting solution was cooled to -15 °C, followed by dropwise addition of NaNO₂ (0.130 g, 1.89 mmol) in water (1 mL). The solution was stirred at -15°C for 30 min, then added dropwise into a solution of Cu powder (0.080 g, 1.26 mmol) and sodium nitrite (1.17 g, 16.9 mmol) in water (2 mL). The reaction mixture was stirred at RT for 1 h, filtered to remove Cu and then the filtrate was extracted with EtOAc (3 × 10 mL). The combined organic extracts were dried over anhydrous Na₂SO₄, filtered, and the filtrate was evaporated in vacuum. The residue was purified by silica gel (60-120 mesh) column chromatography using 5% MeOH/CHCl₃ as an eluant to afford **1e** (0.123 g, 62%) as a gray solid.

(2-nitrothiazol-5-yl)methanol (1f):^{19,20} Compound **25** (0.5 g, 3.16 mmol) was dissolved in



dry MeOH (10 mL). NaBH₄ (0.143 g, 3.79 mmol) was then added at 0 °C and the reaction mixture was allowed to stir at RT for 1.5 h. After completion of the reaction (as monitored by TLC), ice cold water (10 mL) was added and the solution was acidified to pH 7.0 with 3 M HCl. The reaction mixture was extracted with EtOAc (3 × 10 mL) and the combined organic extracts were dried over anhydrous Na₂SO₄, filtered and the filtrate was concentrated *in vacuo*. The residue was purified by silica gel (60-120 mesh) column chromatography using 30-32% EtOAc/hexane as an eluant to give **1f** (0.435 g, 85%) as a dark reddish solid.

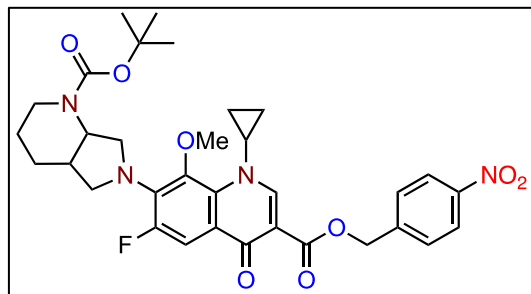
2.5.2.B. General procedure for synthesis of *N*-boc protected nitroheterocyclic esters of MXF (27-32)

Procedure A: A solution of **26** and cesium carbonate (2.14 mmol) in DMF (5 mL) was stirred at RT for 30 min. The aryl bromide (0.61 mmol) in DMF (5 mL) was added to this solution and the mixture was allowed to stir for further 15 h. The crude solution was filtered, diluted

with water (20 mL) and extracted with EtOAc (3×15 mL). The combined organic layer was washed with brine (2×10 mL), dried over Na_2SO_4 , concentrated *in vacuo*. The crude compound was purified by preparative HPLC using Kromasil[®]C-18 column and $\text{H}_2\text{O}:\text{MeOH}$ as mobile phase, under ambient temperature with a flow rate of 8 mL/min to afford pure product. This procedure was followed for the synthesis of **27**.

Procedure B: To a stirred solution of **26**, HBTU (1.96 mmol) and DMAP (0.19 mmol) in dry DCM (100 mL), DIPEA (1.96 mmol) was added. The reaction mixture was stirred for 30 min at RT. The resulting solution turned yellow. To this reaction mixture, alcohol was added and heated to 38 °C for 12 h until the starting material was completely consumed (as monitored by TLC). After completion of the reaction, water (100 mL) was added and the aqueous layer was extracted with DCM (3×100 mL). The organic extracts were combined, washed with brine (2×50 mL), dried over anhydrous Na_2SO_4 , filtered and the filtrate was concentrated under reduced pressure. The residue was purified by preparative HPLC using Kromasil[®]C-18 column at ambient temperature under the gradient elution with $\text{H}_2\text{O}:\text{ACN}$ (20:80, v/v) as mobile phase at a flow rate of 12 mL/min to afford pure products (**28-32**).

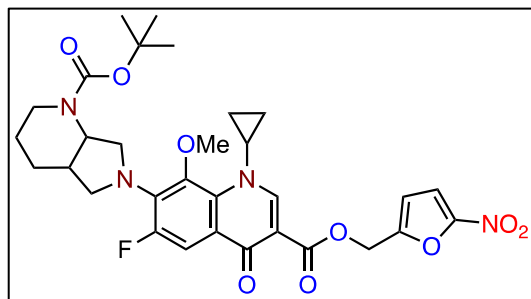
4-nitrobenzyl 7-(-1-(*tert*-butoxycarbonyl)hexahydro-1H-pyrrolo[3,4-b]pyridin-6(2H)-yl)-1-cyclopropyl-6-fluoro-8-methoxy-4-oxo-1,4-dihydroquinoline-3-carboxylate (27):



Starting from **26** (0.197 g, 0.39 mmol) and 4-nitrobenzyl bromide (0.090 g, 0.58 mmol), **27** (183 mg, 73%) was isolated as a white solid; mp = 127-128 °C; R_f (EtOAc:hexane = 70:30) = 0.4; FT-IR (ν_{max} , cm^{-1}): 2924 (C-H stretch), 1729 (ester C=O stretch), 1691 (conjugated ketone C=O stretch),

1457 (asymmetric NO_2 stretch), 1359 (symmetric NO_2 stretch); ^{19}F NMR (376 MHz, CDCl_3): δ -123.3; ^1H NMR (400 MHz, CDCl_3): δ 8.58 (s, 1H), 8.26 – 8.22 (m, 2H), 7.85 (d, J = 14.2 Hz, 1H), 7.72 (d, J = 8.6 Hz, 2H), 5.52 – 5.44 (m, 2H), 4.78 (br, 1H), 4.08 – 4.03 (m, 2H), 3.93 – 3.88 (m, 1H), 3.84 (dt, J = 11.2, 4.9 Hz, 1H), 3.56 (s, 3H), 3.37 (br, 1H), 3.22 (s, 1H), 2.88 (t, J = 10.9 Hz, 1H), 2.28 – 2.21 (m, 1H), 1.77 (s, 2H), 1.48 (s, 11H), 1.24 – 1.22 (m, 1H), 1.08 – 1.00 (m, 2H), 0.84 – 0.76 (m, 1H); ^{13}C NMR (100 MHz, CDCl_3): δ 161.0, 155.4, 151.1, 147.6, 144.1, 140.6, 136.2, 134.6, 133.4, 130.9, 128.0, 123.9, 108.9 (d, J = 122.0 Hz), 80.2, 65.1, 61.2, 56.4, 56.3, 56.0, 39.9, 35.9, 28.6, 25.5, 24.3, 10.6, 8.5; HRMS (ESI-TOF) for $\text{C}_{33}\text{H}_{37}\text{FN}_4\text{O}_8$ $[\text{M}+\text{H}]^+$: Calcd., 637.2673, Found, 637.2673.

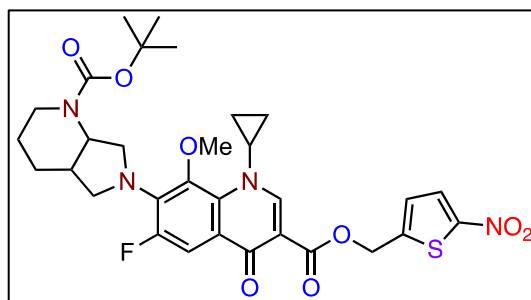
(5-nitrofuran-2-yl)methyl 7-(-1-(tert-butoxycarbonyl)hexahydro-1H-pyrrolo [3,4-b]pyridin-6(2H)-yl)-1-cyclopropyl-6-fluoro-8-methoxy-4-oxo-1,4-dihydroquinoline-3-



carboxylate (28): Starting from **26** (0.160 g, 0.31 mmol) and **1b** (0.068 g, 0.47 mmol), **28** (0.110 g, 56%) was isolated as a white solid; mp = 101-102 °C; R_f (EtOAc:hexane = 70:30) = 0.5; FT-IR (ν_{max} , cm^{-1}): 2988 (C-H stretch), 1732 (ester C=O stretch), 1625 (conjugated ketone C=O stretch),

1449 (asymmetric NO₂ stretch), 1373 (symmetric NO₂ stretch); ¹⁹F NMR (376 MHz, CDCl₃): δ -122.7; ¹H NMR (400 MHz, CDCl₃): δ 8.57 (s, 1H), 7.78 (d, J = 14.0 Hz, 1H), 7.30 (s, 1H), 6.80 (d, J = 3.6 Hz, 1H), 5.40 – 5.31 (m, 2H), 4.78 (br, 1H), 4.07 – 4.02 (m, 2H), 3.94 - 3.81 (m, 1H), 3.84 (t, J = 9.6 Hz, 1H), 3.57 (s, 3H), 3.39 - 3.36 (m, 1H), 3.21 (d, J = 9.1 Hz, 1H), 2.88 (t, J = 11.2 Hz, 1H), 2.28 - 2.22 (m, 1H), 1.81 - 1.75 (m, 2H), 1.48 (s, 10H), 1.30 – 1.19 (m, 2H), 1.12 – 1.00 (m, 2H), 0.86 - 0.77 (m, 1H); ¹³C NMR (100 MHz, CDCl₃): δ 172.8, 164.8, 155.4, 153.5, 152.3 (d, $J_{\text{C-F}}$ = 161.2 Hz), 151.0, 141.5, 136.0 (d, $J_{\text{C-F}}$ = 43.1 Hz), 133.3, 122.1, 113.5, 112.5, 108.8 (d, $J_{\text{C-F}}$ = 94.7 Hz), 108.5, 80.2, 60.9, 57.7, 56.4, 56.3, 39.8, 35.7, 28.5, 25.5, 24.3, 10.5, 8.5; DEPT-135 NMR (100 MHz, CDCl₃): δ 151.0 (CH), 113.6 (CH), 112.5 (CH), 108.5 (CH), 60.9 (CH₃), 57.6 (CH₂), 56.4 (CH₂), 56.3 (CH₂), 39.7 (CH), 35.7 (CH), 28.8 (CH₃), 25.8 (CH₂), 24.4 (CH₂), 10.5 (CH₂), 8.5 (CH₂); HRMS (ESI-TOF) for C₃₁H₃₅FN₄O₉ [M+H]⁺: Calcd., 627.2466, Found, 627.2469.

(5-nitrothiophen-2-yl)methyl-7-(-1-(tert-butoxycarbonyl)hexahydro-1H-pyrrolo[3,4-b]pyridin-6(2H)-yl)-1-cyclopropyl-6-fluoro-8-methoxy-4-oxo-1,4-dihydro quinoline-3-



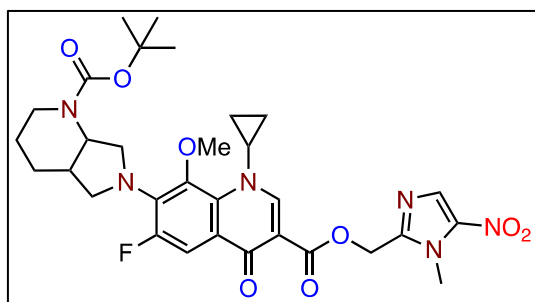
carboxylate (29): Starting from **26** (0.150 g, 0.30 mmol) and **1c** (0.071 g, 0.44 mmol), **29** (0.114 g, 59%) was isolated as a white solid; mp = 97-98 °C; R_f (EtOAc:hexane = 70:30) = 0.5; FT-IR (ν_{max} , cm^{-1}): 1732 (ester C=O stretch), 1684 (conjugated ketone C=O stretch), 1455 (asymmetric NO₂

stretch), 1327 (symmetric NO₂ stretch); ¹⁹F NMR (376 MHz, CDCl₃): δ -122.5; ¹H NMR (400 MHz, CDCl₃): δ 8.58 (s, 1H), 7.84 – 7.80 (m, 2H), 7.15 (d, J = 4.1 Hz, 1H), 5.52 – 5.44 (m, 2H), 4.77 (br, 1H), 4.08 – 4.02 (m, 2H), 3.94 – 3.88 (m, 1H), 3.83 (td, J = 9.9, 2.1 Hz, 1H), 3.56 (s, 3H), 3.36 (br, 1H), 3.21 (d, J = 9.8 Hz, 1H), 2.88 (t, J = 12.2 Hz, 1H), 2.28 – 2.21 (m,

1H), 1.82 – 1.75 (m, 2H), 1.48 (s, 10 H), 1.28 – 1.22 (m, 2H), 1.11 – 1.01 (m, 2H), 0.85 – 0.78 (m, 1H); ¹³C NMR (100 MHz, CDCl₃): δ 172.7, 165.5, 155.4, 152.3 (d, *J*_{C-F} = 144.6 Hz), 151.1, 147.0, 141.5, 136.0 (d, *J*_{C-F} = 44.6 Hz), 133.3, 128.4, 126.9, 122.1, 122.0, 108.9 (d, *J*_{C-F} = 95.5 Hz), 108.6, 100.1, 80.2, 60.9, 60.7, 56.5, 56.4, 56.3, 39.9, 35.8, 28.6, 25.5, 24.3, 10.5, 8.5; DEPT-135 NMR (100 MHz, CDCl₃): δ 151.1 (CH), 128.4 (CH), 126.9 (CH), 109.0 (CH), 61.0 (CH₃), 60.7 (CH₂), 56.4 (CH₂), 56.3 (CH₂), 39.9 (CH), 35.7 (CH), 28.6 (CH₃), 25.5 (CH₂), 24.3 (CH₂), 10.5 (CH₂); HRMS (ESI-TOF) for C₃₁H₃₅FN₄O₈S[M+H]⁺: Calcd., 643.2238, Found, 643.2242.

(1-methyl-5-nitro-1*H*-imidazol-2-yl)methyl 7-(1-(*tert*-butoxycarbonyl)octahydro-6*H*-pyrrolo[3,4-*b*]pyridin-6-yl)-1-cyclopropyl-6-fluoro-8-methoxy-4-oxo-1,4-

dihydroquinoline-3-carboxylate (30): Starting from **26** (0.150 g, 0.30 mmol) and **1d** (0.071

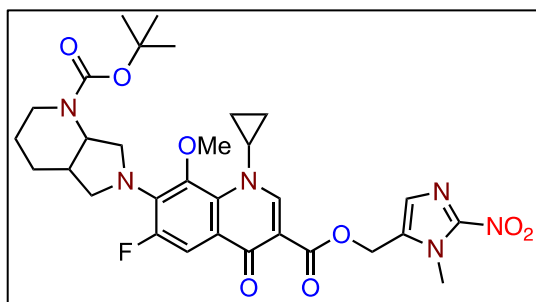


g, 0.45 mmol), **30** (0.181 g, 94%) was isolated as a gray solid; mp = 104-105 °C; *R*_f (MeOH:CHCl₃ = 05:95) = 0.4; FT-IR (*v*_{max}, cm⁻¹): 2931 (C-H stretch), 1731 (ester C=O stretch), 1687 (conjugated ketone C=O stretch), 1616 (asymmetric NO₂ stretch); ¹⁹F NMR (376 MHz,

CDCl₃): δ -122.8; ¹H NMR (400 MHz, CDCl₃): δ 8.56 (s, 1H), 7.97 (s, 1H), 7.79 (d, *J* = 14.1 Hz, 1H), 5.44 (q, *J* = 13.4 Hz, 2H), 4.77 (s, 1H), 4.19 (s, 3H), 4.07 – 4.01 (m, 2H), 3.92 – 3.87 (m, 1H), 3.83 (td, *J* = 10.0, 2.2 Hz, 1H), 3.56 (s, 3H), 3.36 (br, 1H), 3.21 (d, *J* = 9.1 Hz, 1H), 2.87 (t, *J* = 11.8 Hz, 1H), 2.28 – 2.22 (m, 1H), 1.81 – 1.72 (m, 2H), 1.72 (s, 1H), 1.48 (s, 10H), 1.26 – 1.21 (m, 1H), 1.08 – 1.00 (m, 2H), 0.83 – 0.75 (m, 1H); ¹³C NMR (100 MHz, CDCl₃): δ 172.7, 165.1, 155.4, 155.0, 152.5, 151.1, 147.2, 139.8, 136.1 (d, *J* = 43.6 Hz), 133.4, 132.1, 122.0, 108.7 (d, *J* = 95.6 Hz), 108.5, 80.2, 61.0, 58.3, 56.4, 56.3, 39.9, 35.8, 34.1, 28.6, 25.5, 24.3, 10.5, 8.5; DEPT-135 NMR (100 MHz, CDCl₃): δ 151.0 (CH), 132.0 (CH), 108.8 (CH), 60.8 (CH₃), 58.1 (CH₂), 56.3 (CH₂), 56.2 (CH₂), 39.7 (CH), 35.6 (CH), 34.0 (CH₃), 28.5 (CH₃), 25.4 (CH₂), 24.2 (CH₂), 10.4 (CH₂), 8.5 (CH₂); HRMS (ESI-TOF) for C₃₁H₃₇FN₆O₈ [M+H]⁺: Calcd., 641.2735, Found, 641.2726.

(1-methyl-2-nitro-1H-imidazol-5-yl)methyl 7-(-1-(*tert*-butoxy carbonyl) octa hydro-6H-pyrrolo[3,4-b]pyridin-6-yl)-1-cyclopropyl-6-fluoro-8-methoxy-4-oxo-1,4-

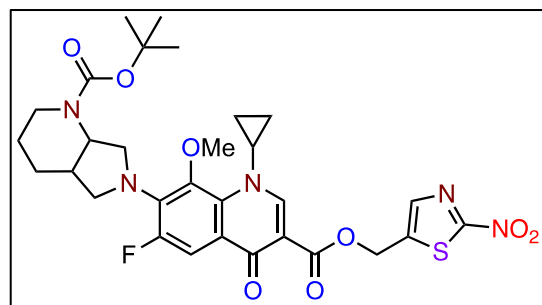
dihydroquinoline-3-carboxylate (31): Starting from **26** (0.170 g, 0.33 mmol) and **1e** (0.080



mg, 0.50 mmol), **31** (0.124 mg, 57%) was isolated as a gray solid; mp = 144-145 °C; R_f (MeOH:CHCl₃ = 05:95) = 0.2; FT-IR (ν_{max} , cm⁻¹): 2974 (C-H stretch), 1731 (ester C=O stretch), 1684 (conjugated ketone C=O stretch), 1539 (asymmetric NO₂ stretch), 1364 (symmetric NO₂

stretch); ¹⁹F NMR (376 MHz, CDCl₃): δ -122.7; ¹H NMR (400 MHz, CDCl₃): δ 8.54 (s, 1H), 7.76 (d, J = 14.1 Hz, 1H), 7.27 (d, J = 10.1 Hz, 1H), 5.36 (q, J = 13.6 Hz, 2H), 4.77 (s, 1H), 4.21 (s, 3H), 4.07 – 4.02 (m, 2H), 3.93 – 3.88 (m, 1H), 3.83 (td, J = 10.0, 2.7 Hz, 1H), 3.56 (s, 3H), 3.35 (br, 1H), 3.21 (d, J = 8.6 Hz, 1H), 2.88 (t, J = 11.2 Hz, 1H), 2.27 – 2.22 (m, 1H), 1.80 – 1.75 (m, 2H), 1.48 (s, 10H), 1.32 – 1.19 (m, 2H), 1.10 – 1.01 (m, 2H), 0.84 – 0.76 (m, 1H); ¹³C NMR (100 MHz, CDCl₃): δ 172.6, 165.5, 155.4, 155.0, 152.5, 151.1, 146.3, 141.5 (d, J_{C-F} = 25.0 Hz), 136.1 (d, J_{C-F} = 44.0 Hz), 133.3, 132.6, 129.6, 122.0, 121.9, 108.9, 108.6, 80.2, 60.9, 56.4, 56.3, 55.2, 39.9, 35.7, 34.7, 28.5, 25.4, 24.3, 10.5, 8.5; DEPT-135 NMR (100 MHz, CDCl₃): δ 151.0 (CH), 129.5 (CH), 108.6 (CH), 60.8 (CH₃), 56.3 (CH₂), 56.2 (CH₂), 55.1 (CH₂), 39.8 (CH), 35.6 (CH), 34.6 (CH₃), 28.4 (CH₃), 25.3 (CH₂), 24.2 (CH₂), 10.4 (CH₂), 8.4 (CH₂); HRMS (ESI-TOF) for C₃₁H₃₇FN₆O₈ [M+H]⁺: Calcd., 641.2735, Found, 641.2737.

(2-nitrothiazol-5-yl)methyl 7-(-1-(*tert*-butoxycarbonyl)octahydro-6H-pyrrolo [3,4-b]pyridin-6-yl)-1-cyclopropyl-6-fluoro-8-methoxy-4-oxo-1,4-dihydroquinoline-3-

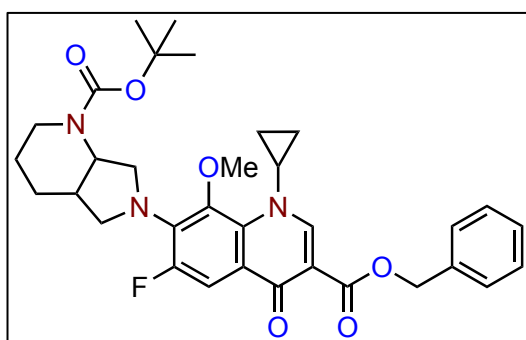


carboxylate (32): Starting from **26** (0.125 g, 0.25 mmol) and **1f** (0.060 g, 0.37 mmol), **32** (0.125 g, 78%) was isolated as yellowish white solid; mp = 110-111 °C; FT-IR (ν_{max} , cm⁻¹): 2992 (C-H stretch), 1739 (ester C=O stretch), 1681 (conjugated ketone C=O stretch), 1358

(symmetric NO₂ stretch); R_f (EtOAc:hexane = 70:30) = 0.5; ¹⁹F NMR (376 MHz, CDCl₃): δ -122.6; ¹H NMR (400 MHz, CDCl₃): δ 8.58 (s, 1H), 7.91 (s, 1H), 7.80 (d, J = 14.0 Hz, 1H), 5.54 (s, 2H), 4.76 (s, 1H), 4.07 – 4.02 (m, 2H), 3.94 – 3.89 (m, 1H), 3.83 (td, J = 9.8, 1.9 Hz, 1H), 3.56 (s, 3H), 3.36 (s, 1H), 3.21 (d, J = 9.2 Hz, 1H), 2.88 (t, J = 11.5 Hz, 1H), 2.28 – 2.23

(m, 1H), 1.80 – 1.75 (m, 2H), 1.48 (s, 11H), 1.32 – 1.23 (m, 1H), 1.11 – 1.00 (m, 2H), 0.83 – 0.77 (m, 1H); ^{13}C NMR (100 MHz, CDCl_3): δ 172.6, 166.8, 165.8, 155.4, 151.3, 142.1, 142.0, 136.1 (d, $J_{\text{C-F}} = 43.7$ Hz), 133.3, 122.0, 108.8 (d, $J_{\text{C-F}} = 95.0$ Hz), 108.2, 80.2, 60.9, 58.1, 56.4, 56.3, 39.9, 35.7, 28.6, 25.5, 24.3, 10.5, 8.5; DEPT-135 NMR (100 MHz, CDCl_3): δ 156.0 (CH), 141.9 (CH), 108.8 (CH), 60.8 (CH_3), 58.0 (CH_2), 56.2 (CH_2), 39.8 (CH), 35.6 (CH), 28.4 (CH_3), 25.4 (CH_2), 24.2 (CH_2), 10.4 (CH_2), 8.4 (CH_2); HRMS (ESI-TOF) for $\text{C}_{30}\text{H}_{34}\text{FN}_5\text{O}_8\text{S}$ $[\text{M}+\text{H}]^+$: Calcd., 644.2190, Found, 644.2184.

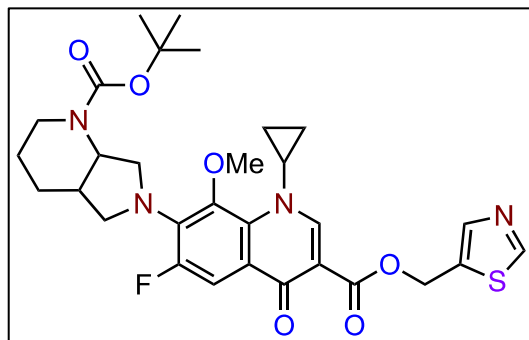
Benzyl 7-(-1-(*tert*-butoxycarbonyl)hexahydro-1H-pyrrolo[3,4-b]pyridin-6(2H)-yl)-1-cyclopropyl-6-fluoro-8-methoxy-4-oxo-1,4-dihydroquinoline-3-carboxylate (39): Starting



from **26** (0.150 g, 0.30 mmol) and benzyl alcohol (0.048 g, 0.44 mmol), **39** (0.115 g, 65%) was isolated as a white solid; mp = 109-110 °C; R_f (EtOAc:hexane = 70:30) = 0.5; FT-IR (ν_{max} , cm^{-1}): 2932 (C-H stretch), 1685 (conjugated ketone C=O stretch), 1614 (conjugated ketone C=O stretch); ^{19}F NMR (376 MHz, CDCl_3): δ -123.2;

^1H NMR (400 MHz, CDCl_3): δ 8.55 (s, 1H), 7.84 (d, $J = 14.2$ Hz, 1H), 7.53 – 7.50 (m, 2H), 7.39 – 7.35 (m, 2H), 7.32 – 7.29 (m, 1H), 5.42 – 5.34 (m, 2H), 4.76 (s, 1H), 4.06 – 4.01 (m, 2H), 3.89 – 3.80 (m, 2H), 3.55 (s, 3H), 3.35 (s, 1H), 3.20 (d, $J = 8.4$ Hz, 1H), 2.88 (t, $J = 12.0$ Hz, 1H), 2.27 – 2.20 (m, 1H), 1.83 – 1.75 (m, 4H), 1.48 (s, 9H), 1.24 – 1.17 (m, 1H), 1.08 – 0.97 (m, 2H), 0.80 – 0.73 (m, 1H); ^{13}C NMR (100 MHz, CDCl_3): δ 173.0, 165.7, 155.4, 150.7, 136.6, 135.8 (d, $J_{\text{C-F}} = 44.2$ Hz), 133.4, 128.6, 128.1, 128.0, 122.2, 122.1, 109.7, 108.9 (d, $J_{\text{C-F}} = 96.5$ Hz), 80.2, 66.4, 60.9, 56.4, 56.3, 39.6, 35.7, 28.6, 25.5, 24.3, 10.4, 8.5; DEPT-135 NMR (100 MHz, CDCl_3): δ 150.7 (CH), 128.6 (CH), 128.0 (CH), 127.9 (CH), 108.9 (CH), 66.4 (CH_2), 60.8 (CH_3), 56.3 (CH_2), 56.2 (CH_2), 39.6 (CH), 35.7 (CH), 28.5 (CH_3), 25.4 (CH_2), 24.3 (CH_2), 10.4 (CH_2), 8.5 (CH_2); HRMS (ESI-TOF) for $\text{C}_{33}\text{H}_{38}\text{FN}_3\text{O}_6$ $[\text{M}+\text{H}]^+$: Calcd., 592.2817, Found, 592.2818.

Thiazol-5-ylmethyl 7-(1-(*tert*-butoxycarbonyl)octahydro-6*H*-pyrrolo[3,4-*b*]pyridin-6-yl)-1-cyclopropyl-6-fluoro-8-methoxy-4-oxo-1,4-dihydroquinoline-3-carboxylate (40):



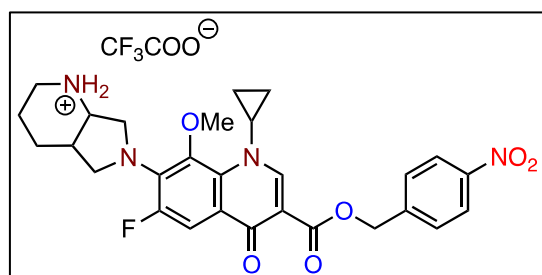
Starting from **26** (0.130 g, 0.26 mmol) and thiazol-5-yl methanol (0.045 g, 0.38 mmol), **40** (0.105 g, 67%) was isolated as yellowish white solid; mp = 129-130 °C; R_f (EtOAc:hexane = 70:30) = 0.5; FT-IR (ν_{max} , cm^{-1}): 2971 (C-H stretch), 1742 (ester C=O stretch), 1668 (conjugated ketone C=O stretch); ^{19}F NMR (376 MHz, CDCl_3): δ -123.0; ^1H

NMR (400 MHz, CDCl_3): δ 8.80 (s, 1H), 8.54 (s, 1H), 7.97 (s, 1H), 7.81 (d, $J = 14.2$ Hz, 1H), 5.60 – 5.53 (m, 2H), 4.76 (s, 1H), 4.07 – 4.01 (m, 2H), 3.90 – 3.85 (m, 1H), 3.83 (td, $J = 9.8, 2.0$ Hz, 1H), 3.55 (s, 3H), 3.35 (s, 1H), 3.20 (d, $J = 8.2$ Hz, 1H), 2.87 (t, $J = 11.7$ Hz, 1H), 2.28 – 2.20 (m, 1H), 1.81 – 1.75 (m, 2H), 1.48 (s, 11H), 1.26 – 1.19 (m, 1H), 1.07 – 0.97 (m, 2H), 0.81 – 0.74 (m, 1H); ^{13}C NMR (100 MHz, CDCl_3): δ 172.7, 165.4, 155.5, 155.0, 154.7, 152.5, 150.9, 144.0, 141.5 (d, $J_{\text{C-F}} = 24.3$ Hz), 135.9 (d, $J_{\text{C-F}} = 43.9$ Hz), 133.3, 122.2, 122.1, 109.0, 108.8, 80.2, 60.9, 58.0, 56.4, 56.3, 39.7, 35.7, 28.5, 25.5, 24.3, 10.4, 8.5; DEPT-135 NMR (100 MHz, CDCl_3): δ 150.8 (CH), 143.9 (CH), 108.8 (CH), 60.8 (CH_3), 57.9 (CH_2), 56.2 (CH_2), 39.6 (CH), 35.6 (CH), 28.4 (CH_3), 25.4 (CH_2), 24.2 (CH_2), 10.3 (CH_2), 8.4 (CH_2); HRMS (ESI-TOF) for $\text{C}_{30}\text{H}_{35}\text{FN}_4\text{O}_6\text{S}$ [$\text{M}+\text{H}$] $^+$: Calcd., 599.2339, Found, 599.2343.

2.5.2.C. General procedure for *N*-boc deprotection of NTR-MXF derivatives (33-38, 41 and 42)

To a solution of compound in dry DCM (15 mL), TFA (26.47 mmol) was added dropwise at 0 °C under nitrogen atmosphere. The resulting reaction mixture was stirred at RT (~ 4-6 h) until the starting material had been completely consumed (determined by TLC) and the solvent was concentrated *in vacuo* at ~5 °C. The product was precipitated by diethyl ether on sonication and the ether solution was then carefully decanted. The obtained solid was washed twice with diethyl ether, and the ethereal solution was concentrated *in vacuo* to afford prodrugs **33-38, 41 and 42** as pure products.

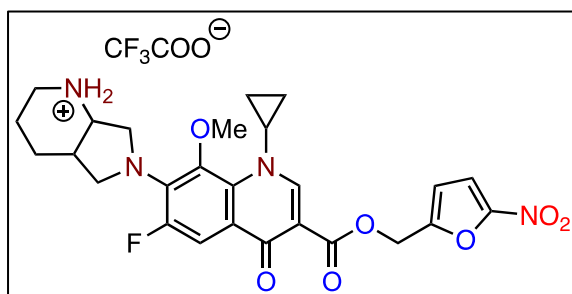
6-(1-cyclopropyl-6-fluoro-8-methoxy-3-(((4-nitrobenzyl)oxy)carbonyl)-4-oxo-1,4-dihydroquinolin-7-yl)octahydro-1H-pyrrolo[3,4-b]pyridin-1-ium 2,2,2-trifluoro acetate (33): Starting from **27** (0.100 g, 0.16 mmol), **33** (0.090 g, 83%) was obtained as a white solid;



mp = 217-218 °C; R_f (MeOH:CHCl₃ = 10:90) = 0.2; FT-IR (ν_{max} , cm⁻¹): 3394 (N-H stretch), 2924 (C-H stretch), 1691 (ester C=O stretch), 1616 (conjugated ketone C=O stretch); ¹⁹F NMR (376 MHz, DMSO-*d*₆): δ -74.4, -122.8; ¹H NMR (400 MHz, DMSO-*d*₆): δ 9.24 (d, J = 9.6 Hz, 1H), 8.59

(d, J = 10.1 Hz, 1H), 8.55 (s, 1H), 8.27 (d, J = 8.7 Hz, 2H), 7.79 (d, J = 8.7 Hz, 2H), 7.60 (d, J = 14.4 Hz, 1H), 5.47 – 5.39 (m, 2H), 4.03 – 4.00 (m, 2H), 3.90 (s, 1H), 3.79 (td, J = 9.8, 4.6 Hz, 1H), 3.70 (t, J = 7.7 Hz, 1H), 3.57 (s, 3H), 3.50 (d, J = 11.7 Hz, 1H), 3.24 (d, J = 9.4 Hz, 1H), 2.99 (q, J = 9.5, 8.0 Hz, 1H), 2.68 – 2.65 (m, 1H), 1.83 -1.70 (m, 4H), 1.18 – 1.10 (m, 1H), 1.07 – 0.94 (m, 2H), 0.85 – 0.78 (m, 1H); ¹³C NMR (100 MHz, DMSO-*d*₆): δ 171.3, 164.4, 153.5, 151.2, 147.0, 144.7, 141.0 (d, J = 26.6 Hz), 134.9 (d, J = 41.3 Hz), 133.3, 128.1, 123.6, 120.9 (d, J = 29.4 Hz), 108.2, 107.3 (d, J = 94.1 Hz), 64.2, 61.5, 54.4, 54.1 (d, J = 31.2 Hz), 51.6 (d, J = 38.0 Hz), 41.9, 34.3, 20.7, 17.8, 9.5, 8.4; DEPT-135 NMR (100 MHz, DMSO-*d*₆): δ 150.9 (CH), 127.8 (CH), 123.3 (CH), 107.0 (CH), 63.9 (CH₂), 61.3 (CH₃), 54.2 (CH), 54.0 (CH₂), 51.3 (CH₂), 41.6 (CH₂), 34.0 (CH), 20.4 (CH₂), 17.5 (CH₂), 9.2 (CH₂), 8.1 (CH₂); HRMS (ESI-TOF) for C₂₈H₃₀FN₄O₆ [M]⁺: Calcd., 537.2144, Found, 537.2146.

6-(1-cyclopropyl-6-fluoro-8-methoxy-3-(((5-nitrofuran-2-yl)methoxy) carbonyl)-4-oxo-1,4-dihydroquinolin-7-yl)octahydro-1H-pyrrolo[3,4-b]pyridin-1-ium 2,2,2-trifluoro acetate (34): Starting from **28** (0.100 mg, 0.15 mmol), **34** (0.092 mg, 85%) was obtained as a

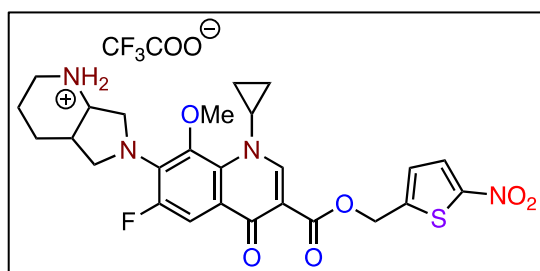


reddish yellow solid; mp = 198-199 °C; R_f (MeOH:CHCl₃ = 10:90) = 0.2; FT-IR (ν_{max} , cm⁻¹): 3427 (N-H stretch), 2971 (C-H stretch), 1690 (ester C=O stretch), 1660 (conjugated ketone C=O stretch), 1451 (asymmetric NO₂ stretch), 1361 (symmetric NO₂ stretch); ¹⁹F NMR (376

MHz, DMSO-*d*₆): δ -74.6, -122.8; ¹H NMR (400 MHz, DMSO-*d*₆): δ 9.21 (d, J = 11.4 Hz, 1H), 8.55 (d, J = 9.0 Hz, 1H), 8.51 (s, 1H), 7.71 (d, J = 3.7 Hz, 1H), 7.55 (d, J = 13.5 Hz, 1H), 6.99 (d, J = 3.7 Hz, 1H), 5.38 – 5.31 (m, 2H), 4.02 – 3.98 (m, 2H), 3.89 (s, 1H), 3.77 (td, J =

10.0, 4.5 Hz, 1H), 3.72 – 3.67 (m, 1H), 3.56 (s, 3H), 3.51 (d, $J = 11.9$ Hz, 1H), 3.25 – 3.22 (m, 1H), 2.98 (q, $J = 9.6$ Hz, 1H), 2.67 – 2.63 (m, 1H), 1.83 – 1.66 (m, 4H), 1.16 – 1.07 (m, 1H), 1.04 – 0.96 (m, 2H), 0.82 – 0.77 (m, 1H); ^{13}C NMR (100 MHz, DMSO- d_6): δ 171.3, 163.7, 158.4 (d, $J = 140.6$ Hz), 153.9, 153.5, 151.3, 151.1, 141.0 (d, $J = 26.7$ Hz), 135.0 (d, $J = 41.6$ Hz), 133.3, 120.8 (d, $J = 29.4$ Hz), 114.1, 113.9, 107.8, 107.2 (d, $J = 95.1$ Hz), 61.6, 57.2, 54.5, 54.2 (d, $J = 12.4$ Hz), 51.5 (d, $J = 37.7$ Hz), 41.9, 34.3, 20.7, 17.7, 9.5, 8.4; DEPT-135 NMR (100 MHz, DMSO- d_6): δ 151.0 (CH), 113.7 (CH), 113.5 (CH), 106.9 (CH), 61.3 (CH₃), 56.8 (CH₂), 54.1 (CH), 53.9 (CH₂), 51.2 (CH₂), 41.5 (CH₂), 34.0 (CH), 20.4 (CH₂), 17.4 (CH₂), 9.2 (CH₂), 8.1 (CH₂); HRMS (ESI-TOF) for C₂₈H₂₈FN₄O₇ [M]⁺: Calcd., 527.1937, Found, 527.1938.

6-(1-cyclopropyl-6-fluoro-8-methoxy-3-(((5-nitrothiophen-2-yl)methoxy) carbonyl)-4-oxo-1,4-dihydroquinolin-7-yl)octahydro-1H-pyrrolo[3,4-b]pyridin-1-ium 2,2,2-trifluoroacetate (35): Starting from **29** (0.100 mg, 0.15 mmol), **35** (0.094 mg, 85%) was

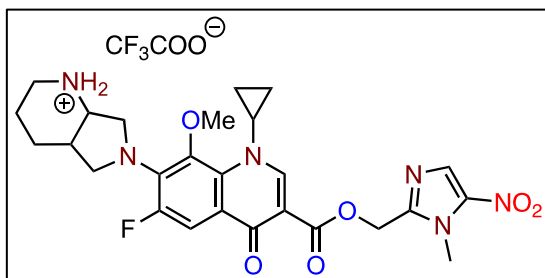


obtained as a yellow solid; mp = 211-212 °C; R_f (MeOH:CHCl₃ = 10:90) = 0.2; FT-IR (ν_{max} , cm⁻¹): 3425 (N-H stretch), 2999 (C-H stretch), 1670 (ester C=O stretch), 1659 (conjugated ketone C=O stretch), 1423 (asymmetric NO₂ stretch), 1314

(symmetric NO₂ stretch); ^{19}F NMR (376 MHz, DMSO- d_6): δ -74.8, -122.7; ^1H NMR (400 MHz, DMSO- d_6): δ 9.13 (s, 1H), 8.53 (s, 2H), 8.07 (d, $J = 3.8$ Hz, 1H), 7.59 (d, $J = 14.4$ Hz, 1H), 7.36 (d, $J = 4.4$ Hz, 1H), 5.53 – 5.46 (m, 2H), 4.06 – 3.98 (m, 2H), 3.88 (t, $J = 5.4$ Hz, 1H), 3.76 (td, $J = 10.0, 4.5$ Hz, 1H), 3.69 (dt, $J = 8.2$ Hz, 2.9 Hz, 1H), 3.57 (s, 3H), 3.50 (d, $J = 12.0$ Hz, 1H), 3.23 (d, $J = 12.9$ Hz, 1H), 2.99 (d, $J = 11.4$ Hz, 1H), 2.67 – 2.60 (m, 1H), 1.84 – 1.66 (m, 4H), 1.17 – 1.10 (m, 1H), 1.06 – 0.94 (m, 2H), 0.87 – 0.78 (m, 1H); ^{13}C NMR (100 MHz, DMSO- d_6): δ 171.2, 164.0, 153.5, 151.3, 151.0, 150.8, 148.1, 141.0 (d, $J = 26.7$ Hz), 134.9 (d, $J = 41.9$ Hz), 133.2, 129.7, 127.5, 120.9 (d, $J = 29.1$ Hz), 107.6, 107.2 (d, $J = 95.3$ Hz), 61.5, 60.3, 54.4, 54.1 (d, $J = 16.3$ Hz), 51.5 (d, $J = 36.4$ Hz), 41.8, 34.2, 20.6, 17.7, 9.4, 8.4; DEPT-135 NMR (100 MHz, DMSO- d_6): δ 151.1 (CH), 129.4 (CH), 127.3 (CH), 107.0 (CH), 61.3 (CH₃), 60.1 (CH₂), 54.2 (CH), 53.9 (CH₂), 51.2 (CH₂), 41.5 (CH₂), 34.0 (CH), 20.4 (CH₂), 17.4 (CH₂), 9.2 (CH₂), 8.1 (CH₂); HRMS (ESI-TOF) for C₂₆H₂₈FN₄O₆S [M]⁺: Calcd., 543.1708, Found, 543.1716.

6-(1-cyclopropyl-6-fluoro-8-methoxy-3-(((1-methyl-5-nitro-1*H*-imidazol-2-yl)methoxy)carbonyl)-4-oxo-1,4-dihydroquinolin-7-yl)octahydro-1*H*-pyrrolo[3,4-

b]pyridin-1-ium 2,2,2-trifluoroacetate (36): Starting from **30** (0.180 g, 0.28 mmol), **36**

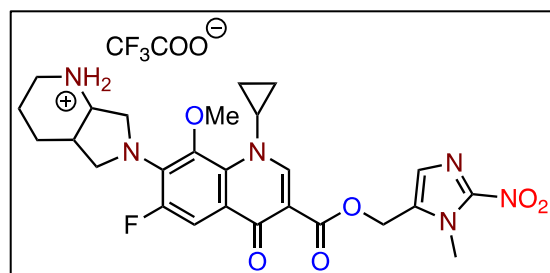


(0.179 g, 97%) was obtained as a yellow solid; mp = 109-110 °C; R_f (MeOH:DCM = 10:90) = 0.1; FT-IR (ν_{max} , cm^{-1}): 2932 (C-H stretch), 1685 (conjugated ketone C=O stretch), 1614 (N-H bend); ^{19}F NMR (376 MHz, DMSO- d_6): δ -75.0, -

122.7; ^1H NMR (400 MHz, DMSO- d_6): δ 9.21 (d, J = 10.5 Hz, 1H), 8.55 (d, J = 9.1 Hz, 1H), 8.52 (s, 1H), 8.09 (s, 1H), 7.56 (d, J = 14.3 Hz, 1H), 5.43 – 5.36 (m, 2H), 4.02 (s, 4H), 3.99 – 3.98 (m, 2H), 3.89 (br, 1H), 3.77 (td, J = 10.0, 4.6 Hz, 1H), 3.72 – 3.67 (m, 1H), 3.56 (s, 3H), 3.51 (d, J = 11.7 Hz, 1H), 3.24 (d, J = 11.4 Hz, 1H), 2.99 (dd, J = 19.2, 9.8 Hz, 1H), 2.68 – 2.62 (m, 1H), 1.85 – 1.68 (m, 4H), 1.17 – 1.10 (m, 1H), 1.05 – 0.94 (m, 2H), 0.84 – 0.77 (m, 1H); ^{13}C NMR (100 MHz, DMSO- d_6): δ 171.7, 164.1, 159.4, 159.0, 158.6, 158.3, 153.9, 151.5, 148.2, 141.4 (d, J = 26.6 Hz), 140.0, 135.4, (d, J = 42.0 Hz), 133.7, 132.1, 121.3, 121.2, 108.2, 107.6 (d, J = 94.8 Hz), 62.0, 58.1, 54.9, 54.5 (d, J = 14.1 Hz), 51.9 (d, J = 36.3 Hz), 42.2, 34.7, 34.6, 34.0, 21.0, 18.1, 9.9, 8.8; DEPT-135 NMR (100 MHz, DMSO- d_6): δ 151.0 (CH), 131.5 (CH), 106.9 (CH), 61.3 (CH₃), 57.4 (CH₂), 54.1 (CH), 53.8 (CH₂), 51.2 (CH₂), 41.5 (CH₂), 34.0 (CH), 33.9 (CH), 33.3 (CH₃), 20.4 (CH₂), 17.4 (CH₂), 9.2 (CH₂), 8.1 (CH₂); HRMS (ESI-TOF) for C₂₆H₃₀FN₆O₆ [M]⁺: Calcd., 541.2205, Found, 541.2205.

6-(1-cyclopropyl-6-fluoro-8-methoxy-3-(((1-methyl-2-nitro-1*H*-imidazol-5-yl)methoxy)carbonyl)-4-oxo-1,4-dihydroquinolin-7-yl)octahydro-1*H*-pyrrolo[3,4-

b]pyridin-1-ium 2,2,2-trifluoroacetate (37): Starting from **31** (0.180 g, 0.28 mmol), **37**

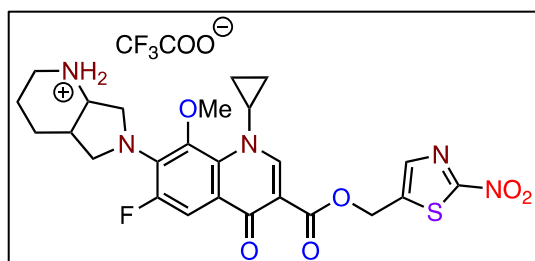


(0.178 g, 97%) was obtained as a white solid; mp = 189-190 °C; R_f (MeOH:DCM = 10:90) = 0.1; FT-IR (ν_{max} , cm^{-1}): 2963 (C-H stretch), 1718 (ester C=O stretch), 1688 (conjugated ketone C=O stretch), 1617 (N-H bend), 1539

(asymmetric NO₂ stretch), 1320 (symmetric NO₂ stretch); ^{19}F NMR (376 MHz, DMSO- d_6): δ -74.3, -122.8; ^1H NMR (400 MHz, DMSO- d_6): δ 9.23 (d, J = 11.5 Hz, 1H), 8.60 – 8.55 (m, 1H), 8.48 (s, 1H), 7.56 (d, J = 14.4 Hz, 1H), 7.33 (s, 1H), 5.38 (s, 2H), 4.04 (s, 3H), 4.02 - 3.97 (m, 2H), 3.90 (s, 1H), 3.76 (td, J = 10.1, 4.8 Hz, 1H), 3.72 – 3.67 (m, 1H), 3.56 (s, 3H), 3.50

(d, $J = 10.1$ Hz, 1H), 3.23 (d, $J = 13.4$ Hz, 1H), 2.98 (d, $J = 10.6$ Hz, 1H), 2.68 – 2.65 (m, 1H), 1.86 – 1.72 (m, 4H), 1.16 – 1.07 (m, 1H), 1.05 – 0.94 (m, 2H), 0.81 – 0.76 (m, 1H); ^{13}C NMR (100 MHz, DMSO- d_6): δ 171.3, 163.9, 158.5, 158.2, 153.5, 151.2, 151.0, 146.1, 141.0 (d, $J = 26.2$ Hz), 134.9 (d, $J = 42.2$ Hz), 133.4, 133.3, 128.6, 120.8 (d, $J = 29.1$ Hz), 108.0, 107.2 (d, $J = 93.2$ Hz), 61.5, 55.1, 54.4, 54.1 (d, $J = 14.1$ Hz), 51.4 (d, $J = 36.4$ Hz), 41.8, 34.4, 34.2, 20.6, 17.7, 9.4, 8.4; DEPT-135 NMR (100 MHz, DMSO- d_6): δ 150.9 (CH), 128.4 (CH), 107.0 (CH), 61.3 (CH₃), 54.8 (CH₂), 54.2 (CH), 53.9 (CH₂), 51.3 (CH₂), 41.6 (CH₂), 34.1 (CH), 34.0 (CH), 20.4 (CH₂), 17.4 (CH₂), 9.2 (CH₂), 8.1 (CH₂); HRMS (ESI-TOF) for C₂₆H₃₀FN₆O₆ [M]⁺: Calcd., 541.2205, Found, 541.2209.

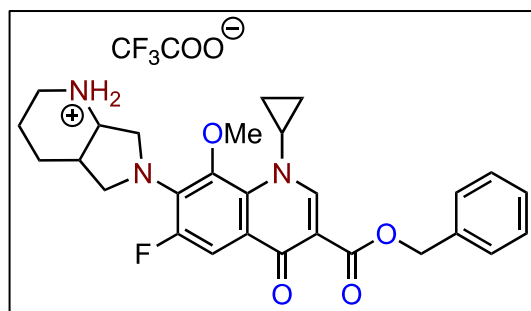
6-(1-cyclopropyl-6-fluoro-8-methoxy-3-(((2-nitrothiazol-5-yl)methoxy) carbonyl)-4-oxo-1,4-dihydroquinolin-7-yl)octahydro-1H-pyrrolo[3,4-b]pyridin-1-ium **2,2,2-trifluoroacetate (38)**: Starting from **32** (0.180 g, 0.27 mmol), **38** (0.178 g, 97%) was obtained as orange yellow solid; mp = 207-208 °C; R_f (MeOH: DCM = 10:90) = 0.1; FT-IR (ν_{\max} , cm⁻¹): 2924 (C-H stretch), 1716 (ester C=O stretch), 1680 (conjugated ketone C=O stretch), 1617 (N-H bend), 1543 (asymmetric NO₂ stretch), 1322 (symmetric NO₂ stretch); ^{19}F NMR (376 MHz, DMSO- d_6): δ -74.6, -122.7; ^1H NMR (400 MHz, DMSO- d_6): δ 9.25 (d, $J = 9.7$ Hz, 1H), 8.58 (d, $J = 9.1$ Hz, 1H), 8.53 (s, 2H), 8.16 (s, 1H), 7.57 (d, $J = 14.2$ Hz, 1H), 5.56 (s, 2H), 4.03 – 3.98 (m, 2H), 3.89 (t, $J = 5.7$ Hz, 1H), 3.77 (td, $J = 10.0, 4.6$ Hz, 1H), 3.72 – 3.67 (m, 1H), 3.56 (s, 3H), 3.50 (d, $J = 12.2$ Hz, 1H), 3.23 (d, $J = 12.8$ Hz, 1H), 2.98 (t, $J = 10.6$ Hz, 1H), 2.68 – 2.64 (m, 1H), 1.83 – 1.70 (m, 4H), 1.15 – 1.10 (m, 1H), 1.04 – 0.96 (m, 2H), 0.83 – 0.79 (m, 1H); ^{13}C NMR (100 MHz, DMSO- d_6): δ 171.2, 166.3, 164.2, 153.5, 151.4, 151.0, 142.8, 141.9, 141.0 (d, $J = 26.5$ Hz), 135.0 (d, $J = 41.8$ Hz), 120.8 (d, $J = 28.3$ Hz), 107.5, 107.2 (d, $J = 94.7$ Hz), 61.5, 57.9, 54.4, 54.0 (d, $J = 13.6$ Hz), 51.5 (d, $J = 36.8$ Hz), 41.8, 34.2, 20.6, 17.7, 9.5, 8.4; DEPT-135 NMR (100 MHz, DMSO- d_6): δ 151.1 (CH), 141.6 (CH), 107.0 (CH), 61.3 (CH₃), 57.7 (CH₂), 54.2 (CH), 53.9 (CH₂), 51.2 (CH₂), 41.5 (CH₂), 34.0 (CH), 20.4 (CH₂), 17.4 (CH₂), 9.2 (CH₂), 8.1 (CH₂); HRMS (ESI-TOF) for C₂₅H₂₇FN₅O₆S [M]⁺: Calcd., 544.1661, Found, 544.1669.



2,2,2-trifluoroacetate (38): Starting from **32** (0.180 g, 0.27 mmol), **38** (0.178 g, 97%) was obtained as orange yellow solid; mp = 207-208 °C; R_f (MeOH: DCM = 10:90) = 0.1; FT-IR (ν_{\max} , cm⁻¹): 2924 (C-H stretch), 1716 (ester C=O stretch), 1680

(conjugated ketone C=O stretch), 1617 (N-H bend), 1543 (asymmetric NO₂ stretch), 1322 (symmetric NO₂ stretch); ^{19}F NMR (376 MHz, DMSO- d_6): δ -74.6, -122.7; ^1H NMR (400 MHz, DMSO- d_6): δ 9.25 (d, $J = 9.7$ Hz, 1H), 8.58 (d, $J = 9.1$ Hz, 1H), 8.53 (s, 2H), 8.16 (s, 1H), 7.57 (d, $J = 14.2$ Hz, 1H), 5.56 (s, 2H), 4.03 – 3.98 (m, 2H), 3.89 (t, $J = 5.7$ Hz, 1H), 3.77 (td, $J = 10.0, 4.6$ Hz, 1H), 3.72 – 3.67 (m, 1H), 3.56 (s, 3H), 3.50 (d, $J = 12.2$ Hz, 1H), 3.23 (d, $J = 12.8$ Hz, 1H), 2.98 (t, $J = 10.6$ Hz, 1H), 2.68 – 2.64 (m, 1H), 1.83 – 1.70 (m, 4H), 1.15 – 1.10 (m, 1H), 1.04 – 0.96 (m, 2H), 0.83 – 0.79 (m, 1H); ^{13}C NMR (100 MHz, DMSO- d_6): δ 171.2, 166.3, 164.2, 153.5, 151.4, 151.0, 142.8, 141.9, 141.0 (d, $J = 26.5$ Hz), 135.0 (d, $J = 41.8$ Hz), 120.8 (d, $J = 28.3$ Hz), 107.5, 107.2 (d, $J = 94.7$ Hz), 61.5, 57.9, 54.4, 54.0 (d, $J = 13.6$ Hz), 51.5 (d, $J = 36.8$ Hz), 41.8, 34.2, 20.6, 17.7, 9.5, 8.4; DEPT-135 NMR (100 MHz, DMSO- d_6): δ 151.1 (CH), 141.6 (CH), 107.0 (CH), 61.3 (CH₃), 57.7 (CH₂), 54.2 (CH), 53.9 (CH₂), 51.2 (CH₂), 41.5 (CH₂), 34.0 (CH), 20.4 (CH₂), 17.4 (CH₂), 9.2 (CH₂), 8.1 (CH₂); HRMS (ESI-TOF) for C₂₅H₂₇FN₅O₆S [M]⁺: Calcd., 544.1661, Found, 544.1669.

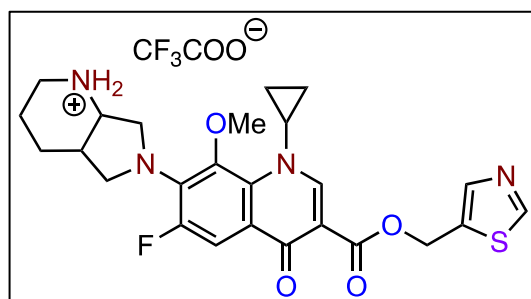
6-(3-((benzyloxy)carbonyl)-1-cyclopropyl-6-fluoro-8-methoxy-4-oxo-1,4-dihydroquinolin-7-yl)octahydro-1H-pyrrolo[3,4-b]pyridin-1-ium 2,2,2-trifluoroacetate



(41): Starting from **39** (0.100 g, 0.17 mmol), **41** (0.090 g, 88%) was isolated as a yellow solid; mp = 147-148 °C; R_f (MeOH: DCM = 10:90) = 0.2; FT-IR (ν_{max} , cm^{-1}): 3522 (N-H stretch), 2981 (C-H stretch), 1709 (ester C=O stretch), 1610 (conjugated ketone C=O stretch); ^{19}F NMR (376

MHz, DMSO- d_6): δ -74.2, -122.9; ^1H NMR (400 MHz, DMSO- d_6): δ 9.16 (d, J = 9.2 Hz, 1H), 8.55 (d, J = 11.2 Hz, 1H), 8.50 (s, 1H), 7.58 (d, J = 14.3 Hz, 1H), 7.50 – 7.47 (m, 2H), 7.42 – 7.37 (m, 2H), 7.35 – 7.31 (m, 1H), 5.31 – 5.24 (m, 2H), 4.02 – 3.97 (m, 2H), 3.90 (br, 1H), 3.77 (td, J = 10.0, 4.4 Hz, 1H), 3.72 – 3.67 (m, 1H), 3.56 (s, 3H), 3.50 (d, J = 11.3 Hz, 1H), 3.23 (d, J = 12.4 Hz, 1H), 2.98 (d, J = 10.9 Hz, 1H), 2.68 – 2.62 (m, 1H), 1.84 – 1.66 (m, 4H), 1.16 – 1.07 (m, 1H), 1.04 – 0.94 (m, 2H), 0.84 – 0.76 (m, 1H); ^{13}C NMR (100 MHz, DMSO- d_6): δ 171.3, 164.3, 151.0, 150.9, 141.0 (d, J = 26.0 Hz), 136.7, 134.8 (d, J = 42.2 Hz), 133.3, 128.4, 127.8, 127.6, 120.9 (d, J = 29.7 Hz), 108.5, 107.2 (d, J = 95.5 Hz), 65.2, 61.5, 54.4, 54.1 (d, J = 12.2 Hz), 51.4 (d, J = 35.8 Hz), 41.8, 40.2, 34.2, 20.6, 17.7, 9.4, 8.4; DEPT-135 NMR (100 MHz, DMSO- d_6): δ 150.6 (CH), 128.1 (CH), 127.5 (CH), 127.4 (CH), 106.9 (CH), 64.9 (CH₂), 61.2 (CH₃), 54.1 (CH), 53.8 (CH₂), 51.1 (CH₂), 41.5 (CH₂), 33.9 (CH), 20.4 (CH₂), 17.4 (CH₂), 9.2 (CH₂), 8.1 (CH₂); HRMS (ESI-TOF) for C₂₈H₃₁FN₃O₄ [M]⁺: Calcd., 492.2293, Found, 492.2297.

6-(1-cyclopropyl-6-fluoro-8-methoxy-4-oxo-3-((thiazol-5-ylmethoxy)carbonyl)-1,4-dihydroquinolin-7-yl)octahydro-1H-pyrrolo[3,4-b]pyridin-1-ium 2,2,2-trifluoroacetate



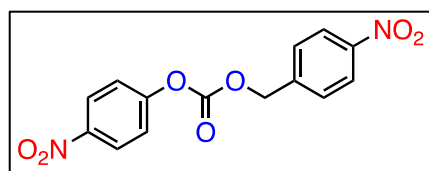
(42): Starting from **40** (0.100 g, 0.16 mmol), **42** (0.090 g, 88%) was isolated as a yellow solid; mp = 188-189 °C; R_f (MeOH: DCM = 10:90) = 0.2; FT-IR (ν_{max} , cm^{-1}): 2952 (C-H stretch), 1716 (ester C=O stretch), 1686 (conjugated ketone C=O stretch), 1617 (N-H stretch); ^{19}F NMR (376 MHz,

DMSO- d_6): δ -74.3, -122.8; ^1H NMR (400 MHz, DMSO- d_6): δ 9.18 – 9.12 (m, 2H), 8.53 – 8.48 (m, 2H), 8.02 (s, 1H), 7.54 (d, J = 14.3 Hz, 1H), 5.49 (s, 2H), 4.01 – 3.97 (m, 2H), 3.89 (br, 1H), 3.76 (td, J = 9.9, 4.3 Hz, 1H), 3.71 – 3.66 (m, 1H), 3.55 (s, 3H), 3.49 (d, J = 11.2 Hz,

1H), 3.23 (d, $J = 14.3$ Hz, 1H), 2.98 (q, $J = 10.8$ Hz, 1H), 2.67 – 2.64 (m, 1H), 1.84 – 1.66 (m, 4H), 1.15 – 1.07 (m, 1H), 1.03 – 0.93 (m, 2H), 0.83 – 0.75 (m, 1H); ^{13}C NMR (100 MHz, DMSO- d_6): δ 171.2, 164.0, 158.4, 158.1, 155.9, 153.4, 151.1, 151.0, 143.7, 141.0 (d, $J = 25.8$ Hz), 135.0 (d, $J = 41.8$ Hz), 133.3, 120.8 (d, $J = 30.1$ Hz), 115.7, 108.0, 107.2 (d, $J = 94.3$ Hz), 61.5, 57.5, 54.4, 54.1 (d, $J = 16.0$ Hz), 51.4 (d, $J = 38.4$ Hz), 41.8, 34.2, 20.6, 17.7, 9.4, 8.4; DEPT-135 NMR (100 MHz, DMSO- d_6): δ 150.8 (CH), 143.4 (CH), 106.9 (CH), 61.3 (CH₃), 57.2 (CH₂), 54.2 (CH), 53.9 (CH₂), 51.2 (CH₂), 41.6 (CH₂), 34.0 (CH), 20.4 (CH₂), 17.4 (CH₂), 9.2 (CH₂), 8.1 (CH₂); HRMS (ESI-TOF) for C₂₅H₂₈FN₄O₄S [M]⁺: Calcd., 499.1810, Found, 499.1816.

2.5.2.D. Synthesis of carbonates

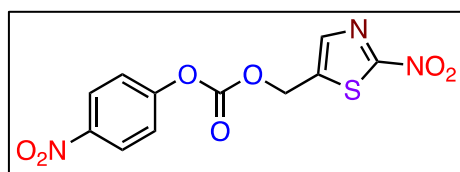
4-nitrobenzyl (4-nitrophenyl) carbonate (43): A solution of 4-nitrophenyl chloroformate



(0.987 g, 4.90 mmol) in anhydrous DCM (3 mL) was slowly added after 10 min to a stirred solution of **1a** (0.5 g, 3.27 mmol) and Et₃N (0.911 mL, 6.53 mmol) in anhydrous DCM (6 mL). The reaction mixture was stirred under

nitrogen atmosphere at RT for 16 h and then partitioned between DCM (20 mL) and water (20 mL). The organic layer was washed with water (30 mL) and brine (30 mL). The combined organic extracts were dried and the solvent was evaporated. The residue was purified by silica gel (60-120 mesh) column chromatography using 12% EtOAc/hexane to obtain **43** (0.702 g, 68%) as a white solid. The analytical data is consistent with the reported literature.²³

4-nitrophenyl ((2-nitrothiazol-5-yl)methyl) carbonate (44): A solution of 4-nitrophenyl



chloroformate (1.36 g, 6.75 mmol) in anhydrous THF (3 mL) was slowly added to a stirred solution of **1f** (0.901 g, 5.63 mmol) and pyridine (0.543 mL, 6.75 mmol) in anhydrous THF (6 mL) after 20 min at room

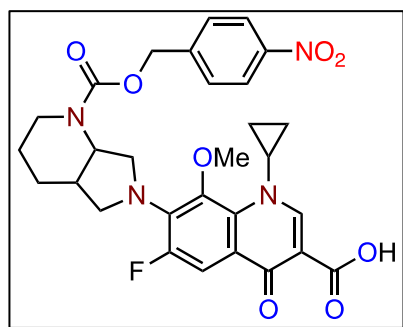
temperature. The reaction mixture was allowed to stir under nitrogen atmosphere at RT for 12 h and then partitioned between EtOAc (20 mL) and water (20 mL). The organic layer was washed with water (30 mL) and brine (30 mL). The combined extracts were dried and the solvent was evaporated. The residue was purified by silica gel (60-120 mesh) column chromatography using 10% EtOAc/hexane to obtain **44** (0.280 g, 16%) as yellow solid. R_f (EtOAc:hexane = 20:80) = 0.5; ^1H NMR (400 MHz, CDCl₃): δ 8.32 – 8.29 (m, 2H), 7.96 (s,

1H), 7.42 – 7.38 (m, 2H), 5.51 (s, 2H). HRMS (ESI-TOF) for C₁₁H₇N₃O₇S [M+H]⁺: Calcd., 326.0083, Found, 326.0078.

2.5.2.E. General procedure for synthesis of nitroheterocyclic carbamates of MXF (45-46)

To a dried two-neck round bottom flask charged with a stir bar and carbonate derivative **43** or **44** (0.383 mmol) in anhydrous DMF (2 mL), Et₃N (0.106 mL, 0.766 mmol) was added. This was followed by dropwise addition of a solution of MXF (0.200 g, 0.498 mmol) in anhydrous DMF (2 mL). The reaction mixture was left to stir at RT overnight under a positive pressure of nitrogen. After completion of the reaction (determined by TLC), the crude product was adsorbed onto celite. The resulting filtrate was diluted with water (10 mL), and the aqueous layer was extracted with EtOAc (3 × 10 mL). The organic extracts were combined, washed with brine (2 × 10 mL), dried over anhydrous Na₂SO₄, filtered and the filtrate was concentrated under reduced pressure. The residue was subjected to purification by column chromatography over silica gel (60-120) with 5-10% MeOH/CHCl₃ to provide MXF carbamates **45-46** as pure products.

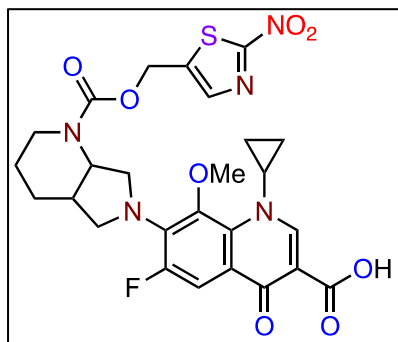
1-cyclopropyl-6-fluoro-8-methoxy-7-(1-(((4-nitrobenzyl)oxy)carbonyl)octahydro-6H-pyrrolo[3,4-*b*]pyridin-6-yl)-4-oxo-1,4-dihydroquinoline-3-carboxylic acid (45): Starting from **43** (0.122 g, 0.383 mmol) and MXF, **45** (0.126 g, 56%) was isolated as a yellow solid;



mp = 183-184 °C; *R_f* (EtOAc:hexane = 50:50) = 0.5; FT-IR (*v*_{max}, cm⁻¹): 3502 (N-H stretch), 2930 (C-H stretch), 1727 (ester C=O stretch), 1701 (conjugated ketone C=O stretch), 1619 (N-H stretch), 1442 (asymmetric NO₂ stretch), 1319 (symmetric NO₂ stretch); ¹⁹F NMR (376 MHz, CDCl₃): δ -121.0; ¹H NMR (400 MHz, CDCl₃): δ 14.94 (s, 1H), 8.78 (s, 1H), 8.23 (d, *J* = 6.7 Hz, 2H), 7.80 (d, *J* = 13.8 Hz, 1H), 7.53 (d, *J* = 8.8 Hz, 2H), 5.27 (s, 2H), 4.88 (s, 1H), 4.20 – 4.09 (m, 2H), 4.02 – 3.96 (m, 1H), 3.93 (td, *J* = 10.1, 2.6 Hz, 1H), 3.58 (s, 3H), 3.29 (s, 1H), 3.02 (s, 1H), 2.38 – 2.30 (m, 1H), 1.89 – 1.82 (m, 2H), 1.60 – 1.50 (m, 2H), 1.35 – 1.27 (m, 1H), 1.17 – 1.05 (m, 2H), 0.90 – 0.79 (m, 2H); ¹³C NMR (100 MHz, CDCl₃): δ 176.9, 167.1, 155.5, 149.9, 147.8, 144.0, 134.5, 128.4, 124.0, 119.1 (d, *J* = 35.0 Hz), 108.2 (d, *J* = 94.7 Hz), 107.9, 66.1, 61.3, 56.5 (d, *J* = 30.6 Hz), 52.9, 40.5, 39.9, 35.7, 29.8, 25.3, 10.7, 8.6; DEPT-135 NMR (100 MHz, CDCl₃): δ 149.8 (CH), 128.3 (CH), 123.9 (CH), 108.1 (CH), 66.0 (CH₂), 61.2 (CH₃), 56.5 (CH₂), 52.8 (CH), 40.4 (CH), 39.8 (CH₂), 35.6 (CH), 25.1

(CH₂), 10.6 (CH₂), 8.5 (CH₂); HRMS (ESI-TOF) for C₂₉H₂₉FN₄O₈ [M+H]⁺: Calcd., 581.2047, Found, 581.2051.

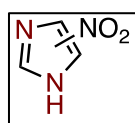
1-cyclopropyl-6-fluoro-8-methoxy-7-(1-(((2-nitrothiazol-5-yl) methoxy) carbonyl) octahydro-6H-pyrrolo[3,4-b]pyridin-6-yl)-4-oxo-1,4-dihydroquinoline-3-carboxylic acid



(46): Starting from **44** (0.124 g, 0.383 mmol) and MXF, **46** (0.140 g, 62%) was isolated as a yellow solid; mp = 131-132 °C; *R_f* (EtOAc:hexane = 50:50) = 0.35; FT-IR (ν_{max} , cm⁻¹): 3647 (N-H stretch), 2933 (C-H stretch), 1725 (ester C=O stretch), 1701 (conjugated ketone C=O stretch), 1619 (N-H stretch), 1439 (asymmetric NO₂ stretch), 1319 (symmetric NO₂ stretch); ¹⁹F NMR (376 MHz, CDCl₃): δ -121.1; ¹H NMR

(400 MHz, CDCl₃): δ 14.93 (s, 1H), 8.78 (s, 1H), 7.84 (s, 1H), 7.79 (d, *J* = 13.8 Hz, 1H), 5.35 (d, *J* = 4.7 Hz, 2H), 4.87 – 4.84 (m, 1H), 4.14 – 4.09 (m, 1H), 4.02 – 3.96 (m, 1H), 3.91 (td, *J* = 10.1, 2.6 Hz, 1H), 3.59 (s, 3H), 3.28 (d, *J* = 7.9 Hz, 1H), 3.01 (s, 1H), 2.36 – 2.30 (m, 1H), 1.86 – 1.82 (m, 2H), 1.58 – 1.49 (m, 2H), 1.35 – 1.27 (m, 1H), 1.18 – 1.03 (m, 3H), 0.90 – 0.80 (m, 2H); ¹³C NMR (100 MHz, CDCl₃): δ 176.9, 167.1, 155.2, 149.9, 142.2, 141.9, 134.5, 119.1 (d, *J* = 35.0 Hz), 108.3 (d, *J* = 94.7 Hz), 107.8, 61.3, 59.1, 56.5 (d, *J* = 30.6 Hz), 52.9, 40.5, 40.0, 35.6, 29.8, 25.1, 10.7, 8.6; DEPT-135 NMR (100 MHz, CDCl₃): δ 149.9 (CH), 141.9 (CH), 108.2 (CH), 61.3 (CH₃), 58.7 (CH₂), 56.5 (CH₂), 52.9 (CH), 40.5 (CH), 40.0 (CH₂), 35.6 (CH), 25.1 (CH₂), 24.1 (CH₂), 10.7 (CH₂); HRMS (ESI-TOF) for C₂₆H₂₆FN₅O₈S [M+H]⁺: Calcd., 588.1564, Found, 588.1572.

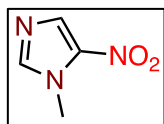
4(5)-nitro-1H-imidazole (5):⁵ Nitric acid (86 mL, 68%, 0.93 mol) was added dropwise to



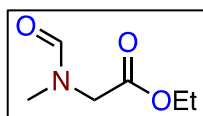
imidazole (10 g, 0.15 mol) in a round-bottom flask with a magnetic stir bar over an ice bath. The solution was stirred at 0 °C for 10 min. Then, sulphuric acid (41 mL, 98%, 0.41 mol) was added and further stirred for 30 min over an ice bath.

The reaction mixture was then refluxed overnight and then allowed to cool down to room temperature. The reaction mixture was then cooled down in the fridge and crushed ice was added to the solution. The white precipitate formed was filtered and washed with distilled water and dried under vacuum to obtain off-white crystals of **5** (2.5 g, 16%).

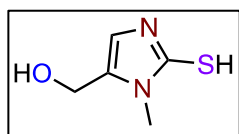
1-methyl-5-nitro-1*H*-imidazole (7):⁶ To a stirred solution of **5** (1 g, 8.84 mmol) in 1,4-dioxane (15 mL), dimethyl sulfate (1.26 mL, 13.27 mmol) was added. The reaction mixture was refluxed for 4 h. The reaction mixture was then concentrated and the oily residue was neutralized with a saturated solution of NaHCO₃ (15 mL) and then extracted with DCM (3 × 25 mL). The organic layers were combined, dried over Na₂SO₄, filtered, and the filtrate was concentrated *in vacuo*. The residue was purified by silica gel (60-120 mesh) column chromatography using 2% MeOH/DCM as an eluant to give **7** (0.612 g, 54%) as a dark greenish solid.



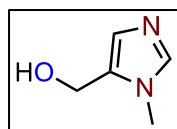
Ethyl *N*-formyl-*N*-methylglycinate (15):^{10,14} To a suspension of **12** (3 g, 25.6 mmol) in a mixture of EtOH (20 mL) and EtOCHO (12.6 mL), K₂CO₃ (4 g, 29.4 mmol) was added and vigorously stirred at RT overnight. The reaction mixture was filtered, filtrate was concentrated, dissolved in a minimum amount of water (3 mL) and then extracted with EtOAc (4 × 20 mL). The combined organic layers were dried over Na₂SO₄, filtered and concentrated under reduced pressure to provide **7** (0.612 g, 54%) as a yellow liquid.



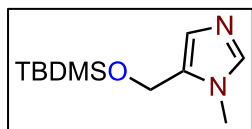
(2-mercapto-1-methyl-1*H*-imidazol-5-yl)methanol (18):^{16,17} To a mixture of *n*BuOH (200 mL) and AcOH (30 mL), dihydroxyacetone dimer (**17**) (25 g, 1.38 mol), KSCN (40.4 g, 4.16 mol) and methylamine hydrochloride (10.7 g, 3.46 mol) were added and stirred at 25 °C. After 5 days, water (50 mL) was added and the solid was isolated by filtration. The solid residue was washed with water (125 mL) and Et₂O (125 mL) and dried in vacuum to afford compound **18** (11.9 g, 59%) as a white powder.



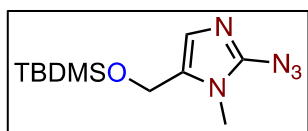
(1-methyl-1*H*-imidazol-5-yl)methanol (19):^{16,17} The intermediate **18** (8.16 g, 56.62 mmol) was added in small portions to a vigorously stirred solution of NaNO₂ (160 mg, 2.32 mmol) in aq. HNO₃ (20 mL, 2.4 M) at 0 °C over a period of 1 h. The resulting yellow solution was stirred at RT for 2 h. The reaction mixture was adjusted to pH 9.0 by adding solid NaHCO₃ and evaporated to dryness in vacuum. The residue was extracted with hot CHCl₃ (3 × 25 mL), dried over anhydrous Na₂SO₄, filtered, and the filtrate was concentrated *in vacuo* to give compound **19** (1.30 g, 20%) as a pale yellow solid.



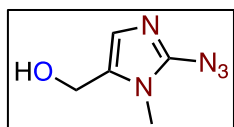
5-(((*tert*-butyldimethylsilyl)oxy)methyl)-1-methyl-1*H*-imidazole (20):¹⁸ To a solution of compound **19** (1.32 g, 11.77 mmol) in *N,N*-DMF (10 mL), imidazole (2.40 g, 35.32 mmol) and TBDMSCl (1.95 g, 12.95 mmol) was added. The reaction was stirred at RT for 6 h under nitrogen atmosphere, and the resulting mixture was poured into water (20 mL) and extracted with DCM (3 × 20 mL). The organic layer was dried over anhydrous Na₂SO₄, concentrated in *vacuo*, and purified by silica gel (60-120 mesh) using 1% EtOAc/hexane as an eluant to yield **20** (0.710 g, 60%) as a yellow solid.



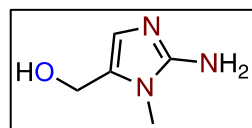
2-azido-5-(((*tert*-butyldimethylsilyl)oxy)methyl)-1-methyl-1*H*-imidazole (21):⁹ *n*BuLi (1.5 mL, 3.75 mmol, 2.4 N in hexane) was added dropwise at -78 °C to a solution of compound **20** (1 g, 4.42 mmol) in anhydrous THF (10 mL). TsN₃ (0.609 mL, 3.98 mmol) was then added dropwise and the reaction was continued stirring at -78 °C for 1 h. The reaction mixture was quenched with aq. NH₄Cl (15 mL) and extracted with EtOAc water (3 × 20 mL) and the combined organic extracts were washed with brine, dried over anhydrous Na₂SO₄ (2 g), filtered and the filtrate was concentrated *in vacuo* to afford the crude product. The residue was purified by column chromatography on silica gel (60-120 mesh) using 2% EtOAc/hexane as an eluant to give **21** (0.710 g, 60%) as yellow oil.



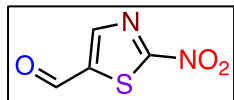
(2-azido-1-methyl-1*H*-imidazol-5-yl)methanol (22):⁹ The intermediate **21** (0.5 g, 1.87 mmol) was stirred in 1 N HCl/MeOH (5 mL) at RT for 4 h. The pH of the reaction was adjusted to 7.0 by adding a few drops of Et₃N. The reaction mixture was concentrated and then the crude product was washed with Et₂O (5 mL) to afford compound **22** (0.225 g, 78%) as a yellow solid.



(2-amino-1-methyl-1*H*-imidazol-5-yl)methanol (23):⁹ The compound **22** (0.220 g, 1.44 mmol) was dissolved in MeOH (5 mL). Pd/C (10%, 0.022 g) was then added and the mixture was hydrogenated under H₂ balloon at RT for 3 h. After reaction, the catalyst was removed by filtration and the filtrate was concentrated *in vacuo* to provide compound **23** (0.162 g, 89%) as a gray solid.

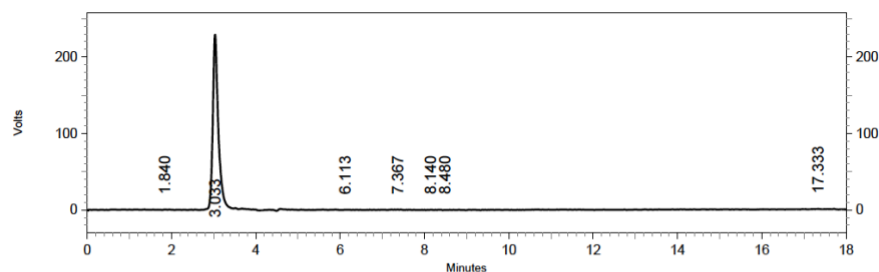


2-nitrothiazole-5-carbaldehyde (25):^{19,20} To a solution of **24** in fluoroboric acid (48% w/v, 6.12 mL), NaNO₂ (0.538 g, 7.80 mmol) in water (10 mL) was added dropwise at 0 °C for 1 h. The resulting solution was then added dropwise into a mixture of Cu powder (1.61 g, 25.3 mmol) and 30 % w/v solution of sodium nitrite in water (10 mL). The reaction mixture was stirred at RT for 1 h, filtered to remove Cu, and the filtrate was extracted with EtOAc (3 × 20 mL). The combined organic extracts were dried over anhydrous Na₂SO₄ and the filtrate was evaporated in vacuum. The residue was purified by silica gel (60-120 mesh) column chromatography using 10-12% EtOAc/hexane as an eluant to afford **25** (0.990 g, 80%) as a dark reddish solid.



2.5.3. Purity of prodrugs by HPLC

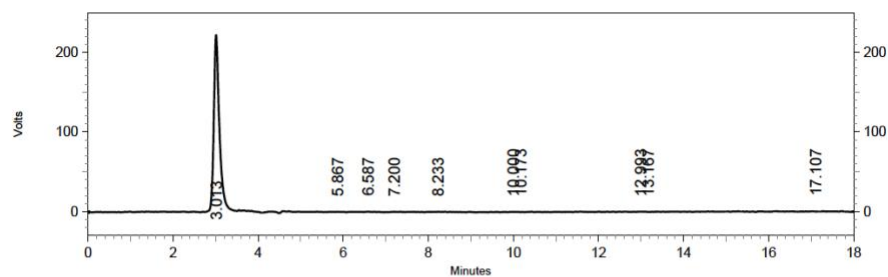
Stock solutions (1 mM) of **33-38**, **45** and **46** were independently prepared in DMSO. A solution of 25 μM of respective prodrug (5 μL, 1 mM stock) was added to 195 μL of ACN and then injected (25 μL) in an HPLC instrument attached with a diode-array detector (detection wavelength 280 nm). The stationary phase used was C-18 reversed phase column (4.6 mm × 100 mm, 5 μm). The mobile phase used was 0.1 % HCOOH in H₂O:ACN at a flow rate of 0.5 mL/min with a run time of 18 min starting with 40:60 → 0-4 min, 20:80 → 4-12 min, 40:60 → 12-15 min, 40:60 → 15-18 min.



DAD: Signal A,
280 nm/Bw:4 nm
Results

| Retention Time | Area | Area % | Height | Height % |
|----------------|---------|--------|--------|----------|
| 1.840 | 21342 | 0.46 | 1156 | 0.24 |
| 3.033 | 4382848 | 94.90 | 479452 | 98.53 |
| 6.113 | 9281 | 0.20 | 924 | 0.19 |
| 7.367 | 64021 | 1.39 | 1635 | 0.34 |
| 8.140 | 21134 | 0.46 | 1017 | 0.21 |
| 8.480 | 18011 | 0.39 | 596 | 0.12 |
| 17.333 | 101557 | 2.20 | 1809 | 0.37 |
| Totals | 4618194 | 100.00 | 486589 | 100.00 |

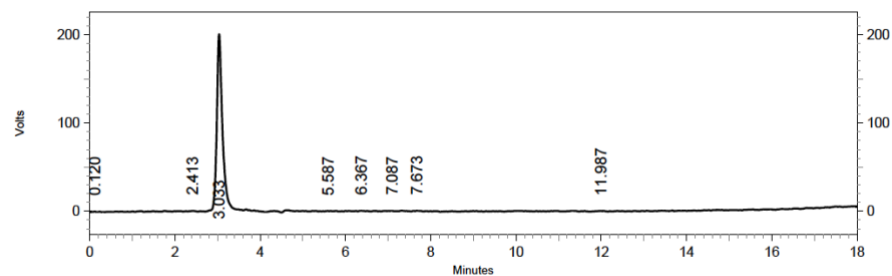
Figure 2.16. HPLC trace of **33**



DAD: Signal A,
280 nm/Bw:4 nm
Results

| Retention Time | Area | Area % | Height | Height % |
|----------------|---------|--------|--------|----------|
| 3.013 | 4249534 | 95.33 | 464587 | 98.29 |
| 5.867 | 18237 | 0.41 | 1100 | 0.23 |
| 6.587 | 47590 | 1.07 | 1756 | 0.37 |
| 7.200 | 48370 | 1.09 | 1342 | 0.28 |
| 8.233 | 60716 | 1.36 | 1430 | 0.30 |
| 10.000 | 14193 | 0.32 | 910 | 0.19 |
| 10.173 | 52 | 0.00 | 0 | 0.00 |
| 12.993 | 10661 | 0.24 | 642 | 0.14 |
| 13.167 | 24 | 0.00 | 0 | 0.00 |
| 17.107 | 8411 | 0.19 | 917 | 0.19 |
| Totals | 4457788 | 100.00 | 472684 | 100.00 |

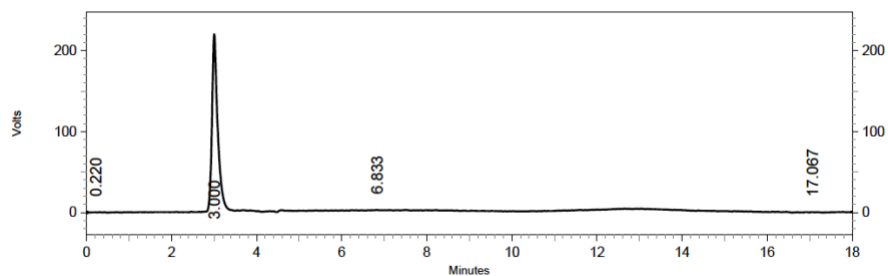
Figure 2.17. HPLC trace of 34



DAD: Signal A,
280 nm/Bw:4 nm
Results

| Retention Time | Area | Area % | Height | Height % |
|----------------|---------|--------|--------|----------|
| 0.120 | 8733 | 0.21 | 968 | 0.22 |
| 2.413 | 16169 | 0.40 | 1723 | 0.40 |
| 3.033 | 3864401 | 94.54 | 419994 | 97.47 |
| 5.587 | 12252 | 0.30 | 934 | 0.22 |
| 6.367 | 38289 | 0.94 | 1776 | 0.41 |
| 7.087 | 72793 | 1.78 | 1836 | 0.43 |
| 7.673 | 55056 | 1.35 | 2274 | 0.53 |
| 11.987 | 19815 | 0.48 | 1379 | 0.32 |
| Totals | 4087508 | 100.00 | 430884 | 100.00 |

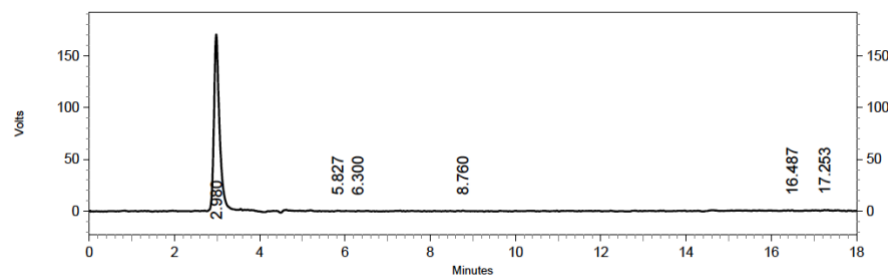
Figure 2.18. HPLC trace of 35



DAD: Signal A,
280 nm/Bw:4 nm
Results

| Retention Time | Area | Area % | Height | Height % |
|----------------|---------|--------|--------|----------|
| 0.220 | 11140 | 0.26 | 580 | 0.13 |
| 3.000 | 4261878 | 98.28 | 458484 | 99.40 |
| 6.833 | 44946 | 1.04 | 1067 | 0.23 |
| 17.067 | 18333 | 0.42 | 1114 | 0.24 |
| Totals | 4336297 | 100.00 | 461245 | 100.00 |

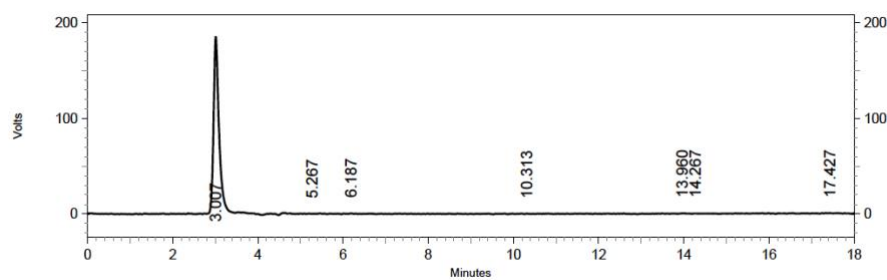
Figure 2.19. HPLC trace of 36



DAD: Signal A,
280 nm/Bw:4 nm
Results

| Retention Time | Area | Area % | Height | Height % |
|----------------|---------|--------|--------|----------|
| 2.980 | 3265485 | 95.52 | 357050 | 97.92 |
| 5.827 | 23674 | 0.69 | 1381 | 0.38 |
| 6.300 | 14342 | 0.42 | 1229 | 0.34 |
| 8.760 | 28198 | 0.82 | 1389 | 0.38 |
| 16.487 | 18731 | 0.55 | 1576 | 0.43 |
| 17.253 | 68362 | 2.00 | 2028 | 0.56 |
| Totals | 3418792 | 100.00 | 364653 | 100.00 |

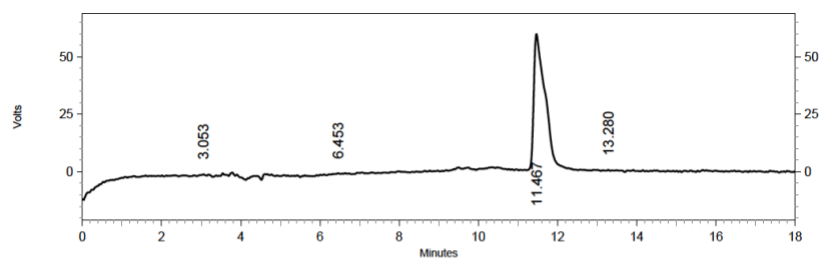
Figure 2.20. HPLC trace of 37



DAD: Signal A,
280 nm/Bw:4 nm
Results

| Retention Time | Area | Area % | Height | Height % |
|----------------|---------|--------|--------|----------|
| 3.007 | 3435313 | 96.56 | 387705 | 98.32 |
| 5.267 | 7606 | 0.21 | 689 | 0.17 |
| 6.187 | 18837 | 0.53 | 1559 | 0.40 |
| 10.313 | 24065 | 0.68 | 927 | 0.24 |
| 13.960 | 13319 | 0.37 | 1205 | 0.31 |
| 14.267 | 18752 | 0.53 | 821 | 0.21 |
| 17.427 | 39816 | 1.12 | 1411 | 0.36 |
| Totals | 3557708 | 100.00 | 394317 | 100.00 |

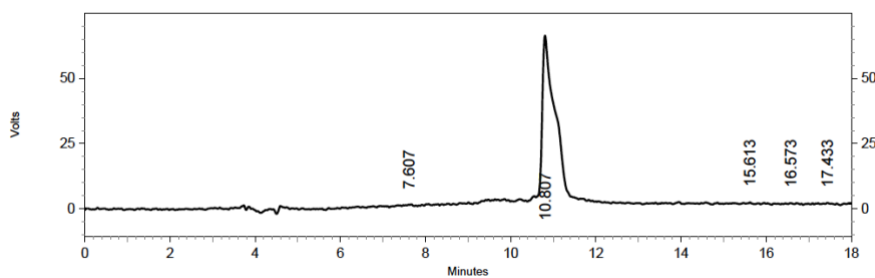
Figure 2.21. HPLC trace of 38



DAD: Signal A,
280 nm/Bw:4 nm
Results

| Retention Time | Area | Area % | Height | Height % |
|----------------|---------|--------|--------|----------|
| 3.053 | 27623 | 1.09 | 1876 | 1.46 |
| 6.453 | 26293 | 1.04 | 1334 | 1.04 |
| 11.467 | 2476755 | 97.55 | 124152 | 96.81 |
| 13.280 | 8286 | 0.33 | 876 | 0.68 |
| Totals | 2538957 | 100.00 | 128238 | 100.00 |

Figure 2.22. HPLC trace of 45



DAD: Signal A,
280 nm/Bw: 4 nm
Results

| Retention Time | Area | Area % | Height | Height % |
|----------------|---------|--------|--------|----------|
| 7.607 | 35855 | 1.29 | 1480 | 1.08 |
| 10.807 | 2626734 | 94.66 | 130403 | 95.55 |
| 15.613 | 30280 | 1.09 | 1487 | 1.09 |
| 16.573 | 35370 | 1.27 | 1359 | 1.00 |
| 17.433 | 46566 | 1.68 | 1748 | 1.28 |
| Totals | 2774805 | 100.00 | 136477 | 100.00 |

Figure 2.23. HPLC trace of **46**

2.5.4. Electrochemical studies by Cyclic voltammetry

Cyclic voltammetry studies were conducted using a standard three-electrode setup connected to a CHI760E electrochemical workstation. Glassy carbon and platinum wire were used as the working electrode and counter electrode respectively. Ag/AgCl was used as a reference electrode. These experiments were conducted under an atmosphere of argon in anhydrous ACN with tetra-butyl ammonium hexafluorophosphate (TBAP; 0.1 M) as supporting electrolyte. Stock solutions of compounds **33-38**, **45** and **46** (10 mM in DMSO) were prepared, added to respective 25 mL volumetric flasks and diluted (20-fold; final conc. 0.5 mM) with electrolyte solution. The cyclic voltammograms (CV) were recorded at 20 °C in a potential range between -2 V to +2 V at a scan rate of 100 mV/s with 10 sweep segments, 0.001 V sample interval, 2 s quiet time and 1×10^{-5} A/V sensitivity. Potentials (V) were calibrated using an internal standard Fc/Fc⁺ redox couple and are reported vs. Ag/AgCl.

2.5.5. Monitoring the absorbance and fluorescence of MXF by fluorimetry

A stock solution of MXF (1 mM) was prepared in DMSO. MXF (10 μ L, 1 mM stock) was diluted with 990 μ L of pH 7.4 phosphate buffer (10 mM) in a 1.5 mL eppendorf tube and then transferred into a quartz micro-fluorescence cuvette (Hellma, path length 1 cm). Absorption spectra was recorded on a SHIMADZU UV-2600 UV-Vis spectrophotometer. Fluorescence spectra ($\lambda_{\text{ex}} = 289$ nm and $\lambda_{\text{em}} = 488$ nm) was recorded using a HORIBA Jobin Yvon Fluorolog fluorescence spectrophotometer with an excitation and emission slit width of 1 nm.

2.5.6. Monitoring the release of MXF upon chemoreduction of prodrugs

(A) Sodium dithionite induced chemoreduction of NTR-MXF prodrugs

A stock solution of sodium dithionite (38.2 mM) was prepared in 15 mL of methanol-water (1:1 v/v). A solution of 10 μ M of prodrug (2 μ L, 1 mM stock) was added to 198 μ L of 38.2 mM Na₂S₂O₄ solution in a 96-well plate. The plate was incubated at 25 °C inside microplate reader (EnSight) with shaking (60 rpm) and the fluorescence response was recorded after 15 min.

(B) Zinc/Ammonium formate mediated chemoreduction of prodrugs

Chemoreduction assays were conducted as previously reported with some modifications.²⁸ A stock solution of ammonium formate (3 mM) was prepared in deionised water. The reaction samples were prepared by adding 30 μ M of ammonium formate (18 μ L, 3 mM stock) followed by zinc dust (15 mg) to a 2 mL eppendorf tubes containing a solution of 10 μ M of prodrugs (18 μ L, 1 mM stock) in 1764 μ L of methanol-water (1:1 v/v). The reaction mixtures were incubated at 37 °C in an Eppendorf thermomixer comfort (800 rpm). Aliquots (250 μ L) were taken from the reaction mixture after 30 min (or at periodic intervals to monitor the time course of MXF release from **37** and **38**), and centrifuged (9,391 \times g for 2 min). The supernatant (200 μ L) was then carefully transferred to a 96-well plate (Tarson). Reduction of the prodrugs were monitored by measurement of fluorescence ($\lambda_{\text{ex}} = 289$ nm and $\lambda_{\text{em}} = 488$ nm) using a microplate reader (EnSight).

2.5.7. Kinetics of dithionite-dependent reduction of NTR-MXF prodrugs

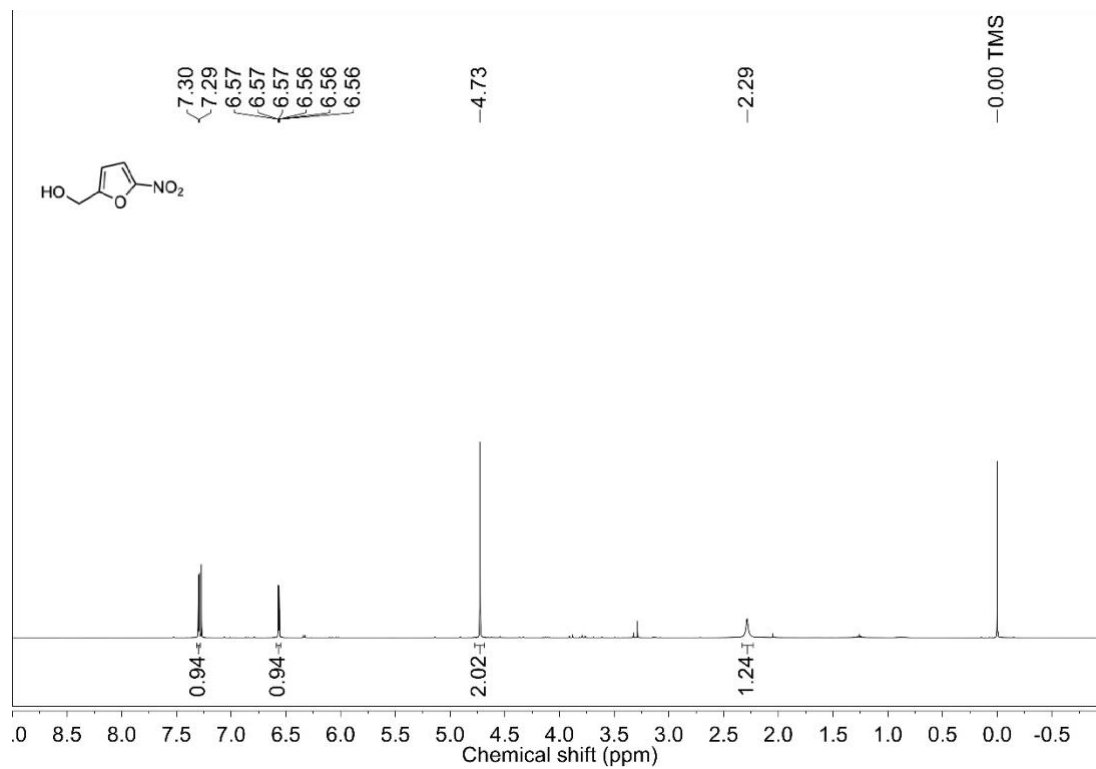
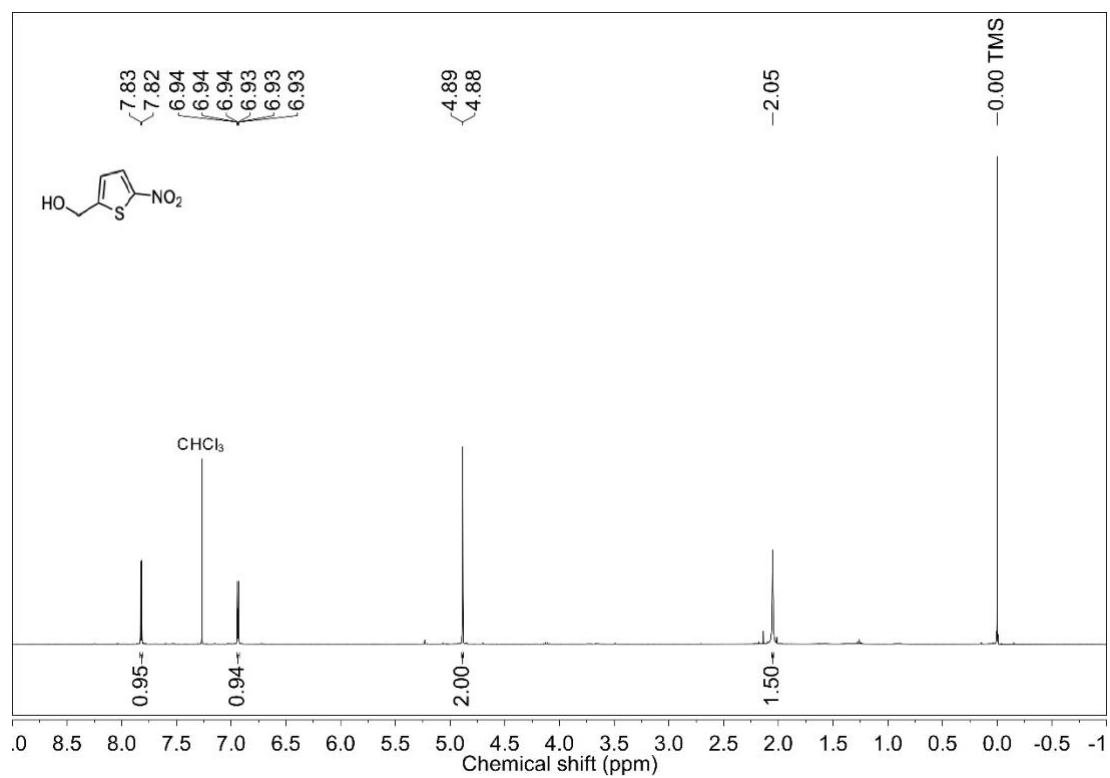
Varying concentrations of sodium dithionite (Na₂S₂O₄; 2.5-7.5 mM) in 15 mL of methanol-water (1:1 v/v) were independently prepared. Reduction reactions were performed in a 96-well microtiter plate by addition of 10 μ M of compound (2 μ L; 1 mM stock) to 198 μ L of Na₂S₂O₄ solution with a fixed (2.5 mM) or a range of concentrations of dithionite (2.5-7.5 mM). The kinetics of dithionite-dependent changes in fluorescence ($\lambda_{\text{ex}} = 289$ nm and $\lambda_{\text{em}} = 488$ nm) was recorded at 25 °C for a period of 4 min (frequency of measurement was 1 s) using a microplate reader (EnSight).

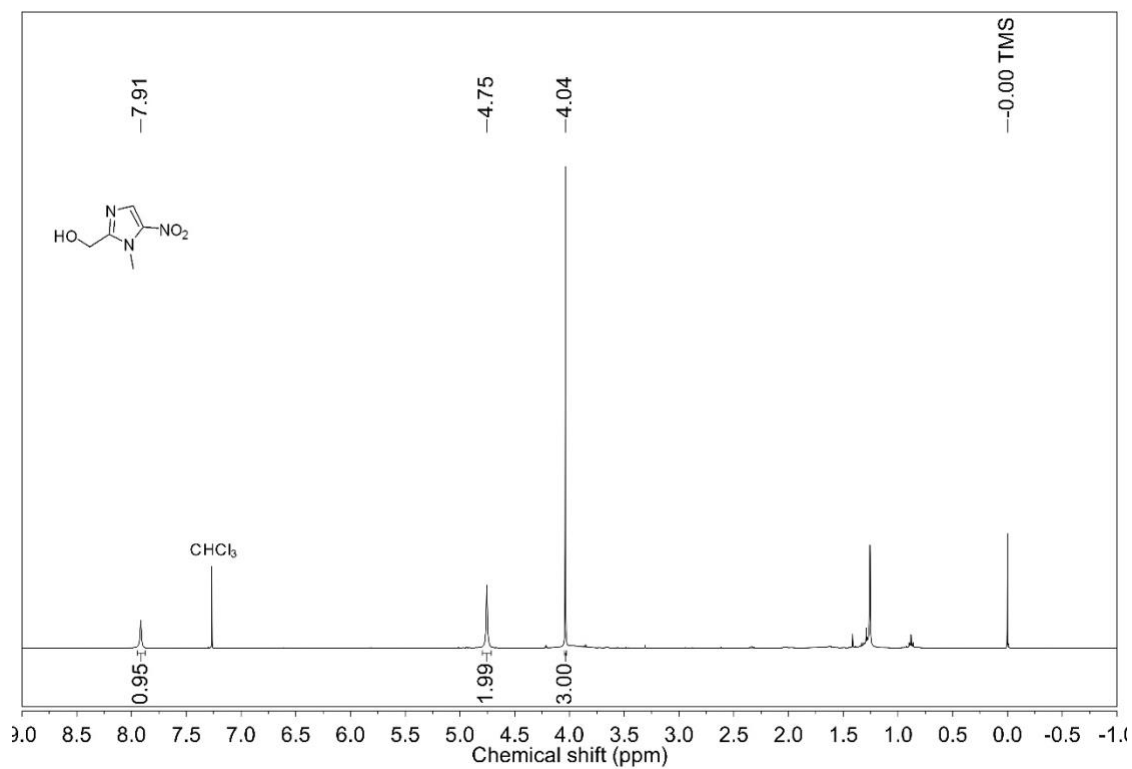
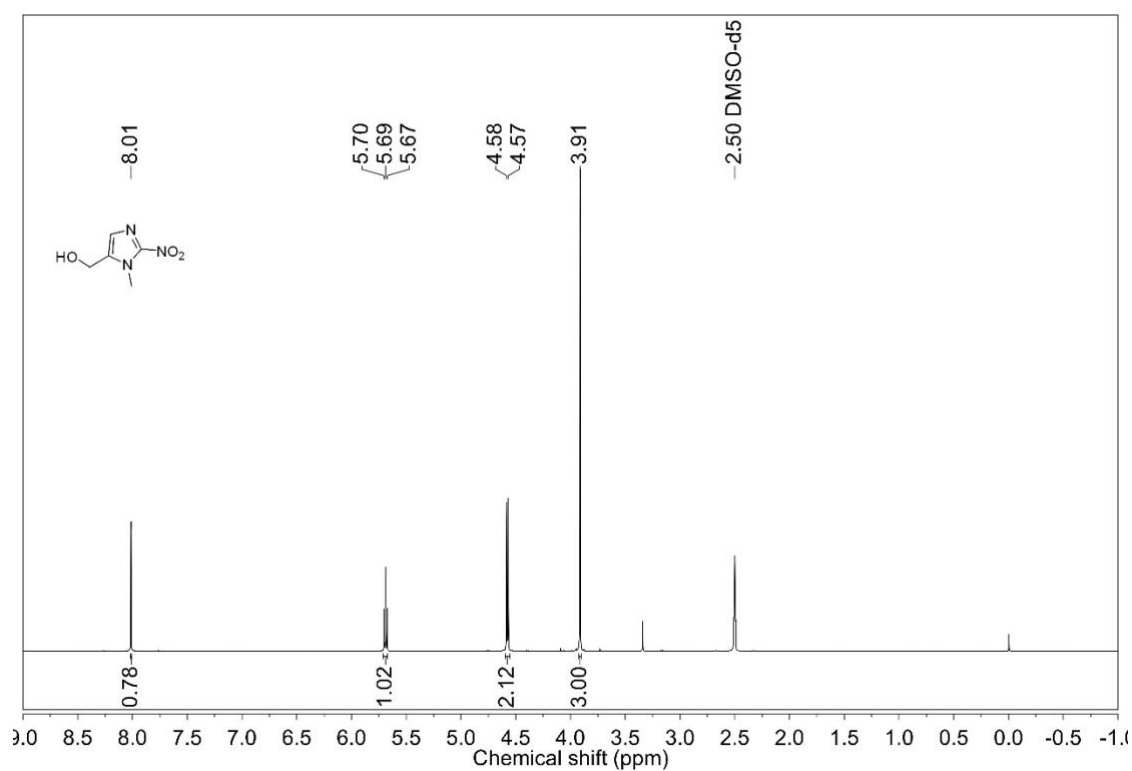
2.5.8. Decomposition studies by HPLC

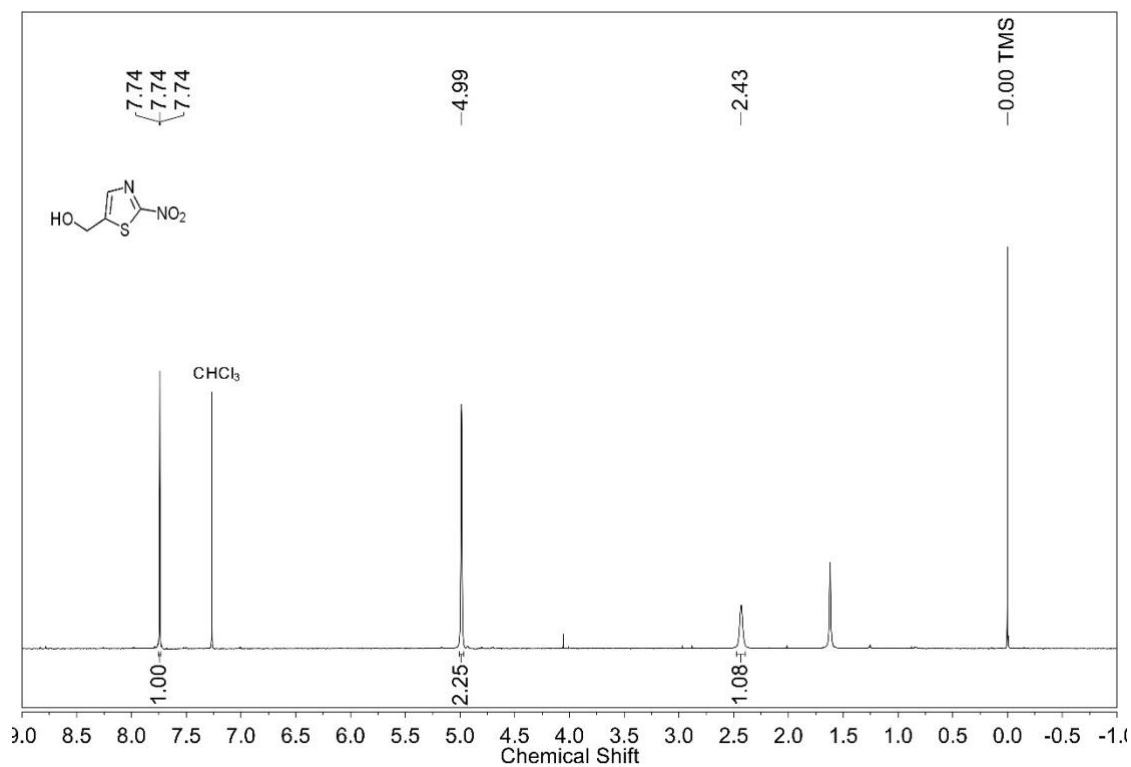
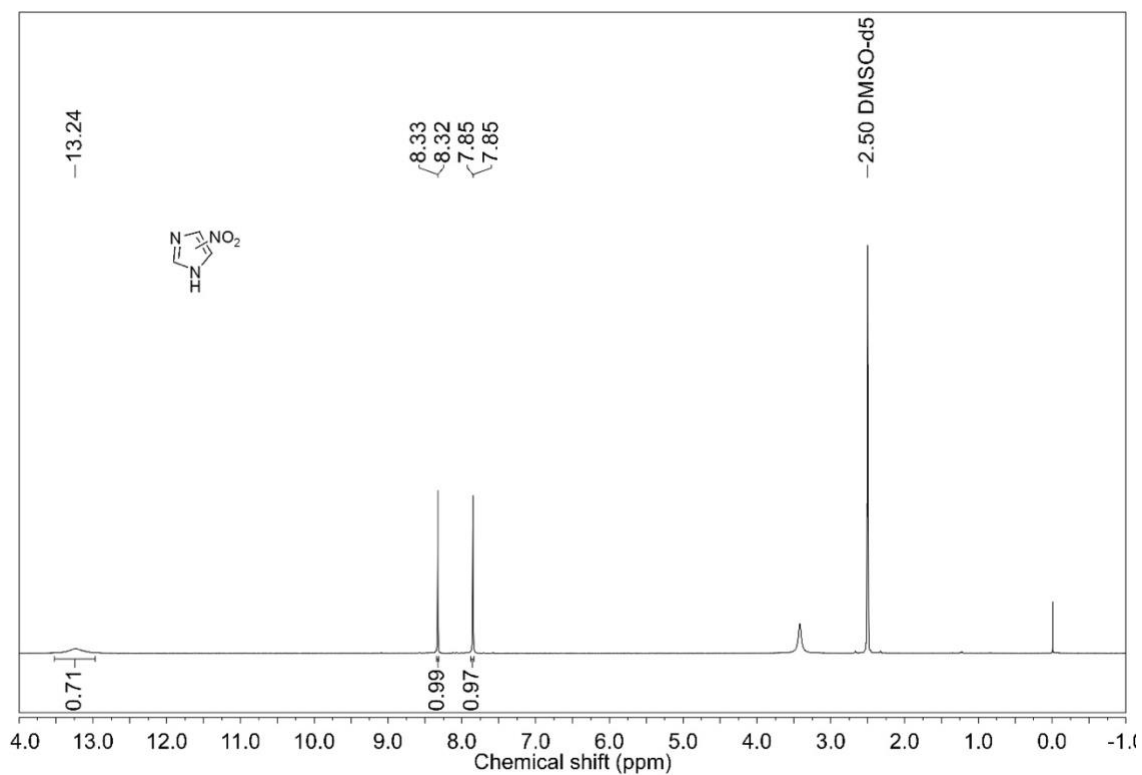
Stock solutions of **33** (5 mM), **41** (5 mM) and MXF (5 mM) were prepared in DMSO independently. The reactions were initiated by adding 30 μ M of ammonium formate (18 μ L, 3 mM stock) followed by zinc dust (15 mg) to a 2 mL eppendorf tubes containing a solution of 10 μ M of prodrugs (18 μ L, 1 mM stock) in 1764 μ L of methanol-water (1:1 v/v). The reaction

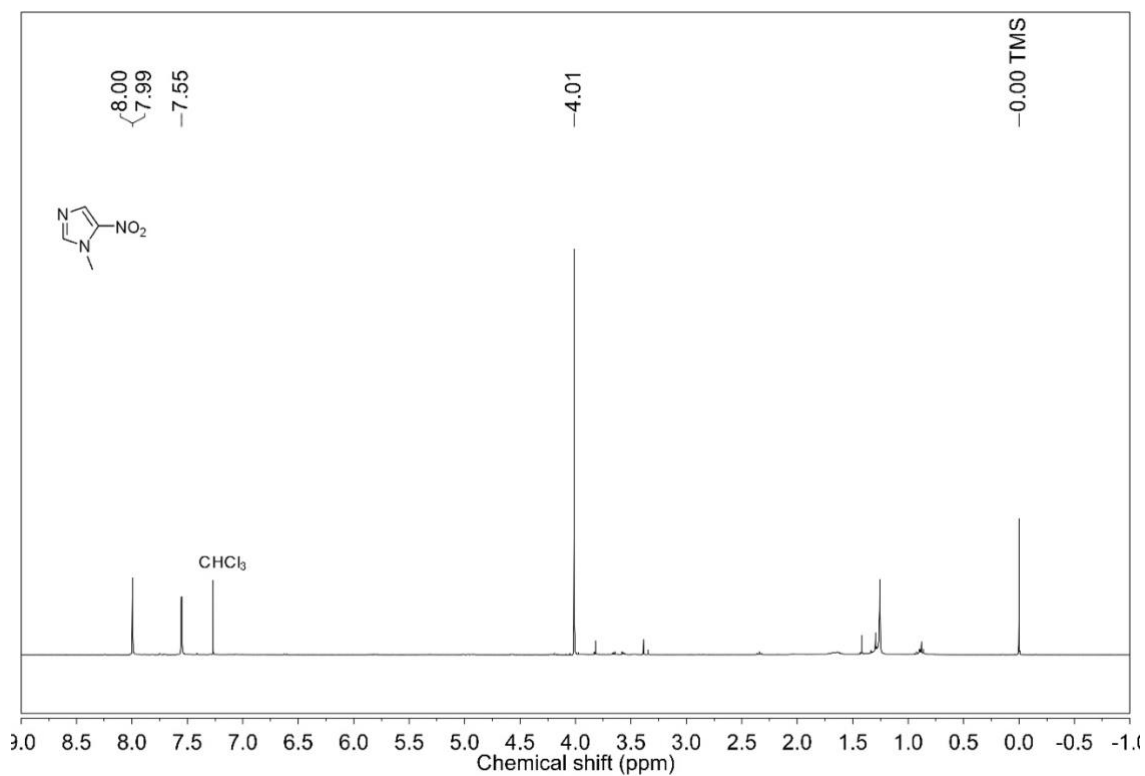
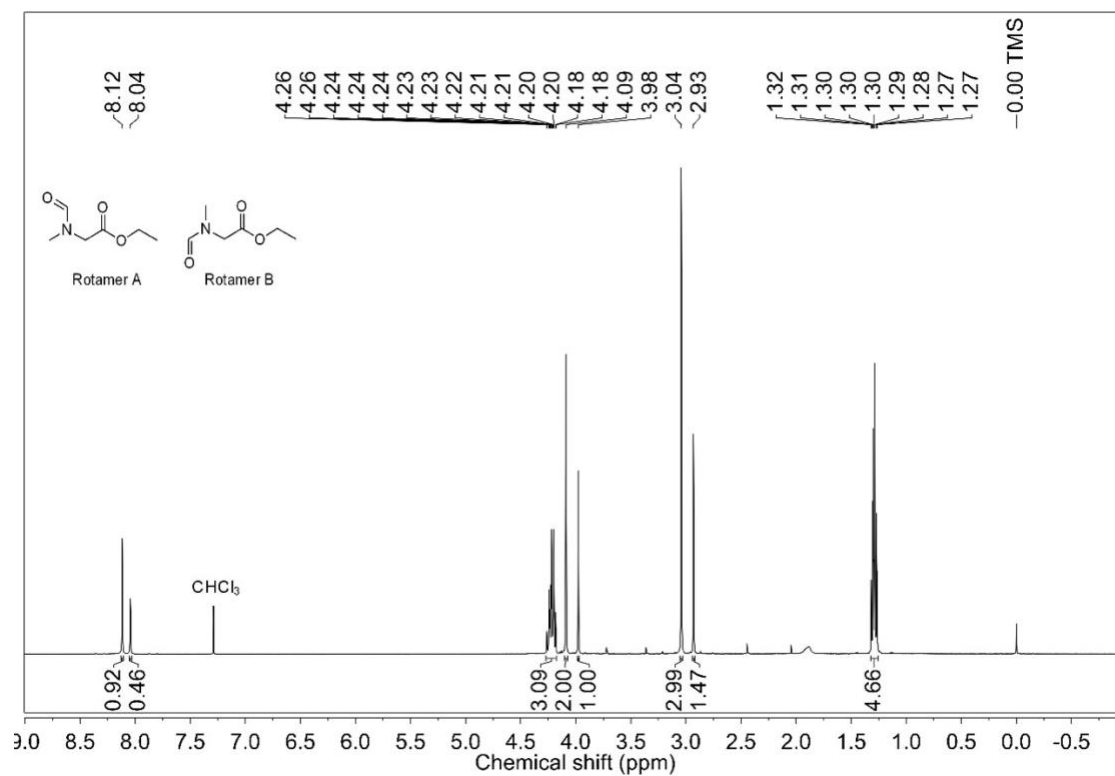
mixtures were incubated at 37 °C in an Eppendorf thermomixer comfort (800 rpm). Aliquots (250 µL) were taken at designated time points from the reaction mixture and centrifuged (9,391 x g for 2 min). The supernatant (200 µL) was then injected (25 µL) in an HPLC instrument attached with a diode-array detector (detection wavelength 280 nm). The stationary phase used was C-18 reversed phase column (4.6 mm × 100 mm, 5 µm). The mobile phase used was 0.0005 % TFA in ACN:H₂O with a run time of 20 min with flow rate of 1 mL/min starting with 81:19 → 0-5 min, 80:20 → 5-10 min, 70:30 → 10-12 min, 50:50 → 12-14 min, 30:70 → 14-16 min, 70:30 → 16-18, 81:19 → 18-20 min and the reduction of the test compounds were analyzed using HPLC by monitoring disappearance of the peak for the test compound.

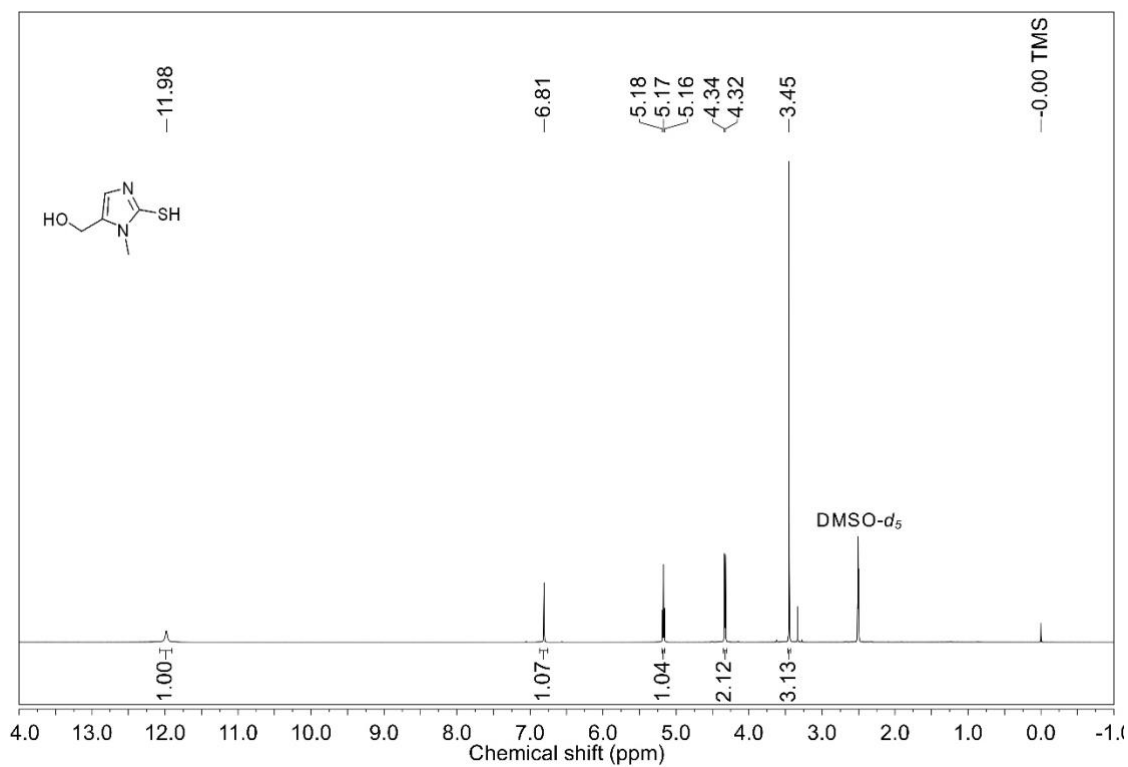
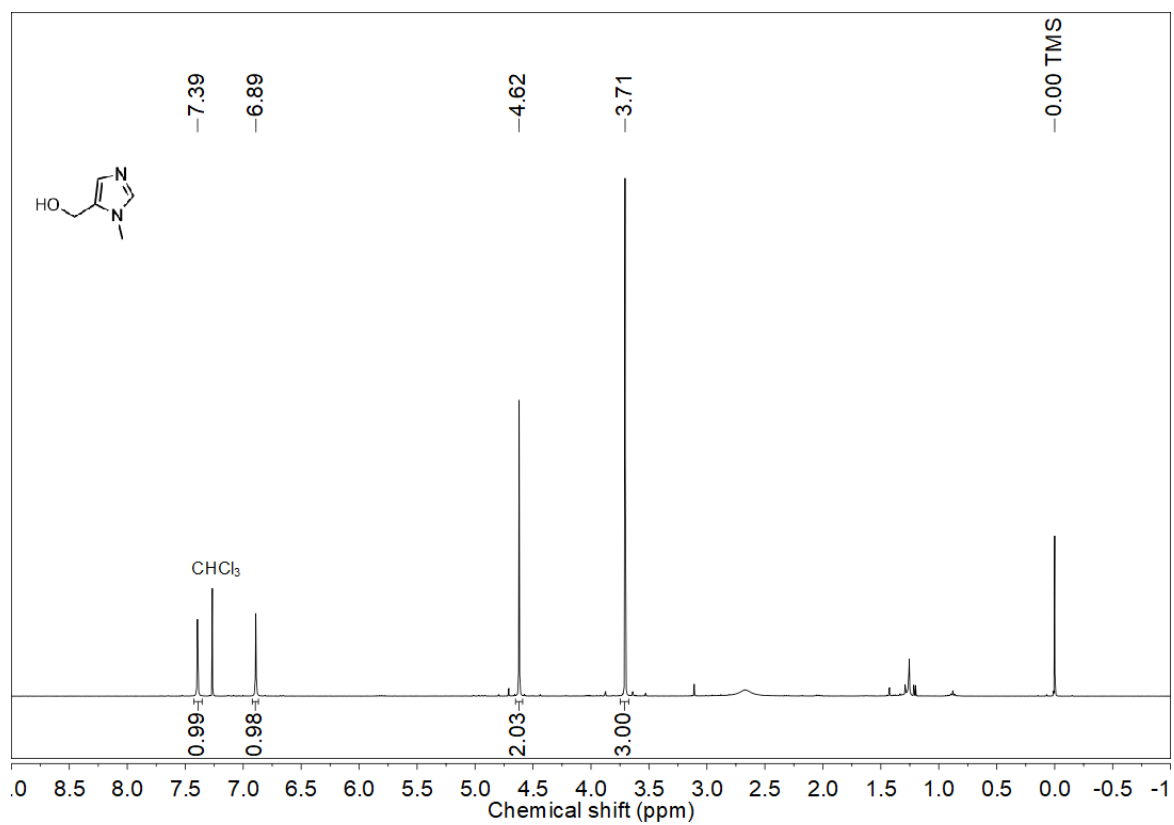
2.6. NMR spectral data

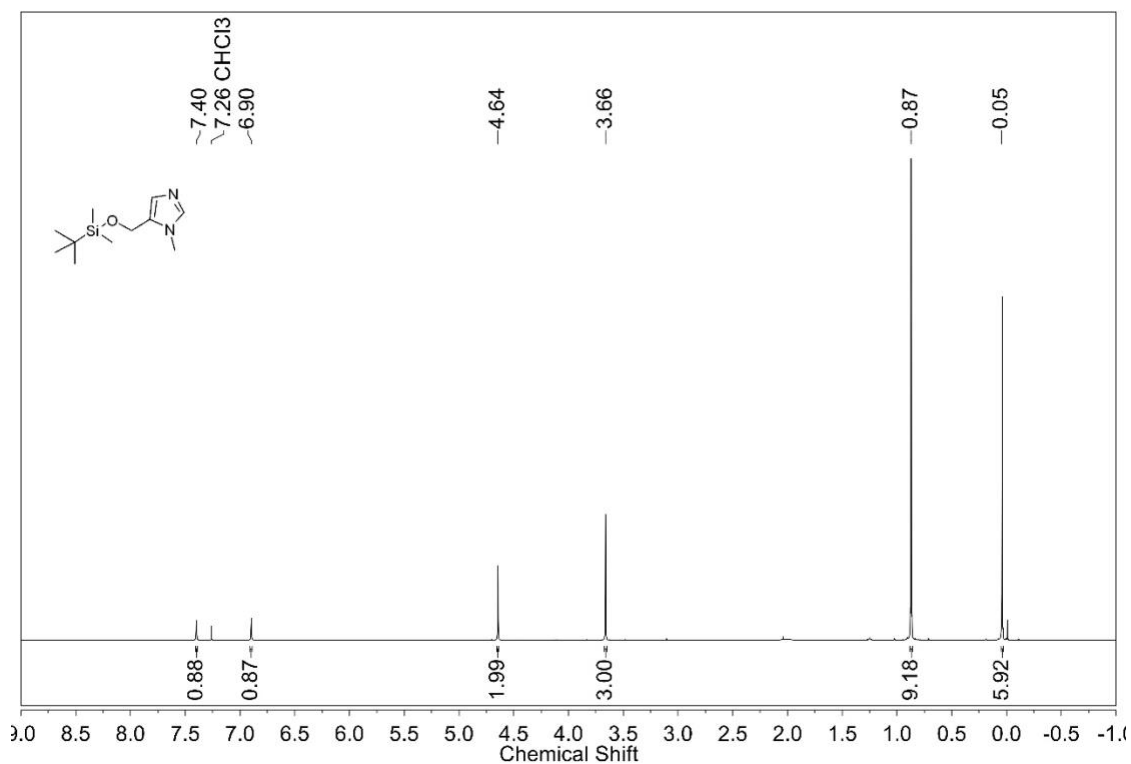
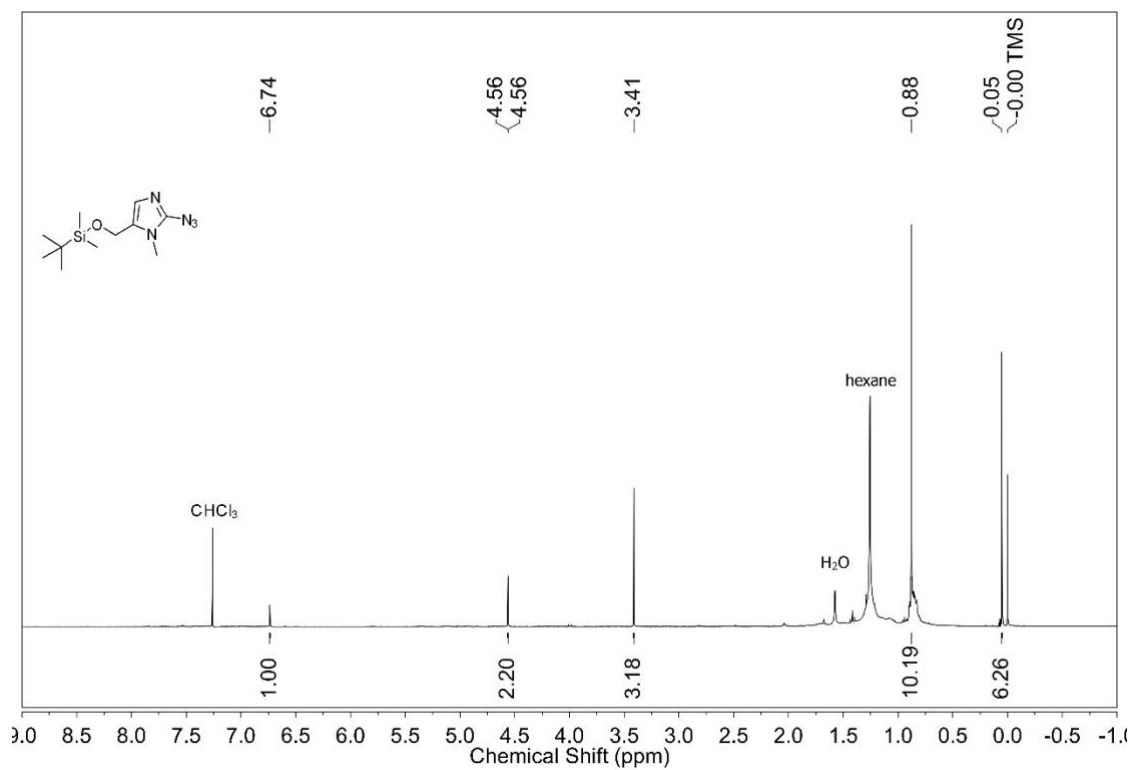
 ^1H NMR spectrum (400 MHz, CDCl_3) of **1b** ^1H NMR spectrum (400 MHz, CDCl_3) of **1c**

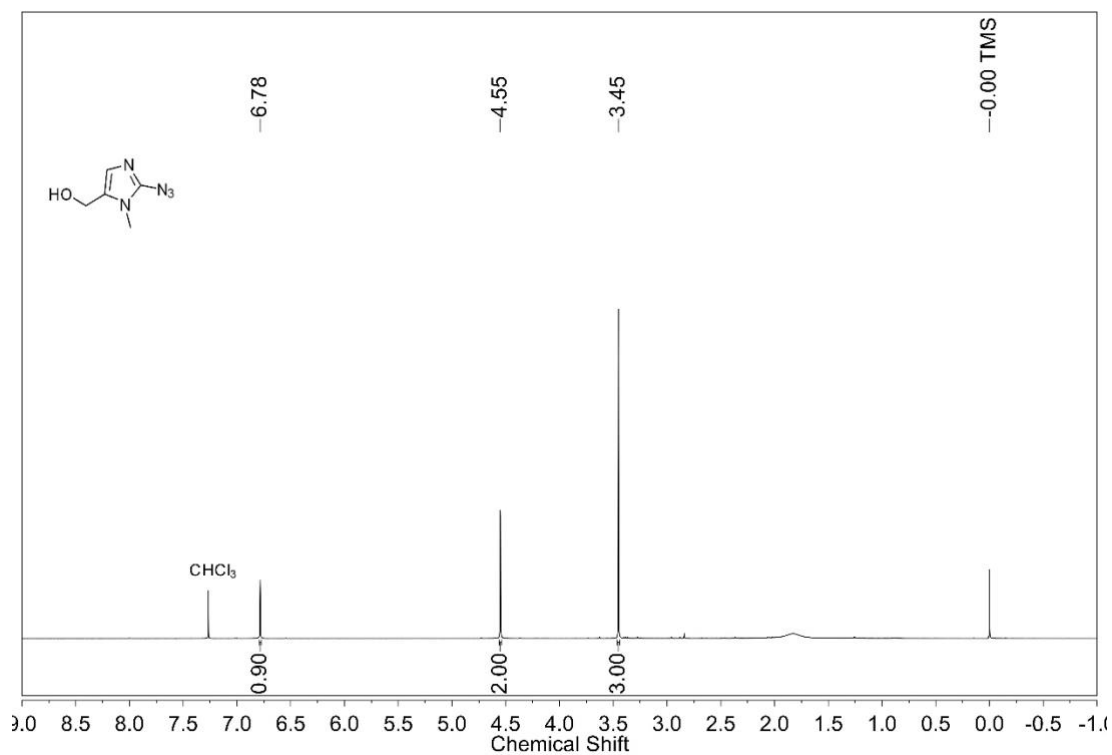
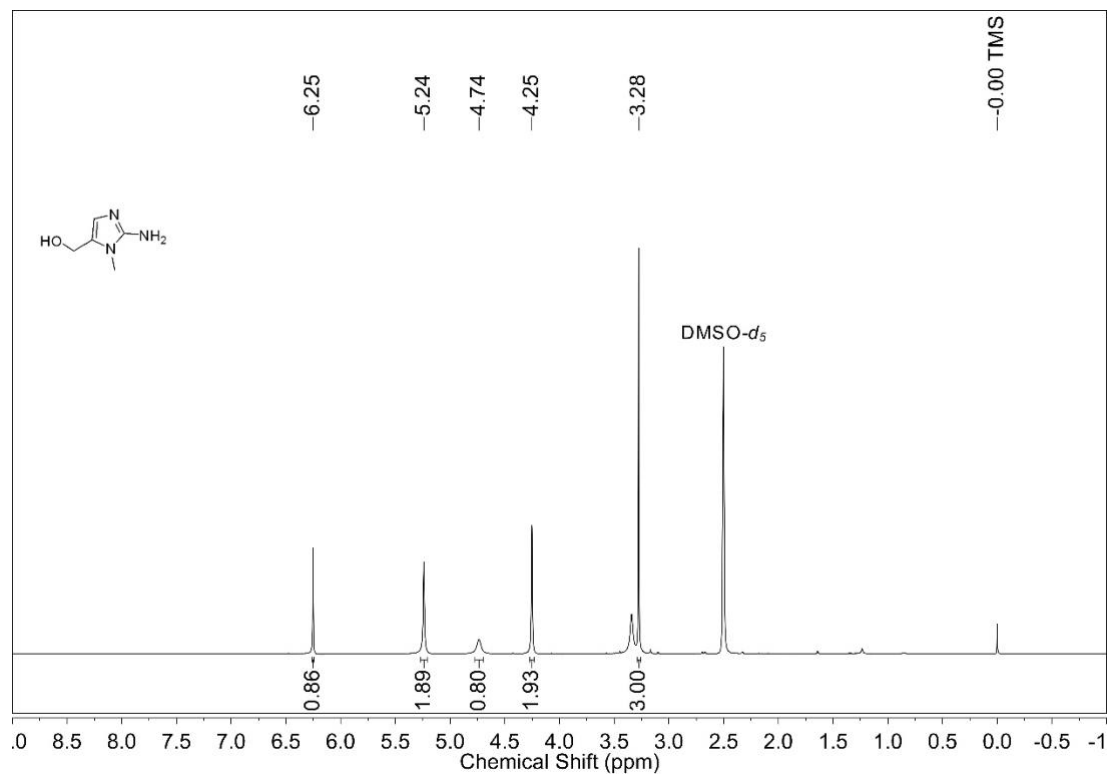
^1H NMR spectrum (400 MHz, CDCl_3) of **1d** ^1H NMR spectrum (400 MHz, $\text{DMSO}-d_6$) of **1e**

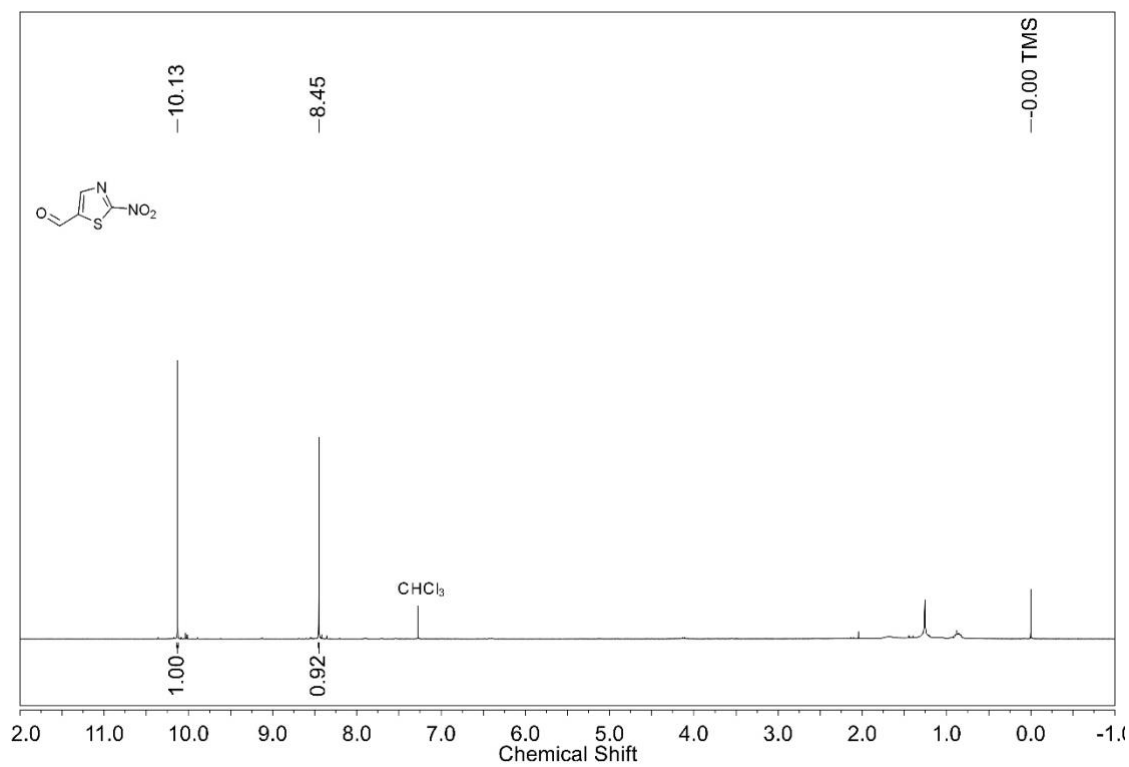
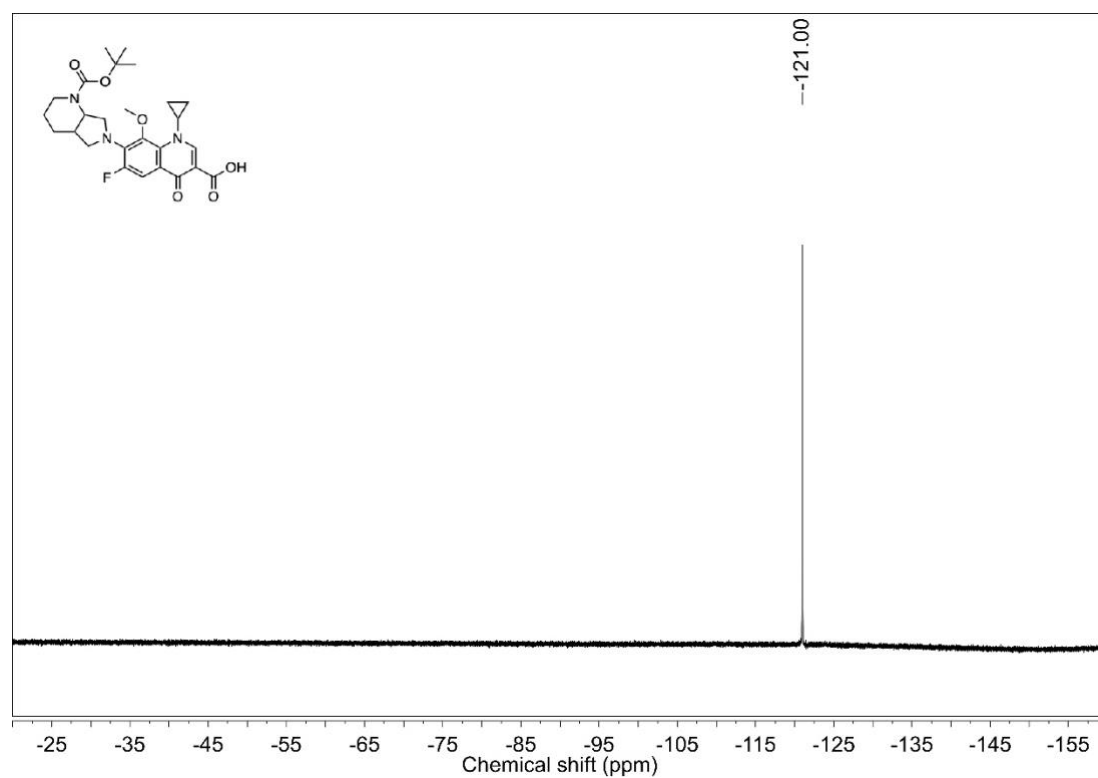
^1H NMR spectrum (400 MHz, CDCl_3) of **1f** ^1H NMR spectrum (400 MHz, $\text{DMSO-}d_6$) of **5**

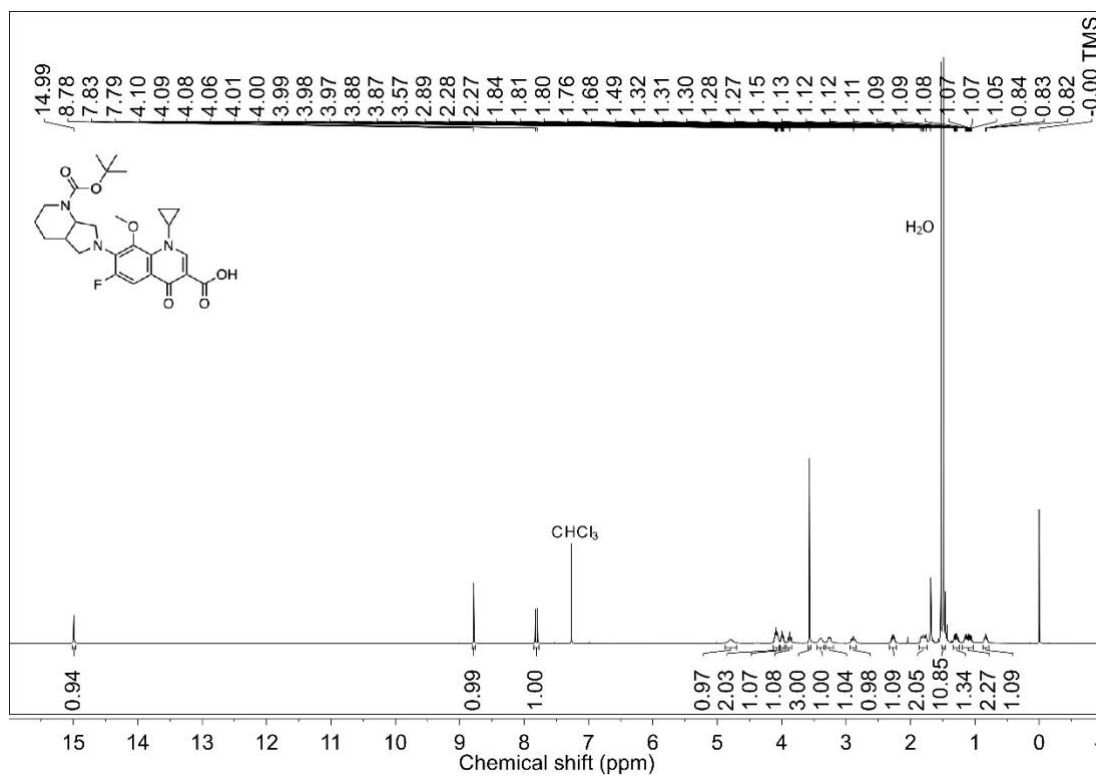
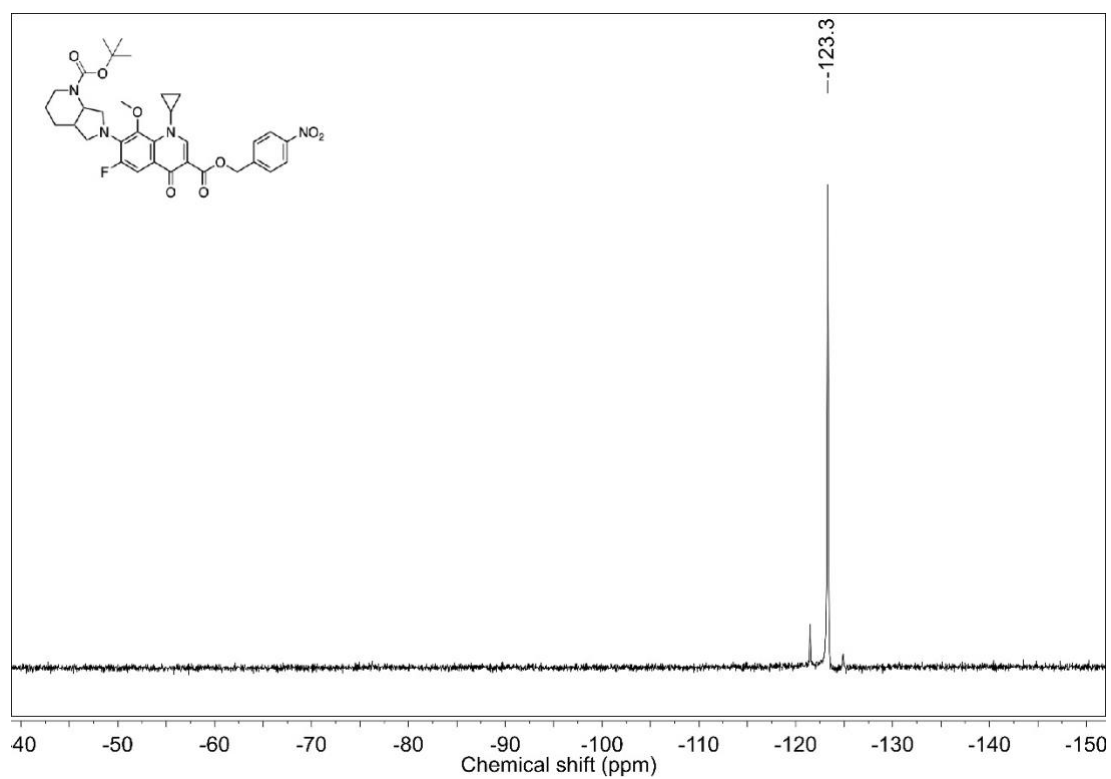
^1H NMR spectrum (400 MHz, CDCl_3) of **7** ^1H NMR spectrum (400 MHz, CDCl_3) of **15**

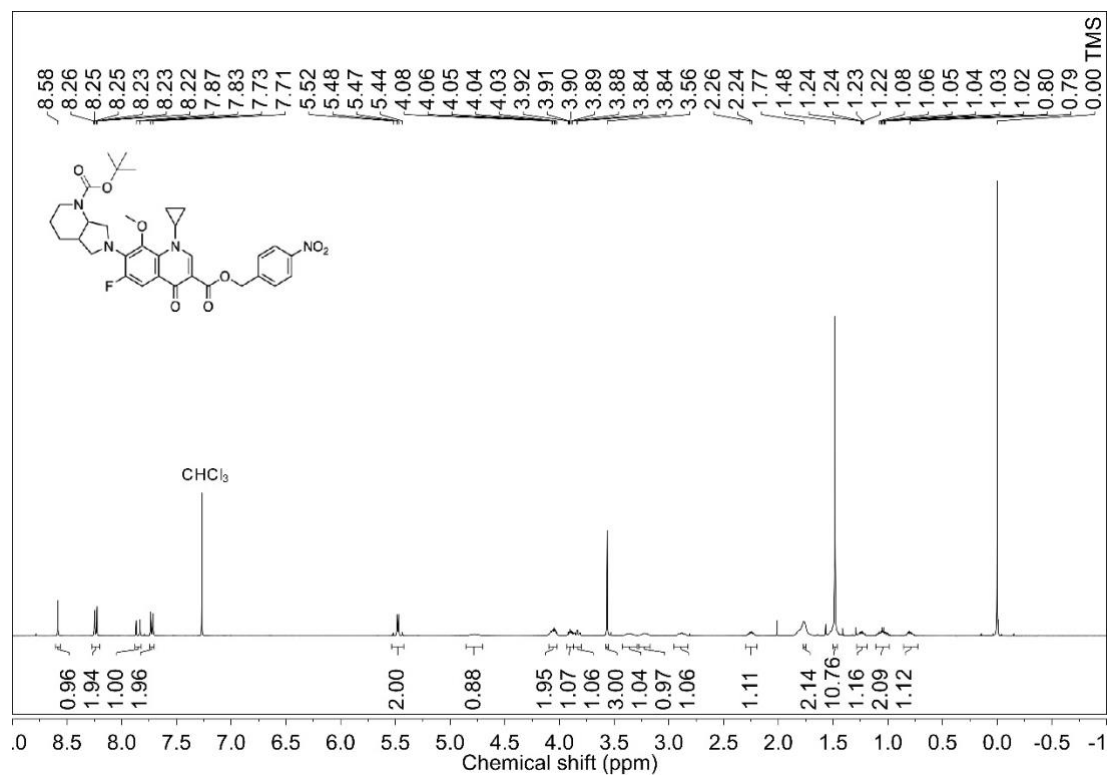
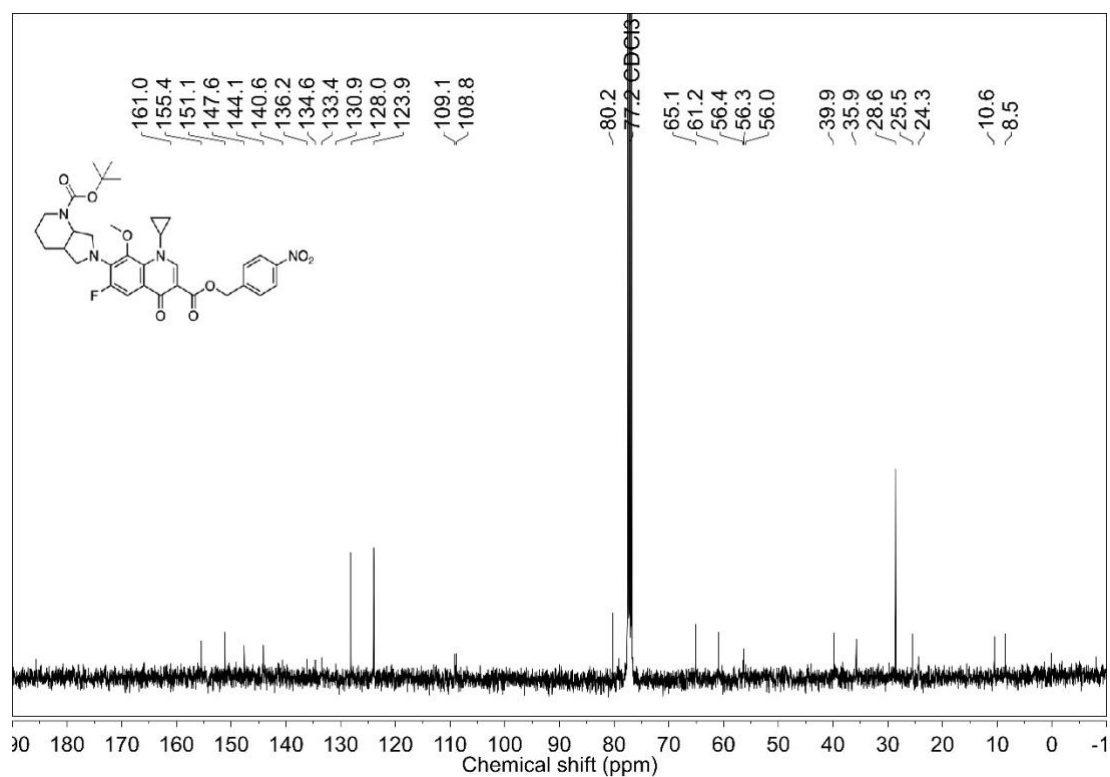
^1H NMR spectrum (400 MHz, $\text{DMSO-}d_6$) of **18** ^1H NMR spectrum (400 MHz, CDCl_3) of **19**

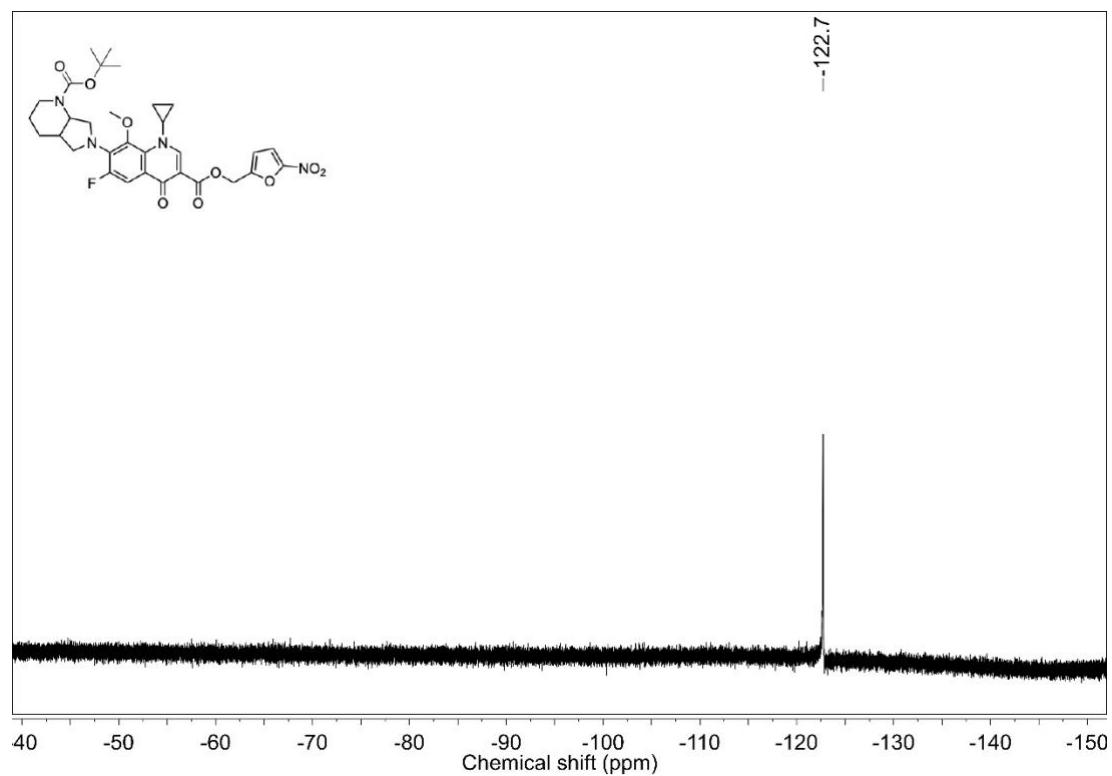
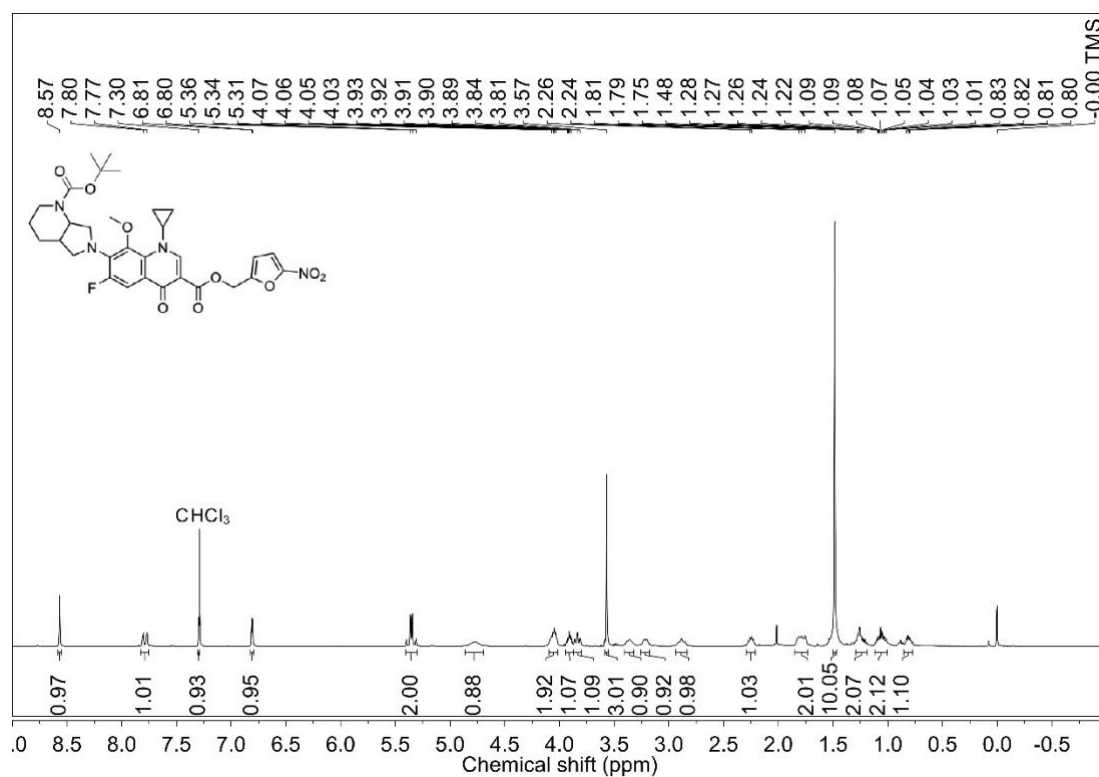
^1H NMR spectrum (400 MHz, CDCl_3) of **20** ^1H NMR spectrum (400 MHz, CDCl_3) of **21**

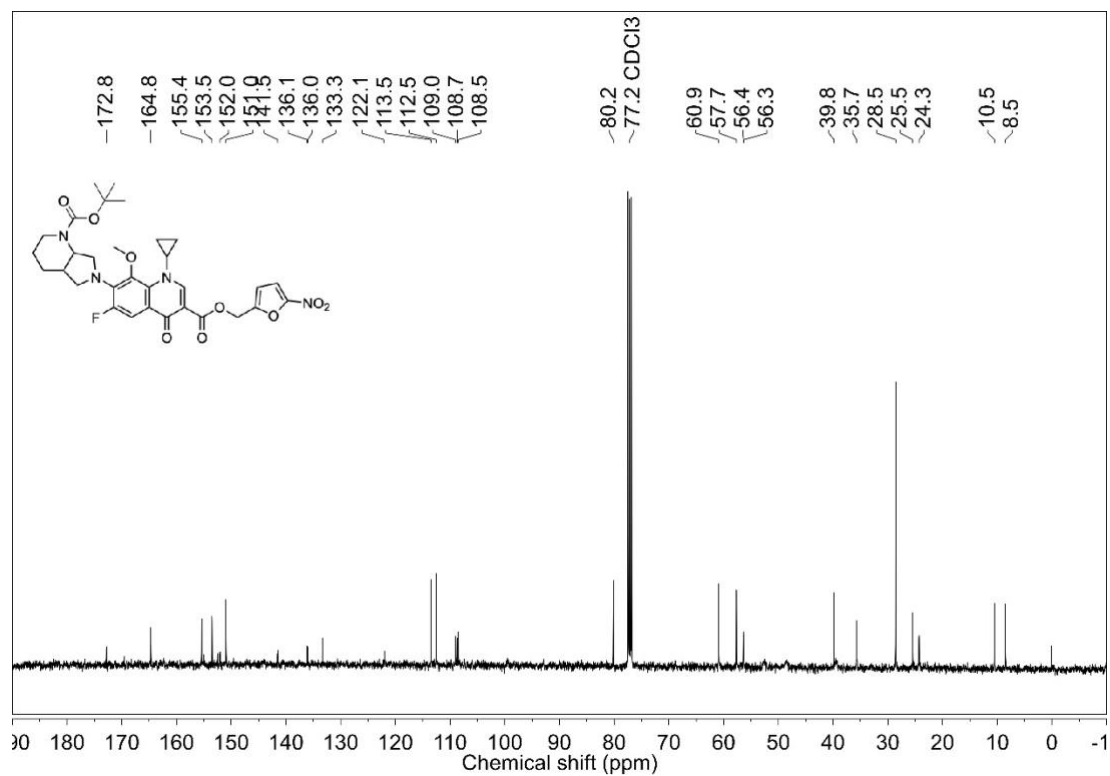
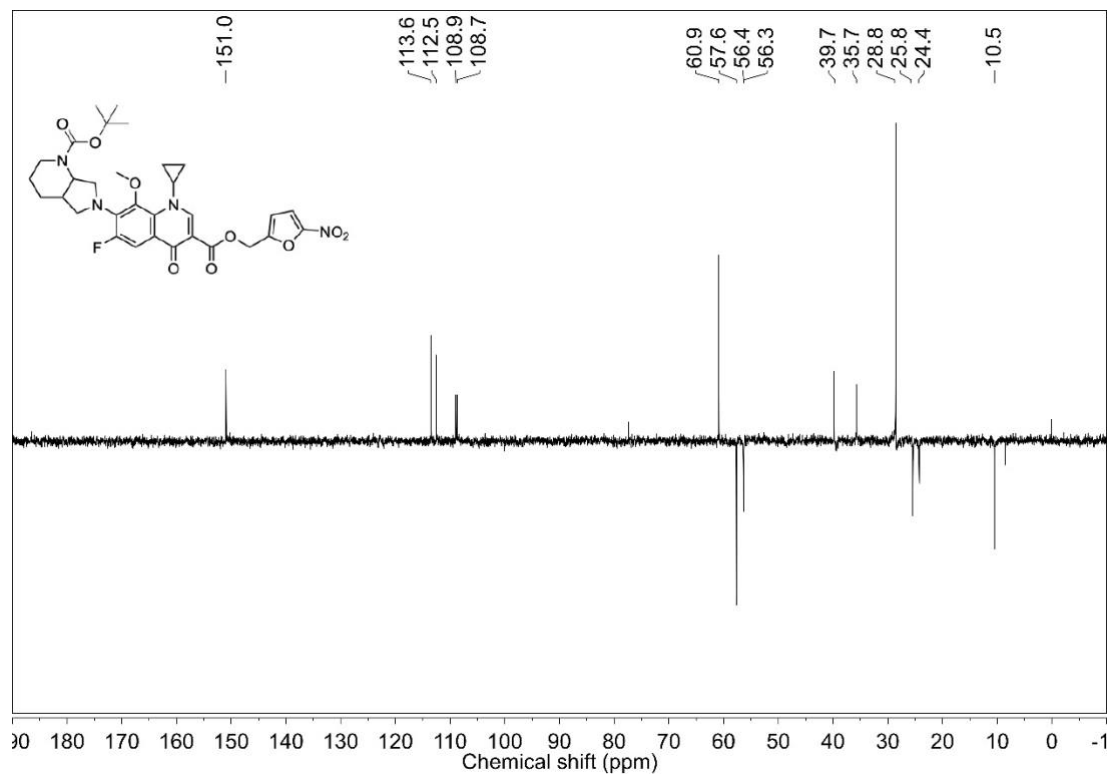
^1H NMR spectrum (400 MHz, CDCl_3) of **22** ^1H NMR spectrum (400 MHz, $\text{DMSO}-d_6$) of **23**

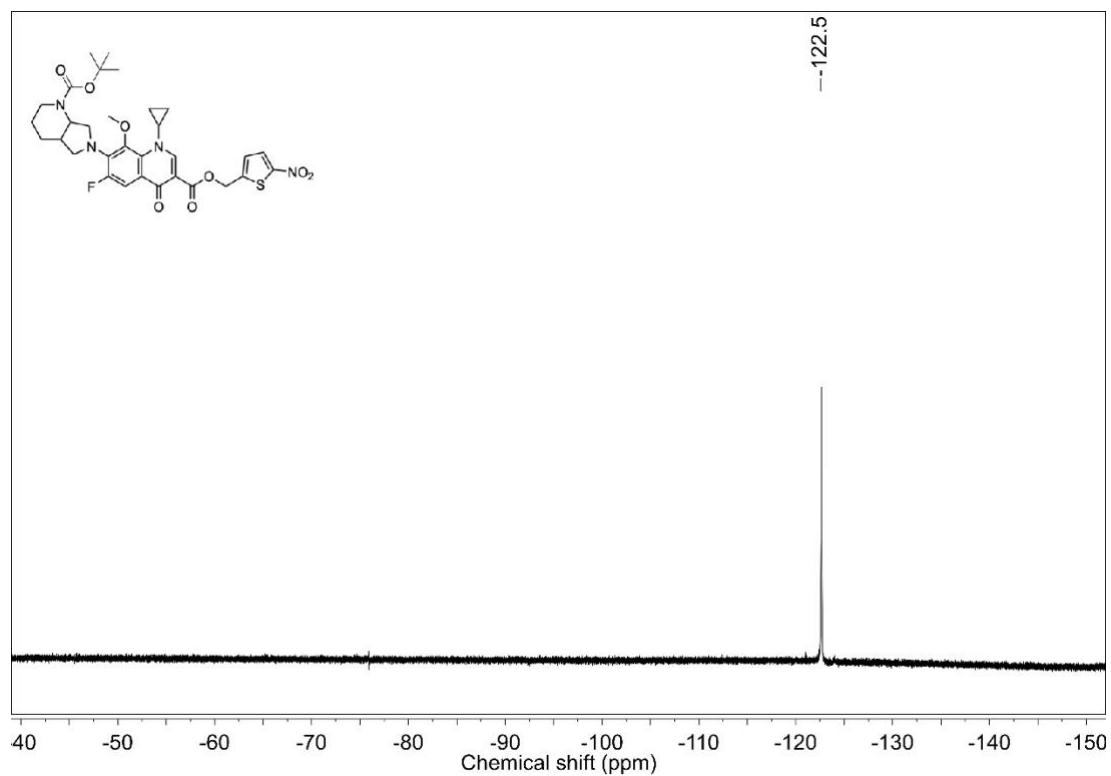
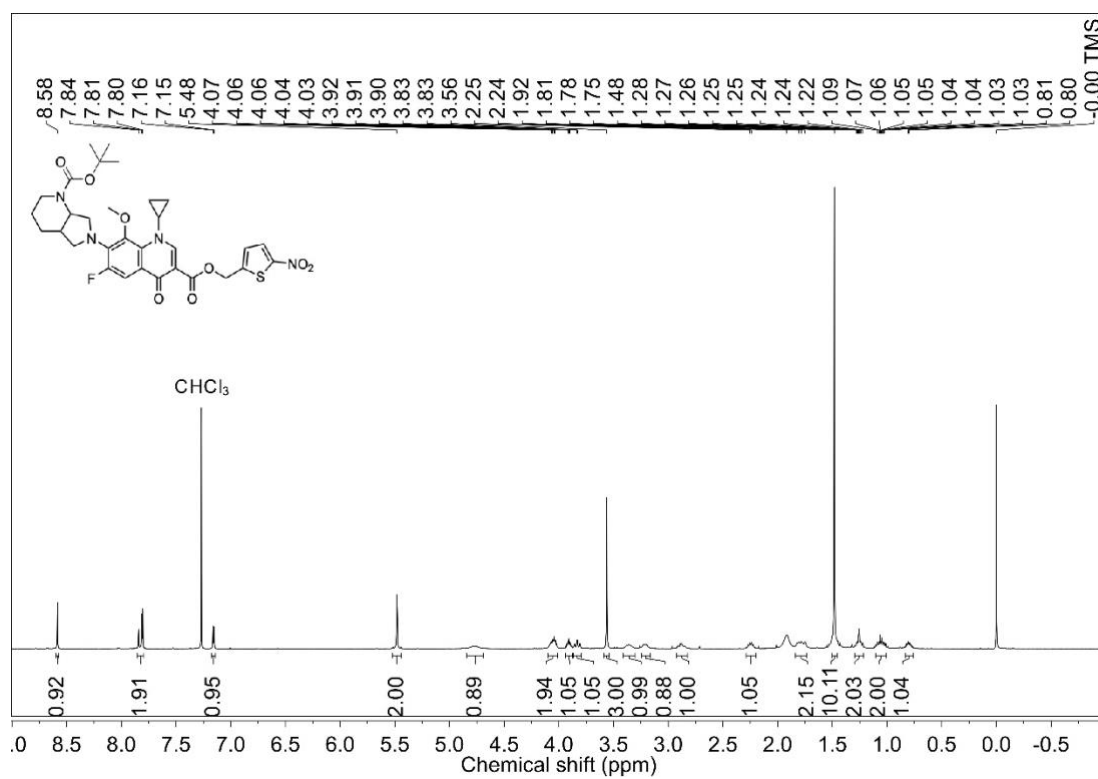
^1H NMR spectrum (400 MHz, CDCl_3) of **25** ^{19}F NMR spectrum (376 MHz, CDCl_3) of **26**

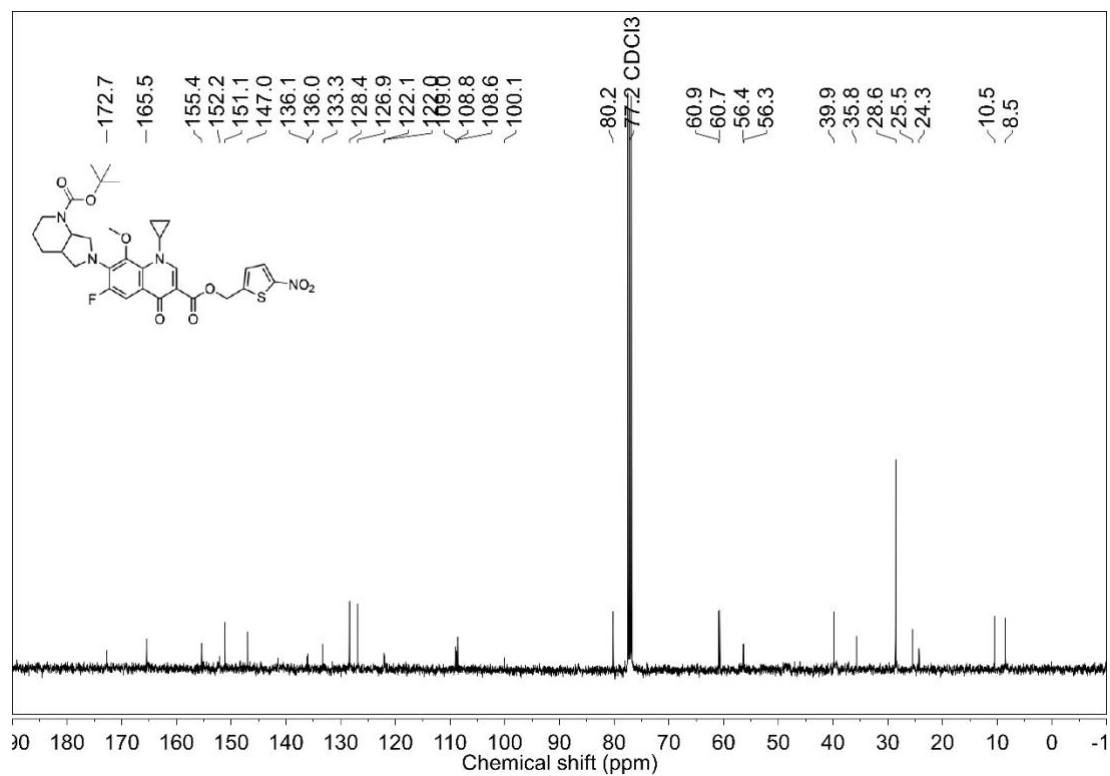
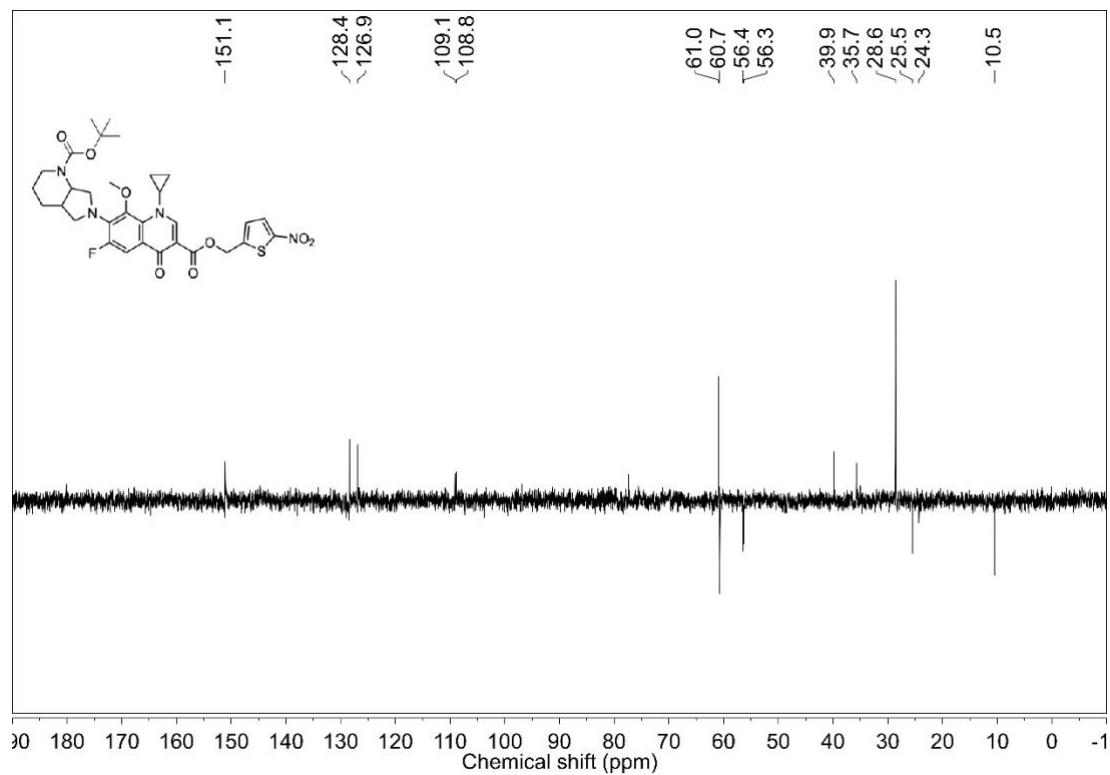
^1H NMR spectrum (400 MHz, CDCl_3) of **26** ^{19}F NMR spectrum (376 MHz, CDCl_3) of **27**

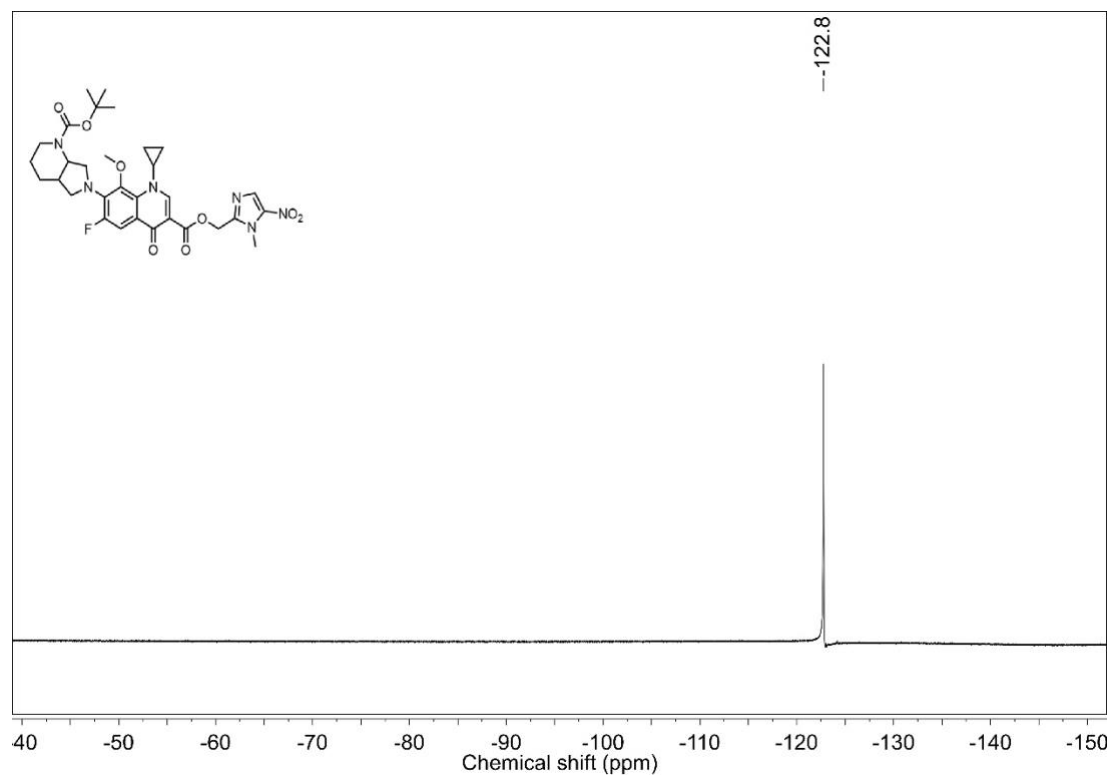
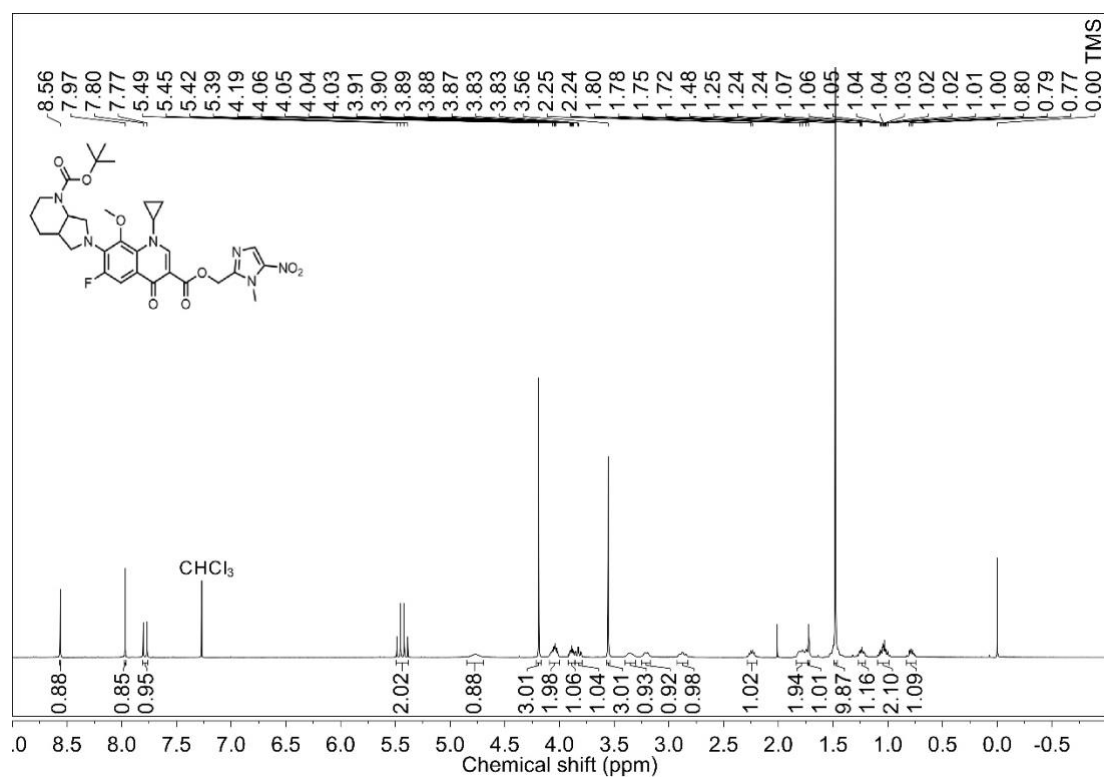
^1H NMR spectrum (400 MHz, CDCl_3) of **27** ^{13}C NMR spectrum (100 MHz, CDCl_3) of **27**

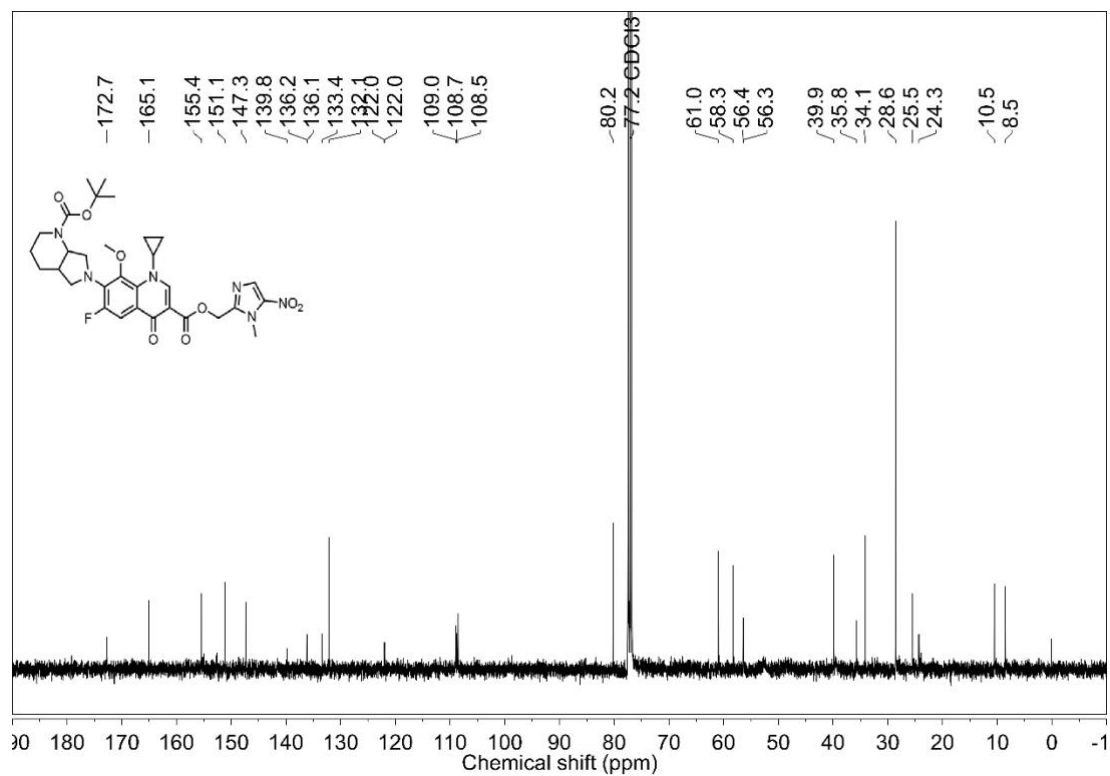
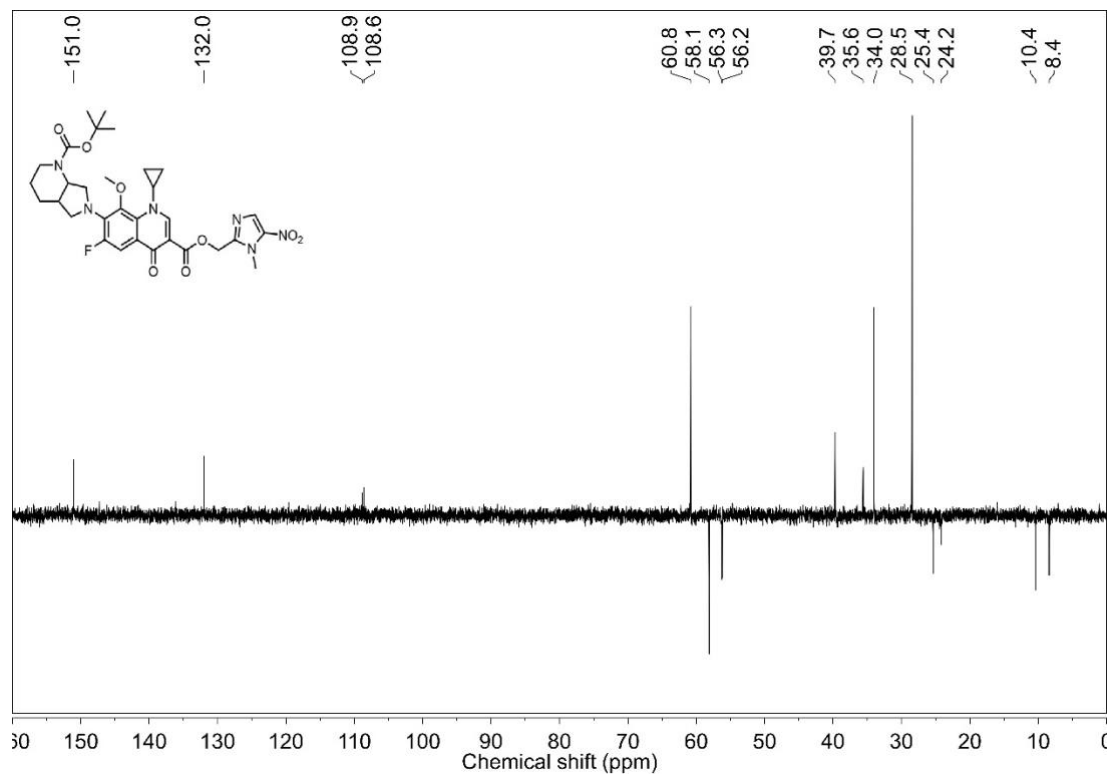
^{19}F NMR spectrum (376 MHz, CDCl_3) of **28** ^1H NMR spectrum (400 MHz, CDCl_3) of **28**

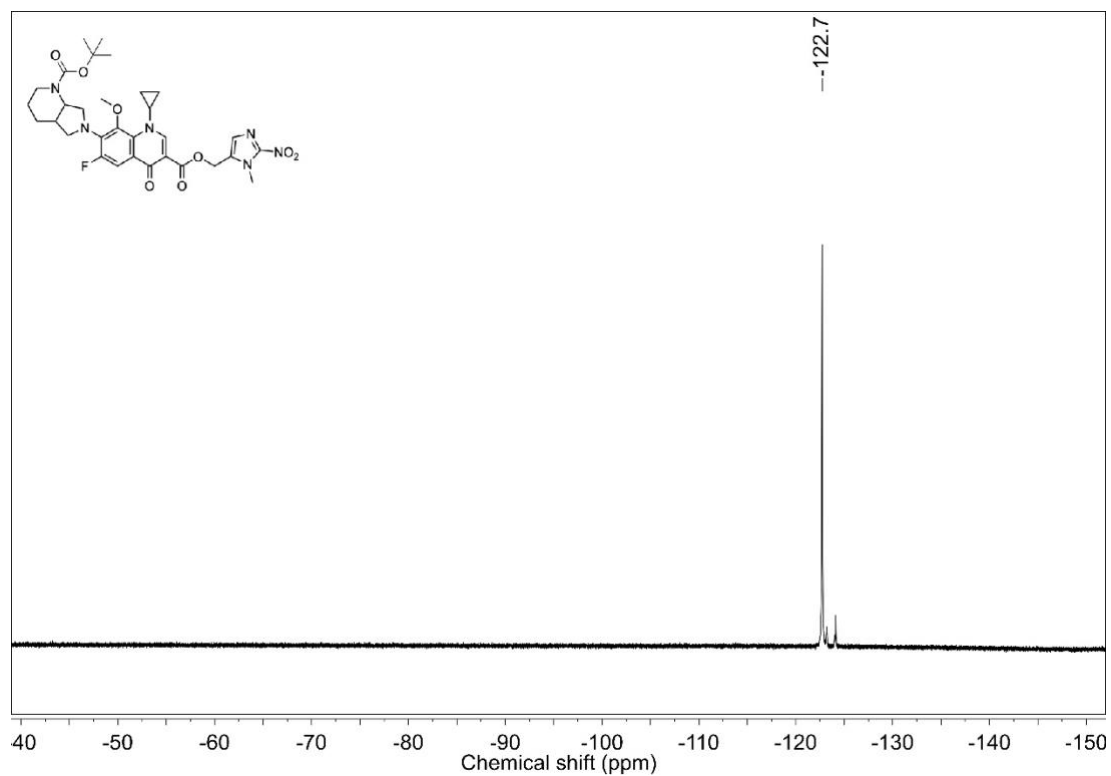
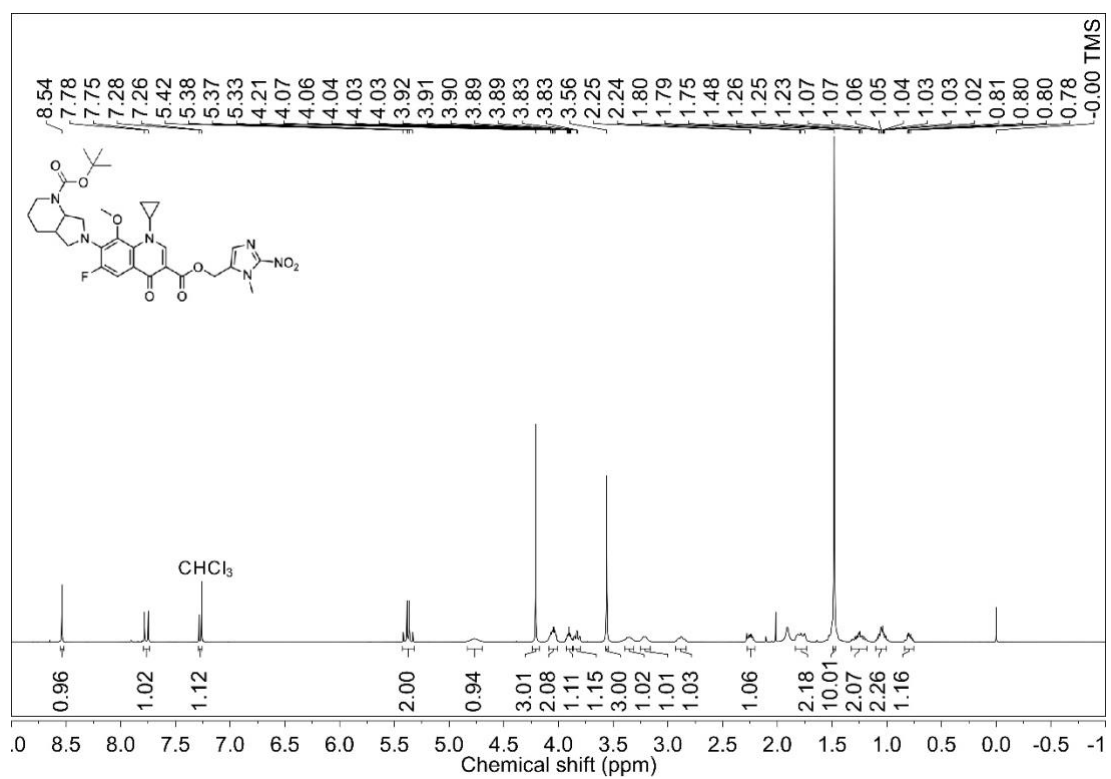
^{13}C NMR spectrum (100 MHz, CDCl_3) of **28**DEPT-135 NMR spectrum (100 MHz, CDCl_3) of **28**

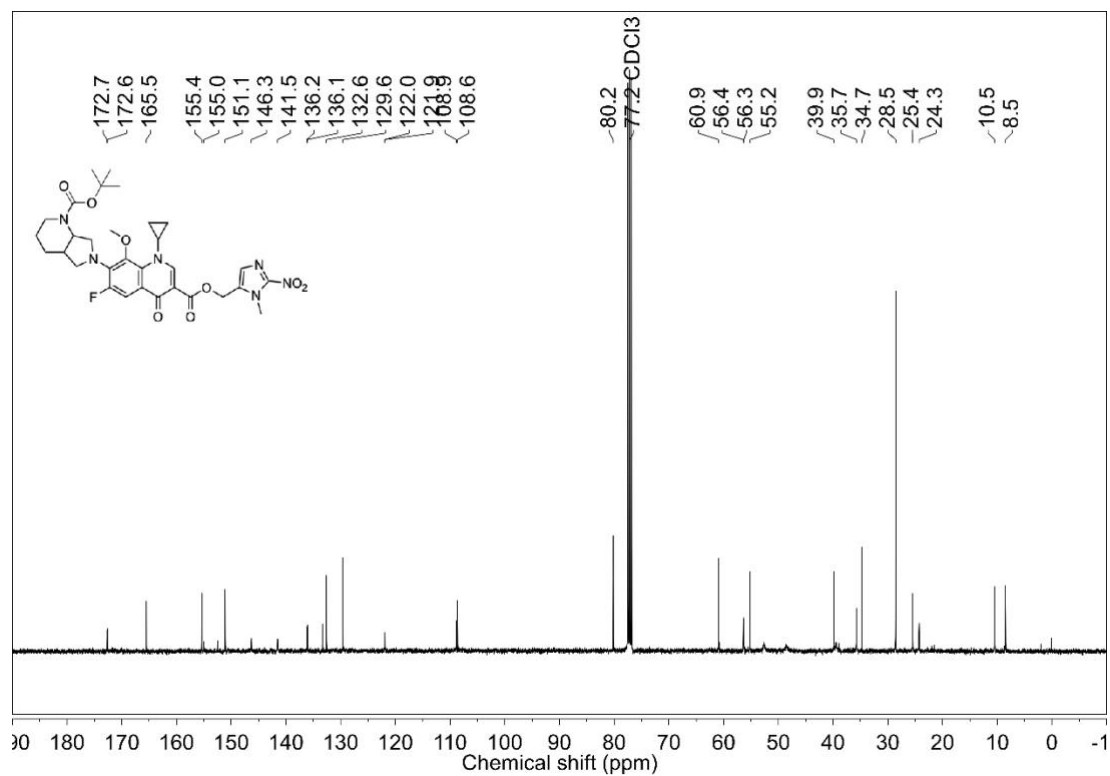
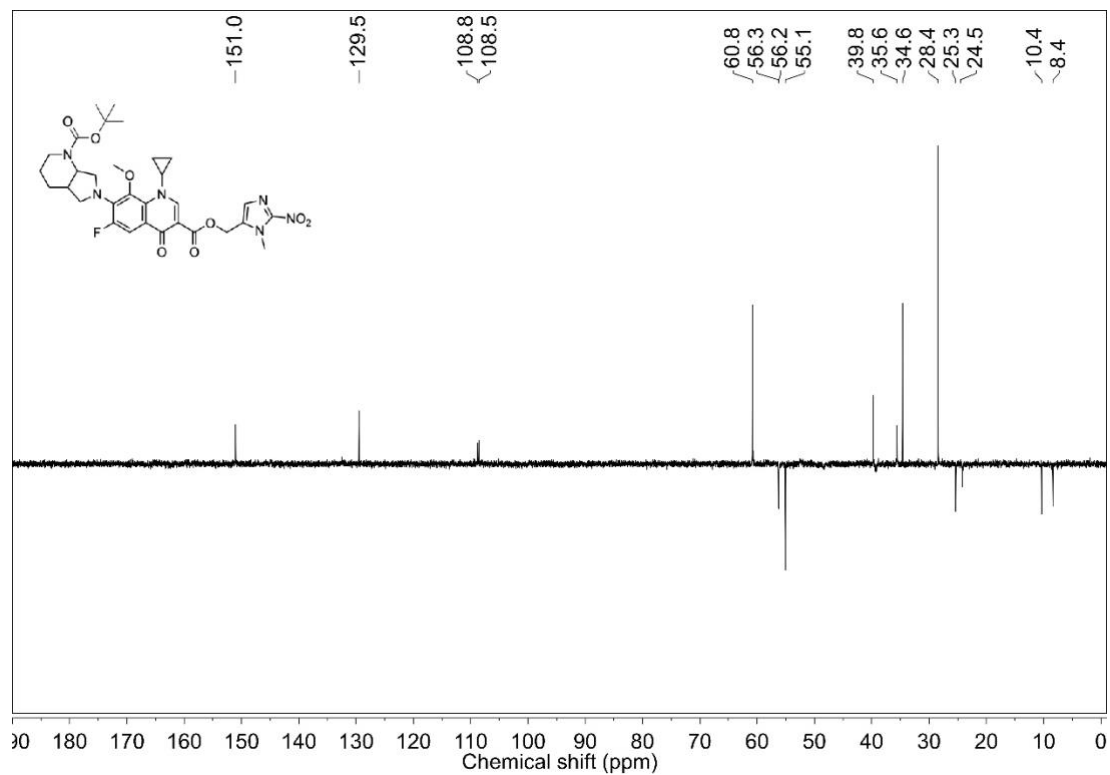
^{19}F NMR spectrum (376 MHz, CDCl_3) of **29** ^1H NMR spectrum (400 MHz, CDCl_3) of **29**

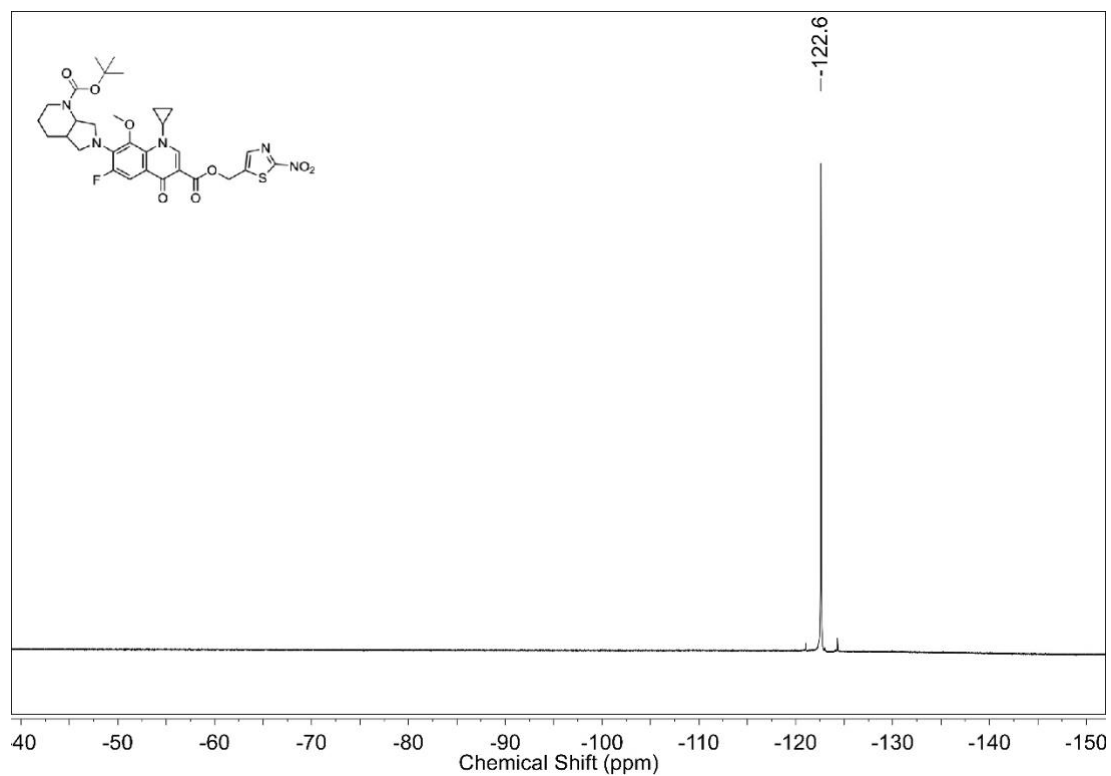
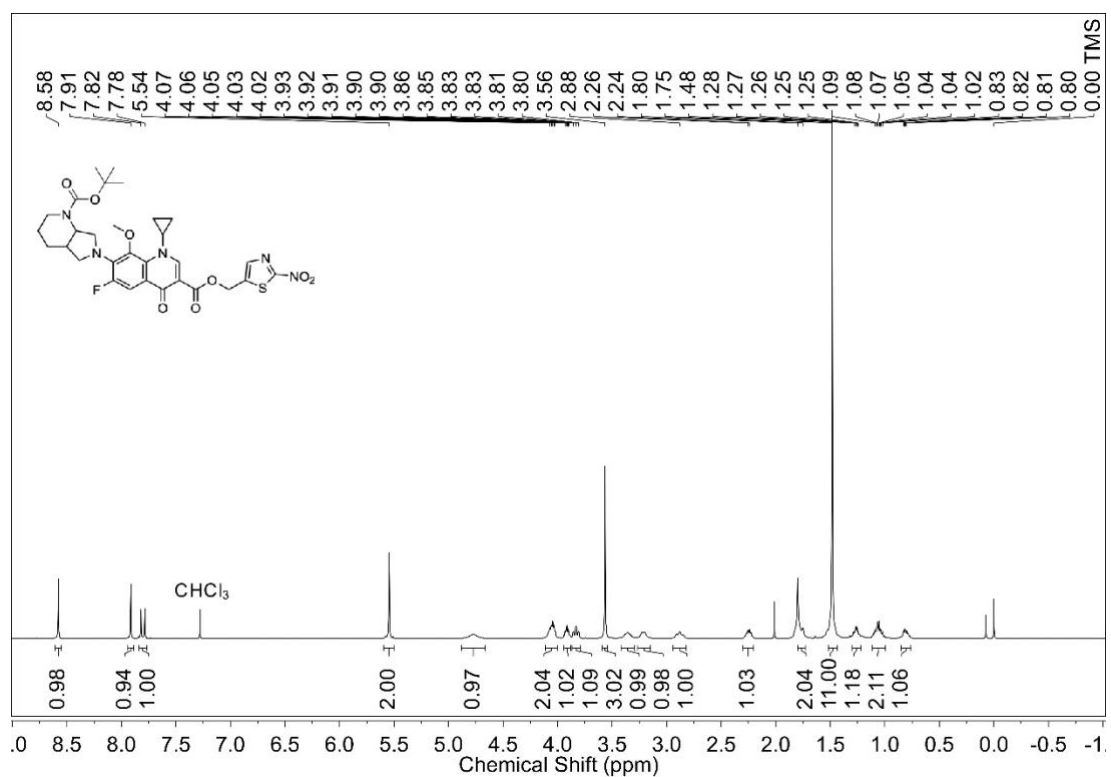
^{13}C NMR spectrum (100 MHz, CDCl_3) of **29**DEPT-135 NMR spectrum (100 MHz, CDCl_3) of **29**

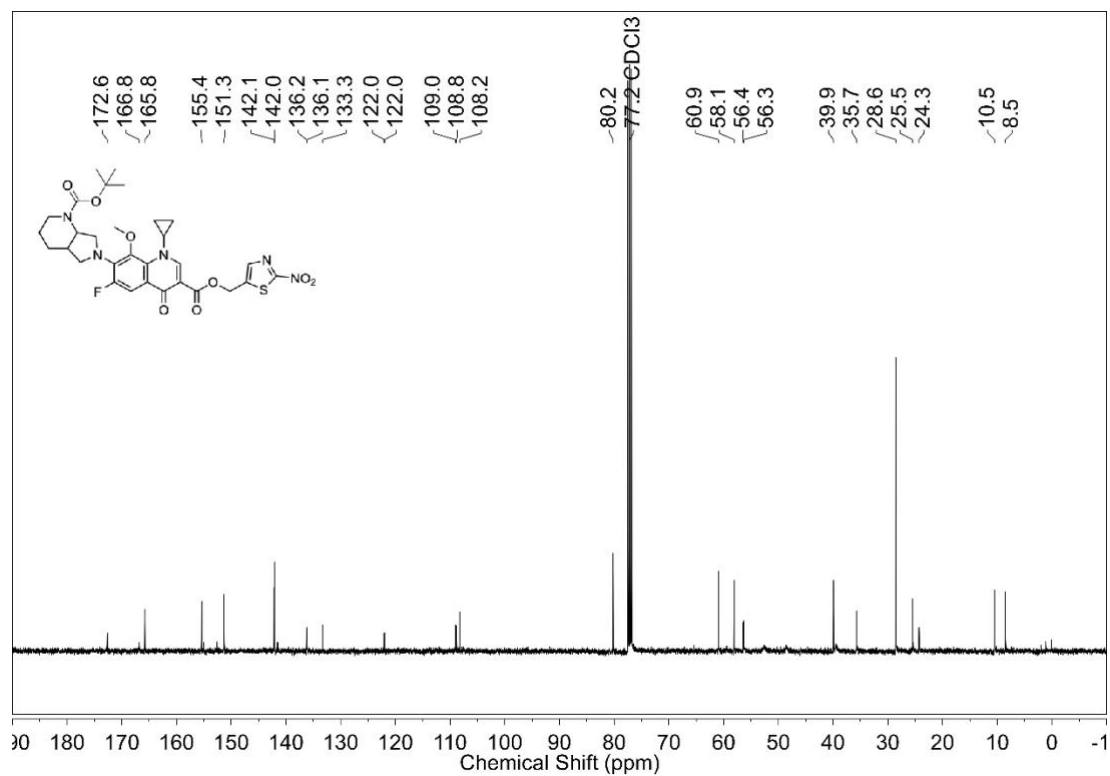
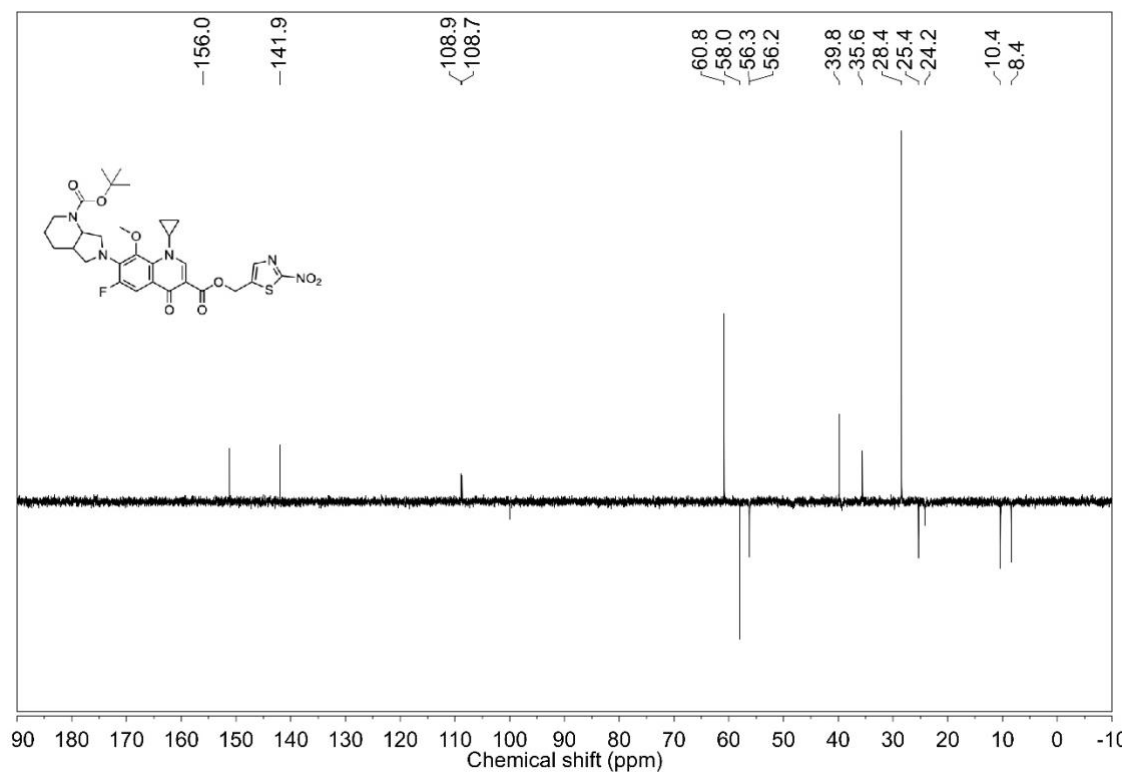
^{19}F NMR spectrum (376 MHz, CDCl_3) of **30** ^1H NMR spectrum (400 MHz, CDCl_3) of **30**

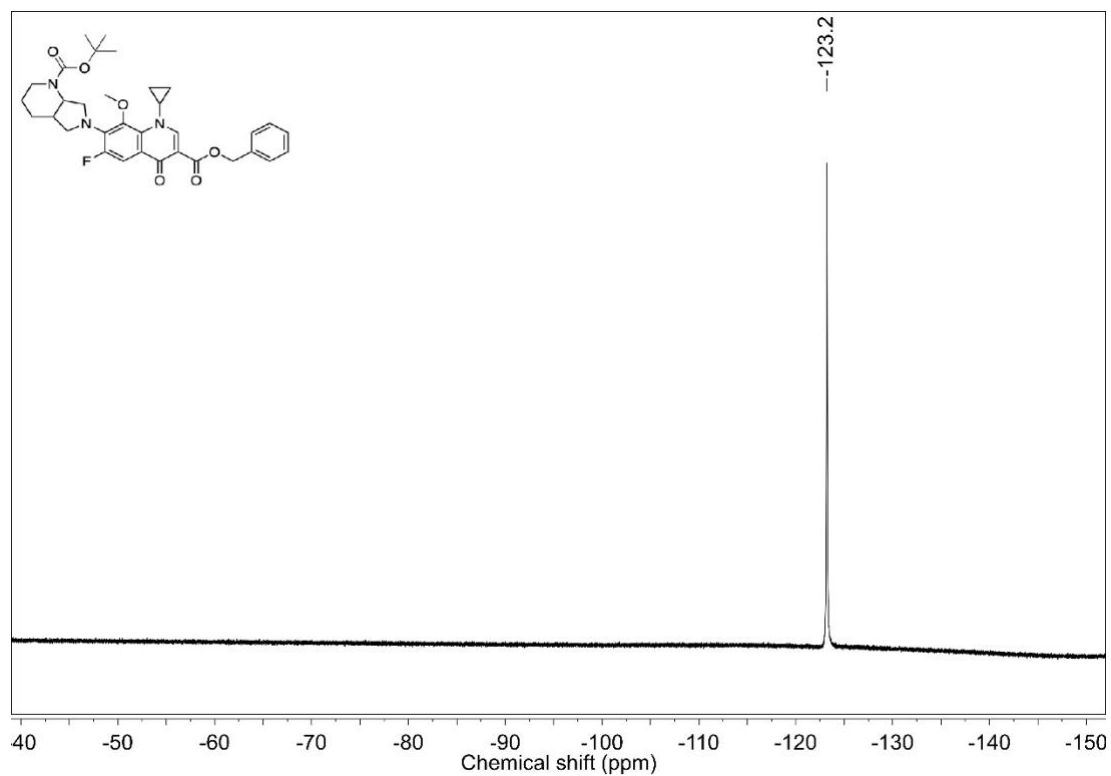
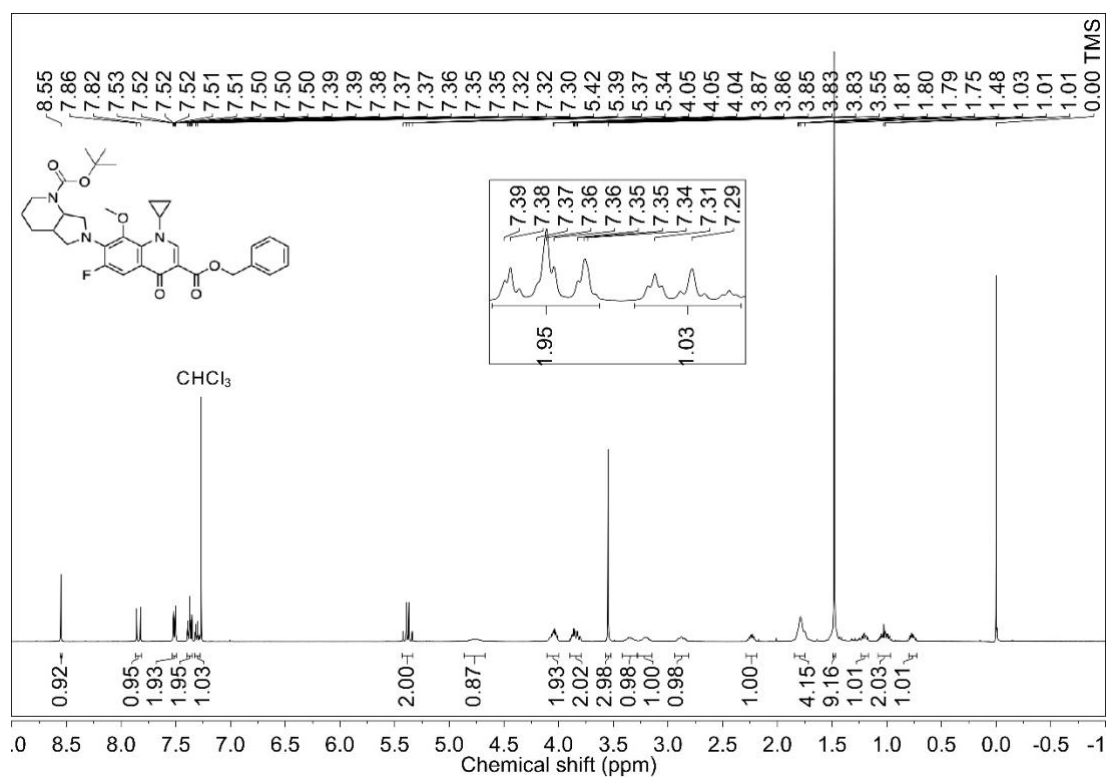
^{13}C NMR spectrum (100 MHz, CDCl_3) of **30**DEPT-135 NMR spectrum (100 MHz, CDCl_3) of **30**

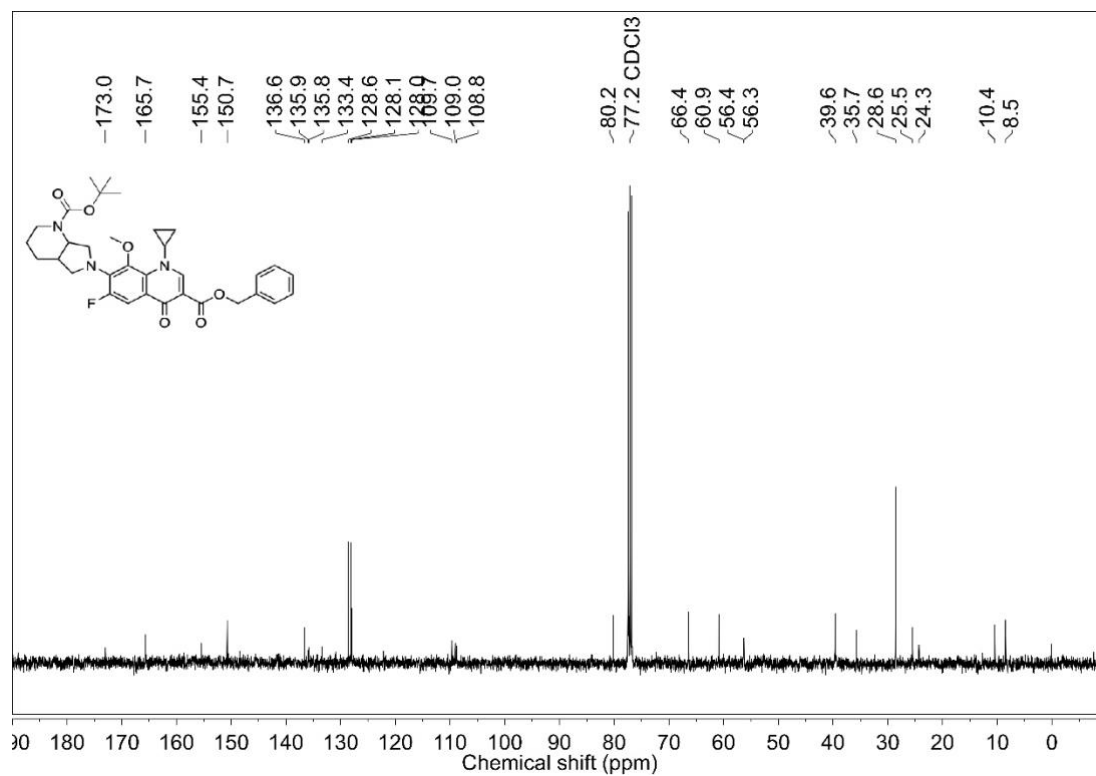
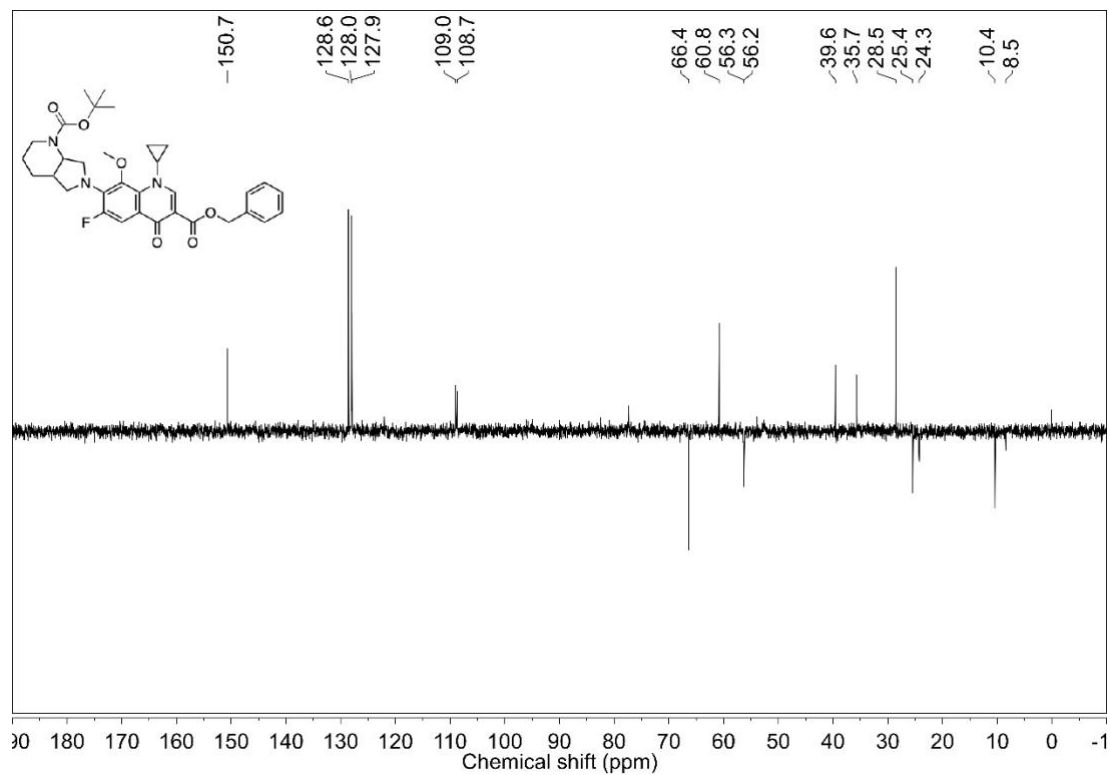
^{19}F NMR spectrum (376 MHz, CDCl_3) of **31** ^1H NMR spectrum (400 MHz, CDCl_3) of **31**

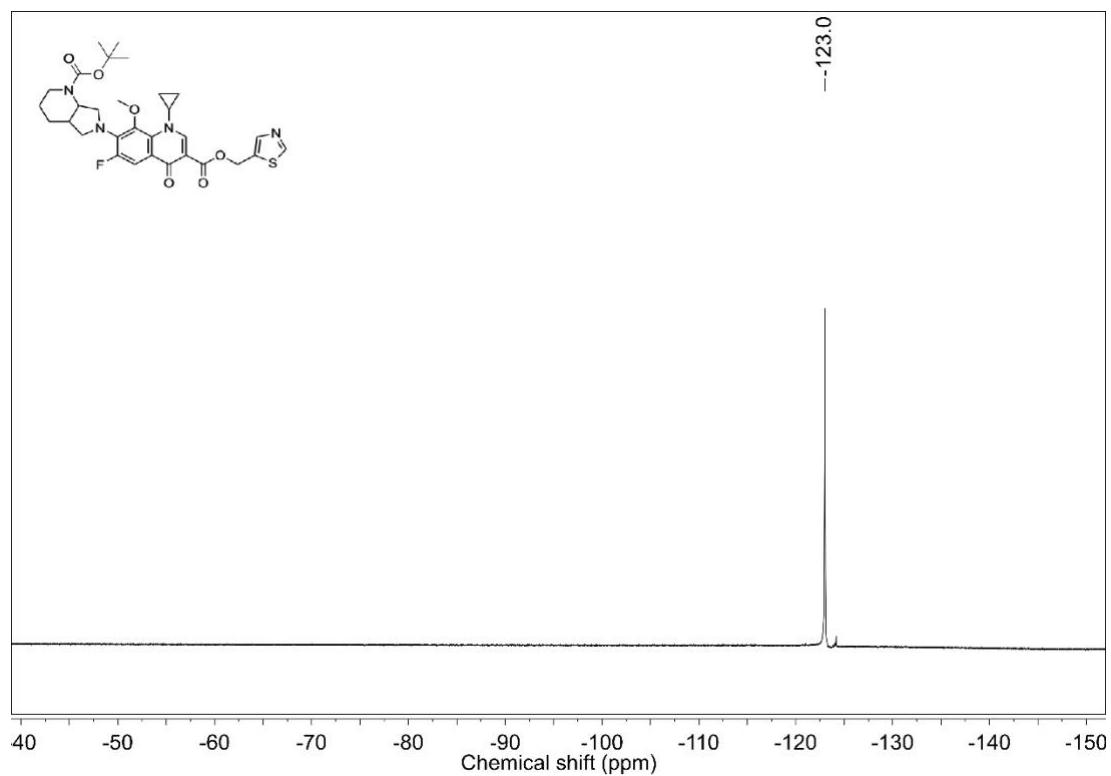
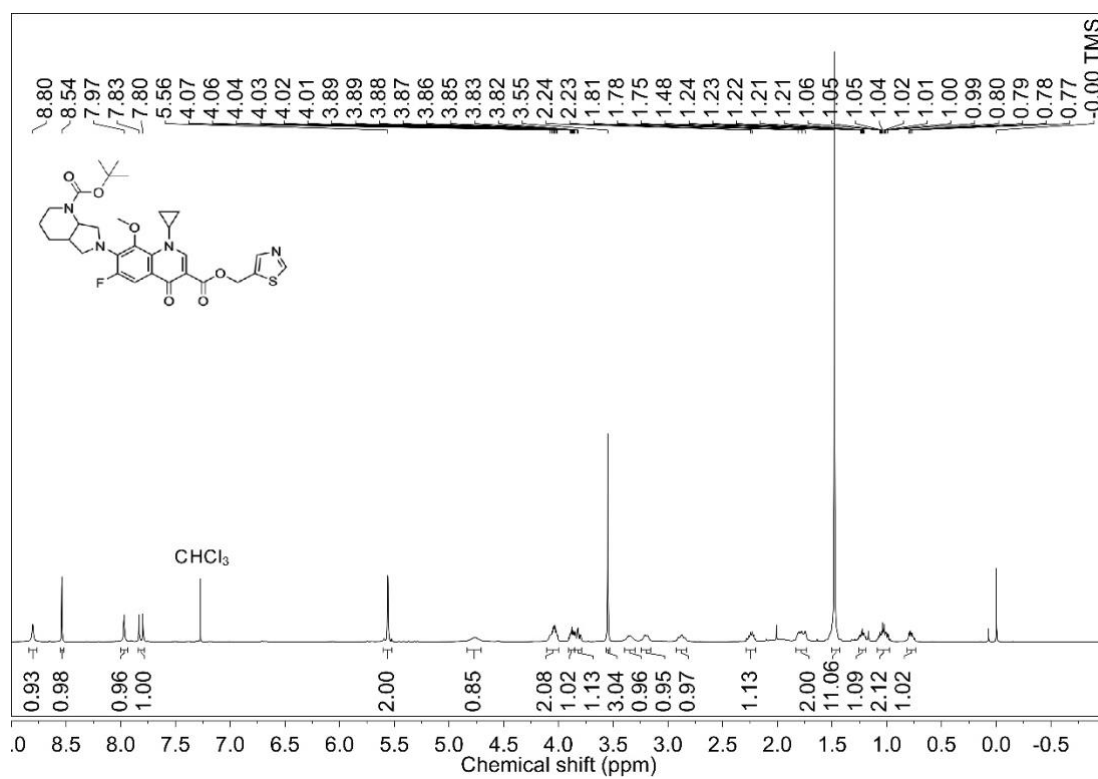
^{13}C NMR spectrum (100 MHz, CDCl_3) of **31**DEPT-135 NMR spectrum (100 MHz, CDCl_3) of **31**

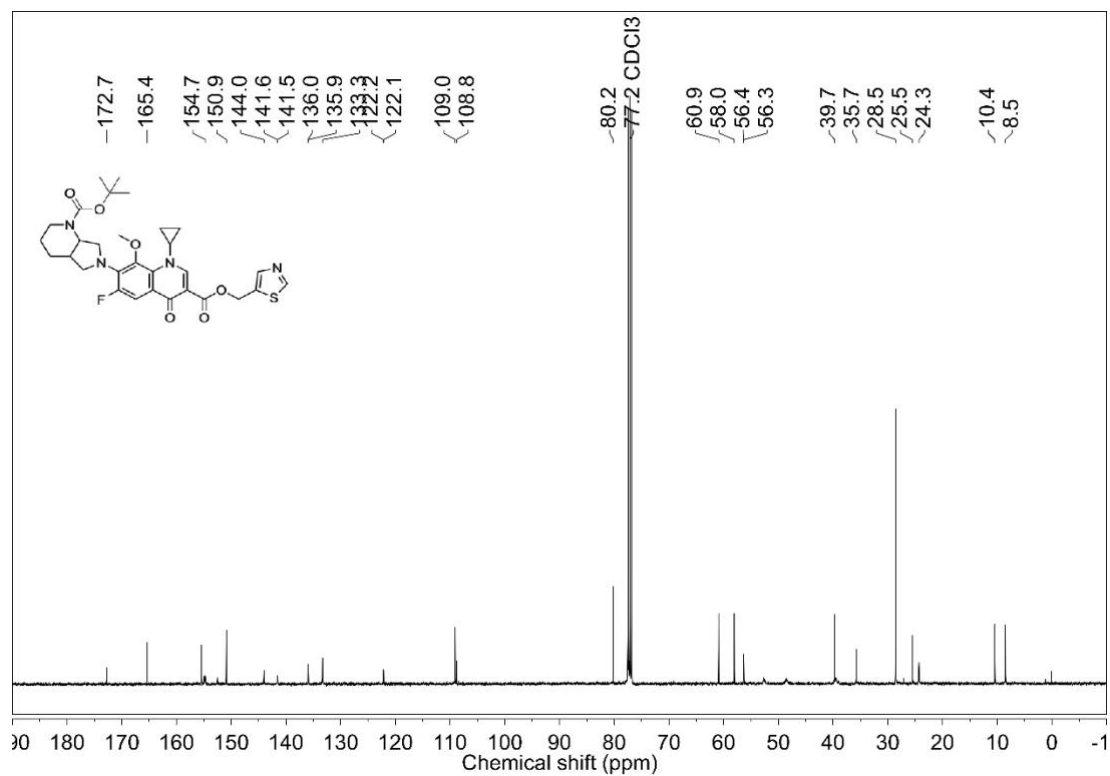
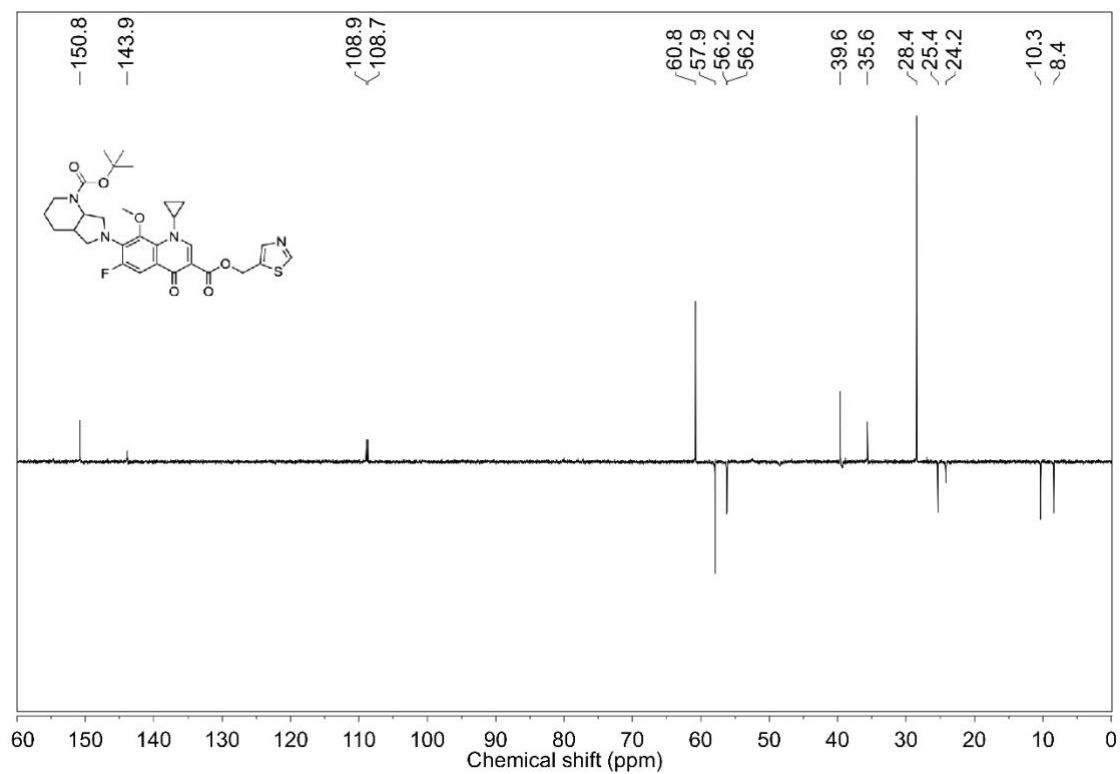
^{19}F NMR spectrum (376 MHz, CDCl_3) of **32** ^1H NMR spectrum (400 MHz, CDCl_3) of **32**

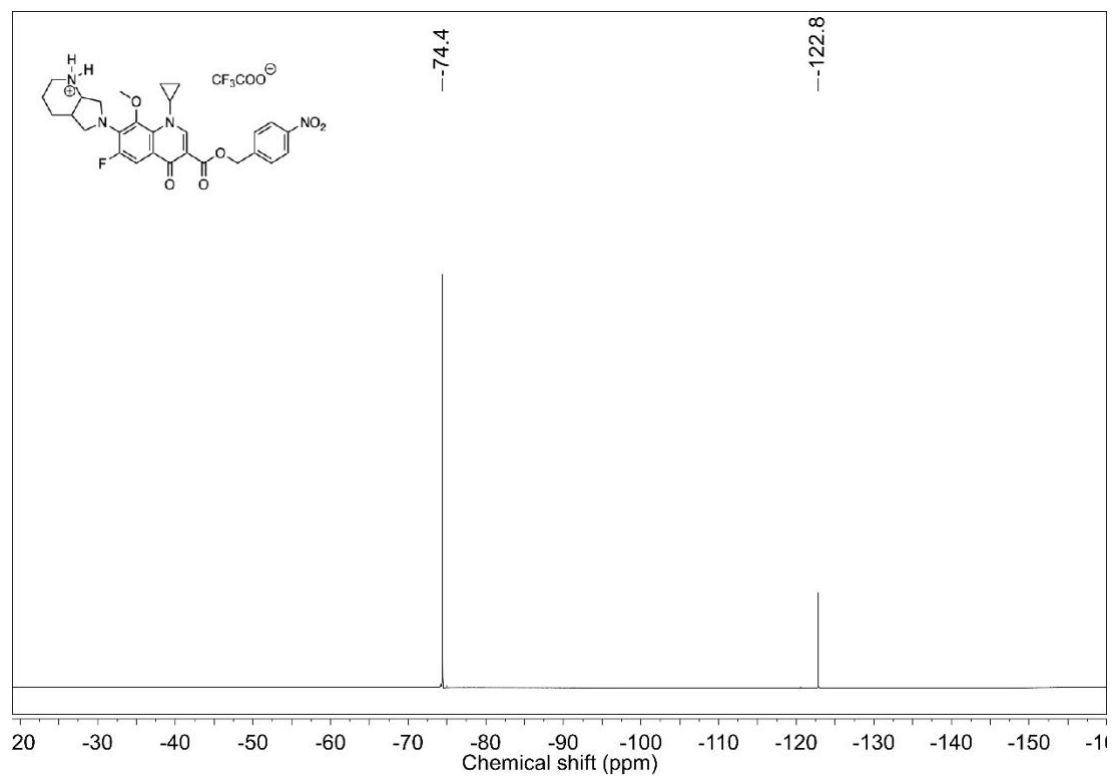
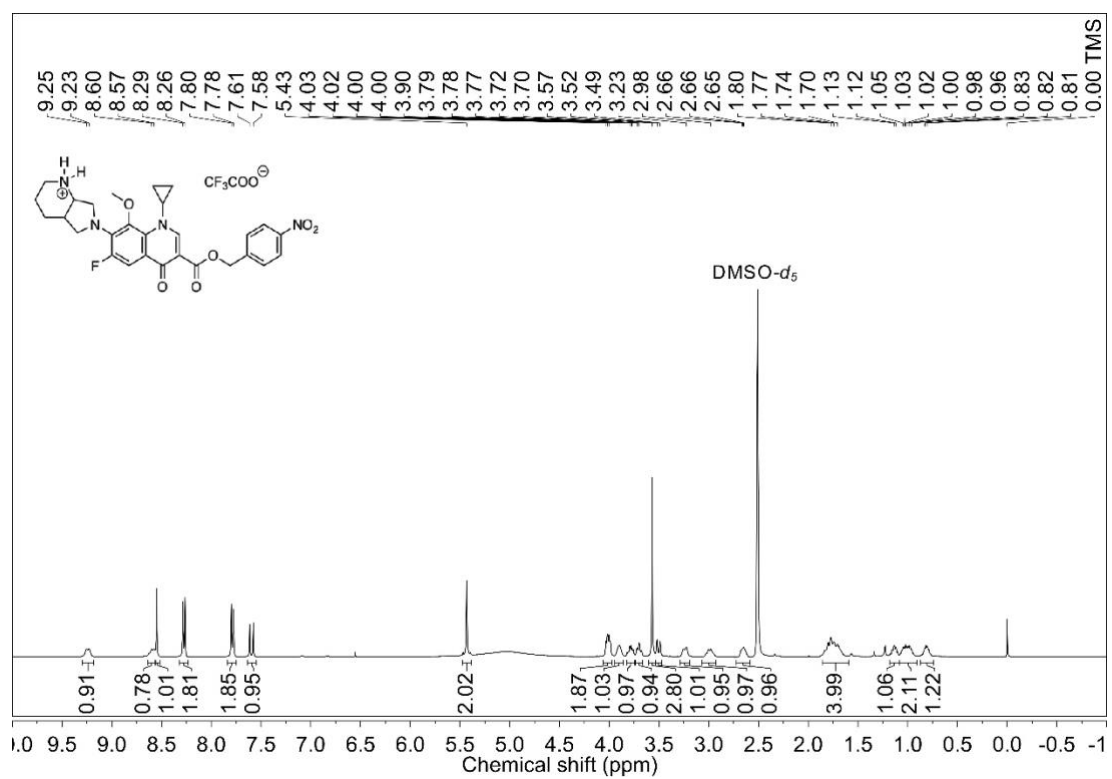
^{13}C NMR spectrum (100 MHz, CDCl_3) of **32**DEPT-135 NMR spectrum (100 MHz, CDCl_3) of **32**

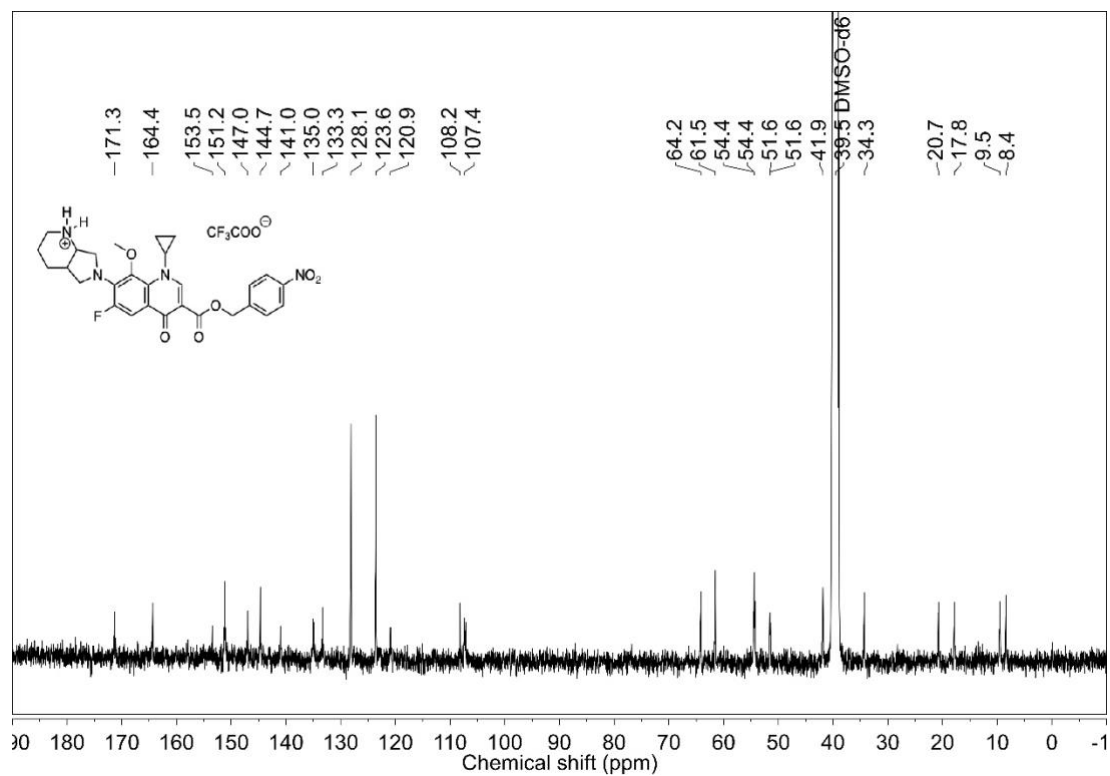
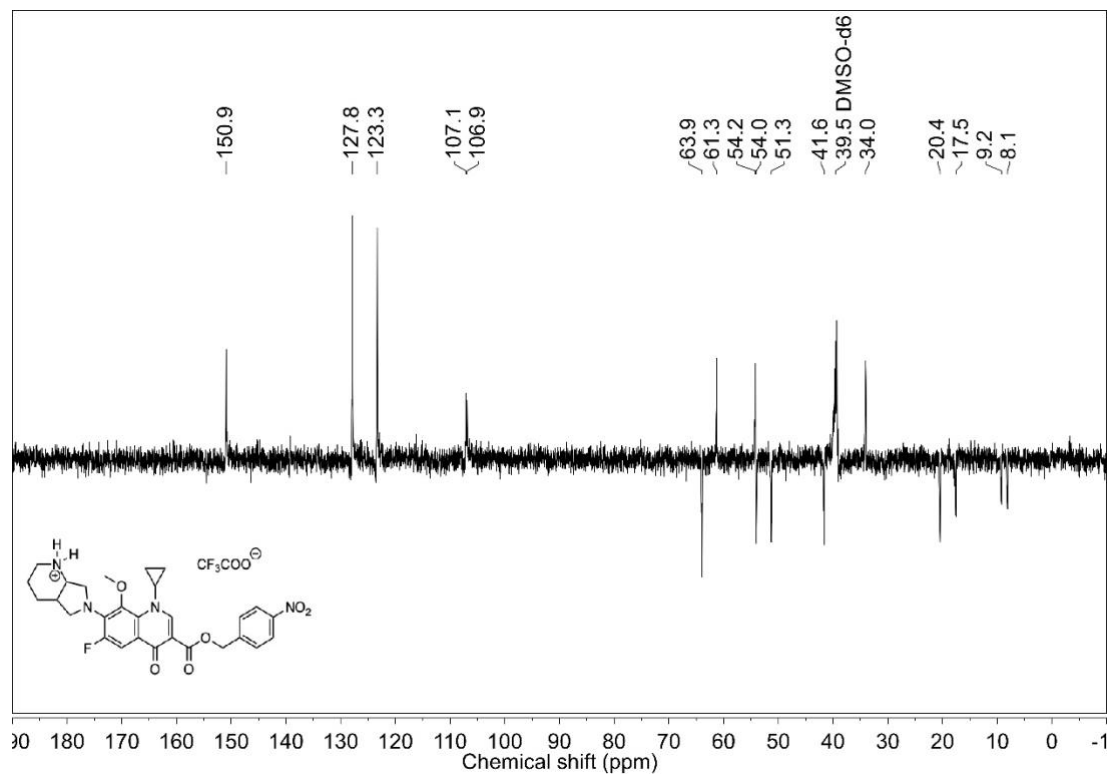
^{19}F NMR spectrum (376 MHz, CDCl_3) of **39** ^1H NMR spectrum (400 MHz, CDCl_3) of **39**

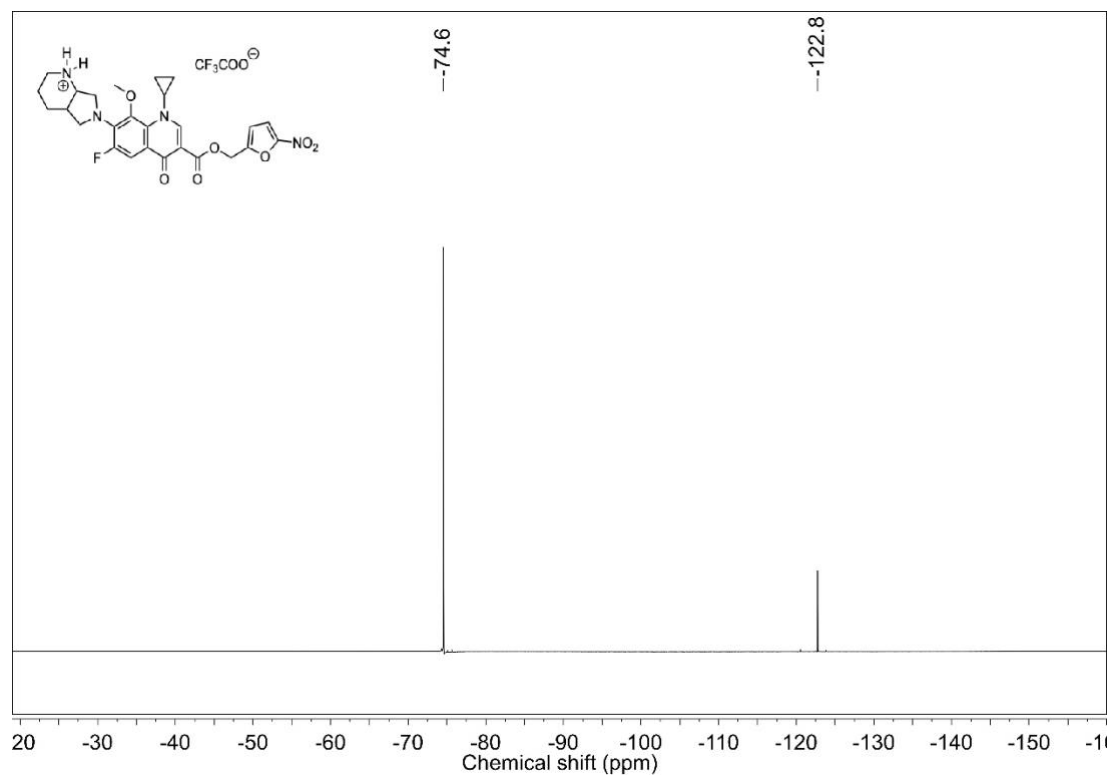
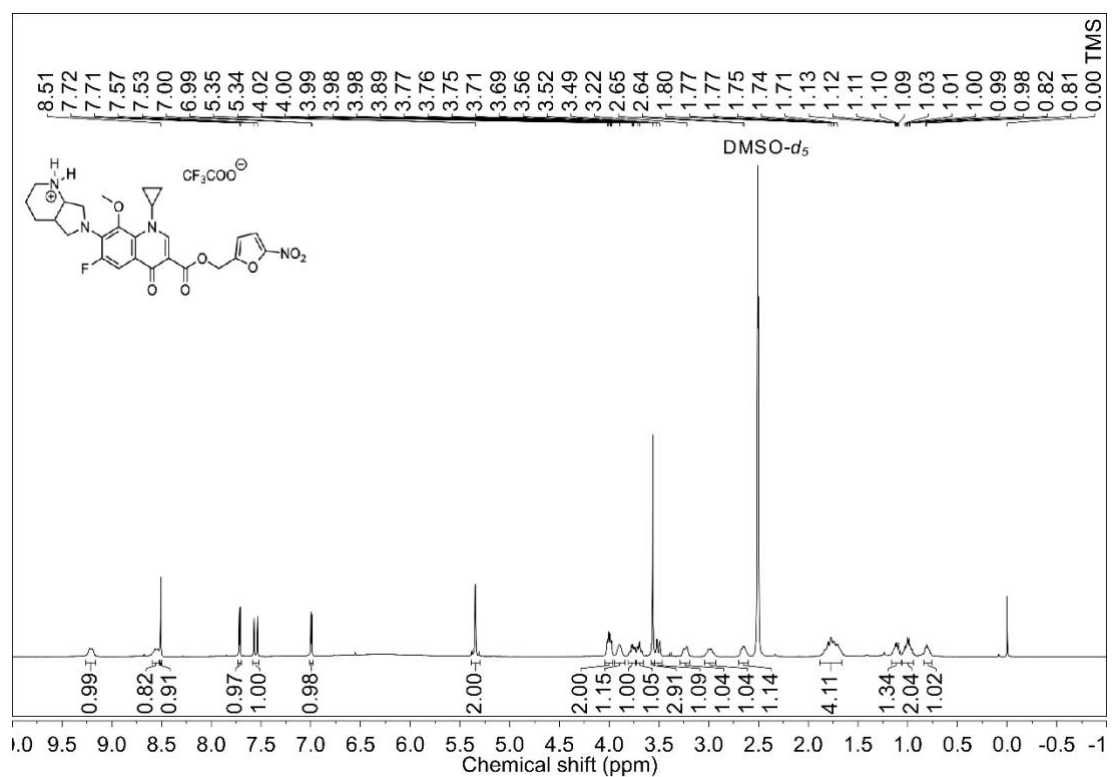
^{13}C NMR spectrum (100 MHz, CDCl_3) of **39**DEPT-135 NMR spectrum (100 MHz, CDCl_3) of **39**

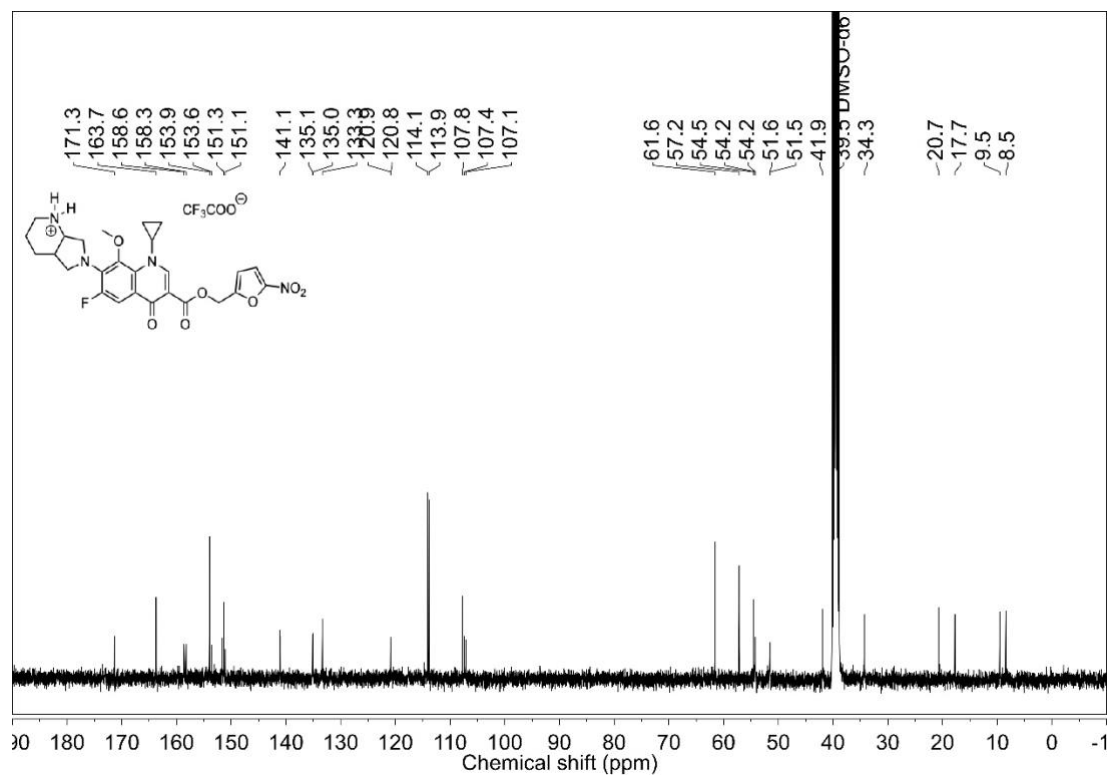
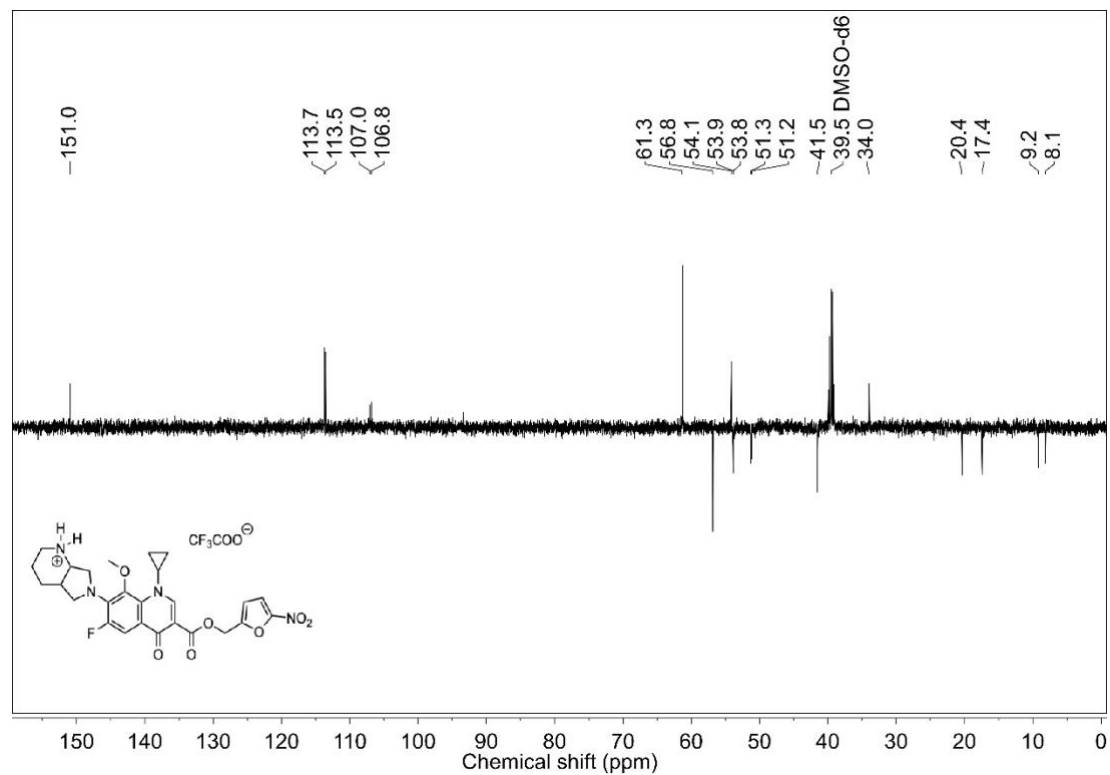
^{19}F NMR spectrum (376 MHz, CDCl_3) of **40** ^1H NMR spectrum (400 MHz, CDCl_3) of **40**

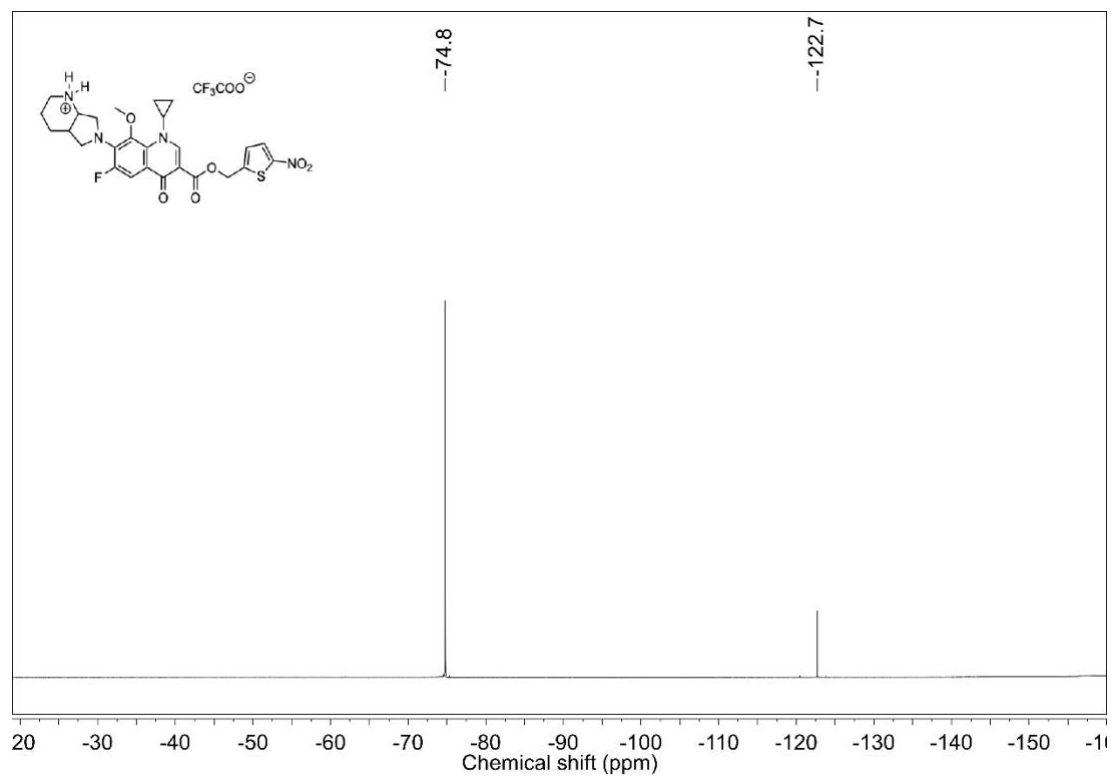
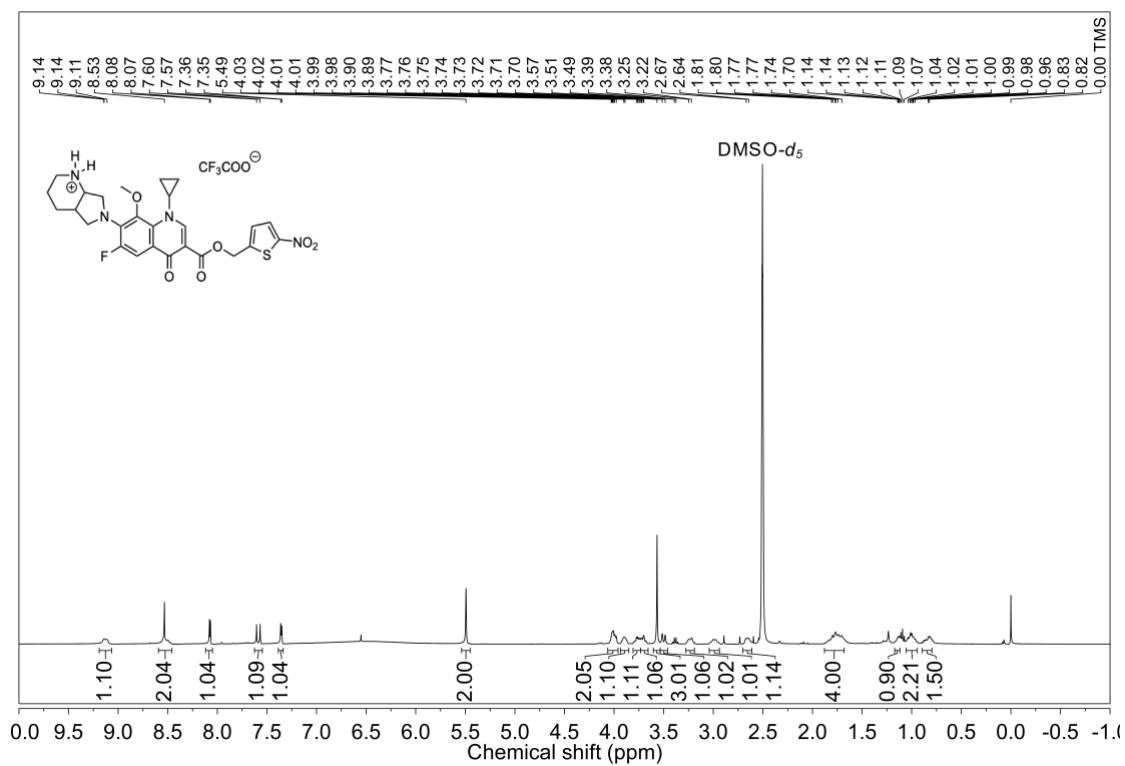
^{13}C NMR spectrum (100 MHz, CDCl_3) of **40**DEPT-135 NMR spectrum (100 MHz, CDCl_3) of **40**

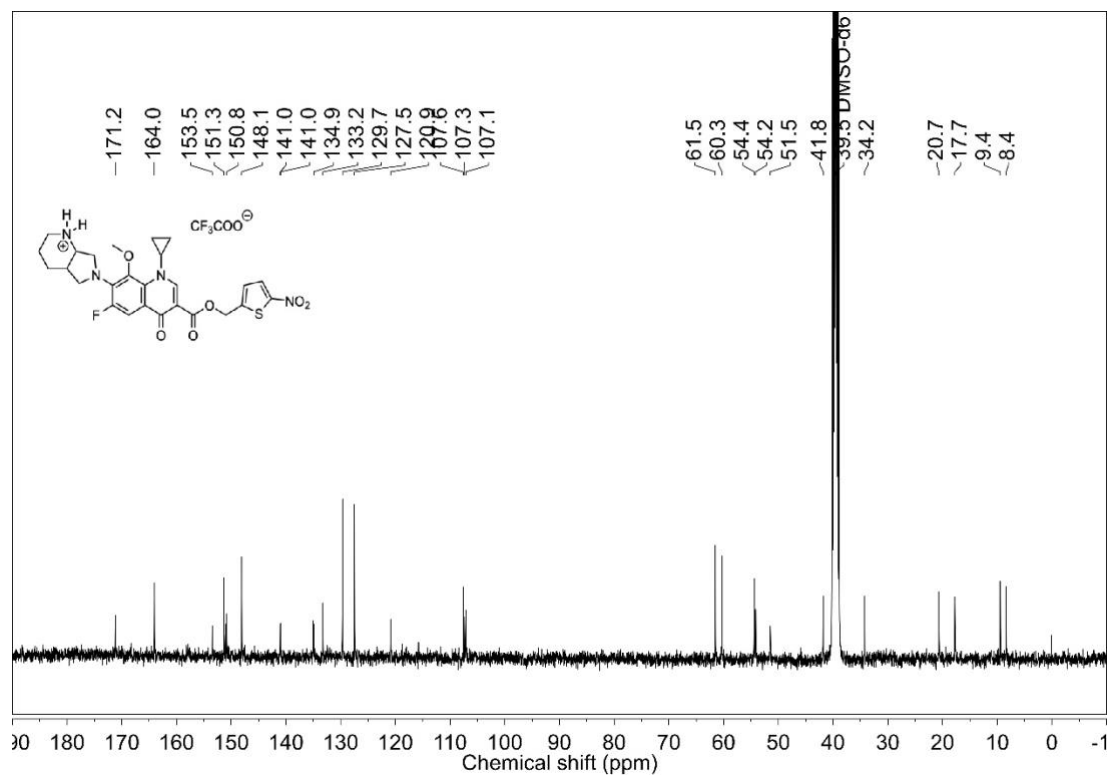
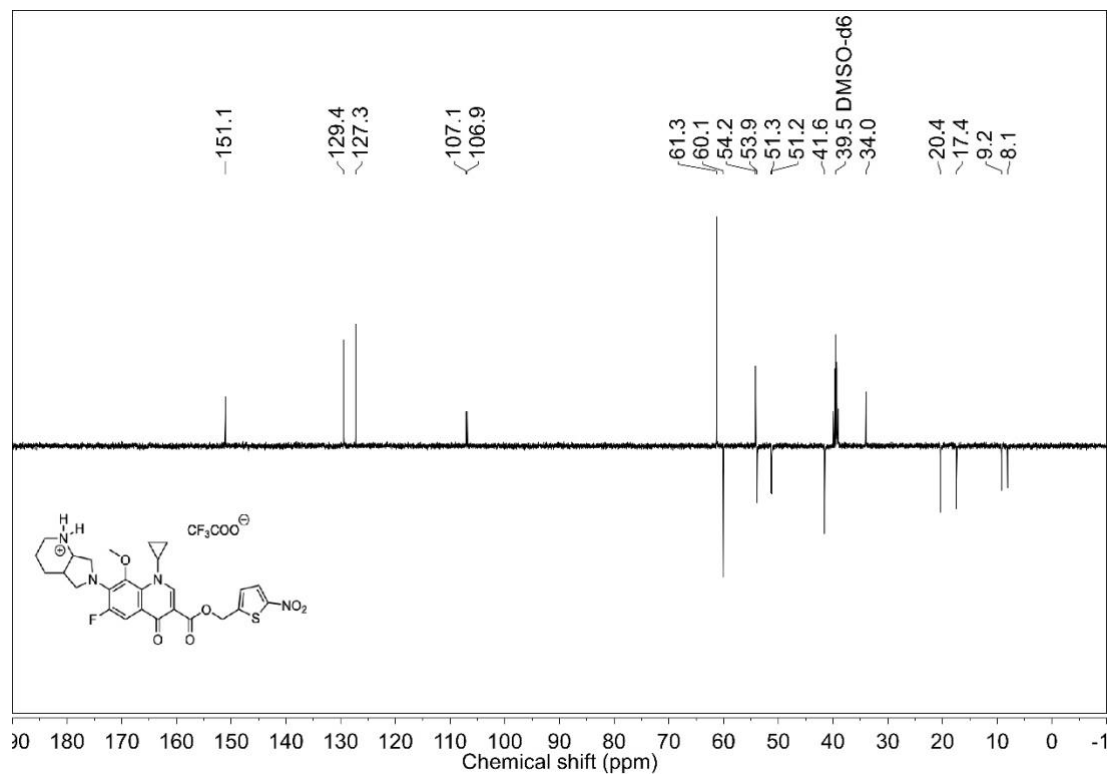
^{19}F NMR spectrum (376 MHz, $\text{DMSO-}d_6$) of **33** ^1H NMR spectrum (400 MHz, $\text{DMSO-}d_6$) of **33**

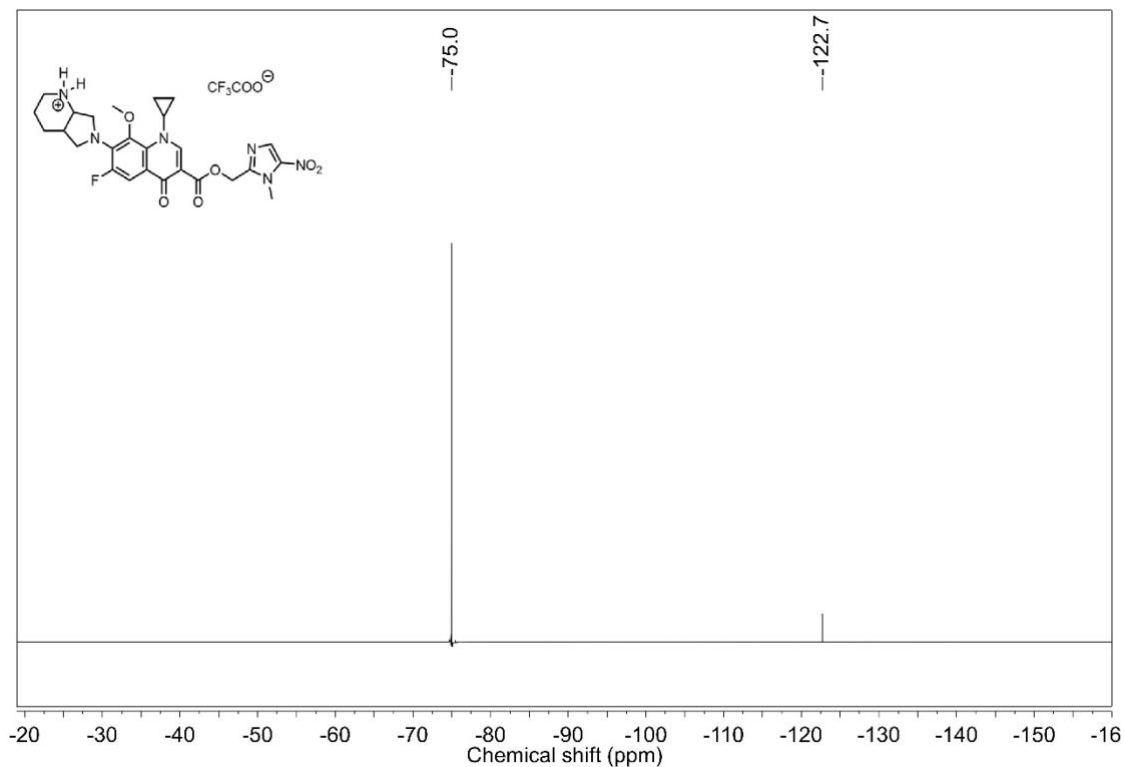
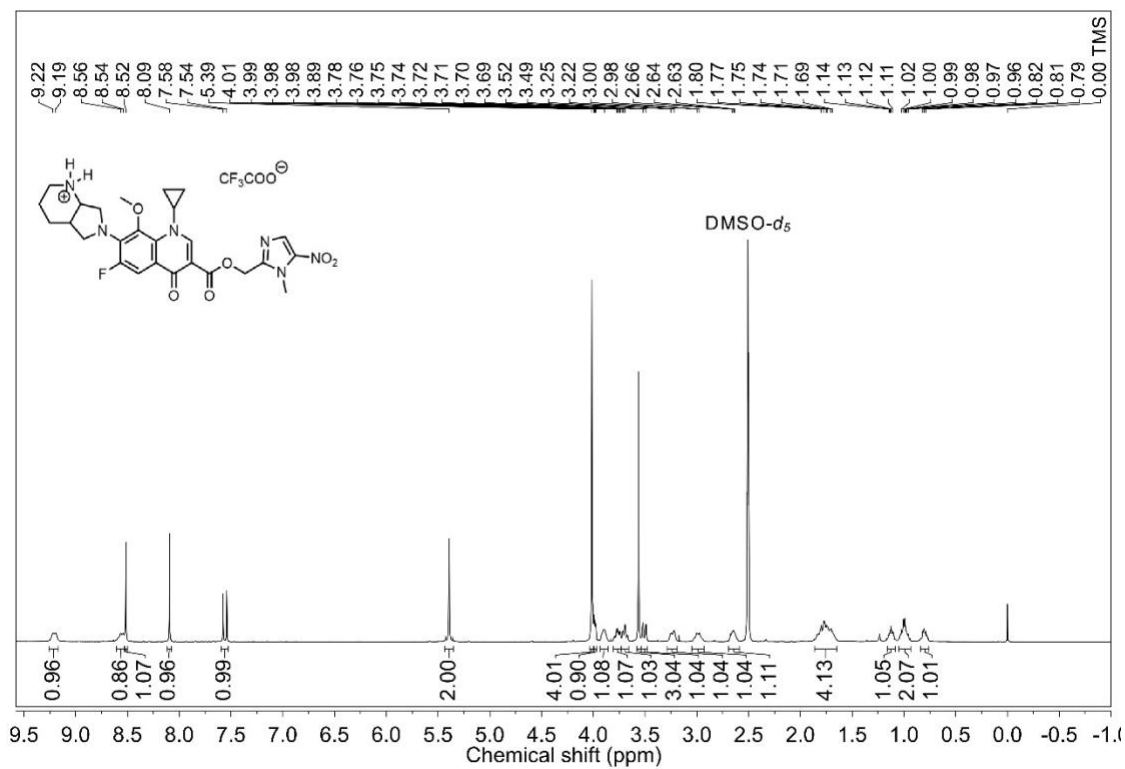
^{13}C NMR spectrum (100 MHz, $\text{DMSO-}d_6$) of **33**DEPT-135 NMR spectrum (100 MHz, $\text{DMSO-}d_6$) of **33**

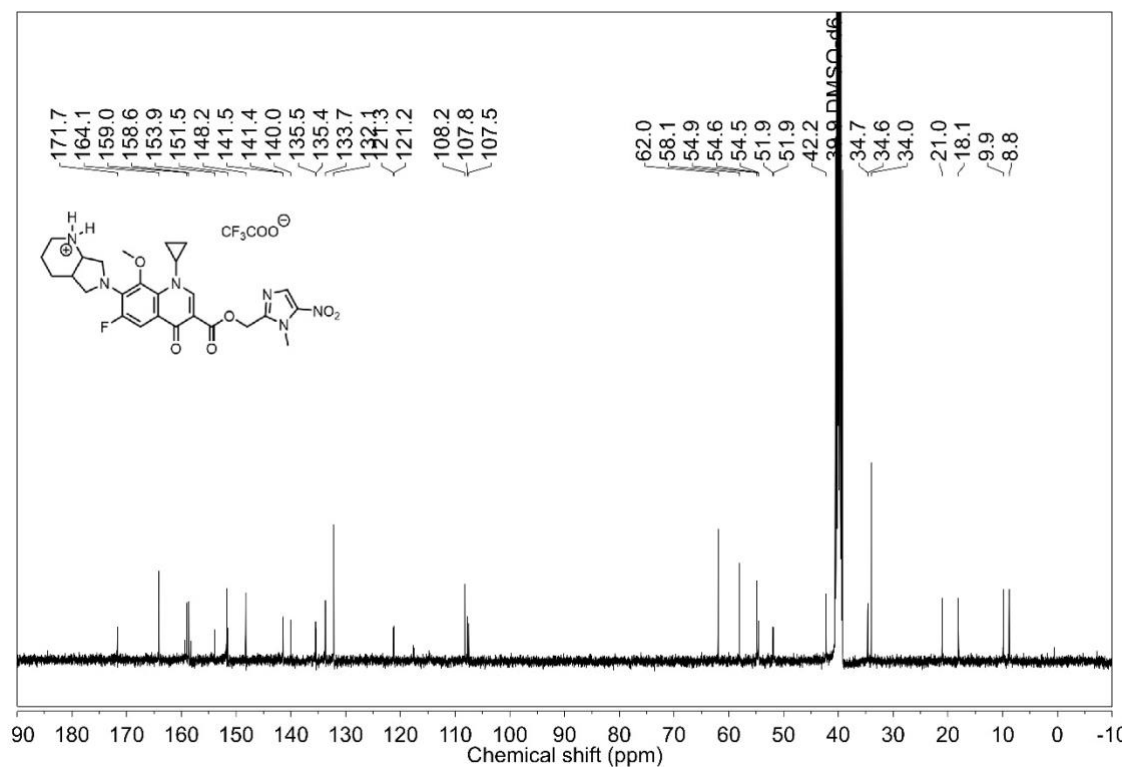
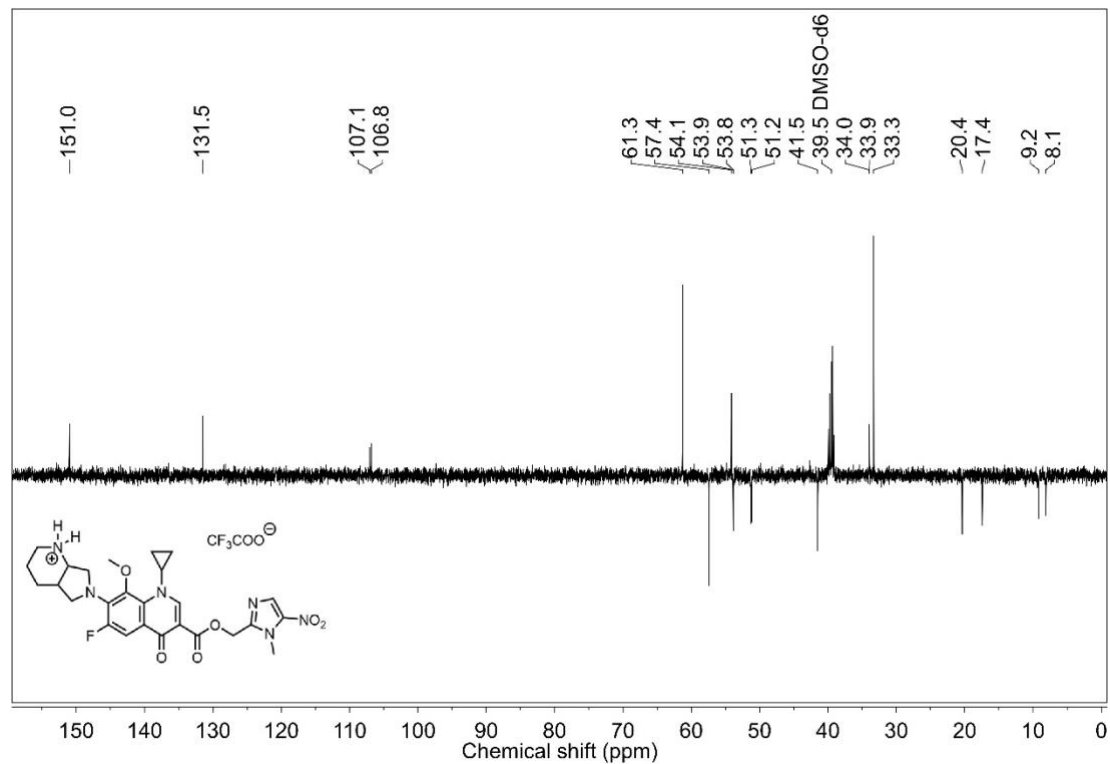
^{19}F NMR spectrum (376 MHz, $\text{DMSO-}d_6$) of **34** ^1H NMR spectrum (400 MHz, $\text{DMSO-}d_6$) of **34**

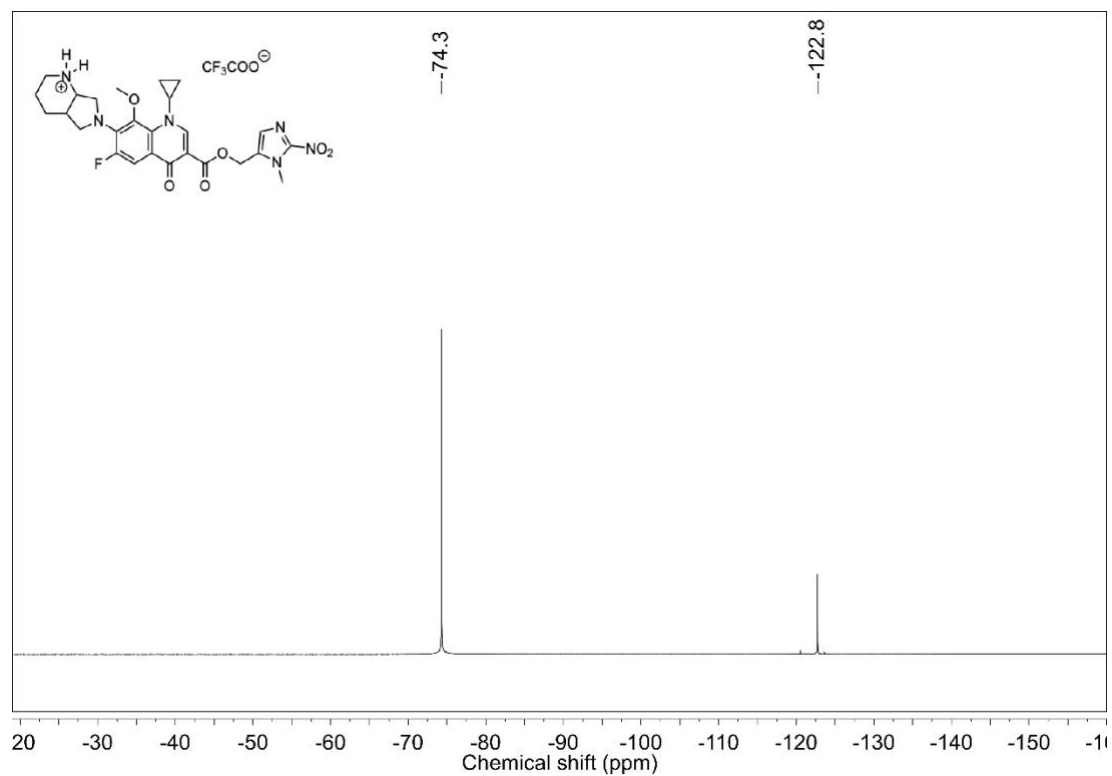
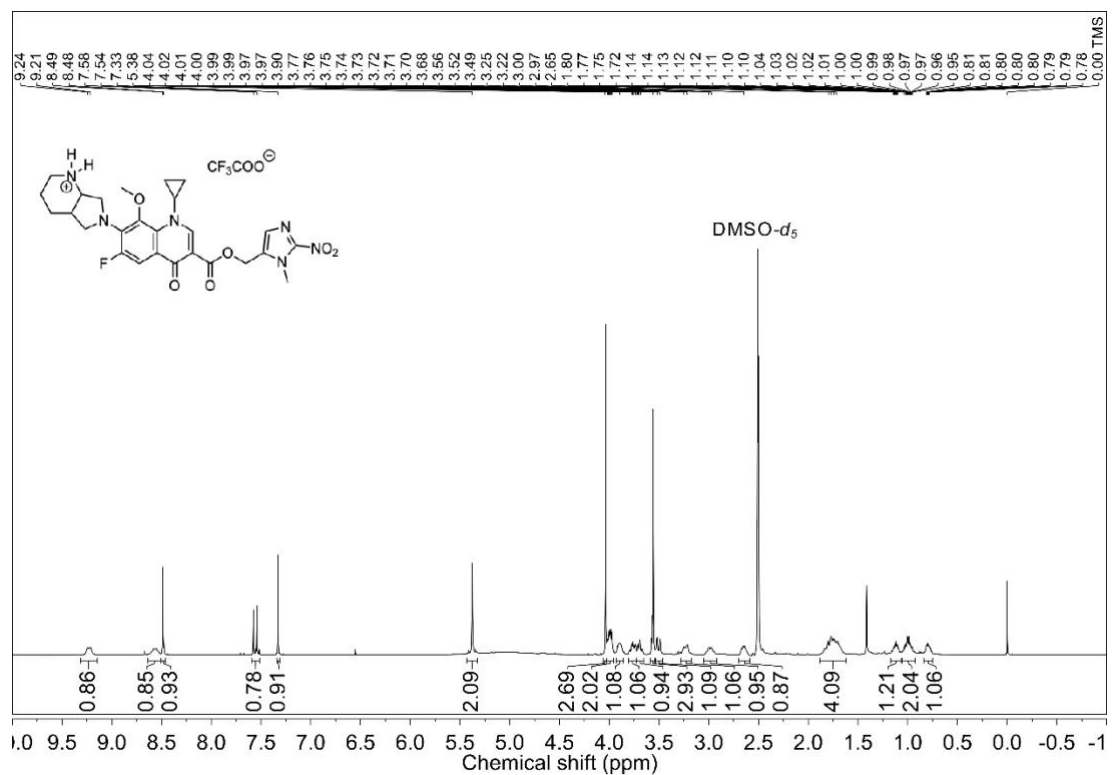
^{13}C NMR spectrum (100 MHz, $\text{DMSO-}d_6$) of **34**DEPT-135 NMR spectrum (100 MHz, $\text{DMSO-}d_6$) of **34**

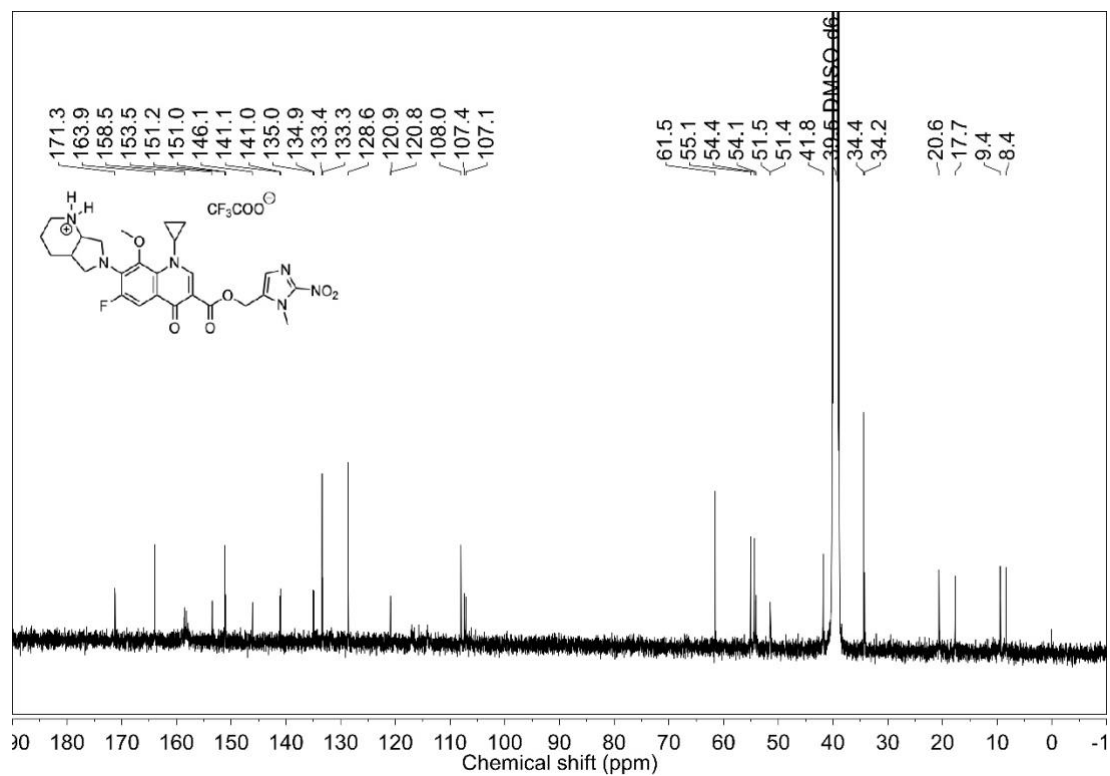
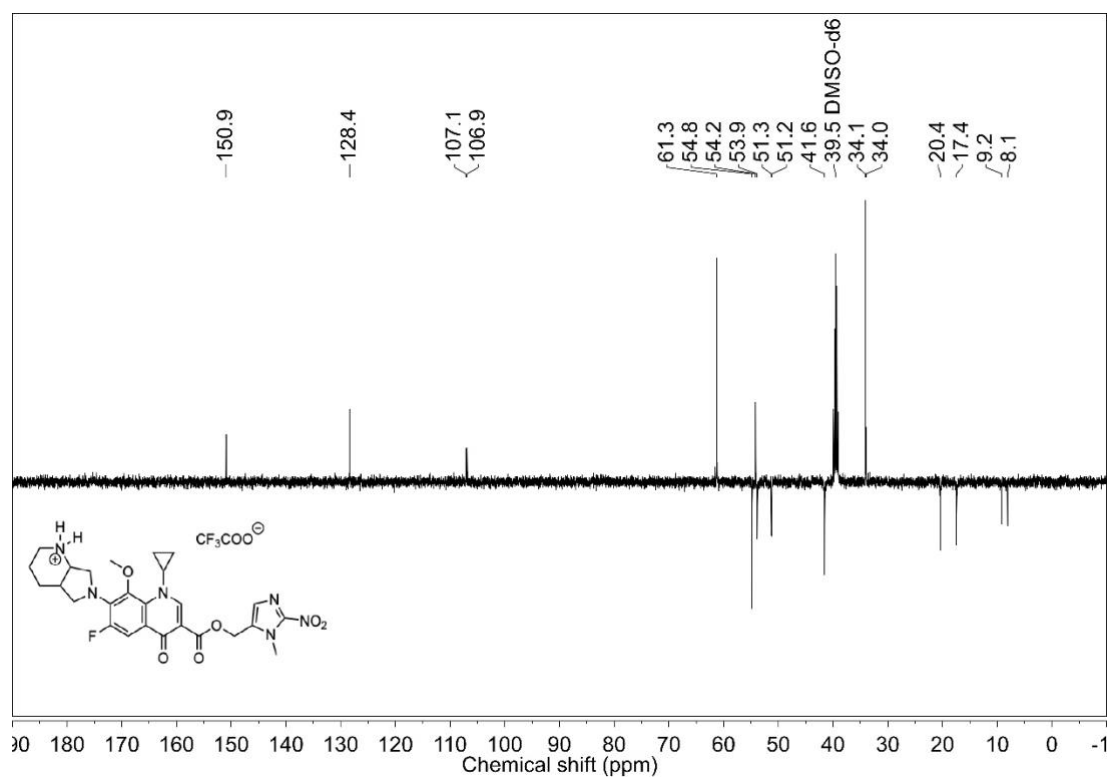
^{19}F NMR spectrum (376 MHz, $\text{DMSO-}d_6$) of **35** ^1H NMR spectrum (400 MHz, $\text{DMSO-}d_6$) of **35**

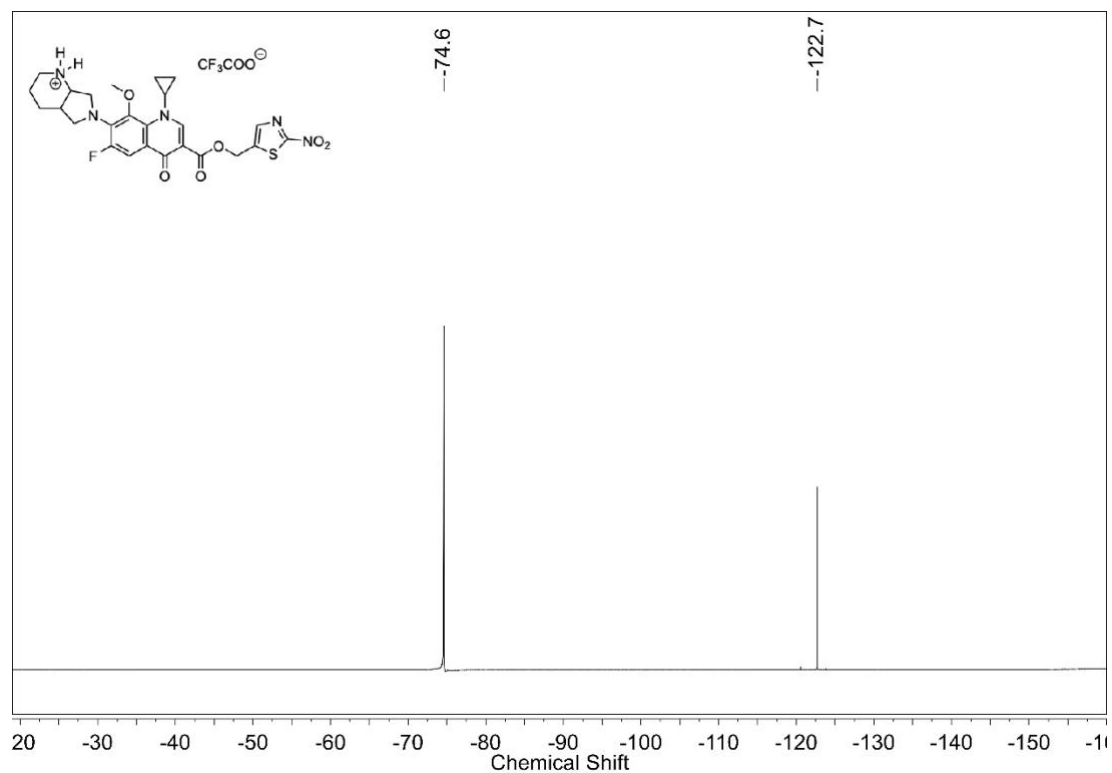
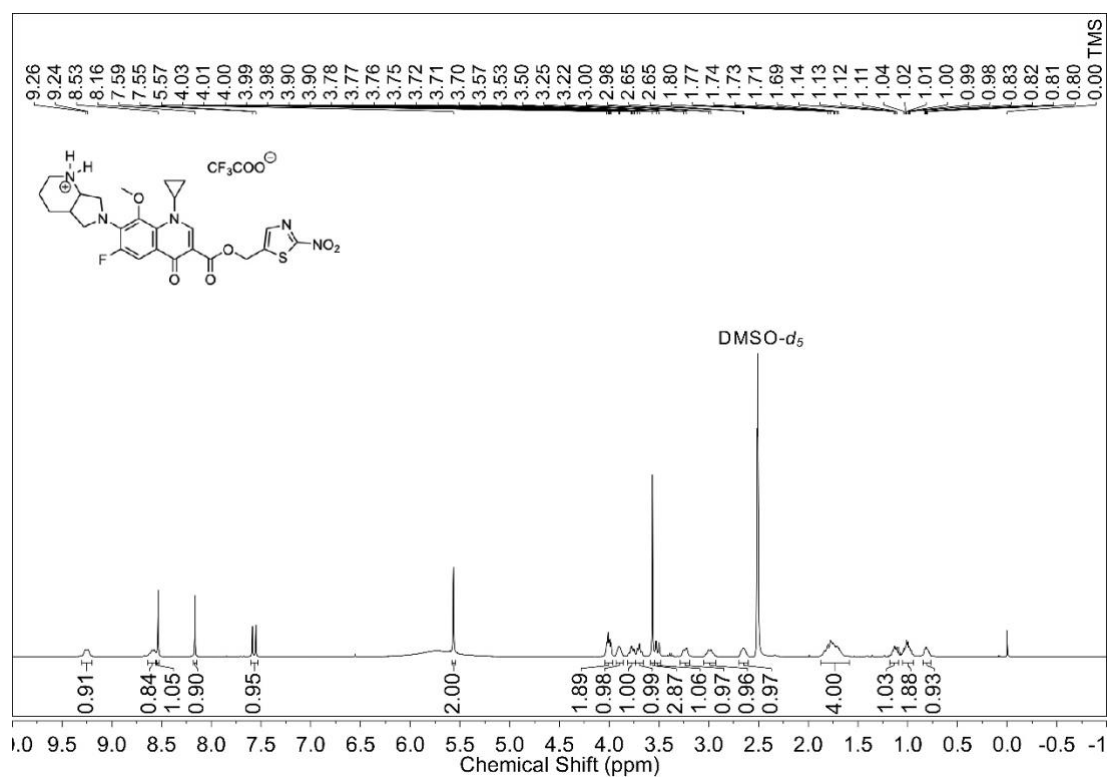
^{13}C NMR spectrum (100 MHz, $\text{DMSO-}d_6$) of **35**DEPT-135 NMR spectrum (100 MHz, $\text{DMSO-}d_6$) of **35**

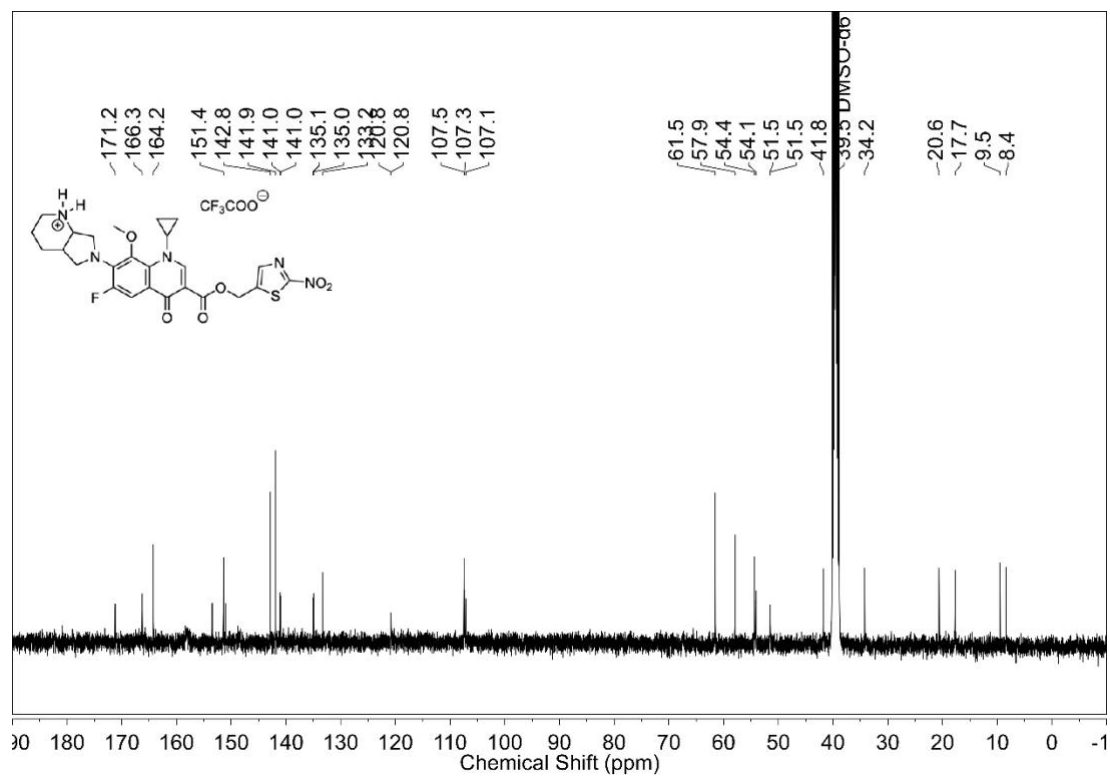
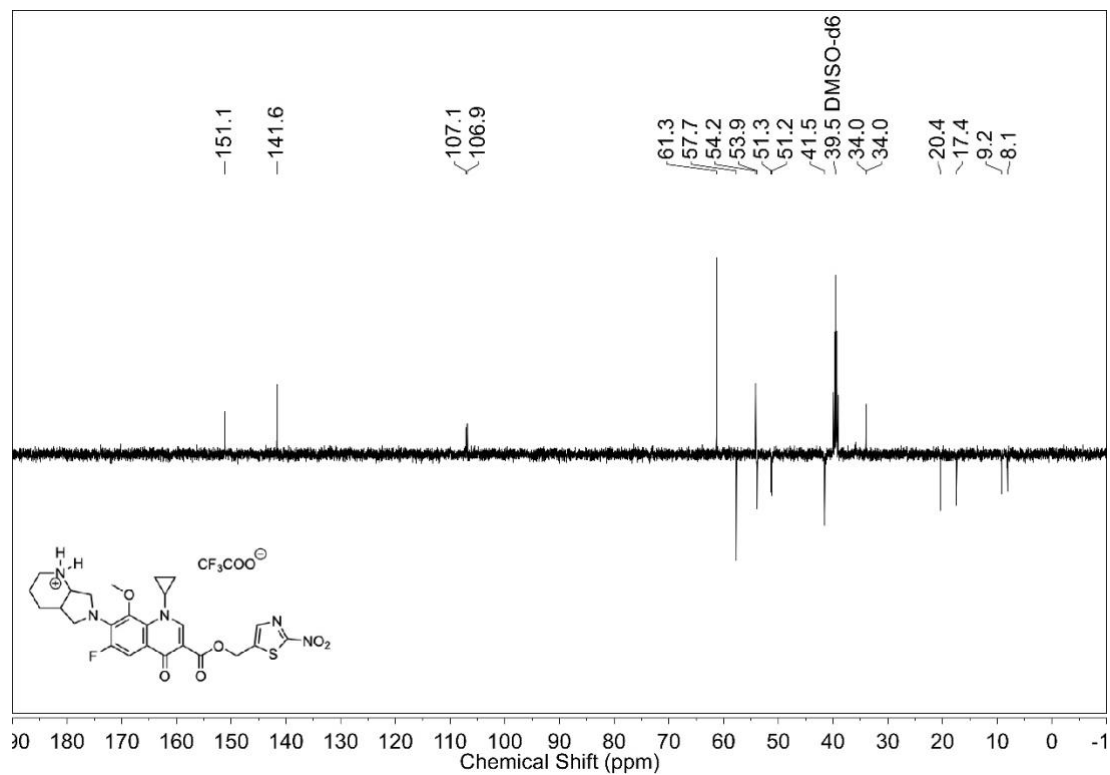
^{19}F NMR spectrum (376 MHz, $\text{DMSO-}d_6$) of **36** ^1H NMR spectrum (400 MHz, $\text{DMSO-}d_6$) of **36**

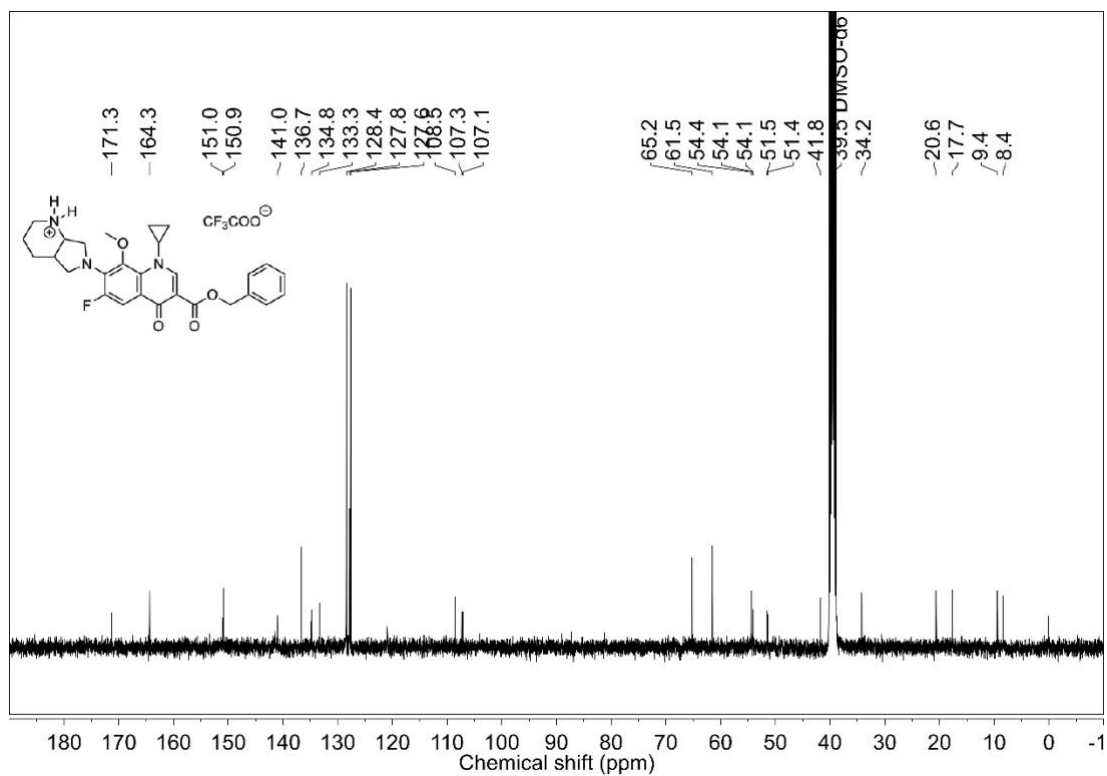
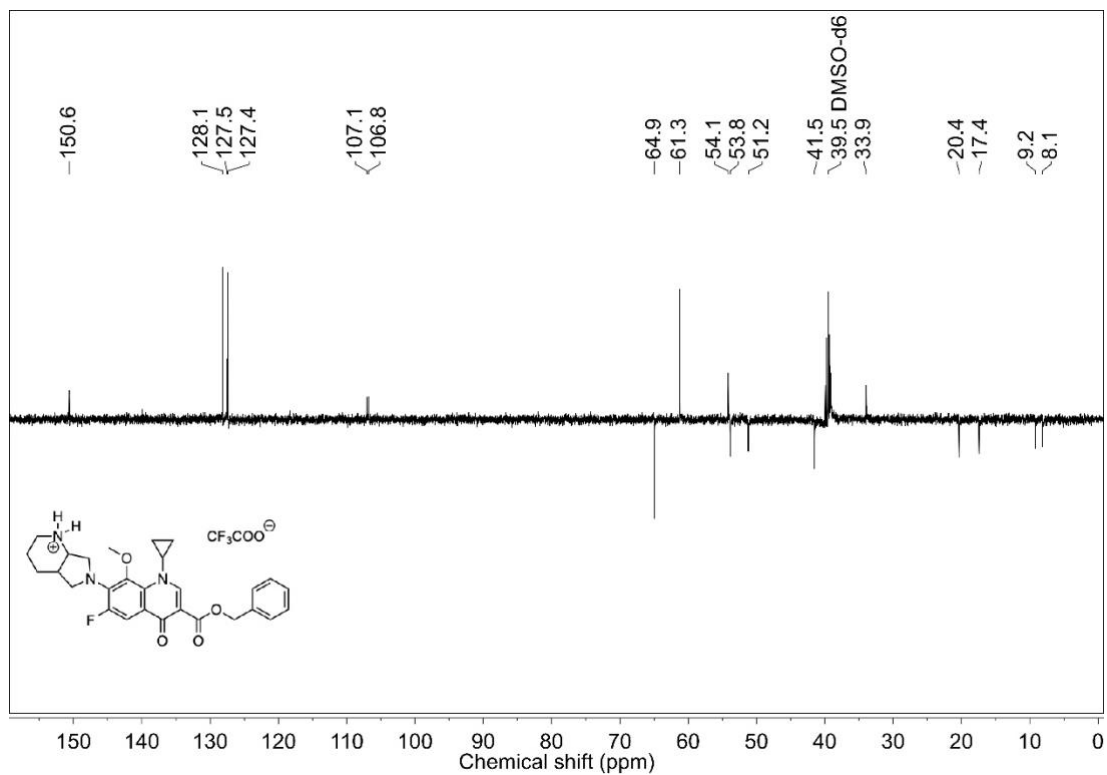
^{13}C NMR spectrum (100 MHz, $\text{DMSO-}d_6$) of **36**DEPT-135 NMR spectrum (100 MHz, $\text{DMSO-}d_6$) of **36**

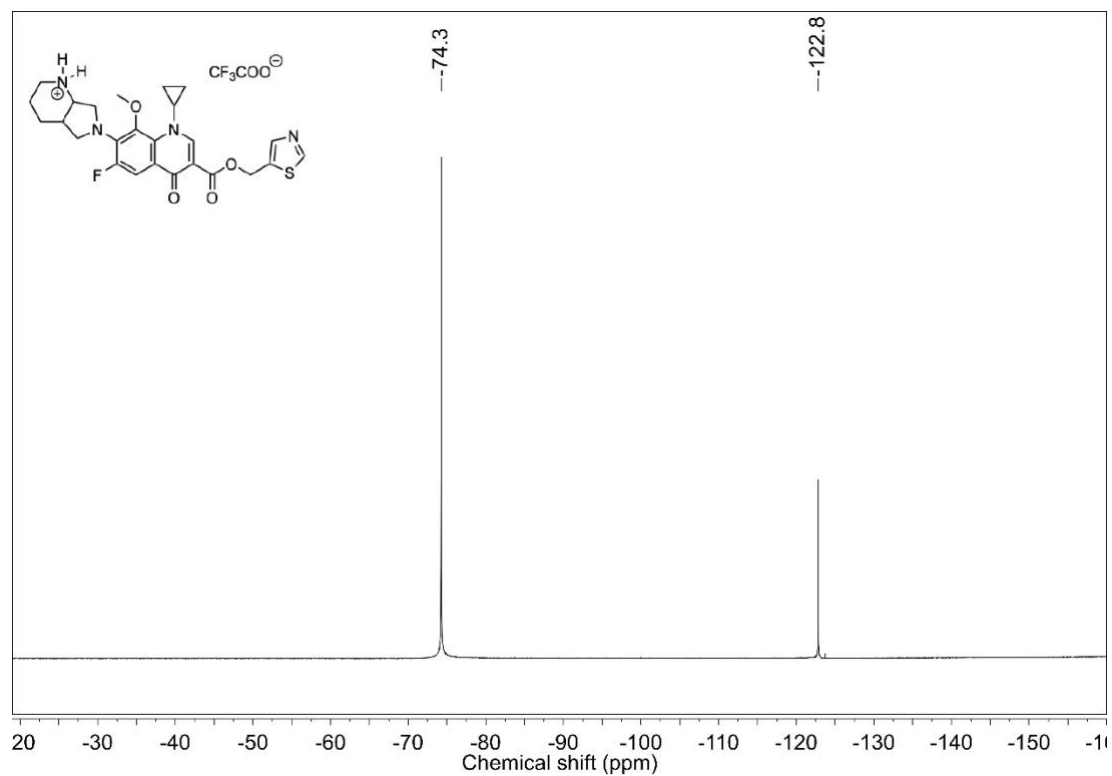
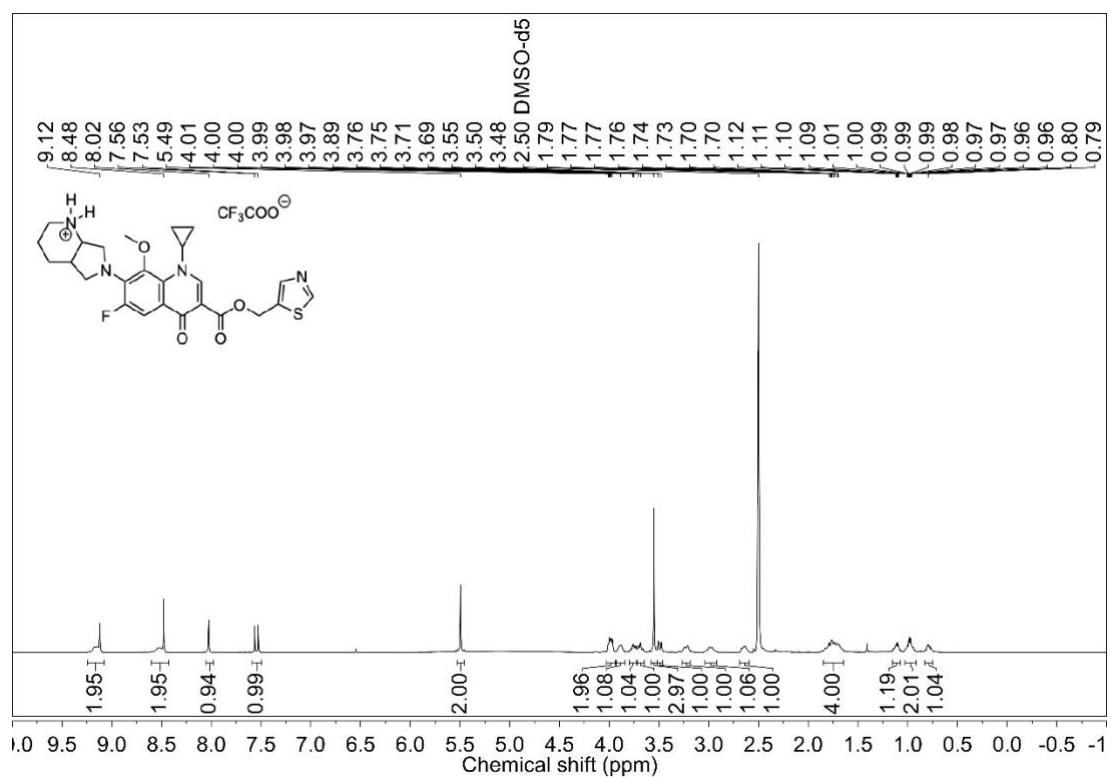
^{19}F NMR spectrum (376 MHz, $\text{DMSO-}d_6$) of **37** ^1H NMR spectrum (400 MHz, $\text{DMSO-}d_6$) of **37**

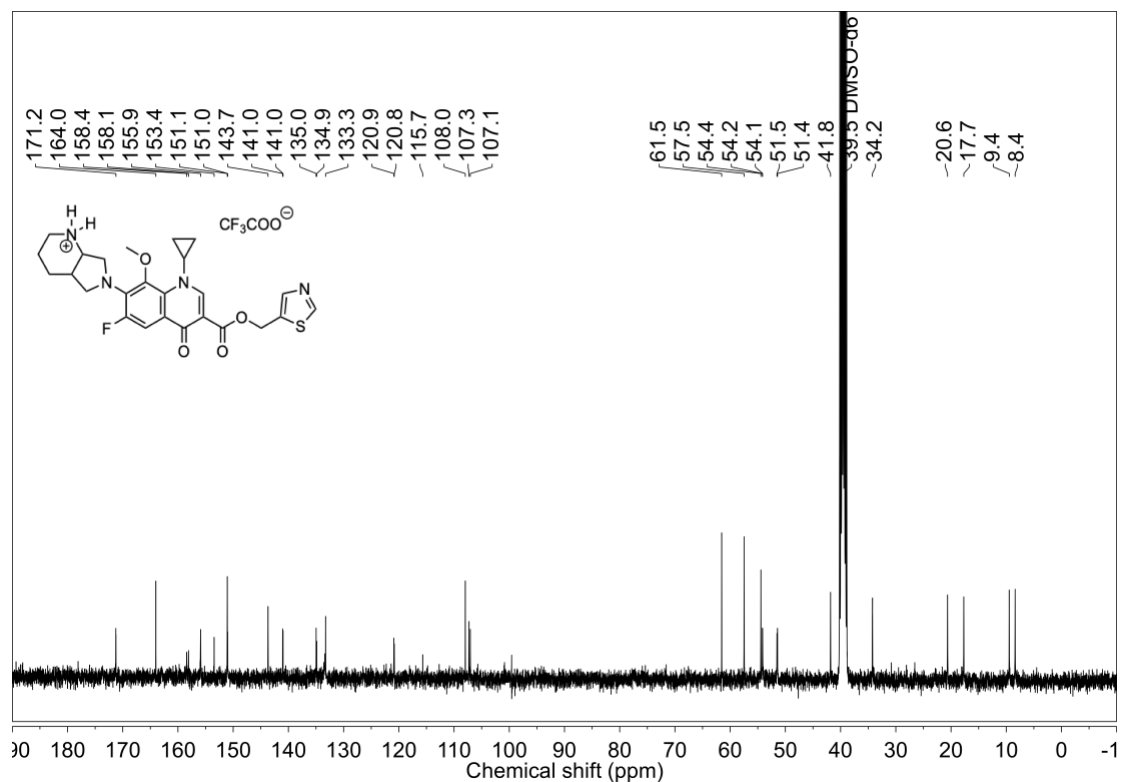
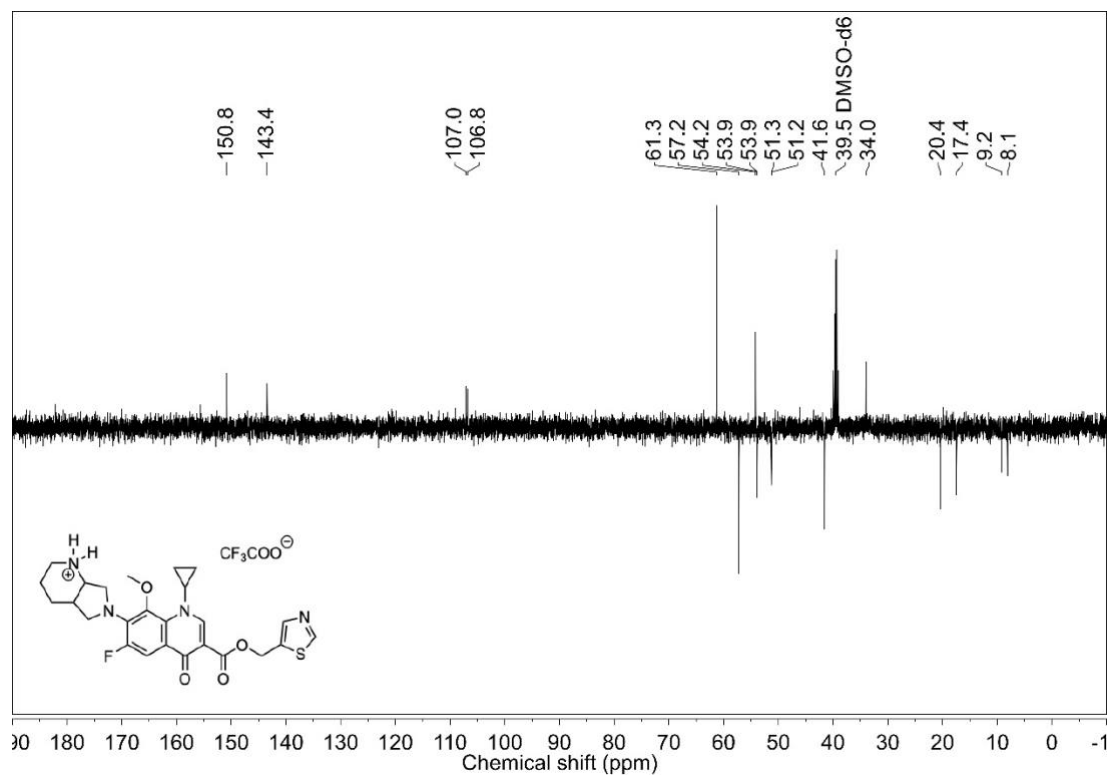
^{13}C NMR spectrum (100 MHz, $\text{DMSO-}d_6$) of **37**DEPT-135 NMR spectrum (100 MHz, $\text{DMSO-}d_6$) of **37**

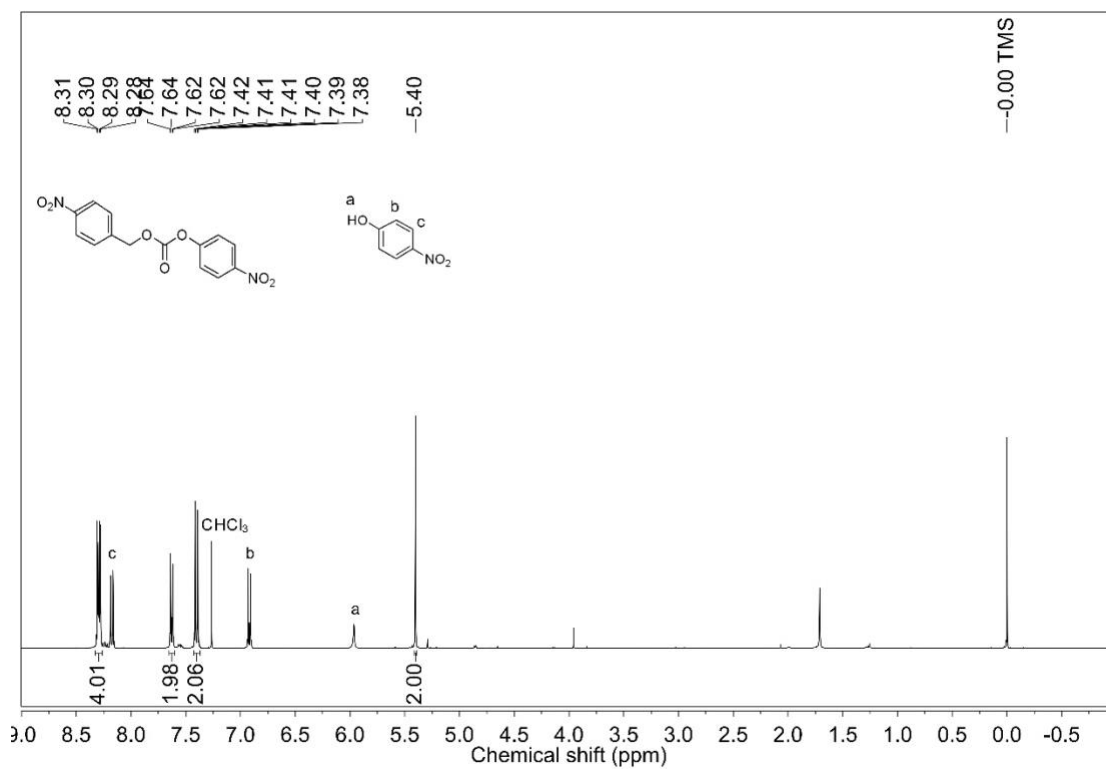
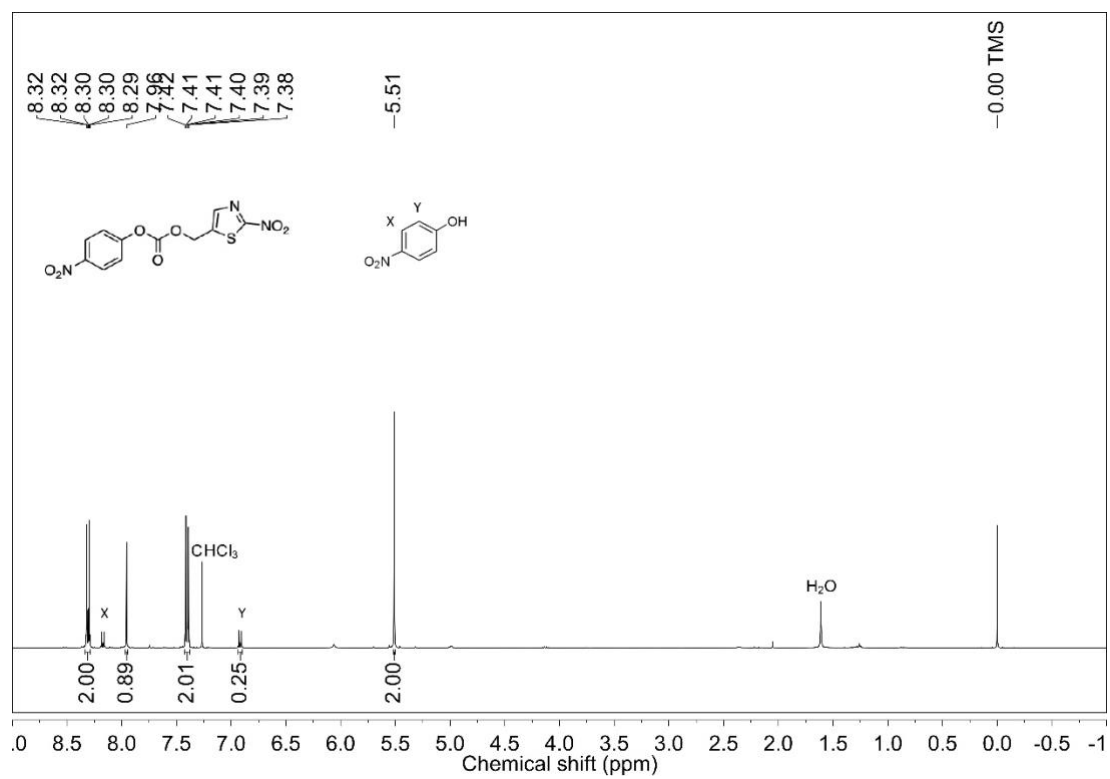
^{19}F NMR spectrum (376 MHz, $\text{DMSO-}d_6$) of **38** ^1H NMR spectrum (400 MHz, $\text{DMSO-}d_6$) of **38**

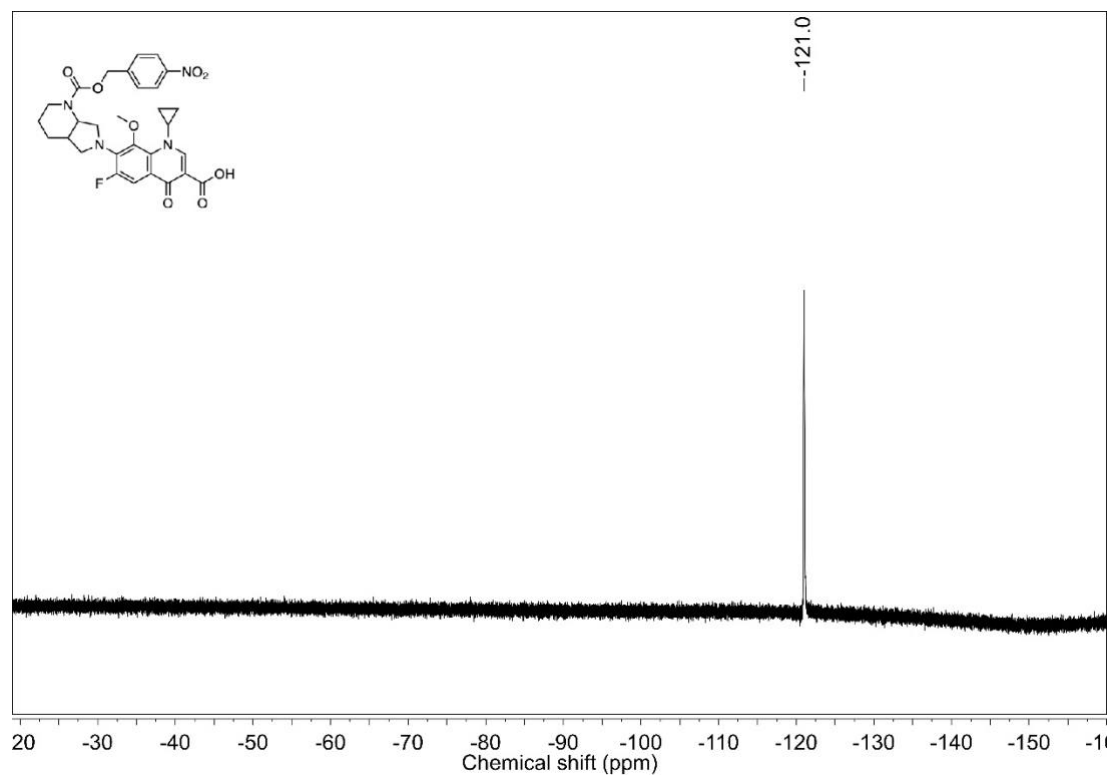
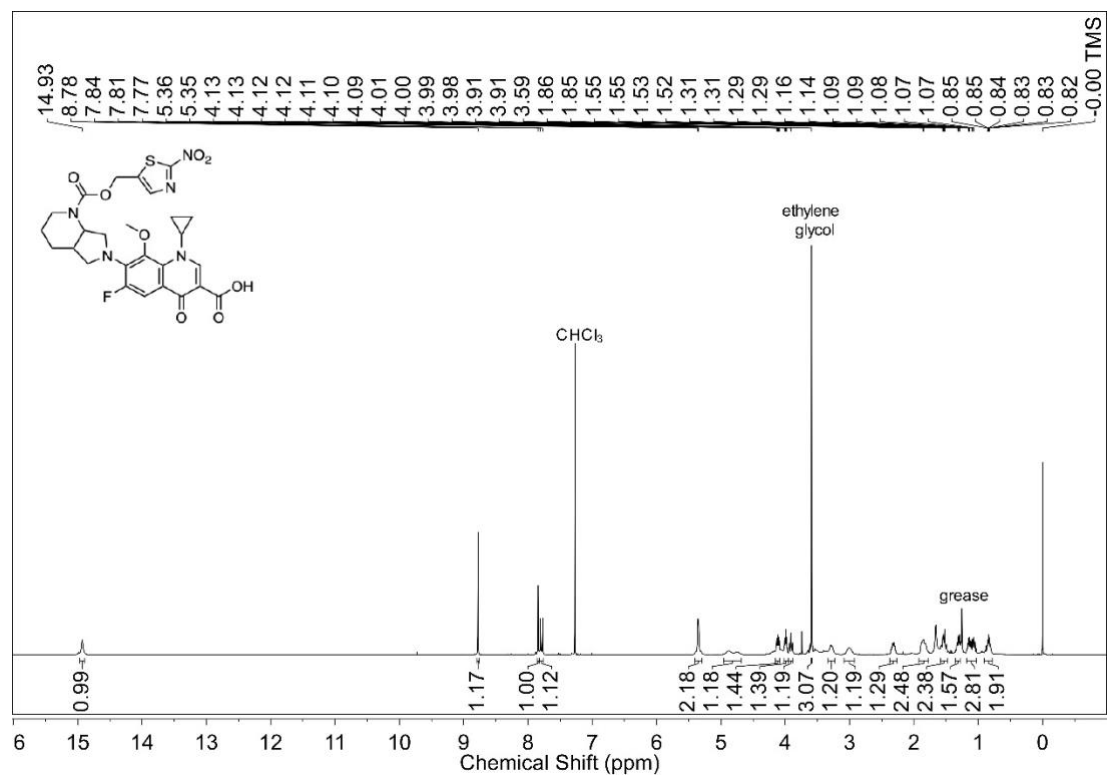
^{13}C NMR spectrum (100 MHz, $\text{DMSO-}d_6$) of **38**DEPT-135 NMR spectrum (100 MHz, $\text{DMSO-}d_6$) of **38**

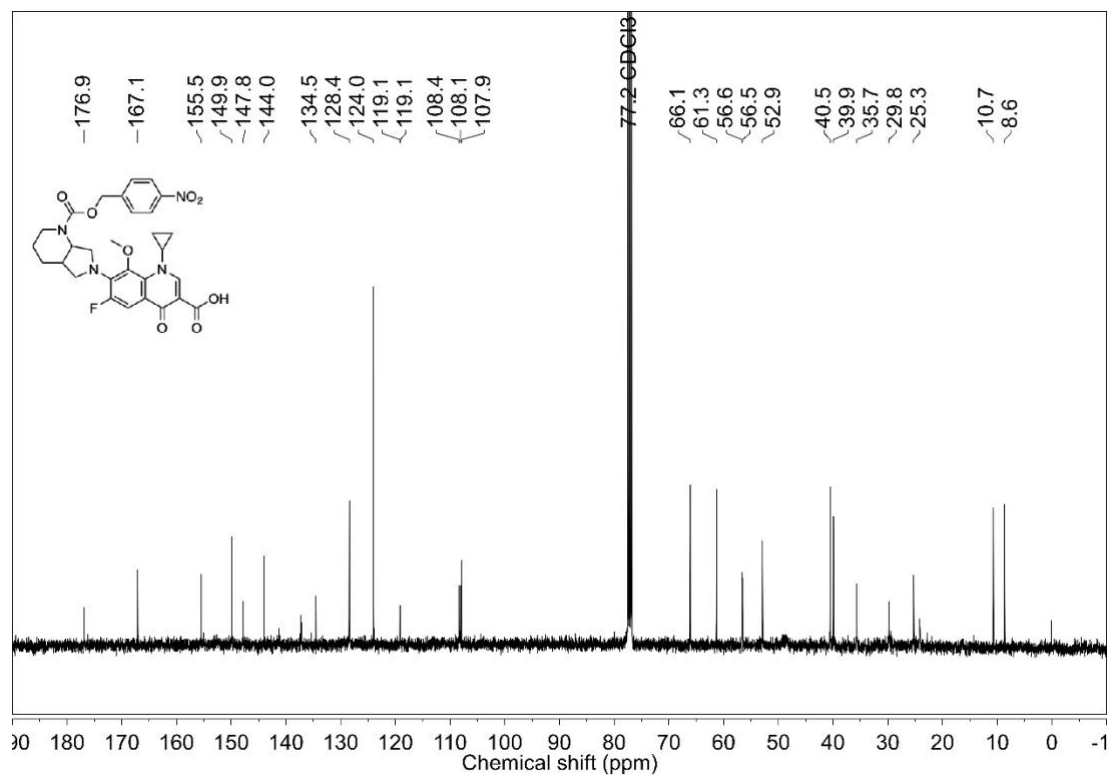
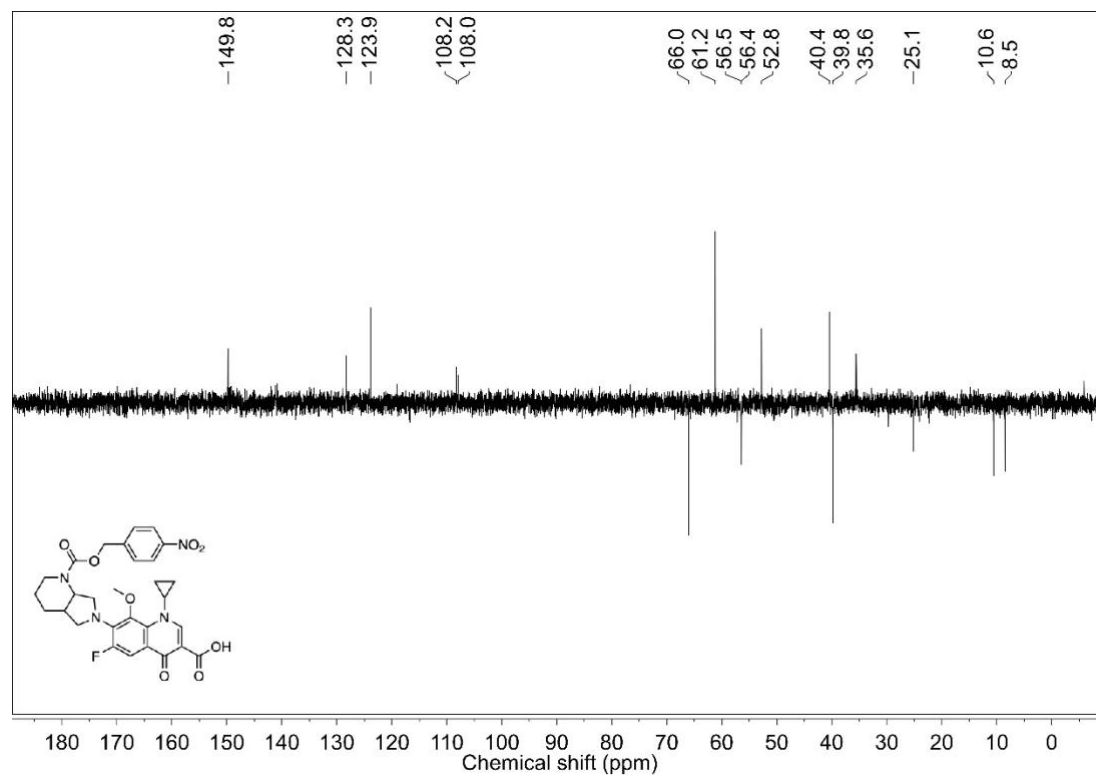
^{13}C NMR spectrum (100 MHz, $\text{DMSO-}d_6$) of **41**DEPT-135 NMR spectrum (100 MHz, $\text{DMSO-}d_6$) of **41**

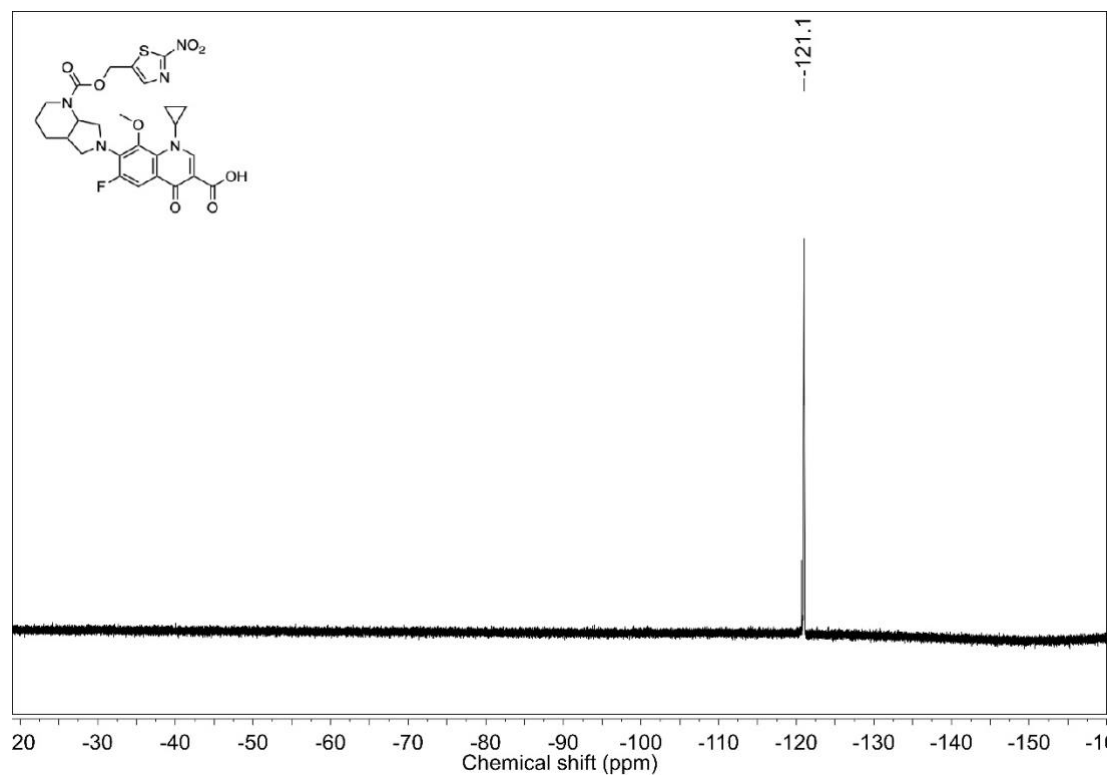
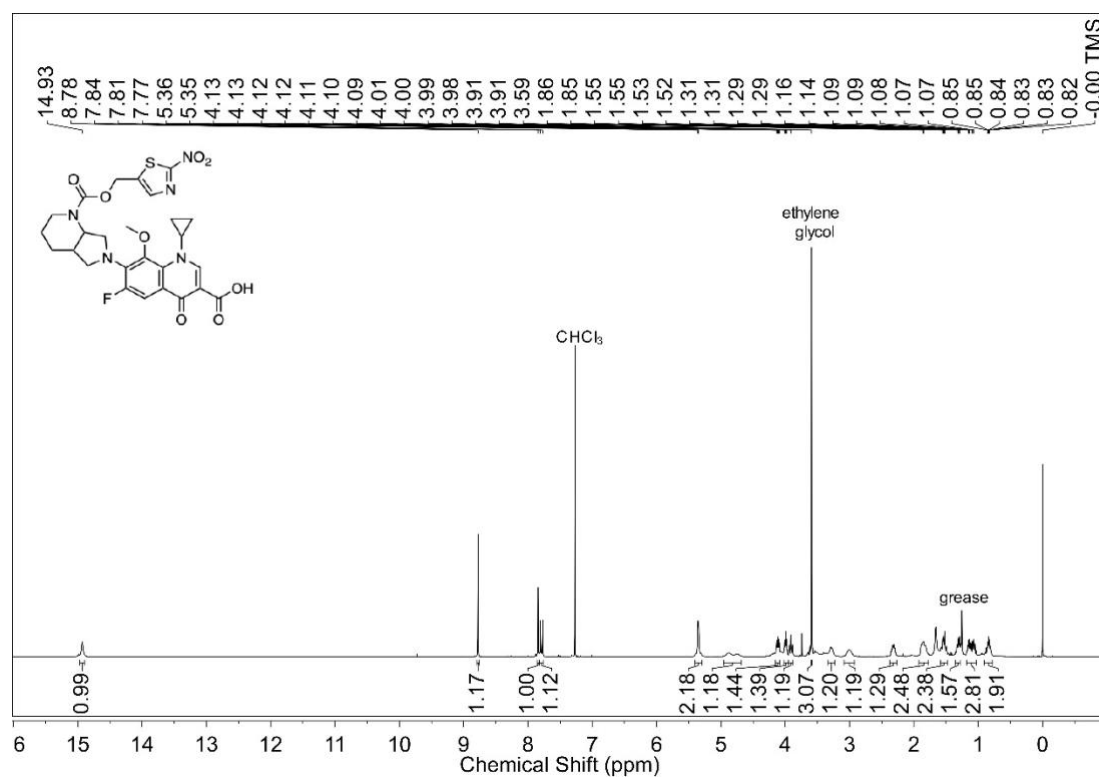
^{19}F NMR spectrum (376 MHz, $\text{DMSO-}d_6$) of **42** ^1H NMR spectrum (400 MHz, $\text{DMSO-}d_6$) of **42**

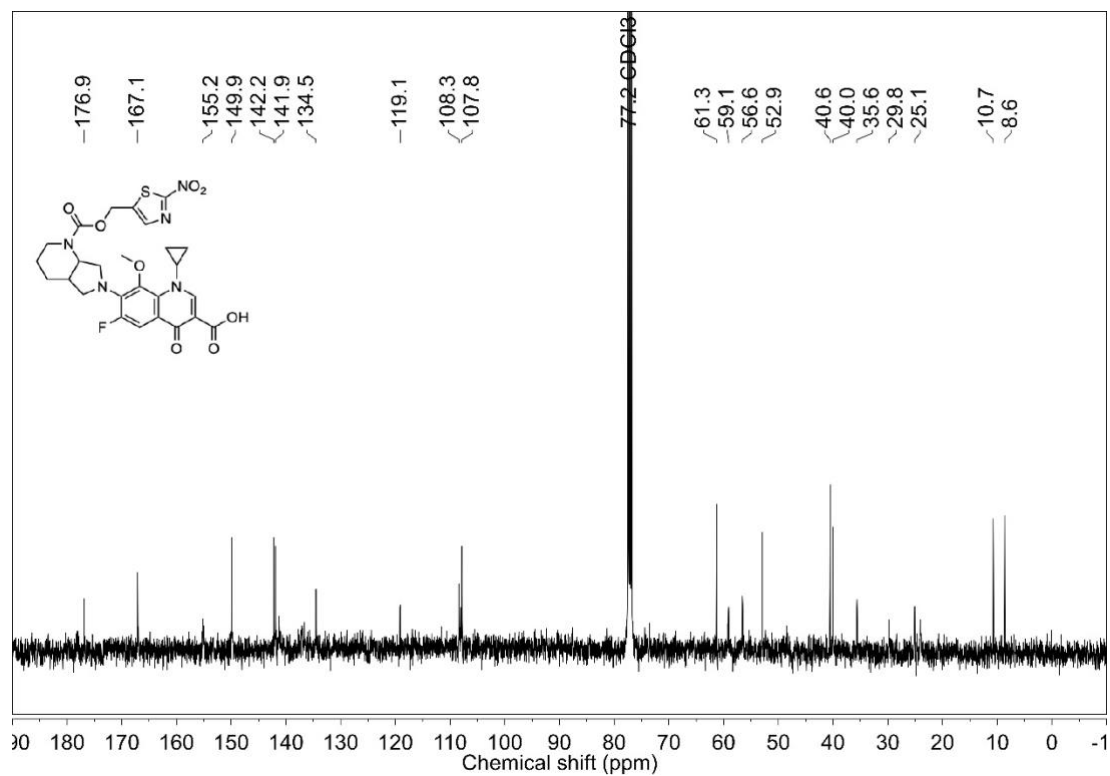
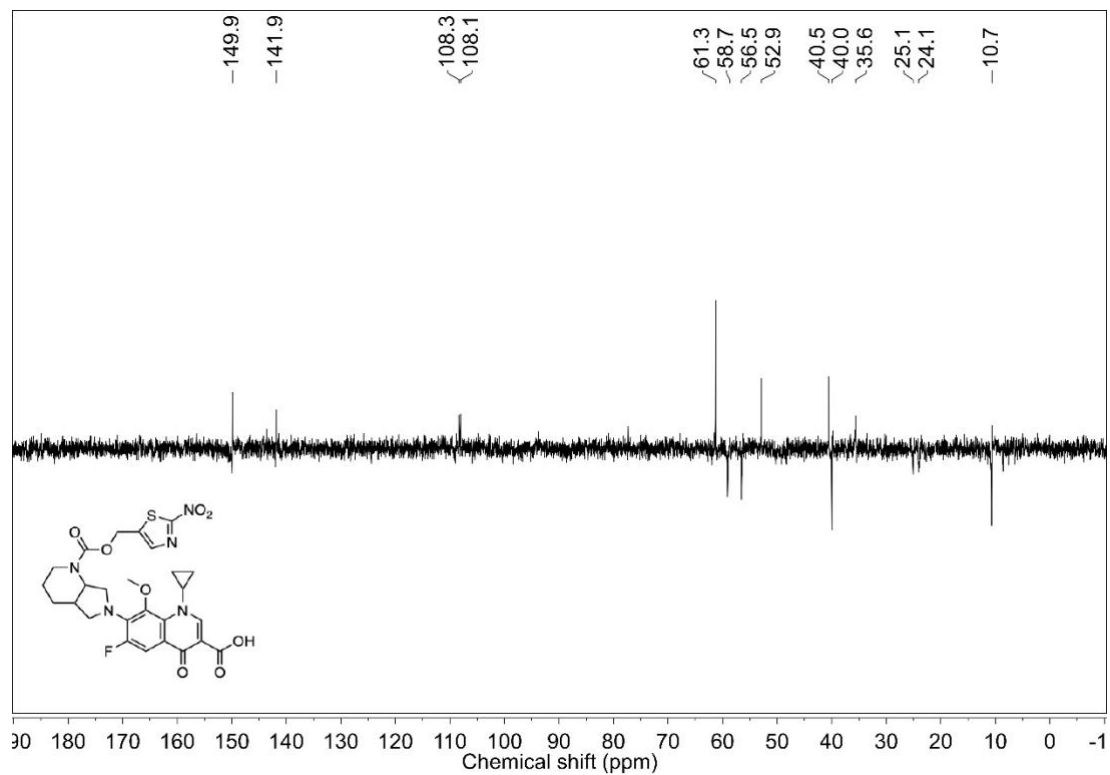
^{13}C NMR spectrum (100 MHz, $\text{DMSO-}d_6$) of **42**DEPT-135 NMR spectrum (100 MHz, $\text{DMSO-}d_6$) of **42**

^1H NMR spectrum (400 MHz, CDCl_3) of **43** ^1H NMR spectrum (400 MHz, CDCl_3) of **44**

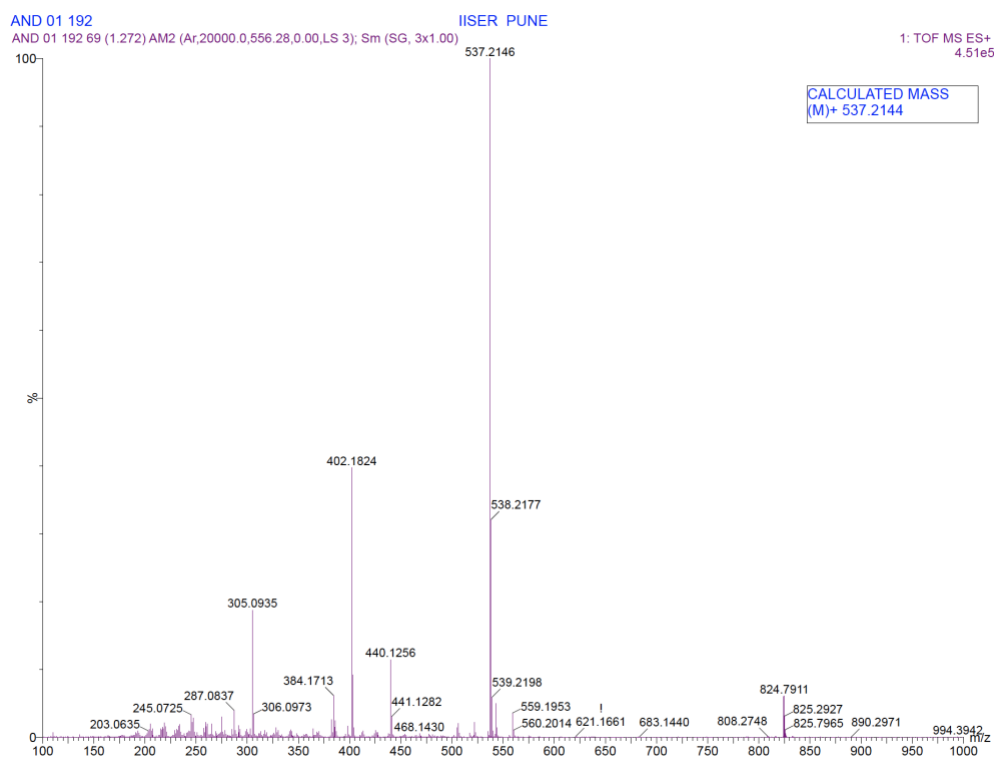
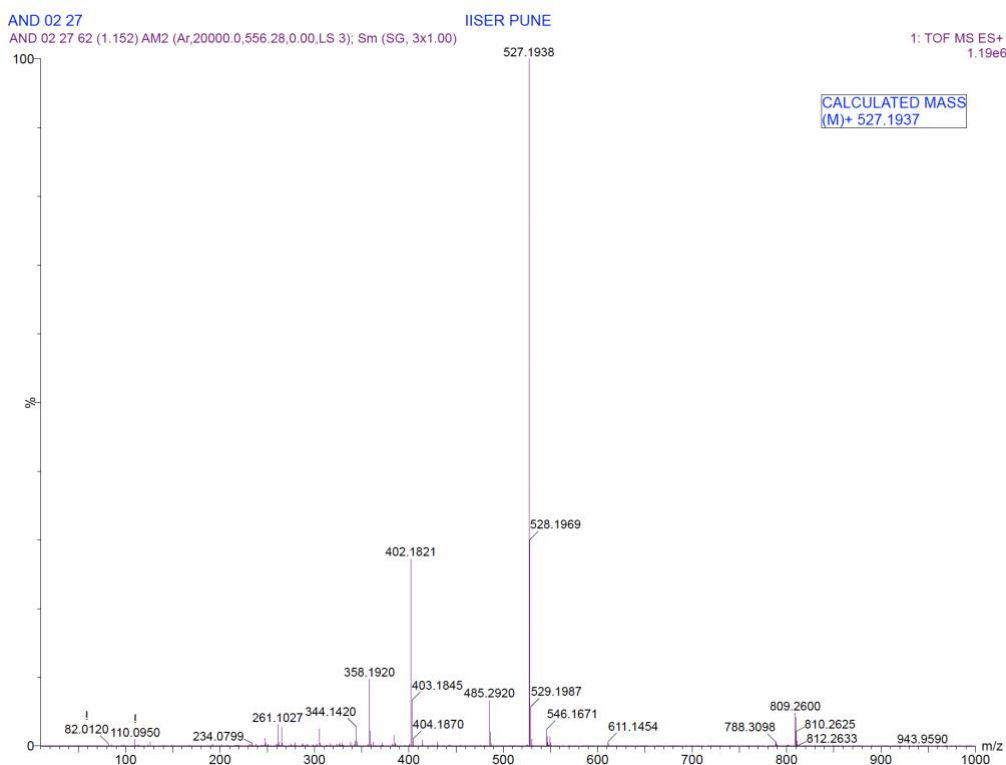
^{19}F NMR spectrum (376 MHz, CDCl_3) of **45** ^1H NMR spectrum (400 MHz, CDCl_3) of **45**

^{13}C NMR spectrum (100 MHz, CDCl_3) of **45**DEPT-135 NMR spectrum (100 MHz, CDCl_3) of **45**

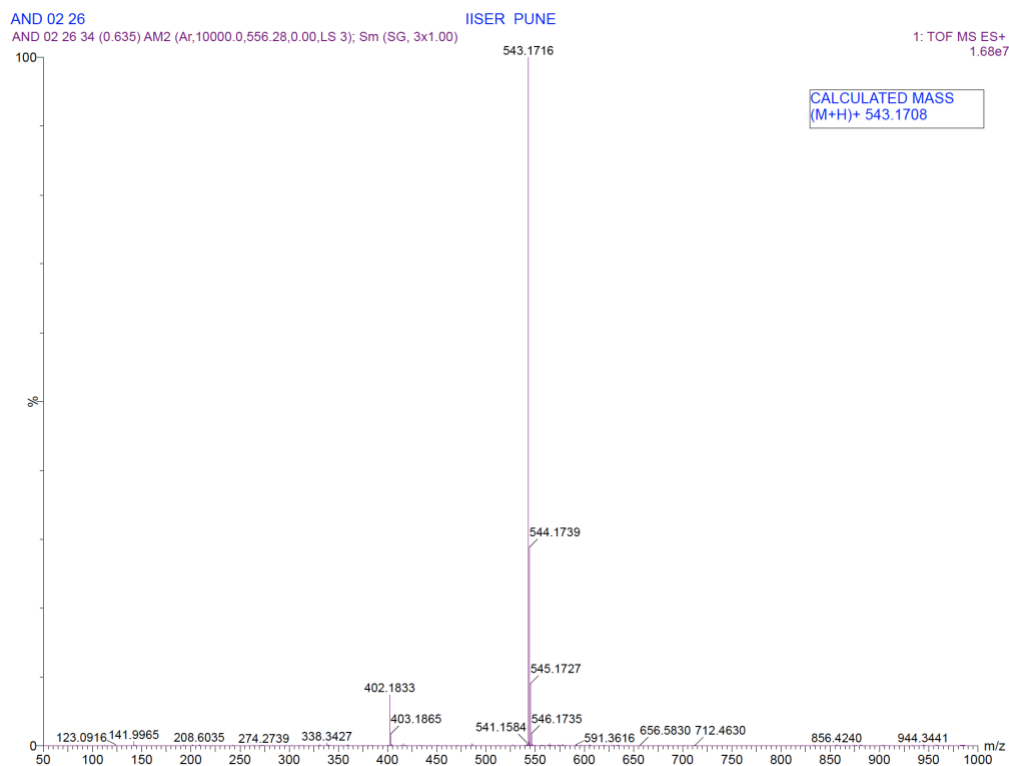
^{19}F NMR spectrum (376 MHz, CDCl_3) of **46** ^1H NMR spectrum (400 MHz, CDCl_3) of **46**

^{13}C NMR spectrum (100 MHz, CDCl_3) of **46**DEPT-135 NMR spectrum (100 MHz, CDCl_3) of **46**

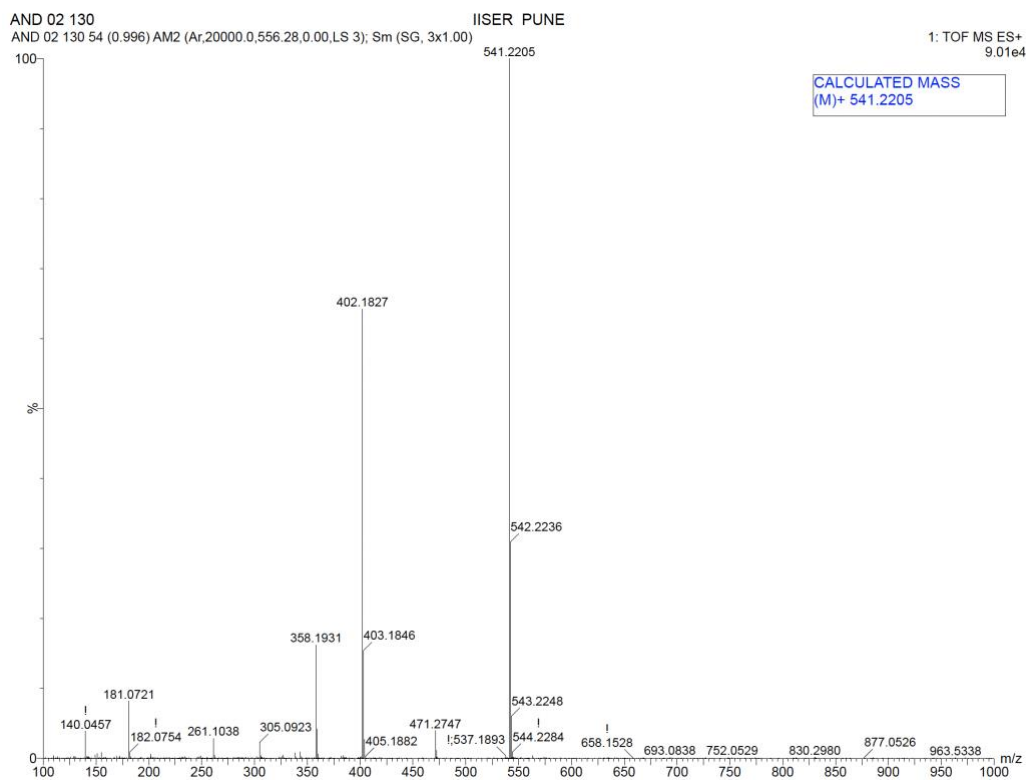
2.7. HRMS spectra of final compounds

HRMS spectrum of **33**HRMS spectrum of **34**

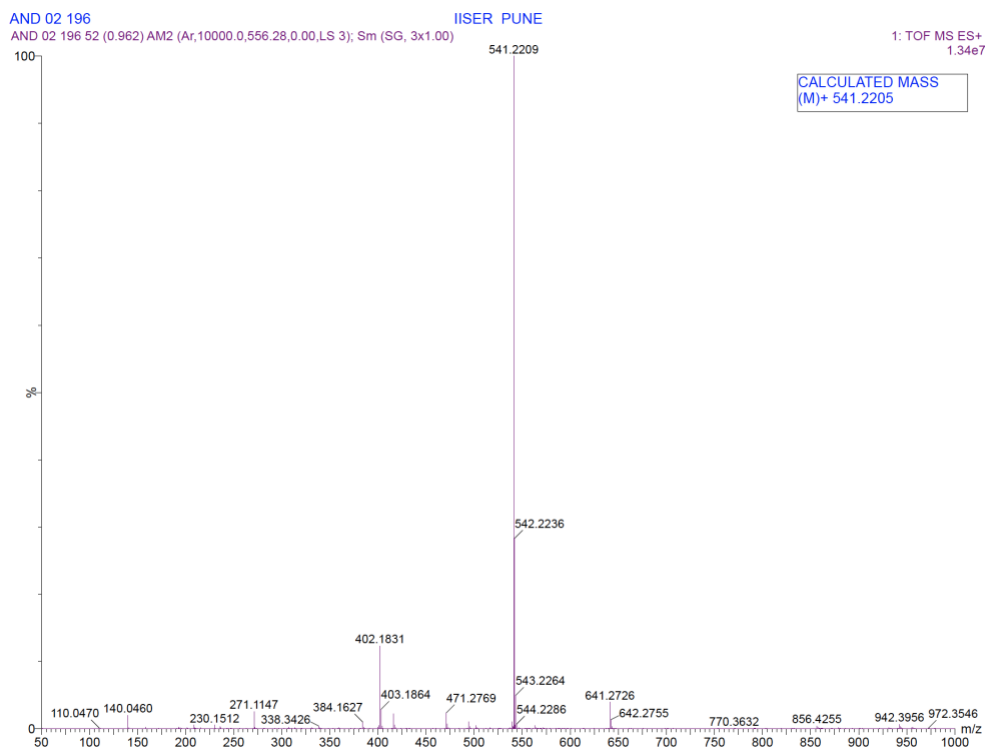
HRMS spectrum of 35



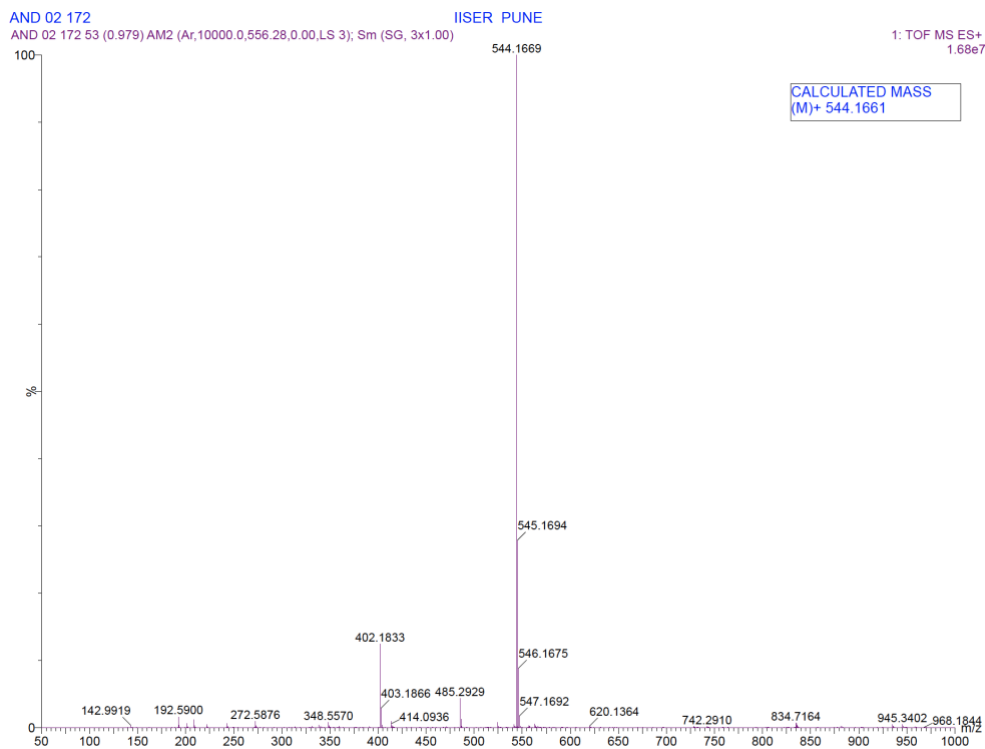
HRMS spectrum of 36



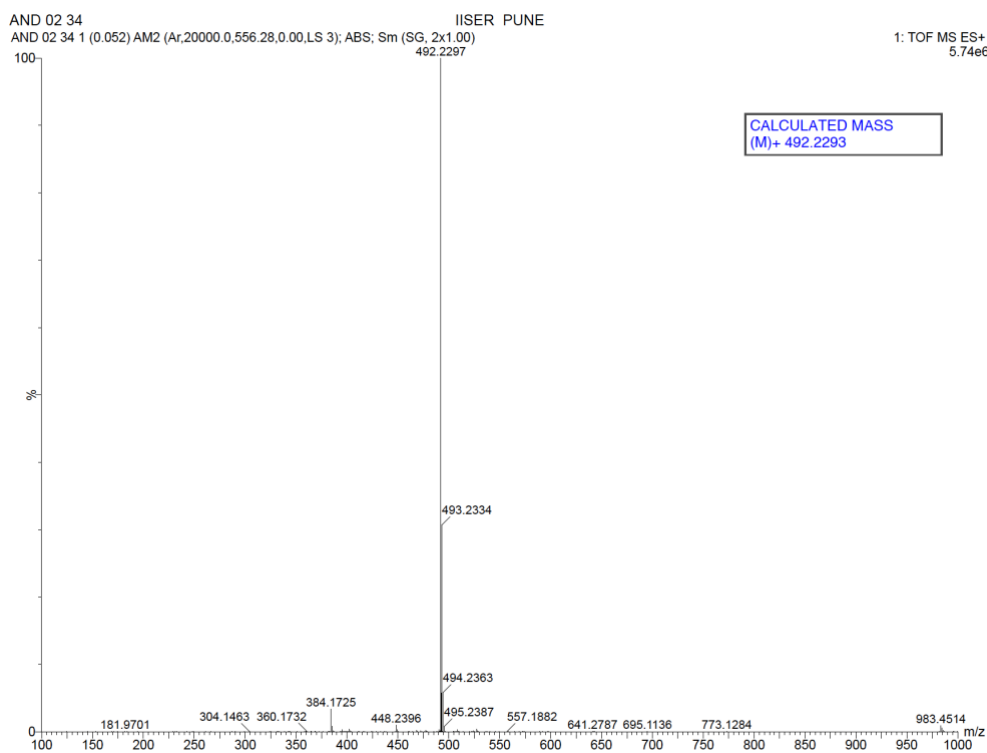
HRMS spectrum of 37



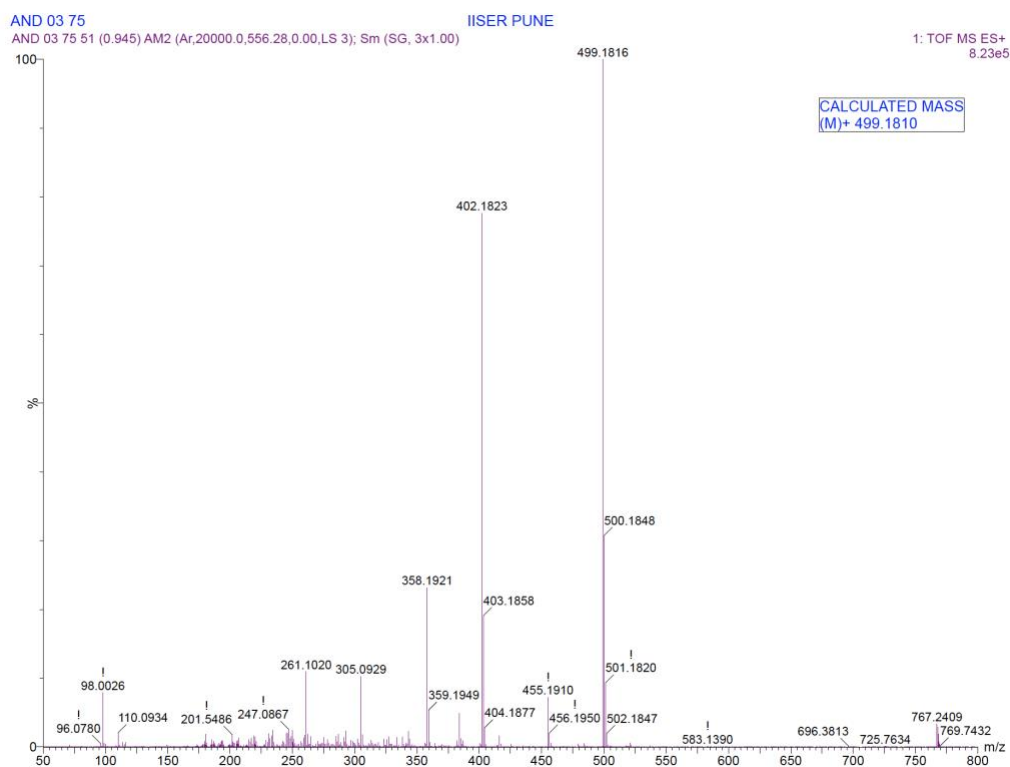
HRMS spectrum of 38



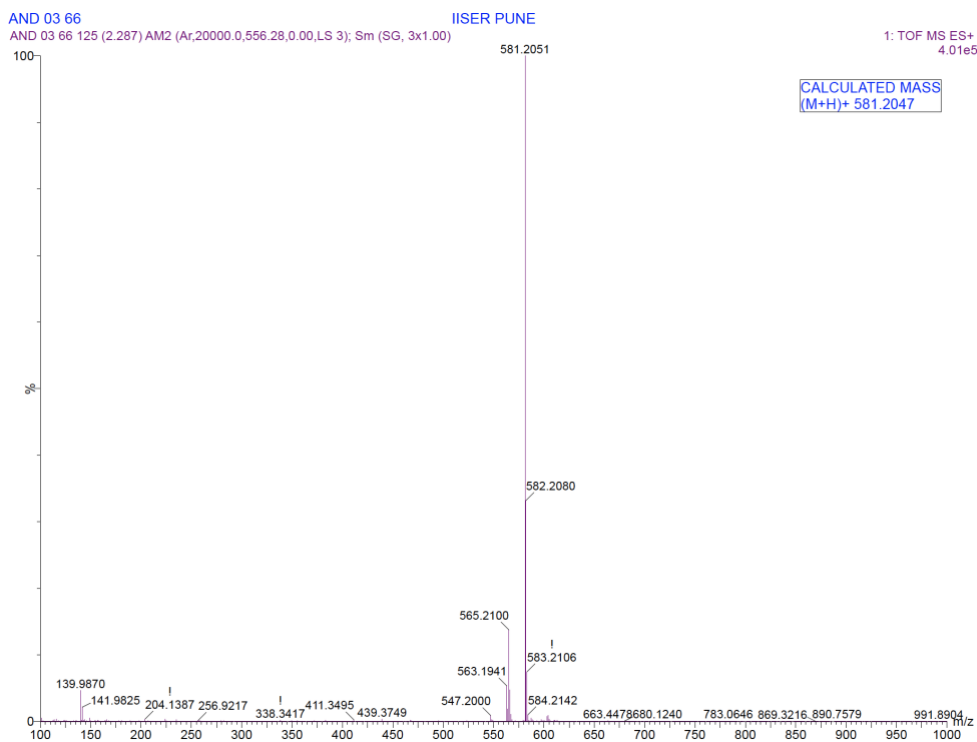
HRMS spectrum of 41



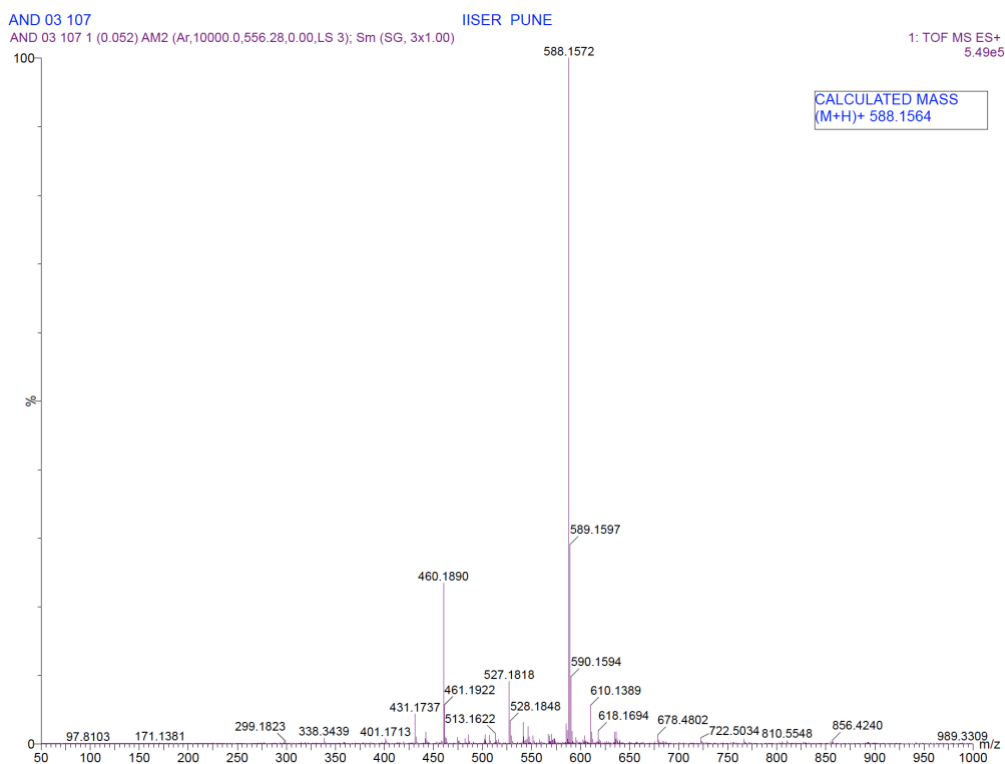
HRMS spectrum of 42



HRMS spectrum of 45



HRMS spectrum of 46



2.8. References

- (1) Sarathy, J.; Dartois, V.; Dick, T.; Gengenbacher, M. Reduced Drug Uptake in Phenotypically Resistant Nutrient-Starved Nonreplicating Mycobacterium Tuberculosis. *Antimicrob. Agents Chemother.* **2013**, *57* (4), 1648-1653.
- (2) Yuan, T.; Sampson, N. S. Hit Generation in TB Drug Discovery: From Genome to Granuloma. *Chem. Rev.* **2018**, *118* (4), 1887-1916.
- (3) Hughes, J. P.; Rees, S.; Kalindjian, S. B.; Philpott, K. L. Principles of Early Drug Discovery. *Br. J. Pharmacol.* **2011**, *162* (6), 1239-1249.
- (4) Winn, B. A.; Shi, Z.; Carlson, G. J.; Wang, Y.; Nguyen, B. L.; Kelly, E. M.; Ross, R. D.; Hamel, E.; Chaplin, D. J.; Trawick, M. L.; Pinney, K. G. Bioreductively Activatable Prodrug Conjugates of Phenstatin Designed to Target Tumor Hypoxia. *Bioorg. Med. Chem. Lett.* **2017**, *27* (3), 636-641.
- (5) Morais, E. M.; Grillo, I. B.; Stassen, H. K.; Seferin, M.; Scholten, J. D. The Effect of an Electron-Withdrawing Group in the Imidazolium Cation: The Case of Nitro-Functionalized Imidazolium Salts as Acidic Catalysts for the Acetylation of Glycerol. *New J. Chem.* **2018**, *42* (13), 10774-10783.
- (6) Samant, B. S.; Sukhthankar, M. G. Compounds Containing 2-Substituted Imidazole Ring for Treatment against Human African Trypanosomiasis. *Bioorg. Med. Chem. Lett.* **2011**, *21* (3), 1015-1018.
- (7) Chauvière, G.; Bouteille, B.; Enanga, B.; de Albuquerque, C.; Croft, S. L.; Dumas, M.; Périé, J. Synthesis and Biological Activity of Nitro Heterocycles Analogous to Megazol, a Trypanocidal Lead. *J. Med. Chem.* **2003**, *46* (3), 427-440.
- (8) Meng, F.; Bhupathi, D.; Sun, J. D.; Liu, Q.; Ahluwalia, D.; Wang, Y.; Matteucci, M. D.; Hart, C. P. Enhancement of Hypoxia-Activated Prodrug TH-302 Anti-Tumor Activity by Chk1 Inhibition. *BMC Cancer* **2015**, *15* (422) 1-17.
- (9) Jin, C.; Zhang, Q.; Lu, W. Synthesis and Biological Evaluation of Hypoxia-Activated Prodrugs of SN-38. *Eur. J. Med. Chem.* **2017**, *132*, 135-141.
- (10) O'Connor, L. J.; Cazares-Körner, C.; Saha, J.; Evans, C. N. G.; Stratford, M. R. L.; Hammond, E. M.; Conway, S. J. Design, Synthesis and Evaluation of Molecularly Targeted Hypoxia-Activated Prodrugs. *Nat. Protoc.* **2016**, *11* (4), 781-794.

-
- (11) Luo, S.; Zou, R.; Wu, J.; Landry, M. P. A Probe for the Detection of Hypoxic Cancer Cells. *ACS Sens.* **2017**, *2* (8), 1139-1145.
- (12) Cavalleri, B.; Ballotta, R.; Lancini, G. C. Synthesis of 1-Alkyl-2-Nitroimidazole-5-Carboxaldehydes. *J. Heterocycl. Chem.* **1972**, *9* (5), 979-984.
- (13) M. Matteucci; J. X. Duan; H. Jiao; J. Kaizerman; S. Ammons; M. H. Hopkins. US Patent Office, WO 2007/002931 A2, **2007**.
- (14) O'Connor, L. J.; Cazares-Körner, C.; Saha, J.; Evans, C. N. G.; Stratford, M. R. L.; Hammond, E. M.; Conway, S. J. Efficient Synthesis of 2-Nitroimidazole Derivatives and the Bioreductive Clinical Candidate Evofosfamide (TH-302). *Org. Chem. Front.* **2015**, *2* (9), 1026-1029.
- (15) Ghedira, D.; Voissière, A.; Peyrode, C.; Kraiem, J.; Gerard, Y.; Maubert, E.; Vivier, M.; Miot-Noirault, E.; Chezal, J.-M.; Farhat, F.; Weber, V. Structure-Activity Relationship Study of Hypoxia-Activated Prodrugs for Proteoglycan-Targeted Chemotherapy in Chondrosarcoma. *Eur. J. Med. Chem.* **2018**, *158*, 51-67.
- (16) Dener, J. M.; Zhang, L. H.; Rapoport, H. An Effective Chiroselective Synthesis of (+)-Pilocarpine from L-Aspartic Acid. *J. Org. Chem.* **1993**, *58* (5), 1159-1166.
- (17) Collman, J. P.; Zhong, M.; Costanzo, S.; Zhang, C. New Imidazole-Based Tripodal Ligands as CuB Site Mimics of Cytochrome c Oxidase. *J. Org. Chem.* **2001**, *66* (24), 8252-8256.
- (18) de Figueiredo, R. M.; Coudray, L.; Dubois, J. Synthesis and Biological Evaluation of Potential Bisubstrate Inhibitors of Protein Farnesyltransferase. Design and Synthesis of Functionalized Imidazoles. *Org. Biomol. Chem.* **2007**, *5* (20), 3299-3309.
- (19) Asato, G.; Berkelhammer, G.; Moon, E. L. Nitroheterocyclic Antimicrobial Agents. I. Nitrothiazolecarboxaldehyde Derivatives. *J. Med. Chem.* **1969**, *12* (3), 374-379.
- (20) Sun, Z.; Zhang, H.; Zhang, H.; Wu, J.; Gao, F.; Zhang, C.; Hu, X.; Liu, Q.; Wei, Y.; Wei, Y.; Zhuang, J.; Zhuang, J.; Huang, X. A Novel Model System for Understanding Anticancer Activity of Hypoxia-Activated Prodrugs. *Mol. Pharm.* **2020**, *17* (6), 2072-2082.
- (21) Tanaka, K. S. E.; Houghton, T. J.; Kang, T.; Dietrich, E.; Delorme, D.; Ferreira, S. S.; Caron, L.; Viens, F.; Arhin, F. F.; Sarmiento, I.; Lehoux, D.; Fadhil, I.; Laquerre, K.;

- Liu, J.; Ostiguy, V.; Poirier, H.; Moeck, G.; Parr, T. R.; Rafai Far, A. Bisphosphonated Fluoroquinolone Esters as Osteotropic Prodrugs for the Prevention of Osteomyelitis. *Bioorg. Med. Chem.* **2008**, *16* (20), 9217–9229.
- (22) Ambrus, I. J. Development of Potential Dual-Action Antibacterial Agents. Ph.D. dissertation, University of Wollongong, **2008**.
- (23) Warnecke, A.; Kratz, F. 2,4-Bis(Hydroxymethyl)Aniline as a Building Block for Oligomers with Self-Eliminating and Multiple Release Properties. *J. Org. Chem.* **2008**, *73* (4), 1546–1552.
- (24) Daina, A.; Michielin, O.; Zoete, V. SwissADME: A Free Web Tool to Evaluate Pharmacokinetics, Drug-Likeness and Medicinal Chemistry Friendliness of Small Molecules. *Sci. Rep.* **2017**, *7* (42717), 1-13.
- (25) Elgrishi, N.; Rountree, K. J.; McCarthy, B. D.; Rountree, E. S.; Eisenhart, T. T.; Dempsey, J. L. A Practical Beginner's Guide to Cyclic Voltammetry. *J. Chem. Educ.* **2018**, *95* (2), 197–206.
- (26) Shah, J.; Rasul Jan, M.; Naeem Khan, M. Micellar-Enhanced Spectrofluorometric Quantification of Moxifloxacin in Pharmaceutical Formulations, Human Urine and Plasma Samples Selective Removal of 2,4-Dichlorophenol and 2,4,6-Trichlorophenol in Aqueous Solutions by Polyaniline-Modified Magnetic Nanoparticles Using High-Performance Liquid Chromatography-UV Detection View Project Micellar-Enhanced Spectrofluorometric Quantification of Moxifloxacin in Pharmaceutical Formulations, Human Urine and Plasma Samples. *Afr. J. Pharmacy Pharmacol.* **2011**, *5* (5), 616–624.
- (27) Wang, J.; Liu, J.; Yang, Z. Recent Advances in Peptide-Based Nanomaterials for Targeting Hypoxia. *Nanoscale Adv.* **2021**, *3*, 6027–6039.
- (28) Pardeshi, K. A.; Kumar, T. A.; Ravikumar, G.; Shukla, M.; Kaul, G.; Chopra, S.; Chakrapani, H. Targeted Antibacterial Activity Guided by Bacteria-Specific Nitroreductase Catalytic Activation to Produce Ciprofloxacin. *Bioconjug. Chem.* **2019**, *30* (3), 751–759.

Chapter 3. Nitroreductase (NTR) mediated bioreductive activation of Moxifloxacin (MXF) prodrugs

3.1. Introduction

Having established that chemical reduction facilitated the release of MXF from nitroheterocyclic prodrugs in Chapter 2, we evaluated their substrate specificities towards bacterial nitroreductases (NTRs). The minor oxygen-insensitive NTR, NfsB of *E. coli* is one of the most recognized enzyme and is widely used as a model system, largely due to its potential for inducible targeted cell/tissue ablation^{1,2} and gene directed enzyme prodrug therapy (GDEPT) for cancer treatment.³⁻⁷ It has been exploited in a variety of research areas, including prodrug activation for the treatment of leishmaniasis⁸⁻¹² and cancer,¹³⁻¹⁶ development of fluorescent probes for the detection of hypoxia,¹⁷⁻³⁷ and real-time detection of bacteria.³⁸⁻⁴⁰ This enzyme has been used in delivery of several reactive species such as NO^{41,42} and H₂S using donor molecules.⁴³ Additionally, NTRs have garnered a lot of attention due to their ability to bioremediate nitrocompounds,⁴⁴⁻⁴⁷ serve as a biosensor,⁴⁸⁻⁵⁰ to enhance the efficacy of existing antibiotics as prodrug⁵¹ and reduce the incidence of resistance.⁵² A recent piece of compelling evidence suggests that the expression of NTR in *E. coli* conferred resistance to chloramphenicol antibiotic.⁵³ Furthermore, the development of aplastic anemia, a rare but serious adverse effect of chloramphenicol, has been postulated to emerge as a result of chloramphenicol nitroreduction by host-associated bacteria.^{53,54}

Biochemical screening using purified enzyme revealed that *E. coli* NfsB catalyzes the reduction of nitroaromatic and several nitroheteroaromatic compounds, including nitrofurans, nitrothiophene, and nitroimidazole groups. Previously, it has been shown that 1-methyl-2-nitroimidazole was the optimal substrate *in vitro* using a panel of fluorophore masked ethers and carbamates respectively.^{28,29} This group was utilized as a favorable prodrug moiety for NTR-mediated release of lysine-specific demethylase 1 (LSD1) inhibitor.⁵⁵ Furthermore, 1-methyl-2-nitroimidazole was found to be an efficient NTR-labile modular uncaging moiety for cyclopropane-tetrazine ligation.⁵⁶

Despite the wide popularity of the 1-methyl-2-nitroimidazole bioreductive group, the efficiency of NTRs in bioactivation of structurally resembling nonimidazole five-membered nitroheterocycles, such as nitrooxazole and nitrothiazole has not yet been systematically studied. Owing to the fact that 5-nitrothiazole core conferred antiparasitic,^{52,57,58} antibacterial^{59,60} and antimycobacterial activity,⁶¹⁻⁶³ there has been a resurgence in interest in the

application of nitrothiazole prodrugs. The reduction of the nitro group by bacterial NTR is a prerequisite for the mutagenic activity of these prodrugs.^{44,64} Halicin, a 5-nitrothiazole antibiotic, has been identified as a powerful, broad-spectrum bactericidal antibiotic using a ground-breaking machine-learning approach. Despite the fact that halicin is not a substrate for *E. coli* NfsA or NfsB, the antibiotic showed antibacterial activity by inducing the expression of iron acquisition genes and dissipating cytoplasmic transmembrane potential.⁶⁵

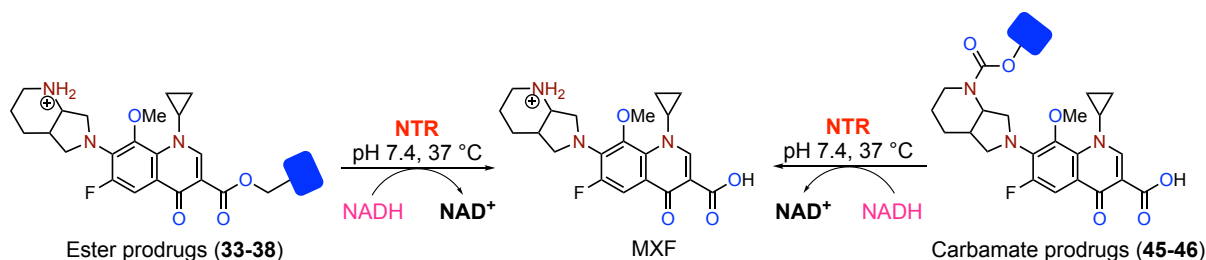
Recently, the 2-nitrothiazolyl moiety was used as a bioreductive trigger and has garnered significant attention in the development of hypoxia-activated prodrugs (HAPs) to specifically target hypoxic tumors.⁶⁶ Nevertheless, to date, 2-nitrothiazoles have not been reported as a substrate for bacterial NTR, including *E. coli* and mycobacterial NTR. In light of this, attempts were made in this chapter to broaden the range of substrates for bacterial NTRs and identify a novel substrate with a profile resembling that of the exquisitely selective nitroaryl substrate, 1-methyl-2-nitroimidazolyl group.

3.2. Results and discussion

3.2.1. Enzymatic nitroreduction of prodrugs and evaluation of release of MXF

First, we tested the feasibility of the *E. coli* NTR-mediated decomposition of prodrugs by measuring the change in fluorescence corresponding to the formation of MXF (Scheme 3.1). The prodrugs (10 μM) were intrinsically less fluorescent in the absence of NTR, supporting the notion that they are stable in buffer. However, the prodrugs elicited a pronounced enhancement in fluorescence to varied degrees after 1 h of incubation with the lowest concentration of *E. coli* NTR (15 nM) under the same conditions (pH 7.4, 37 $^{\circ}\text{C}$). Owing to the higher reactivity than nitrobenzyl tethered prodrug **33**, it was expected that nitrothiophene prodrug **35** would result in enhanced fluorescence signal. Interestingly, the 2-nitrothiazole prodrugs **38** and **46** also displayed the highest increase in fluorescence response similar to **35**. These results were in line with the results of the chemoreductive study (Figure 3.1).

Scheme 3.1. Proposed strategy for NTR-dependent bioactivation of prodrugs



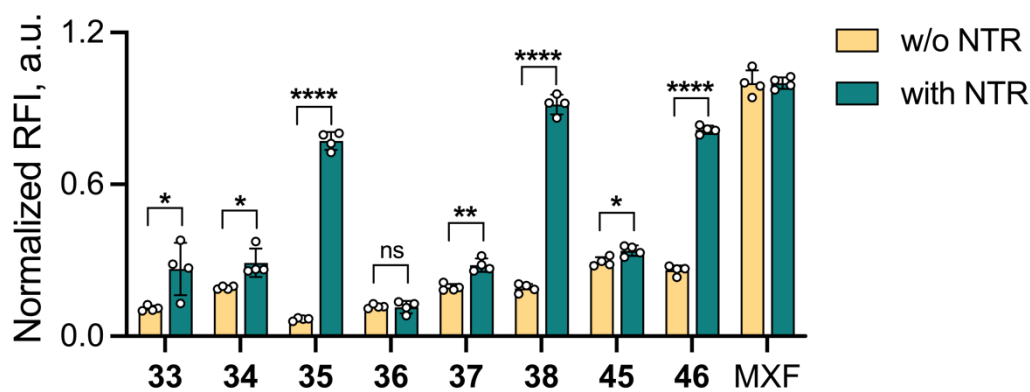


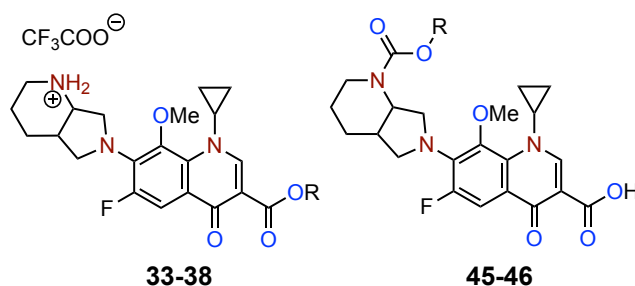
Figure 3.1. Monitoring the *E. coli* NTR mediated bio-reductive activation of prodrugs by fluorescence ($\lambda_{\text{ex}} = 289$ nm and $\lambda_{\text{em}} = 488$ nm) after 1 h of incubation with *E. coli* NTR (15 nM) and NADH (100 μM) in pH 7.4 phosphate buffer (10 mM) at 37 $^{\circ}\text{C}$. All the data represent mean \pm SD from three independent experiments performed in triplicate. p values were determined using the student's two-tailed unpaired parametric t -test relative to the NTR untreated control. (* $p < 0.05$, ** $p \leq 0.01$, **** $p \leq 0.001$ and ns indicate not significant).

3.2.2. Kinetics of *E. coli* NTR dependent reductive activation of MXF prodrugs

To gain a better understanding of the differences in the rate of *E. coli* NTR catalyzed nitro-reduction of various prodrugs, reaction progress curves were generated by using a fixed concentration of enzyme (15 nM) and NADH (100 μM) with a broad range of substrate concentrations and the fluorescence response was measured as a function of time (Figure 3.2). We chose a lowest concentration of enzyme adequate enough to catalyse a reaction and differentiate the fluorescence response among the substrates during an enzymatic reaction. Initial reaction rates were obtained from the linear portion of the experimental progress curves (Table 3.1), fitted to the Michaelis-Menten equation, and plotted as a function of initial substrate concentration in order to provide kinetic parameters (Table 3.2).

Table 3.1. Estimation of linearity from the reaction progress curves of NTR-MXF prodrugs

| Prodrug | 33 | 34 | 35 | 36 | 37 | 38 | 45 | 46 |
|----------------------|------|-----|-----|-----|-----|-------|--------|-------|
| Linear portion (min) | 0-12 | 0-2 | 0-2 | 0-7 | 0-6 | 0-0.3 | 0-12.5 | 0-0.3 |

Table 3.2. Comparative analysis of kinetic parameters of NTR-MXF prodrugs

| Entry | Prodrug | R | Initial rate V ($\mu\text{M min}^{-1}$) | k_{cat} (min^{-1}) | K_{m} (μM) | $k_{\text{cat}}/K_{\text{m}}$ ($\mu\text{M}^{-1} \text{min}^{-1}$) | Relative rate* |
|--|-----------|---|--|---|----------------------------------|---|-------------------|
| 4-nitrophenyl | | | | | | | |
| 1 | 33 | | 0.15 ± 0.005 | 10.0 | 7.28 ± 0.75 | 1.37 | 1.9 |
| 5-membered heterocycles with one heteroatom | | | | | | | |
| 2 | 34 | | 0.54 ± 0.056 | 36.6 | 5.98 ± 1.59 | 6.11 | 6.8 |
| 3 | 35 | | 0.77 ± 0.016 | 51.6 | 5.08 ± 0.39 | 10.16 | 10 |
| 5-membered heterocycles with two heteroatoms | | | | | | | |
| 4 | 36 | | 0.07 ± 0.005 | 4.90 | 9.57 ± 1.57 | 0.51 | 0.9 |
| 5 | 37 | | 0.08 ± 0.003 | 5.85 | 9.59 ± 0.87 | 0.61 | 1 |
| 6 | 38 | | 7.41 ± 0.98 | 494.3 | 19.81 ± 5.18 | 24.95 | 93 |
| Carbamates | | | | | | | |
| 7 | 45 | | 0.045 ± 0.002 | 3.05 | 6.66 ± 0.93 | 0.45 | 0.6 |
| 8 | 46 | | 3.28 ± 1.14 | 218.9 | 22.5 ± 14.95 | 9.72 | 41 |

*Initial rates were recorded relative to the rate of NTR-catalyzed nitro-reduction for **37** under the defined conditions

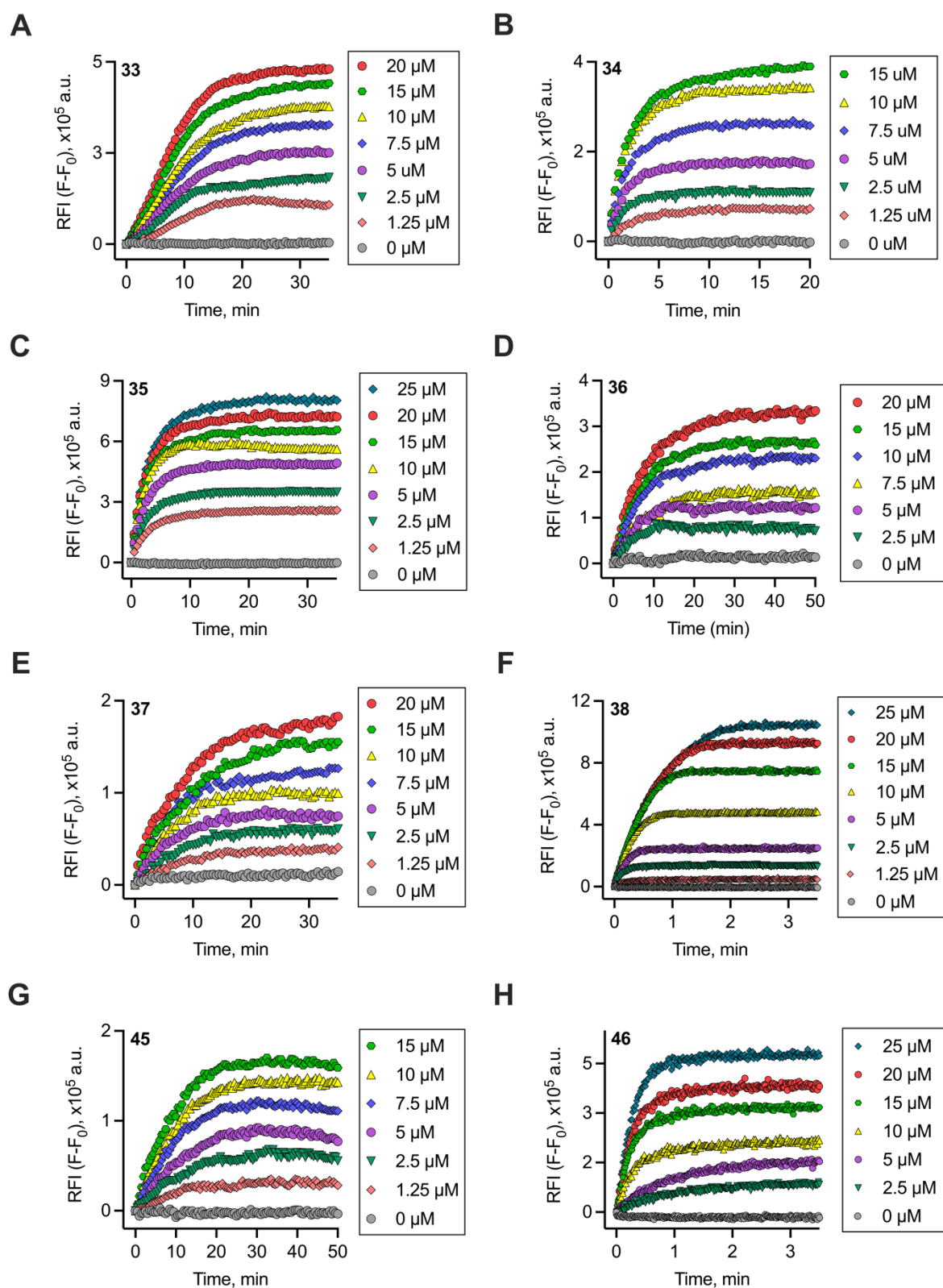


Figure 3.2. Representative reaction progress curves obtained by monitoring the release of MXF ($\lambda_{\text{ex}} = 289 \text{ nm}$ and $\lambda_{\text{em}} = 488 \text{ nm}$) as a function of time from (A) **33**, (B) **34**, (C) **35**, (D) **36**, (E) **37**, (F) **38**, (G) **45** and (H) **46** using a fluorescence-based assay. The reactions were performed with a broad range of substrate concentrations (reported on the right of each curve) in the presence of NADH (100 μM) and a fixed concentration

of *E. coli* NTR (15 nM) in phosphate buffer (pH 7.4, 10 mM). The kinetic experiments were performed at either 37 °C (for **33-37** and **45**) or 25 °C (for **38** and **46**).

Kinetic analysis revealed that nitrobenzyl prodrugs **33** and **45** were least preferred by *E. coli* NTR over 5-membered nitro-heterocyclic prodrugs containing one heteroatom, **34** and **35**, and these results were in good agreement with the earlier findings.^{28,29,55} Despite having higher onset reduction potential, 5-nitrothiophenyl MXF ester prodrug ($E^\circ = -0.88$ V) exhibited higher k_{cat} and k_{cat}/K_m values than 5-nitrofuranyl prodrug ($E^\circ = -0.81$ V) (Figure 3.3; Table 3.2, entries 1-3 and 7).

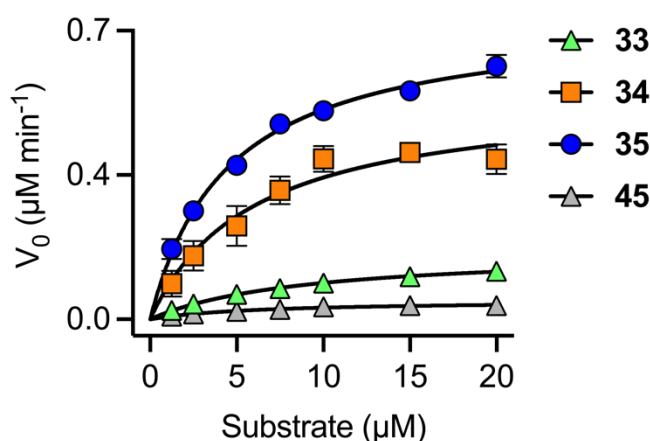


Figure 3.3. Michaelis-Menten analyses demonstrating the nitroreduction of prodrugs by *E. coli* NTR. Values are averages ($n = 3$, mean \pm SD).

A closer inspection of the Michaelis-Menten kinetic curves in Figure 3.4.A leads to two significant observations upon substitution of 4-nitrophenyl moiety with a 5-membered nitroimidazolyl group. First, the 2-nitroimidazole MXF ester prodrug **37** was least preferred by *E. coli* NTR over other prodrugs, including the nitrobenzyl derivative **33**. This result is not in agreement with earlier studies, albeit with a different leaving group.^{28,29,55,56} Second, prodrugs **36** and **37** were activated by NTR to a similar extent and showed lower k_{cat}/K_m values, despite **36** being less reactive than **37** (Figure 3.4.A; Table 3.2, entries 1, 4, and 5, respectively). We reckoned that the differential substrate specificities could be due to the accessibility of the prodrug to the active site of NTR, steric hinderance with the bound FMN or active site residues, nature of the leaving group, and ease of enzyme mediated nitroreduction. Surprisingly, 2-nitrothiazole prodrugs **38** and **46** were found to be the most favored active substrates for *E. coli* NTR *in vitro*, as evidenced by their higher V_{max} and catalytic efficiency values. The higher k_{cat}/K_m values of $24.95 \mu\text{M}^{-1}\text{min}^{-1}$ and $9.72 \mu\text{M}^{-1}\text{min}^{-1}$ for **38** and **46**, respectively, which

were 93- and 41- fold more efficient than **37** with a k_{cat}/K_m of $0.61 \mu\text{M}^{-1}\text{min}^{-1}$, clearly demonstrate that *E. coli* NTR had the highest catalytic efficiency for 2-nitrothiazole prodrugs (Figure 3.4.B; Table 3.2, entries 6 and 8, respectively).

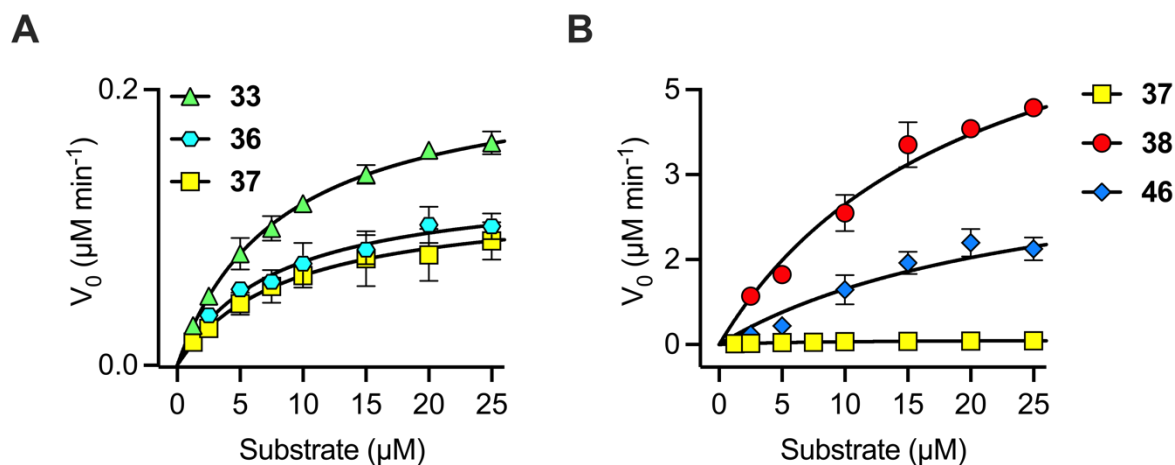


Figure 3.4. Michaelis-Menten analyses showing the nitroreduction of (A) nitrobenzyl versus nitroimidazolyl and (B) 2-nitroimidazolyl versus 2-nitrothiazolyl prodrugs by *E. coli* NTR. Values are averages ($n = 3$, mean \pm SD).

Encouraged by the distinct specificities of **37** and **38** towards NTR, we then examined the degree of enzyme-dependent cleavage of these ester-based prodrugs with varied concentrations of NTR ranging from 1.875 to 60 nM. Fluorescence studies indicated that prodrug **37** responded to NTR far more slowly than was predicted. The reaction reached the fluorescence plateau after 10 min, although it was still only partially complete, even with a higher concentration (60 nM) of NTR (Figure 3.5. A-C). On the other hand, lower concentrations (3.75 to 15 nM) of NTR promoted an instantaneous and complete reduction of **38** to MXF at 25 °C and 37 °C, allowing the reaction progress curves to plateau within a minute, even at 25 °C (Figure 3.5. A, D and E). These results collectively demonstrated that 2-nitrothiazolyl MXF prodrugs were the superior substrates for *E. coli* NTR among the analogues tested as evident by greater sensitivity and quick response kinetics for NTR.

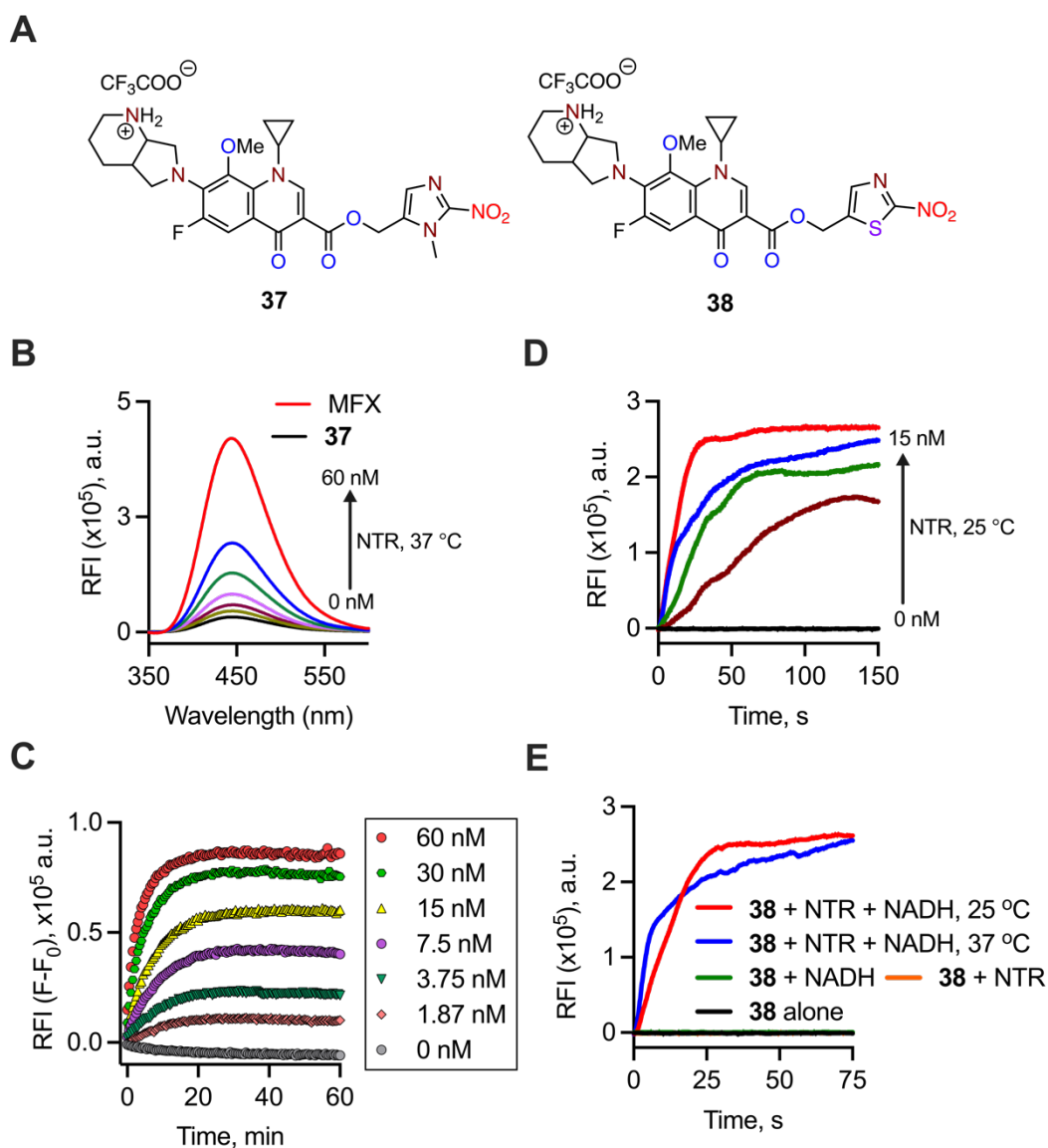


Figure 3.5. Comparative NTR-dependent fluorescence response of **37** and **38**. (A) Structures of **37** and **38**. (B) Emission spectra of MXF recorded post-incubation of **37** (10 μM) for 30 min with various concentrations of NTR (0, 3.75, 7.5, 15, 30 and 60 nM) in the presence of NADH (100 μM) in phosphate buffer (10 mM, pH 7.4) at 37 °C. (C) Representative reaction progress curves were obtained by monitoring the release of MXF as a function of time from **37** using a fluorescence-based assay. (D) Time-dependent fluorimetric analysis of reaction mixtures containing **38** with or without NTR at different concentrations (0, 1.875, 3.75, 7.5 and 15 nM) in the presence of NADH (100 μM) in phosphate buffer (pH 7.4, 10 mM) at 25 °C for 150 s. (E) Time-dependent fluorimetric analysis of reaction mixtures containing **38** with a fixed concentration of NTR (15 nM) at 25 °C and 37 °C in the presence of NADH (100 μM). The generation of MXF in the reaction mixtures were monitored at $\lambda_{\text{ex}} = 289 \text{ nm}$ and $\lambda_{\text{em}} = 488 \text{ nm}$. The data was smoothed using second order with twenty neighboring points in GraphPad Prism 9.

3.2.3. Assessment of bioreduction of prodrugs

To more thoroughly investigate the release of MXF from prodrugs upon enzymatic nitro-reduction, fluorescence spectral characteristics were examined in the presence and absence of NTR. As seen in (Figure 3.6.A-C), the prodrugs showed almost no fluorescence, whereas treatment with NTR after 15 min resulted in a prominent increase in fluorescence intensity, indicating the release of MXF. Consistent with the *in vitro* enzyme kinetic findings, prodrugs **38** and **46** showed a prominent fluorescence emission peak centered at 488 nm ($\lambda_{\text{ex}} = 289$ nm) corresponding to MXF. Furthermore, the fluorescence responses of **38** and **46** were respectively 11-fold and 7.5-fold higher than those of the prodrug tethered with the 2-nitroimidazole functional group, **37** (4.8 fold). To unequivocally confirm the generation of MXF and identify the specific reaction products formed upon incubation of prodrugs with NTR, LC-MS analysis was performed.

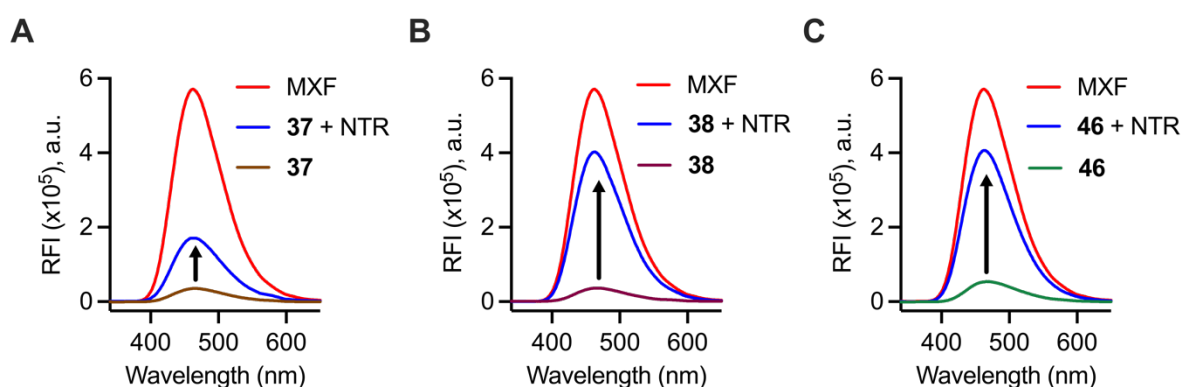


Figure 3.6. Fluorescence spectra before and after incubation of prodrugs (A) **37** (10 μM), (B) **38** (10 μM) and (C) **46** (10 μM) with *E. coli* NTR (15 nM) in the presence of NADH (100 μM) in PB (pH 7.4, 10 mM) at 37 $^{\circ}\text{C}$. A pronounced enhancement in fluorescence attributable to the generation of MXF ($\lambda_{\text{ex}} = 289$ nm and $\lambda_{\text{em}} = 488$ nm) was observed from 2-nitrothiazole prodrugs when compared to **37**.

Prior to LC-MS analysis, the stability of prodrugs was initially evaluated under buffered conditions using HPLC. The prodrugs **38** and **46** alone remained stable during incubation in buffer for 2 h at 37 $^{\circ}\text{C}$ (Figure 3.7).

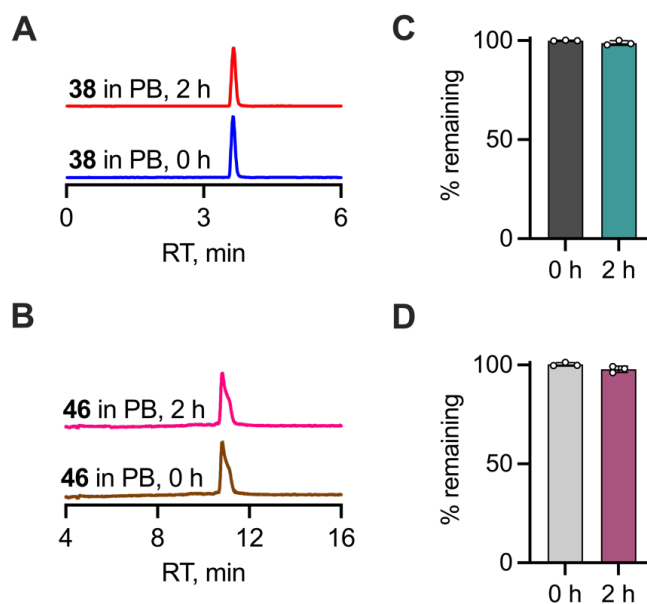


Figure 3.7. Stability of 2-nitrothiazole prodrugs in buffer. HPLC traces of stability of (A) **38** and (B) **46** in pH 7.4 buffer (10 mM) at 37 °C. Area under the curve corresponding to (C) **38** at 3.6 min and (D) **46** at 10.8 min remaining in buffer after 2 h of incubation (absorbance 280 nm).

The enzymatic activation of prodrugs **38** (10 μ M) and **46** (10 μ M) was next carried out with a fixed concentration of enzyme (*E. coli*; 15 nM) and cofactor (NADH; 100 μ M). The prodrugs were incubated with NTR at 37 °C. After 30 min of incubation, the reaction mixtures were analyzed using LC-MS. The prodrugs underwent bioreduction as anticipated, followed by fragmentation to liberate MXF. In line with expectations, the peak corresponding to **38** (expected, $[M+H]^+ = 544.1661$; observed, $[M+H]^+ = 544.1664$) at 11.7 min completely disappeared after being treated with NTR and NADH, demonstrating that the prodrug was, in fact, entirely consumed in the reaction. This was followed by the appearance of a second peak at 9.3 min in almost quantitative yield with a characteristic LC-MS feature like that of MXF (expected, $[M+H]^+ = 402.1824$; observed, $[M+H]^+ = 402.1826$) (Figure 3.8.A).

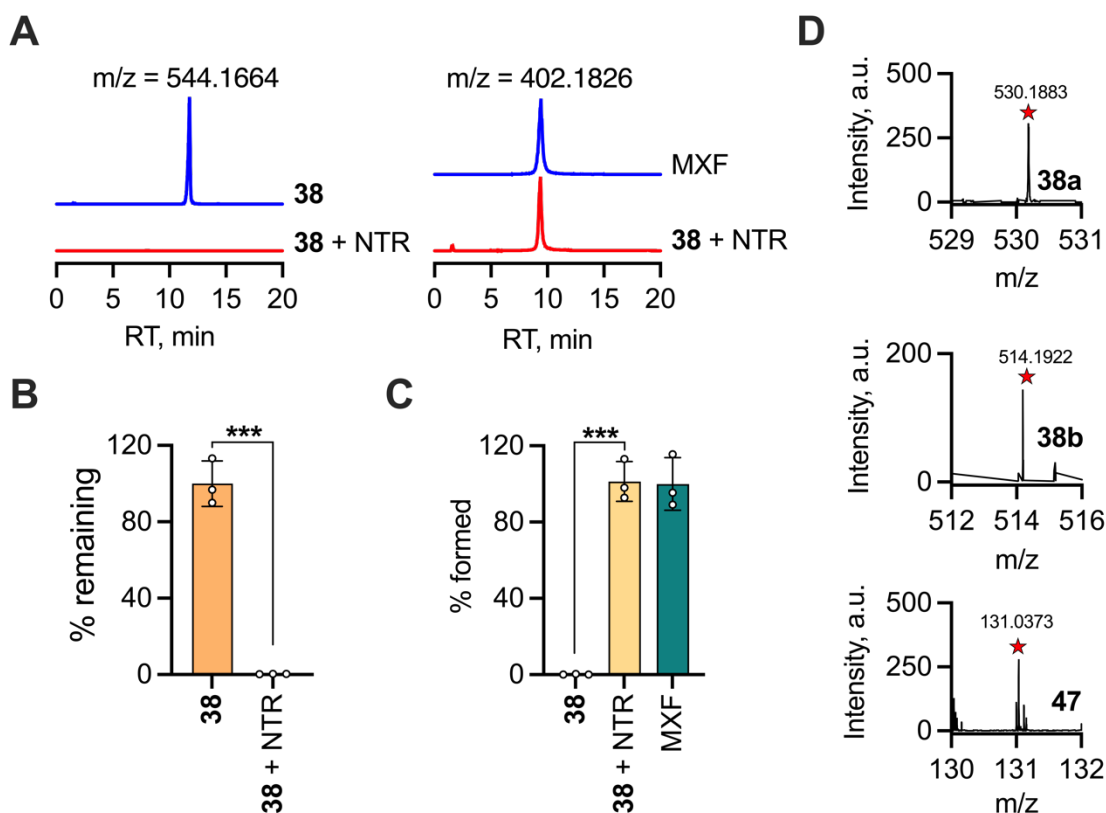


Figure 3.8. *E. coli* NTR mediated nitro-reduction of **38** resulted in the release of MXF. (A) LC/MS analysis showing the disappearance of **38** (left panel) and formation of MXF (right panel). Representative extracted ion chromatograms (EIC) are shown. (B-C) Area under the curve (AUC) for the peaks corresponding to (B) disappearance of **38** and (C) formation of MXF. Ctrl represents enzyme alone. All data presented as means \pm SD of peak areas for extracted ion chromatograms from triplicate experiments. p value was determined by unpaired two-tailed student's t -test analyzed relative to **38** alone. (***, $p \leq 0.001$). (D) Positive-ion-mode mass spectrum of the protonated singly charged $[M+1]^+$ molecular ion of the reaction products **38a** (top), **38b** (middle), and **47** (bottom) formed in the enzymatic reaction of **38** with *E. coli* NTR.

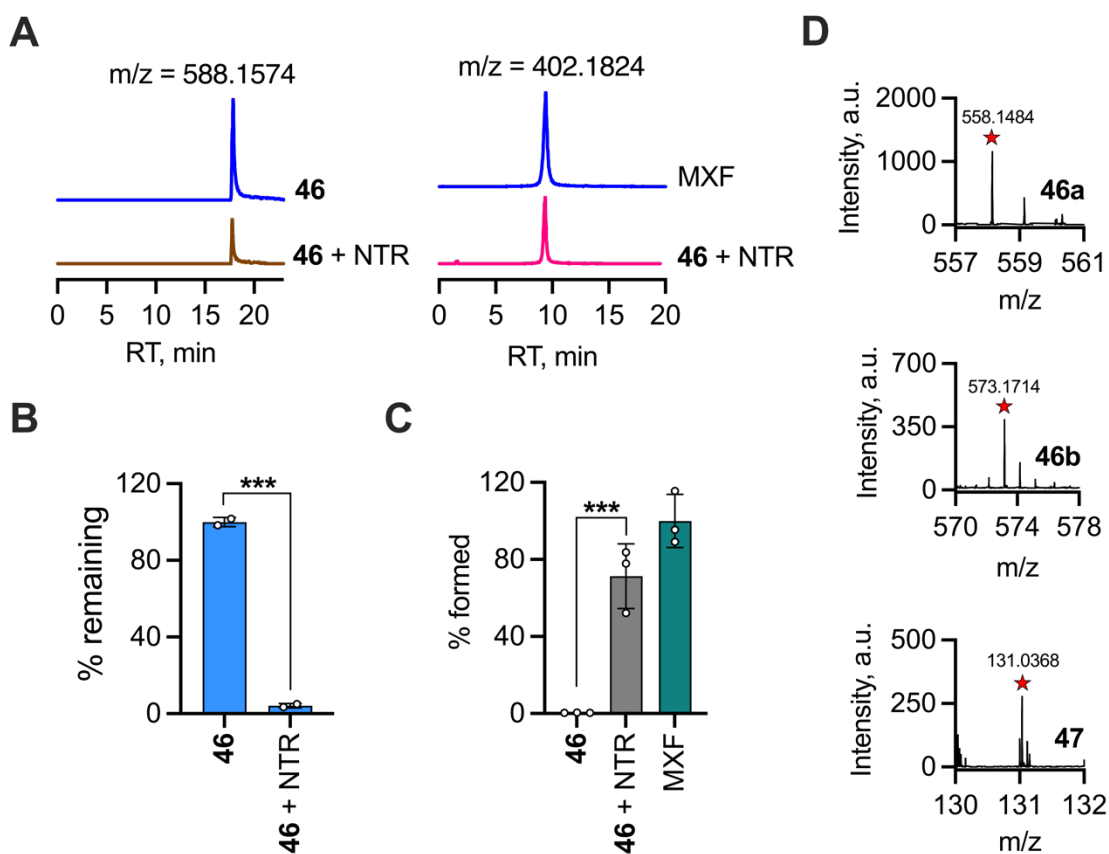


Figure 3.9. *E. coli* NTR mediated nitro-reduction of **46** resulted in the release of MXF. (A) LC/MS analysis showing the disappearance of **46** (left panel) and formation of MXF (right panel). Representative extracted ion chromatograms (EIC) are shown. (B-C) Area under the curve (AUC) for the peaks corresponding to (B) disappearance of **46** and (C) formation of MXF. Ctrl represents enzyme alone. All data presented as means \pm SD of peak areas for extracted ion chromatograms from duplicate experiments. *p* value was determined by unpaired two-tailed student's *t*-test analyzed relative to **46** alone. (***, *p* \leq 0.001). (D) Positive-ion-mode mass spectrum of the protonated singly charged $[M+1]^+$ molecular ion of the reaction products **46a** (top), **46b** (middle), and **47** (bottom) formed in the enzymatic reaction of **46** with *E. coli* NTR.

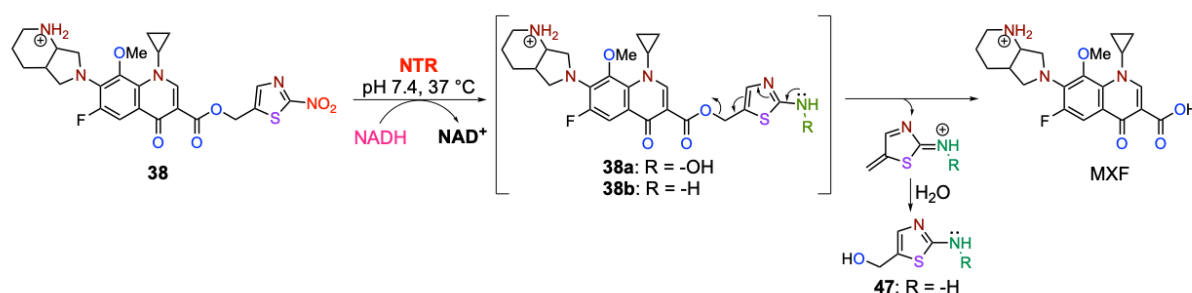
Moreover, LC-MS analysis revealed a good correlation between the consumption of **38** and the formation of MXF during the enzymatic reaction (Figure 3.8.B-C). Mass peaks corresponding to the hydroxylamino (**38a**, *m/z* 530.18) and amino (**38b**, *m/z* 514.19) intermediates formed during the enzymatic reduction of **38** were detected at very low intensities (Figure 3.8.D). A similar observation was made in the case of **46** (Figure 3.9.A-D). The prodrug was readily converted to MXF upon treatment with NTR and NADH after 30 min of incubation. The consumption of prodrug **46** (96%) and the generation of MXF (71%), however, showed a discernible difference (Figure 3.9.B-C). This incongruity could most likely be attributable to

the nature of leaving group (carboxylic acid in case of **38** and a secondary amine in case of **46**) and the degree of fragmentation of intermediates. During the enzymatic biotransformation of the ester and carbamate prodrugs of MXF, the final byproduct 2-aminothiazolylmethanol (**47**, m/z 131.03) was found to be a common intermediate (Figure 3.8.D and 3.9.D; *bottom panel*).

3.2.4. Mechanism

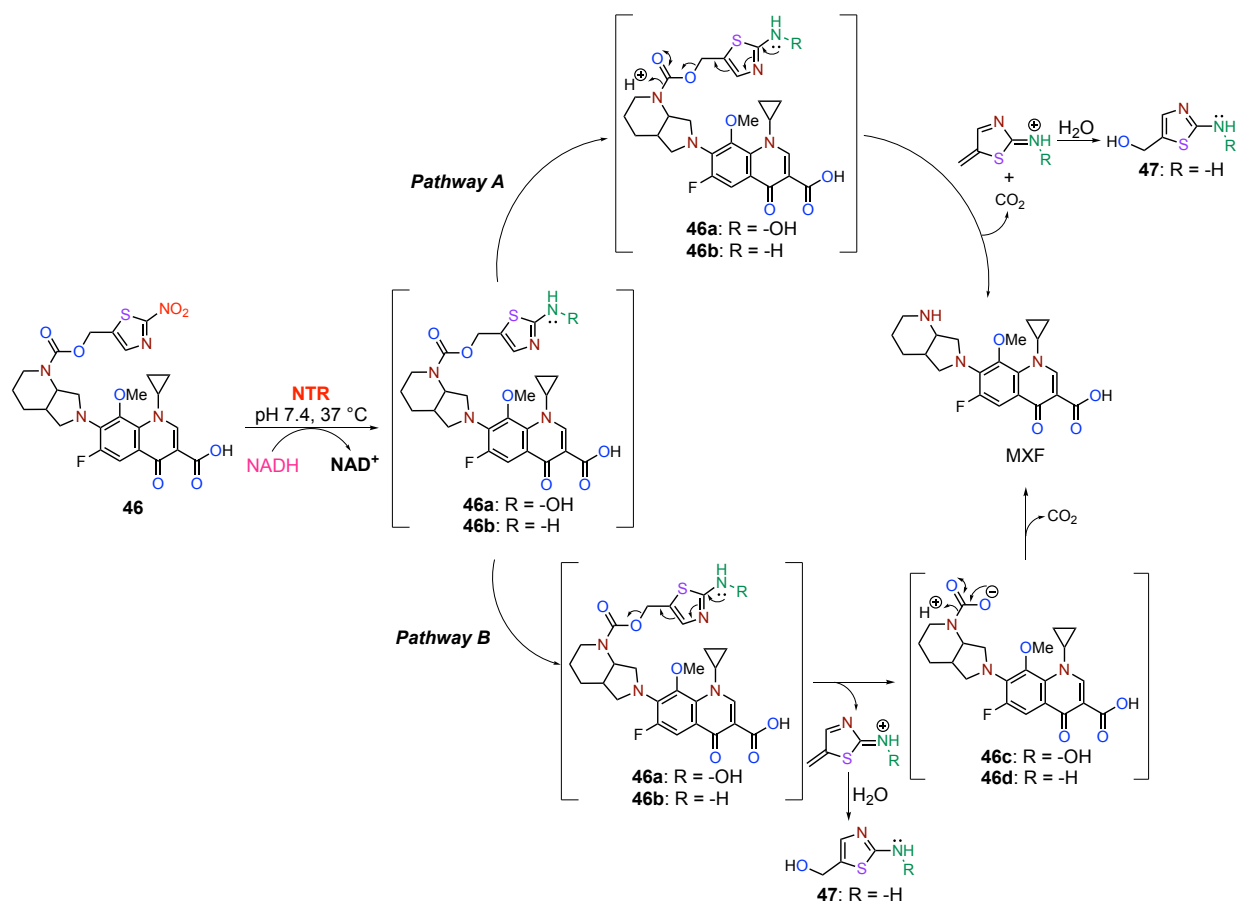
On the basis of the existence of the aforementioned intermediates, a mechanism for the release of MXF from ester and carbamate prodrugs was proposed (Scheme 3.2 and 3.3). The chemoselective reduction of the nitro group in the nitrothiazole motif of **38** catalyzed by *E. coli* NTR resulted in the formation of hydroxylamine intermediate **38a**. Subsequently, this intermediate is reduced to the electron-rich amine intermediate **38b**, which promotes self-immolation *via* a 1,5-elimination reaction. This, in turn, inevitably leads to trigger detachment and release of MXF and quinone-methide intermediate. The latter species produced 2-aminothiazole methanol, **47** with ease when quenched in an aqueous solution (Scheme 3.2).

Scheme 3.2. Plausible mechanism for bioreductive activation of **38**



Reductive elimination from **46** can take place in one of two ways. (a) Pathway A: Intermediate **46a** or **46b** can undergo fragmentation in a concerted fashion to afford MXF and carbon dioxide after protonation of the amine group. (b) Pathway B: Intermediate **46a** or **46b** can dissociate to produce intermediate **46c** or **46d**. Subsequent protonation of the amine with concomitant decarboxylation afforded MXF and 2-aminothiazole methanol, **47**. As opposed to the carboxylic acid (pK_a 6.3) in prodrug **38**, the existence of secondary amine with a pK_{aH} of 9.3, most likely led to the slower fragmentation of intermediate and promoted the formation of MXF from **46** to a lesser extent (Scheme 3.3).

Scheme 3.3. Plausible mechanism for bioreductive activation of 46



3.2.5. Computational studies

3.2.5.1. Docking analysis

Computational studies were then conducted to comprehend the structural basis for the distinct differences in the reactivity and kinetic profile of prodrugs towards *E. coli* NTR. The target protein *E. coli* NTR exists as a homodimer with two identical subunits (chain A and B) that form two FMN-binding active sites located at the dimeric interface⁶⁷ (Figure 3.10). Owing to the fact that the FMN bound active pocket is formed as a result of the intertwining of the two monomers, the entire protein was considered for targeted docking. Prior to docking the designed prodrugs, the docking protocol was validated by removing the co-crystal bound ligand (FMN) from the chain A of oxidized (*E. coli*; PDB 1DS7) NTR and then re-docking into the catalytic binding site. The minimal RMSD value (0.001 Å) between the resultant and native conformations of FMN in the chain A of *E. coli* NTR attests to the precision of the docking approach (Figure 3.11.A). The resemblance between the experimental and docked structures is illustrated by a molecular surface view of the active pocket (Figure 3.11.B). Furthermore, the top-ranked pose of the docked conformer revealed interactions with the active site residues

that were identical to those of the native conformer (Figure 3.11.C and D). Among other amino acids, K14, K74, N71, E165, and G166 play a crucial role in the binding of the cofactor at the active site. The active conformation of the homodimer is influenced by the polar interaction of lysine (K205) and arginine residues (R10 and R207) with the phosphate moiety of FMN from the first monomer. The phosphate group of FMN is stabilized by R10, S12, N200, K205, S206 and R207 through hydrogen-bond interactions. The benzenoid component of FMN makes hydrophobic interactions with residues like E165 and P163. The isoalloxazine ring of FMN adopts a butterfly bend conformation along the N5-N10 axis. As it has already been seen in the other structurally related proteins, the *si* face is buried, whereas the solvent-accessible *re* face provides the putative binding site for nitroaryl substrates.

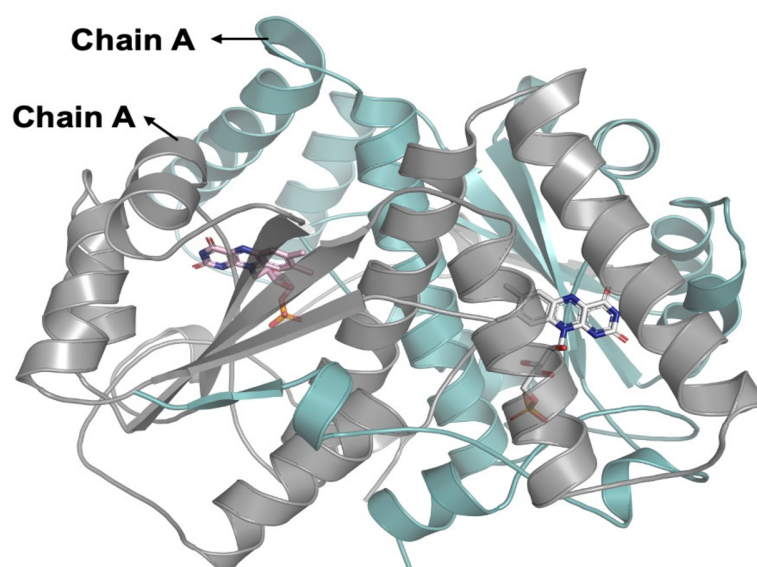


Figure 3.10. Structure of *E. coli* NTR (NfsB, PDB 1DS7). The FMN ligands bound at the dimeric interface of both the chains are shown.

Once the docking protocol was validated, targeted docking was performed using AutoDock Vina into the predicted binding site to delineate the role of active site architecture in NTR-catalyzed nitro-reduction of prodrugs. This generated twenty different docking poses for each prodrug, which were then ranked according to their respective binding energies. The prodrugs, in particular, showed predicted binding energies that were lower than those of FMN and considerably weaker interactions with NTR. As a consequence, the enzyme is easily departed following the reduction of nitro functionality in prodrugs. This outcome is primarily determined by the relative rate of enzyme mediated nitroreduction and the reduction potential of the prodrug. The top-

ranked docked poses with the lowest binding energy were chosen for further analysis and are shown in Table 3.3.

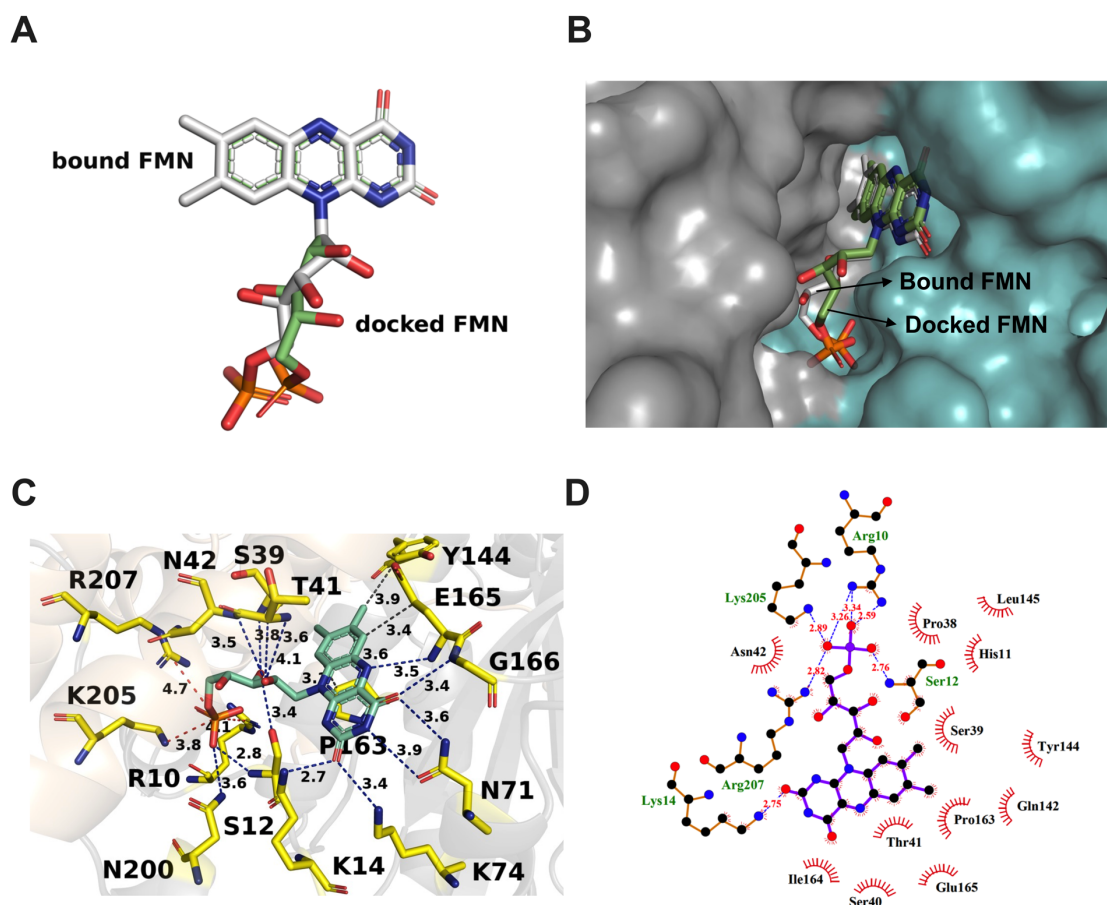
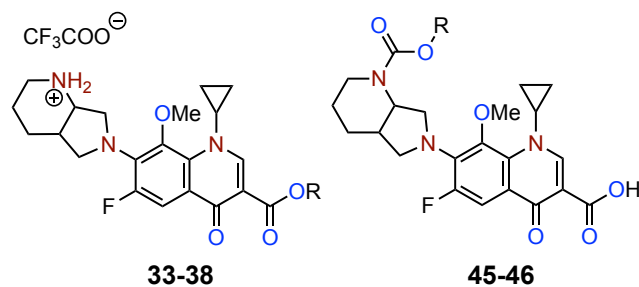


Figure 3.11. (A) Alignment of the bound and docked conformer of FMN using Ligand alignment tool of PyMOL. The RMSD value between the conformations was found to be 0.001 Å. (B) Molecular surface view of bound and docked pose of FMN at the dimeric interface of *E. coli* NTR (PDB: 1DS7). (C) Cartoon representation of the docked FMN at the active site of oxidized NTR of *E. coli* (PDB: 1DS7). The docked ligands and bound FMN are shown in a stick model, and the active site residues are indicated by a 1-letter code. The hydrogen, hydrophobic interactions, and salt bridges are drawn as blue, dark gray, and red dotted lines respectively and the lengths are indicated. (D) 2D LigPlot representation of the docking interaction of *E. coli* NTR (PDB: 1DS7) with FMN. Receptor residues involved in hydrophobic interactions are represented by brick red spoked arcs, hydrogen bonding shown by blue dotted lines. Receptor residues involved in H-bonding are colored green. Ligand residues involved in H-bonding are shown in red color.

Table 3.3. Comparative analysis of the docking results of NTR-MXF prodrugs against *E. coli* NTR (PDB: 1DS7)



| Entry | Ligand/ Prodrug | R | Binding affinity (kcal/mol) | Distance (Å) from FMN to nitro group | |
|-------|--------------------|---|--------------------------------|---|----------|
| | | | | N5 (FMN) | N1 (FMN) |
| 1 | FMN | - | -10.2 | - | - |
| 2 | 33 | | -9.2 | 2.7 | 3.5 |
| 3 | 34 | | -9.7 | 12.3 | 10.0 |
| 4 | 35 | | -9.3 | 12.2 | 9.7 |
| 5 | 36 | | -9.6 | 11.5 | 8.9 |
| 6 | 37 | | -9.7 | 11.5 | 8.9 |
| 7 | 38 | | -9.6 | 9.0 | 7.8 |
| 8 | 45 | | -9.3 | 16.9 | 13.4 |
| 8 | 46 | | -9.4 | 8.7 | 5.9 |

stabilized by many hydrogen bonds, hydrophobic contacts, and salt bridges with the active site residues close to the FMN cofactor. The profound exception to this trend was 2-nitrothiazolyl carbamate, **46**. Contrary to ester prodrug **38**, the nitro group in carbamate **46** was directed towards N5 of FMN with a distance of 8.7 Å (Figure 3.13.H).

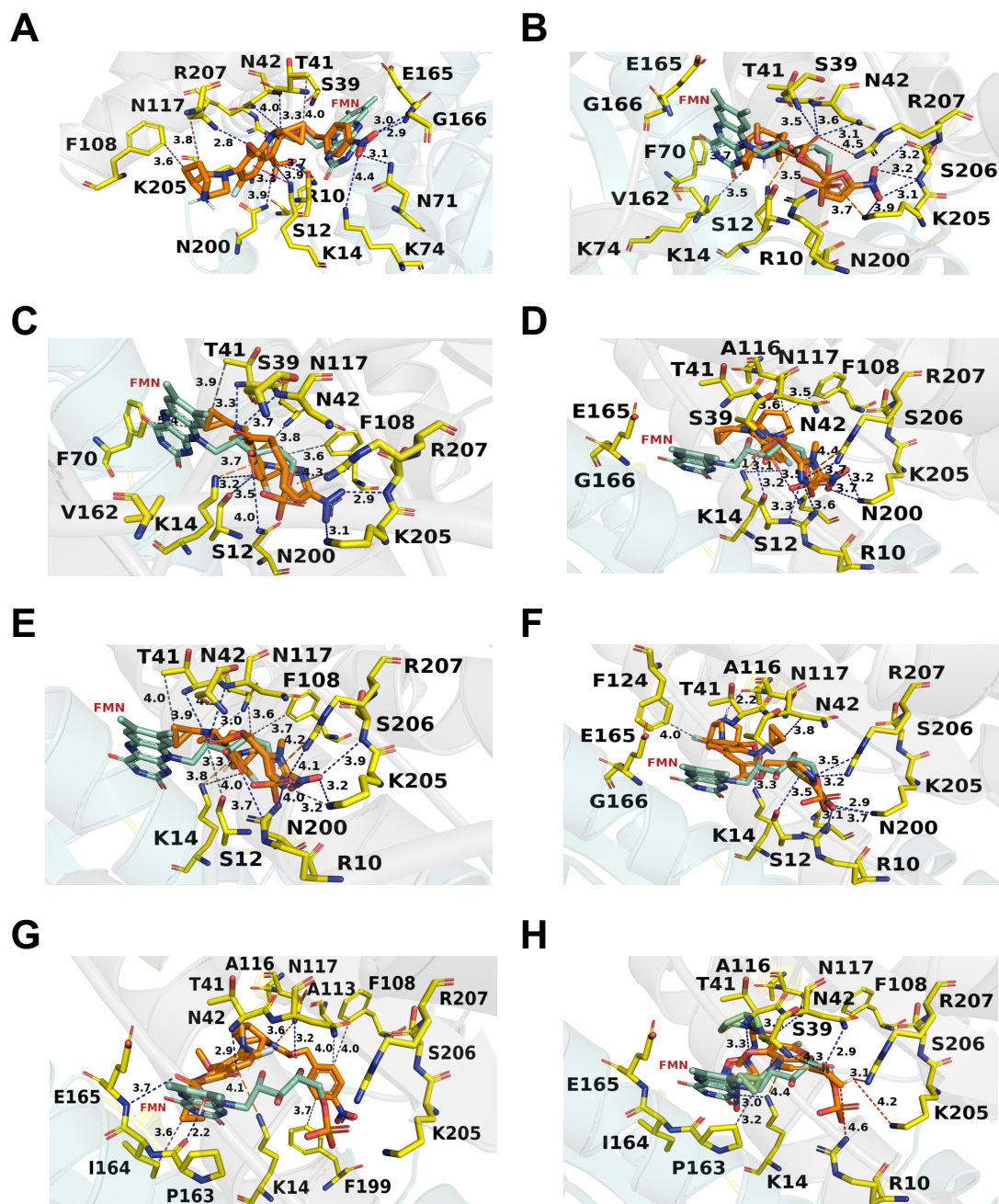


Figure 3.13. Cartoon representation of (A) **33**, (B) **34**, (C) **35**, (D) **36**, (E) **37**, (F) **38**, (G) **45** and (H) **46** docked at the active site of chain A of *E. coli* NTR (PDB: 1DS7). The docked ligands and bound FMN are shown in a stick model and the active site residues are indicated by a 1-letter code. The hydrogen, hydrophobic interactions, π interactions and salt bridges are drawn as blue, dark gray, orange, and red dotted lines, respectively, and the lengths are indicated.

Given that the nitro group is within van der waal's radii (14 Å) of flavin,⁷⁵ FMN-mediated nitroreduction of **34–38** and **45** could possibly occur *via* electron transfer coupled to proton transfer rather than hydride transfer. It is interesting to note that 2-nitrothiazole prodrugs, **38** and **46** showed shortest distance (8.7 Å and 9.0 Å respectively) between the nitro group from N5 of FMN among the tested prodrugs except **33**. Unfortunately, the docking score and the interactions generated with the active site residues were not adequate to rationalize the discrepancies in the kinetic profiles of the prodrugs.

3.2.5.2. Molecular dynamics simulations

To shed light on the notable differences in the kinetic profiles, the top ranked docked pose of all the prodrugs (**33–38**, **45** and **46**) with its target (*E. coli* NTR; PDB 1DS7) were used as structural models for running Molecular Dynamics (MD) simulations. These studies were performed by Dr. SharathChandra M. (Prof. Jennifer Hirschi Lab, University of Binghamton, New York, U.S.A). The models were then reduced without constraints after being solvated in a TIP3P water box (Transferable intermolecular potential with 3 points, a widely used 3-point water model). The system was brought to 300K using simulated annealing with a 2 ns equilibration and a 1 fs time step. Using a Nosé-Hoover thermostat, the reduced geometries were then put through 50 ns production cycles. The overlay of the docked conformations of **33**, **37** and **38** from FMN in the active site is displayed in Fig 3.14, and the average distance between the nitro groups of the prodrugs from FMN cofactor, bound to the same monomer was found to be within 6-8 Å.

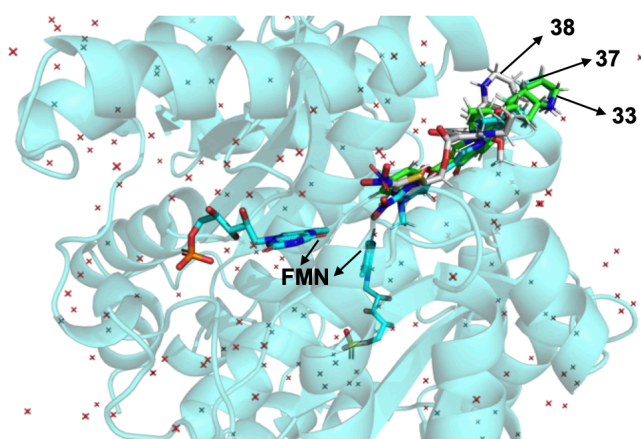


Figure 3.14. Simulation model showing the overlaid docked conformers of **33**, **37** and **38** from FMN in the active site of *E. coli* NTR. Data was provided by Dr. SharathChandra M. (Prof. Jennifer Hirschi Lab, University of Binghamton, USA).

Three possible mechanistic scenarios are illustrated in Scheme 3.4 *viz.* (1) proton transfer (PT) followed by a formal hydride transfer (HT), (2) a formal hydride transfer followed by a proton transfer, and (3) two consecutive electron transfer (ET)-proton transfer sequences can be envisioned for the reduction of nitro groups by NTR. A direct hydride transfer from FMN is improbable, based on the distances discovered through the aforementioned molecular dynamics simulations and the literature precedent found for CB1954 with other bacterial nitroreductase variations (1YKI and 1IDT).⁶⁸ Furthermore, a plausible mechanistic model that involves an electron transfer followed by protonation *via* water is supported by the active site's abundance of water.

The electron transfer barriers were computed using Marcus theory in order to investigate the electron transfer step from FMN.^{69,70} The estimated electron transfer barriers listed in Table 3.4 are in good agreement with the yields measured for *E. coli* NTR. These outcomes are consistent with the findings in related NTR activated prodrugs developed by Wilke and colleagues.⁶⁸ Notably, 2-nitrothiazole ester prodrug **38** has the lowest barrier for electron transfer reaction. Compared to **38**, the steric effect imposed by methyl substituent in **37** might contribute to a higher electron transfer barrier, which would likely result in a slower rate of nitroreduction. Conversely, the rate of nitroreduction of 2-nitrothiazole carbamate prodrug **46** was comparatively lower than that of the ester prodrug, presumably due to a ~ 1.7 -fold higher electron transfer barrier. This indubitably demonstrated that the *E. coli* NTR mediated nitroreduction of **38** is more kinetically and thermodynamically feasible than other prodrugs.

Scheme 3.4. Plausible mechanistic scenarios for the reduction of nitro group by NTR

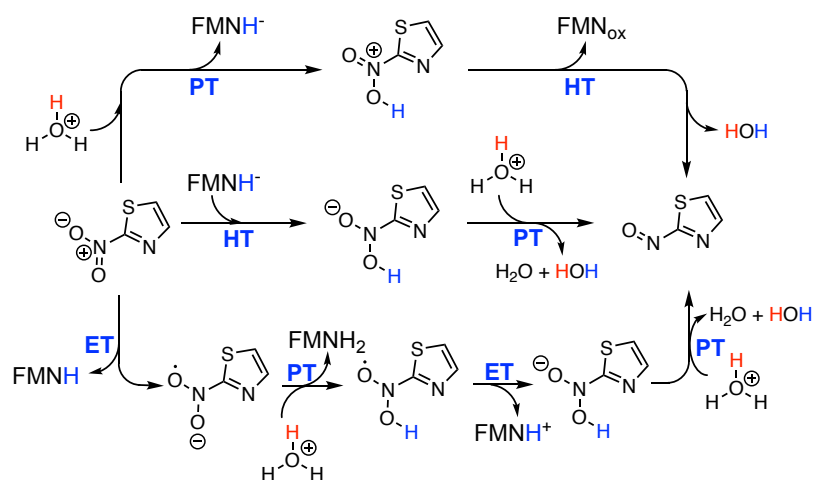
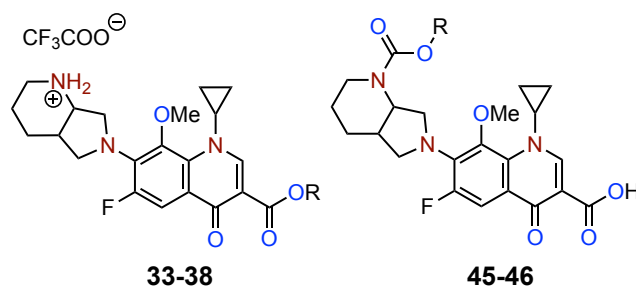


Table 3.4. Comparative analysis of electron transfer barriers with the rate and amount of MXF generated from prodrugs

| Entry | Prodrug | R | Electron transfer barrier (kcal/mol) | % of MXF | Relative rate |
|-------|-----------|---|--------------------------------------|----------|---------------|
| 1 | 33 | | 9.6 | 13 | 1.9 |
| 2 | 34 | | 6.7 | 8 | 6.8 |
| 3 | 35 | | 5.9 | 64 | 10 |
| 4 | 37 | | 9.5 | 7 | 0.9 |
| 5 | 38 | | 3.6 | 86 | 1 |
| 6 | 45 | | 13.5 | 3 | 93 |
| 7 | 46 | | 6.4 | 49 | 0.6 |

Taken together, the simulation studies offered empirical evidence behind the superiority of 2-nitrothiazole ester prodrug **38** over the carbamate prodrug, **46** as well as other nitroaryl prodrugs. These results are in agreement with the experimental findings, supporting the outstanding reactivity of **38** towards NTR that favours the rapid and complete reduction of the prodrug to generate MXF in a quantitative manner. These results motivated us to seek prodrug **38** for further studies.

3.2.6. Selectivity of **38** towards NTR

Next, the selectivity of **38** to NTR was evaluated by determining the changes in fluorescence intensity. As clearly illustrated in (Figure 3.15), **38** displayed no significant enhancement in fluorescence response in the presence of biologically relevant analytes such as thiols (Cys, GSH), saccharides (Glu, Gal), reductants (Vit-C), amino acids (His), oxidizing agents (H_2O_2), esterase enzyme (Es), NADH or NTR alone. However, **38** uniquely responded to *E. coli* NTR in the presence of NADH under the same conditions and produced an intense fluorescence signal within a minute at 37 °C.

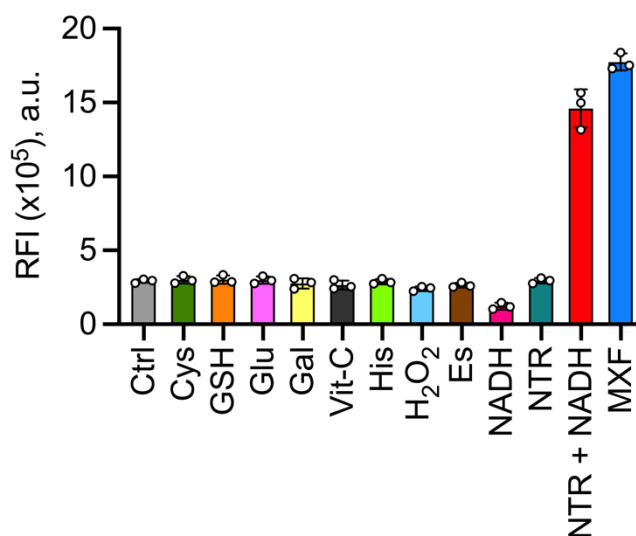


Figure 3.15. Fluorescence response of **38** (10 μM) to various biological analytes (100 μM) in phosphate buffer (pH 7.4, 10 mM) after 15 min at 37 °C. Ctrl = **38** alone; Cys = cysteine; GSH = glutathione; Glu = glucose; Gal = galactose; Vit-C = ascorbic acid; H_2O_2 = hydrogen peroxide; Es = esterase 1 U/mL; NADH = reduced nicotinamide adenine dinucleotide (100 μM); NTR = *E. coli* nitroreductase (15 nM). All data are presented as means \pm SD of three independent experiments performed in triplicate.

3.2.7. *E. coli* mediated bioreductive activation of prodrugs

Guided by the impressive selectivity of the 2-nitrothiazolyl group towards NTR, the bioreductive ability of **38** was evaluated and compared to other prodrugs in a variety of bacterial lysates. Congruent with our *invitro* enzymatic kinetic findings, **38** exhibited a high degree of *E. coli* lysate dependent conversion into MXF than other prodrugs (Figure 3.16.A). A distinct time-dependent strong fluorescence was observed upon incubation with *E. coli* lysate, indicative of MXF generation. As anticipated, pretreatment with NTR inhibitor, Dicoumarol (DCOM)⁷¹ and heat-inactivation of the lysate significantly reduced the fluorescence intensity, underlining its specificity to FMN-dependent *E. coli* NTR (Figure 3.16.B).

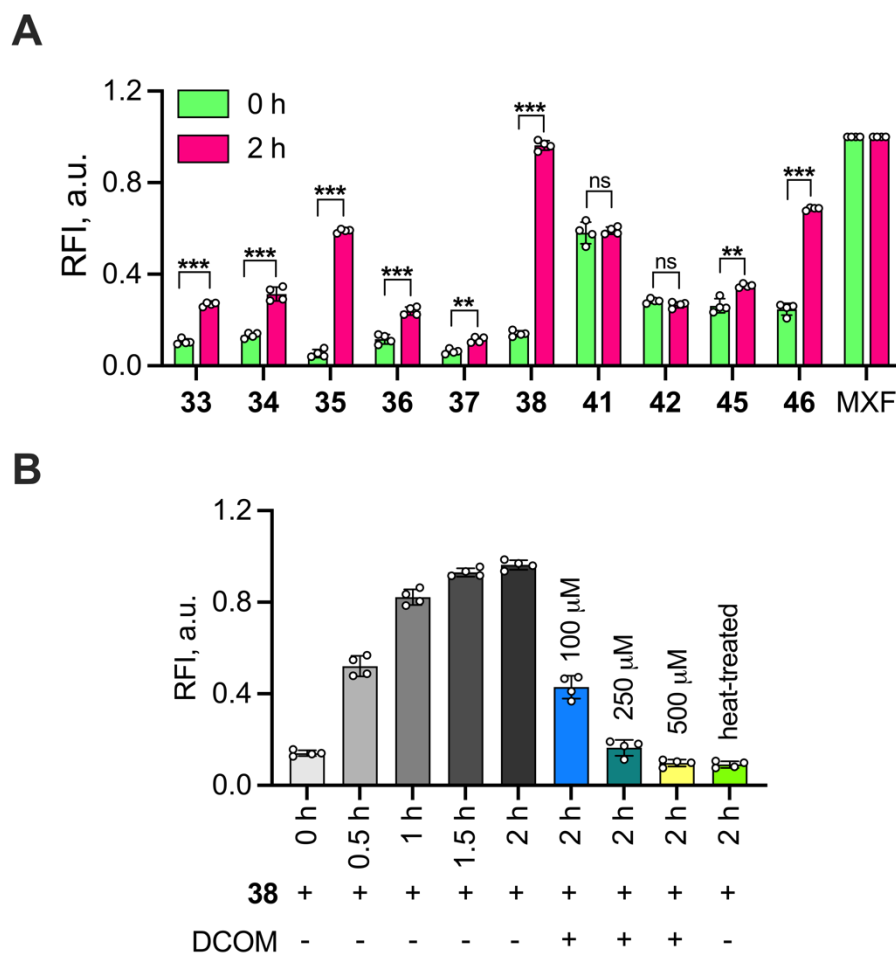


Figure 3.16. (A) Bioreductive activation of prodrugs (10 μM) in *E. coli* ATCC 25922 lysate (1 mg/mL). All data are presented as means \pm SD from quadruplicate experiments performed in triplicate. p value was determined by the student's two-tailed unpaired parametric t -test relative to 0 h. (** $p \leq 0.01$; *** $p \leq 0.001$ and ns indicates not significant). (B) Monitoring the release of MXF from **38** (10 μM) by measuring fluorescence ($\lambda_{\text{ex}} = 289$ nm and $\lambda_{\text{em}} = 488$ nm) in lysates (1 mg/mL) of *E. coli* alone or in the presence of various concentrations of NTR inhibitor, dicoumarol (DCOM; 100, 250 or 500 μM) and heat-inactivated lysates.

3.2.8. *In silico* modeling of the interaction of prodrug with Mycobacterial NTRs

Compared to *E. coli*, *mycobacteria* possess several NTRs that rely on canonical flavin cofactors, such as FMN or FAD and deazaflavin cofactors. For instance, overexpression of NfnB, an FMN-dependent NTR in *Mycobacterium smegmatis* (*M.smegmatis*), conferred resistance to anti-TB drugs such as dinitrobenzamides (DNBs)⁷² and benzothiazinones (BTZs)^{72,73} by reducing the more active nitrocompound into considerably less active hydroxylamino or amino derivatives. Conversely, another recent study indicated that the NfnB-dependent reduction of nitro derivative into

potentially active hydroxylamine rendered *M. smegmatis* sensitive to the nitazoxanide prodrug (TP053).⁷⁴ The nitroreductase activity of NfnB uses both NADH and NADPH as physiological electron donors, similar to *E. coli* NTR. Considering that the FMN-binding domain of mycobacterial NfnB shares a significant amount of sequence similarity (35%) with the *E. coli* NTR (Figure 3.17),⁷³ we reasoned that mycobacterial NfnB-catalyzed nitroreduction of prodrugs could liberate MXF.

```

E.coli_NfsB      1 MDIISVAL-----KRHSTKAFDASKKLTPEQAEQIKTLLQ
M.smegmatis_NfnB 1 MSVPTLPTGPTVDLAQAAERLIKGRAVRAFRPD-EVPEETMRAVFELAG
* . . . . . * . . . . . * . . . . . *

E.coli_NfsB      36 YSPSSNSQPWHFIVASTEEGKARVAKSAAGNYVFNERKILDASHVVVFC
M.smegmatis_NfnB 50 HAPSNNTQPWHVEVSG-AARDRLAEALVTAH-----
* * . * . * * * * * . . . . . * *

E.coli_NfsB      86 AKTAMDDAWLKLVVDQEDADGRFATPEAKA-----
M.smegmatis_NfnB 82 -----AEERVTVDFPYREGLFQGVLQERRADFGSRLYAALGIARDQTD
.....* . . * * . * * . . . . .

E.coli_NfsB      116 ----ANDKGRKFFADMHRKDLH---DDAEWMAKQVYLVNGNFLLVAAALG
M.smegmatis_NfnB 125 LLQGYNTESLRFYGAPHVAMLFAPNNTEARIAGDMGIYAQTLMLAMTAHG
.....* . . . . * * . . . . * * . . . . * *

E.coli_NfsB      159 LDAVP--IEGFDAAILDAEFGLKEKGYTSLVVVPVGHHSVEDFNATLPKS
M.smegmatis_NfnB 175 IASCPQALLSFYADTVRAELGVENRKLLMGISFGYADDTAAVNGVRIPRA
. * . . . * * . * * * . . . . . *

E.coli_NfsB      207 RLPQNITLTEV
M.smegmatis_NfnB 225 GLSETTRFSR-
* . . .

```

Figure 3.17. Sequence alignment of NfsB from *E. coli* and NfnB from *M. smegmatis*. Alignments were performed using T-coffee and visualized with Jalview. The consensus symbols: “*” and “.” under the amino acids indicate identical and semi-conserved residues that are highlighted in red and blue color, respectively. The FMN binding region shown in bold shared 35% sequence identity.

In order to validate our hypothesis, **38** was docked using AutoDock Vina into the active site of *M. smegmatis* NfnB (PDB: 2WZW). Molecular docking analysis demonstrated the interaction of prodrug into the FMN-bound active site of NfnB. Specifically, the prodrug is positioned on the *re* face of FMN bound at the dimer interface and surrounded by amino acid residues R105, S55, R29, and S53 through hydrogen bonds. More crucially, it is conceivable that the presence of possible polar interactions between the nitro group of **38** and residues of NfnB, such as A27, R25, and R223 contributed to enhanced binding with NTR and facile reduction of the prodrug (Figure 3.18). Furthermore, **38** has a higher predicted binding of -10.8 kcal/mol than FMN (-12.8 kcal/mol), indicating that the 2-nitrothiazolyl moiety favours the quick departure of the enzyme following reduction of the prodrug. This was supported by the fact that the average distance between nitrogen of the nitro group in **38** and FMN cofactor bound to the same monomer was ~6.5 Å (Figure 3.19).

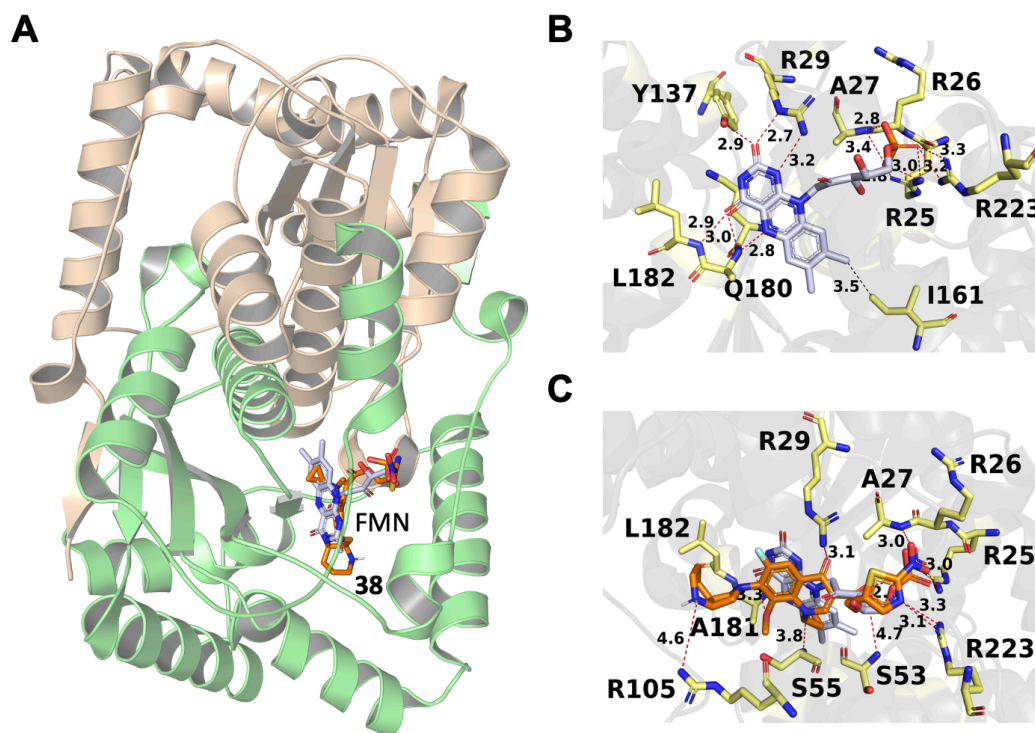


Figure 3.18. Predicted binding mode of **38** to FMN cofactor bound *M. smegmatis* NfnB (A) Ribbon model showing the docked pose of **38** to FMN bound chain A of NfnB (PDB: 2WZV). (B and C) Close-up view of the catalytic site of *M. smegmatis* NfnB showing top-ranked docked poses of (B) bound FMN and (C) **38** in the presence of bound FMN (cyan) resulting from docking simulations. The residues presenting interactions with FMN and **38** are labelled by a one-letter code and shown as a stick model. The red and black dashed lines represent polar and hydrophobic contacts, respectively, and the lengths are indicated.

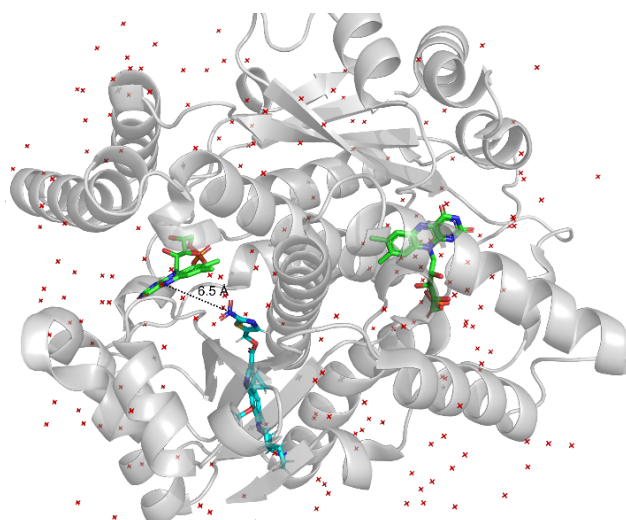


Figure 3.19. Simulation model showing the binding interaction of **38** with *E. coli* NTR. The average distance between the nitro group of **38** and FMN is displayed. Data was provided by Dr. SharathChandra M. (Prof. Jennifer Hirschi Lab, University of Binghamton, USA).

3.2.9. Bioreductive transformation of 38 in mycobacterial lysates

To substantiate the docking results and demonstrate that a similar conversion prevails within mycobacteria, we tested the feasibility of **38** to generate MXF. As expected, fluorescence studies confirmed that prodrug **38** underwent a greater degree of *M. smegmatis* (WT) lysate dependent biotransformation into MXF than the other prodrugs (Figure 3.20.A). Similar results were also observed in lysates from MshA deletion mutants of *M. smegmatis* (Δ mshA) with defects in mycothiol biosynthesis (Figure 3.20.B). This suggests that the likelihood of prodrugs being activated in a mycothiol-dependent manner is low. However, this does not exclude the possibility of an alternate route of prodrug activation triggered by F₄₂₀H₂ dependent nitroreductases⁷⁵ or unusual FMN-dependent MsAcg putative NTR⁷⁶ that does not require NADH/NADPH for reductive catalysis.

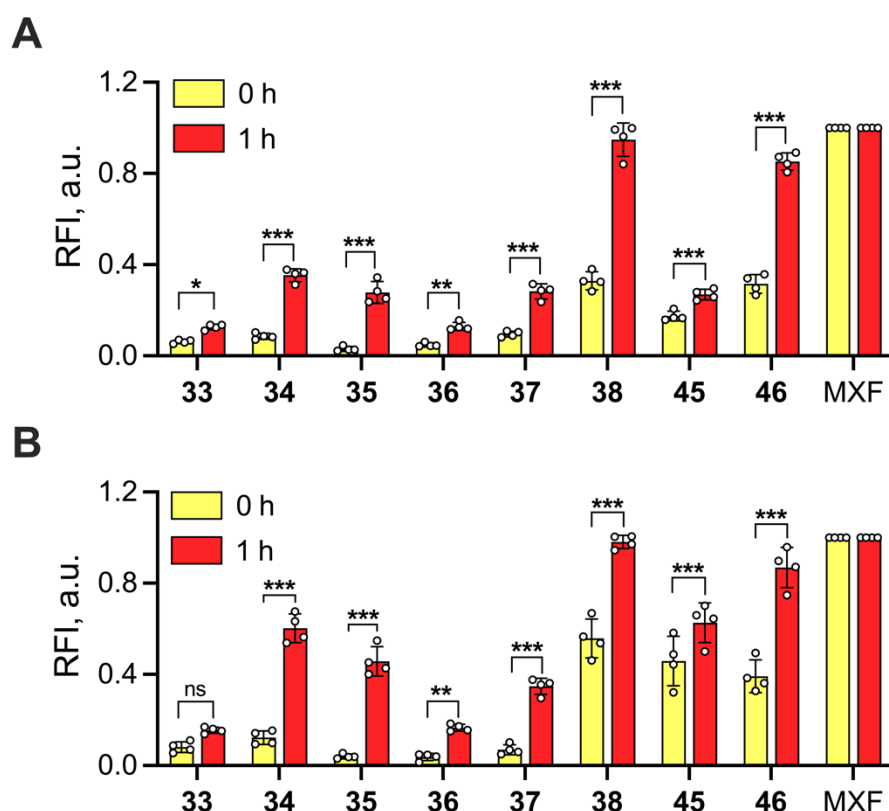


Figure 3.20. *In vitro* determination of the generation of MXF by measuring the increase in fluorescence ($\lambda_{\text{ex}} = 289$ nm and $\lambda_{\text{em}} = 488$ nm) after incubation of prodrugs (10 μ M) in lysates of (A) wild-type (WT) and (B) MshA deficient (Δ mshA) *M. smegmatis* (1 mg/mL). All data are presented as means \pm SD from quadruplicate experiments performed in triplicate. *p* value was determined by the student's two-tailed unpaired parametric *t*-test relative to 0 h. (**p* < 0.05; ***p* ≤ 0.01; ****p* ≤ 0.001 and ns indicates not significant).

The fluorescence signal was significantly diminished when **38** was added to *M. smegmatis* lysate that had already been subjected to treatment with different concentrations of DCOM. Furthermore, a marked reduction in the fluorescence signal was observed in **38** treated heat-inactivated *Msm* lysate. These results presented evidence of the specificity of the prodrug for FMN-dependent NTRs that are reliant on either NADH or NADPH (Figure 3.21).

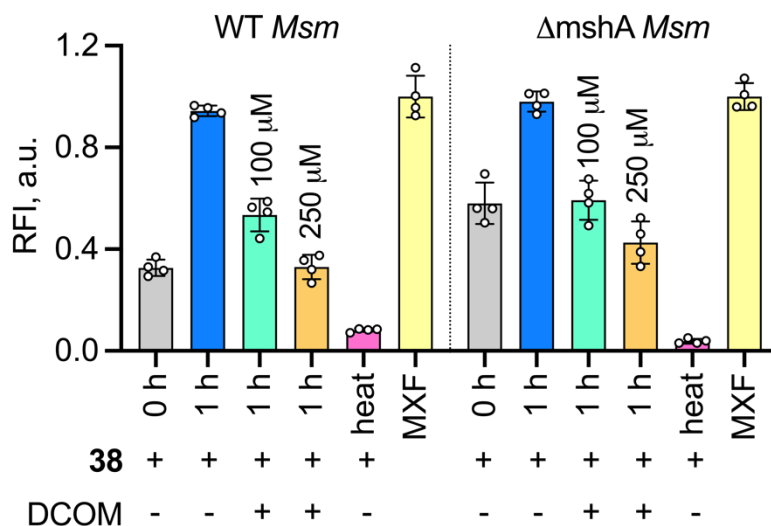


Figure 3.21. Monitoring the release of MXF from **38** (10 μ M) by measuring enhancement in fluorescence in lysates (1 mg/mL) of wild-type (WT) and MshA deficient (Δ mshA) *M. smegmatis* alone or in the presence of various concentrations of NTR inhibitor, dicoumarol (DCOM; 100 and 250 μ M) and heat-inactivated lysates.

Although, several NTRs have been recognised in *Mtb*, their precise role in *Mtb* pathogenesis remains unclear. These NTRs probably contribute to combat nitrosative and oxidative stress encountered by *Mtb* inside host macrophage to survive and establish infection.⁷⁷⁻⁸⁰ It has been well established that hypoxia is one of the commonly encountered stress by *Mtb* residing in the granulomas of the lungs of TB patients. These hypoxic regions are a privileged reservoir for non-replicating *Mtb* persisters. Under hypoxic stress, these drug-tolerant bacilli strongly induce DevR regulon-controlled genes encoding several nitroreductases (NTRs) such as Rv2032, Rv3131 and Rv3127.⁸⁰⁻⁸⁴ Because *Mtb* lacks orthologues of *M. smegmatis* NfnB,⁷³ we posited that *Mtb* specific NTR driven reduction of **38** would release MXF. To test this idea, lysates from actively replicating and dormant cultures of *Mtb* were exposed to **38** (25 μ M) and the fluorescence corresponding to the generation of MXF was monitored. The enhanced fluorescence of MXF in *Mtb* lysates indicated the involvement of *Mtb* specific NTRs in the bioreductive activation of **38** (Figure 3.22). However, further studies are warranted to identify

Mtb's specific NTR and understand their precise role in the putative bioreduction of **38** to MXF in *Mtb*. Nevertheless, these results indisputably provide evidence that **38** served as a substrate for nitroreductases of *E. coli*, *M. smegmatis* and *M. tuberculosis*.

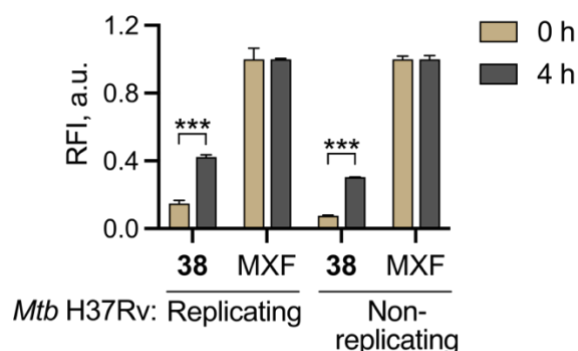


Figure 3.22. Monitoring the release of MXF from **38** (25 μ M) by measuring enhancement of fluorescence ($\lambda_{\text{ex}} = 289$ nm and $\lambda_{\text{em}} = 488$ nm) in lysates of replicating (normoxic) and non-replicating (hypoxic) cultures of *Mtb*. Data was provided by Dr. Piyali Mukherjee (Prof. Amit Singh Lab, IISc Bangalore).

3.2.10. Stability of **38** in mammalian lysate

Given that the carboxylester linkage in **38** is prone to hydrolysis, we also tested the stability in mammalian lysate owing to higher levels of ubiquitous esterase enzymes. After incubating **38** (10 μ M) in mammalian (A549) lysate at 37 $^{\circ}$ C, the cleavage of the prodrug was evaluated by measuring the change in fluorescence intensity over time. As shown in (Figure 3.23.A), no discernible increase in fluorescence was seen, indicating the stability of **38**. However, a small increase in fluorescence was observed only after 4 h of incubation in MEF cell lysate (Figure 3.23.B). These results suggested that **38** was stable under physiological conditions and undergoes exclusive rapid bioreduction in bacteria.

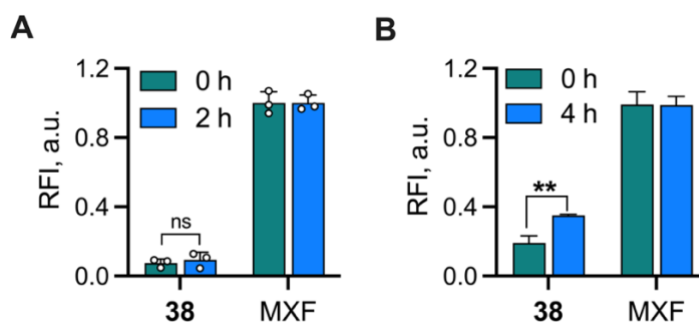


Figure 3.23. Evaluation of the stability of **38** in lysates (1 mg/mL) of mammalian cell line (A) A549 (lung-cancer cell line) after 2 h and (B) MEF (mouse embryonic fibroblast) after 4 h by measuring fluorescence ($\lambda_{\text{ex}} = 289$ nm and $\lambda_{\text{em}} = 488$ nm) corresponding to MXF.

3.3. Conclusion

Numerous investigations have demonstrated the superiority of the 1-methyl-2-nitroimidazole group in rapid, and sensitive turn-on fluorescence detection of *E. coli* NTR. Due to the challenges involved in the synthesis of the 1-methyl-2-nitroimidazolyl moiety, efforts towards identification of a novel resembling substrates which can be easily synthesized are gaining traction. In this chapter, a systematic study was conducted to tune the selectivity and enhance the reactivity of substrates toward *E. coli* NTR. Our investigation revealed that the prodrugs tethered with 2-nitrothiazolyl moiety were the optimal substrates with an outstanding selectivity to *E. coli* NTR, which upon enzymatic nitroreduction provided MXF in quantitative yield. Compared to the 2-nitroimidazolyl prodrug **37**, *E. coli* NTR promoted an instantaneous and complete reduction in the 2-nitrothiazole prodrugs **38** and **46** to MXF. The relative sensitivity and superiority of ester prodrug **38** to *E. coli* NTR over 2-nitrothiazole carbamate prodrug is even more striking. Among all the prodrugs, *E. coli* NTR has demonstrated the highest catalytic efficiency with 2-nitrothiazolyl ester prodrug, **38** with a $k_{\text{cat}}/K_{\text{M}}$ of $24.95 \mu\text{M}^{-1}\text{min}^{-1}$. These remarkable experimental findings were also complemented by the docking results. Furthermore, the MD simulations indicate that the mechanism of reduction is likely to be mediated by electron transfer from FMN followed by proton transfer *via* water at the active site. The lower electron transfer barrier between the bound FMN and prodrug allows the efficient and rapid reduction of the nitro group in **38**. In agreement with these findings, the prodrug **38** showed remarkable stability in mammalian lysates under physiological conditions. Furthermore, the prodrug **38** was preferentially activated in a range of lysates derived from bacteria such as *E. coli*, *M. smegmatis*, and *M. tuberculosis*. This is a further testament to the incredible versatility and specificity of 2-nitrothiazole substrate, **38** towards a variety of bacterial NTRs.

3.4. Experimental protocols

3.4.1. General methods

Stock solutions of MXF (1 mM), compounds **33-38**, **45** and **46** (1 mM) were prepared in DMSO whereas the stock solutions of *E. coli* NTR (1 mg/mL) and NADH (5 mM) were prepared in phosphate buffer (pH 7.4, 10 mM). Unless otherwise specified, the reaction mixtures were prepared in 10 mM pH 7.4 phosphate buffer (PB) and the fluorescence corresponding to MXF ($\lambda_{\text{ex}} = 289$ nm and $\lambda_{\text{em}} = 488$ nm) was measured using an EnSight Multimode Plate Reader (PerkinElmer).

3.4.2. Investigating the release of MXF from prodrugs using a fluorescence-based assay

The reactions in the 96-well plate were initiated by the addition of 15 nM *E. coli* NTR (30 μL ; 0.1 μM) and 100 μM of NADH (4 μL ; 5 mM stock) to a solution of 10 μM prodrugs (2 μL , 1 mM stock) in 164 μL of buffer. The enhancement of the fluorescence signal corresponding to the release of MXF relative to the NTR untreated control was recorded at 37 °C using an EnSight microplate reader (PerkinElmer) for 1 h.

3.4.3. Determination of steady-state apparent kinetic parameters for NTR-mediated release of MXF from ester and carbamate derivatives (**33-38**, **45** and **46**)

Two-fold serial dilutions were prepared from compound stocks (10 mM in DMSO) yielding a concentration range of 0 to 4 mM. Kinetic measurements were carried out in a total volume of 200 μL /well containing 164 μL of buffer, 100 μM of NADH (4 μL ; 5 mM stock) with varying substrate concentrations ranged from 0 μM - 40 μM (2 μL ; 0 to 4 mM stock). The final DMSO concentration was 1%. Reactions were initiated by the addition of 15 nM *E. coli* NTR (30 μL ; 0.1 μM stock) with a multichannel pipette. The control wells contained only substrates with or without either NADH or NTR. Fluorescence attributable to the formation of MXF was followed using a microplate reader in a 96-well plate format. The following parameters were used for fluorescence measurement: Readings were collected from the top at every 37 s interval for a period of 40 min (for prodrugs **33-37** and **45** at 37 °C) or at every 1 s interval for a period of 4 min (for prodrugs **38** and **46** at 25 °C) with 15 flashes per well and a focus height adjusted to 9.5 mm. The background fluorescence was subtracted for each time point from the total fluorescence signal to obtain corrected relative fluorescence intensity (RFI) values. Next, the change in fluorescence (ΔF , RFI/min) upon addition of enzyme was obtained by subtracting the fluorescence signal in the absence of enzyme (F_0) of the varying concentrations of substrates for given time points from the total fluorescence signal (F). The change in

fluorescence (ΔF) vs. time was plotted. The standard curve of MXF was generated by plotting the corrected RFI values vs. concentration (Figure 3.23). The slope and intercept were determined using linear regression ($R^2 = 0.99$) and used to calculate the amount of MXF formed. The RFI/min was converted into $\mu\text{M}/\text{min}$ of MXF produced from various concentrations of substrates using eq. 1.

$$\mu\text{M}/\text{min} = \frac{\Delta F (\text{RFU}/\text{min}) - \text{Intercept (Std.curve)}}{\text{Slope of Std. curve (RFU}/\mu\text{M})} \quad \dots\text{eq. 1}$$

Linear regression analysis was performed to determine the initial reaction rates by taking the slope during the linear stage of the resulting curves of varying concentrations of substrates using OriginPro 8.5.1. These initial reaction velocities were replotted against substrate concentrations and kinetic parameters (V_{max} , K_m , and k_{cat}/K_m) for each concentration were calculated by nonlinear regression using the GraphPad Prism 9 (GraphPad Software, San Diego, California USA) according to the Michaelis-Menten equation (eq. 2). All data are shown as mean \pm standard deviation for three biological replicates.

$$V = \frac{V_{max} [S]}{K_m + [S]} \quad \dots\text{eq. 2}$$

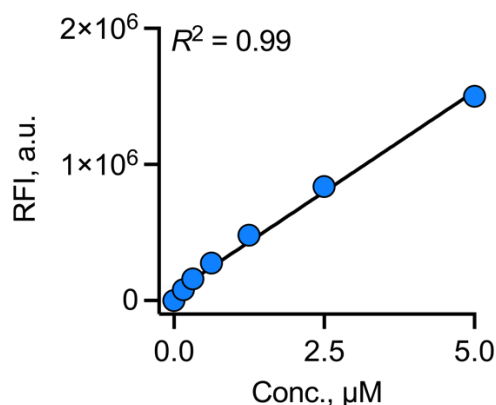


Figure 3.24. Calibration curve for MXF in pH 7.4 phosphate buffer (10 mM) at 37 °C.

3.4.4. Monitoring the release of MXF from 37

(a) Fluorimetry studies

To an eppendorf tube (1.5 mL) containing 10 μM solution of **37** (10 μL , 1 mM stock) in 870 μL of buffer, 100 μM of NADH (20 μL , 5 mM stock) and varied concentrations of NTR ranged from 0 to 60 nM (100 μL , 0 to 0.6 μM stock) were added. Control reactions containing only **37** or lacking NADH or NTR were also carried out. These reaction mixtures were transferred to a quartz micro-fluorescence cuvette (Hellma, path length 1 cm) after incubation at 37 °C on

an Eppendorf thermomixer comfort (700 rpm) for 30 min. The fluorescence measurements were performed using a HORIBA Jobin Yvon Fluorolog fluorescence spectrophotometer with an excitation and emission slit width of 1 nm.

(b) Fluorescence-based analysis

A similar experiment as mentioned above was carried out in a 96-well plate to monitor the enzyme catalyzed reaction of **37** with different concentrations of NTR. The reaction mixture either contained only 10 μM of **37** (2 μL , 1 mM stock) or 10 μM of **37** (2 μL , 1 mM stock), 100 μM of NADH (4 μL , 5 mM stock) with varied concentrations of NTR ranged from 0 to 60 nM (30 μL , 0 to 0.4 μM stock) in 164 μL of buffer. The reactions were incubated at 37 $^{\circ}\text{C}$, and the progression of the NTR-dependent reaction was assessed by change in fluorescence over time using a microplate reader (EnSight) with readings collected from the top at every 30 s intervals for a period of 60 min with the same parameters as stated earlier in Section 3.4.3.

3.4.5. Time- and concentration-dependent kinetics of **38 with NTR**

The reaction mixture contained 10 μM of **38** (10 μL , 1 mM stock), with or without 100 μM of NADH (20 μL , 5 mM stock) in 870 μL of buffer were independently added to a clean 1 mL micro-fluorescence cuvette (Hellma, path length 1 cm). The cuvette was placed in the fluorescence instrument with slow stirring condition by a magnetic stirrer equipped with the instrument (at $t = 0$ s). The fluorescence response was continuously recorded at an $\lambda_{\text{em}} = 488$ nm ($\lambda_{\text{ex}} = 289$ nm) either at 25 $^{\circ}\text{C}$ or 37 $^{\circ}\text{C}$ on a Fluoromax-4 spectrophotometer (Jobin Yvon Edison) following addition of NTR ranged from 0 to 15 nM (100 μL , 0 to 0.15 μM stock) at ($t = 50$ s) for 150 s. The time-axis was normalized according to eq. 3 and fluorescence intensity vs. time was plotted.

$$t = t - 50 \quad \dots\text{eq. 3}$$

3.4.6. Assessing the selectivity of **38**

Stock solutions of porcine liver esterase (50 U/mL), GSH (10 mM), Cys (10 mM), vitamin-C (10 mM), glucose (10 mM), galactose (10 mM), histidine (10 mM), and H_2O_2 (30%, 10 mM) in phosphate buffer were prepared independently from commercial sources. In a typical reaction, 10 μM of **38** (2 μL , 1 mM stock), 100 μM of NADH (4 μL , 5 mM stock), and 15 nM of NTR (30 μL ; 0.1 μM stock) were added to 164 μL of buffer. Similarly, a reaction mixture of 10 μM of **38** (2 μL , 1 mM stock) and 100 μM of various analytes (2 μL , 10 mM stock) was prepared in 196 μL of buffer. In a separate experiment, the reaction mixture was prepared by adding compound 10 μM of **38** (2 μL , 1 mM stock) along with 1 U/mL esterase (4 μL , 50

U/mL stock) in 194 μ L of buffer. The reaction mixtures were incubated for 1 min at 37 $^{\circ}$ C, and then fluorescence response was recorded using a microplate reader (EnSight).

3.4.7. Stability assessment of **38** and **46** by HPLC

A stock solution of **38** and **46** (2.5 mM) was prepared independently in DMSO. In a typical reaction, the compound **38** or **46** (5 μ L, final conc. 25 μ M) was added to 495 μ L of PB (pH 7.4, 10 mM). Reaction mixtures were incubated at 37 $^{\circ}$ C on an Eppendorf thermomixer comfort (800 rpm). Aliquots were taken at determined time points (0 h and 2 h), and injected (25 μ L) in an HPLC instrument attached with a diode-array detector (detection wavelength 280 nm). The stationary phase used was C-18 reversed phase column (4.6 mm \times 250 mm, 5 μ m). The mobile phase used was 0.1% HCOOH in H₂O:ACN at a flow rate of 0.5 mL/min with a run time of 18 min, starting with 40:60 \rightarrow 0-4 min, 20:80 \rightarrow 4-12 min, 40:60 \rightarrow 12-15 min, 40:60 \rightarrow 15-18 min.

3.4.8. LC-MS analysis of NTR-dependent decomposition of **38** and **46**

The reaction mixture was prepared by adding compound 20 μ M of **38** or **46** (10 μ L, 2 mM stock) to a solution of 100 μ M NADH (20 μ L, 5 mM stock), and 15 nM of NTR (150 μ L; 0.1 μ M) in 820 μ L of buffer. The reaction samples containing only prodrug (**38** or **46**) or MXF served as reference controls, while the reaction mixture with NADH and NTR was used as a blank. The reaction mixtures were incubated at 37 $^{\circ}$ C on an Eppendorf thermomixer comfort (700 rpm) for 30 min. An aliquot (100 μ L) was withdrawn from the reaction mixtures and centrifuged (9,391 \times g) at RT for 5 min. The supernatants (100 μ L) were carefully sampled, diluted with ACN (100 μ L), and assessed thereafter by LC/MS. All measurements were done using a LC-MS method in the positive ion mode using a high resolution multiple reaction monitoring (MRM-HR) analysis on a Sciex X500R quadrupole time-of flight (QTOF) mass spectrometer fitted with an Exion UHPLC system using a Kinetex 2.6 mm hydrophilic interaction liquid chromatography (HILIC) column with 100 \AA particle size, 150 mm length, and 3 mm internal diameter (Phenomenex). Nitrogen was the nebulizer gas, with the nebulizer pressure set at 50 psi. MS was calibrated in positive mode and samples were injected (50 μ L) and analyzed with the following parameters: Mode: Electrospray ionization (ESI), ion source gas 1 = 40 psi, ion source gas 2 = 50 psi, curtain gas = 30, CAD gas = 7, spray voltage = 5500 V and temperature = 500 $^{\circ}$ C. The MRM-HR mass spectrometry parameters are as follows: MXF (Q1, M + H⁺) = 402.18, **38** (Q2, M + H⁺) = 544.17 or **46** (Q2, M + H⁺) = 588.16, **38a** (Q3, M + H⁺) = 514.19 and **46a** (Q3, M + H⁺) = 574.18, **38b** (Q4, M + H⁺) = 530.19 and **46b**

(Q4, M + H⁺) = 558.18, **47** (Q5, M + H⁺) = 131.03, declustering potential = 80 V, declustering potential spread = 20 V, collision energy = 10 V, collision exit potential = 5 V and accumulation time = 0.24 s. The LC runs were for 30 min with a gradient of 100% solvent A (0.1% HCOOH in milliQ water) for 5 min, a linear gradient of solvent B (ACN, 0% to 100%) for 25 min followed by 100% solvent A for 5 min all at a flow rate of 0.5 mL per min.

3.4.9. Sequence alignment

The sequences of NfsB (*E. coli*; UniProtKB ID: P38489) and NfnB (*M. smegmatis*; UniProtKB ID: A0R6D0) were obtained from Uniprot database. The unweighted sequence alignments between NfsB and NfnB from *E. coli* and *M. smegmatis* were performed using T-coffee, a web-server maintained by the European Bioinformatics Institute website (<https://www.ebi.ac.uk>) using the default settings and displayed using Jalview. The sequence name indicates the organism of origin, the Uniprot code, and the numbers indicate the amino acid residues displayed. The consensus symbols: ‘*’, ‘.’ and ‘.’ under the amino acids indicate identical, conserved, and semi-conserved residues respectively.

3.4.10. *In silico* molecular docking studies

The structures of compounds (**33-38**, **45**, and **46**) were built with standard bond length and angles using ChemDraw and then energy minimized with Chem3D using the integrated MM2 energy minimization script. The X-ray crystal structures of FMN-bound oxidized *E. coli* NTR (PDB ID: 1DS7; resolution = 2.0 Å), and FMN-bound *M. smegmatis* NfnB (PDB ID: 2WZW; resolution = 1.8 Å) were retrieved from PDB. The protein and ligand PDBQT files were prepared using AutoDock Tools 1.5.6 (ADT) following the standard protocol. The following docking parameters of FMN-bound active sites were employed for (a) *E. coli* NTR (PDB ID: 1DS7): grid box (9.52 × 9.52 × 9.52 Å³) at the coordinates (x = 18.533, y = -32.728, z = 48.114); (c) *M. smegmatis* NfnB (PDB ID: 2WZW): grid box (9.6 × 9.6 × 9.6 Å³) at the coordinates (x = -14.253, y = -81.909, z = -25.468) with default settings: exhaustiveness = 24, energy range = 3 kcal/mol and number of modes = 20. The best-scored docking pose with the lowest binding energy was selected for analysis and figures were visualized using PyMOL (The PyMOL Molecular Graphics System, Version 2.0 Schrödinger, LLC). LigPLOT+ was used to depict the 2D interactions of the ligand and the protein.

3.4.11. *In situ* detection of MXF generated from prodrugs in bacterial lysates (*E. coli*, WT and Δ mshA *M. smegmatis*) using fluorescence-based assay

E. coli ATCC 25922 was grown in LB media at 37 °C in a rotary shaker for overnight. *M. smegmatis* mc²155 bacteria was grown with agitation of 180 rpm in Middlebrook 7H9 broth media supplemented with glycerol (0.2%), and tween-80 (0.1%) at 37 °C for 24 h. The bacterial cells were harvested by centrifugation at 2486 x g (10 min for *E. coli*; 15 min for *M. smegmatis*) at 4 °C. The bacterial pellets were washed twice with PBS buffer (1X, pH 7.4), resuspended in PBS (1X, 2 mL), and transferred to a microcentrifuge tube. The cells were lysed by sonication using (130 W ultrasonic processor, VX 130W) stepped microtip for 2 minutes pulse on time (with 5 s ON and 10 s OFF pulse, 60% amplitude, 20 kHz frequency for *E. coli*) or 5 minutes pulse on time (with 3 s ON and 3 s OFF pulse, 60% amplitude, 20 kHz frequency for *M. smegmatis*) under ice cold conditions. The total protein concentration of the whole cell lysate was determined by Bradford assay using bovine serum albumin (BSA) and further adjusted to 1 mg/mL with PBS (1X). The reactions were conducted by treatment of 10 μ M of various prodrugs (5 μ L, 1 mM stock) with 495 μ L of *E. coli* or *M. smegmatis* lysate (1 mg/mL) at 37 °C on an Eppendorf thermomixer comfort (800 rpm). An aliquot (100 μ L) was taken after 1 h or 2 h of incubation (for prodrugs **33-38**, **45** and **46**) or at predetermined time points (for prodrug **38**), transferred to a 96-well microplate, and fluorescence for the release of MXF was recorded using a microplate reader (EnSight). A similar protocol was followed to determine the specificity of **38** toward *E. coli* and *M. smegmatis* NTR by treatment of 485 μ L bacterial lysate with varying amounts of NTR inhibitor, DCOM ranging from 100 to 500 μ M (10 μ L, 5 to 25 mM stocks) for 10 min prior to the addition of 10 μ M of **38** (5 μ L, 1 mM stock). Furthermore, a control experiment was performed by incubating **38** in heat-inactivated bacterial lysates. These lysates were prepared by heating the bacterial lysates at 90 °C for 45 min on an Eppendorf Thermomixer comfort (800 rpm) followed by cooling down to 37 °C.

3.4.12. Assessing the stability of **38** in mammalian cellular lysate by fluorescence

MEF cells were grown in culture flask in complete DMEM medium supplemented with 5% FBS (fetal bovine serum) and 1% antibiotic solution in an atmosphere of 5% CO₂ at 37 °C. When the cells were 70% confluent, old media was removed and the cells were washed with PBS buffer (1x). The cells were then detached by trypsinization, subsequently resuspended in PBS (1x) and transferred to a microcentrifuge tube. The cells were lysed by sonication using (130 W ultrasonic processor, VX 130W) stepped microtip for 2 minutes (with 5 s ON

and 10 s OFF pulse, 60% amplitude) under ice cold conditions. The total protein concentration of the whole cell lysate was determined by Bradford assay and further adjusted to 1 mg/mL with PBS (1x). The stability of **1e** was assessed by treatment of 10 μ M of **1e** (5 μ L, 1 mM stock) with 495 μ L of whole cell lysate in PBS (pH 7.4, 10 mM) at 37 °C on an Eppendorf Thermomixer comfort (800 rpm). At predetermined time points, aliquots (100 μ L) were transferred to a 96-well microplate and the fluorescence was recorded using a microplate reader (EnSight).

3.5. References

- (1) White, D. T.; Mumm, J. S. The nitroreductase system of inducible targeted ablation facilitates cell-specific regenerative studies in zebrafish. *Methods* **2013**, *62* (3), 232-240.
- (2) Sharrock, A. v; Mulligan, T. S.; Hall, K. R.; Williams, E. M.; White, D. T.; Zhang, L.; Matthews, F.; Nimmagadda, S.; Washington, S.; Le, K.; Meir-Levi, D.; Cox, O. L.; Saxena, M. T.; Calof, A. L.; Lopez-Burks, M. E.; Lander, A. D.; Ding, D.; Ji, H.; Ackerley, D. F.; Mumm, J. S. NTR 2.0: A rationally-engineered prodrug converting enzyme with substantially enhanced efficacy for targeted cell ablation. *Nat. Methods* **2022**, 205-215.
- (3) Hay, M. P.; Anderson, R. F.; Ferry, D. M.; Wilson, W. R.; Denny, W. A. Synthesis and evaluation of nitroheterocyclic carbamate prodrugs for use with nitroreductase-mediated gene-directed enzyme prodrug therapy. *J. Med. Chem.* **2003**, *46* (25), 5533-5545.
- (4) Bhaumik, S.; Sekar, T. V.; Depuy, J.; Klimash, J.; Paulmurugan, R. Noninvasive optical imaging of nitroreductase gene-directed enzyme prodrug therapy system in living animals. *Gene Ther.* **2012**, *19* (3), 295-302.
- (5) Copp, J. N.; Mowday, A. M.; Williams, E. M.; Guise, C. P.; Ashoorzadeh, A.; Sharrock, A. v.; Flanagan, J. U.; Smaill, J. B.; Patterson, A. v.; Ackerley, D. F. Engineering a multifunctional nitroreductase for improved activation of prodrugs and PET probes for cancer gene therapy. *Cell Chem. Biol.* **2017**, *24* (3), 391-403.
- (6) Vass, S. O.; Jarrom, D.; Wilson, W. R.; Hyde, E. I.; Searle, P. F. E. coli NfsA: An Alternative Nitroreductase for Prodrug Activation Gene Therapy in Combination with CB1954. *Br. J. Cancer* **2009**, *100* (12), 1903-1911.
- (7) Friedlos, F.; Denny, W. A.; Palmer, B. D.; Springer, C. J. Mustard prodrugs for activation by Escherichia coli nitroreductase in gene-directed enzyme prodrug therapy. *J. Med. Chem.* **1997**, *40* (8), 1270-1275.
- (8) Torreele, E.; Trunz, B. B.; Tweats, D.; Kaiser, M.; Brun, R.; Mazué, G.; Bray, M. A.; Pécoul, B. Fexinidazole - a new oral nitroimidazole drug candidate entering clinical development for the treatment of sleeping sickness. *PLoS Negl. Trop. Dis.* **2010**, *4* (12), 1-15.

-
- (9) Voak, A. A.; Gobalakrishnapillai, V.; Seifert, K.; Balczon, E.; Hu, L.; Hall, B. S.; Wilkinson, S. R. An essential type I nitroreductase from *Leishmania major* can be used to activate leishmanicidal prodrugs. *J. Biol. Chem.* **2013**, *288* (40), 28466-28476.
- (10) Voak, A. A.; Seifert, K.; Helsby, N. A.; Wilkinson, S. R. Evaluating aziridinyl nitrobenzamide compounds as leishmanicidal prodrugs. *Antimicrob. Agents Chemother.* **2014**, *58* (1), 370-377.
- (11) Wyllie, S.; Roberts, A. J.; Norval, S.; Patterson, S.; Foth, B. J.; Berriman, M.; Read, K. D.; Fairlamb, A. H. Activation of bicyclic nitro-drugs by a novel nitroreductase (NTR2) in *Leishmania*. *PLoS Pathog.* **2016**, *12* (11) 1-22.
- (12) Hall, B. S.; Wu, X.; Hu, L.; Wilkinson, S. R. Exploiting the drug-activating properties of a novel trypanosomal nitroreductase. *Antimicrob. Agents Chemother.* **2010**, *54* (3), 1193-1199.
- (13) Shi, S.; Du, Y.; Zou, Y.; Niu, J.; Cai, Z.; Wang, X.; Qiu, F.; Ding, Y.; Yang, G.; Wu, Y.; Xu, Y.; Zhu, Q. Rational Design for Nitroreductase (NTR)-responsive proteolysis targeting chimeras (PROTACs) selectively targeting tumor tissues. *J. Med. Chem.* **2022**, *65* (6), 5057-5071.
- (14) Prosser, G. A.; Copp, J. N.; Syddall, S. P.; Williams, E. M.; Smaill, J. B.; Wilson, W. R.; Patterson, A. v.; Ackerley, D. F. Discovery and evaluation of *Escherichia coli* nitroreductases that activate the anti-cancer prodrug CB1954. *Biochem. Pharmacol.* **2010**, *79* (5), 678-687.
- (15) Meng, F.; Bhupathi, D.; Sun, J. D.; Liu, Q.; Ahluwalia, D.; Wang, Y.; Matteucci, M. D.; Hart, C. P. Enhancement of hypoxia-activated prodrug TH-302 anti-tumor activity by Chk1 inhibition. *BMC Cancer* **2015**, *15* (422), 1-17.
- (16) Thomson, P.; Naylor, M. A.; Everett, S. A.; Stratford, M. R. L.; Lewis, G.; Hill, S.; Patel, K. B.; Wardman, P.; Davis, P. D. Synthesis and biological properties of bioreductively targeted nitrothienyl prodrugs of combretastatin A-4. *Mol. Cancer Ther.* **2006**, *5* (11), 2886-2894.
- (17) Okuda, K.; Okabe, Y.; Kadonosono, T.; Ueno, T.; Youssif, B. G. M.; Kizaka-Kondoh, S.; Nagasawa, H. 2-Nitroimidazole-tricarbo-cyanine conjugate as a near-infrared fluorescent probe for in vivo imaging of tumor hypoxia. *Bioconjug. Chem.* **2012**, *23* (3), 324-329.

-
- (18) Liu, J. N.; Bu, W.; Shi, J. Chemical design and synthesis of functionalized probes for imaging and treating tumor hypoxia. *Chem. Rev.* **2017**, *117* (9), 6160–6224.
- (19) Zhang, J.; Liu, H. W.; Hu, X. X.; Li, J.; Liang, L. H.; Zhang, X. B.; Tan, W. Efficient two-photon fluorescent probe for nitroreductase detection and hypoxia imaging in tumor cells and tissues. *Anal. Chem.* **2015**, *87* (23), 11832-11839.
- (20) Luo, S.; Zou, R.; Wu, J.; Landry, M. P. A probe for the detection of hypoxic cancer cells. *ACS Sens.* **2017**, *2* (8), 1139-1145.
- (21) Ao, X.; Bright, S. A.; Taylor, N. C.; Elmes, R. B. P. 2-nitroimidazole based fluorescent probes for nitroreductase; monitoring reductive stress in cellulose. *Org. Biomol. Chem.* **2017**, *15* (29), 6104-6108.
- (22) Kiyose, K.; Hanaoka, K.; Oushiki, D.; Nakamura, T.; Kajimura, M.; Suematsu, M.; Nishimatsu, H.; Yamane, T.; Terai, T.; Hirata, Y.; Nagano, T. Hypoxia-sensitive fluorescent probes for in vivo real-time fluorescence imaging of acute ischemia. *J. Am. Chem. Soc.* **2010**, *132* (45), 15846-15848.
- (23) Li, Z.; Li, X.; Gao, X.; Zhang, Y.; Shi, W.; Ma, H. Nitroreductase detection and hypoxic tumor cell imaging by a designed sensitive and selective fluorescent probe, 7-[(5-Nitrothiophen-2-Yl)methoxy]-3H-phenoxazin-3-one. *Anal. Chem.* **2013**, *85* (8), 3926-3932.
- (24) Li, Y.; Sun, Y.; Li, J.; Su, Q.; Yuan, W.; Dai, Y.; Han, C.; Wang, Q.; Feng, W.; Li, F. Ultrasensitive near-infrared fluorescence-enhanced probe for in vivo nitroreductase imaging. *J. Am. Chem. Soc.* **2015**, *137* (19), 6407-6416.
- (25) Li, Z.; Gao, X.; Shi, W.; Li, X.; Ma, H. 7-[(5-Nitrothiophen-2-Yl)methoxy]-3H-phenoxazin-3-one as a spectroscopic off-on probe for highly sensitive and selective detection of nitroreductase. *Chem. Commun.* **2013**, *49* (52), 5859-5861.
- (26) Jin, C.; Zhang, Q.; Lu, W. Selective turn-on near-infrared fluorescence probe for hypoxic tumor cell imaging. *RSC Adv.* **2017**, *7* (30), 18217-18223.
- (27) Xu, K.; Wang, F.; Pan, X.; Liu, R.; Ma, J.; Kong, F.; Tang, B. High selectivity imaging of nitroreductase using a near-infrared fluorescence probe in hypoxic tumor. *Chem. Commun.* **2013**, *49* (25), 2554-2556.

- (28) Wang, S.; Wu, X.; Zhang, Y.; Zhang, D.; Xie, B.; Pan, Z.; Ouyang, K.; Peng, T. Discovery of a highly efficient nitroaryl group for detection of nitroreductase and imaging of hypoxic tumor cells. *Org. Biomol. Chem.* **2021**, *19* (15), 3469-3478.
- (29) Gruber, T. D.; Krishnamurthy, C.; Grimm, J. B.; Tadross, M. R.; Wysocki, L. M.; Gartner, Z. J.; Lavis, L. D. Cell-specific chemical delivery using a selective nitroreductase-nitroaryl pair. *ACS Chem. Biol.* **2018**, *13* (10), 2888-2896.
- (30) Cui, L.; Zhong, Y.; Zhu, W.; Xu, Y.; Du, Q.; Wang, X.; Qian, X.; Xiao, Y. A new prodrug-derived ratiometric fluorescent probe for hypoxia: high selectivity of nitroreductase and imaging in tumor cell. *Org. Lett.* **2011**, *13* (5), 928-931.
- (31) Porterfield, W. B.; Jones, K. A.; McCutcheon, D. C.; Prescher, J. A. A “Caged” luciferin for imaging cell-cell contacts. *J. Am. Chem. Soc.* **2015**, *137* (27), 8656-8659.
- (32) Shi, Y.; Zhang, S.; Zhang, X. A novel near-infrared fluorescent probe for selectively sensing nitroreductase (NTR) in an aqueous medium. *Analyst* **2013**, *138* (7), 1952-1955.
- (33) Guo, T.; Cui, L.; Shen, J.; Zhu, W.; Xu, Y.; Qian, X. A highly sensitive long-wavelength fluorescence probe for nitroreductase and hypoxia: selective detection and quantification. *Chem. Commun.* **2013**, *49* (92), 10820-10822.
- (34) Li, H.; Jintao, F.; Wang, Z.; Jia, Y.; Li, P.; Yao, C.; Qu, Z. A highly selective fluorescent probe for the detection of nitroreductase based on a naphthalimide scaffold. *J. Fluoresc.* **2022**, *32* (5), 1825-1832.
- (35) Grimm, J. B.; Gruber, T. D.; Ortiz, G.; Brown, T. A.; Lavis, L. D. Virginia orange: A versatile, red-shifted fluorescein scaffold for single- and dual-input fluorogenic probes. *Bioconjug. Chem.* **2016**, *27* (2), 474-480.
- (36) Li, M.; Kong, X.; Yin, Y.; Zhang, Y.; Dai, X.; Wang, J.; Lin, W. A novel red-emitting two-photon fluorescent probe for imaging nitroreductases in cancer cells and tumor tissues with hypoxia conditions. *J. Photochem. Photobiol. A: Chem.* **2022**, *424* (113657), 1-5.
- (37) Zhou, Y.; Bobba, K. N.; Lv, X. W.; Yang, D.; Velusamy, N.; Zhang, J. F.; Bhuniya, S. A biotinylated piperazine-rhodol derivative: A “turn-on” probe for nitroreductase triggered hypoxia imaging. *Analyst* **2017**, *142* (2), 345-350.

- (38) Liu, T.; Wang, Y.; Feng, L.; Tian, X.; Cui, J.; Yu, Z.; Wang, C.; Zhang, B.; James, T. D.; Ma, X. 2D strategy for the construction of an enzyme-activated nir fluorophore suitable for the visual sensing and profiling of homologous nitroreductases from various bacterial species. *ACS Sens.* **2021**, *6* (9), 3348-3356.
- (39) Xu, S.; Wang, Q.; Zhang, Q.; Zhang, L.; Zuo, L.; Jiang, J. D.; Hu, H. Y. Real time detection of ESKAPE pathogens by a nitroreductase-triggered fluorescence turn-on probe. *Chem. Commun.* **2017**, *53* (81), 11177-11180.
- (40) Lee, M. K.; Williams, J.; Twieg, R. J.; Rao, J.; Moerner, W. E. Enzymatic activation of nitro-aryl fluorogens in live bacterial cells for enzymatic turnover-activated localization microscopy. *Chem. Sci.* **2013**, *4* (1), 220-225.
- (41) Sharma, K.; Sengupta, K.; Chakrapani, H. Nitroreductase-activated nitric oxide (NO) prodrugs. *Bioorg. Med. Chem. Lett.* **2013**, *23* (21), 5964-5967.
- (42) Hibbard, H. A. J.; Reynolds, M. M. Synthesis of novel nitroreductase enzyme-activated nitric oxide prodrugs to site-specifically kill bacteria. *Bioorg. Chem.* **2019**, *93* (103318), 1-7.
- (43) Shukla, P.; Khodade, V. S.; SharathChandra, M.; Chauhan, P.; Mishra, S.; Siddaramappa, S.; Pradeep, B. E.; Singh, A.; Chakrapani, H. "On Demand" redox buffering by H₂S contributes to antibiotic resistance revealed by a bacteria-specific H₂S donor. *Chem. Sci.* **2017**, *8* (7), 4967-4972.
- (44) Spain, J. C. Biodegradation of nitroaromatic compounds. *Annu. Rev. Microbiol.* **1995**, *49* (1), 523-555.
- (45) Ramos, J. L.; González-Pérez, M. M.; Caballero, A.; Dillewijn, P. van. Bioremediation of polynitrated aromatic compounds: plants and microbes put up a fight. *Curr. Opin. Biotechnol.* **2005**, *16*, 275-281.
- (46) Lewis, T. A.; Goszczyński, S.; Crawford, R. L.; Korus, R. A.; Admassu, W. Products of anaerobic 2,4,6-Trinitrotoluene (TNT) transformation by *Clostridium bifermentans*. *Appl. Environ. Microbiol.* **1996**, *62* (12), 4669-4674.
- (47) Rieger, P.-G.; Meier, H.-M.; Gerle, M.; Vogt, U.; Groth, T.; Knackmuss, H.-J. Xenobiotics in the environment: present and future strategies to obviate the problem of biological persistence. *J. Biotechnol.* **2002**, *94* (1), 101-123.

- (48) Vorobyeva, A. G.; Stanton, M.; Godinat, A.; Lund, K. B.; Karateev, G. G.; Francis, K. P.; Allen, E.; Gelovani, J. G.; McCormack, E.; Tangney, M.; Dubikovskaya, E. A. development of a bioluminescent nitroreductase probe for preclinical imaging. *PLoS One* **2015**, *10* (6), e0131037, 1-18.
- (49) Yang, X.; Li, Z.; Jiang, T.; Du, L.; Li, M. A coelenterazine-type bioluminescent probe for nitroreductase imaging. *Org. Biomol. Chem.* **2017**, *16* (1), 146-151.
- (50) Feng, P.; Zhang, H.; Deng, Q.; Liu, W.; Yang, L.; Li, G.; Chen, G.; Du, L.; Ke, B.; Li, M. Real-time bioluminescence imaging of nitroreductase in mouse model. *Anal. Chem.* **2016**, *88* (11), 5610-5614.
- (51) Çelik, A.; Yetiş, G.; Ay, M.; Güngör, T. Modification of existing antibiotics in the form of precursor prodrugs that can be subsequently activated by nitroreductases of the target pathogen. *Bioorg. Med. Chem. Lett.* **2016**, *26* (16), 4057-4060.
- (52) Galeh, T. M.; Kazemi, A.; Mahami-Oskouei, M.; Baradaran, B.; Spotin, A.; Sarafraz, S.; Karamat, M. Introducing nitazoxanide as a promising alternative treatment for symptomatic to metronidazole-resistant giardiasis in clinical isolates. *Asian Pac. J. Trop. Med.* **2016**, *9* (9), 887-892.
- (53) Crofts, T. S.; Sontha, P.; King, A. O.; Wang, B.; Bidy, B. A.; Zanolli, N.; Gaumnitz, J.; Dantas, G. Discovery and characterization of a nitroreductase capable of conferring bacterial resistance to chloramphenicol. *Cell Chem. Biol.* **2019**, *26* (4), 559-570.e6.
- (54) Holt, R. The Bacterial Degradation of Chloramphenicol. *Lancet* **1967**, *1*, 1259-1260.
- (55) Herrlinger, E.-M.; Hau, M.; Melanie Redhaber, D.; Greve, G.; Willmann, D.; Steimle, S.; Müller, M.; Lübbert, M.; Cornelius Miething, C.; Schüle, R.; Jung, M. Nitroreductase-mediated release of inhibitors of lysine-specific demethylase 1 (LSD1) from prodrugs in transfected acute myeloid leukaemia cells. *ChemBioChem.* **2020**, *21* (16), 2329-2347.
- (56) Jiang, T.; Kumar, P.; Huang, W.; Kao, W. S.; Thompson, A. O.; Camarda, F. M.; Laughlin, S. T. Modular enzyme- and light-based activation of cyclopropene-tetrazine ligation. *ChemBioChem.* **2019**, *20* (17), 2222-2226.
- (57) Islip, P. J.; Closier, M. D.; Neville, M. C. Antiparasitic 5-nitrothiazoles and 5-nitro-4-thiazolines. *J. Med. Chem.* **1974**, *17* (2), 207-209.

- (58) Müller, J.; Wastling, J.; Sanderson, S.; Müller, N.; Hemphill, A. A novel giardia lamblia nitroreductase, G1NR1, interacts with nitazoxanide and other thiazolides. *Antimicrob Agents. Chemother.* **2007**, *51* (6), 1979-1986.
- (59) Hof, H.; Zakt, O.; Schweizerf, E.; Denzler, A. Antibacterial activities of nitrothiazole derivatives. *J. Antimicrob. Chemother.* **1984**, *14* (1), 31-39.
- (60) Koenig, H. N.; Durling, G. M.; Walsh, D. J.; Livinghouse, T.; Stewart, P. S. Novel nitro-heteroaromatic antimicrobial agents for the control and eradication of biofilm-forming bacteria. *Antibiotics* **2021**, *10* (7), 855.
- (61) Odingo, J.; Bailey, M. A.; Files, M.; Early, J. v.; Alling, T.; Dennison, D.; Bowman, J.; Dalai, S.; Kumar, N.; Cramer, J.; Masquelin, T.; Hipskind, P. A.; Parish, T. In vitro evaluation of novel nitazoxanide derivatives against Mycobacterium tuberculosis. *ACS Omega* **2017**, *2* (9), 5873-5890.
- (62) Jeankumar, V. U.; Chandran, M.; Samala, G.; Alvala, M.; Koushik, P. V.; Yogeewari, P.; Salina, E. G.; Sriram, D. Development of 5-nitrothiazole derivatives: identification of leads against both replicative and latent Mycobacterium tuberculosis. *Bioorg. Med. Chem. Lett.* **2012**, *22* (24), 7414-7417.
- (63) de Carvalho, L. P.; Lin, G.; Jiang, X.; Nathan, C. Nitazoxanide kills replicating and nonreplicating Mycobacterium tuberculosis and evades resistance. *J. Med. Chem.* **2009**, *52* (19), 5789-5792.
- (64) Roldán, M. D.; Pérez-Reinado, E.; Castillo, F.; Moreno-Vivián, C. Reduction of polynitroaromatic compounds: the bacterial nitroreductases. *FEMS Microbiol. Rev.* **2008**, *32* (3), 474-500.
- (65) Stokes, J. M.; Yang, K.; Swanson, K.; Jin, W.; Cubillos-Ruiz, A.; Donghia, N. M.; MacNair, C. R.; French, S.; Carfrae, L. A.; Bloom-Ackerman, Z.; Tran, V. M.; Chiappino-Pepe, A.; Badran, A. H.; Andrews, I. W.; Chory, E. J.; Church, G. M.; Brown, E. D.; Jaakkola, T. S.; Barzilay, R.; Collins, J. J. A deep learning approach to antibiotic discovery. *Cell* **2020**, *180* (4), 688-702.e13.
- (66) Sun, Z.; Zhang, H.; Zhang, H.; Wu, J.; Gao, F.; Zhang, C.; Hu, X.; Liu, Q.; Wei, Y.; Wei, Y.; Zhuang, J.; Zhuang, J.; Huang, X. A novel model system for understanding anticancer activity of hypoxia-activated prodrugs. *Mol. Pharm.* **2020**, *17* (6), 2072–2082.

- (67) Parkinson, G. N.; Skelly, J. v.; Neidle, S. Crystal Structure of FMN-dependent nitroreductase from *Escherichia coli* b: a prodrug-activating enzyme. *J. Med. Chem.* **2000**, *43* (20), 3624–3631.
- (68) Christofferson, A.; Wilkie, J. Mechanism of CB1954 reduction by *Escherichia coli* nitroreductase. *Biochem. Soc. Trans.* **2009**, *37* (2), 413–418.
- (69) Marcus, R. A. On the theory of oxidation-reduction reactions involving electron transfer. I. *J. Chem. Phys.* **1956**, *24* (5), 966–978.
- (70) Marcus, R. A. Electron transfer reactions in chemistry: theory and experiment. *Angew. Chem. Int. Ed. Engl.* **1993**, *32* (8), 1111–1121.
- (71) Johansson, E.; Parkinson, G. N.; Denny, W. A.; Neidle, S. Studies on the nitroreductase prodrug-activating system. crystal structures of complexes with the inhibitor dicoumarol and dinitrobenzamide prodrugs and of the enzyme active form. *J. Med. Chem.* **2003**, *46* (19), 4009–4020.
- (72) de Jesus Lopes Ribeiro, A. L.; Degiacomi, G.; Ewann, F.; Buroni, S.; Incandela, M. L.; Chiarelli, L. R.; Mori, G.; Kim, J.; Contreras-Dominguez, M.; Park, Y. S.; Han, S. J.; Brodin, P.; Valentini, G.; Rizzi, M.; Riccardi, G.; Pasca, M. R. Analogous mechanisms of resistance to benzothiazinones and dinitrobenzamides in *Mycobacterium smegmatis*. *PLoS One* **2011**, *6* (11) 1-7.
- (73) Manina, G.; Bellinzoni, M.; Pasca, M. R.; Neres, J.; Milano, A.; de Jesus Lopes Ribeiro, A. L.; Buroni, S.; Škovierová, H.; Dianišková, P.; Mikušová, K.; Marák, J.; Makarov, V.; Giganti, D.; Haouz, A.; Lucarelli, A. P.; Degiacomi, G.; Piazza, A.; Chiarelli, L. R.; de Rossi, E.; Salina, E.; Cole, S. T.; Alzari, P. M.; Riccardi, G. Biological and structural characterization of the *mycobacterium smegmatis* nitroreductase NfnB, and its role in benzothiazinone resistance. *Mol. Microbiol.* **2010**, *77* (5), 1172–1185.
- (74) Buchieri, M. v.; Cimino, M.; Rebollo-Ramirez, S.; Beauvineau, C.; Cascioferro, A.; Favre-Rochex, S.; Helynck, O.; Naud-Martin, D.; Larrouy-Maumus, G.; Munier-Lehmann, H.; Gicquel, B. Nitazoxanide analogs require nitroreduction for antimicrobial activity in *Mycobacterium smegmatis*. *J. Med. Chem.* **2017**, *60* (17), 7425–7433.
- (75) Jirapanjawat, T.; Ney, B.; Taylor, M. C.; Warden, A. C.; Afroze, S.; Russell, R. J.; Lee, B. M.; Jackson, C. J.; Oakeshott, J. G.; Pandey, G.; Greening, C. The redox cofactor

- F420 protects mycobacteria from diverse antimicrobial compounds and mediates a reductive detoxification system. *Appl. Environ. Microbiol.* **2016**, *82* (23), 6810–6818.
- (76) Chauviac, F. X.; Bommer, M.; Yan, J.; Parkin, G.; Daviter, T.; Lowden, P.; Raven, E. L.; Thalassinos, K.; Keep, N. H. Crystal structure of reduced MsAcg, a putative nitroreductase from mycobacterium smegmatis and a close homologue of mycobacterium tuberculosis Acg. *J. Biol. Chem.* **2012**, *287* (53), 44372–44383.
- (77) Hu, Y.; Coates, A. R. M. Mycobacterium tuberculosis Acg gene is required for growth and virulence in vivo. *PLoS One* **2011**, *6* (6) 1-11.
- (78) Cellitti, S. E.; Shaffer, J.; Jones, D. H.; Mukherjee, T.; Gurumurthy, M.; Bursulaya, B.; Boshoff, H. I.; Choi, I.; Nayyar, A.; Lee, Y. S.; Cherian, J.; Niyomrattanakit, P.; Dick, T.; Manjunatha, U. H.; Barry, C. E.; Spraggon, G.; Geierstanger, B. H. Structure of Ddn, the deazaflavin-dependent nitroreductase from Mycobacterium tuberculosis involved in bioreductive activation of PA-824. *Structure*, **2012**, *20* (1–2), 101–112.
- (79) Negri, A.; Javidnia, P.; Mu, R.; Zhang, X.; Vendome, J.; Gold, B.; Roberts, J.; Barman, D.; Ioerger, T.; Sacchettini, J. C.; Jiang, X.; Burns-Huang, K.; Warriar, T.; Ling, Y.; Warren, J. D.; Oren, D. A.; Beuming, T.; Wang, H.; Wu, J.; Li, H.; Rhee, K. Y.; Nathan, C. F.; Liu, G.; Somersan-Karakaya, S. Identification of a mycothiol-dependent nitroreductase from Mycobacterium tuberculosis. *ACS Infect. Dis.* **2018**, *4* (5), 771–787.
- (80) Peddireddy, V.; Doddam, S. N.; Qureshi, I. A.; Yerra, P.; Ahmed, N. A Putative Nitroreductase from the DosR Regulon of mycobacterium tuberculosis induces pro-inflammatory cytokine expression via TLR2 signaling pathway. *Sci. Rep.* **2016**, *6* (24535), 1–9.
- (81) Dong, W.; Shi, J.; Chu, P.; Liu, R.; Wen, S.; Zhang, T.; Pang, Y.; Lu, J. Rv3131, a gene encoding nitroreductase, is essential for metronidazole activation in Mycobacterium tuberculosis under hypoxic condition. *Res. Sq.* **2020**.
- (82) Chauhan, S.; Sharma, D.; Singh, A.; Surolia, A.; Tyagi, J. S. Comprehensive insights into mycobacterium tuberculosis DevR (DosR) regulon activation switch. *Nucleic Acids Res.* **2011**, *39* (17), 7400–7414.
- (83) Sherman, D. R.; Voskuil, M.; Schnappinger, D.; Liao, R.; Harrell, M. I.; Schoolnik, G. K. Regulation of the Mycobacterium tuberculosis hypoxic response gene encoding α -Crystallin. *Proc. Natl. Acad. Sci. U. S. A.* **2001**, *98* (13), 7534 LP – 7539.

- (84) Purkayastha, A.; McCue, L. A.; McDonough, K. A. Identification of a mycobacterium tuberculosis putative classical nitroreductase gene whose expression is coregulated with that of the Acr gene within macrophages, in standing versus shaking cultures, and under low oxygen conditions. *Infect. Immun.* **2002**, *70* (3), 1518–1529.

Chapter 4: Evaluation of Antibacterial and Antimycobacterial activity of NTR-MXF prodrugs

4.1. Introduction

As described in the previous chapters, a focussed library of nitroheterocyclic esters and carbamates of MXF were synthesized and then their ability to generate MXF under chemo- and bio-reductive conditions in Chapter 2 and Chapter 3 respectively was investigated. Detailed analysis showed that one of the analogues **38** was efficiently activated by bacterial NTR to produce MXF quantitatively. Herein, the antibacterial activity of prodrugs, including **38** against gram-positive and gram-negative bacteria as well as mycobacteria was evaluated.

4.2. Results and discussion

4.2.1. *In vitro* antibacterial activity

The antibacterial activity of NTR-MXF prodrugs were assessed against *S. aureus* ATCC 29213 (gram-positive) and *E. coli* ATCC 25922 (gram-negative) by our collaborator Dr. Sidharth Chopra Lab, CSIR-CDRI, Lucknow. Although the prodrugs **33-38**, **45** and **46** (Table 4.1) differ only in nature of bioreductive functional group, they exhibit different antibacterial activities. Among the prodrugs evaluated, **38** was remarkably active and exhibited significant potency (MIC, 0.09 μ M) against *E. coli* and *S. aureus*, comparable to that of MXF (MIC of 0.078 μ M against *S. aureus* and 0.039 μ M against *E. coli*), parent FQ (Table 4.1, entries 1 and 7) presumably due to higher amount of MXF release triggered by bacterial NTR as shown earlier in Chapter 3. Furthermore, **38** showed a significant reduction in bacterial burden of *E. coli* in a neutropenic thigh infection murine model similar to MXF (Figure 4.1).

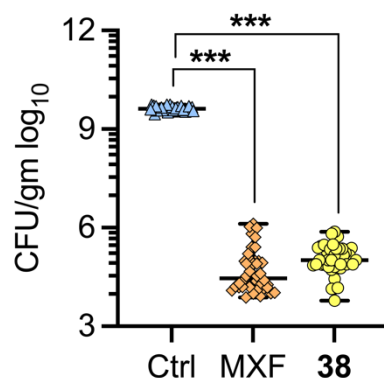


Figure 4.1. *In vivo* efficacy of **38** (10 mg/kg) against *E.coli* ATCC 25922 in a neutropenic murine thigh infection model. MXF (10 mg/kg) was used as a reference compound while Ctrl is untreated mice. Statistical significance was established with respect to Ctrl (***) ($p < 0.001$). Data was provided by Dr. Sidharth Chopra Lab, CSIR-CDRI, Lucknow.

4.2.2. *In vitro* antimycobacterial activity

4.2.2.1. Against *M. smegmatis mc²155*

These prodrugs were evaluated against *Mycobacterium smegmatis* (*Msm*), a rapidly growing mycobacterial species using resazurin reduction microplate assay (REMA). REMA is a reliable colorimetric method used to test the drug susceptibility for mycobacteria. The cellular metabolic activity was assessed by the reduction of oxidized non-fluorescent blue resazurin to a highly fluorescent pink colored resorufin (Scheme 4.1).¹ The presence of blue color indicate an absence of bacterial growth, while the pink color show resazurin reduction as a result of bacterial growth and metabolism. As expected, MXF (MIC = 0.25 μ M) was effective against *Msm* (Table 4.1, entry 1). Of those tested, prodrugs **38** again displayed potent activity against *Msm* equivalent to MXF (MIC = 0.25 μ M) (Figure 4.2, Figure 4.3 and Table 4.1, entries 2-7).

Scheme 4.1. Reduction of Resazurin

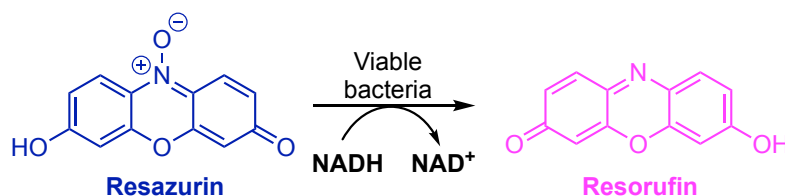
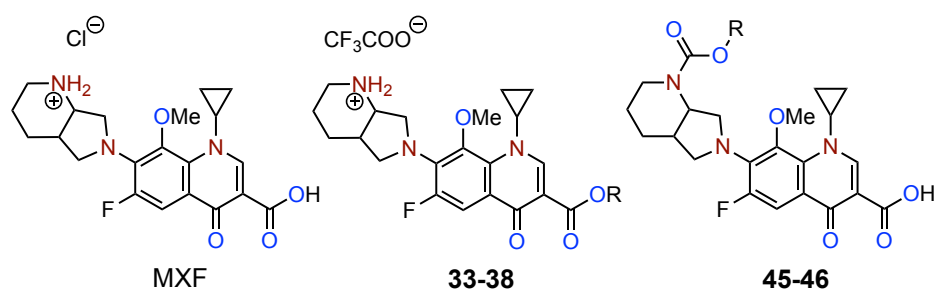


Table 4.1. Antibacterial activity of MXF prodrugs against *E. coli*, *S. aureus* and *M. smegmatis*

| Entry | Prodrug/ Drug, MIC (μM) | R | <i>S. aureus</i> (ATCC 29213)* | <i>E. coli</i> (ATCC 25922)* | <i>M. smegmatis</i> <i>mc</i> ² 155 |
|-------|---|---|--------------------------------------|------------------------------------|---|
| 1 | MXF | - | 0.078 | 0.039 | 0.25 |
| 2 | 33 | | 6.1 | 3.0 | 4 |
| 3 | 34 | | 1.5 | 0.39 | 2 |
| 4 | 35 | | 3.0 | 1.5 | 4 |
| 5 | 36 | | 24.4 | 6.1 | 4 |
| 6 | 37 | | 1.5 | 1.5 | 2 |
| 7 | 38 | | 0.09 | 0.09 | 0.25 |
| 8 | 45 | | 3.4 | 13 | - |
| 9 | 46 | | 0.05 | 0.85 | 0.5 |

*Data was provided by Dr. Sidharth Chopra Lab, CSIR-CDRI, Lucknow

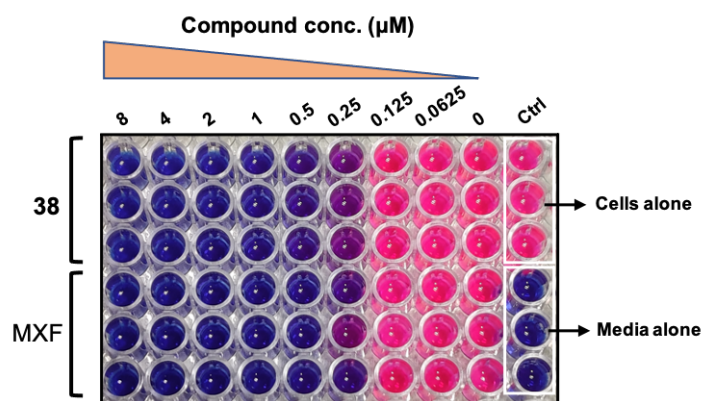


Figure 4.2. Minimum inhibitory concentrations (MIC) of **38** and MXF against *Mycobacterium smegmatis* (mc²155; *Msm*) determined by Resazurin reduction microplate assay (REMA)

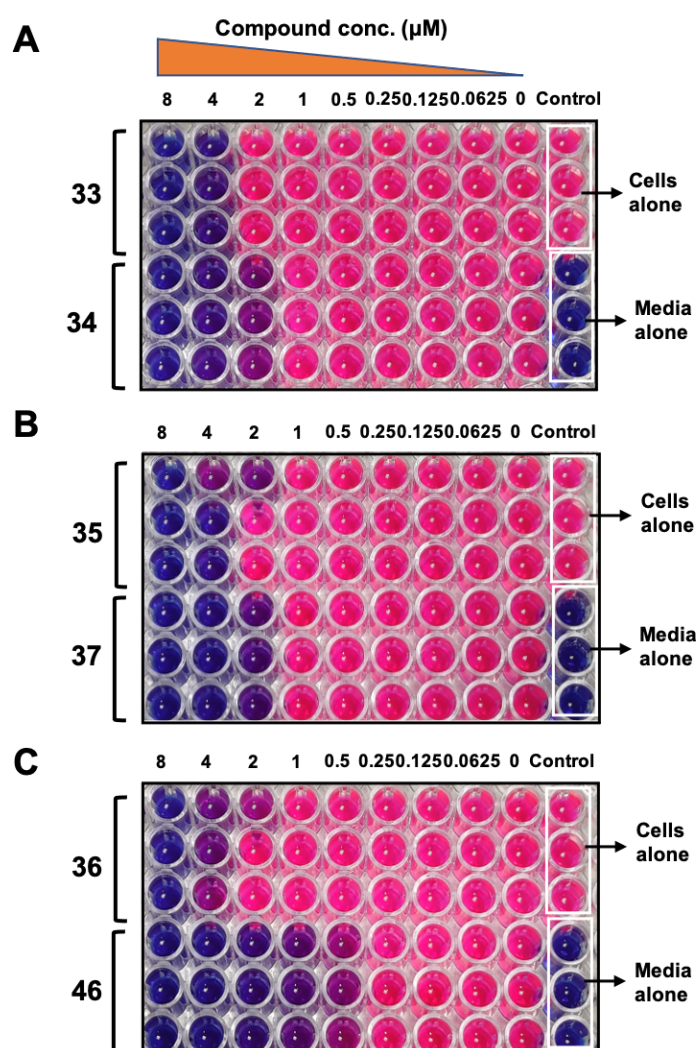


Figure 4.3. Minimum inhibitory concentrations (MIC) of prodrugs (A) **33** and **34**, (B) **35** and **37**, and (C) **36** and **46** against *Mycobacterium smegmatis* (mc²155; *Msm*) determined by Resazurin reduction microplate assay (REMA)

4.2.2.2. Against *M. tuberculosis* H37Rv

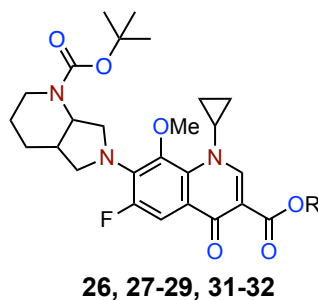
With the results from *Msm* study in hand, the prodrugs were then evaluated against pathogen *Mtb* H37Rv. The data was provided by Prof. Amit Singh, IISc Bangalore. The prodrugs **38** and **46** (MIC = 0.25 μ M) exhibited remarkable potent anti-mycobacterial activity equivalent to MXF (MIC = 0.25 μ M) against drug-susceptible *Mtb* (Table 4.2, entries 1, 7 and 11). Furthermore, these prodrugs were more potent than other prodrugs (Table 4.2, entries 2-11).

Interestingly, *N*-boc protected counterparts lacked activity, likely as a result of reduced permeability into bacterial cells or due to poor engagement with its targets (DNA gyrase or topoisomerase IV) (Table 4.3).

Table 4.2. Antimycobacterial activity of prodrugs against *Mtb*

| Entry | Prodrug/Drug | MIC (μ M), <i>M.tuberculosis</i> H37Rv |
|-------|--------------|--|
| 1 | MXF | 0.25 |
| 2 | 33 | 2 |
| 3 | 34 | 8 |
| 4 | 35 | 2-8 |
| 6 | 37 | 1 |
| 7 | 38 | 0.25 |
| 8 | 41 | 1 |
| 9 | 42 | 2-8 |
| 10 | 45 | >8 |
| 11 | 46 | 0.25 |

*Data was provided by Prof. Amit Singh Lab, IISc, Bangalore

Table 4.3. Antimycobacterial activity of *N*-boc protected MXF derivatives against *Mtb*

| Entry | Prodrug/Drug | R | MIC (μM), <i>M. tuberculosis</i> H37Rv |
|-------|--------------|---|--|
| 1 | 26 | H | >8 |
| 2 | 27 | | >8 |
| 3 | 28 | | >8 |
| 4 | 29 | | >8 |
| 5 | 31 | | >8 |
| 6 | 32 | | >8 |

*Data was provided by Prof. Amit Singh Lab, IISc, Bangalore

The cytotoxicity studies of prodrugs were then examined in VERO cells. The prodrugs **37** and **38** exhibited a better selective index than the tested compounds (Table 4.4). Although both the prodrugs were better tolerated by mammalian cells, the prodrug **38** demonstrated more potent antibacterial and antimycobacterial activity than **37** and **46** (Table 4.1, entries 6-7 and Table 4.4, entries 5-6 and 8). This encouraged us to pursue prodrug **38** for further studies. The prodrug **38** demonstrated significant anti-mycobacterial activity similar to MXF against patient derived clinical isolates of *Mtb* (MDR = multidrug-resistant and XDR = extensively drug-resistant) resistant to first- and second-line anti-TB drugs (Table 4.5).

Table 4.4. Selective indices of MXF prodrugs

| Entry | Prodrug/Drug | ^a CC ₅₀ | ^b MIC ₉₀ | ^c Selective Index (SI) |
|-------|--------------|-------------------------------|--------------------------------|-----------------------------------|
| 1 | MXF | 20 | 0.109 | 183 |
| 2 | 33 | 40 | 1.30 | 30 |
| 3 | 34 | 10 | 5.12 | 2 |
| 4 | 35 | 40 | 1.31-5.25 | 8-30 |
| 5 | 37 | 40 | 0.65 | 61 |
| 6 | 38 | 10 | 0.16 | 62 |
| 7 | 45 | 80 | 4.64 | 17 |
| 8 | 46 | 5 | 0.14 | 36 |

^aCC₅₀ (µg/mL) = cytotoxic concentration 50% against monkey (Vero cells); ^bMIC₉₀ (µg/mL) = minimum concentration required to inhibit 90% of *Mtb* growth; ^cSI = CC₅₀/ MIC₉₀; ^{a,b}Data was provided by Dr. Sidharth Chopra, CSIR-CDRI, Lucknow and Prof. Amit Singh, IISc Bangalore respectively.

Table 4.5. MIC of MXF and **38** against drug resistant clinical isolates of *Mtb*

| Entry | <i>M. tuberculosis</i> strains | | MIC (µM) | |
|-------|--------------------------------|---------|----------|-----------|
| | | | MXF | 38 |
| 1 | ^a MDR | BND320 | 0.25 | 0.125 |
| 2 | ^b XDR | Jal1934 | 0.25 | 0.25 |
| 3 | | Jal2261 | 0.25 | 0.25 |
| 4 | | MYC431 | 0.25 | 0.25 |

^aMultidrug-resistant (MDR) and ^bExtensively drug-resistant (XDR) strains of *Mtb*; Data was provided by Prof. Amit Singh, IISc Bangalore)

Time-kill analysis indicated that the prodrug **38** was bactericidal and significantly reduced viable bacteria of *Mtb* at 5x MIC comparable to MXF (Figure 4.4).

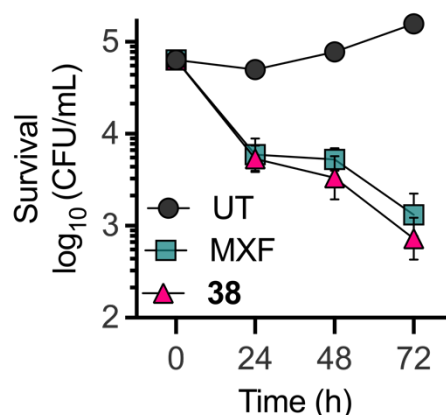


Figure 4.4. Bacterial survival kinetics after treatment of THP-1 macrophages infected with *Mtb* H37Rv at 5x MIC of **38** and MXF. Data was provided by Prof. Amit Singh, IISc Bangalore.

The efficacy of **38** against dormant *Mtb* was evaluated against non-replicating *Mtb* in Wayne hypoxia dormancy model. Hypoxic *Mtb* cells were challenged with MXF and **38** at 10x MIC and the viability of cells were evaluated by hypoxia resazurin reduction assay (HyRRA) and CFU enumeration (Figure 4.5.A-B). Interestingly, the non-replicating *Mtb* cells were highly tolerant to INH (Isoniazid, first-line drug) and MXF but were rather more susceptible to **38**, MXF prodrug. Collectively, prodrug **38** exhibited potent antimycobacterial activity against non-replicating *Mtb* while retaining mycobactericidal activity similar to MXF against replicating *Mtb*.

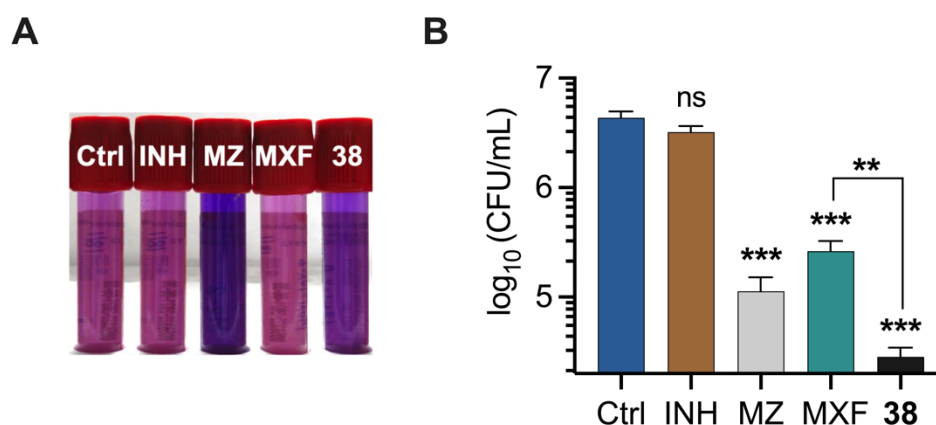


Figure 4.5. Bactericidal activity of **38** against non-replicating *Mtb*. (A) Mycobactericidal effect of MXF and **38** at indicated concentrations (10x MIC) on hypoxia-adapted *Mtb* bacilli

based on visual hypoxia resazurin reduction assay (HyRRA). Isoniazid (INH, 10 μ M) and Metronidazole (MZ, 10 mM) served as a negative and positive control respectively. The pink colour in the tube indicates cell viability under hypoxia while blue colour indicates no growth. (B) Survival of *Mtb* under hypoxia was measured as log₁₀ of colony-forming units (CFU) after treatment with 10x MIC of MXF and **38** for 5 days. Data represent at least three independent experiments performed in triplicate. Error bars represent standard deviation from the mean. Statistical significance was established relative to untreated bacteria control (Ctrl) using unpaired *t*-test with welch's correction student's (** $p \leq 0.01$, *** $p \leq 0.001$ and ns indicate not significant).

4.2.3. Plausible mechanisms behind the enhanced efficacy of **38**

Because **38** is a prodrug of MXF, we posited that NTR triggered decomposition of prodrug would exert the antibacterial activity as a result of the inhibition of DNA gyrase by the released active antibiotic MXF. We examined the antibacterial activity of **38** and MXF against FQ-resistant clinical isolates of *E. coli* (Table 4.6).

Table 4.6. MIC of MXF and **38** against FQ-sensitive and resistant strains of *E. coli*

| Entry | <i>E. coli</i> | MIC (μ M)* | |
|-------|----------------|-----------------|-----------|
| | | MXF | 38 |
| 1 | ATCC 25922 | 0.039 | 0.09 |
| 2 | NR 17661 | 73 | >97 |
| 3 | NR 48983 | 73 | >97 |
| 4 | NR 51487 | 73 | >97 |

(Data was provided by Dr. Sidharth Chopra, CSIR-CDRI, Lucknow)

As anticipated, mutants (NR 17661, NR 48983 and NR 51487) challenged with **38** displayed a particularly high MIC value as compared to the wild-type strain (ATCC 25922) similar to MXF (Table 4.6, entries 1-4). These results indicate that **38** and MXF operate through a common mode of action.

Despite the fact that these studies unequivocally show that the prodrug behaves identical to MXF against replicating *Mtb*, these findings do not provide an explanation underlying the enhanced lethality of **38** over MXF in non-replicating *Mtb*. As mentioned earlier, the presence of lipid enriched thickened cell wall is one of the important factors that contributes to the

reduced permeation of MXF in non-replicating *Mtb*.²⁻⁴ Given that the prodrug **38** (clogP = 1.05) is more lipophilic than MXF (clogP = -0.49), the prodrug could augment the efficacy of MXF by increasing its intracellular concentration in non-replicating *Mtb*. Therefore, studies were conducted to quantitate the intracellular concentrations of MXF and **38**.

4.2.4. Accumulation studies

Radiolabelled and fluorescence-based compounds are often used to detect and quantify the intracellular concentration of the compounds within bacteria.⁵⁻¹² The intrinsic fluorescence of fluoroquinolones has frequently been used as a surrogate to measure the cellular internalization of clinically relevant quinolone antibiotics into bacteria.^{5,13,14} Initially, we chose to optimize spectrofluorimetric based permeability study using *E. coli* as a model organism.

4.2.4.1. Fluorescence based accumulation studies

Infact, Pandeya and co-workers relied on the fluorescence emission intensity of FQ to quantify the uptake and subcellular distribution of the drug by gram-negative bacteria.¹⁴ A preliminary fluorescence-based accumulation assay was performed with MXF (5 μ M). After incubation of *E. coli* ATCC 25922 at 37 °C for 15 min with MXF, the drug-treated bacteria were centrifuged through silicone oil. This silicone oil method eliminates the need for numerous washes to remove the extracellular compound and results in a greater signal of the compound. After centrifugation, the resulting bacterial pellets were resuspended in pH 3.0 glycine-HCl buffer and lysed by sonication to afford whole-cell lysates. To evaluate the relative distribution of MXF in the periplasmic and cytoplasmic compartments of *E. coli* cells, the drug-treated bacterial pellets collected above were subjected to osmotic shock. After centrifugation, supernatant with the periplasmic fraction was carefully separated from the bacterial pellet. The cell pellet enriched with the cytoplasmic component was resuspended in glycine-HCl buffer and lysed. The fluorescence intensity of MXF ($\lambda_{\text{ex}} = 289$ nm and $\lambda_{\text{em}} = 488$ nm) was recorded in all the collected fractions, and then the amount of accumulated drug was quantified by using a calibration curve (Figure 4.6 and 4.7).

Strikingly, MXF accumulated in periplasm, cytoplasm and whole cell fractions of *E. coli*. It was found that the fluorescence intensity corresponding to MXF in the periplasmic compartment was higher than in the cytoplasmic and whole-cell components. This observation suggested that MXF accumulated in the periplasm at a higher concentration (Figure 4.7). This false positive result could originate either from

possible non-specific binding of MXF to uncharacterized periplasmic proteins or from leakage of MXF from the cytoplasmic compartment during osmotic shock. These findings are again congruent with the outcomes obtained by Pandeya and coworkers.¹⁴

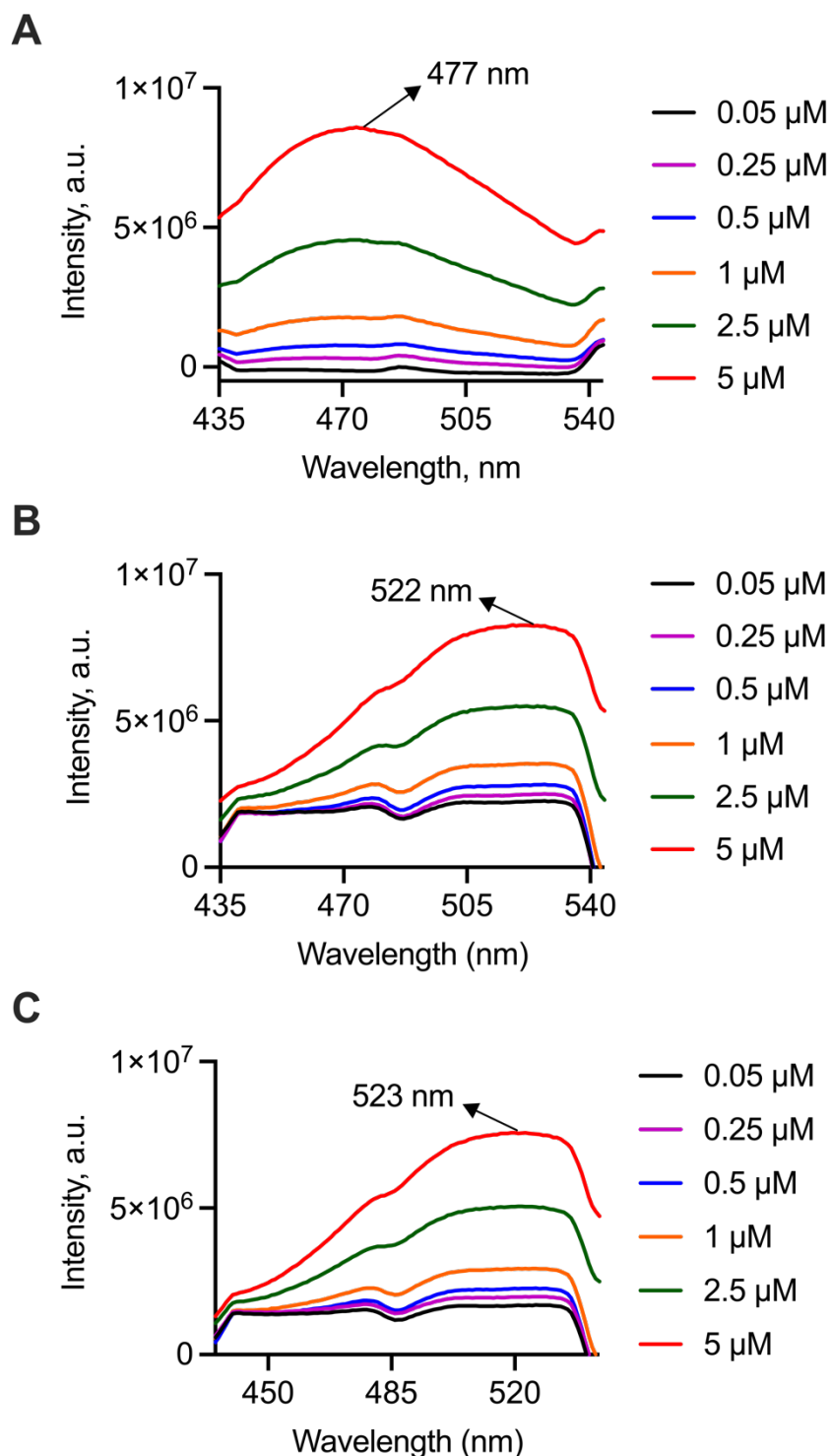


Figure 4.6. Emission spectra of MXF (excited at 289 nm) in (A) periplasmic, (B) cytosolic fractions and (C) whole-cell fractions lysates of *E. coli* ATCC 25922

Furthermore, MXF accumulated in the cytoplasmic and whole-cell fractions to a similar extent, albeit to a lesser degree in the whole-cell lysate. However, all drug-treated samples showed a marked alteration in the emission spectra of MXF (Figure 4.6). This may be due to an interference from background fluorescence from the media and/or bacterial autofluorescence, among other things. This prompted us to utilize LC-MS/MS, a more popular and straightforward technique, to measure the intracellular accumulation of MXF. Moreover, this method has advantages over fluorimetry for detecting intracellular levels of drug, even at nanomolar or picomolar concentrations.

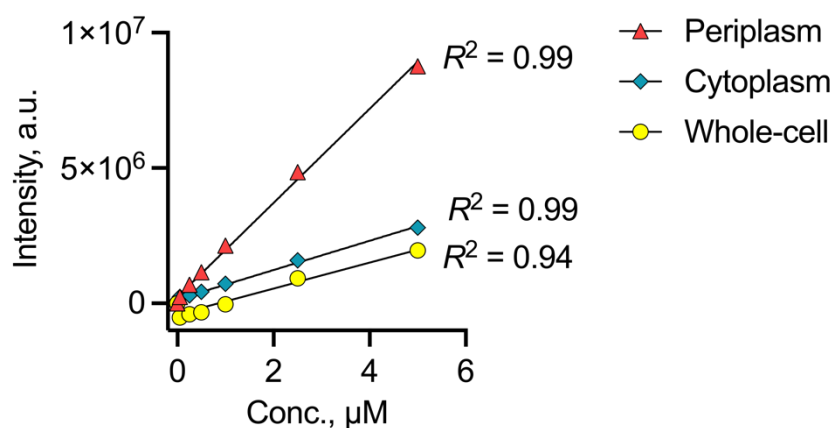


Figure 4.7. Calibration curve for MXF ($\lambda_{\text{ex}} = 289 \text{ nm}$ and $\lambda_{\text{em}} = 488 \text{ nm}$) in periplasmic, cytoplasmic fractions and whole cell lysate of *E. coli* in pH 3.0 glycine-HCl buffer (0.1 M)

4.2.4.2. LC-MS/MS based accumulation studies

4.2.4.2.A. Drug uptake studies in *E. coli* ATCC 25922

Owing to the high degree of sensitivity to detect compounds at low concentrations, a liquid chromatography coupled tandem mass spectrometry (LC-MS/MS) was used to directly quantify intracellular accumulation of MXF and **38** within bacteria. A schematic diagram of the assay is shown in Figure 4.8. During optimization of the assay, several factors were taken into account. Some of these factors include compound concentration, incubation time to achieve steady-state accumulation, and cell lysis method.

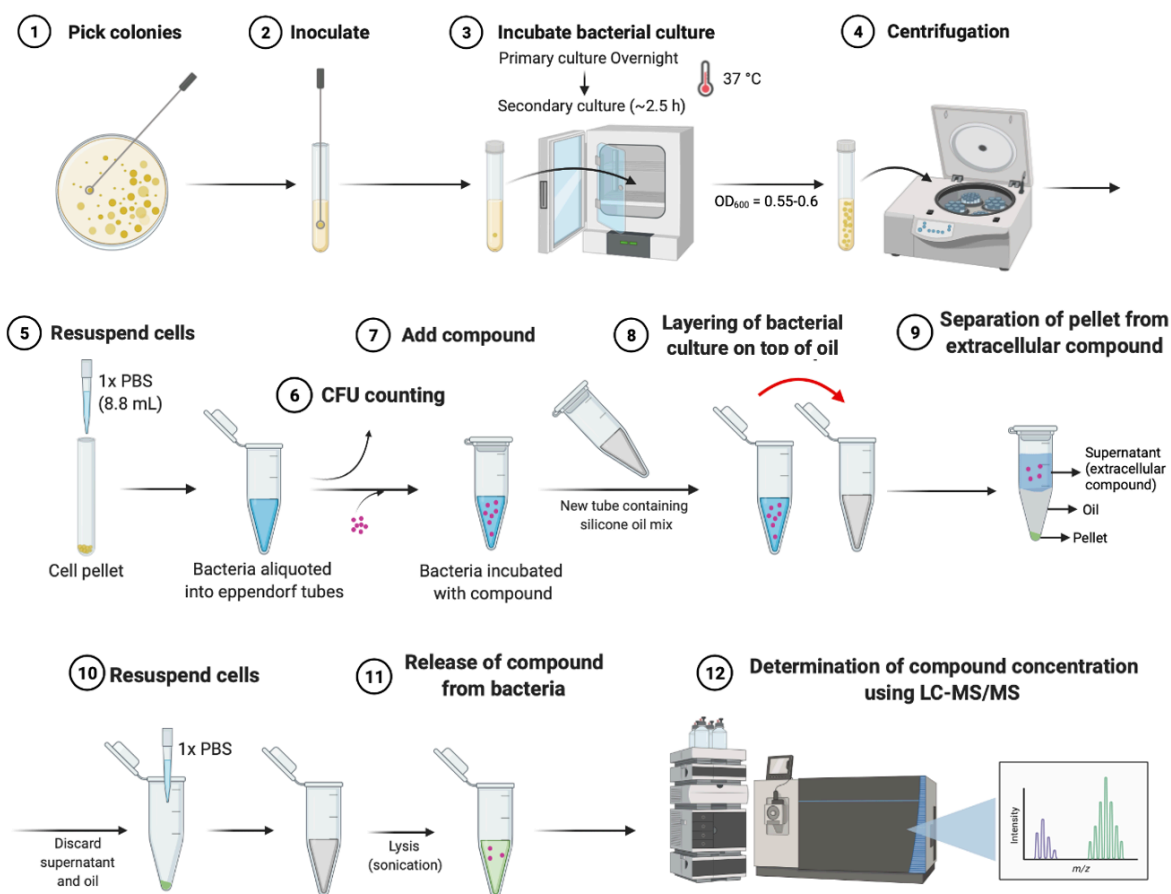


Figure 4.8. Schematic workflow for LC-MS/MS based accumulation assay in *E. coli*

Initial pilot studies with *E. coli* ATCC 25922 were conducted to optimize the concentration and incubation time with MXF to avoid complications due to bactericidal effects. Following a protocol highlighted in a recent study by Hergenrother's group, exponentially growing *E. coli* were incubated at 37 °C in pH 7.4 PBS (1x) with MXF at a final concentration of 50 μM for 10 min.^{11,15} This incubation time period is sufficient to achieve steady-state concentrations of many fluoroquinolones, including MXF.^{13,14} PBS was used as the preferred medium for the assay to eliminate the possibility of bacterial growth during incubation with MXF. A significant reduction in bacterial viability was observed, likely as a result of the rapid bactericidal effect of MXF (Figure 4.9). The assay was modified and bacteria were incubated with a 10-fold lower concentration of MXF (5 μM). At this concentration, bacteria maintained the cell viability of 80% relative to DMSO treated sample (Figure 4.9). Finally, a concentration of 5 μM and incubation time of 10 min with MXF and its prodrug **38** was used for the accumulation studies. Another FQ, Ciprofloxacin (CIP; 5 μM) served as a positive control in this study.

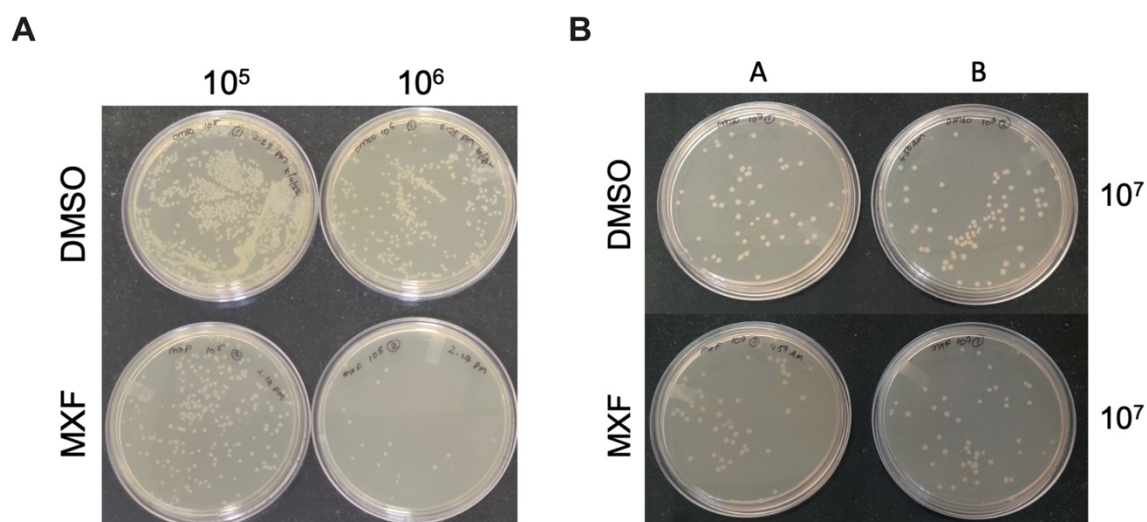


Figure 4.9. Optimization of the concentration of MXF at (A) 50 μM and (B) 5 μM with *E. coli* ATCC 25922 to ensure bacterial cell viability during incubation

After incubation of the bacteria with the test compound in PBS, the bacterial pellets were centrifuged through silicone oil to remove the unbound drug. Bacteria were lysed by sonication under ice-cold conditions. The compound was extracted from the resultant whole cell lysate, and the intracellular concentration (nM) was determined using a standard curve generated for the test compound by LC-MS/MS. These values were multiplied with the volume of the bacterial lysate (mL) to obtain accumulation values (nmol), normalized with the entire bacterial population (10^{10} CFUs), and then reported as drug accumulation (nmol/ 10^{10} CFUs). Three MRM transitions (one quantifier and two qualifiers) for each analyte were monitored in pH 7.4 PBS (1x) on a Sciex X500R quadrupole time-of flight (QTOF) mass spectrometer in a positive ion mode (Figure 4.10 and Table 4.7). The analyte peak area of the quantifier transition was correlated with the standard concentration of the analyte to construct a linear calibration curve to accurately quantify the intracellular concentration of the compound of interest (Figure 4.11).

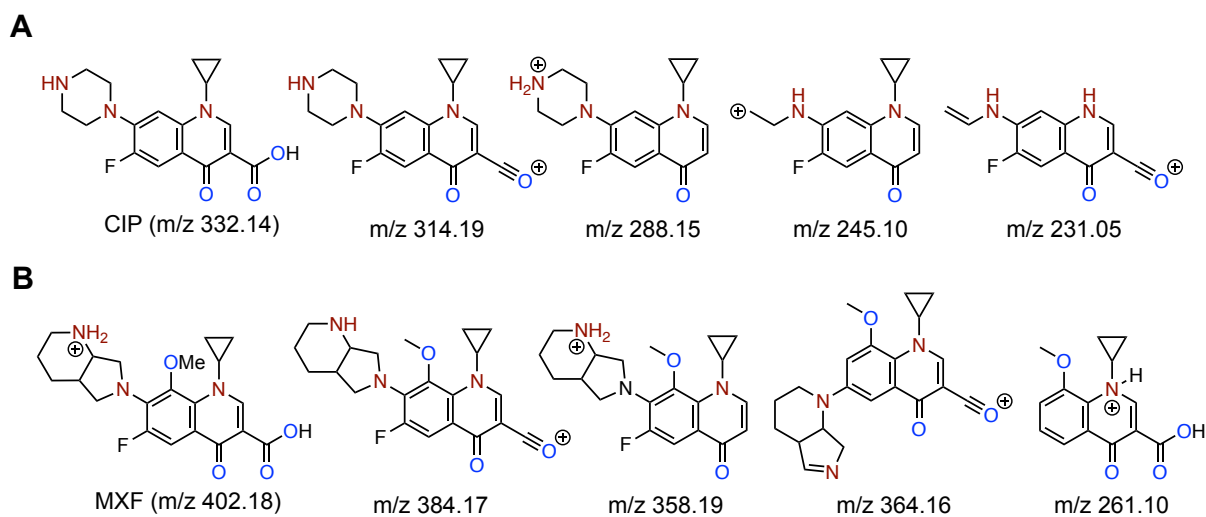


Figure 4.10. Structures of parent and fragment ions of (A) CIP and (B) MXF

Table 4.7. MRM transitions for the compounds used in the accumulation assay

| Entry | Compound | ESI polarity | Parent ion (m/z) | Fragment ion (m/z) |
|-------|-----------|--------------|------------------|--|
| 1 | CIP | Positive | 332.14 | 314.19 (Quantifier) 288.15 (Qualifier) |
| 2 | MXF | Positive | 402.18 | 384.17 (Quantifier) 358.19 (Qualifier) 364.16 (Qualifier) |
| 3 | 38 | Positive | 544.17 | 402.18 (Quantifier) 384.17 (Quantifier) 358.19 (Qualifier) 364.16 (Qualifier) |

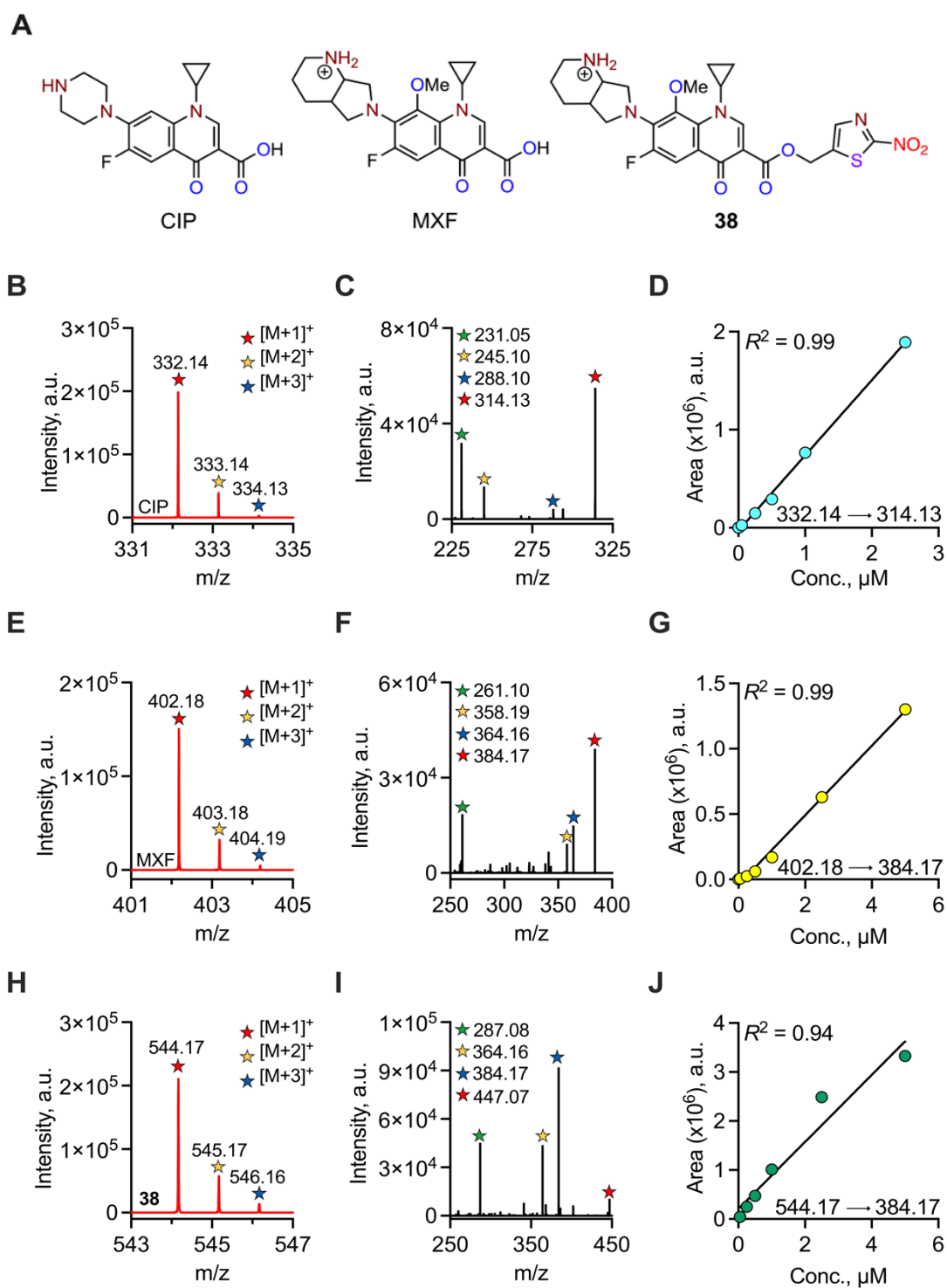


Figure 4.11. (A) Structures of analytes (CIP, MXF and **38**) used in the accumulation assay. Optimization of LC-MS/MS conditions for the detection of CIP, MXF and **38** in pH 7.4 PBS (1x). The (B, E, and H) MS1 and (C, F, and I) MS2 signals for CIP, MXF and **38** are shown, respectively. The calibration curve was constructed by monitoring the transition of (D) CIP (m/z 332.14 \rightarrow 314.13), (G) MXF (m/z 402.18 \rightarrow 384.17) and (J) **38** (m/z 544.17 \rightarrow m/z 384.17).

Compared to fluorescence-based assay, *E. coli* accumulated MXF (m/z 402.18 → 384.17) at 3.8-fold higher intracellular concentration than CIP (m/z 332.14 → 314.19) under these conditions (Figure 4.12). This could probably be due to differences in the outer membrane permeability between strains of the same bacteria (MG1655 in the study and ATCC 25922 in our study). Treatment of *E. coli* with **38** led to enhanced accumulation of the parent FQ antibiotic, MXF. Under these conditions, only the MRM transition was observed at m/z 544.16 → 384.17 (characteristic quantifier ion of MXF) for **38**. Furthermore, no evidence of the prodrug **38** peak at m/z 544.16 was found. This suggested that the prodrug was efficiently converted to the parent antibiotic, MXF by bacterial NTR following internalization of the compound into *E. coli*. In contrast to direct treatment with MXF, treatment of *E. coli* with **38** showed a considerable increase (4.5 fold) in the intracellular accumulation of MXF generated from the prodrug (Figure 4.12). Overall, these results indicated that the use of prodrug **38** led to an increased accumulation of MXF. However, the higher accumulation of the prodrug did not lead to any appreciable decrease in MIC (0.09 μM) of **38** as compared to MXF (0.039 μM). This suggest that a steady state concentration is necessary for efficient engagement or inhibition of the target within the bacteria and above this threshold, differences in efficacy may not be seen.

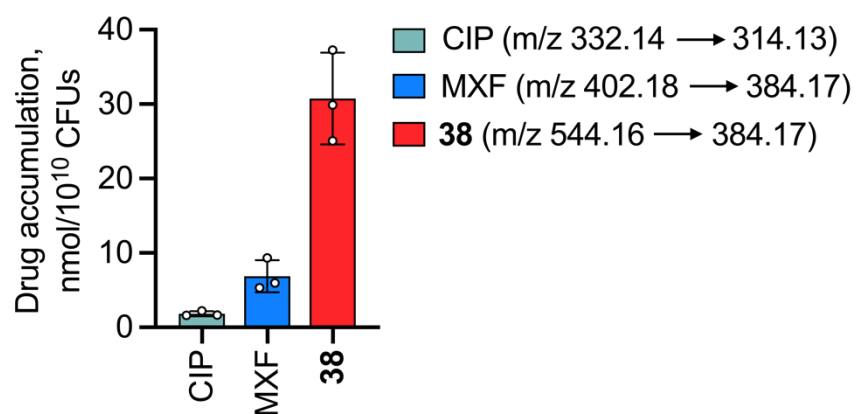


Figure 4.12. Whole cell intracellular accumulation of drug in *E. coli*

4.2.4.2.B. Drug uptake studies in *Mtb* H37Rv

Next, accumulation of MXF and **38** in mycobacteria was studied using a similar protocol (Figure 4.13).

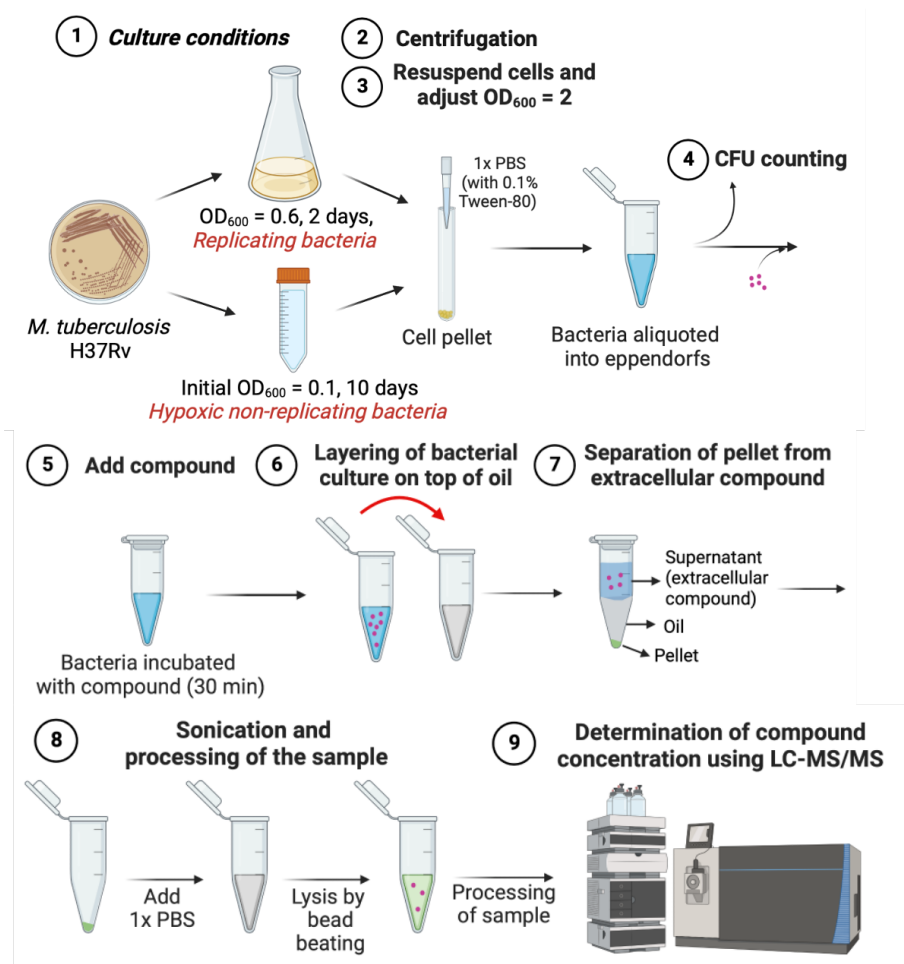


Figure 4.13. Schematic workflow for LC-MS based accumulation assay in replicating and non-replicating *Mtb*

Due to the differences observed in the permeability barrier observed among bacteria (*E. coli* vs. *Mtb*), a number of factors including compound concentration, incubation time, and matrix effects were initially optimized for the drug penetration assay in mycobacteria. Prior studies have shown that FQs have achieved steady-state accumulation in *Mtb* within minutes following drug exposure.^{3,16,17} Another study showed that the accumulation of FQs is rapid and reaches equilibrium within 30 min of exposure.³ Hence, an incubation period of 30 min was used for this study.

It is well known that matrix effects can adversely affect the LC-MS parameters (limit of detection, accuracy, and linearity) of the analyte.^{18,19} Next, we assessed the effects of various matrices, such as PBS and *Mtb* lysate on the signal of MXF. Although the absolute concentration of MXF in both the tested samples remained the same, a decrease in the response of MXF was observed with *Mtb* lysate, more likely as a result of ion suppression (Figure 4.14). Therefore, blank untreated *Mtb* lysates were prepared, and

treated with different concentrations of MXF or **38** to construct calibration curves (Figure 4.15 and 4.16). These were then used to quantitate the intracellular concentration of analyte.

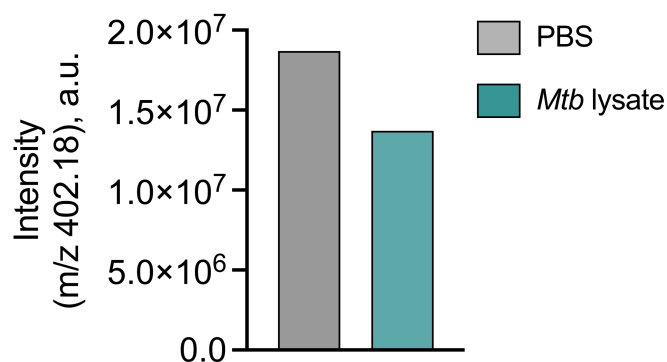


Figure 4.14. Suppressive effect of *Mtb* lysate on MXF signal

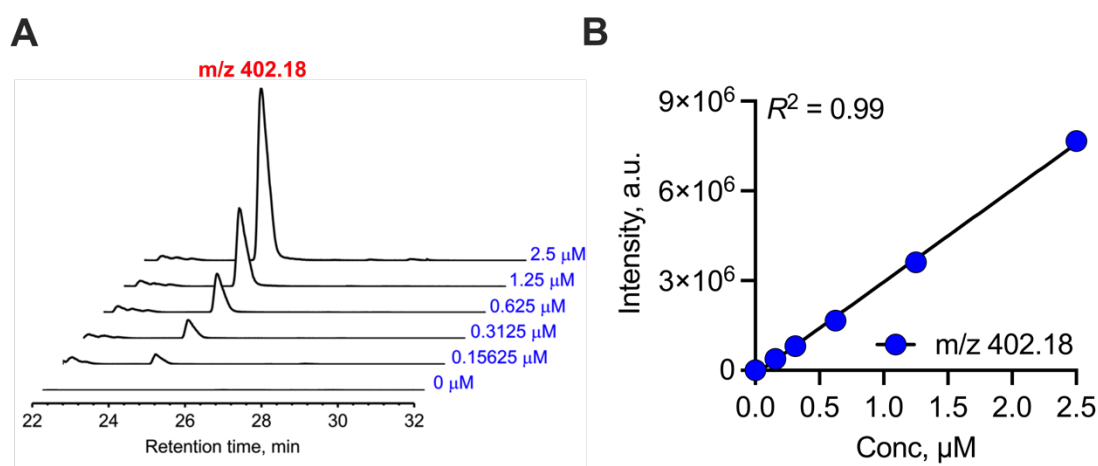


Figure 4.15. (A) Representative extracted ion chromatograms (EIC) and (B) standard calibration curve obtained with different concentrations of MXF (m/z 402.18)

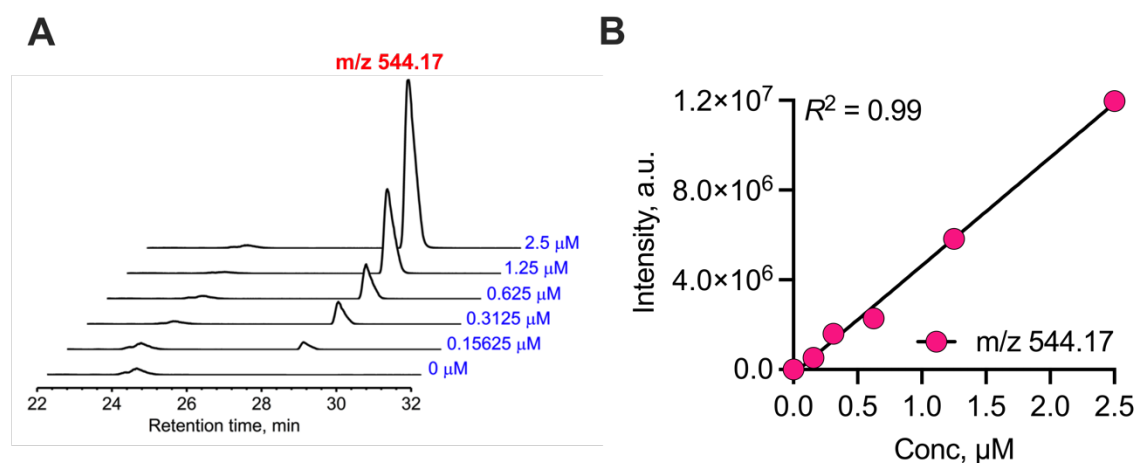


Figure 4.16. (A) Representative extracted ion chromatograms (EIC) and (B) standard calibration curve obtained with different concentrations of **38** (m/z 544.17)

Following a validated protocol mentioned earlier, exponentially growing and non-replicating hypoxic *Mtb* were incubated at 37 °C in pH 7.4 PBS (1x) with either MXF or **38** at a final concentration of 5 μM. After incubation (30 min) of the bacteria with test compound, the replicating and non-replicating bacterial pellets were centrifuged through silicone oil and then lysed through bead beating. The compounds were extracted from the resultant whole cell clarified lysates using PBS-MeOH and filtered through a 3 kDa Amicon® centrifugal filter. The intracellular concentrations (nM) were determined by LC-MS using a standard calibration curve, and then converted into accumulation values (nmol) by multiplying with the volume of lysate (mL) used for the assay. These values were normalized with the bacterial count (10⁸ CFUs) and are represented as drug accumulation (nmol/10⁸ CFUs).

Compared to replicating bacilli, a marked reduction in the intracellular accumulation of MXF was observed in hypoxic non-replicating cultures of *Mtb* (Figure 4.17). This observation is consistent with previous reports of diminished permeation of MXF in nutrient-starved non-replicating cultures of *Mtb*.³ Exposure of replicating and non-replicating *Mtb* with **38** again led to the formation of MXF (m/z 544.16 → 402.18). Again, there was no evidence of intact prodrug under these conditions, suggesting that **38** was converted into MXF following permeation into *Mtb*. There was a marked difference in the intracellular amounts of MXF (m/z 402.18) in replicating and non-replicating *Mtb* treated with **38** (Figure 4.18.A-B). In accordance with the earlier results, accumulation of MXF from the prodrug was much lower in hypoxic *Mtb* compared to the replicative state. In contrast to the findings in *E. coli* (Figure 4.12), intracellular

concentrations of MXF in MXF and **38** treated replicating bacteria were comparable (Figure 4.18.A). The accumulation values of MXF from the prodrug were, however, found to be higher than those from the MXF alone in hypoxic non-replicating *Mtb* (Figure 4.18.B).

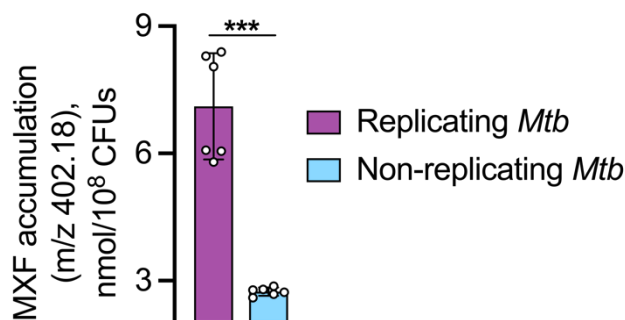


Figure 4.17. LC-MS analysis of intracellular concentration of MXF (m/z 402.18) in replicating and non-replicating cultures of *Mtb* following incubation with MXF (5 μ M) for 30 min.

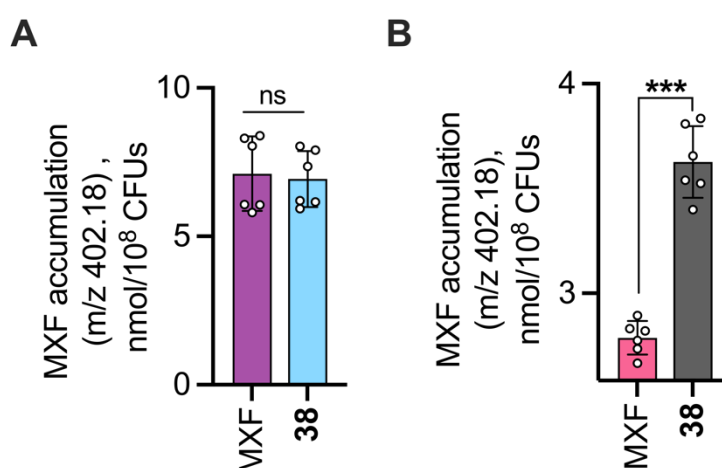


Figure 4.18. LC-MS analysis of intracellular concentration of MXF (m/z 402.18) in (A) replicating and (B) non-replicating cultures of *Mtb* following incubation for 30 min with a fixed concentration (5 μ M) of MXF and **38**. Statistical significance was established relative to MXF treated sample using an unpaired *t*-test (***) $p \leq 0.001$ and ns indicate not significant).

Overall, LC-MS/MS based studies demonstrated the increased intracellular accumulation of MXF from the prodrug as compared to MXF alone, and this could contribute to enhanced potency in the non-replicating *Mtb* model.

4.3. Conclusion

The activity of the prodrugs were evaluated against gram-positive, gram-negative, and mycobacteria. Our analysis showed that one of the analogues, 2-nitrothiazole prodrug **38** exhibited potent antibacterial activity that was comparable to MXF against gram-positive and gram-negative bacteria in both cellular and animal models. The prodrug displayed antimycobacterial activity equivalent to MXF against drug-susceptible and drug-resistant strains of *Mtb*. Furthermore, our results demonstrated that **38** had superior inhibitory activity against non-replicating *Mtb* when compared with MXF. LC-MS based studies further supported that the enhanced efficacy could be due to increased intracellular accumulation of **38**. Together, we employed a prodrug strategy to enhance the potency of a clinical drug against non-replicating *Mtb* while retaining the antimycobacterial activity similar to MXF against replicating *Mtb*. This strategy may have a significant therapeutic benefit in the treatment of latent TB caused by mycobacterial persisters.

4.4. Experimental protocols

4.4.1. Determination of Minimum Inhibitory Concentrations (MICs) of prodrugs against *M. smegmatis*

WT *M. smegmatis* mc²155 bacteria was grown with agitation (180 rpm) at 37 °C in Middlebrook 7H9 broth (Himedia) supplemented with 10% ADS (albumin-dextrose-saline), glycerol (0.2%), and tween-80 (0.05%) until exponential phase ($OD_{600} = 0.4-0.8$). The MIC experiments were performed in Middlebrook 7H9 broth supplemented with 0.2% glycerol and 10% (v/v) ADS in sterile 96-well flat bottom plates. Briefly, aliquots (100 μ L) of Middlebrook 7H9 broth supplemented with 0.2% glycerol and 10% (v/v) ADS were dispensed into each well of a 96-well plate, and serial 2-fold dilutions of each drug were prepared directly in the plate. The exponential phase cultures of bacteria ($OD_{600} = 0.4-0.8$) were diluted in experimental medium. Aliquots (100 μ L) of inoculums (approximately 1×10^6 bacteria/ml, $OD_{600} = 0.006$) were added into triplicate wells. Growth and sterile controls were also included in the assay. 7H9 medium was added to all peripheral wells to avoid evaporation. The plate was covered, sealed, and incubated at 37 °C under a normal static condition. After 16 h of incubation, 0.02% w/v of resazurin solution (30 μ L) was added to each well, and the plate was further incubated for ~6 h or till the color of the growth well transforms from blue to pink. The intensity of the pink colour directly correlates with the extent of bacterial growth and the fluorescence was measured in EnSight Multimode Plate Reader (PerkinElmer) in bottom-reading mode with excitation wavelength 530 nm and emission wavelength 590 nm and converted as a percentage of growth inhibition.

4.4.2. Fluorimetry-based method to evaluate the intracellular accumulation of compounds in *E. coli*

An overnight culture (6 mL) of *E. coli* ATCC 25922 was diluted in fresh LB media (600 mL; 1:100 dilution) and grown to the mid-exponential phase ($OD_{600} = 0.60-0.65$; ~ 2 h) in a shaking incubator at 37 °C. Bacteria were harvested by centrifugation (2,486 x g) for 10 min at 4 °C, supernatant was removed, and the pellet was resuspended in PBS to be again centrifuged under the same conditions. The pooled pellets were then resuspended in pH 7.4 PBS (1x, 13.5 mL) to reach an $OD_{600} = 5$. Aliquots of bacterial solution (875 μ L) were distributed in 2 mL microcentrifuge tubes and equilibrated at 37 °C in a thermomixer for 5 min prior to incubation with compounds. Bacterial viability was measured by enumerating CFUs by serial dilutions using a L-spreader on nutrient agar (NA) plates before and after exposure to compound/antibiotic. The plates were incubated at 37 °C for 16 h and CFUs were counted.

Unless otherwise stated, accumulation assays were performed at a drug concentration of 5 μ M. Bacterial samples (875 μ L) were either left untreated or treated with DMSO (8.75 μ L) or 5 μ M of MXF (8.75 μ L, 0.5 mM stock) in triplicate and incubated with shaking at 180 rpm at 37 $^{\circ}$ C. An aliquot (800 μ L) was removed after 15 min from each reaction and then transferred into a 2 mL microcentrifuge tube containing silicone oil mix (700 μ L; 9:1 AR20/sigma high temperature) pre-cooled to -78 $^{\circ}$ C. The samples were pelleted by centrifugation (13,000 x g) for 4.5 min at RT and then the supernatant was discarded.

For whole-cell samples, the pellets were resuspended in 1 mL of pH 3.0 glycine-HCl buffer. The samples were then directly lysed by sonication using the 130 Watt ultrasonic processor (Vx 130W) by stepping a microtip with a 2 min pulse on time (with 3s ON and 3s OFF pulse, 60% amplitude, 20 kHz frequency) under ice-cold conditions. The cell debris was removed through centrifugation at 13,000 x g at RT for 2.5 min. The supernatant was collected and the fluorescence emission spectra was then recorded. For fractionated samples, the pellets were resuspended in 100 μ L of periplasm preparation buffer and incubated at RT for 5 min. The samples were subjected to osmotic shock by the addition of 200 μ L of ice-cold milliQ water, and then the mixture was incubated on ice for 2 min. Next, the samples were centrifuged at 15,000 x g for 1 min. The supernatant (250 μ L) containing periplasmic component was diluted to 1 mL with pH 3.0 glycine-HCl buffer, and then the fluorescence emission spectra was recorded. The pellet containing the cytoplasmic fraction was resuspended in 1 mL of pH 3.0 glycine-HCl buffer and then lysed by sonication as described above. The samples were centrifuged at 15,000 x g for 2.5 min and the collected supernatant was used to measure the fluorescence emission profile at $\lambda_{\text{ex}} = 289$ nm. The peak intensity at the corresponding emission wavelength (488 nm) was used to construct a standard calibration curve for MXF.

4.4.3. LC-MS/MS based accumulation studies in *E. coli*

Bacterial samples (875 μ L) were prepared in a similar manner as mentioned above. These samples were either left untreated or treated with DMSO (8.75 μ L) or compounds (8.75 μ L of CIP or MXF or **38**; final conc. 5 μ M) in triplicate and incubated with shaking at 180 rpm at 37 $^{\circ}$ C. An aliquot (800 μ L) was removed after 10 min from each reaction and then transferred into a 2 mL microcentrifuge tube containing silicone oil mix (700 μ L; 9:1 AR20/sigma high temperature) pre-cooled to -78 $^{\circ}$ C. The bacteria were pelleted by centrifugation (13,000 x g) at RT for 2 min and the supernatants (oil and aqueous layer containing extracellular compound)

were removed by pipetting. Bacilli were then resuspended in sterile PBS (200 μ L), transferred to a new microcentrifuge tube, and lysed by sonication as described in the previous section. The resultant lysate was subjected to centrifugation (13,000 \times g for 2 min at RT) and supernatant (100 μ L) was collected in a new microcentrifuge tube. The bacterial pellet was washed with MeOH (50 μ L), vortexed (1 min), centrifuged (13,000 \times g at RT for 2 min), and methanolic wash (100 μ L) was added to the previously collected aqueous supernatant. Bacterial lysates (150 μ L) were further clarified by centrifugation (15,000 \times g at RT for 2 min). The resultant supernatant (100 μ L) was carefully sampled and assessed thereafter by LC-MS/MS.

All measurements were made using a LC-MS method in the positive ion mode using high resolution multiple reaction monitoring (MRM-HR) analysis on a Sciex X500R quadrupole time-of flight (QTOF) mass spectrometer fitted with an Exion UHPLC system using a Kinetex 2.6 mm hydrophilic interaction liquid chromatography (HILIC) column with 100 Å particle size, 150 mm length and 3 mm internal diameter (Phenomenex). Nitrogen was the nebulizer gas, with the nebulizer pressure set at 50 psi. Samples were injected (20 μ L) and analyzed with the following parameters: Mode: Electrospray ionization (ESI), ion source gas 1 = 40 psi, ion source gas 2 = 50 psi, curtain gas = 30, CAD gas = 7, spray voltage = 5500 V and temperature = 500 °C. The LC runs of 23 min were performed using a mobile phase of solvent A (0.1% HCOOH in milliQ water) and solvent B (ACN) with a gradient starting with 100:0 \rightarrow 0 min, 100:0 to 90:10 \rightarrow 0 - 0.3 min, 90:10 to 90:10 \rightarrow 0.3 - 3 min, 90:10 to 75:25 \rightarrow 3 - 9 min, 75:25 to 75:25 \rightarrow 9 - 11 min, 75:25 to 50:50 \rightarrow 11 - 13 min, 50:50 to 10:90 \rightarrow 13 - 17 min, 10:90 to 10:90 \rightarrow 17 - 20 min, 10:90 to 90:10 \rightarrow 20 - 21 min, 90:10 to 90:10 \rightarrow 21 - 23 min at a flow rate of 0.5 mL per min. The TOF MS/MS parameters are: MXF (Q1, M + H⁺; m/z = 402.18 to Q3, M + H⁺; m/z = 384.17), **38** (Q1, M + H⁺; m/z = 544.17 to Q3, M + H⁺; m/z = 384.17 and Q1, M + H⁺; m/z = 544.17 to Q3, M + H⁺; m/z = 402.18) and CIP (Q1, M + H⁺; m/z = 332.14 to Q3, M + H⁺; m/z = 314.13). Blank untreated cell lysates were extracted using the procedure described above and were used to construct calibration curves to quantitate the intracellular concentration (nM) of compound/antibiotic in each respective sample. These are reported as accumulation values (nmol/CFU) following normalization with CFU/mL of untreated bacteria.

4.4.4. Evaluation of accumulation of compounds within *M. tuberculosis* using LC-MS

Replicating and non-replicating (hypoxic) pellets of *Mtb* were prepared by Ms. Shalini (Prof. Amit Singh lab, IISc Bangalore).

(A) For replicating *Mtb*: The bacterial suspension was aliquoted to different tubes. Drugs were added (5 μ M) to the tubes and incubated at 37 °C for 30 min. For CFU enumeration, bacterial suspension was collected from control tube, plated on 7H11-OADC agar and incubated at 37 °C. After incubation, equal volume of pre-chilled (-80 °C) silicone oil mix (9:1 AR20/sigma high temperature) was added to each tube containing the suspension and centrifuged at 13000 x *g* for 5 min. The pellet was collected, suspended in PBS (pH 7.4, 10 mM) and lysed. The resultant lysate was treated as described above in the section 4.4.3. The concentration of compounds were quantified using a LC-MS method in the positive ion mode on a Bruker Daltonics ESI-QTOF (Maxis Impact) mass spectrometer connected to a Thermo Dionex (Ultimate 3000) micro-LC system. Chromatographic separation was performed on C18 reverse phase column (4.6 X 150 mm, 2.7 μ m; Agilent Poroshell 120) using a mobile phase of solvent A (0.1 % HCOOH in milliQ water) and solvent B (ACN) with a run time of 64 min and a multistep gradient 95:5 \rightarrow 0–3 min, 95:5 to 5:95 \rightarrow 3–50 min, 5:95 to 5:95 \rightarrow 50–55 min, 5:95 to 95:5 \rightarrow 55–64 min at a flow rate of 0.3 mL/min. The TOF MS parameters were same as described above in the section 4.4.3.

(B) For non-replicating *Mtb*: The above mentioned modified protocol was used to prepare *Mtb* under hypoxic condition. 40 mL ($OD_{600} = 0.1$) bacterial culture were added in 50 mL conical tubes followed by incubation at 37 °C in shaking condition. Achievement of hypoxia was observed as decolorization of methylene blue. The culture were grown till $OD_{600} \sim 0.6$, harvested and were treated as above.

4.5. References

- (1) Taneja, N. K.; Tyagi, J. S. Resazurin reduction assays for screening of anti-tubercular compounds against dormant and actively growing *Mycobacterium tuberculosis*, *Mycobacterium bovis* BCG and *Mycobacterium smegmatis*. *J. Antimicrob. Chemother.* **2007**, *60* (2), 288–293.
- (2) Cunningham, A. F.; Spreadbury, C. L. Mycobacterial stationary phase induced by low oxygen tension: cell wall thickening and localization of the 16-kilodalton-crystallin homolog. *J. Bacteriol.* **1998**, *180* (4), 801-8.
- (3) Sarathy, J.; Dartois, V.; Dick, T.; Gengenbacher, M. Reduced drug uptake in phenotypically resistant nutrient-starved nonreplicating *Mycobacterium tuberculosis*. *Antimicrob. Agents Chemother.* **2013**, *57* (4), 1648–1653.
- (4) Jakkala, K.; Ajitkumar, P. Hypoxic non-replicating persistent *Mycobacterium tuberculosis* develops thickened outer layer that helps in restricting rifampicin entry. *Front. Microbiol.* **2019**, *10*, 2339.
- (5) Bazile S, Moreau N, Bouzard D, Essiz M. Relationships among antibacterial activity, inhibition of DNA gyrase, and intracellular accumulation of 11 fluoroquinolones. *Antimicrob. Agents Chemother.* **1992**, *36* (12), 2622-7.
- (6) Cai, H.; Rose, K.; Liang, L. H.; Dunham, S.; Stover, C. Development of a liquid chromatography/mass Spectrometry-based drug accumulation assay in *Pseudomonas aeruginosa*. *Anal. Biochem.* **2009**, *385* (2), 321–325.
- (7) Capobianco, J. O.; Goldman, R. C. Macrolide transport in *Escherichia coli* strains having normal and altered OmpC and/or OmpF porins. *Int. J. Antimicrob. Agents*, **1994**, *4* (3), 183-189.
- (8) Chopra I. Transport of tetracyclines into *Escherichia coli* requires a carboxamide group at the C2 position of the molecule. *J. Antimicrob. Chemother.* **1986**, *18* (6), 661-6.
- (9) Li, X. Z.; Livermore, D. M.; Nikaidol, H.; Role of efflux pump(s) in intrinsic resistance of *Pseudomonas Aeruginosa*: Resistance to tetracycline, chloramphenicol, and norfloxacin. *Antimicrob. Agents Chemother.* **1994**, *38* (8), 1732-41.
- (10) Williams, K. J.; Piddock, L. J. Accumulation of rifampicin by *Escherichia coli* and *Staphylococcus aureus*. *J. Antimicrob. Chemother.* **1998**, *42* (5), 597-603.

-
- (11) Richter, M. F.; Drown, B. S.; Riley, A. P.; Garcia, A.; Shirai, T.; Svec, R. L.; Hergenrother, P. J. Predictive compound accumulation rules yield a broad-spectrum antibiotic. *Nature* **2017**, *545* (7654), 299–304.
- (12) de Cristóbal, R. E.; Vincent, P. A.; Salomón, R. A. Multidrug resistance pump AcrAB-TolC is required for high-Level, Tet(A)-mediated tetracycline resistance in *Escherichia coli*. *J. Antimicrob. Chemother.* **2006**, *58* (1), 31-6.
- (13) Piddock, L. J.; Jin, Y. F.; Ricci, V.; Asuquo, A.E. Quinolone accumulation by *Pseudomonas aeruginosa*, *Staphylococcus aureus* and *Escherichia coli*. *J. Antimicrob. Chemother.* **1999**, *43* (1), 61-70.
- (14) Pandeya, A.; Alegun, O.; Cai, Y.; Wei, Y. Distribution of fluoroquinolones in the two aqueous compartments of *Escherichia coli*. *Biochem. Biophys. Rep.* **2020**, *24* (100849), 1-8.
- (15) Geddes, E. J.; Li, Z.; Hergenrother, P. J. An LC-MS/MS Assay and complementary web-based tool to quantify and predict compound accumulation in *E. coli*. *Nat. Protoc.* **2021**, *16* (10), 4833–4854.
- (16) Piddock, L. J.; Jin, Y. F. Antimicrobial activity and accumulation of moxifloxacin in quinolone-susceptible bacteria. *J. Antimicrob. Chemother.* **1999**, *43* (Suppl B), 39-42.
- (17) Piddock, L.J.; Ricci, V. Accumulation of five fluoroquinolones by *Mycobacterium tuberculosis* H37Rv. *J. Antimicrob. Chemother.*, **2001**, *48* (6), 787–791.
- (18) Matuszewski, B. K.; Constanzer, M. L.; Chavez-Eng, C. M. Matrix effect in quantitative LC/MS/MS analyses of biological fluids: a method for determination of finasteride in human plasma at picogram per milliliter concentrations. *Anal. Chem.* **1998**, *70* (5), 882-889.
- (19) Trufelli, H.; Palma, P.; Famigliini, G.; Cappiello, A. An overview of matrix effects in liquid chromatography-mass spectrometry. *Mass Spectrom. Rev.* **2011**, *30* (3), 491-509.

In previous chapters, the 2-nitrothiazolyl moiety was utilized to mask carboxylic acid as well as secondary amine and develop NTR sensitive ester and carbamate prodrugs of MXF (Figure 5.1.1).

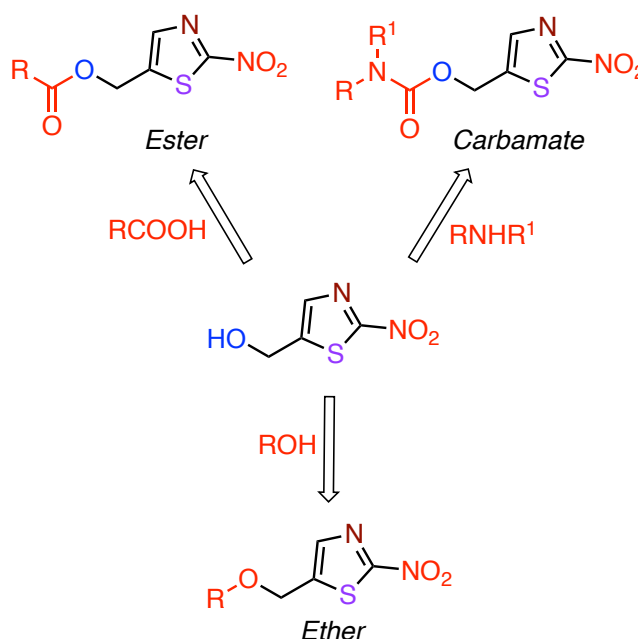


Figure 5.1.1. Scope and utility of 2-nitrothiazolyl moiety as NTR-sensitive bioreductive trigger

Having established that 2-nitrothiazole group as an improved bioreductive trigger compared to 1-methyl-2-nitroimidazole and other nitroaryl groups, the scope and utility of this group in masking drugs and fluorophores was investigated in this chapter (Figure 5.1.1). Two selective strategies to mask carboxylic acid and phenolic compounds as an ester (Chapter 5.1) and an ether (Chapter 5.2) based NTR-sensitive caged compounds respectively were considered.

Chapter 5.1. Design, synthesis and evaluation of Nitroreductase (NTR) activated prodrugs of Ciprofloxacin (CIP)

5.1.1. Introduction

A detailed experimental and computational analysis in Chapter 2-4 unequivocally demonstrated that the 2-nitrothiazole tethered prodrug was more sensitive and underwent complete transformation into MXF in the presence of bacterial NTR. Moreover, this prodrug showed potent antibacterial and antimycobacterial activity equivalent to MXF. In this chapter, 2-nitrothiazolyl moiety was further exploited to develop an ester prodrug that would retain antibacterial activity similar to another parent FQ antibiotic against gram-positive and gram-

negative bacteria. This prodrug strategy was employed to design and synthesize nitroreductase (NTR) sensitive conjugates of a broad spectrum second generation FQ antibiotic, Ciprofloxacin (CIP).¹⁻⁷ Upon activation by bacterial NTR, the efficient cleavage of the prodrug would liberate CIP (Figure 5.1.2).

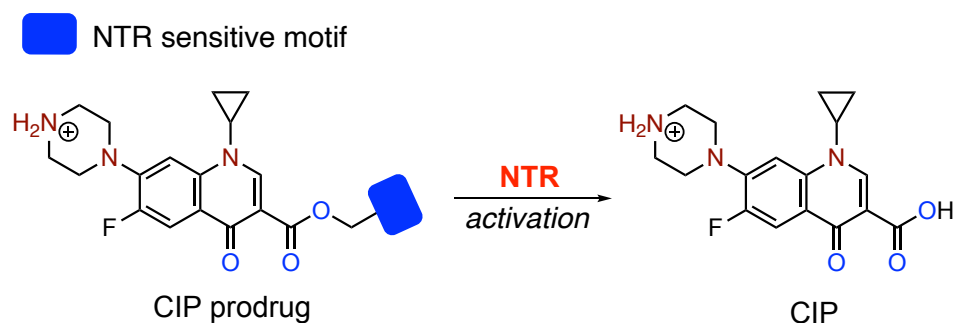


Figure 5.1.2. Proposed strategy for the release of CIP from ester prodrug

5.1.2. Results and discussion

5.1.2.1. Synthesis

The piperazine ring of CIP was protected using $(\text{Boc})_2\text{O}$, and the resulting intermediate **47** was coupled with primary alcohols (**1a** and **1f**) in the presence of HBTU to afford esters **48** and **49** in moderate yields.⁸ This was followed by *N*-boc deprotection under acidic conditions to provide **50** and **51** (Scheme 5.1.1 and Table 5.1.1).

Scheme 5.1.1. Synthesis of **50** and **51**

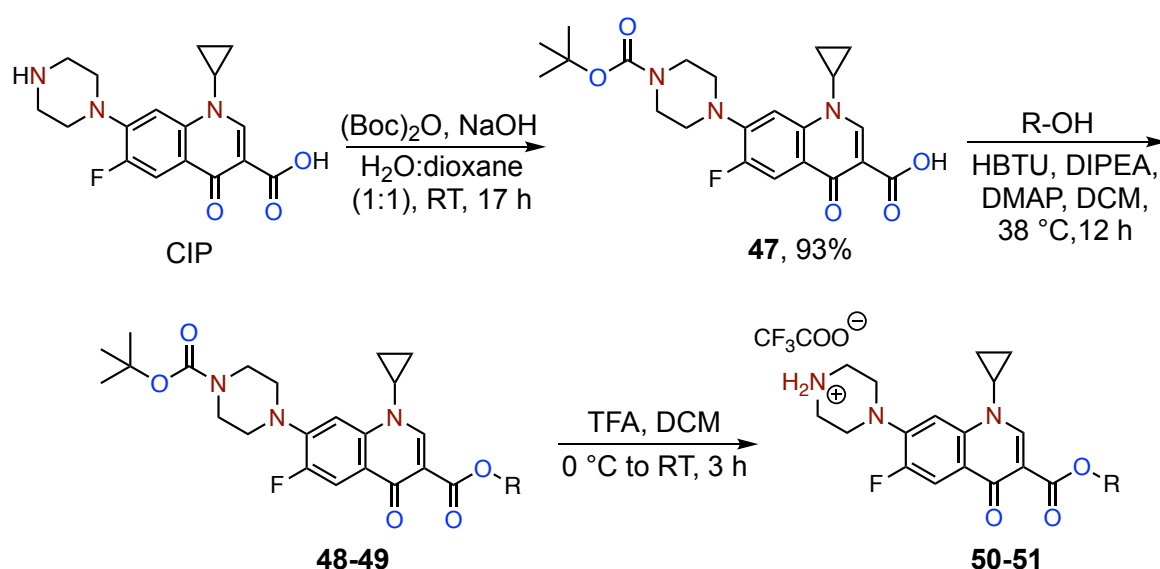
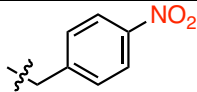
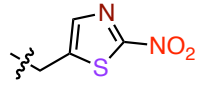


Table 5.1.1. Synthesis of nitro(hetero)aryl esters of CIP

| Entry | R | Alcohol | Ester | % Yield | Ester | % Yield |
|-------|---|-----------|-----------|---------|-----------|---------|
| 1 |  | 1a | 48 | 65 | 50 | 92 |
| 2 |  | 1f | 49 | 74 | 51 | 95 |

5.1.2.2. *E. coli* NTR mediated nitroreduction of prodrugs

Next, the ability of the prodrugs to generate CIP was monitored in the presence of *E. coli* NTR by recording the fluorescence response after 1 h of incubation (Scheme 5.1.2). The 2-nitrothiazole prodrug **51** displayed highest fluorescence response than 4-nitrobenzyl prodrug **50** under these conditions (Figure 5.1.3). These results were in agreement with the findings shown earlier in Chapter 3, suggesting that 2-nitrothiazole moiety is an optimal substrate for *E. coli* NTR.

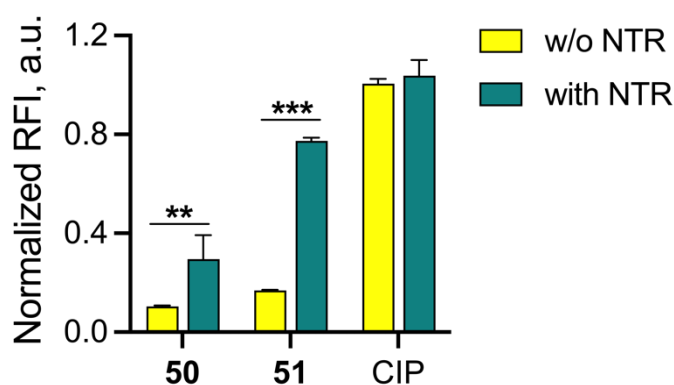
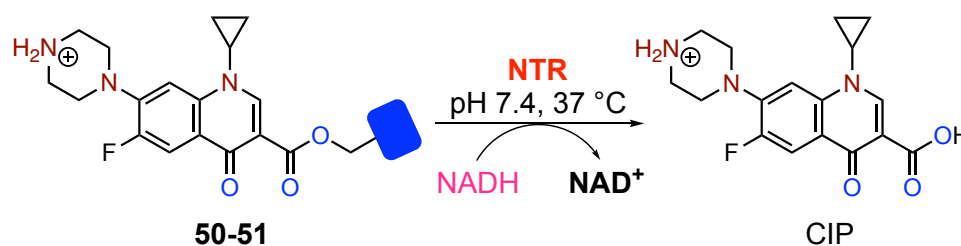
Scheme 5.1.2. Proposed strategy for NTR-mediated bioactivation of prodrugs

Figure 5.1.3. Monitoring the *E. coli* NTR mediated bioreductive activation of prodrugs by fluorescence ($\lambda_{\text{ex}} = 281 \text{ nm}$ and $\lambda_{\text{em}} = 445 \text{ nm}$) after 1 h of incubation with *E. coli* NTR (15 nM) and NADH (100 μM) in pH 7.4 phosphate buffer (10 mM) at 37 $^\circ\text{C}$.

5.1.2.3. Bioreductive activation of prodrugs

The bioreductive ability of the prodrugs were then assessed in bacterial lysates (*E. coli* and *M. smegmatis*). A distinct fluorescence signal was observed upon incubation of the prodrugs with lysates of *E. coli* (Figure 5.1.4.A) and *M. smegmatis* (Figure 5.1.4.B). Among the prodrugs, **51** showed the highest fluorescence response, indicating a greater degree of biotransformation of the prodrug into CIP. Furthermore, a significant reduction in the fluorescence response of **51** was observed following pretreatment with dicoumarol (DCOM; NTR inhibitor) in bacterial lysates (Figure 5.1.5.A-B). These results suggest that the activation of the prodrug is mostly likely mediated by NADH or NADPH dependent FMN-dependent NTR.

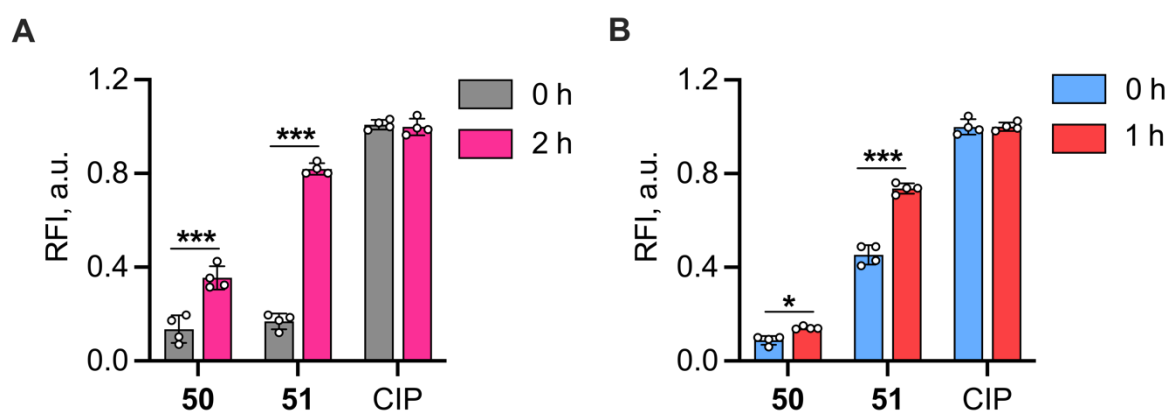


Figure 5.1.4. Bioreductive activation of prodrugs (10 μ M) after incubation in lysates (1 mg/mL) of (A) *E. coli* ATCC 25922 for 2 h and (B) *M. smegmatis* mc²155 in 1 h.

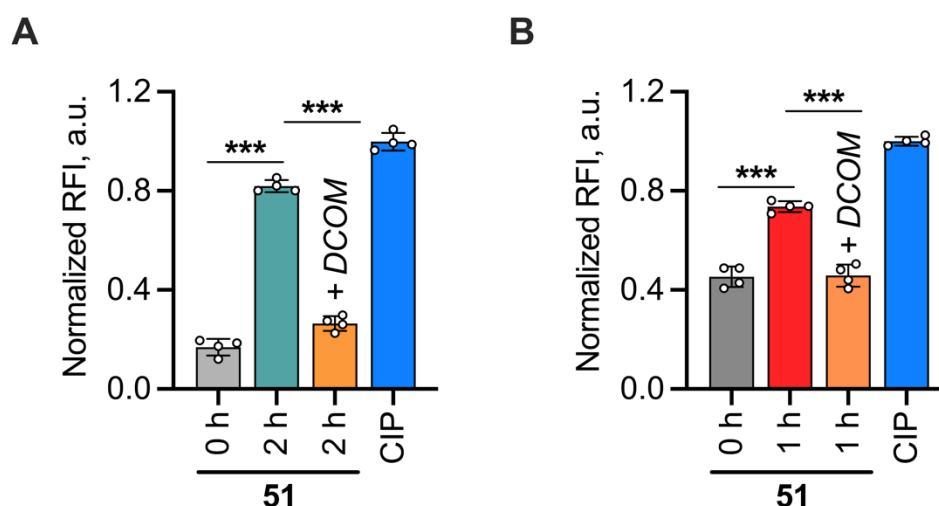
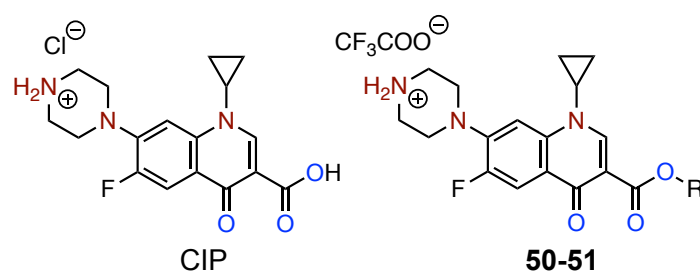


Figure 5.1.5. Monitoring the release of CIP from prodrugs (10 μ M) after incubation in lysates (1 mg/mL) of (A) *E. coli* ATCC 25922 for 2 h and (B) *M. smegmatis* mc²155 in 1 h alone or in the presence of NTR inhibitor, dicoumarol (DCOM; 250 μ M).

5.1.2.4. Antibacterial activity

Furthermore, the antibacterial activity of prodrugs were evaluated against *S. aureus* ATCC 29213 and *E. coli* ATCC 25922 (Table 5.1.2). Data was provided by our collaborator Dr. Sidharth Chopra Lab, CSIR-CDRI, Lucknow. Consistent with the results described in the previous chapter, 4-nitrobenzyl derivative was less potent and exhibited substantially higher MIC than parent antibiotic, CIP. Again, **51** demonstrated equipotent antibacterial activity against *S. aureus* and *E. coli* comparable to CIP.

Table 5.1.2. Antibacterial activity of CIP prodrugs against *E. coli*, and *S. aureus*



| Entry | Prodrug/ Drug, | R | MIC (μM) | |
|-------|-------------------|---|-----------------------------------|---------------------------------|
| | | | <i>S. aureus</i> (ATCC 29213)* | <i>E. coli</i> (ATCC 25922)* |
| 1 | CIP | - | 1.50 | 0.047 |
| 2 | 50 | | 55.1 | 3.44 |
| 3 | 51 | | 0.85 | 0.10 |

Data was provided by Dr. Sidharth Chopra Lab, CSIR-CDRI, Lucknow

5.1.3. Conclusion

The superiority of 2-nitrothiazolyl moiety over other nitro(hetero)aryl functional groups towards *E. coli* NTR was demonstrated in Chapter 3. Our investigation revealed that 2-nitrothiazolyl tethered CIP prodrug was the optimal substrate for *E. coli* NTR, which upon enzymatic nitroreduction provided CIP in quantitative yield. The prodrug was activated in a variety of bacterial lysates, indicating the specificity of the prodrug towards bacterial NTRs. These results suggest changing the leaving group from MXF (fourth-generation FQ) to CIP (second-generation FQ) in the prodrug has no impact on *E. coli* dependent nitroreduction. The 2-nitrothiazolyl tethered prodrug retained antibacterial activity equivalent to CIP against gram-positive and gram-negative

bacteria. Overall, these studies strongly indicate that 2-nitrothiazole functional group is a promising bioreductive trigger.

5.1.4. Experimental protocols

5.1.4.1. Synthesis and characterization

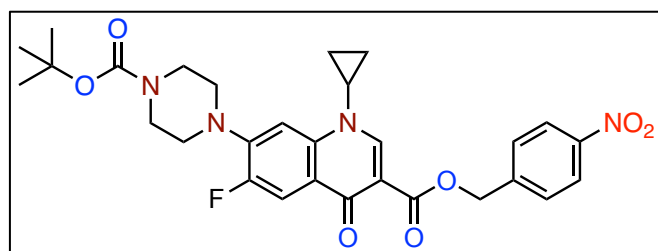
Compound **47**⁸ was synthesized following previously reported protocols and the analytical data for each compound was consistent with reported values.

5.1.4.1.A. General procedure for synthesis of *N*-boc protected nitroheterocyclic esters of CIP (48-49)

To a stirred solution of **47**, HBTU (1.74 mmol) and DMAP (0.13 mmol) in dry DCM (100 mL), DIPEA (1.74 mmol) was added. The reaction mixture was stirred for 30 min at RT. The resulting solution turned yellow. To this reaction mixture, alcohol was added and heated to 38 °C for 12 h until the starting material was completely consumed (as monitored by TLC). After completion of the reaction, water (100 mL) was added and the aqueous layer was extracted with DCM (3 × 100 mL). The organic extracts were combined, washed with brine (2 × 50 mL), dried over anhydrous Na₂SO₄ (2 g), filtered and the filtrate was concentrated under reduced pressure. The residue was purified by preparative HPLC using Kromasil[®]C-18 column at ambient temperature under the gradient elution with H₂O:ACN (20:80, v/v) as mobile phase at a flow rate of 12 mL/min to afford pure products (**48-49**).

4-nitrobenzyl 7-(4-(*tert*-butoxycarbonyl)piperazin-1-yl)-1-cyclopropyl-6-fluoro-4-oxo-1,4-dihydroquinoline-3-carboxylate (**48**)

Starting from **47** (0.150 g, 0.34 mmol), **48** (0.130 g, 65%) was obtained as a white solid; mp =

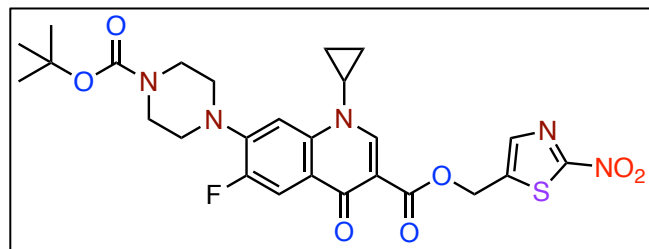


167-168 °C; *R_f* (EtOAc:hexane = 70:30) = 0.5; ¹⁹F NMR (376 MHz, CDCl₃): δ –123.2; ¹H NMR (400 MHz, CDCl₃): δ 8.57 (s, 1H), 8.24 (d, *J* = 11.0 Hz, 1H), 8.07 (d, *J* = 13.1 Hz, 1H), 7.73 (d, *J* = 8.8

Hz, 2H), 7.29 (d, *J* = 7.1 Hz, 1H), 5.48 (s, 2H), 3.67-3.65 (m, 1H), 3.43 (tt, *J* = 7.1, 4.0 Hz, 1H), 3.24-3.22 (m, 4H), 1.50 (s, 9H), 1.34 (d, *J* = 6.5 Hz, 2 H), 1.14 (d, *J* = 3.5 Hz, 1H).

(2-nitrothiazol-5-yl)methyl 7-(4-(tert-butoxycarbonyl)piperazin-1-yl)-1-cyclopropyl-6-fluoro-4-oxo-1,4-dihydroquinoline-3-carboxylate (49)

Starting from **47** (0.150 g, 0.34 mmol), **49** (0.145 g, 74%) was obtained as a yellow solid; mp =



= 135-136 °C; R_f (EtOAc:hexane = 70:30)

= 0.4; ^{19}F NMR (376 MHz, CDCl_3): δ -

122.9; ^1H NMR (400 MHz, CDCl_3): δ

8.56 (s, 2H), 8.02 (d, J = 13.1 Hz, 2H),

7.91 (s, 2H), 7.29 (s, 1H), 5.55 (s, 2H),

3.69 – 3.60 (m, 4H), 3.48 – 3.43 (m, 1H), 3.24 – 3.21 (m, 4H), 1.50 (s, 9H), 1.36 (q, J = 6.9

Hz, 2 H), 1.16 (q, J = 6.5 Hz, 2H); ^{13}C NMR (100 MHz, CDCl_3): δ 172.9, 165.8, 165.7, 154.8,

154.7, 152.4, 149.1, 144.8 (d), 142.1, 142.0, 138.0, 123.2 (d), 113.4 (d), 108.8, 105.2, 80.4,

58.2, 50.0, 34.9, 28.5, 8.3; DEPT-135 NMR (100 MHz, $\text{DMSO}-d_6$): δ 149.0 (CH), 142.0 (CH),

113.4 (CH), 105.1 (CH), 58.1 (CH_2), 50.0 (CH_2), 34.8 (CH), 28.4 (CH_3), 8.2 (CH_2); HRMS

(ESI-TOF) for $\text{C}_{26}\text{H}_{28}\text{FN}_5\text{O}_7\text{S}$ $[\text{M}+\text{H}]^+$: Calcd., 574.1771, Found, 574.1768.

5.1.4.1.B. General procedure for N-boc deprotection of NTR-CIP derivatives (50 and 51)

To a solution of compound in dry DCM (10 mL), TFA (26.47 mmol) was added dropwise at 0

°C under nitrogen atmosphere. The resulting reaction mixture was stirred at RT (~ 4-6 h) until

the starting material had been completely consumed (determined by TLC) and the solvent was

concentrated *in vacuo* at ~5 °C . The product was precipitated by diethyl ether on sonication

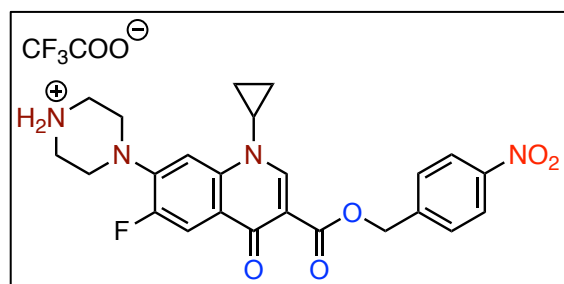
and the ether solution was then carefully decanted. The obtained solid was washed twice with

diethyl ether, and the ethereal solution was concentrated *in vacuo* to afford prodrugs **50** and **51**

as pure products.

4-(1-cyclopropyl-6-fluoro-3-(((4-nitrobenzyl)oxy)carbonyl)-4-oxo-1,4-dihydroquinolin-7-yl)piperazin-1-ium 2,2,2-trifluoroacetate (50)

Starting from **48** (150 mg, 0.26 mmol), **50** (113 mg, 92%) was isolated as a white solid; mp =



121-122 °C; R_f (MeOH: CHCl_3 = 10:90) = 0.2;

^{19}F NMR (400 MHz, $\text{DMSO}-d_6$): δ -124.4, -74.2;

^1H NMR (400 MHz, $\text{DMSO}-d_6$): δ 9.04 (s, 2H),

8.53 (s, 1H), 8.26 (d, J = 8.6 Hz, 2H), 7.84 (d, J

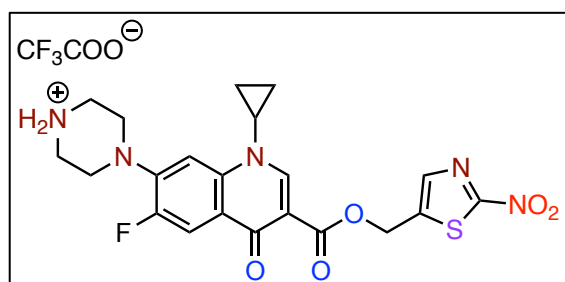
= 13.2 Hz, 1H), 7.79 (d, J = 8.6 Hz, 2H), 7.49 (d,

J = 7.3 Hz, 1H), 5.43 (s, 2H), 3.73 – 3.67 (m,

1H), 3.47 – 3.45 (m, 4H), 3.34 (br, 4H), 1.29 – 1.25 (m, 2H), 1.14 – 1.10 (br, 2H); ^{13}C (100

MHz, DMSO-*d*₆): δ 171.6, 164.4, 153.9, 151.3, 148.9, 146.9, 144.6, 142.8 (d), 138.0, 128.1, 123.5, 122.6 (d), 111.8 (d), 108.6, 106.9, 64.2, 46.6, 42.8, 35.2, 7.7; DEPT-135 NMR (100 MHz, DMSO-*d*₆): δ 148.8 (CH), 127.9 (CH), 123.2 (CH), 111.6 (CH), 106.6 (CH), 64.2 (CH₂), 46.3 (CH₂), 42.5 (CH₂), 34.7 (CH), 7.4 (CH₂); HRMS (ESI-TOF) for C₂₄H₂₄FN₄O₅ [M]⁺: Calcd., 467.1725, Found, 467.1726.

4-(1-cyclopropyl-6-fluoro-3-(((2-nitrothiazol-5-yl)methoxy)carbonyl)-4-oxo-1,4-dihydroquinolin-7-yl)piperazin-1-ium 2,2,2-trifluoroacetate (**51**)



Starting from **49** (150 mg, 0.26 mmol), **51** (118 mg, 95%) was isolated as a yellow solid; mp = 171-172 °C; *R_f* (MeOH:CHCl₃ = 10:90) = 0.2; ¹⁹F NMR (400 MHz, DMSO-*d*₆): δ -124.3, -74.7; ¹H NMR (400 MHz, DMSO-*d*₆): δ 8.95 (s, 2H), 8.53 (s, 1H), 8.16 (s, 1H), 7.83 (d, *J* = 13.2 Hz,

1H), 7.49 (d, *J* = 7.4 Hz, 1H), 5.57 (s, 2H), 3.72 – 3.67 (m, 1H), 3.49 – 3.42 (m, 4H), 3.33 (s, 4H), 1.27 (d, *J* = 5.9 Hz, 2H), 1.14 – 1.09 (m, 2H); ¹³C (100 MHz, DMSO-*d*₆): δ 171.5, 166.3, 164.3, 158.5, 158.1, 153.8, 151.3, 149.1, 142.9, 142.8, 141.9, 138.0, 122.5 (d *J* = 26.2 Hz), 111.9 (d, *J* = 89.4 Hz), 107.9, 106.9, 58.0, 46.6, 42.8, 35.1, 7.6; HRMS (ESI-TOF) for C₂₁H₂₁FN₅O₅S [M]⁺: Calcd., 474.1242, Found, 474.1246.

5.1.4.2. General methods

Stock solutions of CIP (1 mM), compounds **50** and **51** (1 mM) were prepared in DMSO whereas the stock solutions of *E. coli* NTR (1 mg/mL) and NADH (5 mM) were prepared in phosphate buffer (pH 7.4, 10 mM). Unless otherwise specified, the reaction mixtures were prepared in 10 mM pH 7.4 phosphate buffer (PB) and the fluorescence corresponding to MXF ($\lambda_{\text{ex}} = 281$ nm and $\lambda_{\text{em}} = 445$ nm) was measured using an EnSight Multimode Plate Reader (PerkinElmer).

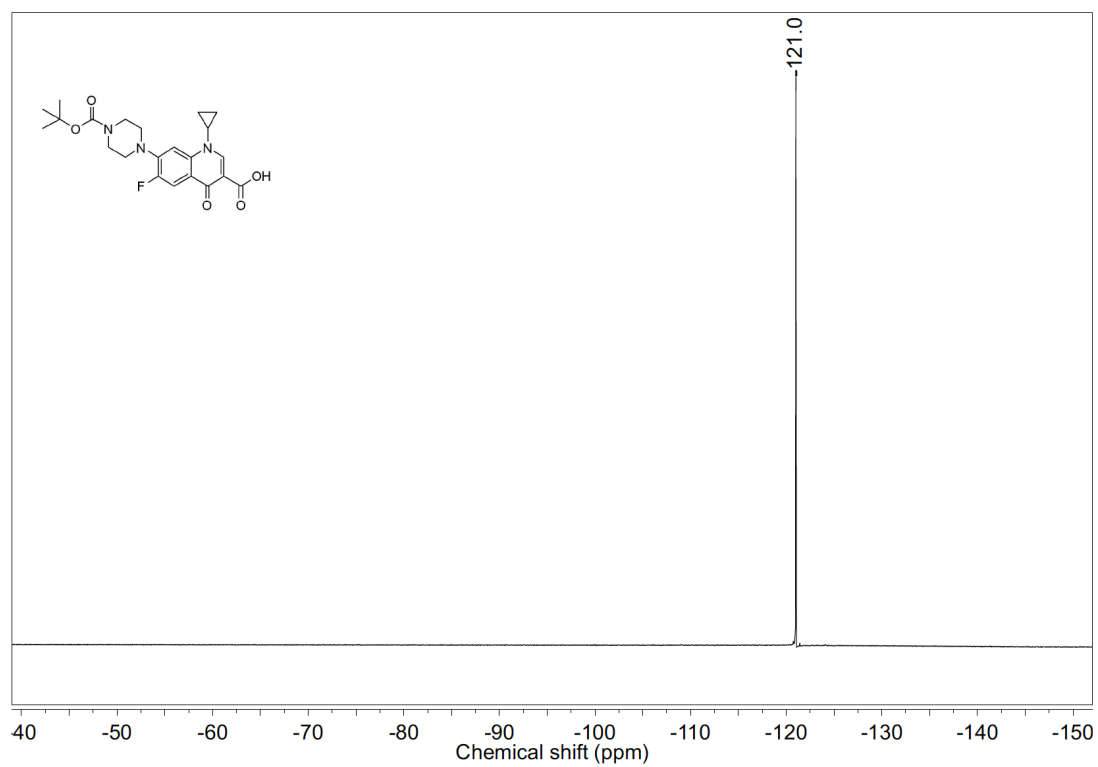
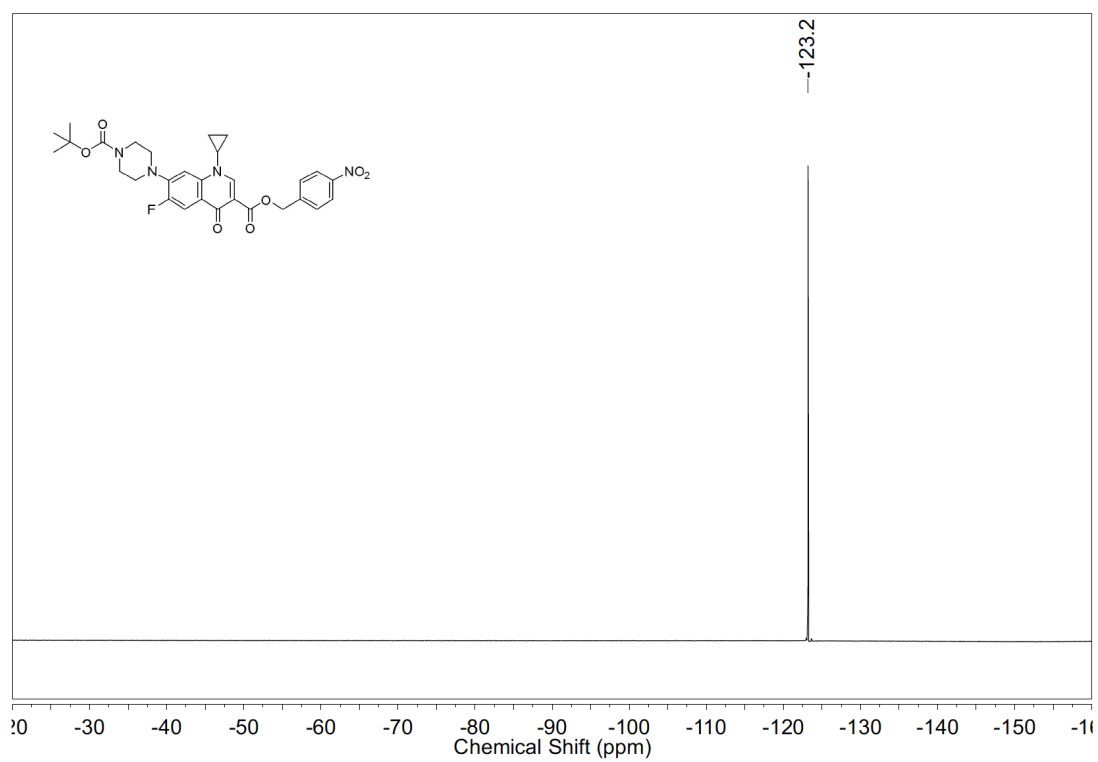
5.1.4.3. Investigating the release of CIP from prodrugs using a fluorescence-based assay

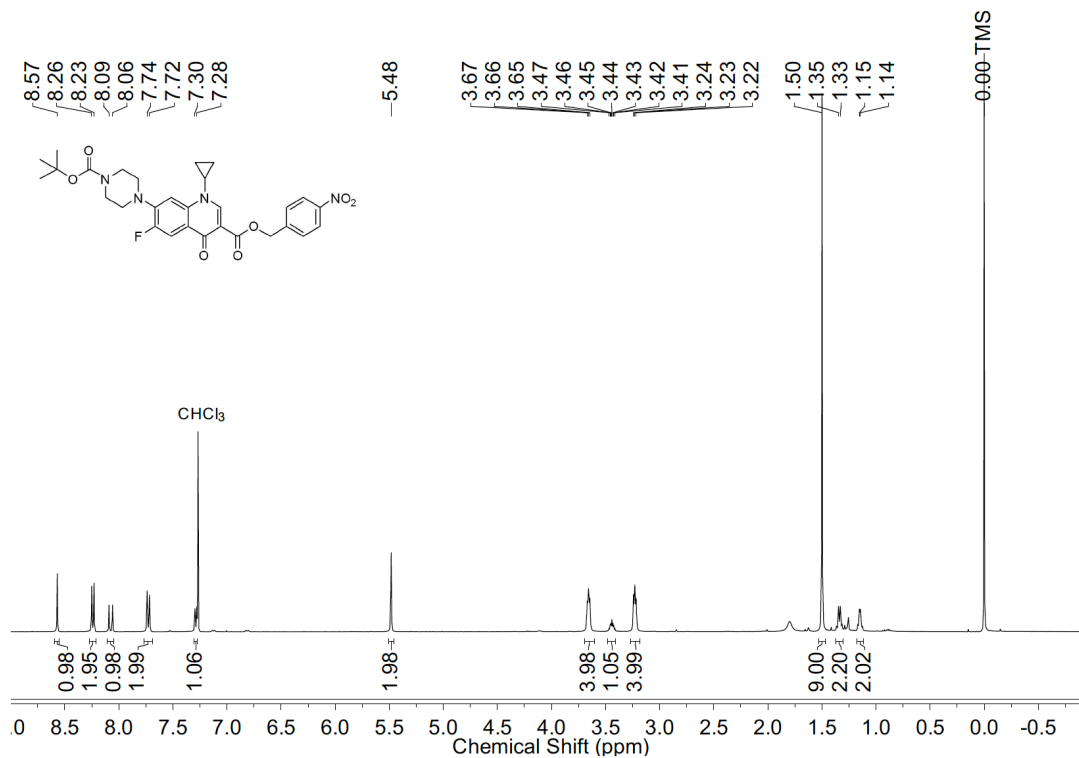
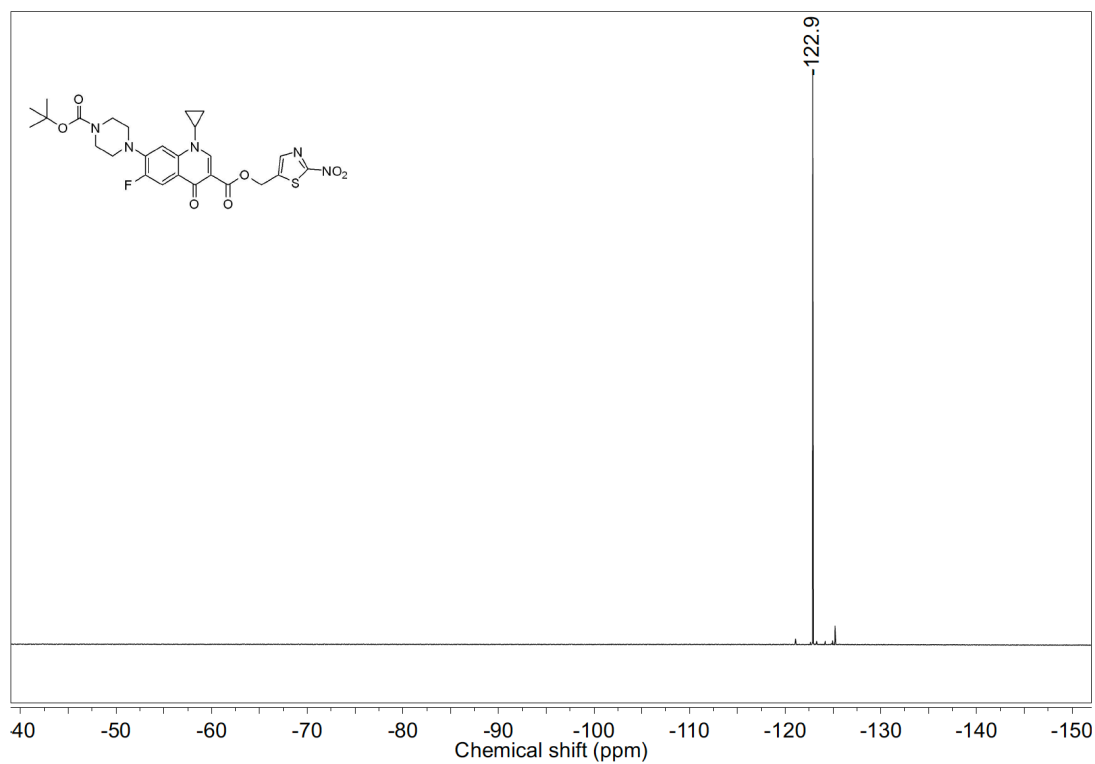
The reactions in the 96-well plate were initiated by the addition of 15 nM *E. coli* NTR (30 μ L; 0.1 μ M) and 100 μ M of NADH (4 μ L; 5 mM stock) to a solution of 10 μ M prodrugs (2 μ L, 1 mM stock) in 164 μ L of buffer. The enhancement of the fluorescence signal corresponding to the release of CIP relative to the NTR untreated control was recorded at 37 °C using an EnSight microplate reader (PerkinElmer) for 1 h.

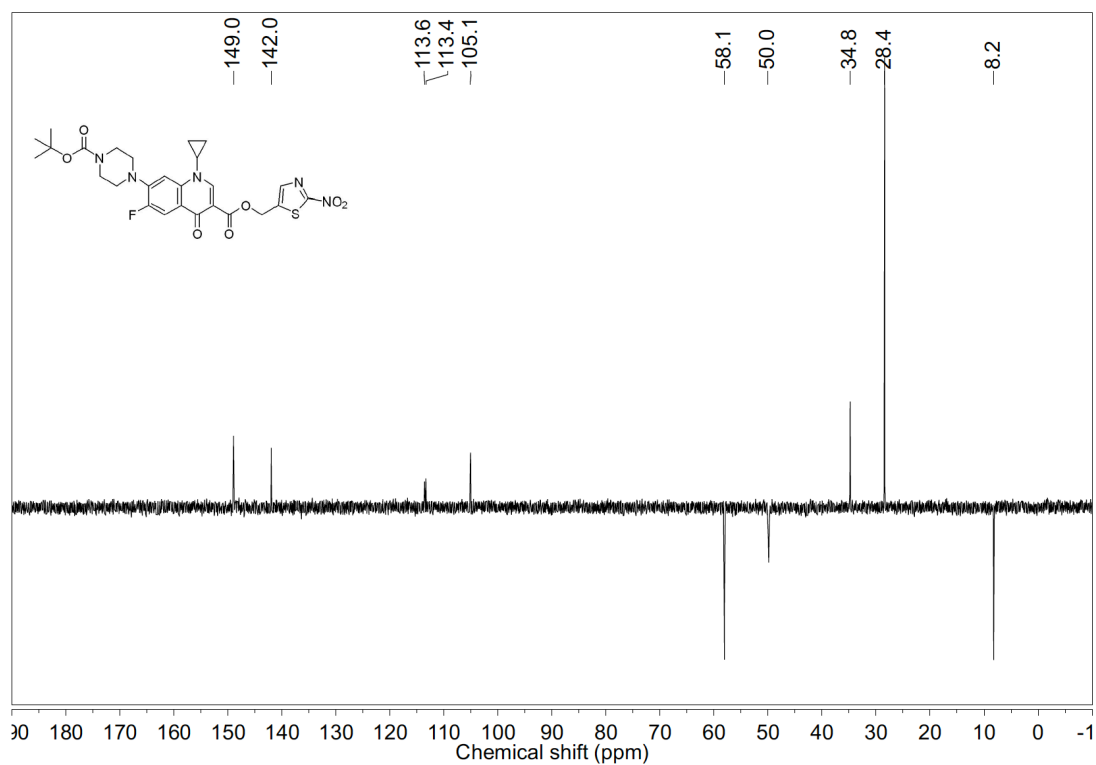
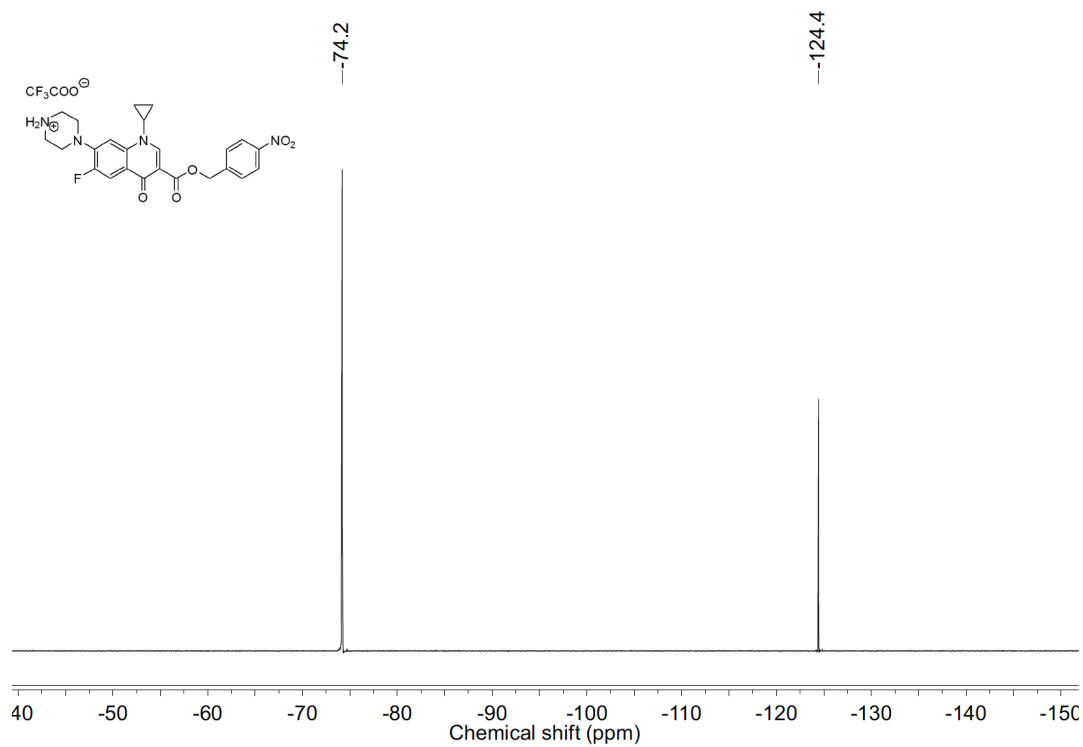
5.1.4.4. *In situ* detection of CIP generated from prodrugs in bacterial lysates (*E. coli*, and *M. smegmatis*) using fluorescence-based assay

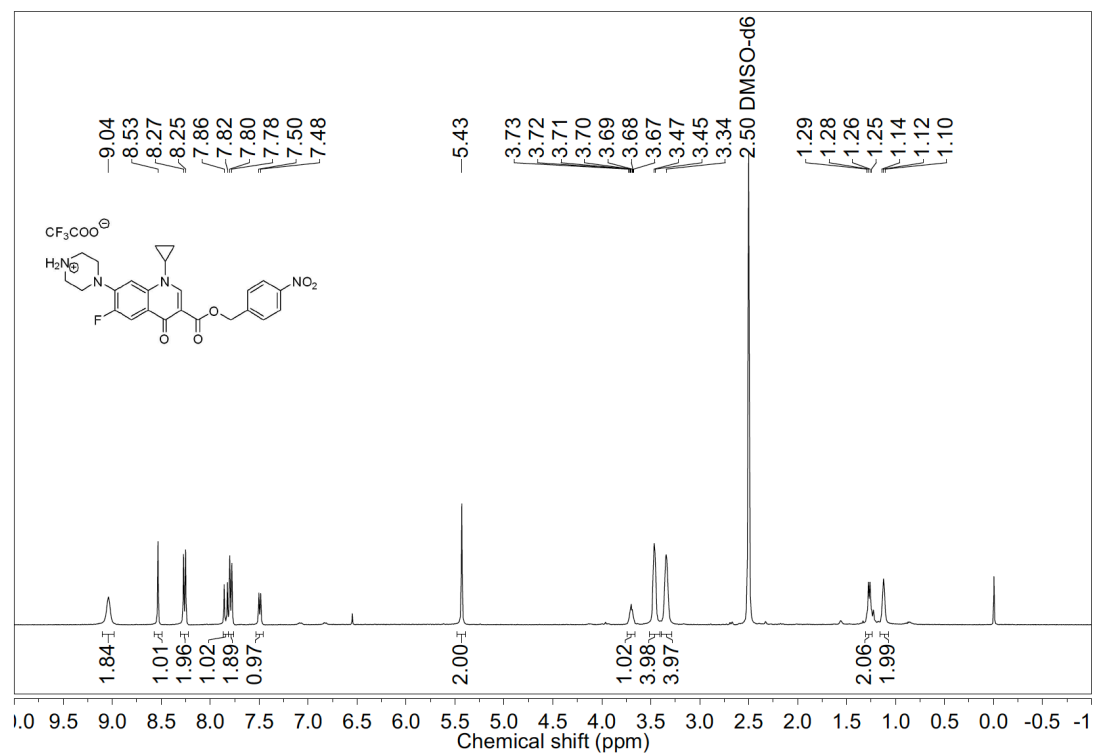
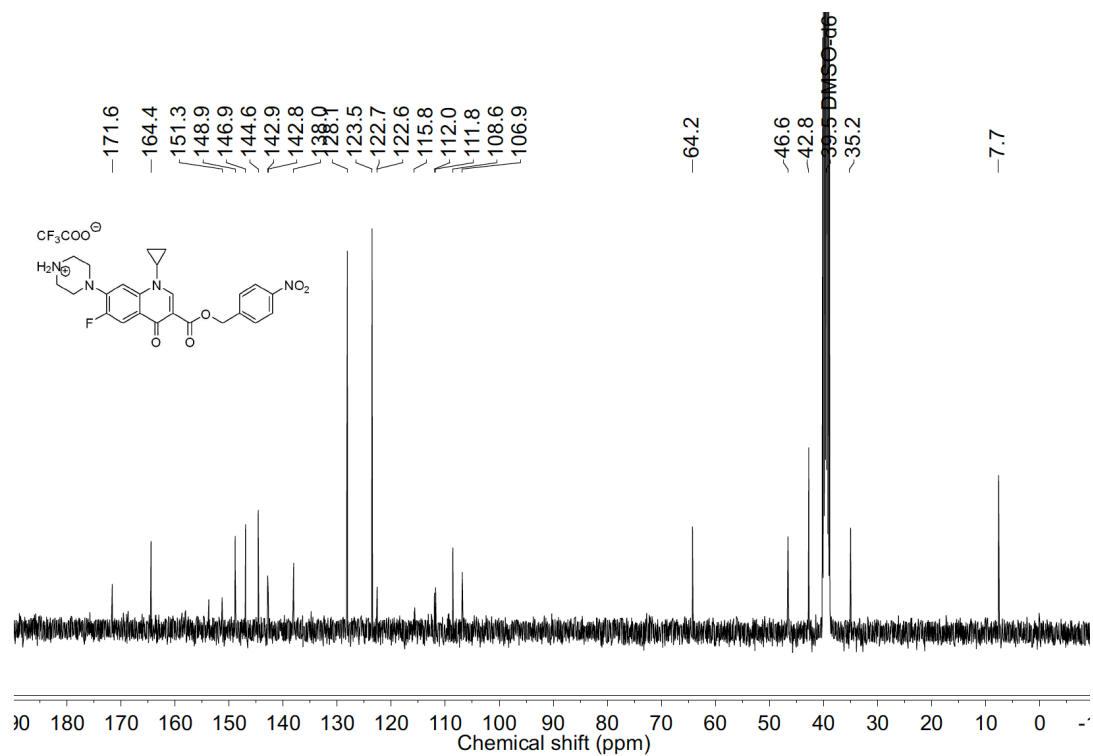
E. coli ATCC 25922 was grown in LB media at 37 °C in a rotary shaker for overnight. *M. smegmatis* mc²155 bacteria was grown with agitation of 180 rpm in Middlebrook 7H9 broth media supplemented with glycerol (0.2%), and tween-80 (0.1%) at 37 °C for 24 h. The bacterial cells were harvested by centrifugation at 2486 x g (10 min for *E. coli*; 15 min for *M. smegmatis*) at 4 °C. The bacterial pellets were washed twice with PBS buffer (1x, pH 7.4), resuspended in PBS (1x, 2 mL), and transferred to a microcentrifuge tube. The cells were lysed by sonication using (130 W ultrasonic processor, VX 130W) stepped microtip for 2 minutes pulse on time (with 5 s ON and 10 s OFF pulse, 60% amplitude, 20 kHz frequency for *E. coli*) or 5 minutes pulse on time (with 3 s ON and 3 s OFF pulse, 60% amplitude, 20 kHz frequency for *M. smegmatis*) under ice cold conditions. The total protein concentration of the whole cell lysate was determined by Bradford assay using bovine serum albumin (BSA) and further adjusted to 1 mg/mL with PBS (1x). The reactions were conducted by treatment of 10 µM of various prodrugs (5 µL, 1 mM stock) with 495 µL of *E. coli* or *M. smegmatis* lysate (1 mg/mL) at 37 °C on an Eppendorf thermomixer comfort (800 rpm). An aliquot (100 µL) was taken after 1 h or 2 h of incubation (for prodrugs **50** and **51**), transferred to a 96-well microplate, and fluorescence for the release of CIP was recorded using a microplate reader (EnSight). A similar protocol was followed to determine the specificity of **51** toward *E. coli* and *M. smegmatis* NTR by treatment of 490 µL bacterial lysate with 250 µM of DCOM (5 µL, 25 mM stocks) for 10 min prior to the addition of 10 µM of **51** (5 µL, 1 mM stock).

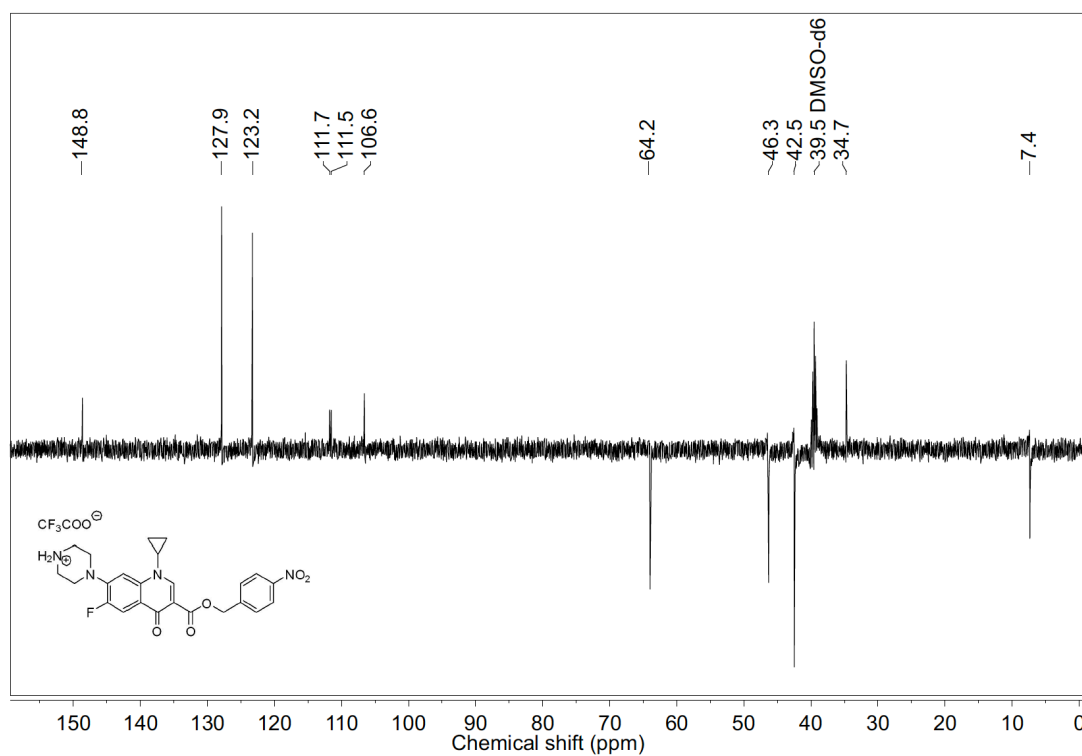
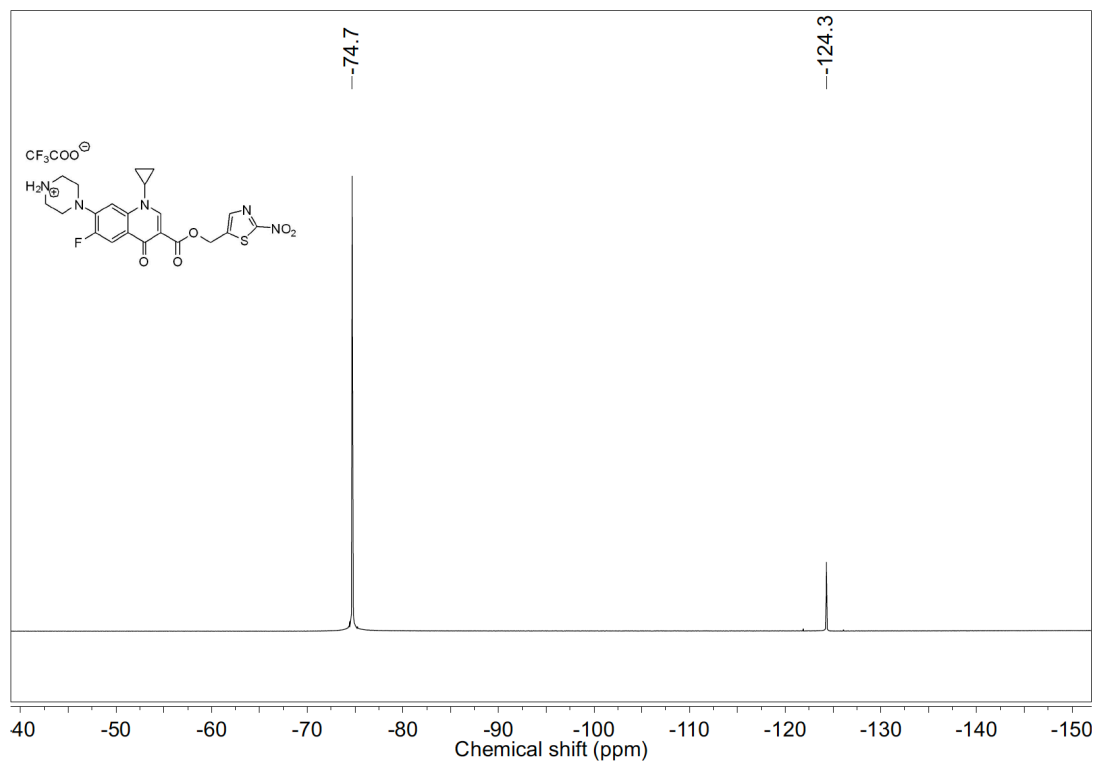
5.1.5. NMR spectral data

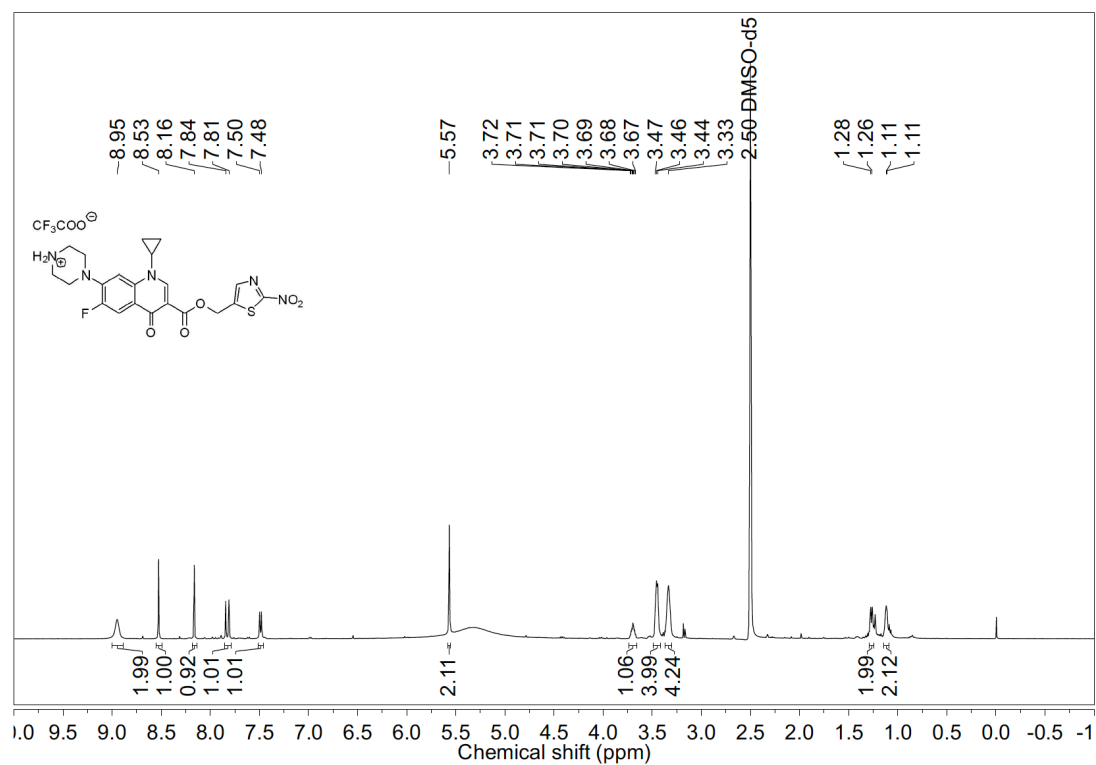
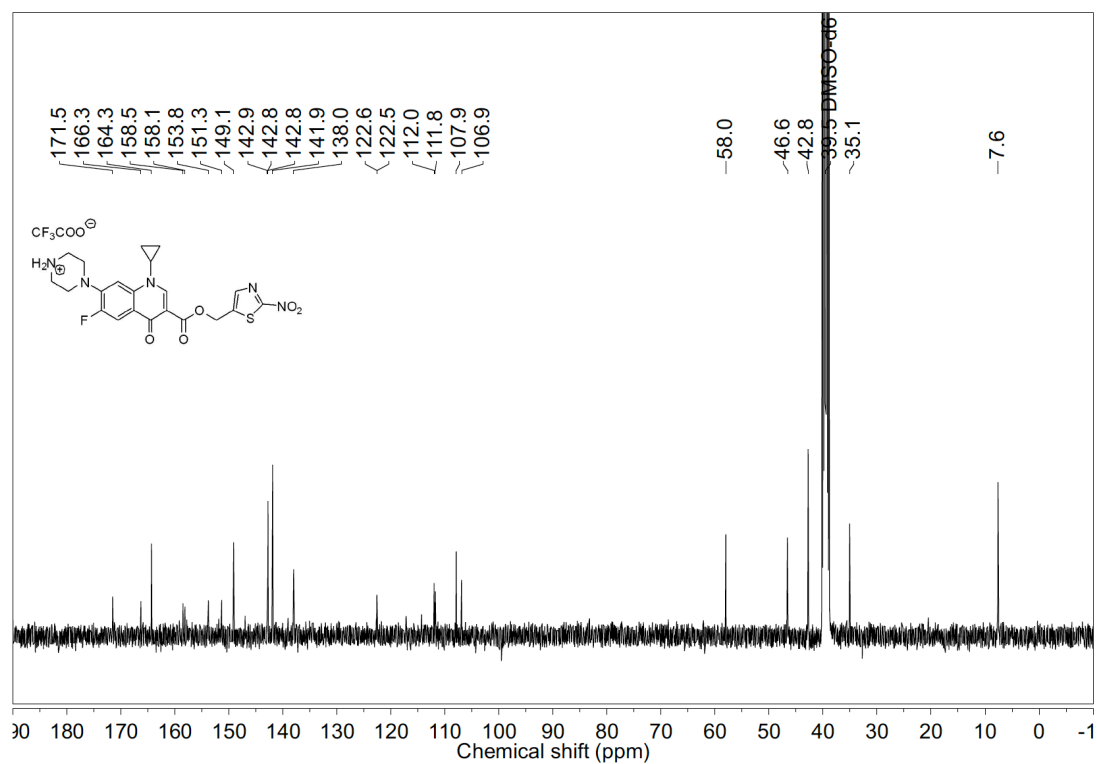
 ^{19}F NMR spectrum (400 MHz, CDCl_3) of **47** ^{19}F NMR spectrum (400 MHz, CDCl_3) of **48**

^1H NMR spectrum (400 MHz, CDCl_3) of **48** ^{19}F NMR spectrum (400 MHz, CDCl_3) of **49**

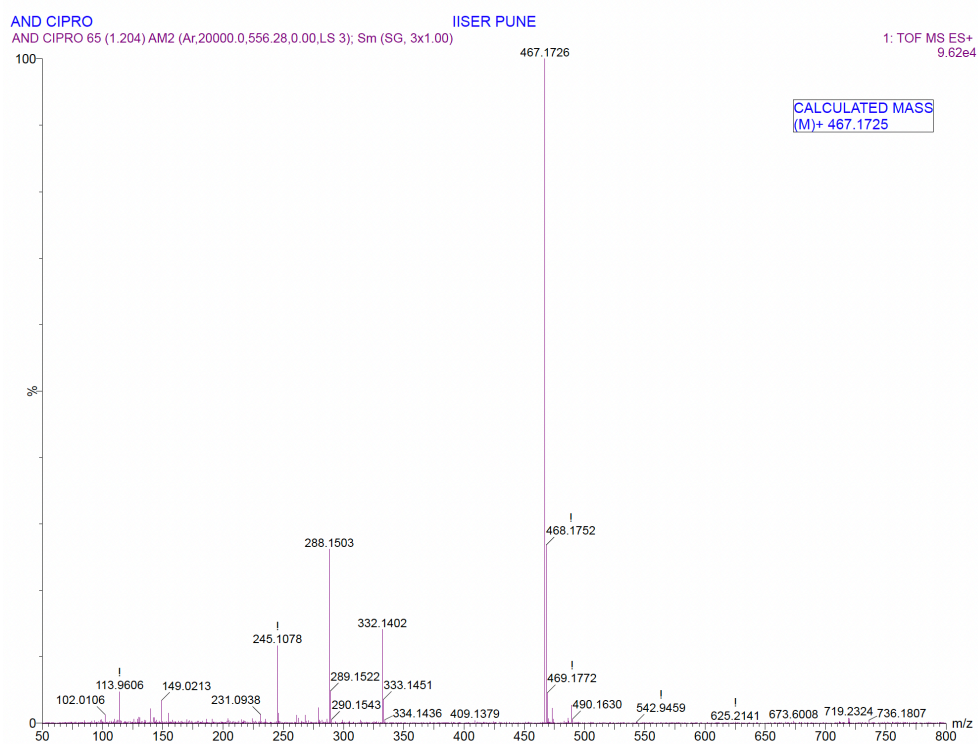
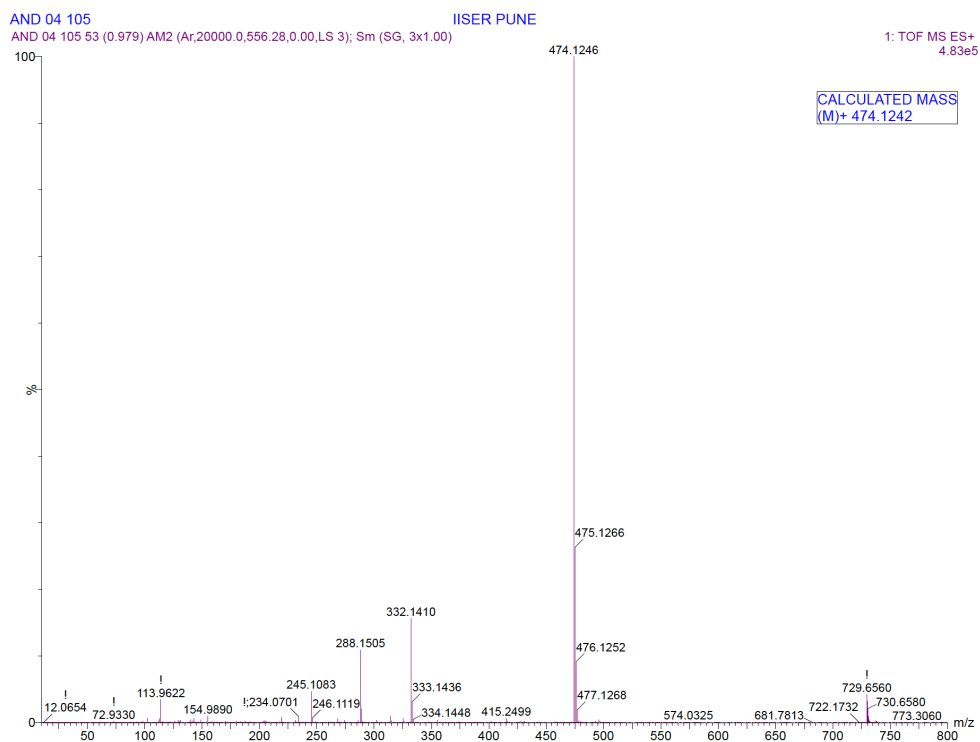
DEPT-135 NMR spectrum (100 MHz, CDCl₃) of **49**¹⁹F NMR spectrum (400 MHz, DMSO-*d*₆) of **50**

¹H NMR spectrum (400 MHz, DMSO-*d*₆) of **50**¹³C NMR spectrum (100 MHz, DMSO-*d*₆) of **50**

DEPT-135 NMR spectrum (100 MHz, DMSO-*d*₆) of **50** ^{19}F NMR spectrum (400 MHz, DMSO-*d*₆) of **51**

^1H NMR spectrum (400 MHz, $\text{DMSO-}d_6$) of **51** ^{13}C NMR spectrum (100 MHz, $\text{DMSO-}d_6$) of **51**

5.1.6. HRMS spectra of final compounds

HRMS spectrum of **50**HRMS spectrum of **51**

5.1.7. References

- (1) Walker, R. C. The Fluoroquinolones. *Mayo Clin. Proc.* **1999**, *74* (10), 1030–1037.
- (2) Andriole, V. T. The Quinolones: past, present, and future. *Clin. Infect. Dis.* **2005**, *41*, S113–S119.
- (3) Andriole, V. T. *The Quinolones*, 2nd edn.; Academic Press, San Diego, CA, 1998.
- (4) Tillotson, G. S. Quinolones: structure-activity relationships and future predictions. *J. Med. Microbiol.* **1996**, *44* (5), 320–324.
- (5) Pham, T. D. M.; Ziora, Z. M.; Blaskovich, M. A. T. Quinolone Antibiotics. *Medchemcomm* **2019**, *10* (10), 1719–1739.
- (6) Campoli-Richards, D. M.; Monk, J. P.; Price, A.; Benfield, P.; Todd, P. A.; Ward, A. Ciprofloxacin. A review of its antibacterial activity, pharmacokinetic properties and therapeutic use. *Drugs*. **1988**, *35* (4), 373-447
- (7) Aldred, K. J.; Kerns, R. J.; Osheroff, N. Mechanism of Quinolone Action and Resistance. *Biochemistry* **2014**, *53*, 1565–1574.
- (8) Pardeshi, K. A.; Kumar, T. A.; Ravikumar, G.; Shukla, M.; Kaul, G.; Chopra, S.; Chakrapani, H. targeted antibacterial activity guided by bacteria-specific nitroreductase catalytic activation to produce ciprofloxacin. *Bioconjug. Chem.* **2019**, *30* (3), 751–759.

Chapter 5.2. Design and Development of Nitroreductase (NTR) Responsive Dual Colorimetric Fluorescence “Turn OFF-ON” Probes

5.2.1. Introduction

The widespread and long-term overuse use of antibiotics has spurred the rise of drug resistant pathogenic bacteria, which poses a major risk to human health worldwide. The severity of infections varies, ranging from self-limiting to a potentially fatal condition, causing significant morbidity and mortality. A recent study estimated that ~1.27 million people died due to drug resistant infections.¹ Therefore, rapid detection of bacteria is critical for early diagnosis and effective treatment of infections as well as the development of new antibiotics. Several techniques, including polymerase chain reaction (PCR), immunological assays, and use of staining agents have been widely used for the detection of bacteria. These standardized time-consuming methods involve many steps and can often produce false positive results.²⁻⁷

To accommodate such needs, significant progress has been made in the area of fluorescence imaging employing bacterial-specific small molecule fluorescent probes. These probes generate “TURN-ON” fluorescence through a specific interactions either with cell wall components or reaction of bacterial enzymes allowing real-time fluorescent imaging of bacteria under *in vitro* and *in vivo* conditions.^{8,9} Many fluorescent probes reported in the literature rely on activation by bacterial specific enzymes such as alkaline phosphatase (ALP), β -glucuronidase, β -lactamase, and Nitroreductase (NTR).^{7,10-15} Due to the prevalence of nitroreductases (NTRs) in bacteria, this enzyme is a highly relevant diagnostic marker for the detection of bacterial infections.^{16,17} Owing to the presence of NTRs in several pathogenic bacteria belonging to ESKAPE family (*E. faecium*, *S. aureus*, *K. pneumoniae*, *A. baumannii*, *P. aeruginosa* and *Enterbacter* sp.) responsible for the majority of hospital-acquired drug-resistant infections, numerous research groups have developed NTR responsive probes for real time detection of bacteria.^{16,18-22} Although probes capable of detecting NTRs in bacteria have been developed, the utilization of NTRs as diagnostic markers for rapid detection of bacterial infections by visual and fluorescence readout remains scarce.

Owing to the prominent photophysical properties, tricyanofuran based long wavelength fluorescent probe, TCF-OH has been widely employed in several *in vitro* and *in vivo* settings for real-time detection of analytes.²³⁻²⁷ In this chapter, we utilized TCF-OH as a prototype to develop nitroreductase (NTR) responsive dual colorimetric fluorescence “turn OFF-ON” probe.

5.2.2. Design of Nitroreductase (NTR)-responsive dual colorimetric fluorescent probe

Despite the common use of 4-nitrobenzyl bio-reductive group, various nitro heterocyclic triggers such as 2-nitroimidazole, nitro-furan and nitro-thiophene have been widely employed to develop bio-reductive prodrugs, hypoxia activated prodrugs and fluorescent probes for nitroreductase enzyme due to their ease of undergoing facile reduction.^{28–30} Earlier results in this thesis showed that the bacterial NTR favoured 2-nitrothiazole-based prodrugs over other substrates, clearly suggesting an impressive selectivity of 2-nitrothiazolyl moiety towards the bacterial NTR. Inspired by these differences in the sensitivity and specificity of nitro(hetero)aryl groups towards NTR, a dual colorimetric fluorescent probe sensitive to bacterial NTR was constructed. Herein, TCF-OH was caged with a nitro(hetero)aromatic functionality to develop latent fluorophores. The presence of electron-withdrawing nitro group induces an electron-transfer process and as a result quenches the fluorescence emission of the probe. However, NTR-catalyzed reduction of nitro group will be accompanied by a significant bathochromic shift and “turn OFF-ON” fluorescence, enabling the visual and fluorescence based detection of bacteria (Figure 5.2.1).³¹

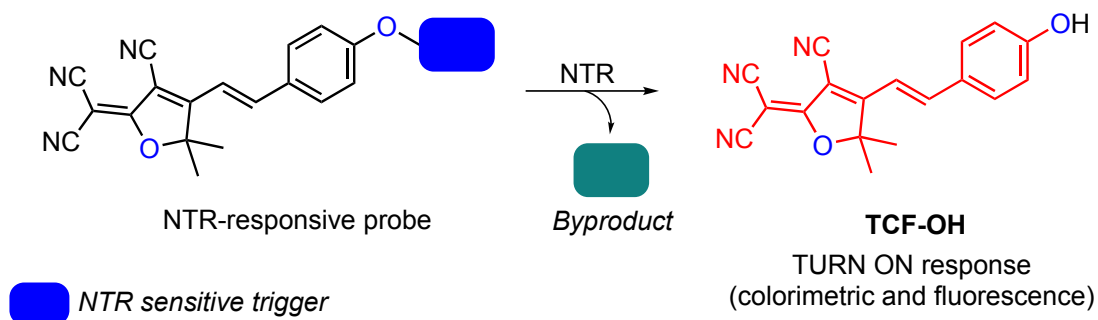
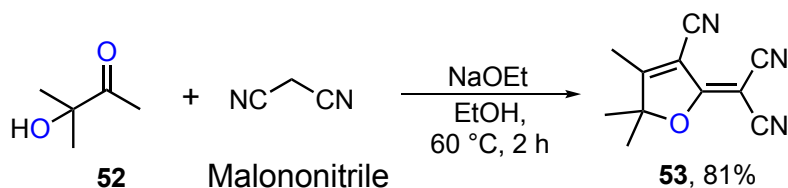


Figure 5.2.1. Proposed mechanism of NTR mediated activation of dual colorimetric fluorescence turn OFF-ON probe

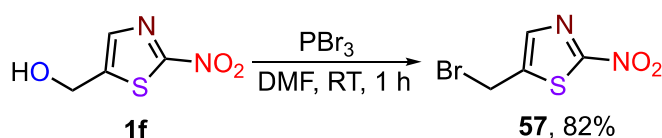
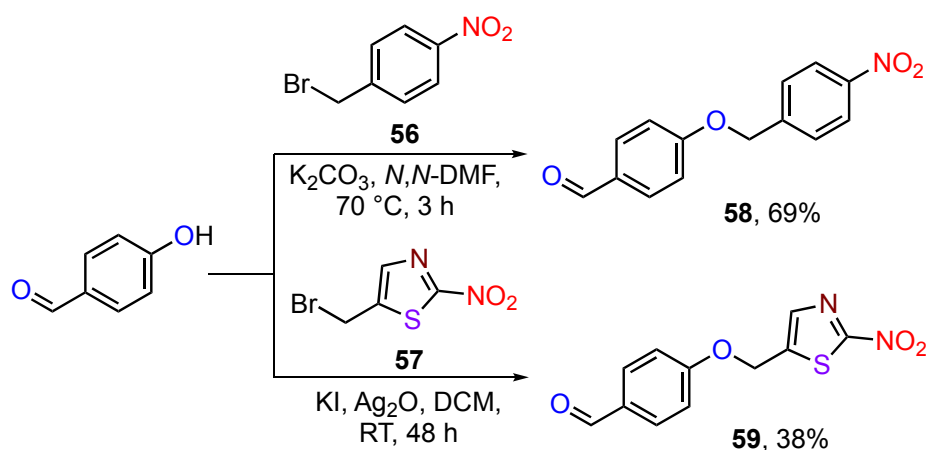
5.2.3. Results and discussion

5.2.3.1. Synthesis

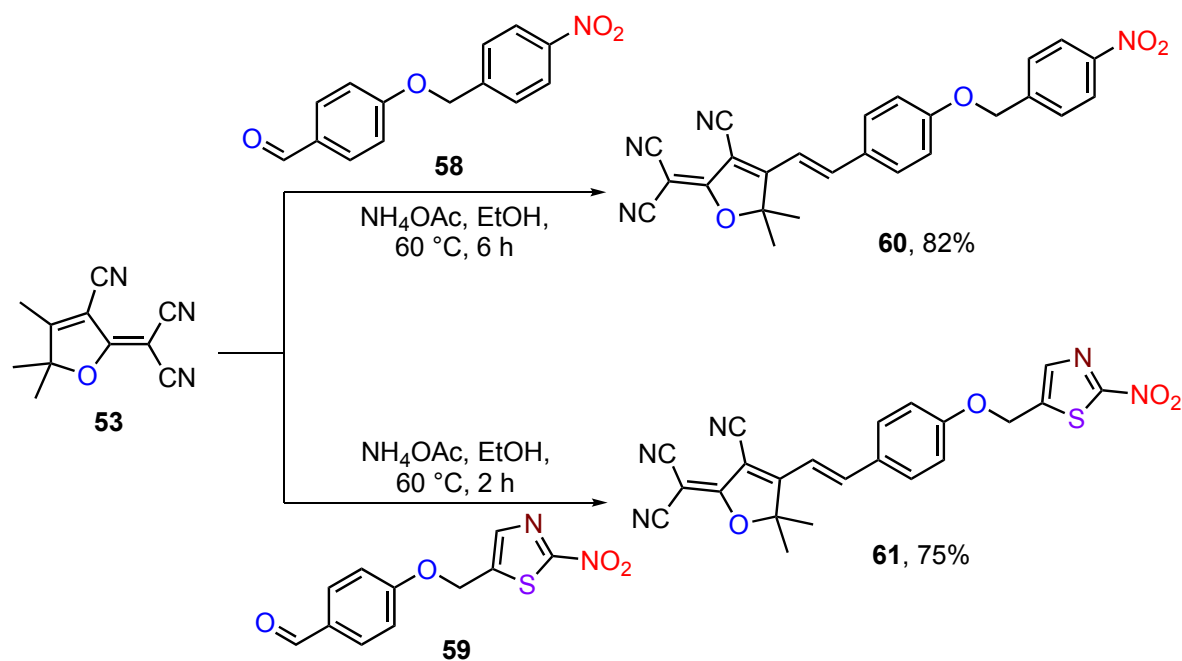
Initially, two building blocks (TCF fluorophore **53** and nitro group containing aldehydes **56** and **57**) were synthesized in order to design NTR-responsive latent fluorophores. The fluorophore **53** was synthesized in one-pot sodium ethoxide promoted reaction of **52** with malononitrile in ethanol (Scheme 5.2.1).²⁵

Scheme 5.2.1. Synthesis of **53**

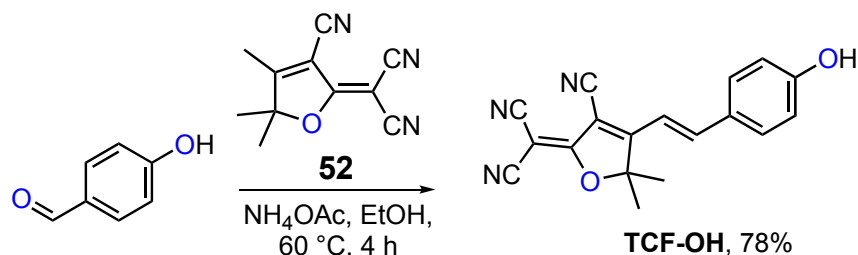
The commercially available 4-nitrobenzyl bromide **56** was used without further purification. Bromination of the primary alcohol **1f** with PBr₃ furnished **57** as a yellowish white solid (Scheme 5.2.2). Etherification of **56** with 4-hydroxy benzaldehyde in the presence of K₂CO₃ gave **58** in good yield (Scheme 5.2.3).³² Unfortunately, **57** underwent decomposition in basic condition and did not provided **59** as a desired compound. Therefore, etherification of **57** with 4-hydroxy benzaldehyde was performed under neutral condition using silver oxide (Ag₂O) in the presence of catalytic amount of KI to obtain **59** (Scheme 5.2.3).

Scheme 5.2.2. Synthesis of **57**Scheme 5.2.3. Synthesis of **58** and **59**

Finally, base catalyzed Knoevenagel condensation of **53** with aldehydes **58** or **59** provided latent fluorophores, **60** and **61** respectively in moderate yields (Scheme 5.2.4). A similar synthetic strategy was used to synthesize the fluorescent probe, TCF-OH from the corresponding aldehyde following a reported protocol (Scheme 5.2.5). All the compounds were well characterized by ¹H-NMR, ¹³C-NMR and HRMS techniques.

Scheme 5.2.4. Synthesis of **60** and **61**

Scheme 5.2.5. Synthesis of TCF-OH



5.2.3.2. Photophysical properties

All photophysical studies were carried out with probes containing 1% of DMSO in PBS (1x, pH 7.4) at $37\text{ }^\circ\text{C}$. Owing to the presence of extended π -conjugation, **TCF-OH** ($50\text{ }\mu\text{M}$) displayed a pinkish color in buffer and exhibited a strong emission at 603 nm upon excitation at 579 nm. However, under these conditions, the probes **60** and **61** ($50\text{ }\mu\text{M}$) displayed no fluorescence and showed yellow coloration in solution (Figure 5.2.2). This could be attributed to the presence of an electron-withdrawing nitro group in the probe, which decreases the π -conjugation resulting in hypsochromic shift.

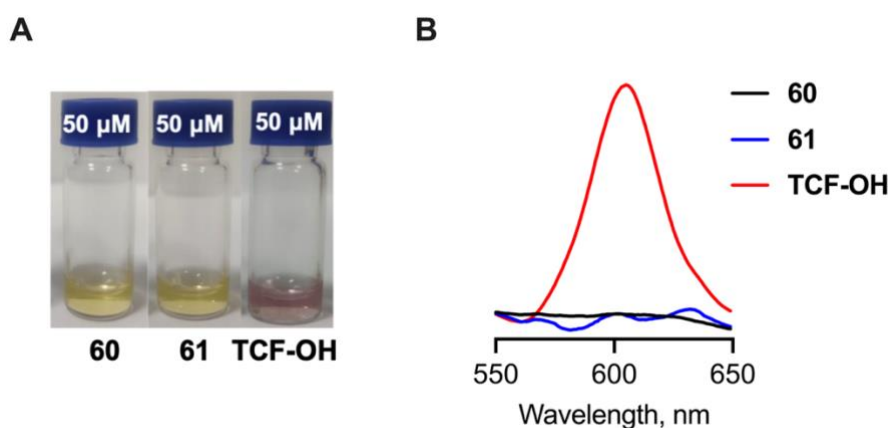


Figure 5.2.2. (A) Colorimetric response and (B) Emission spectra ($\lambda_{\text{ex}} = 579 \text{ nm}$) of probes (50 μM) recorded in pH 7.4 phosphate buffer (10 mM)

5.2.3.3. *E. coli* NTR mediated activation of latent fluorophores

The fluorescence response of probes was assessed in the presence of a fixed concentration of cofactor NADH (100 μM) and NTR (15 nM) in phosphate buffer (pH 7.4, 10 mM). The probes **60** and **61** were non-fluorescent in the absence of NTR, but exhibited an increase in the fluorescence intensity after 30 min upon reaction with NADH and NTR. Consistent with the earlier findings described in this thesis, 2-nitrothiazolyl caged probe **61** remained more sensitive and provided a strong fluorescence signal than widely utilized 4-nitrobenzyl tethered probe **60** (Figure 5.2.3). These results encouraged us to pursue **61** as a chemosensor for NTR for further studies.

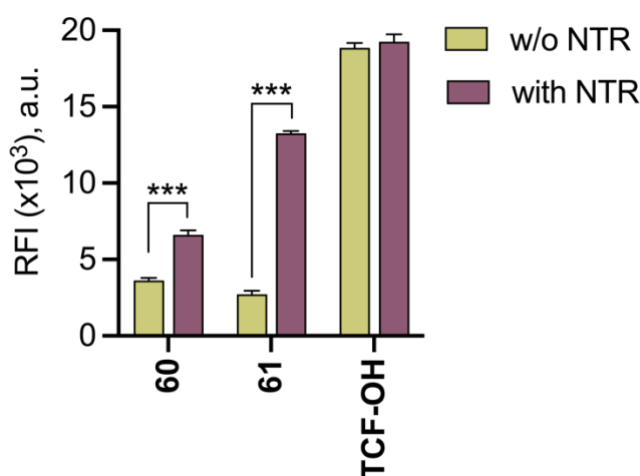


Figure 5.2.3. Monitoring the fluorescence response ($\lambda_{\text{ex}} = 579 \text{ nm}$ and $\lambda_{\text{em}} = 603 \text{ nm}$) of probes after 30 min of incubation with *E. coli* NTR (15 nM) and NADH (100 μM) in pH 7.4 phosphate buffer (10 mM) at 37 °C. p values were determined using the student's two-tailed unpaired parametric t -test relative to the NTR untreated control. (***) $p \leq 0.001$).

5.2.3.4. *E. coli* NTR dependent colorimetric and fluorescence “turn OFF-ON” response

Next, the colorimetric and fluorescence “turn OFF-ON” response of **61** was evaluated in the presence of *E. coli* NTR by UV/Vis spectroscopy and fluorimetry. As anticipated, the probe displayed yellow coloration and was intrinsically non-fluorescent in the absence of NTR. Addition of *E. coli* NTR induced a significant visual change from yellow to pink and a distinct redshift of the absorption band ascribed to the formation of **TCF-OH** after 5 min of incubation (Figure 5.2.4.A and 5.2.4.B). This was also accompanied with a concomitant increase in the fluorescence signal corresponding to the formation of **TCF-OH** formed during the enzymatic reaction (Figure 5.2.4.C).

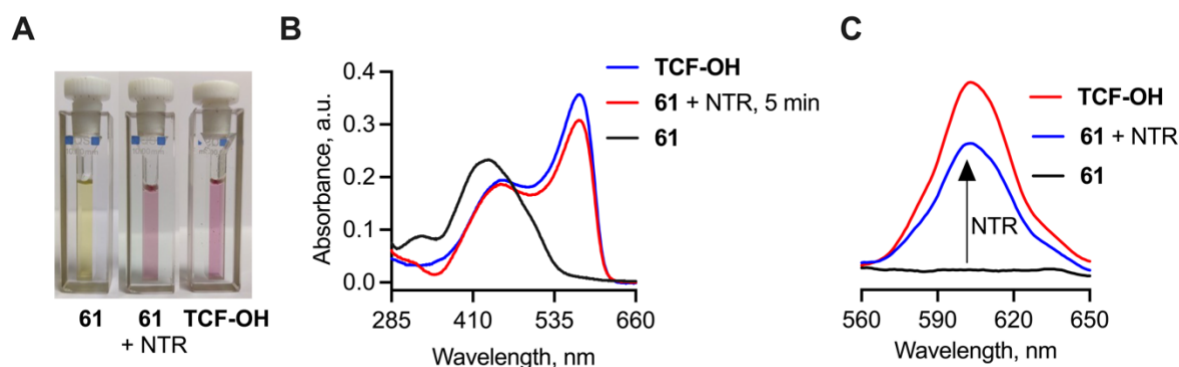


Figure 5.2.4. Monitoring the visual colorimetric response “turn OFF-ON” response of probe **61** (10 μ M) by (A) recording a photographic image and (B) absorption spectra after 5 min of incubation with *E. coli* NTR (15 nM) and NADH (100 μ M) in pH 7.4 phosphate buffer (10 mM) at 37 $^{\circ}$ C. A distinct colorimetric change (yellow to pink) corresponding to the formation of **TCF-OH** was observed after incubation of the probe with NTR. (C) Fluorescence spectra ($\lambda_{\text{ex}} = 579$ nm and $\lambda_{\text{em}} = 603$ nm) upon incubation of **61** (10 μ M) with NTR (15 nM) and NADH (100 μ M) in pH 7.4 phosphate buffer (10 mM).

HPLC analysis revealed the stability of **61** in pH 7.4 buffer over 1 h (Figure 5.2.5.A). Next, the enzymatic activation of probe **61** in the presence of a fixed concentration of NTR (*E. coli*; 15 nM) and cofactor (NADH; 100 μ M) was investigated. The probe was incubated with NTR at 37 $^{\circ}$ C for 15 min. Aliquots from the reaction mixture were taken at predetermined time points and were analyzed using HPLC. As anticipated, the peak corresponding to probe **61** at 14.98 min completely disappeared within 15 min in the presence of NTR and NADH. This was accompanied with the formation of a new peak corresponding to **TCF-OH** at 9.98 min in almost quantitative yield (Figure 5.2.5.B and 5.2.5.C). Altogether, these results corroborated the rapid and complete conversion of **61** to **TCF-OH** in the presence of NTR (Scheme 5.2.6).

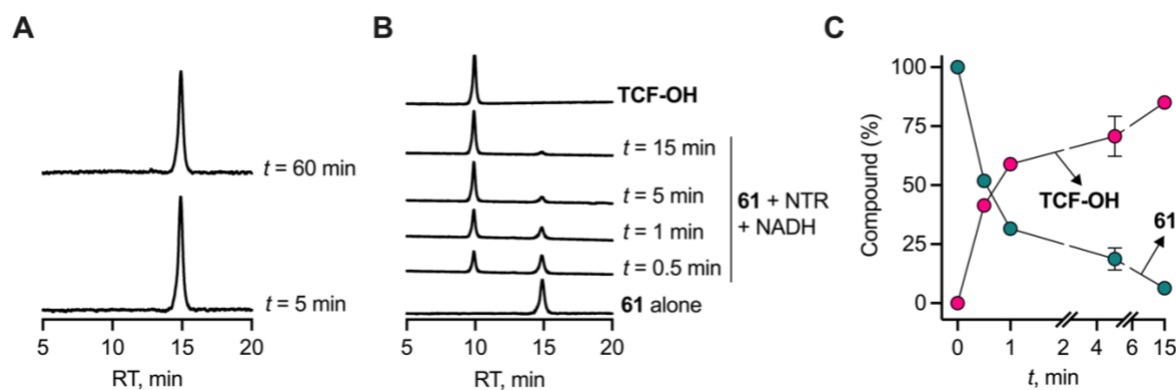
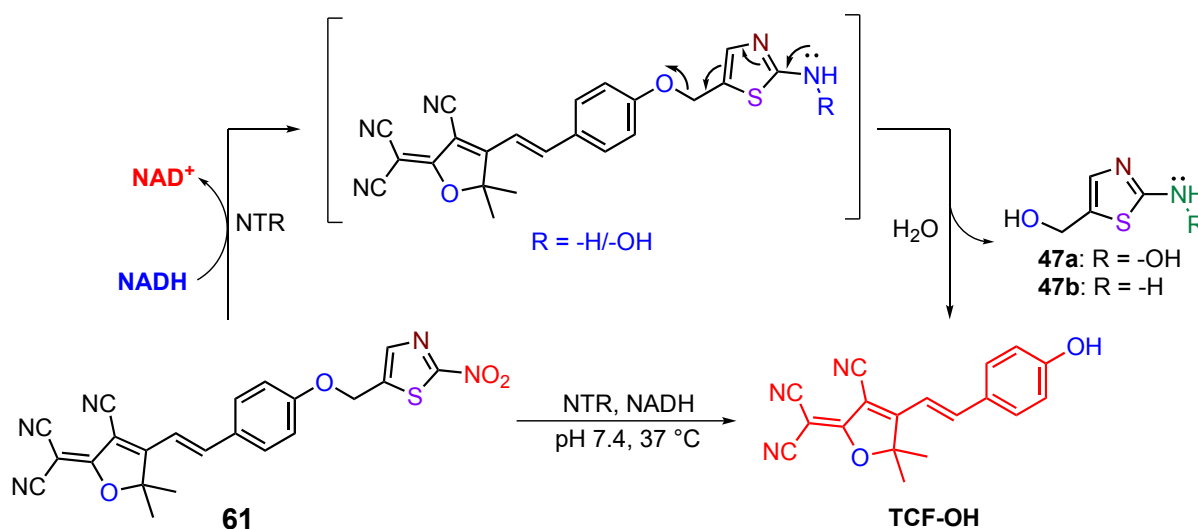


Figure 5.2.5. HPLC traces of (A) stability of the probe **61** and (B) enzyme dependent reductive activation of probe **61** ($12.5 \mu\text{M}$) in the presence of *E. coli* NTR (15 nM) and NADH ($100 \mu\text{M}$) in pH 7.4 phosphate buffer. **TCF-OH** ($12.5 \mu\text{M}$) was used as a positive control. The signal was detected using the UV detector set at 440 nm. (C) Decomposition of **61** and formation of **TCF-OH** upon incubation with NTR (15 nM) and NADH ($100 \mu\text{M}$) in pH 7.4 phosphate buffer at 37°C as monitored by HPLC.

Scheme 5.2.6. Proposed mechanism of NTR dependent colorimetric and fluorescent turn-on response of **61**



5.2.3.5. Selectivity and sensitivity of **61** towards *E. coli* NTR

Next, the colorimetric and fluorescence response of **61** at various concentrations (10 , 25 , 50 and $100 \mu\text{M}$) was evaluated in the presence of *E. coli* NTR by monitoring the visual change in colour ascribed to the formation of **TCF-OH**. As anticipated, the probe displayed yellow coloration in the absence of NTR. However, a marked concentration dependent colorimetric response from yellow to pink was observed in the presence of NTR after 5 min of incubation (Figure 5.2.6.A). This was also accompanied with a concomitant increase in the absorbance and fluorescence signal in a concentration dependent manner (Figure 5.2.6.B and 5.2.6.C).

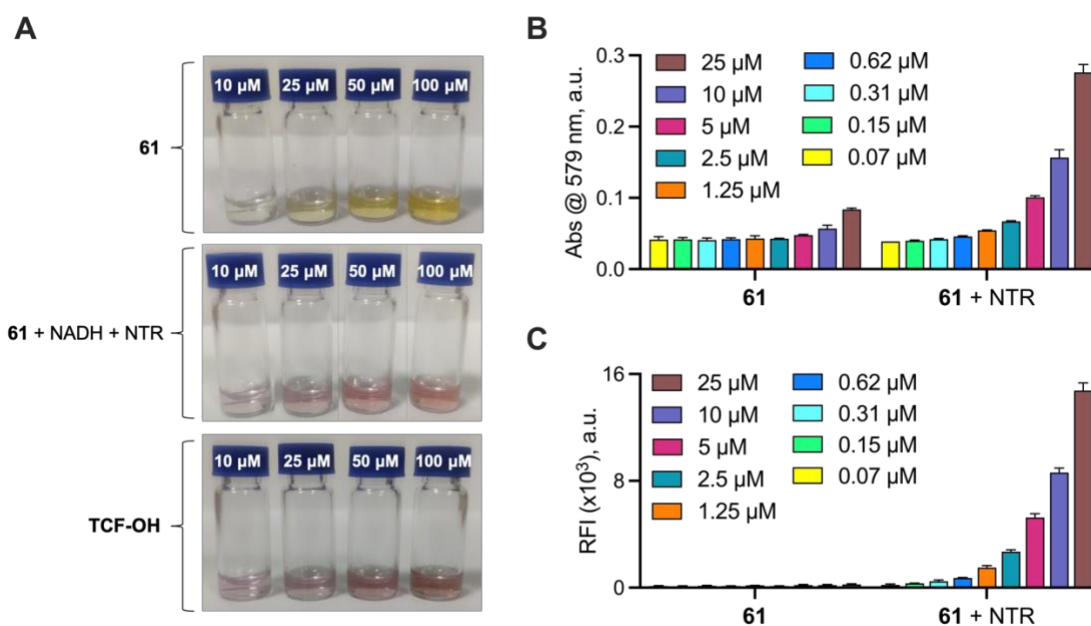


Figure 5.2.6. (A) Comparative visual colorimetric response of **61** at different concentrations (10, 25, 50 and 100 μM) before (*top panel*) and after (*middle panel*) incubation (5 min) with *E.coli* NTR relative to **TCF-OH** (*bottom panel*). (B-C) Changes in (B) absorbance signal and (C) fluorescence intensity with different concentrations (0.07 μM to 25 μM) of probe **61** in the presence of NADH (100 μM) and NTR (15 nM) after 5 min of incubation in pH 7.4 phosphate buffer at 37 $^{\circ}\text{C}$.

Next, the sensing ability of **61** toward NTR was investigated under *in vitro* conditions. The absorption and fluorescence spectra of **61** was recorded after 5 min of incubation in the presence of NADH with a wide range of NTR concentration in phosphate buffer (pH 7.4, 10 mM) (Figure 5.2.7.A-C). Strikingly, a good linearity between the increase in absorbance or fluorescence intensity of probe **61** with the varying concentrations of NTR in the range from 0.025 nM to 0.9375 nM (or 0.6 ng/mL to 22.5 ng/mL) was observed (Figure 5.2.7.D and 5.2.7.E).

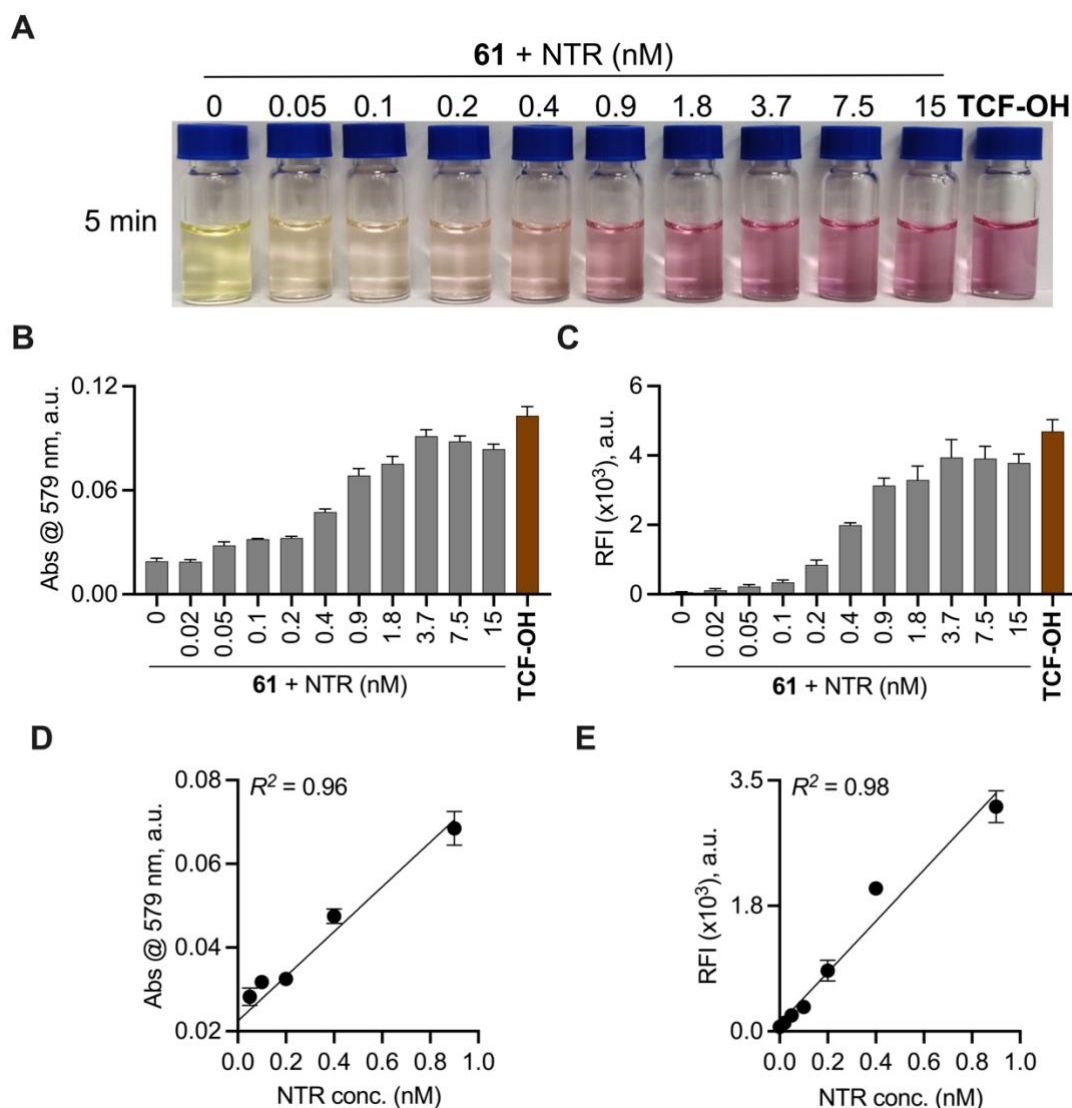


Figure 5.2.7. (A) Photometric images of visual colour change of probe **61** upon addition of different concentration of NTR (0-15 nM) in the presence of NADH (100 μ M) in pH 7.4 phosphate buffer at 37 $^{\circ}$ C. (B-C) Changes in (B) absorbance signal and (C) fluorescence intensity of probe **61** with increasing concentrations of NTR (0-15 nM) in the presence of NADH (100 μ M) in pH 7.4 phosphate buffer. (D-E) Linear correlation between enhancement in (D) absorbance and (E) fluorescence intensity of **61** with concentrations of NTR.

Next, the selectivity of the probe **61** was assessed in the presence of various biologically relevant analytes. As clearly illustrated in (Figure 5.2.8), **61** displayed no significant enhancement in fluorescence response in the presence of biologically relevant analytes such as thiols (Cys, GSH, NAC), saccharides (Glu, Gal, Ara), reductants (Vit-C), amino acids (His), oxidizing agents (H_2O_2), esterase enzyme (Es), NADH or NTR alone. However, **61** uniquely responded to *E. coli* NTR in the presence of NADH under the same conditions and produced an intense fluorescence signal at 37 $^{\circ}$ C within 5 min. The impact of pH on the detection of

NTR was next investigated. As shown in Figure 5.2.9, probe **61** displays a distinct colorimetric response along with an enhancement in absorbance as well as fluorescence signal in a wide range of biologically relevant pH from 7 to 10.

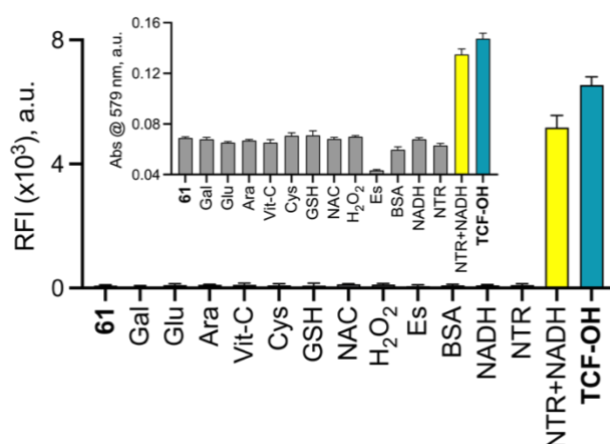


Figure 5.2.8. Fluorescence response (and *inset*: absorbance intensity) of **61** (10 μ M) in the presence of various biological analytes (100 μ M) after 5 min incubation at 37 $^{\circ}$ C. Gal = galactose; Glu = glucose; Ara = arabinose; Vit-C = ascorbic acid; Cys = cysteine; GSH = glutathione; NAC = *N*-acetyl cysteine; H₂O₂ = hydrogen peroxide; Es = esterase 1 U/mL; BSA = bovine serum albumin 1mg/mL; NADH = reduced nicotinamide adenine dinucleotide (100 μ M); NTR = *E. coli* nitroreductase (15 nM); NTR (15 nM) + NADH (100 μ M) reaction.

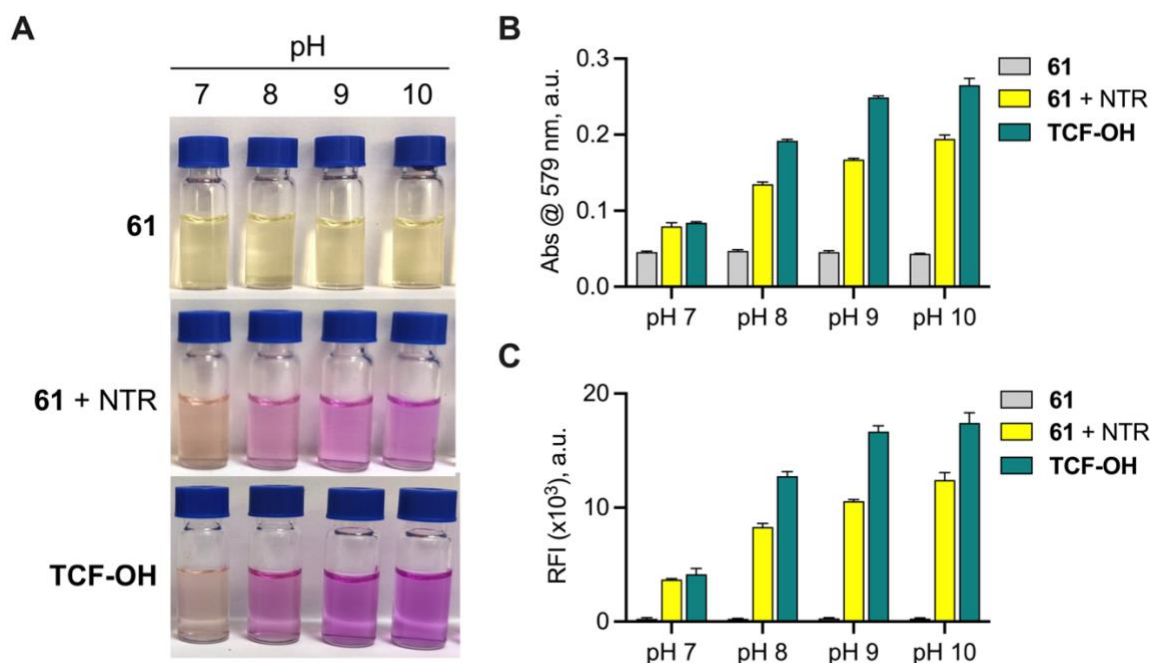


Figure 5.2.9. (A) Photometric images of visual colour change of probe **61** upon addition of NTR (15 nM) and NADH (100 μ M) in different pH (7.0-10.0) at 37 $^{\circ}$ C. Changes in (B) absorbance signal and (C) fluorescence intensity of probe **61** with NTR (15 nM) and NADH (100 μ M) in different pH 7.0-10.0 at 37 $^{\circ}$ C.

Furthermore, the probe was compatible in various bacterial media and displayed a colorimetric and fluorescence turn OFF-ON response only in the presence of NTR and NADH (Figure 5.2.10). Collectively, these findings demonstrate that probe **61** exhibited high selectivity to NTR and a quick response (< 5 min) in the presence of physiologically relevant analytes.

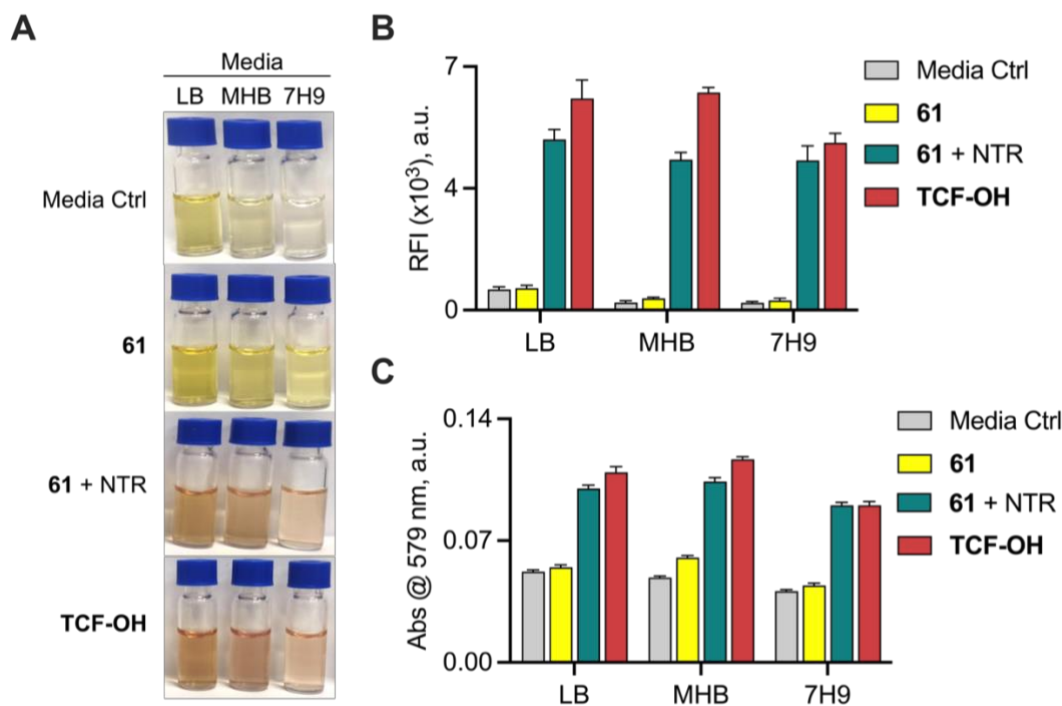


Figure 5.2.10. (A) Photometric images of visual colour change of probe **61** upon addition of NTR (15 nM) and NADH (100 μ M) in various bacterial media at 37 $^{\circ}$ C. Changes in (B) absorbance signal and (C) fluorescence intensity of probe **61** with NTR (15 nM) and NADH (100 μ M) in different bacterial media at 37 $^{\circ}$ C. Media: LB = Luria Bertoni broth for *E. coli*; MHB = Mueller Hinton Broth cation 2 adjusted for *S. aureus*; 7H9 = Middlebrook 7H9 broth for *Mycobacterium* species.

5.2.3.6. Cell viability

The cytotoxicity of **61** and **TCF-OH** was evaluated by determining the cell viability in MEF cells using MTT assay. This assay was conducted by Mr. Suman Manna (Prof. Harinath Chakrapani Lab, IISER-Pune). Cells were treated with varying concentrations of **61** and **TCF-OH** and later incubated for 6 h. While no significant cytotoxicity was observed upto 20 μ M with **TCF-OH**, cytotoxicity from **61** was observed at 10 μ M. Given that the **61** was well tolerated by the cells upto 5 μ M, we used this concentration for confocal imaging experiments in bacteria (Figure 5.2.11).

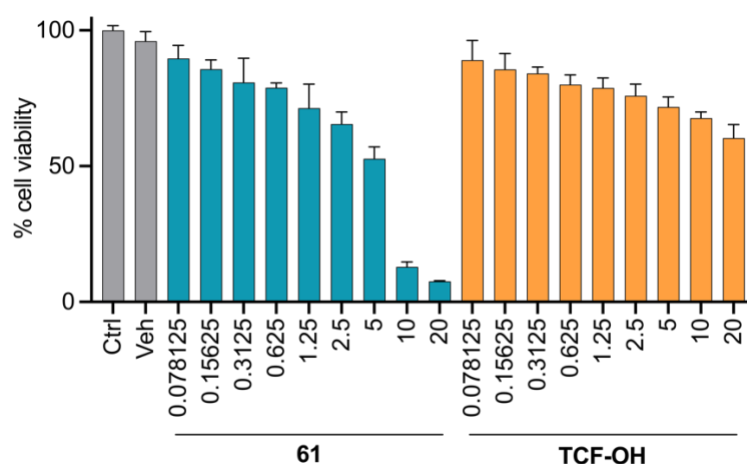


Figure 5.2.11. Cell Viability assay for cytotoxicity of **61** and **TCF-OH** in MEF cells

5.2.3.7. Real-time detection of bacteria by confocal microscopy

We then assessed the ability of **61** to detect the NTR in live pathogenic gram-negative bacteria (*E. coli* ATCC 25922). The bacteria ($OD_{600} = 0.1$) was co-incubated with **61** (5 μ M) in LB media at 37 °C for 2 h. The cell suspension was centrifuged and washed twice with 1x phosphate buffer saline (PBS, pH 7.4). The resulting bacterial pellets were incubated with DAPI (5 μ L, 10 μ g/mL in water), a cell-permeable dye that stains living and dead bacteria. After incubation for 15 min in the dark, the excess unbound dye was removed by PBS washes (x2) and the bacterial suspension was examined under oil-immersion objective (100 \times) by using a Leica SP8 optical microscope employing $\lambda 405$ nm (blue channel) and $\lambda 568$ nm (red channel) lasers. The confocal images (Figure 5.2.12) were provided by Ms. Ruma Ghosh (Prof. M. Jayakannan Lab, IISER Pune).

As shown in Figure 5.2.12, a red fluorescence signal in Alexa fluor 568 (red channel) characteristic of the release of **TCF-OH** from **61** was observed. The blue channel illustrates the visualization of bacteria by DAPI. Superposition of panels (a-b) shows complete overlap of red and blue signals, resulting in a pinkish signal (panel c) around the bacteria. This result indicate that the probe was cell permeable and was able to afford a strong fluorescence response upon NTR-dependent bioreductive activation in bacteria. On the contrary, fluorescence signal from **TCF-OH** was not observed in the red channel (panel e and g) under these conditions, most likely as a result of reduced permeability in bacteria. Collectively, this findings underpins that **61** with NTR-responsive OFF-ON feature has an excellent ability for non-invasive real-time detection of bacteria.

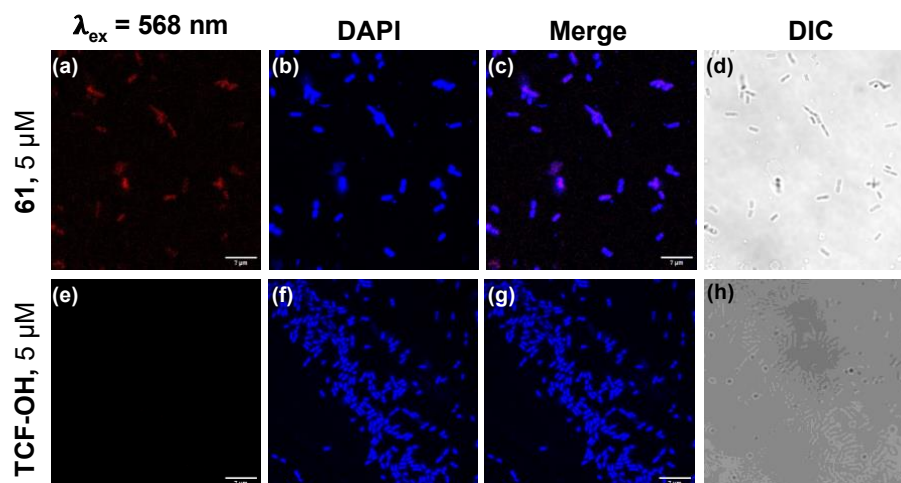


Figure 5.2.12. Confocal microscope images in *E. coli* bacterial cells preincubated with (a-d) **61** (5 μ M) or (e-h) **TCF-OH** (5 μ M) for 2 h. The cells were imaged on the red channel (Alexa fluor 568 for detection of **TCF-OH** (a and e)), DAPI channel (b and f), merged image of red and DAPI channel (c and g) and DIC image (d and h).

5.2.4. Conclusion

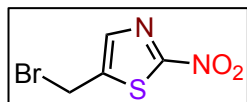
Despite the wide popularity of 4-nitrobenzyl and 1-methyl-2-nitroimidazolyl moiety as preferred substrates for NTR, the development of a dual colorimetric fluorescence “turn OFF-ON” probe for rapid and real time detection of bacteria has been limited. As described in the previous chapters, 2-nitrothiazolyl moiety demonstrated superior sensitivity and reactivity towards NTR over other nitro(hetero)aryl substrates. Therefore, 2-nitrothiazolyl group was used as a caging group for the development of an NTR activatable probe with a colorimetric and fluorescence “turn OFF-ON” response. In this context, TCF-based latent fluorophores **60** and **61** were synthesized and evaluated in the presence of bacterial NTR for visual and fluorescence change over time. Our investigation revealed that the 2-nitrothiazolyl tethered probe **61** provided a strong color change from yellow to pink with concomitant increase in the fluorescence response in the presence of NTR. The probe **61** also exhibited high selectivity to NTR and a quick response (< 5 min) in the presence of physiologically relevant analytes. Confocal imaging studies demonstrated that **61** with NTR-responsive OFF-ON feature has an excellent ability for non-invasive real-time detection of bacteria. Together, these results lay the foundation for the development of NTR-sensitive dual response probes for targeted imaging of bacterial infections.

5.2.5. Experimental protocols

5.2.5.1. Synthesis and characterization

Compounds **53**,²³ **58**³² and TCF-OH²³ were synthesized following previously reported protocols and the analytical data for each compound was consistent with reported values.

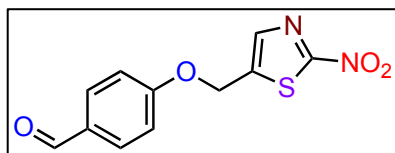
5-(bromomethyl)-2-nitrothiazole (57): To a solution of **1f** (1 g, 6.24 mmol) in anhydrous



DMF (10 mL), PBr₃ (0.89 mL, 9.37 mmol) was added dropwise at 0 °C under nitrogen atmosphere. The resulting reaction was stirred at RT for 1 h until the complete consumption of the starting material. The reaction

mixture was quenched with sat. solution of NaHCO₃, and the aqueous layer was extracted with EtOAc (3 × 10 mL). The organic extracts were combined, washed with brine (3 × 10 mL), dried over anhydrous Na₂SO₄ (1 g), filtered and the filtrate was concentrated under reduced pressure. The residue was subjected to purification by column chromatography over silica gel (60-120) with 10-12% EtOAc/hexane as an eluant to provide **57** (1.1 g, 82% yield) as yellowish white solid. ¹H NMR (400 MHz, CDCl₃): δ 7.83 (s, 1H), 4.68 (s, 2H); ¹³C NMR (100 MHz, CDCl₃): δ 144.9, 141.3, 20.9; DEPT-135 NMR (100 MHz, CDCl₃): δ 141.2 (CH), 20.9 (CH₂).

4-((2-nitrothiazol-5-yl)methoxy)benzaldehyde (59): Potassium iodide (0.2 g, 1.23 mmol)



was added to a solution of **57** (0.274 g, 1.23 mmol) in anhydrous DCM (8 mL) under nitrogen atmosphere. The solution was stirred at RT for 10 min. Then, 4-hydroxybenzaldehyde (0.1 g, 0.81 mmol) and Ag₂O (0.380 g,

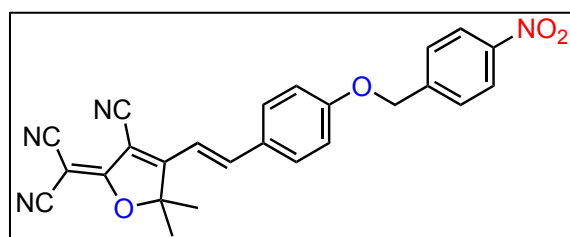
1.64 mmol) was added and further stirred for 48 h. The reaction mixture was filtered through celite, and the filtrate was concentrated *in vacuo* to afford the crude product. The residue was purified by column chromatography on silica gel (60-120 mesh) with 12-15% EtOAc/hexane as an eluant to give **59** (0.082 g, 38%) as yellow solid. ¹H NMR (400 MHz, CDCl₃): δ 9.93 (s, 1H), 7.93 – 7.87 (m, 3H), 7.13 – 7.06 (dt, *J* = 8.7, 2.6 Hz, 2H), 5.40 (s, 2H), 8.28 (d, *J* = 8.7 Hz, 2H), 7.87 (d, *J* = 8.7 Hz, 2H), 7.63 (d, *J* = 8.5 Hz, 2H), 7.09 (d, *J* = 8.7 Hz, 2H), 5.27 (s, 2H); ¹³C NMR (100 MHz, CDCl₃): δ 190.7, 162.1, 142.4, 140.4, 132.3, 131.3, 115.2, 62.7; DEPT-135 NMR (100 MHz, CDCl₃): δ 190.6 (CH), 140.3 (CH), 132.1 (CH), 115.0 (CH), 62.6 (CH₂). HRMS (ESI-TOF) for C₁₁H₇N₃O₇S [M+Na]⁺: Calcd., 347.9897, Found, 347.9898.

General procedure for the synthesis of probes (60 and 61)

NH₄OAc (0.19 mmol) was added to a solution of TCF (0.38 mmol) and respective aromatic aldehyde (0.38 mmol) in EtOH (10 mL). The reaction mixture was refluxed at 60 °C for 2-6 h and then allowed to cool down to room temperature. The resulting reaction mixture was diluted with water (20 mL) and extracted with EtOAc (3 × 20 mL). The organic layer was dried over anhydrous Na₂SO₄, concentrated in *vacuo*, and purified over silica gel (60-120 mesh) with 30-40% EtOAc/hexane to provide probes **60** and **61** as pure products.

(E)-2-(3-cyano-5,5-dimethyl-4-(4-((4-nitrobenzyl)oxy)styryl)furan-2(5H)-ylidene)

malononitrile (60): Starting from **53** (0.077 g, 0.38 mmol) and **58** (0.1 g, 0.38 mmol), **60**



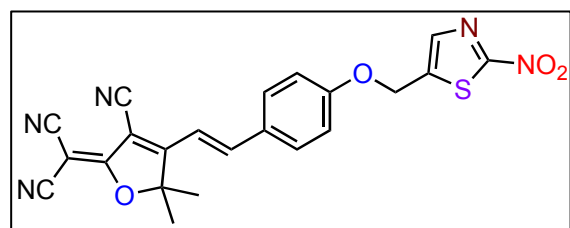
(0.138 g, 82%) was isolated as an orange solid;

¹H NMR (400 MHz, DMSO-*d*₆): δ 8.28 (d, *J* = 8.7 Hz, 2H), 7.98 – 7.87 (m, 3H), 7.75 (d, *J* = 8.7 Hz, 2H), 7.19 (d, *J* = 8.8 Hz, 2H), 7.11 (d, *J* = 16.4 Hz, 1H), 5.41 (s, 2H), 1.79 (s, 6H); ¹³C

NMR (100 MHz, DMSO-*d*₆): δ 177.2, 175.6, 161.5, 147.4, 147.1, 144.3, 131.9, 128.4, 127.7, 123.7, 115.7, 113.2, 112.0, 111.1, 99.2, 97.8, 68.4, 53.8, 25.2; DEPT-135 NMR (100 MHz, DMSO-*d*₆): δ 147.1 (CH), 131.6 (CH), 128.1 (CH), 123.4 (CH), 115.5 (CH), 112.9 (CH), 68.1 (CH₂), 24.9 (CH₃); HRMS (ESI-TOF) for C₂₅H₁₈N₄O₄ [M+H]⁺: Calcd., 439.1404, Found, 439.1398.

(E)-2-(3-cyano-5,5-dimethyl-4-(4-((2-nitrothiazol-5-yl)methoxy)styryl)furan-2(5H)-ylidene)

malononitrile (61): Starting from **53** (0.077 g, 0.38 mmol) and **59** (0.1 g, 0.31 mmol),



61 (0.129 g, 75%) was isolated as an orange solid;

¹H NMR (400 MHz, DMSO-*d*₆): δ 8.16 (s, 1H), 7.97 – 7.89 (m, 3H), 7.22 (d, *J* = 8.9 Hz, 2H), 7.13 (d, *J* = 16.4 Hz, 1H), 5.60 (s, 2H), 1.79 (s, 6H); ¹³C NMR (100 MHz, DMSO-*d*₆): δ

177.2, 175.5, 160.8, 147.2, 143.0, 141.5, 131.8, 128.1, 115.8, 113.5, 112.8, 112.0, 111.0, 99.3, 98.1, 62.2, 53.9, 25.2; DEPT-135 NMR (100 MHz, DMSO-*d*₆): δ 147.0 (CH), 141.3 (CH), 131.6 (CH), 115.5 (CH), 113.2 (CH), 61.9 (CH₂), 25.0 (CH₃); HRMS (ESI-TOF) for C₂₂H₁₅N₅O₄S [M+H]⁺: Calcd., 446.0923, Found, 446.0923.

5.2.5.2. Investigating the release of TCF-OH from probes in a fluorescence-based assay

Stock solutions of **TCF-OH** (1 mM), probes **60** and **61** (1 mM) were prepared in DMSO whereas the stock solutions of *E. coli* NTR (1 mg/mL) and NADH (5 mM) were prepared in phosphate buffer (pH 7.4, 10 mM). The reactions in the 96-well plate were initiated by the addition of 15 nM *E. coli* NTR (30 μ L; 0.1 μ M) and 100 μ M of NADH (4 μ L; 5 mM stock) to a solution of 10 μ M probes (2 μ L, 1 mM stock) in 164 μ L of buffer. The enhancement of the fluorescence signal corresponding to the release of TCF-OH ($\lambda_{\text{ex}} = 579$ nm and $\lambda_{\text{em}} = 603$ nm) relative to the NTR untreated control was recorded at 37 °C using an EnSight microplate reader (PerkinElmer) for 30 min.

5.2.5.3. Monitoring *E. coli* dependent colorimetric and fluorescence turn OFF-ON response for **61**

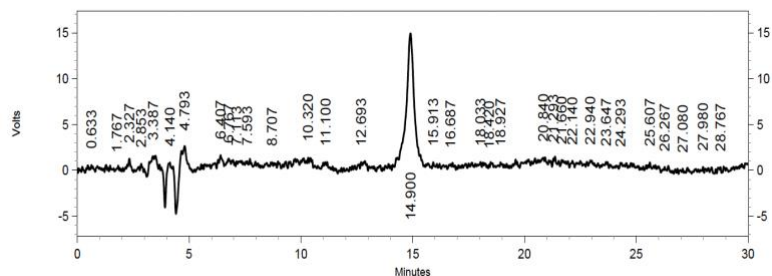
Stock solutions of **61** (1 mM) and **TCF-OH** (1 mM) were prepared in DMSO independently. The enzymatic reactions were initiated by adding 100 μ M of NADH (30 μ L, 5 mM stock) followed by 15 nM of NTR (450 μ L, 50 nM stock) to a 2 mL eppendorf tubes containing 10 μ M of **61** (15 μ L, 1 mM stock) in 1005 μ L of pH 7.4 phosphate buffer (10 mM). The reaction mixture was incubated for 5 min at 37 °C in an Eppendorf thermomixer comfort (700 rpm). Reaction mixture was transferred to a quartz micro-fluorescence cuvette (Hellma, path length 1 cm) and the fluorescence measurements were performed using a HORIBA Jobin Yvon Fluorolog fluorescence spectrophotometer with an excitation and emission slit width of 1 nm. Aliquots were also taken from the reaction mixture, transferred to a 2 mL transparent glass vial and a photograph was taken to visually inspect the colorimetric change. Similarly, aliquots were transferred to a 96-well plate and the emission spectra at $\lambda_{\text{ex}} = 579$ nm corresponding to the generation of **TCF-OH** was recorded.

5.2.5.4. Purity analysis by HPLC

Stock solution of **61** (1 mM) was prepared in DMSO. A solution of 12.5 μ M of **61** (5 μ L, 1 mM stock) was added to 395 μ L of ACN and then injected (50 μ L) in an HPLC instrument attached with a diode-array detector (detection wavelength 280 nm). The stationary phase used was C-18 reversed phase column (4.6 mm \times 100 mm, 5 μ m). The mobile phase used was 0.0001 % TFA in H₂O:ACN with a run time of 30 min with flow rate of 0.5 mL/min starting with 35:65 \rightarrow 0-1 min, 25:75 \rightarrow 1-5 min, 25:75 \rightarrow 5-14 min, 20:80 \rightarrow 14-17 min, 20:80 \rightarrow 17-19 min, 25:75 \rightarrow 19-21 min, 30:70 \rightarrow 21-23 min, 35:65 \rightarrow 23-26, 35:65 \rightarrow 26-30 min.

Area % Report

Data File: C:\Users\HPLC agilent\Desktop\All data\Hari
 Grp\ANAND\Jan-2023_NIR-NTR\13-01-2023\145-12.5-buffer+ACN-0 min-fresh-2.dat
 Method: C:\Users\HPLC agilent\Desktop\All data\Hari Grp\ANAND\Jan-2023_NIR-NTR\method_21
 min_01112023_mod-1.met
 Acquired: 1/13/2023 6:23:27 PM
 Printed: 3/16/2023 6:38:36 PM



DAD: Signal B,
 440 nm/Bw:4 nm
 Results

| Retention Time | Area | Area % | Height | Height % |
|----------------|---------|--------|--------|----------|
| 0.320 | 21247 | 0.37 | 2143 | 0.80 |
| 1.693 | 2322 | 0.04 | 937 | 0.35 |
| 1.800 | 8096 | 0.14 | 1710 | 0.64 |
| 1.907 | 2667 | 0.05 | 889 | 0.33 |
| 5.933 | 2520 | 0.04 | 891 | 0.33 |
| 6.047 | 1037 | 0.02 | 358 | 0.13 |
| 6.160 | 2175 | 0.04 | 535 | 0.20 |
| 7.707 | 761 | 0.01 | 433 | 0.16 |
| 8.640 | 11022 | 0.19 | 1579 | 0.59 |
| 8.813 | 4609 | 0.08 | 1642 | 0.61 |
| 8.973 | 8191 | 0.14 | 1794 | 0.67 |
| 11.713 | 6745 | 0.12 | 1488 | 0.56 |
| 11.787 | 5416 | 0.09 | 1410 | 0.53 |
| 11.893 | 4285 | 0.07 | 1129 | 0.42 |
| 13.287 | 11888 | 0.21 | 2245 | 0.84 |
| 13.380 | 13556 | 0.24 | 3123 | 1.17 |
| 13.560 | 6048 | 0.11 | 1714 | 0.64 |
| 13.627 | 13927 | 0.24 | 3320 | 1.24 |
| 13.713 | 11290 | 0.20 | 2592 | 0.97 |
| 13.900 | 16470 | 0.29 | 3639 | 1.36 |
| 14.907 | 5517541 | 95.99 | 215459 | 80.55 |
| 16.220 | 23013 | 0.40 | 2572 | 0.96 |
| 16.287 | 2856 | 0.05 | 1445 | 0.54 |
| 17.220 | 12494 | 0.22 | 2121 | 0.79 |
| 18.593 | 1936 | 0.03 | 1012 | 0.38 |
| 22.673 | 2260 | 0.04 | 822 | 0.31 |
| 22.733 | 2584 | 0.04 | 1189 | 0.44 |
| 22.907 | 5635 | 0.10 | 1291 | 0.48 |
| 23.640 | 1754 | 0.03 | 856 | 0.32 |
| 25.773 | 1794 | 0.03 | 900 | 0.34 |
| 28.807 | 2829 | 0.05 | 999 | 0.37 |
| 29.613 | 4525 | 0.08 | 1022 | 0.38 |
| 29.767 | 6407 | 0.11 | 1397 | 0.52 |
| 29.860 | 3771 | 0.07 | 1323 | 0.49 |
| 29.913 | 4627 | 0.08 | 1520 | 0.57 |

| | | | | |
|--------|---------|--------|--------|--------|
| Totals | 5748298 | 100.00 | 267499 | 100.00 |
|--------|---------|--------|--------|--------|

Figure 5.2.13. HPLC trace of 61

5.2.5.5. Stability assessment and *E. coli* NTR mediated decomposition study by HPLC

Stock solutions of **61** (1 mM), and **TCF-OH** (1 mM) were prepared in DMSO independently. In a typical reaction, 25 μM of probe **61** (25 μL , 1 mM stock) was added to 975 μL of PB (pH 7.4, 10 mM). The reaction mixtures were incubated at 37 $^{\circ}\text{C}$ on an Eppendorf thermomixer comfort (700 rpm). Aliquots were taken at determined time points (5 min and 60 min), injected (50 μL) in a HPLC instrument attached with a diode-array detector (detection wavelength 440 nm) and the stability of the probe in buffer was assessed.

Similarly, the *E. coli* NTR mediated reactions was initiated by adding 100 μM NADH (20 μL , 5 mM stock) followed by 15 nM NTR (300 μL , 50 nM stock) to a 1.5 mL eppendorf tubes containing a solution of 25 μM of **61** (25 μL , 1 mM stock) in 655 μL of pH 7.4 phosphate buffer (10 mM). The reaction mixtures were incubated at 37 $^{\circ}\text{C}$ in an Eppendorf thermomixer comfort (700 rpm). Aliquots (500 μL) were taken at designated time points from the reaction mixture, diluted with an equal volume of ACN (500 μL) and centrifuged (9,391 $\times g$ for 4 min). The supernatant was then injected (50 μL) in a HPLC instrument attached with a diode-array detector (detection wavelength 440 nm). The stationary phase used was C-18 reversed phase column (4.6 mm \times 100 mm, 5 μm). The mobile phase used was 0.0001 % TFA in $\text{H}_2\text{O}:\text{ACN}$ with a run time of 30 min with flow rate of 0.5 mL/min starting with 35:65 \rightarrow 0-1 min, 25:75 \rightarrow 1-5 min, 25:75 \rightarrow 5-14 min, 20:80 \rightarrow 14-17 min, 20:80 \rightarrow 17-19 min, 25:75 \rightarrow 19-21 min, 30:70 \rightarrow 21-23 min, 35:65 \rightarrow 23-26, 35:65 \rightarrow 26-30 min and the enzyme mediated decomposition for the test compound was analyzed using HPLC.

5.2.5.6. Evaluation of the concentration dependent NTR mediated colorimetric and fluorescence turn OFF-ON response for 61

Stock solutions of probes **61** and **TCF-OH** at varied concentrations (0.0078 to 2.5 mM) were prepared in DMSO independently. The reaction mixture contained various concentrations (0.078 to 25 μM) of **61** (25 μL , 0.0078 to 2.5 mM stock), 100 μM NADH (20 μL , 5 mM stock) and 15 nM NTR (300 μL , 50 nM stock) in 655 μL of pH 7.4 phosphate buffer (10 mM). Control reactions containing only **61** was also carried out. The reaction mixtures were incubated at 37 $^{\circ}\text{C}$ in an Eppendorf thermomixer comfort (700 rpm). An aliquot (0.5 mL) was taken after 5 min from the reaction mixture, transferred to a 2 mL transparent glass vial and a photograph was taken to visually inspect the colorimetric change. Similarly, aliquots (100 μL) were transferred to a 96-well plate and the absorbance signal as well as fluorescence signal ($\lambda_{\text{ex}} = 579$ nm and $\lambda_{\text{em}} = 603$ nm) corresponding to the generation of **TCF-OH** was recorded using a microplate reader (EnSight).

A similar experiment was carried out to monitor the enzyme catalyzed reaction of **61** with different concentrations of NTR. The reaction mixture either contained only 10 μM of **61** or **TCF-OH** (15 μL , 1 mM stock) or 10 μM of **61** (15 μL , 1 mM stock), 100 μM of NADH (30 μL , 5 mM stock) with varied concentrations of NTR ranged from 0 to 60 nM (450 μL , 0 to 200 nM stock) in 1005 μL of buffer. The reactions were incubated at 37 $^{\circ}\text{C}$ for 5 min in an Eppendorf thermomixer comfort (700 rpm). A photograph was taken to visually inspect the colorimetric change. Next, the progression of the NTR-dependent reaction was assessed by change in absorbance and fluorescence signal using a microplate reader (EnSight) with readings collected from the top with 30 flashes per well and a focus height adjusted to 9.5 mm.

5.2.5.7. Assessing the selectivity of **61**

Stock solutions of porcine liver esterase (Es; 50 U/mL), bovine serum albumin (BSA; 1 mg/mL), glutathione (GSH; 10 mM), cysteine (Cys; 10 mM), *N*-acetyl cysteine (NAC; 10 mM), vitamin-C (10 mM), glucose (Glu; 10 mM), galactose (Gal; 10 mM), arabinose (Ara; 10 mM), histidine (His; 10 mM), and H_2O_2 (30%, 10 mM) in phosphate buffer were prepared independently from commercial sources. In a typical reaction, 10 μM of **61** (15 μL , 1 mM stock), 100 μM of NADH (30 μL , 5 mM stock), and 15 nM of NTR (450 μL ; 50 nM stock) were added to 1005 μL of buffer. Similarly, a reaction mixture of 10 μM of **61** (15 μL , 1 mM stock) and 100 μM of various analytes (15 μL , 10 mM stock) was prepared in 1470 μL of buffer. In a separate experiment, the reaction mixture was prepared by adding 10 μM of **61** (15 μL , 1 mM stock) along with either 1 U/mL esterase (15 μL , 100 U/mL stock) or BSA (15 μL , 1 mg/mL stock) in 1470 μL of buffer. Control reactions containing only **61** or lacking NADH or NTR were also carried out. The reaction mixtures were incubated for 5 min at 37 $^{\circ}\text{C}$ in an Eppendorf thermomixer comfort (700 rpm), and then absorbance and fluorescence response were recorded using a microplate reader (EnSight).

5.2.5.8. Monitoring the sensitivity of detection of NTR by **61** in different bacterial media

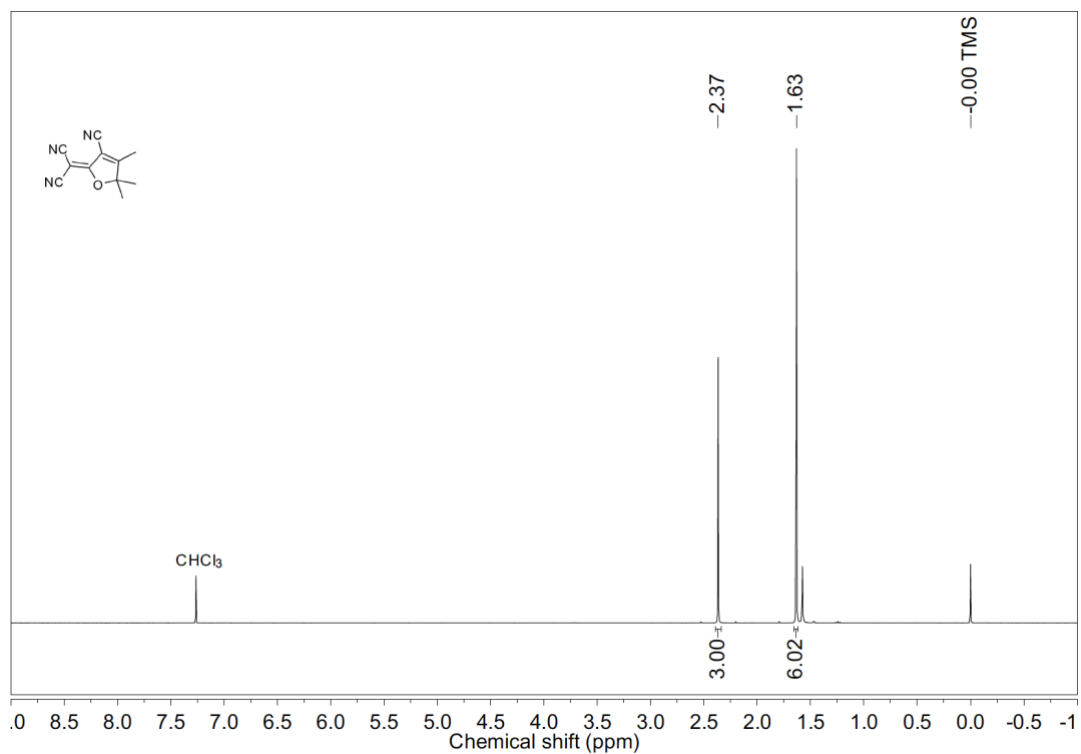
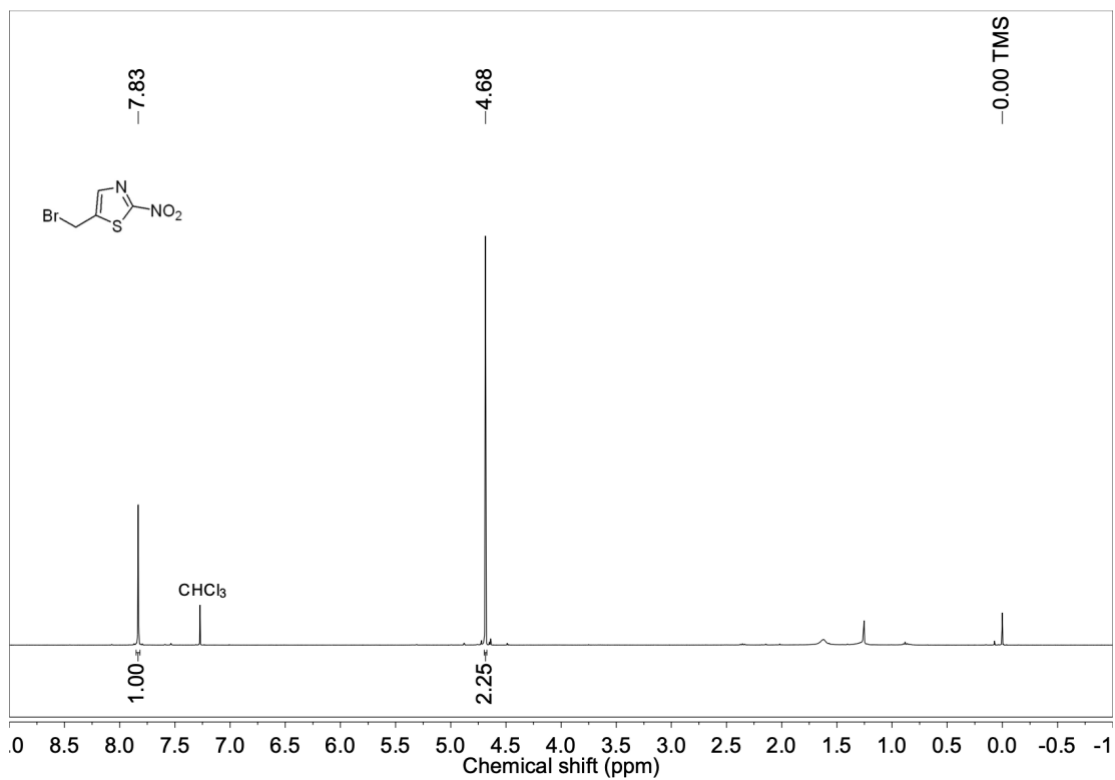
Stock solutions were prepared as mentioned earlier. Different bacterial media (LB = Luria Bertoni broth for *E. coli* (gram-negative bacteria); MHB = Mueller Hinton Broth cation 2 adjusted for *S. aureus* (gram-negative bacteria); 7H9 = Middlebrook 7H9 broth for *Mycobacterium* species) were prepared according to manufacturer's instructions. The reactions were initiated by addition of 10 μM of **61** (15 μL , 1 mM stock) to a solution of 100 μM of NADH (30 μL , 5 mM stock) and 15 nM of NTR (450 μL ; 50 nM stock) in 1005 μL of bacterial media (LB or MHB or 7H9). Control reactions containing only **61** or **TCF-OH** were also

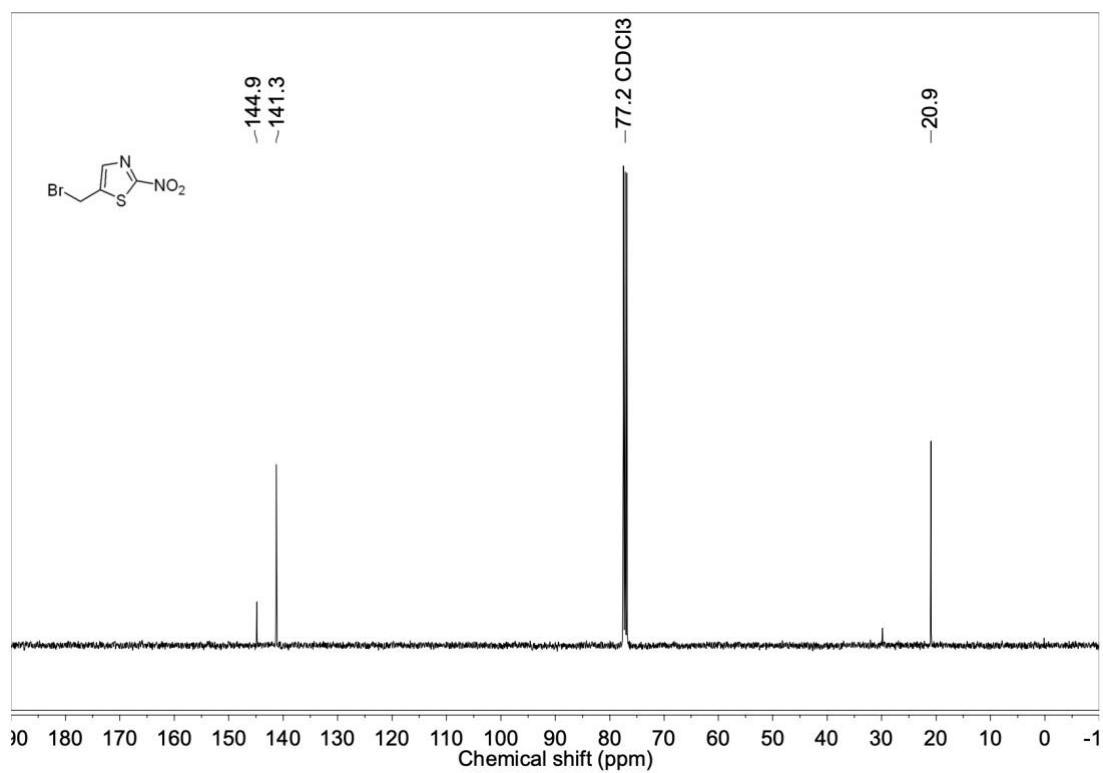
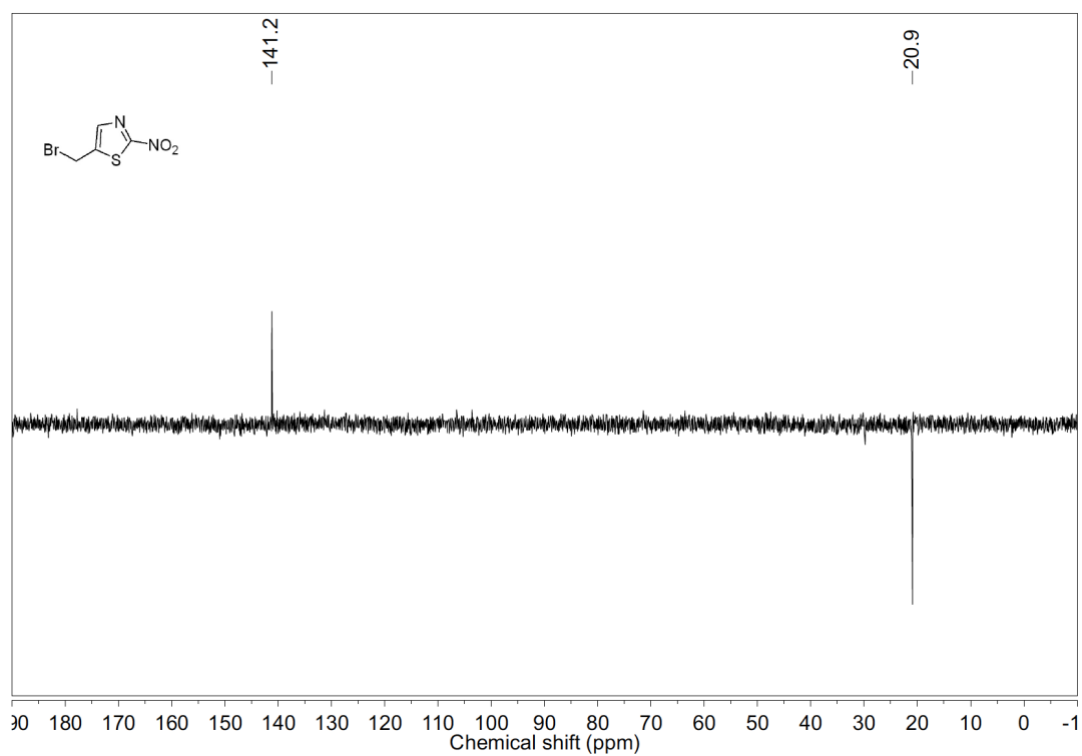
carried out. The reaction mixtures were incubated for 5 min at 37 °C in an Eppendorf thermomixer comfort (700 rpm), and then absorbance and fluorescence response were recorded using a microplate reader (EnSight).

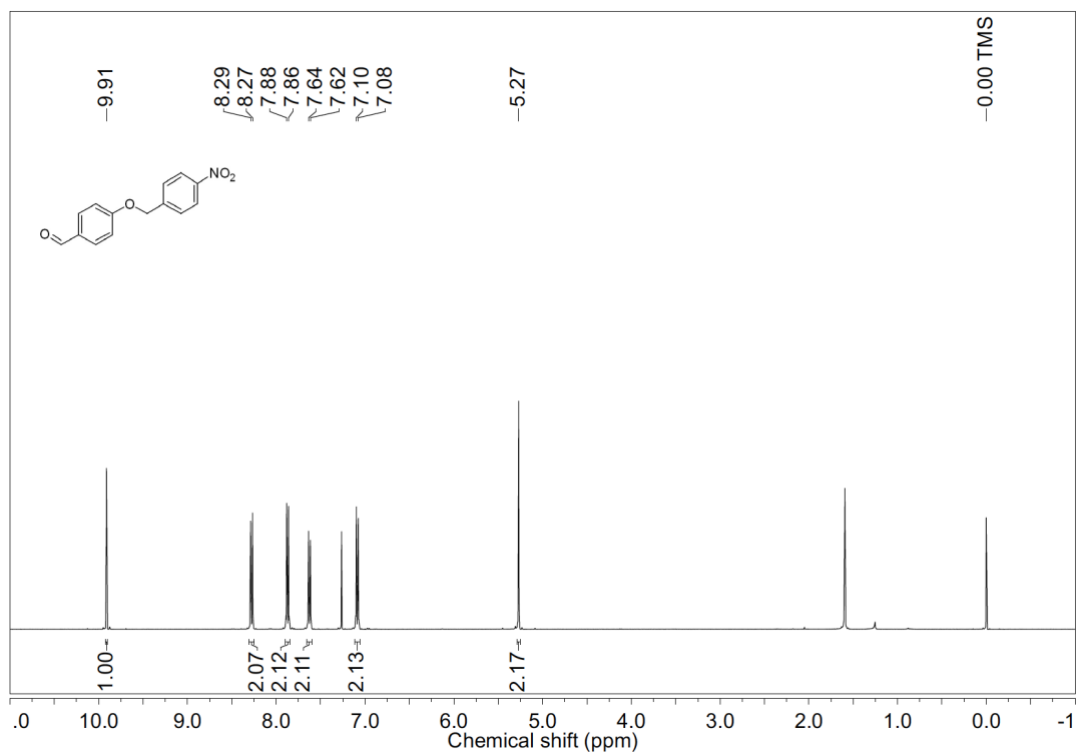
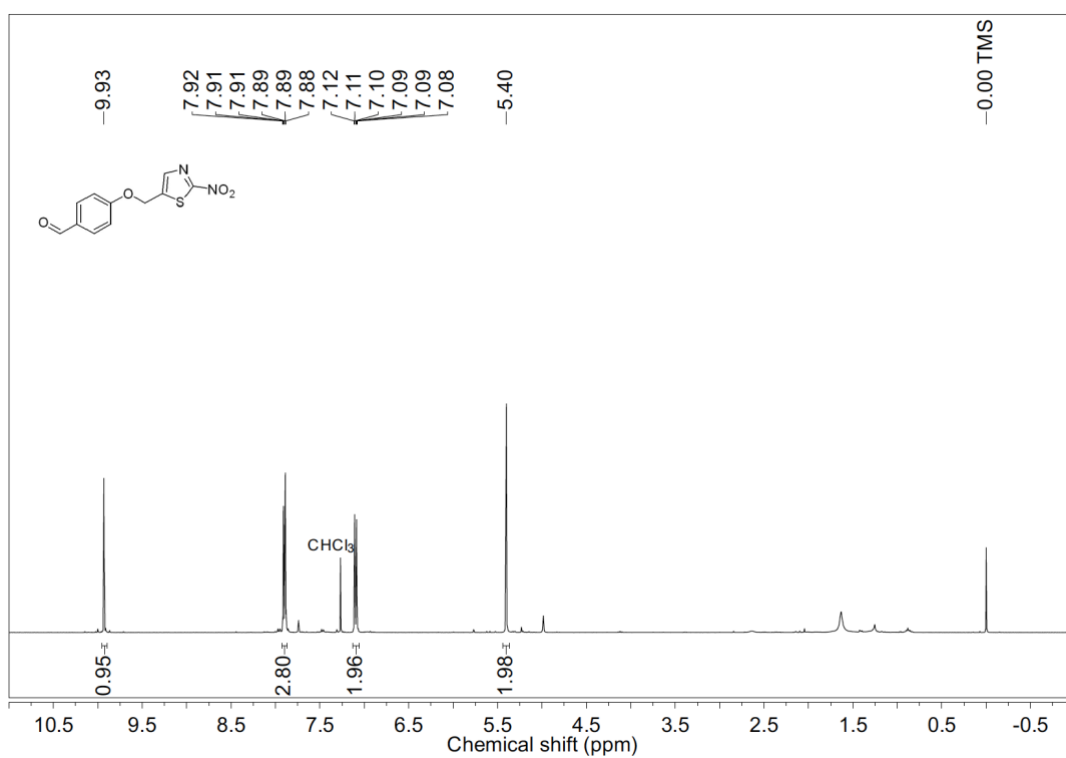
5.2.5.9. Monitoring the impact of pH on detection of NTR by **61**

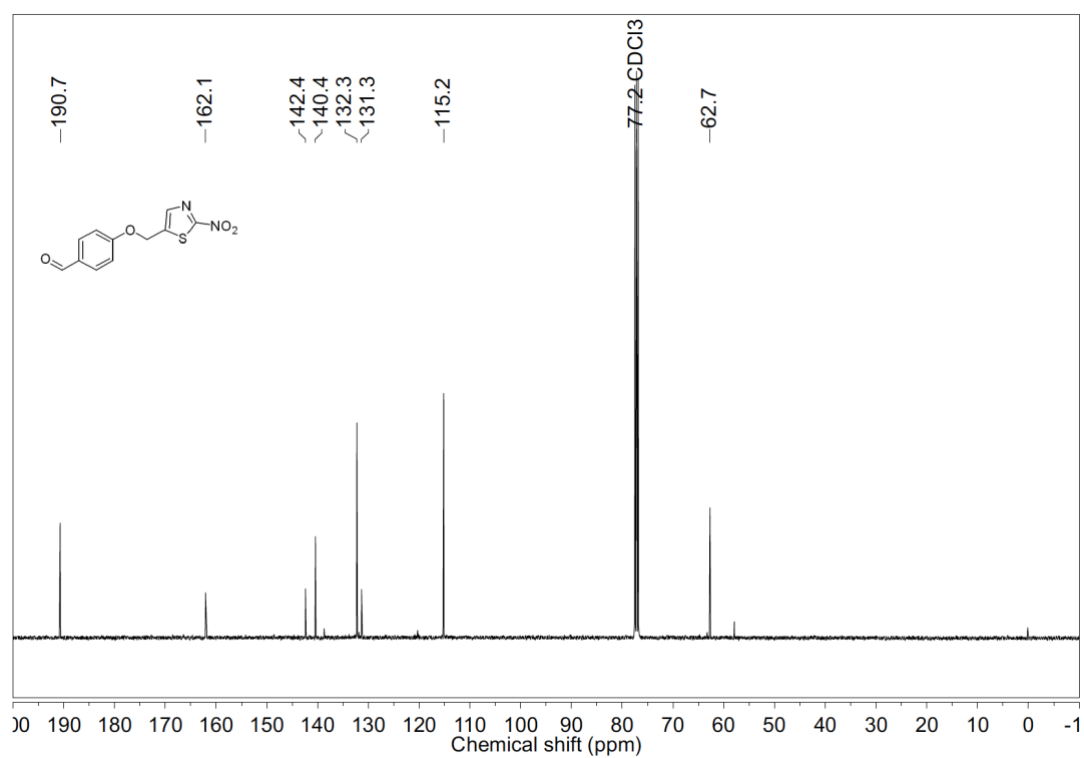
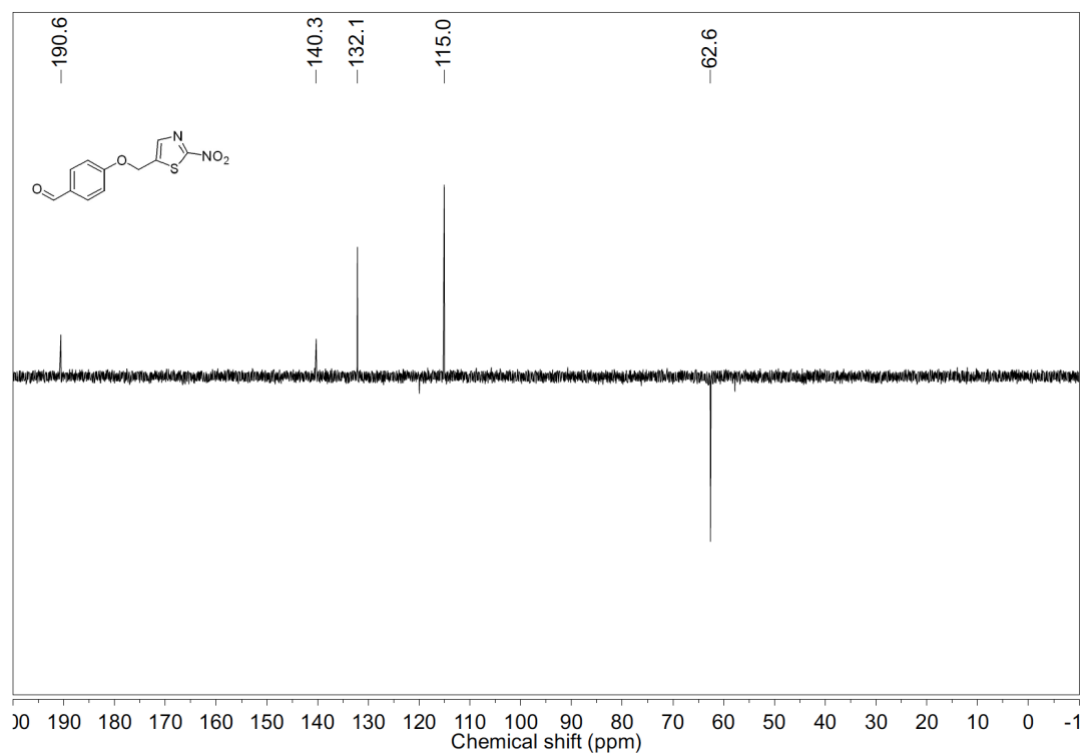
Stock solutions were prepared as mentioned earlier. Different biologically relevant buffers (pH 7 to 10) were prepared following the protocol reported elsewhere. In a typical reaction, 25 μM of probe **61** or **TCF-OH** (25 μL , 1 mM stock) was added to 1485 μL of phosphate buffer with varying pH (pH 7 to 10.0, 10 mM). Similarly, NTR-mediated reaction was carried out by adding 10 μM of **61** (15 μL , 1 mM stock), 100 μM of NADH (30 μL , 5 mM stock), and 15 nM of NTR (450 μL ; 50 nM stock) in 1005 μL of buffer with pH varying from 7 to 10. A photograph was taken to visually inspect the colorimetric change. Aliquots (100 μL) were also transferred to a 96-well plate and the absorbance signal as well as fluorescence signal was recorded using a microplate reader (EnSight).

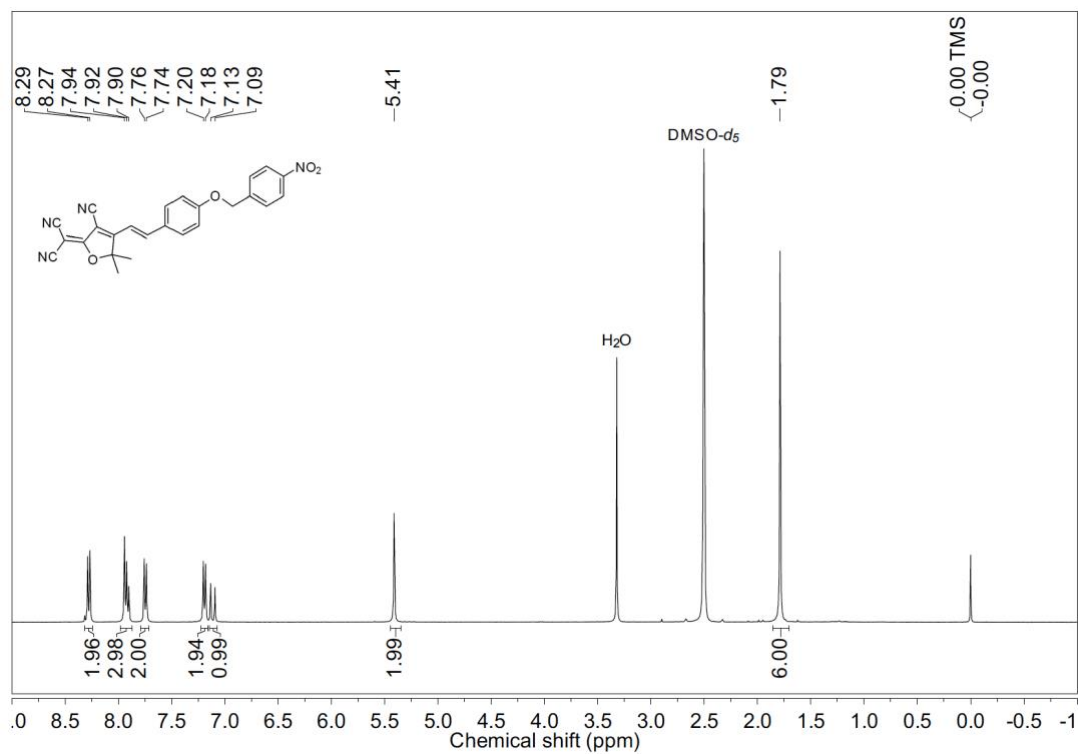
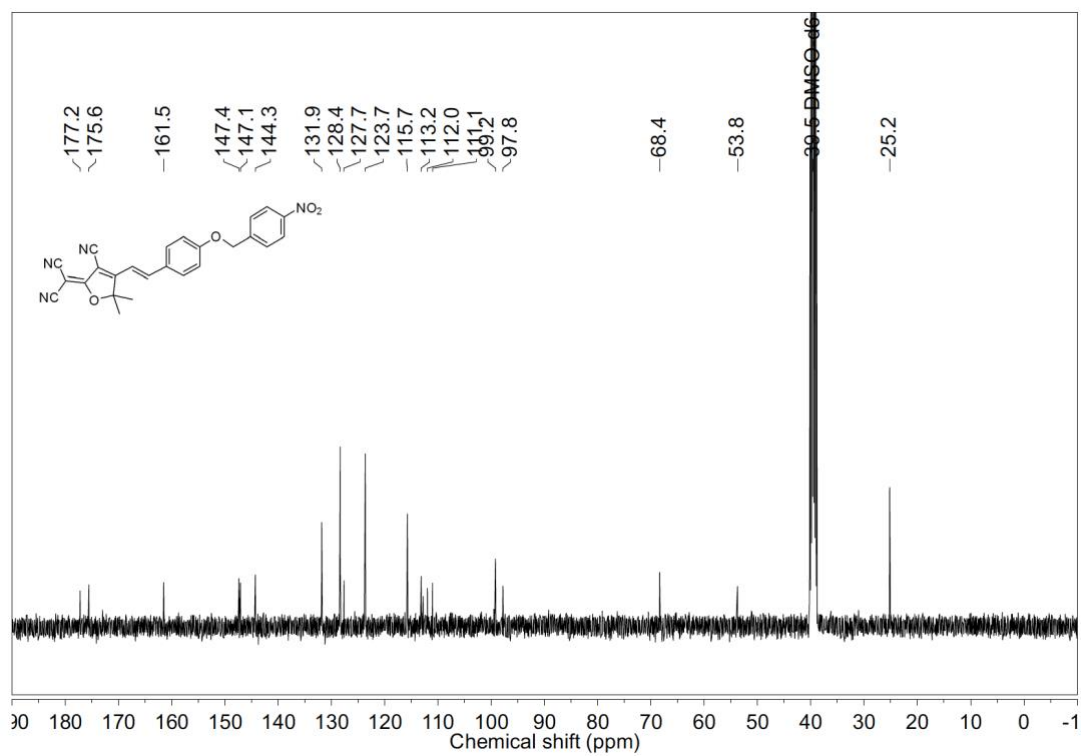
5.2.6. NMR spectral data

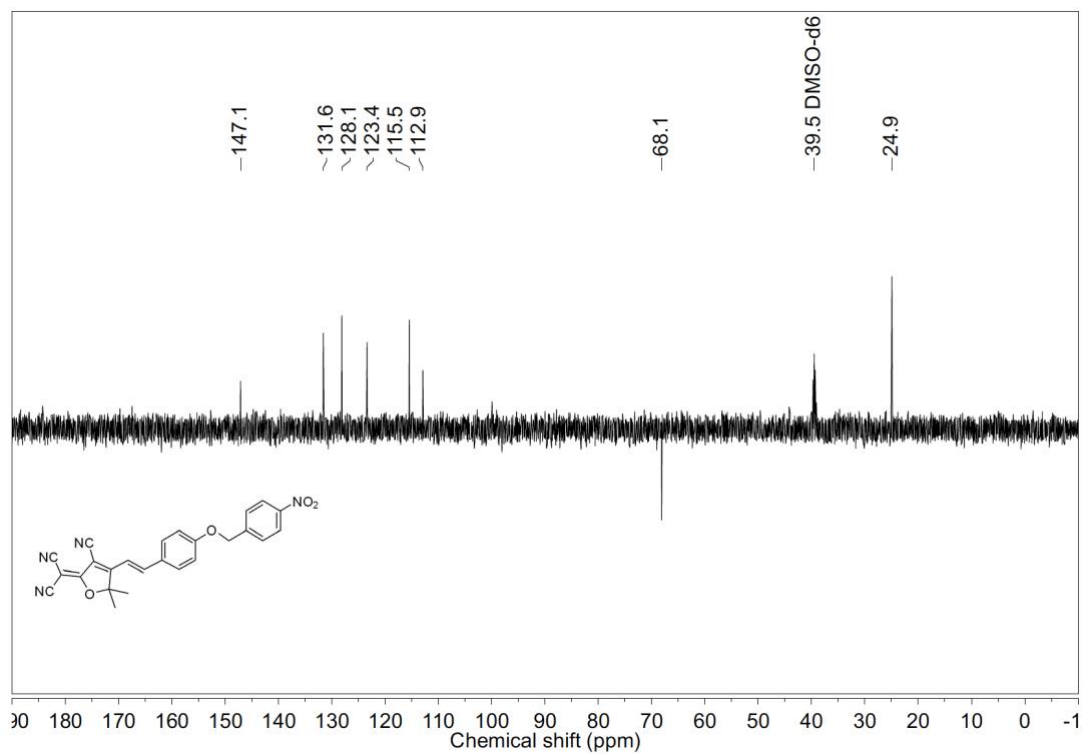
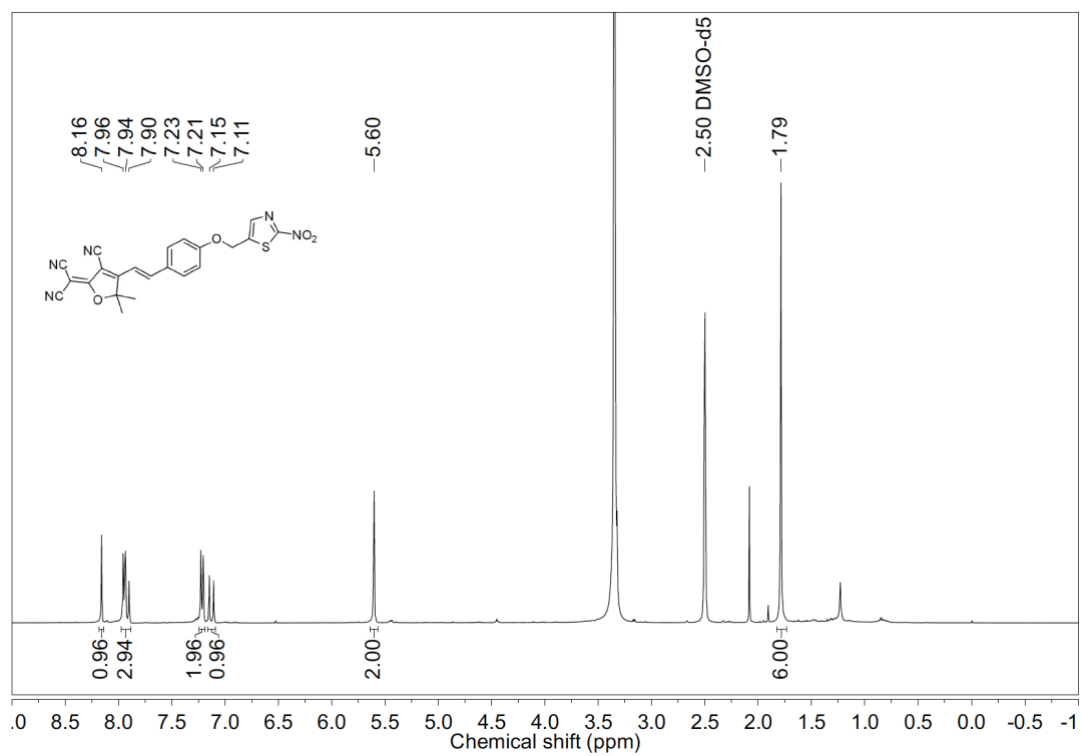
 ^1H NMR spectrum (400 MHz, CDCl_3) of **53** ^1H NMR spectrum (400 MHz, CDCl_3) of **57**

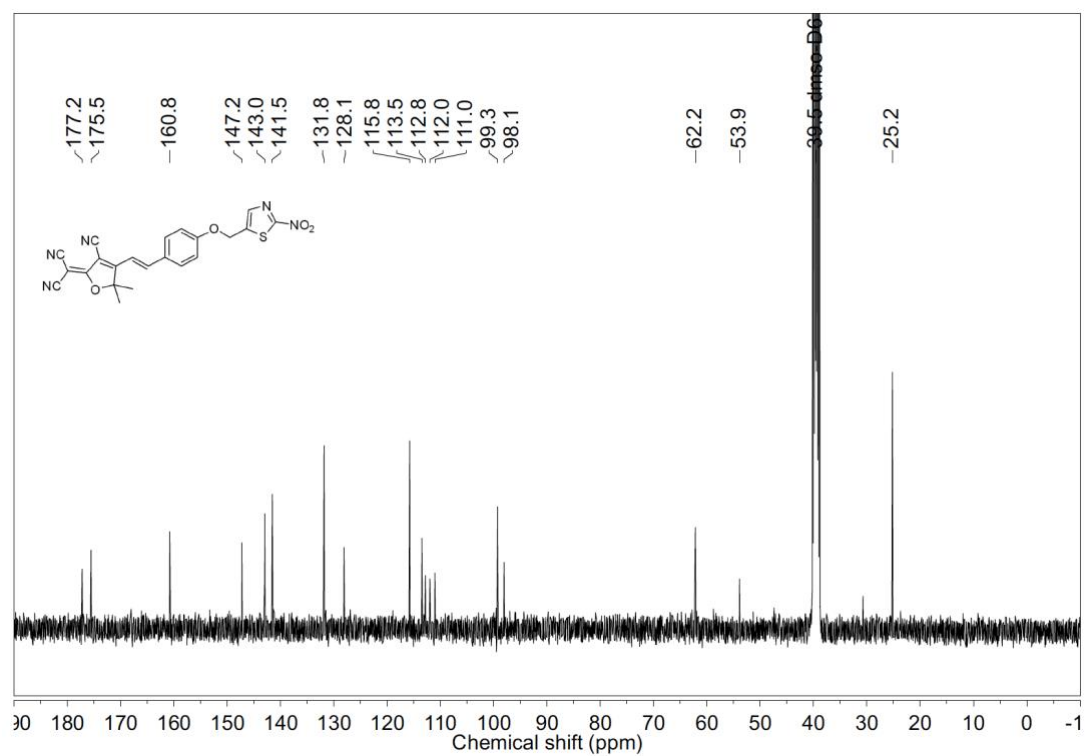
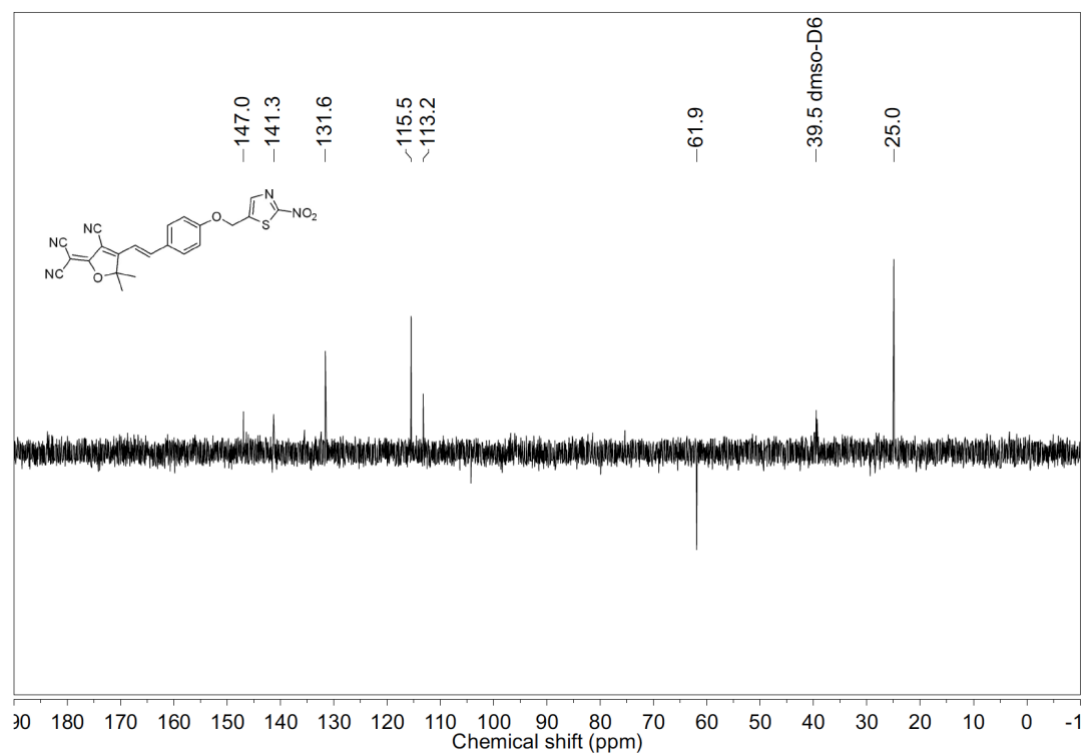
^{13}C NMR spectrum (100 MHz, CDCl_3) of **57**DEPT-135 NMR spectrum (100 MHz, CDCl_3) of **57**

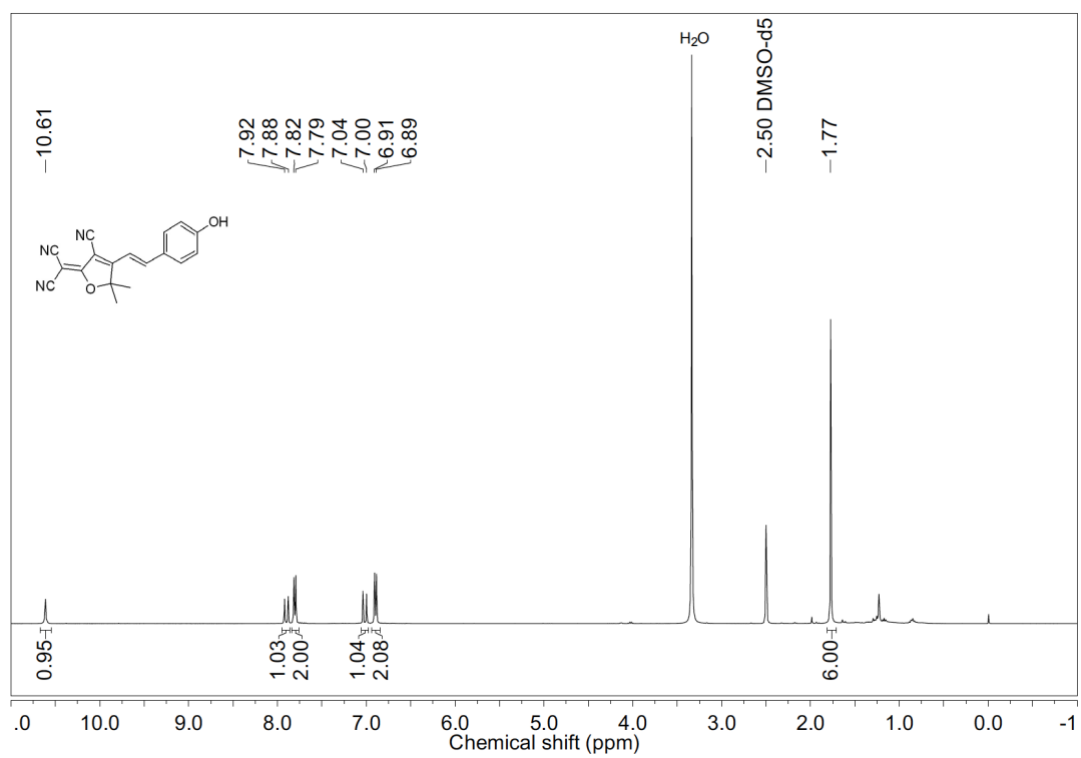
^1H NMR spectrum (400 MHz, CDCl_3) of **58** ^1H NMR spectrum (400 MHz, CDCl_3) of **59**

^{13}C NMR spectrum (400 MHz, CDCl_3) of **59**DEPT-135 NMR spectrum (400 MHz, CDCl_3) of **59**

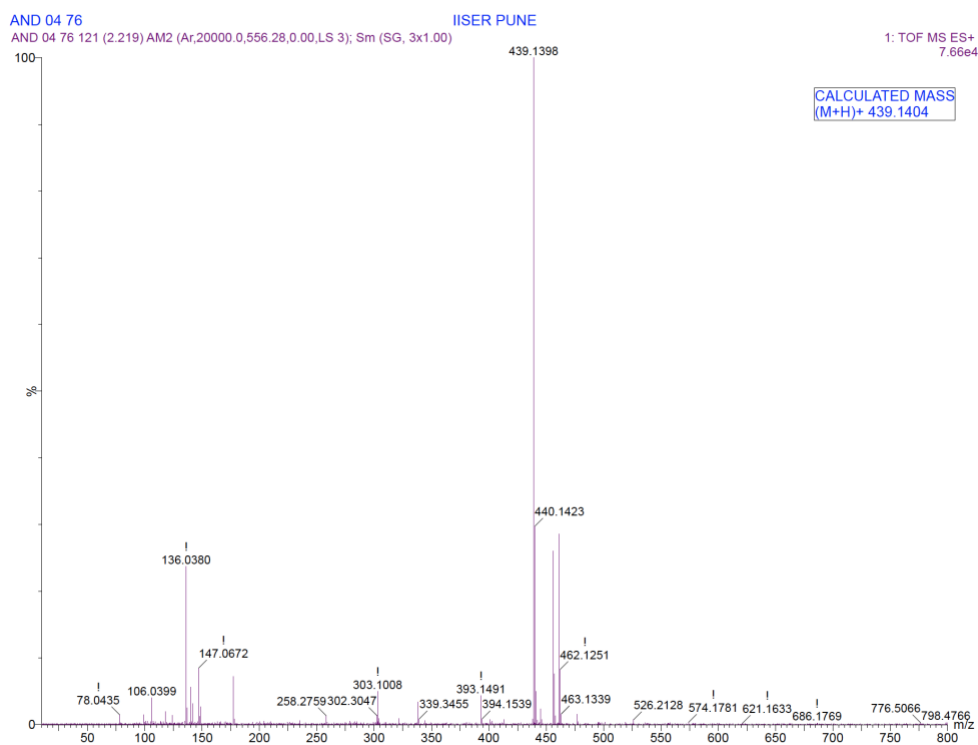
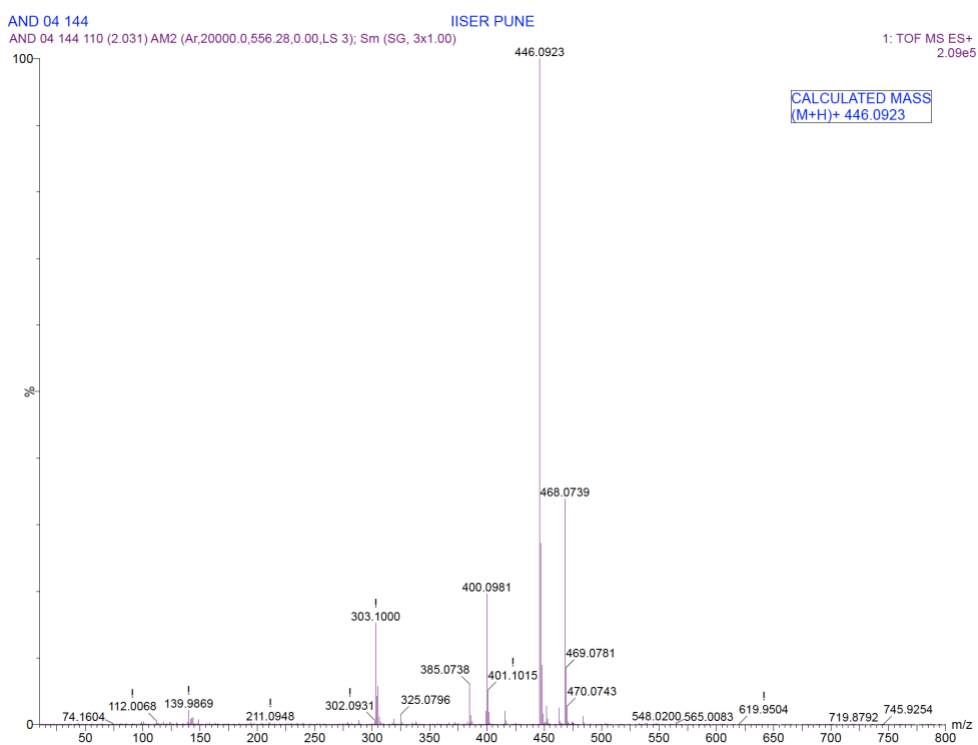
^1H NMR spectrum (400 MHz, $\text{DMSO-}d_6$) of **60** ^{13}C NMR spectrum (400 MHz, $\text{DMSO-}d_6$) of **60**

DEPT-135 NMR spectrum (400 MHz, DMSO-*d*₆) of **60**¹H NMR spectrum (400 MHz, DMSO-*d*₆) of **61**

^{13}C NMR spectrum (400 MHz, $\text{DMSO-}d_6$) of **61**DEPT-135 NMR spectrum (400 MHz, $\text{DMSO-}d_6$) of **61**

^1H NMR spectrum (400 MHz, $\text{DMSO-}d_6$) of TCF-OH

5.2.7. HRMS spectra of final compounds

HRMS spectrum of **60**HRMS spectrum of **61**

5.2.8. References

- (1) Global burden of bacterial antimicrobial resistance in 2019: A systematic analysis. *Lancet* **2022**, 399 (10325), 629–655.
- (2) Váradi, L.; Luo, J. L.; Hibbs, D. E.; Perry, J. D.; Anderson, R. J.; Orenga, S.; Groundwater, P. W. Methods for the detection and identification of pathogenic bacteria: past, present, and future. *Chem. Soc. Rev.* **2017**, 46 (16), 4818-4832.
- (3) Huang, Y.; Chen, W.; Chung, J.; Yin, J.; Yoon, J. Recent Progress in Fluorescent Probes for Bacteria. *Chem. Soc. Rev.*, **2021**, 50, 7725-7744
- (4) Hameed, S.; Xie, L.; Ying, Y. Conventional and emerging detection techniques for pathogenic bacteria in food science: A review. *Trends Food Sci. Technol.* **2018**, 81, 61–73.
- (5) Lazcka, O.; Campo, F. J. del; Muñoz, F. X. Pathogen detection: A perspective of traditional methods and biosensors. *Biosens. Bioelectron.* **2007**, 22 (7), 1205-17.
- (6) Franco-Duarte, R.; Černáková, L.; Kadam, S.; Kaushik, K. S.; Salehi, B.; Bevilacqua, A.; Corbo, M. R.; Antolak, H.; Dybka-Stepień, K.; Leszczewicz, M.; Tintino, S. R.; de Souza, V. C. A.; Sharifi-Rad, J.; Coutinho, H. D. M.; Martins, N.; Rodrigues, C. F. Advances in Chemical and Biological Methods to Identify Microorganisms—from Past to Present. *Microorganisms.* **2019**, 7 (5), 130.
- (7) Yoon, S. A.; Park, S. Y.; Cha, Y.; Gopala, L.; Lee, M. H. Strategies of detecting bacteria using fluorescence-based dyes. *Front. Chem.* **2021**, 9 (743923), 1-19.
- (8) Elmes, R. B. P. Bioreductive fluorescent imaging agents: Applications to tumour hypoxia. *Chem. Commun.* **2016**, 52 (58), 8935–8956.
- (9) Zhang, J.; Shen, Y.; May, S. L.; Nelson, D. C.; Li, S. Ratiometric fluorescence detection of pathogenic bacteria resistant to broad-spectrum β -lactam antibiotics. *Angew. Chem. Int. Ed. Engl.* **2012**, 51 (8), 1865–1868.
- (10) Zhang, X.; Ren, C.; Hu, F.; Gao, Y.; Wang, Z.; Li, H.; Liu, J.; Liu, B.; Yang, C. Detection of bacterial alkaline phosphatase activity by enzymatic in situ self-assembly of the AIEgen-peptide conjugate. *Anal. Chem.* **2020**, 92 (7), 5185–5190.

-
- (11) Zhao, L.; Liu, Y.; Zhang, Z.; Wei, J.; Xie, S.; Li, X. Fibrous testing papers for fluorescence trace sensing and photodynamic destruction of antibiotic-resistant bacteria. *J. Mater. Chem. B*. **2020**, *8* (13), 2709–2718.
- (12) Dai, T.; Xie, J.; Zhu, Q.; Kamariza, M.; Jiang, K.; Bertozzi, C. R.; Rao, J. A fluorogenic trehalose probe for tracking phagocytosed Mycobacterium tuberculosis. *J. Am. Chem. Soc.* **2020**, *142* (36), 15259–15264.
- (13) Zhang, Z.; Lv, T.; Tao, B.; Wen, Z.; Xu, Y.; Li, H.; Liu, F.; Sun, S. A novel fluorescent probe based on naphthalimide for imaging nitroreductase (NTR) in bacteria and cells. *Bioorg. Med. Chem.* **2020**, *28* (3), 115280.
- (14) Yoon, J. W.; Kim, S.; Yoon, Y.; Lee, M. H. A resorufin-based fluorescent turn-on probe responsive to nitroreductase activity and its application to bacterial detection. *Dyes and Pigments*. **2019**, *171*, 107779.
- (15) Wu, L. L.; Wang, Q.; Wang, Y.; Zhang, N.; Zhang, Q.; Hu, H. Y. Rapid differentiation between bacterial infections and cancer using a near-infrared fluorogenic probe. *Chem. Sci.* **2020**, *11* (12), 3141–3145.
- (16) Wong, R. H. F.; Kwong, T.; Yau, K.-H.; Au-Yeung, H. Y. Real time detection of live microbes using a highly sensitive bioluminescent nitroreductase probe. *Chem. Commun.* **2015**, *51* (21), 4440–4442.
- (17) Welling, M. M.; Hensbergen, A. W.; Bunschoten, A.; Velders, A. H.; Scheper, H.; Smits, W. K.; Roestenberg, M.; van Leeuwen, F. W. B. Fluorescent imaging of bacterial infections and recent advances made with multimodal radiopharmaceuticals. *Clin. Transl. Imaging*, **2019**, *7* (2), 125–138.
- (18) Feng, P.; Zhang, H.; Deng, Q.; Liu, W.; Yang, L.; Li, G.; Chen, G.; Du, L.; Ke, B.; Li, M. Real-time bioluminescence imaging of nitroreductase in mouse model. *Anal. Chem.* **2016**, *88* (11), 5610–5614.
- (19) Xu, S.; Wang, Q.; Zhang, Q.; Zhang, L.; Zuo, L.; Jiang, J. D.; Hu, H. Y. Real Time detection of ESKAPE pathogens by a nitroreductase-triggered fluorescence turn-on probe. *Chem. Commun.* **2017**, *53* (81), 11177–11180.

-
- (20) Lee, M. K.; Williams, J.; Twieg, R. J.; Rao, J.; Moerner, W. E. Enzymatic activation of nitro-aryl fluorogens in live bacterial cells for enzymatic turnover-activated localization microscopy. *Chem. Sci.* **2013**, *4* (1), 220–225.
- (21) Liu, T.; Wang, Y.; Feng, L.; Tian, X.; Cui, J.; Yu, Z.; Wang, C.; Zhang, B.; James, T. D.; Ma, X. 2D strategy for the construction of an enzyme-activated NIR fluorophore suitable for the visual sensing and profiling of homologous nitroreductases from various bacterial species. *ACS Sens.* **2021**, *6* (9), 3348–3356.
- (22) Li, X.; Geng, P.; Hong, X.; Sun, Z.; Liu, G. Detecting mycobacterium tuberculosis using a nitrofuranyl calanolide-trehalose probe based on nitroreductase Rv2466c. *Chem. Commun.* **2021**, *57* (97), 13174–13177.
- (23) Sedgwick, A. C.; Han, H. H.; Gardiner, J. E.; Bull, S. D.; He, X. P.; James, T. D. Long-wavelength fluorescent boronate probes for the detection and intracellular imaging of peroxynitrite. *Chem. Commun.* **2017**, *53* (95), 12822–12825.
- (24) Siarkiewicz, P.; Michalski, R.; Sikora, A.; Smulik-Izydorzyc, R.; Szala, M.; Grzelakowska, A.; Modrzejewska, J.; Bailey, A.; Nycz, J. E.; Kalyanaraman, B.; Malecki, J. G.; Zielonka, J.; Podsiadły, R. On the chemical reactivity of tricyanofuran (TCF)-based near-infrared fluorescent redox probes – effects of glutathione on the probe response and product fluorescence. *Dyes and Pigments* **2021**, *192*, 109405.
- (25) Gwynne, L.; Sedgwick, A. C.; Gardiner, J. E.; Williams, G. T.; Kim, G.; Lowe, J. P.; Maillard, J. Y.; Jenkins, T.; Bull, S. D.; Sessler, J. L.; Yoon, J.; James, T. D. Long wavelength TCF-based fluorescence probe for the detection of alkaline phosphatase in live cells. *Front. Chem.* **2019**, *7*, 255.
- (26) Wu, Y.; Deng, X.; Ye, L.; Zhang, W.; Xu, H.; Zhang, B. A TCF-based carbon monoxide NIR-probe without the interference of BSA and its application in living cells. *Molecules* **2022**, *27* (13), 4155.
- (27) Shi, W. J.; Wan, Q. H.; Yang, F.; Wang, X.; Wei, Y. F.; Lin, X. R.; Zhang, J. Y.; Deng, R. H.; Chen, J. Y.; Zheng, L.; Liu, F.; Gao, L. A novel TCF-Aza-BODIPY-based near-infrared fluorescent probe for highly selective detection of hypochlorous acid in living cells. *Spectrochim. Acta. A. Mol. Biomol. Spectrosc.* **2022**, *279*, 121490.

-
- (28) O'Connor, L. J.; Cazares-Körner, C.; Saha, J.; Evans, C. N. G.; Stratford, M. R. L.; Hammond, E. M.; Conway, S. J. Design, synthesis and evaluation of molecularly targeted hypoxia-activated prodrugs. *Nat. Protoc.* **2016**, *11* (4), 781–794.
- (29) Jin, C.; Zhang, Q.; Lu, W. Synthesis and biological evaluation of hypoxia-activated prodrugs of SN-38. *Eur. J. Med. Chem.* **2017**, *132*, 135–141.
- (30) Wang, S.; Wu, X.; Zhang, Y.; Zhang, D.; Xie, B.; Pan, Z.; Ouyang, K.; Peng, T. discovery of a highly efficient nitroaryl group for detection of nitroreductase and imaging of hypoxic tumor cells. *Org. Biomol. Chem.* **2021**, *19* (15), 3469–3478.
- (31) Liu, F.; Wang, Z.; Wang, W.; Luo, J.-G.; Kong, L. Red-emitting fluorescent probe for detection of γ -glutamyltranspeptidase and its application of real-time imaging under oxidative stress in cells and in vivo. *Anal. Chem.* **2018**, *90* (12), 7467–7473.
- (32) Rostami, E.; Hamidi Zare, S. double brønsted acidic media immobilized on carbonized sugarcane bagasse (CSCB) as a new and efficient solid acid catalyst for the synthesis of coumarins, dicoumarols and xanthenes. *ChemistrySelect*, **2019**, *4* (45), 13295–13303.

Synopsis

Design, Synthesis and Evaluation of Bioreductively-Activated Fluoroquinolone Prodrugs

Chapter 1. Introduction

Tuberculosis is one of the world's oldest and deadliest infectious diseases caused by facultative intracellular bacterium *Mycobacterium tuberculosis* (*Mtb*). The recommended standard treatment for drug-susceptible TB has a cure rate of >95% when provided under directly observed therapy (DOT).¹⁻² During the first two months of effective intensive treatment, a subpopulation of actively replicating mycobacteria transitions into a metabolically inactive, non-replicating persistent state that are transiently resistant to antibiotics (Figure 1).³ These persisters provide an evolutionary reservoir that favours the emergence of drug-resistant mutants and also contribute to the protracted regimen required for TB treatment. These non-replicating population can switch to active growth at any point resulting in the recalcitrance and relapse of TB infection.⁴⁻⁷ Hence, their existence often contributes to the development of latent infections which pose a significant problem for those with a weak or compromised immune system.

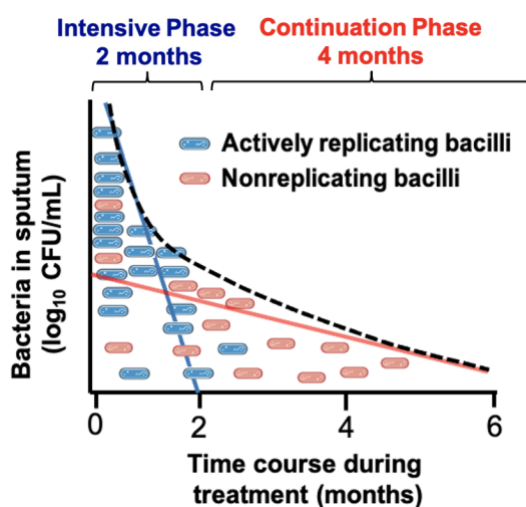


Figure 1. Heterogeneity in the intrinsic drug susceptibility in the bacterial subpopulations of *Mtb*. A rapid rate of decline was seen with the replicating bacilli (blue line), but the number of non-replicating bacilli declined at a slower rate (red line). Adapted from Horsburgh, C. R et al. *New Eng. J. Med.* 2015.⁷

The adaptation into a drug-tolerant non-replicating persistent state is associated with metabolic downshift and cell wall remodelling. Compared to rapidly dividing bacteria, non-replicating *Mtb* exhibited increased thickening of lipid-rich cell walls, as a result of the extensive

accumulation of free mycolates and lipoarabinomannans.⁸⁻¹¹ This distinct feature is a characteristic phenotype of non-replicating tubercle bacilli and contributes to hindering the penetration and accumulation of antibiotics to reach their periplasmic or intracellular targets.¹² LC-MS/MS analysis demonstrated that the intracellular accumulation of different TB drugs is affected to varying degrees in the non-replicating state. The permeability of many anti-TB drugs is significantly impaired and this accounts for the phenotypic drug resistance in non-replicating *Mtb*.¹³

Preclinical and clinical studies have shown that fluoroquinolones (FQs) had excellent inhibitory activity against *Mtb*. A multitude of *in vitro* and *in vivo* studies have demonstrated the superiority of MXF (a fourth-generation FQ) over other FQs in reducing bacterial burden in both mice and rabbit models of TB.¹⁴⁻¹⁵ Recent clinical trial on MXF (RPT-MOXTB, 2020) have led to a shortening of TB treatment to 4-months from standard 6-months.¹⁶⁻¹⁸ Although MXF demonstrated lethality against actively replicating *Mtb*, it has limited efficacy against mycobacterial persisters.¹⁹⁻²³ One important reason for the lack of activity of MXF against non-replicating *Mtb* is its poor accumulation within bacteria. Being relatively hydrophilic (clogP = -0.49), the presence of thickened cell envelope makes the non-replicating bacilli even more impermeable than replicating *Mtb*, contributing to the reduced uptake of MXF in quiescent populations.

To address this problem, the possibility of utilizing a prodrug approach to enhance the efficacy of MXF by increasing its permeability in non-replicating *Mtb* was considered. This strategy is promising considering the fact that many TB drugs unlike many conventional antibiotics share the common characteristic trait of being more hydrophobic. Since bacterial NTRs are prevalent in both replicating and non-replicating *Mtb*,²⁴⁻²⁶ we propose that a MXF prodrug may be cleaved by NTR to generate MXF. Hence, these prodrugs should retain their potency against both replicating and non-replicating *Mtb* (Figure 2).

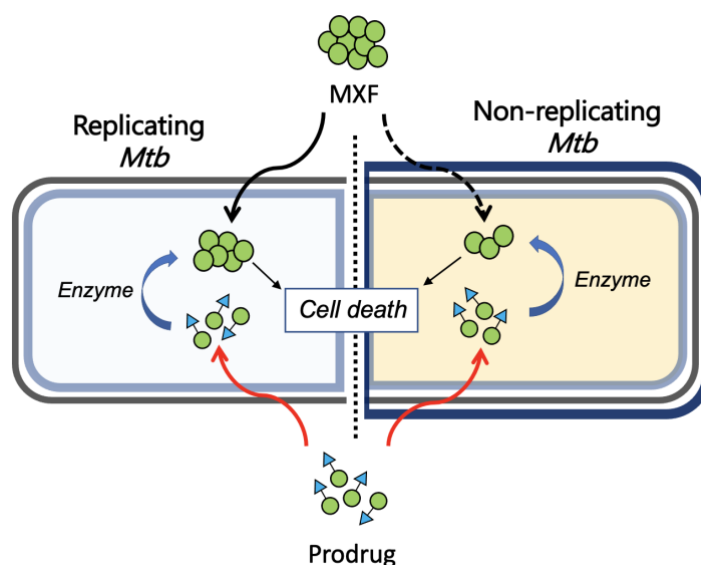


Figure 2. Proposed prodrug strategy to enhance accumulation and efficacy of MXF in non-replicating *Mtb*

In **Chapter 2**, we designed and developed a focussed library of nitroaryl and nitroheteroaryl conjugates of MXF. Two principles were used in the enzyme-prodrug design: first, to use NTR as an enzyme to activate a prodrug to produce MXF with both rate and efficiency serving as optimization criteria; and second, to increase lipophilicity of the ensuing prodrug in order to improve permeability. In **Chapter 3**, a detailed computational and biochemical analysis was conducted to understand the reactivity of substrates toward *E. coli* NTR and identify an optimal substrate. The ability of prodrugs to generate MXF in a variety of bacterial lysates and their stability in mammalian lysates were also tested. Among the tested prodrugs, 2-nitrothiazole-based prodrug was found to undergo rapid and efficient cleavage under both chemo- and bio-reductive conditions to release MXF. In **Chapter 4**, the prodrugs were evaluated for antimycobacterial activity against replicating and non-replicating *Mtb*. Again, 2-nitrothiazole MXF prodrug demonstrated equipotent antimycobacterial activity against replicating *Mtb* and superior inhibitory activity against non-replicating *Mtb* compared to MXF. LC-MS analysis was conducted to correlate the enhanced efficacy of the prodrug with the intracellular accumulation of MXF in non-replicating *Mtb*. The prodrug strategy was further exploited to enhance the antibacterial activity of another fluoroquinolone antibiotic, ciprofloxacin (CIP) in **Chapter 5.1**. Since detection of *Mtb* is challenging and in order to work towards rapid and real detection of *Mtb*, we next utilized the newly identified NTR sensitive 2-nitrothiazole moiety to develop NTR responsive dual colorimetric and fluorescence “turn OFF-ON” NIR probe in **Chapter 5.2**.

Chapter 2. Design, Synthesis, and Evaluation of Nitroheterocyclic prodrugs of Moxifloxacin (MXF)

MXF contains two functional groups that can be modified into a prodrug form. The carboxylic acid can be converted to a nitroaryl ester, and the amine on the piperidine ring can be derivatized as a nitroaryl carbamate (Figure 3).

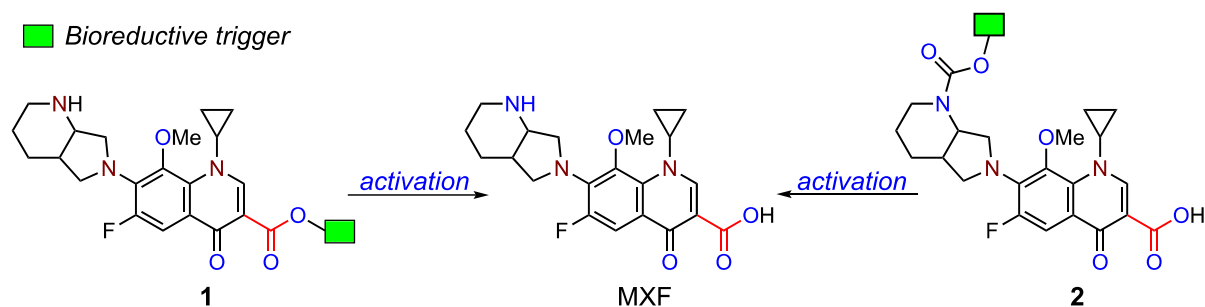


Figure 3. Proposed strategy for the generation of MXF from ester and carbamate prodrugs

Hence, we sought to rationally design MXF prodrugs that could be activated in reductive environments prevalent in replicating and non-replicating *Mtb* (Figure 4). Our strategy involved exploiting the expressed NTRs as an enzyme trigger to activate the prodrug to produce MXF with both rate and efficiency as parameters for optimization; and to increase the lipophilicity of the ensuing prodrug to improve permeability. This strategy may shorten the duration of TB treatment and reduce the relapse rate. Additionally, the prodrug strategy can mitigate FQ-induced host toxicity and reduce its tremendous impact on the host microbial symbiosis by minimizing the unintended systemic exposure of MXF to host cells.

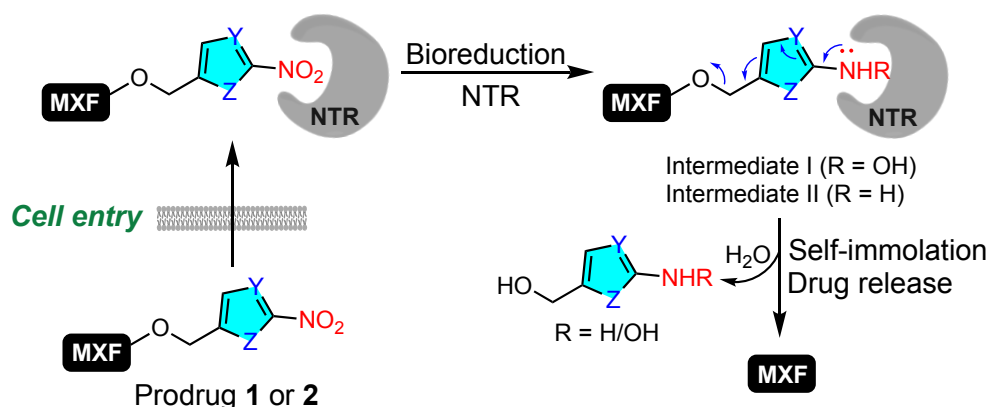


Figure 4. Design and mechanism of bioreductive activation of nitroheteroaryl prodrugs. Reduction of prodrug by NTR results in the formation of hydroxylamine or amine intermediate, which upon subsequent self-immolation releases MXF.

To this end, we synthesized a focussed library of nitro-heterocyclic esters and carbamates of MXF with a wide range of reduction potentials. The prodrugs were evaluated for physicochemical descriptors commonly observed with many anti-tubercular drugs. The prodrugs have shown significantly higher polar surface area and lipophilicity compared to MXF. Encouraged by the fact that lipophilic compounds have increased availability in areas of lipid-rich necrotic regions of lungs of TB patients and enhanced intracellular accumulation inside non-replicating *Mtb*, the prodrugs would presumably have higher accumulation than hydrophilic antibiotic, MXF.

A systematic investigation to identify the optimal nitroaryl prodrug to generate MXF in the presence of mild and strong reducing agents was conducted. Despite the wide use of 2-nitroimidazolyl group in the development of hypoxia-activated prodrugs, the synthesis of 1-methyl-2-nitroimidazole precursor is quite lengthy and reinforces the need for alternatives. To circumvent these problems, the identification of a reliable, time-efficient, high yielding, and more sensitive bioreductive trigger appears to be a more logical and promising approach. Our synthetic endeavour culminated in the utilization of 2-nitrothiazole functionality to design ester and carbamate prodrugs of MXF. Interestingly, 2-nitrothiazole prodrug **38** displayed a significantly lower onset reduction potential than other prodrugs, supporting the reduction of 2-nitrothiazole moiety is more thermodynamically favoured when compared with other similar nitroaryl groups. Moreover, the 2-nitrothiazolyl prodrug **38** demonstrated superior sensitivity and enhanced response towards milder reducing agents than prodrug **37** tethered with extensively employed 2-nitroimidazole moiety. The 2-nitrothiazole ester prodrug **38** also follows a chemoreduction profile similar to the 2-nitroimidazole based prodrug in the presence of strong reducing agents (Figure 5).

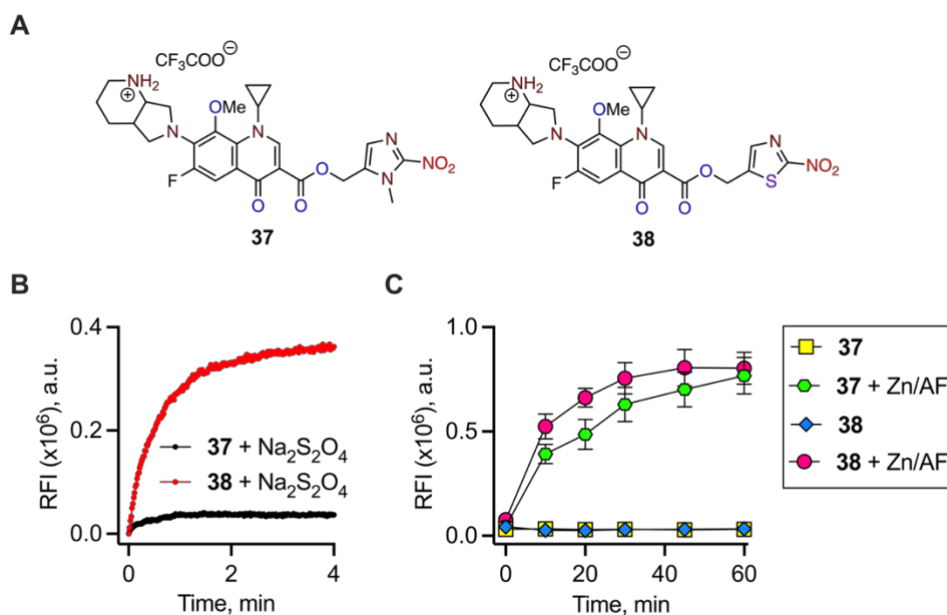


Figure 5. (A) Structures of **37** and **38**. Monitoring time-dependent release kinetics of MXF following chemical reduction with (B) sodium dithionite ($\text{Na}_2\text{S}_2\text{O}_4$) and (B) Zinc/ammonium formate (Zn/AF) from **37** and **38** by a fluorescence-based assay

Overall, these results suggest that 2-nitrothiazole tethered MXF prodrug with the lowest reduction potential demonstrated superior sensitivity and enhanced response towards different reducing agents in an unprecedented fashion.

Chapter 3. Nitroreductase (NTR) mediated bioreductive activation of Moxifloxacin (MXF) prodrugs

Having established that chemical reduction facilitated the release of MXF from nitro-heterocyclic prodrugs in Chapter 2, we evaluated their substrate specificities towards bacterial nitroreductases (NTRs). Despite the wide popularity of the 1-methyl-2-nitroimidazole bioreductive group, the efficiency of NTRs in bioactivation of structurally resembling nonimidazole five-membered nitroheterocycles, such as nitrooxazole and nitrothiazole has not yet been systematically studied. Recently, the 2-nitrothiazolyl moiety was used as a bioreductive trigger and has garnered significant attention in the development of hypoxia-activated prodrugs (HAPs) to specifically target hypoxic tumors.²⁷ Nevertheless, to date, 2-nitrothiazoles have not been reported as a substrate for bacterial NTR, including *E. coli* and mycobacterial NTR. In light of this, a systematic study was conducted to tune the selectivity and enhance the reactivity of substrates toward *E. coli* NTR.

Owing to the higher reactivity than nitrobenzyl tethered prodrug **33**, it was expected that nitrothiophene prodrug **35** would result in enhanced fluorescence signal. Interestingly, the 2-nitrothiazole prodrugs **38** (ester) and **46** (carbamate) also displayed the highest increase in fluorescence response similar to **35**. These results were in line with the results of the chemoreductive study (Figure 6).

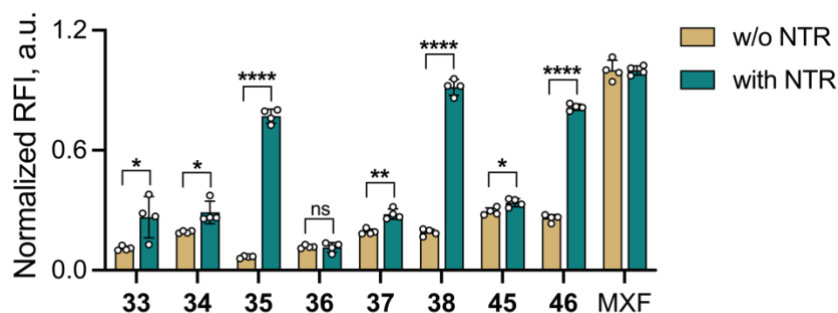


Figure 6. Monitoring the *E. coli* NTR mediated bioreductive activation of prodrugs by fluorescence ($\lambda_{\text{ex}} = 289 \text{ nm}$ and $\lambda_{\text{em}} = 488 \text{ nm}$) after 1 h of incubation with *E. coli* NTR (15 nM) and NADH (100 μM) in pH 7.4 phosphate buffer (10 mM) at 37 °C

The 2-nitrothiazole prodrugs **38** and **46** were found to be the most favoured substrates for *E. coli* NTR *in vitro*, as evidenced by their higher V_{max} and catalytic efficiency values. The higher $k_{\text{cat}}/K_{\text{m}}$ values of 24.95 $\mu\text{M}^{-1}\text{min}^{-1}$ and 9.72 $\mu\text{M}^{-1}\text{min}^{-1}$ for **38** and **46**, respectively, which were 93- and 41- fold more efficient than **37** with a $k_{\text{cat}}/K_{\text{m}}$ of 0.61 $\mu\text{M}^{-1}\text{min}^{-1}$, clearly demonstrate that *E. coli* NTR had the highest catalytic efficiency for 2-nitrothiazole prodrugs (Figure 7).

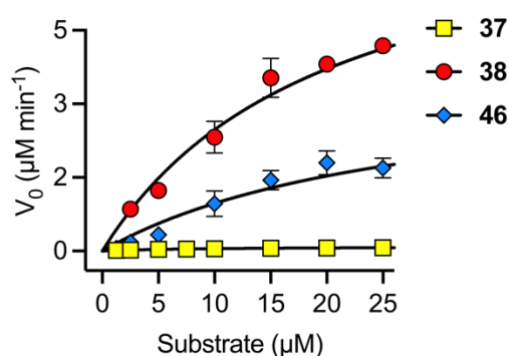


Figure 7. Michaelis-Menten analyses showing the nitroreduction of 2-nitroimidazolyl versus 2-nitrothiazolyl prodrugs by *E. coli* NTR

Furthermore, *E. coli* NTR promoted an instantaneous and complete reduction of the 2-nitrothiazole ester prodrug **38** into MXF (Figure 8). The relative sensitivity and superiority of ester prodrug **38** to *E. coli* NTR over 2-nitrothiazole carbamate prodrug is even more striking.

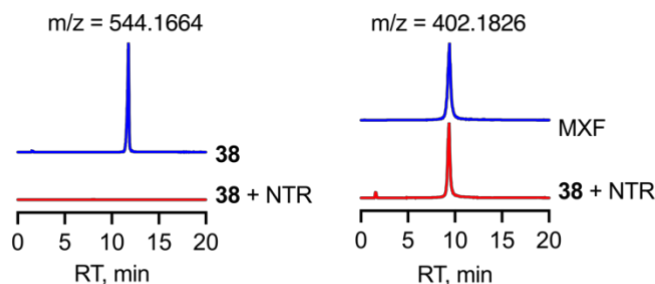


Figure 8. LC-MS analysis of *E. coli* NTR mediated nitro-reduction of **38** resulted in the release of MXF

The experimental findings were also complemented by the docking results. Furthermore, the MD simulations indicate that the mechanism of reduction is likely to be mediated by electron transfer from FMN followed by proton transfer *via* water at the active site. The lower electron transfer barrier between the bound FMN and prodrug allows the efficient and rapid reduction of the nitro group in **38**. In agreement with these findings, the prodrug **38** was stable in mammalian lysates under physiological conditions. Furthermore, the prodrug **38** was preferentially activated in a range of lysates derived from bacteria such as *E. coli*, *M. smegmatis*, and *M. tuberculosis*. This is a further testament to the versatility and specificity of 2-nitrothiazole substrate, **38** towards a variety of bacterial NTRs.

Chapter 4. Antibacterial activity of NTR-MXF prodrugs

The antibacterial activity of prodrugs, including **38** was evaluated against Gram-positive, Gram-negative and mycobacteria (*M. smegmatis* and *M. tuberculosis*). Our analysis showed that one of the analogues, 2-nitrothiazole prodrug **38** exhibited potent antibacterial activity comparable to MXF in both cellular and animal models. The prodrug **38** also exhibited potent anti-mycobacterial activity against drug-susceptible and drug-resistant strains of *Mtb*, including MDR and XDR patient-derived strains (Figure 9).

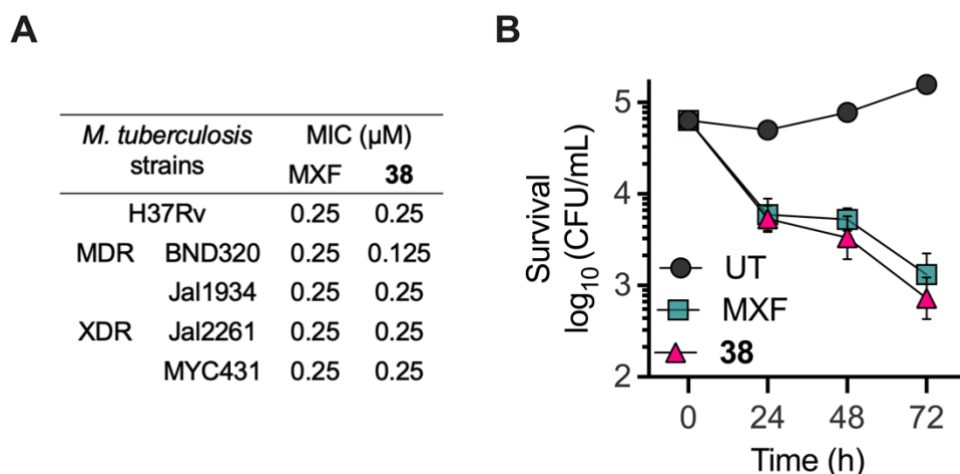


Figure 9. (A) Antimycobacterial activity of MXF and **38** against drug-susceptible and patient-derived drug resistant strains of *Mtb*. (B) Bacterial survival kinetics after treatment of THP-1 macrophages infected with *Mtb* H37Rv at 5x MIC of **38** and MXF. Data was provided by Prof. Amit Singh, IISc Bangalore.

Furthermore, our results demonstrated that **38** had superior inhibitory activity against non-replicating *Mtb* when compared with MXF (Figure 10). These results indicated that the prodrug exhibited potent anti-mycobacterial activity against non-replicating *Mtb* while retaining mycobactericidal activity similar to MXF against replicating *Mtb*.

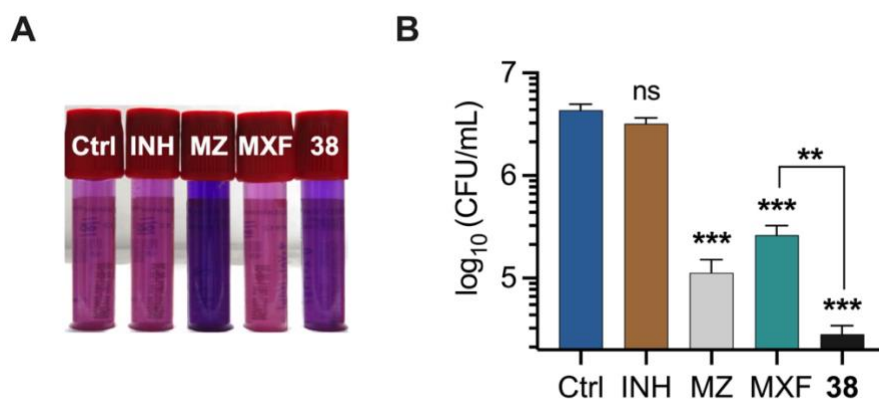


Figure 10. (A) Mycobactericidal effect of MXF and **38** on hypoxia-adapted *Mtb* bacilli based on visual hypoxia resazurin reduction assay (HyRRA). Isoniazid (INH, 10 μM) and Metronidazole (MZ, 10 mM) served as a negative and positive control respectively. The pink colour in the tube indicates cell viability under hypoxia while blue colour indicates no growth. (B) Survival of *Mtb* under hypoxia was measured as log₁₀ of colony-forming units (CFU) after treatment with 10x MIC of MXF and **38** for 5 days. Data was provided by Prof. Amit Singh, IISc Bangalore.

LC-MS based studies demonstrated the increased intracellular accumulation of MXF from **38** as compared to MXF alone, and this could contribute to enhanced potency in the non-replicating *Mtb* model (Figure 11). This strategy may have a significant therapeutic benefit in the treatment of latent TB caused by mycobacterial persisters.

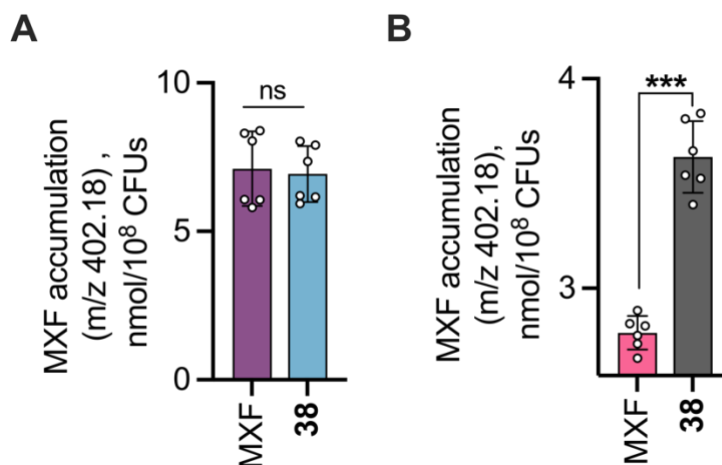


Figure 11. LC-MS analysis of intracellular concentrations of MXF (m/z 402.18) in (A) replicating and (B) non-replicating cultures of *Mtb* following incubation for 30 min with a fixed concentration of MXF and **38** of 5 μ M. The drug content is expressed as the amount of drug (nmol/10⁸ CFUs).

Chapter 5. Understanding the scope of 2-nitrothiazolyl moiety as a masking group for NTR

Having established that 2-nitrothiazole group as an improved bioreductive trigger compared to 1-methyl-2-nitroimidazole and other nitroaryl groups, the scope and utility of this group in masking drugs and fluorophores was investigated in this chapter. Two selective strategies to mask carboxylic acid and phenolic compounds as an ester (Chapter 5.1) and an ether (Chapter 5.2) based NTR-sensitive caged compounds respectively were considered.

Chapter 5.1. Design, Synthesis and Evaluation of Nitroreductase (NTR) activated Prodrugs of Ciprofloxacin (CIP)

In this chapter, 2-nitrothiazolyl moiety was utilized to design and synthesize NTR sensitive ester prodrugs of a broad spectrum second generation FQ antibiotic, Ciprofloxacin (CIP). Upon activation by bacterial NTR, the efficient cleavage of the prodrug would liberate CIP (Figure 12).

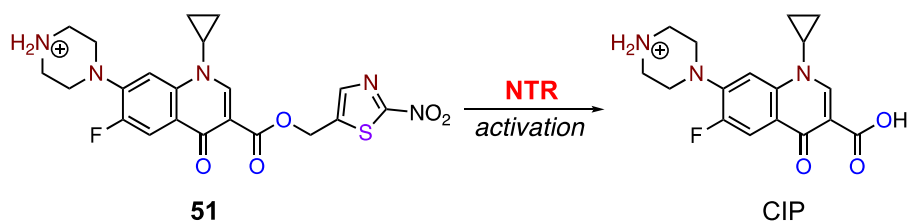


Figure 12. Proposed strategy for the release of CIP from ester prodrug

Detailed investigative analysis revealed that the 2-nitrothiazolyl tethered CIP prodrug **51** was an optimal substrate for *E. coli* NTR and provided CIP upon enzymatic reduction in quantitative yield. The prodrug was activated in a variety of bacterial lysates, indicating the specificity of this prodrug towards bacterial NTRs (Figure 13).

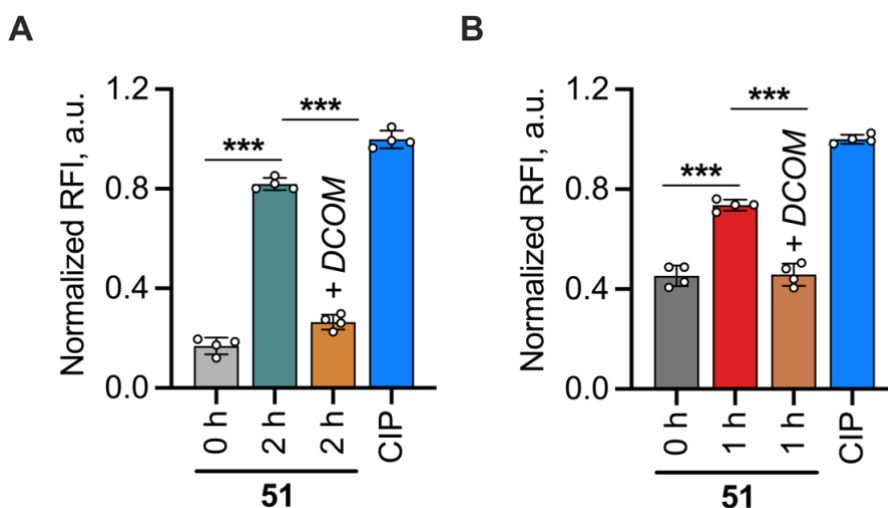


Figure 13. Monitoring the release of CIP from **51** (10 μ M) after incubation in lysates (1 mg/mL) of (A) *E. coli* ATCC 25922 for 2 h and (B) *M. smegmatis* mc²155 in 1 h alone or in the presence of NTR inhibitor, dicoumarol (DCOM; 250 μ M)

These results suggest changing the leaving group from MXF (fourth-generation FQ) to CIP (second-generation FQ) in the prodrug has no impact on *E. coli* dependent nitroreduction. This prodrug also retained antibacterial activity equivalent to CIP against gram-positive and gram-negative bacteria. Overall, these studies strongly indicate that 2-nitrothiazole functional group is a promising bioreductive trigger.

Chapter 5.2. Design and Development of Nitroreductase (NTR) Responsive Dual Colorimetric Fluorescence “Turn OFF-ON” Probes

The widespread and long-term overuse use of antibiotics has spurred the rise of drug resistant pathogenic bacteria, which poses a major risk to human health worldwide.²⁸ The severity of infections varies, ranging from self-limiting to a potentially fatal condition, causing significant morbidity and mortality. Therefore, rapid detection of bacteria is critical for early diagnosis and effective treatment of infections as well as the development of new antibiotics. Owing to the presence of NTRs in several pathogenic bacteria responsible for the majority of hospital-acquired drug-resistant infections, numerous research groups have developed NTR responsive probes for real time detection of bacteria.²⁹⁻³⁴

Despite the wide popularity of 4-nitrobenzyl and 1-methyl-2-nitroimidazolyl moiety as preferred substrates for NTR, the development of a dual colorimetric fluorescence “turn OFF-ON” probe for rapid and real time detection of bacteria has been limited. As described in the previous chapters, 2-nitrothiazolyl moiety demonstrated superior sensitivity and reactivity towards NTR over other nitro(hetero)aryl substrates. Therefore, 2-nitrothiazolyl group was used as a caging group for the development of an NTR activatable probe with a colorimetric and fluorescence “turn OFF-ON” response (Figure 14).

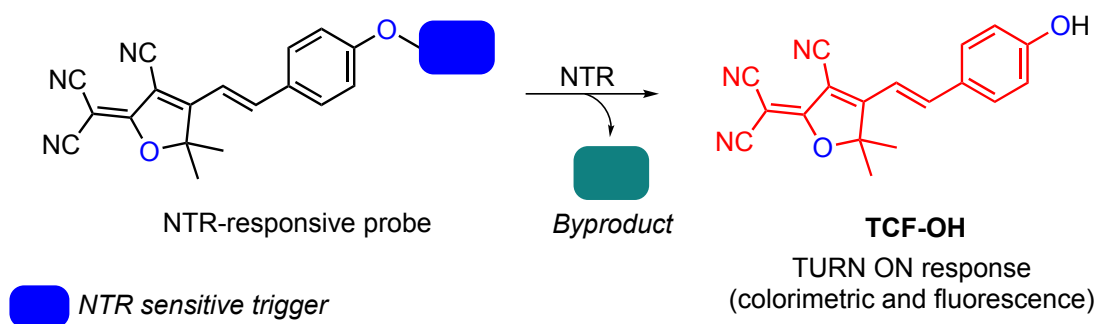


Figure 14. Proposed mechanism of NTR mediated activation of dual colorimetric fluorescence turn OFF-ON probe

In this context, ether based TCF tethered latent fluorophores **60** and **61** were synthesized and evaluated in the presence of bacterial NTR for visual and fluorescence change over time. Our investigation revealed that the 2-nitrothiazolyl tethered probe **61** provided a strong color change from yellow to pink with concomitant increase fluorescence response and change in the absorbance in the presence of NTR (Figure 15). HPLC

analysis also corroborated the rapid and complete conversion of **61** to **TCF-OH** in the presence of NTR (Figure 16 and 17).

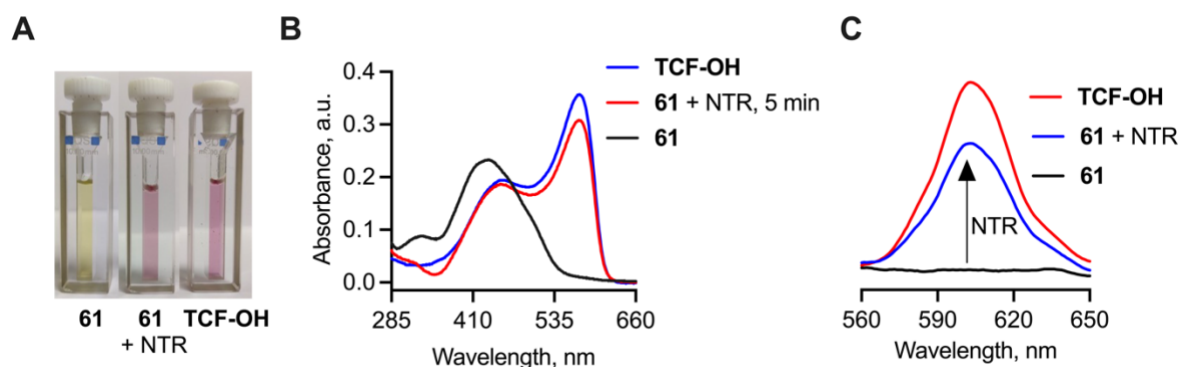


Figure 15. Monitoring the visual colorimetric response “turn OFF-ON” response of probe **61** (10 μ M) by (A) recording a photographic image and (B) absorption spectra after 5 min of incubation with *E. coli* NTR (15 nM) and NADH (100 μ M) in pH 7.4 phosphate buffer (10 mM) at 37 $^{\circ}$ C. A distinct colorimetric change (yellow to pink) corresponding to the formation of **TCF-OH** was observed after incubation of the probe with NTR. (C) Fluorescence spectra ($\lambda_{\text{ex}} = 579$ nm and $\lambda_{\text{em}} = 603$ nm) upon incubation of **61** (10 μ M) with NTR (15 nM) and NADH (100 μ M) in pH 7.4 phosphate buffer (10 mM).

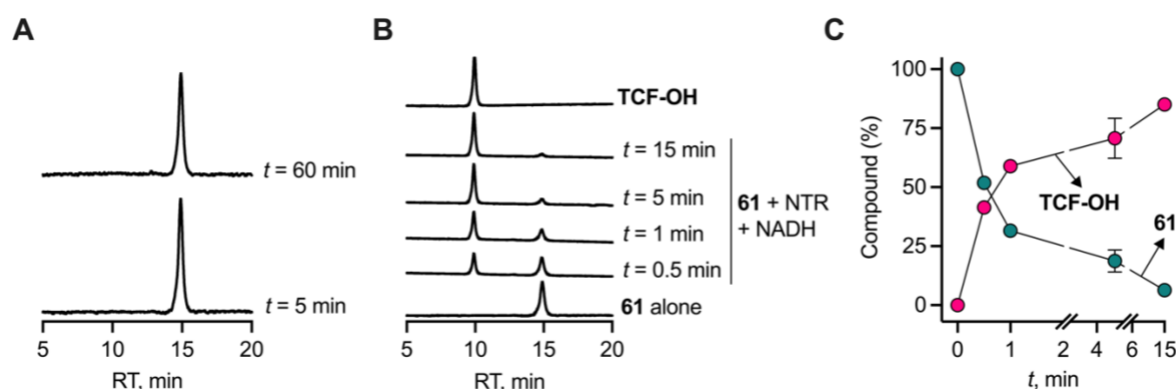


Figure 16. HPLC traces of (A) stability of the probe **61** and (B) enzyme dependent reductive activation of probe **61** (12.5 μ M) in the presence of *E. coli* NTR (15 nM) and NADH (100 μ M) in pH 7.4 phosphate buffer. **TCF-OH** (12.5 μ M) was used as a positive control. The signal was detected using the UV detector set at 440 nm. (C) Decomposition of **61** and formation of **TCF-OH** upon incubation with NTR (15 nM) and NADH (100 μ M) in pH 7.4 phosphate buffer at 37 $^{\circ}$ C as monitored by HPLC.

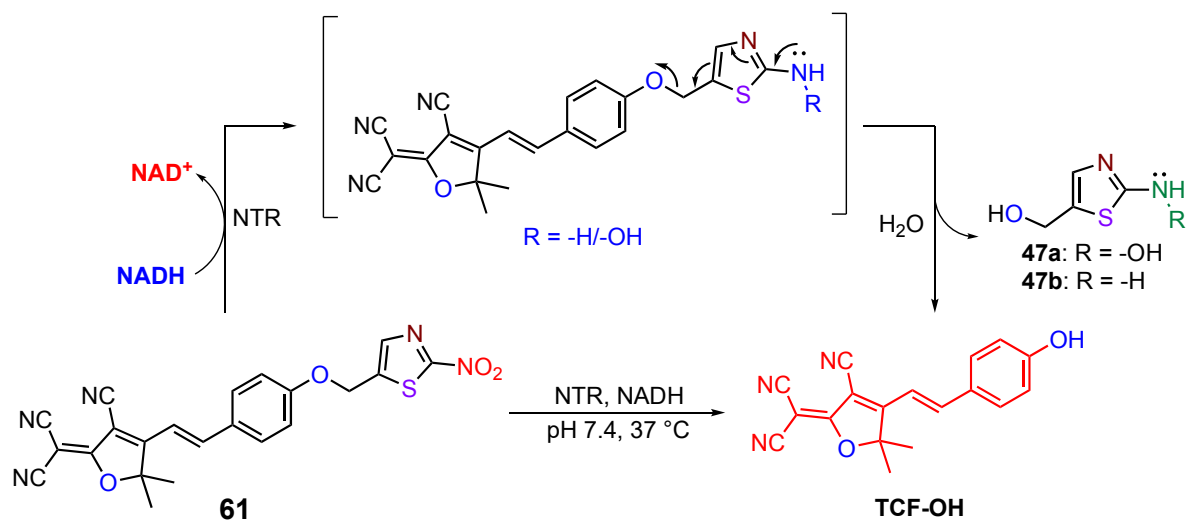


Figure 17. Proposed mechanism of NTR dependent conversion of **61** to TCF-OH

The probe **61** exhibited high selectivity to NTR and a quick response (< 5 min) in the presence of physiologically relevant analytes. Given that the **61** was well tolerated by the mammalian cells, we then assessed the ability of **61** to detect the NTR in live pathogenic gram-negative bacteria (*E. coli* ATCC 25922) using confocal imaging. As shown in Figure 18, a red fluorescence signal in Alexa fluor 568 (red channel) characteristic of the release of **TCF-OH** from **61** was observed. This result indicate that the probe was cell permeable and was able to afford a strong fluorescence response upon NTR-dependent bioreductive activation in bacteria.

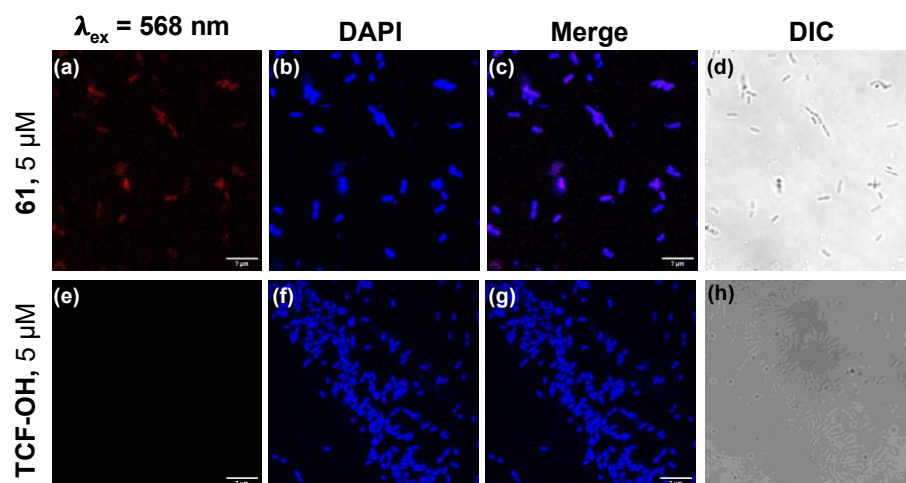


Figure 18. Confocal microscope images in *E. coli* bacterial cells preincubated with (a-d) **61** (5 μM) or (e-h) **TCF-OH** (5 μM) for 2 h. The cells were imaged on the red channel (Alexa fluor 568 for detection of **TCF-OH** (a and e)), DAPI channel (b and f), merged image of red and DAPI channel (c and g) and DIC image (d and h).

Confocal imaging studies demonstrated that **61** with NTR-responsive OFF-ON feature has an excellent ability for non-invasive real-time detection of bacteria. Together, these results lay the foundation for the development of NTR-sensitive dual response probes for targeted imaging of bacterial infections.

The results in this thesis laid the ground work for using 2-nitrothiazole as a bioreductive trigger in the development of NTR-activated prodrugs and NTR-responsive colorimetric and fluorescence ‘turn OFF-ON’ probes.

References:

- (1) Zumla, A.; Nahid, P.; Cole, S. T. Advances in the Development of New Tuberculosis Drugs and Treatment Regimens. *Nat. Rev. Drug Discov.* **2013**, *12*, 388–404.
- (2) Hopewell, P. C.; Pai, M.; Maher, D.; Uplekar, M.; Raviglione, M. C. International standards for tuberculosis care. *Lancet Infect. Dis.* **2006**, *6* (11), 710-25.
- (3) Horsburgh, C. R.; Barry, C. E.; Lange, C. Treatment of Tuberculosis. *New Eng. J. Med.* **2015**, *373* (22), 2149–2160.
- (4) Zhang, Y.; Yew, W. W.; Barer, M. R. Targeting Persisters for Tuberculosis Control. *Antimicrob. Agents Chemother.* **2012**, *56* (5), 2223-30.
- (5) Cohen, N. R.; Lobritz, M. A.; Collins, J. J. Microbial Persistence and the Road to Drug Resistance. *Cell Host Microbe.* **2013**, *13* (6), 632-42.
- (6) Sebastian, J.; Swaminath, S.; Nair, R. R.; Jakkala, K.; Pradhan, A.; Ajitkumar, P. De Novo Emergence of Genetically Resistant Mutants of Mycobacterium Tuberculosis from the Persistence Phase Cells Formed against Antituberculosis Drugs in Vitro. *Antimicrob. Agents Chemother.* **2017**, *61* (2), e01343-16.
- (7) Zhang, Y. Persisters, Persistent Infections and the Yin-Yang Model. *Emerg. Microbes Infect.* **2014**, *3* (1), e3.
- (8) Jakkala, K.; Ajitkumar, P. Hypoxic Non-Replicating Persistent Mycobacterium Tuberculosis Develops Thickened Outer Layer That Helps in Restricting Rifampicin Entry. *Front. Microbiol.* **2019**, *10*, 2339.
- (9) Seiler, P.; Ulrichs, T.; Bandermann, S.; Pradl, L.; Jörg, S.; Krenn, V.; Morawietz, L.; Kaufmann, S. H. E.; Aichele, P.; Kaufmann, S. H. E. Cell-Wall Alterations as an Attribute of Mycobacterium Tuberculosis in Latent Infection. *J. Infect. Dis.* **2003**, *188* (9), 1326-31.
- (10) Wright, C. C.; Hsu, F. F.; Arnett, E.; Dunaj, J. L.; Davidson, P. M.; Pacheco, S. A.; Harriff, M. J.; Lewinsohn, D. M.; Schlesinger, L. S.; Purdy, G. E. The Mycobacterium Tuberculosis MmpL11 Cell Wall Lipid Transporter Is Important for Biofilm Formation, Intracellular Growth, and Nonreplicating Persistence. *Infect. Immun.* **2017**, *85* (8), e00131-17.

- (11) Bacon, J.; Alderwick, L. J.; Allnut, J. A.; Gabasova, E.; Watson, R.; Hatch, K. A.; Clark, S. O.; Jeeves, R. E.; Marriott, A.; Rayner, E.; Tolley, H.; Pearson, G.; Hall, G.; Besra, G. S.; Wernisch, L.; Williams, A.; Marsh, P. D. Non-Replicating Mycobacterium Tuberculosis Elicits a Reduced Infectivity Profile with Corresponding Modifications to the Cell Wall and Extracellular Matrix. *PLoS One*. **2014**, *9* (2), e87329.
- (12) Cunningham, A. F.; Spreadbury, C. L. Mycobacterial Stationary Phase Induced by Low Oxygen Tension: Cell Wall Thickening and Localization of the 16-Kilodalton-Crystallin Homolog. *J. Bacteriol.* **1998**, *180* (4), 801-8.
- (13) Sarathy, J.; Dartois, V.; Dick, T.; Gengenbacher, M. Reduced Drug Uptake in Phenotypically Resistant Nutrient-Starved Nonreplicating Mycobacterium Tuberculosis. *Antimicrob. Agents Chemother.* **2013**, *57* (4), 1648–1653.
- (14) Maitre, T.; Petitjean, G.; Chauffour, A.; Bernard, C.; el Helali, N.; Jarlier, V.; Reibel, F.; Chavanet, P.; Aubry, A.; Veziris, N. Are Moxifloxacin and Levofloxacin Equally Effective to Treat XDR Tuberculosis? *J. Antimicrob. Chemother.* **2017**, *72* (8), 2326–2333.
- (15) Sarathy, J.; Blanc, L.; Alvarez-Cabrera, N.; O'Brien, P.; Dias-Freedman, I.; Mina, M.; Zimmerman, M.; Kaya, F.; Liang, H. P. H.; Prideaux, B.; Dietzold, J.; Salgame, P.; Savic, R. M.; Linderman, J.; Kirschner, D.; Pienaar, E.; Dartois, V. Fluoroquinolone Efficacy against Tuberculosis Is Driven by Penetration into Lesions and Activity against Resident Bacterial Populations. *Antimicrob. Agents Chemother.* **2019**, *63* (5), e02516-18.
- (16) Dorman, S. E.; Nahid, P.; Kurbatova, E. v.; Phillips, P. P. J.; Bryant, K.; Dooley, K. E.; Engle, M.; Goldberg, S. v.; Phan, H. T. T.; Hakim, J.; Johnson, J. L.; Lourens, M.; Martinson, N. A.; Muzanyi, G.; Narunsky, K.; Nerette, S.; Nguyen, N. v.; Pham, T. H.; Pierre, S.; Purfield, A. E.; Samaneka, W.; Savic, R. M.; Sanne, I.; Scott, N. A.; Shenje, J.; Sizemore, E.; Vernon, A.; Waja, Z.; Weiner, M.; Swindells, S.; Chaisson, R. E. Four-Month Rifapentine Regimens with or without Moxifloxacin for Tuberculosis. *New Eng. J. Med.* **2021**, *384* (18), 1705–1718.
- (17) Silva, D. R.; Mello, F. C. de Q.; Migliori, G. B. Shortened Tuberculosis Treatment Regimens: What Is New? *J. Bras. Pneumol.* **2020**, *46* (2), 1–8.
- (18) Gillespie, S. H.; Crook, A. M.; McHugh, T. D.; Mendel, C. M.; Meredith, S. K.; Murray, S. R.; Pappas, F.; Phillips, P. P. J.; Nunn, A. J. Four-Month Moxifloxacin-Based

- Regimens for Drug-Sensitive Tuberculosis. *New Engl. J. Med.* **2014**, 371 (17), 1577–1587.
- (19) Prideaux, B.; Via, L. E.; Zimmerman, M. D.; Eum, S.; Sarathy, J.; O'Brien, P.; Chen, C.; Kaya, F.; Weiner, D. M.; Chen, P.-Y.; Song, T.; Lee, M.; Shim, T. S.; Cho, J. S.; Kim, W.; Cho, S. N.; Olivier, K. N.; Barry III, C. E.; Dartois, V. The Association between Sterilizing Activity and Drug Distribution into Tuberculosis Lesions. *Nat. Med.* **2015**, 21, 1223.
- (20) Sarathy, J. P.; Via, L. E.; Weiner, D.; Blanc, L.; Boshoff, H.; Eugenin, E. A.; Barry, C. E.; Dartois, V. A. Extreme Drug Tolerance of Mycobacterium Tuberculosis in Caseum. *Antimicrob. Agents Chemother.* **2018**, 62 (2), e02266-17.
- (21) Blanc, L.; Daudelin, I. B.; Podell, B. K.; Chen, P. Y.; Zimmerman, M.; Martinot, A. J.; Savic, R. M.; Prideaux, B.; Dartois, V. High-Resolution Mapping of Fluoroquinolones in TB Rabbit Lesions Reveals Specific Distribution in Immune Cell Types. *Elife.* **2018**, 7, 1–21.
- (22) Prideaux, B.; Dartois, V.; Staab, D.; Weiner, D. M.; Goh, A.; Via, L. E.; Barry, C. E. 3rd; Stoeckli, M. High-Sensitivity MALDI-MRM-MS Imaging of Moxifloxacin Distribution in Tuberculosis-Infected Rabbit Lungs and Granulomatous Lesions. *Anal. Chem.* **2011**, 83 (6), 2112–2118.
- (23) Dartois, V. The Path of Anti-Tuberculosis Drugs: From Blood to Lesions to Mycobacterial Cells. *Nat. Rev. Microbiol.* **2014**, 12 (3), 159–167.
- (24) Chauhan, S.; Sharma, D.; Singh, A.; Surolia, A.; Tyagi, J. S. Comprehensive Insights into Mycobacterium Tuberculosis DevR (DosR) Regulon Activation Switch. *Nucleic Acids Res.* **2011**, 39 (17), 7400–7414.
- (25) Dong, W.; Shi, J.; Chu, P.; Liu, R.; Wen, S.; Zhang, T.; Pang, Y.; Lu, J. Rv3131, a Gene Encoding Nitroreductase, is Essential for Metronidazole Activation in Mycobacterium Tuberculosis under Hypoxic Condition. *Res. Sq.* **2020**.
- (26) Sherman, D. R.; Voskuil, M.; Schnappinger, D.; Liao, R.; Harrell, M. I.; Schoolnik, G. K. Regulation of the Mycobacterium Tuberculosis Hypoxic Response Gene Encoding-Crystallin. *Proc. Natl. Acad. Sci. U. S. A.* **2001**, 98 (13), 7534-9.

- (27) Sun, Z.; Zhang, H.; Zhang, H.; Wu, J.; Gao, F.; Zhang, C.; Hu, X.; Liu, Q.; Wei, Y.; Wei, Y.; Zhuang, J.; Zhuang, J.; Huang, X. A novel model system for understanding anticancer activity of hypoxia-activated prodrugs. *Mol. Pharm.* **2020**, *17* (6), 2072–2082.
- (28) Global burden of bacterial antimicrobial resistance in 2019: A systematic analysis. *Lancet* **2022**, *399* (10325), 629–655.
- (29) Wong, R. H. F.; Kwong, T.; Yau, K.-H.; Au-Yeung, H. Y. Real time detection of live microbes using a highly sensitive bioluminescent nitroreductase probe. *Chem. Commun.* **2015**, *51* (21), 4440–4442.
- (30) Feng, P.; Zhang, H.; Deng, Q.; Liu, W.; Yang, L.; Li, G.; Chen, G.; Du, L.; Ke, B.; Li, M. Real-time bioluminescence imaging of nitroreductase in mouse model. *Anal. Chem.* **2016**, *88* (11), 5610–5614.
- (31) Xu, S.; Wang, Q.; Zhang, Q.; Zhang, L.; Zuo, L.; Jiang, J. D.; Hu, H. Y. Real Time detection of ESKAPE pathogens by a nitroreductase-triggered fluorescence turn-on probe. *Chem. Commun.* **2017**, *53* (81), 11177–11180.
- (32) Lee, M. K.; Williams, J.; Twieg, R. J.; Rao, J.; Moerner, W. E. Enzymatic activation of nitro-aryl fluorogens in live bacterial cells for enzymatic turnover-activated localization microscopy. *Chem. Sci.* **2013**, *4* (1), 220–225.
- (33) Liu, T.; Wang, Y.; Feng, L.; Tian, X.; Cui, J.; Yu, Z.; Wang, C.; Zhang, B.; James, T. D.; Ma, X. 2D strategy for the construction of an enzyme-activated NIR fluorophore suitable for the visual sensing and profiling of homologous nitroreductases from various bacterial species. *ACS Sens.* **2021**, *6* (9), 3348–3356.
- (34) Li, X.; Geng, P.; Hong, X.; Sun, Z.; Liu, G. Detecting mycobacterium tuberculosis using a nitrofuranyl calanolide-trehalose probe based on nitroreductase Rv2466c. *Chem. Commun.* **2021**, *57* (97), 13174–13177.

List of Figures

| | | |
|--------------|--|----|
| Figure 1.1. | Heterogeneity in the intrinsic drug susceptibility in the bacterial subpopulations of <i>Mtb</i> . A rapid rate of decline was seen with the replicating bacilli (blue line), but the number of non-replicating bacilli declined at a slower rate (red line). Adapted from Horsburgh, C. R et al. <i>New Eng. J. Med.</i> 2015 . ⁷ | 2 |
| Figure 1.2. | Hypoxia induced progressive transition of replicating into non-replicating persistent states in wayne model | 3 |
| Figure 1.3. | Schematic representation of distinct morphological differences observed in replicating and non-replicating <i>Mtb</i> | 4 |
| Figure 1.4. | Proposed mechanisms of activation by Type I and II NTRs | 5 |
| Figure 1.5. | (A) Structures of bicyclic nitroimidazole anti-tubercular prodrugs and their (B) proposed mechanism of activation by deazaflavin dependent nitroreductase (Ddn) | 7 |
| Figure 1.6. | Proposed mechanism of activation of (A) nitrothienopyrimidine analogue (TP-053) and (B) nitrofuranylcalanolides (NFCs) by mycothiol dependent NTR | 8 |
| Figure 1.7. | Origin of Quinolone's pharmacophore | 9 |
| Figure 1.8. | Discovery and development of FQs | 10 |
| Figure 1.9. | Structures of widely prescribed clinically imperative FQs | 11 |
| Figure 1.10. | UV light triggered uncaging of CIP | 14 |
| Figure 1.11. | UV light triggered release of FQ from photolyzable ester | 15 |
| Figure 1.12 | Visible light mediated release of LVX | 15 |
| Figure 1.13. | Glutathione (GSH) mediated release of LVX from prodrug | 16 |
| Figure 1.14. | Glutathione (GSH) mediated reductive cleavage of siderophore-FQ conjugate | 17 |
| Figure 1.15. | FQ prodrugs activated by enzymes such as (A) human paraoxonase (hPON1), (B) alkaline phosphatase (ALP) and (C) β -glucuronidase | 18 |
| Figure 1.16. | Proposed mechanism of release of CIP from dual-action FQ prodrug | 19 |

| | | |
|--------------|---|----|
| Figure 1.17. | (A) β -lactamase activated ester, carbamate and amine based FQ prodrugs. (B) Proposed mechanism of activation of cephalosporin-CIP prodrug by β -lactamase | 20 |
| Figure 1.18. | Nitroreductase catalyzed activation of prodrug to generate CIP and fluorescence reporter | 21 |
| Figure 1.19. | Lipophilic ester prodrugs of FQs | 21 |
| Figure 1.20. | Structure of moxifloxacin (MXF) | 22 |
| Figure 1.21. | MXF containing TB-drug regimens | 24 |
| Figure 1.22. | Proposed prodrug strategy to enhance accumulation and efficacy of MXF in non-replicating <i>Mtb</i> | 25 |
| Figure 2.1. | Proposed strategy for the generation of MXF from ester and carbamate prodrugs | 45 |
| Figure 2.2. | Design and mechanism of bioreductive activation of nitroheteroaryl prodrugs. Reduction of prodrug by NTR results in the formation of hydroxylamine or amine intermediate, which upon subsequent self-immolation releases MXF. | 46 |
| Figure 2.3. | Monitoring the formation of 33 following <i>N</i> -Boc deprotection of 27 with TFA by TLC using a 1:9 MeOH:CHCl ₃ solvent system. The TLC was visualized under a UV chamber (<i>left panel</i> : 250 nm and <i>right panel</i> :365 nm) after 6 h with (a) authentic 27 , (b) 27 + TFA (100 eq.), and (c) authentic MXF. | 53 |
| Figure 2.4. | Structures of 33-38 | 54 |
| Figure 2.5. | Plot of (A) MR vs molecular weight , (B) TPSA vs molecular weight and (C) clogP vs molecular weight of MXF and its prodrugs (esters and carbamates) | 57 |
| Figure 2.6. | Cyclic voltammograms of (A) controls (blank electrolyte and ferrocene), (B) 33 , (C) 34 , (D) 35 , (E) 36 , (F) 37 , (G) 38 , (H) 45 and (I) 46 recorded in argon saturated 0.1 M TBAP solution in ACN with an initial positive scan (shown by a purple arrow) at a sweep rate of 100 mV/s, sample interval of 1 mV, quiet time of 2 s, and a sensitivity of 1×10^{-5} A/V. The final concentration of analytes was 0.5 mM. The onset reduction potentials are indicated by arrows in the voltammograms. | 59 |

| | | |
|--------------|--|----|
| Figure 2.7. | Comparison of the experimentally measured onset potentials with the computationally derived reduction potentials. | 61 |
| Figure 2.8. | (A) Absorbance spectra and (B) Fluorescence emission spectra of MXF (10 μ M, $\lambda_{\text{ex}} = 289$ nm) in phosphate buffer (pH 7.4, 10 mM) at 37 $^{\circ}$ C. MXF exhibits a strong emission peak at 488 nm. (C) Fluorescence response of MXF prodrugs (10 μ M, $\lambda_{\text{ex}} = 289$ nm; $\lambda_{\text{em}} = 488$ nm) in phosphate buffer (pH 7.4, 10 mM) at 37 $^{\circ}$ C. | 61 |
| Figure 2.9. | Screening and evaluation for release of MXF following sodium dithionite ($\text{Na}_2\text{S}_2\text{O}_4$) induced chemoreduction of compounds (10 μ M) in $\text{H}_2\text{O}:\text{MeOH}$ (1:1) in a fluorescence-assay ($\lambda_{\text{ex}} = 289$ nm; $\lambda_{\text{em}} = 488$ nm). | 62 |
| Figure 2.10. | Kinetics of dithionite-dependent reduction of NTR-MXF prodrugs (10 μ M) in $\text{H}_2\text{O}:\text{MeOH}$ (1:1) by measuring fluorescence attributable to MXF ($\lambda_{\text{ex}} = 289$ nm; $\lambda_{\text{em}} = 488$ nm) at a time interval of 1 s. | 63 |
| Figure 2.11. | Monitoring time-dependent release kinetics of MXF following (A) chemical reduction with 250 eq. (2.5 mM) of sodium dithionite ($\text{Na}_2\text{S}_2\text{O}_4$) from 37 and 38 and (B) with 38 and various equivalents (0, 250, 500 and 750 eq.; 0, 2.5, 5 and 7.5 mM) of sodium dithionite. | 63 |
| Figure 2.12. | (A) Evaluating the release of MXF from 33 and 41 following $\text{Zn}/\text{HCOONH}_4$ mediated chemoreduction of compounds (10 μ M) in $\text{H}_2\text{O}:\text{MeOH}$ (1:1) by monitoring fluorescence ($\lambda_{\text{ex}} = 289$ nm; $\lambda_{\text{em}} = 488$ nm). (B) Investigating the time-dependent release of MXF from 33 following chemical reduction with Zinc/ammonium formate ($\text{Zn}/\text{HCOONH}_4$). | 64 |
| Figure 2.13. | HPLC traces of chemoreduction of compounds 33 and 41 (10 μ M) in the absence and presence of Zn dust and ammonium formate in $\text{H}_2\text{O}:\text{MeOH}$ (1:1). MXF (10 μ M) was used as a positive control. The signal was detected using the UV detector set at 280 nm. | 65 |

| | | |
|--------------|--|-----|
| Figure 2.14. | Screening and evaluation for release of MXF following Zinc/ammonium formate (Zn/HCOONH ₄) based mediated chemoreduction of compounds (10 μM) in H ₂ O:MeOH (1:1) in a fluorescence-assay. | 66 |
| Figure 2.15. | Monitoring time-dependent release of MXF from 37 and 38 following chemical reduction with Zinc/ammonium formate (Zn/HCOONH ₄) by a fluorescence-based assay | 66 |
| Figure 2.16. | HPLC trace of 33 | 87 |
| Figure 2.17. | HPLC trace of 34 | 88 |
| Figure 2.18. | HPLC trace of 35 | 88 |
| Figure 2.19. | HPLC trace of 36 | 89 |
| Figure 2.20. | HPLC trace of 37 | 89 |
| Figure 2.21. | HPLC trace of 38 | 90 |
| Figure 2.22. | HPLC trace of 45 | 90 |
| Figure 2.23. | HPLC trace of 46 | 91 |
| Figure 3.1. | Monitoring the <i>E. coli</i> NTR mediated bioreductive activation of prodrugs by fluorescence ($\lambda_{\text{ex}} = 289 \text{ nm}$ and $\lambda_{\text{em}} = 488 \text{ nm}$) after 1 h of incubation with <i>E. coli</i> NTR (15 nM) and NADH (100 μM) in pH 7.4 phosphate buffer (10 mM) at 37 °C. | 149 |
| Figure 3.2. | Representative reaction progress curves obtained by monitoring the release of MXF ($\lambda_{\text{ex}} = 289 \text{ nm}$ and $\lambda_{\text{em}} = 488 \text{ nm}$) as a function of time from (A) 33 , (B) 34 , (C) 35 , (D) 36 , (E) 37 , (F) 38 , (G) 45 and (H) 46 using a fluorescence-based assay. The reactions were performed with a broad range of substrate concentrations (reported on the right of each curve) in the presence of NADH (100 μM) and a fixed concentration of <i>E. coli</i> NTR (15 nM) in phosphate buffer (pH 7.4, 10 mM). The kinetic experiments were performed at either 37 °C (for 33-37 and 45) or 25 °C (for 38 and 46). | 151 |
| Figure 3.3. | Michaelis-Menten analyses demonstrating the nitroreduction of prodrugs by <i>E. coli</i> NTR. | 152 |
| Figure 3.4. | Michaelis-Menten analyses showing the nitroreduction of (A) nitrobenzyl <i>versus</i> nitroimidazolyl and (B) 2- | 153 |

- nitroimidazolyl *versus* 2-nitrothiazolyl prodrugs by *E. coli* NTR.
- Comparative NTR-dependent fluorescence response of **37** and **38**. (A) Structures of **37** and **38**. (B) Emission spectra of MXF recorded post-incubation of **37** (10 μ M) for 30 min with various concentrations of NTR (0, 3.75, 7.5, 15, 30 and 60 nM) in the presence of NADH (100 μ M) in phosphate buffer (10 mM, pH 7.4) at 37 $^{\circ}$ C. (C) Representative reaction progress curves were obtained by monitoring the release of MXF as a function of time from **37** using a fluorescence-based assay. (D) Time-dependent fluorimetric analysis of reaction mixtures containing **38** with or without NTR at different concentrations (0, 1.875, 3.75, 7.5 and 15 nM) in the presence of NADH (100 μ M) in phosphate buffer (pH 7.4, 10 mM) at 25 $^{\circ}$ C for 150 s. (E) Time-dependent fluorimetric analysis of reaction mixtures containing **38** with a fixed concentration of NTR (15 nM) at 25 $^{\circ}$ C and 37 $^{\circ}$ C in the presence of NADH (100 μ M). The generation of MXF in the reaction mixtures were monitored at $\lambda_{\text{ex}} = 289$ nm and $\lambda_{\text{em}} = 488$ nm.
- Fluorescence spectra before and after incubation of prodrugs (A) **37** (10 μ M), (B) **38** (10 μ M) and (C) **46** (10 μ M) with *E. coli* NTR (15 nM) in the presence of NADH (100 μ M) in PB (pH 7.4, 10 mM) at 37 $^{\circ}$ C.
- Stability of 2-nitrothiazole prodrugs in buffer. HPLC traces of stability of (A) **38** and (B) **46** in pH 7.4 buffer (10 mM) at 37 $^{\circ}$ C. Area under the curve corresponding to (C) **38** at 3.6 min and (D) **46** at 10.8 min remaining in buffer after 2 h of incubation (absorbance 280 nm).
- E. coli* NTR mediated nitro-reduction of **38** resulted in the release of MXF. (A) LC/MS analysis showing the disappearance of **38** (*left panel*) and formation of MXF (*right panel*). Representative extracted ion chromatograms (EIC) are shown. (B-C) Area under the curve (AUC) for the peaks corresponding to (B)

- disappearance of **38** and (C) formation of MXF. Ctrl represents enzyme alone. (D) Positive-ion-mode mass spectrum of the protonated singly charged $[M+1]^+$ molecular ion of the reaction products **38a** (top), **38b** (middle), and **47** (bottom) formed in the enzymatic reaction of **38** with *E. coli* NTR.
- E. coli* NTR mediated nitro-reduction of **46** resulted in the release of MXF. (A) LC/MS analysis showing the disappearance of **46** (*left panel*) and formation of MXF (*right panel*). Representative extracted ion chromatograms (EIC) are shown. (B-C) Area under the curve (AUC) for the peaks corresponding to (B) disappearance of **46** and (C) formation of MXF. Ctrl represents enzyme alone. (D) Positive-ion-mode mass spectrum of the protonated singly charged $[M+1]^+$ molecular ion of the reaction products **46a** (top), **46b** (middle), and **47** (bottom) formed in the enzymatic reaction of **46** with *E. coli* NTR.
- Structure of *E. coli* NTR (NfsB, PDB 1DS7). The FMN ligands bound at the dimeric interface of both the chains are shown.
- (A) Alignment of the bound and docked conformer of FMN using Ligand alignment tool of PyMOL. The RMSD value between the conformations was found to be 0.001 Å. (B) Molecular surface view of bound and docked pose of FMN at the dimeric interface of *E. coli* NTR (PDB: 1DS7). (C) Cartoon representation of the docked FMN at the active site of oxidized NTR of *E. coli* (PDB: 1DS7). The docked ligands and bound FMN are shown in a stick model, and the active site residues are indicated by a 1-letter code. The hydrogen, hydrophobic interactions, and salt bridges are drawn as blue, dark gray, and red dotted lines respectively and the lengths are indicated. (D) 2D LigPlot representation of the docking interaction of *E. coli* NTR (PDB: 1DS7) with FMN. Receptor residues involved in hydrophobic interactions are represented by brick red spoked arcs, hydrogen bonding shown by blue dotted lines. Receptor

- residues involved in H-bonding are colored green. Ligand residues involved in H-bonding are shown in red color.
- 2D LigPlot representation of docking interaction of *E. coli* NTR (PDB: 1DS7) with prodrugs (**33-38**, **45** and **46**). Receptor residues involved in hydrophobic interactions are represented by brick red spoked arcs, hydrogen bonding shown by blue dotted lines. Receptor residues involved in hydrogen bonding are colored green. Ligand residues involved in H-bonding are shown in red color.
- Figure 3.12. 164
- Cartoon representation of (A) **33**, (B) **34**, (C) **35**, (D) **36**, (E) **37**, (F) **38**, (G) **45** and (H) **46** docked at the active site of chain A of *E. coli* NTR (PDB: 1DS7). The docked ligands and bound FMN are shown in a stick model and the active site residues are indicated by a 1- letter code. The hydrogen, hydrophobic interactions, π interactions and salt bridges are drawn as blue, dark gray, orange, and red dotted lines, respectively, and the lengths are indicated.
- Figure 3.13. 165
- Simulation model showing the overlaid docked conformers of **33**, **37** and **38** from FMN in the active site of *E. coli* NTR. Data was provided by Dr. SharathChandra M. (Prof. Jennifer Hirschi Lab, University of Binghamton, USA).
- Figure 3.14. 166
- Fluorescence response of **38** (10 μ M) to various biological analytes (100 μ M) in phosphate buffer (pH 7.4, 10 mM) for 15 min at 37 °C. Ctrl = **38** alone; Cys = cysteine; GSH = glutathione; Glu = glucose; Gal = galactose; Vit-C = ascorbic acid; H₂O₂ = hydrogen peroxide; Es = esterase 1 U/mL; NADH = reduced nicotinamide adenine dinucleotide (100 μ M); NTR = *E. coli* nitroreductase (15 nM).
- Figure 3.15. 169
- (A) Bioreductive activation of prodrugs (10 μ M) in *E. coli* ATCC 25922 lysate (1 mg/mL). (B) Monitoring the release of MXF from **38** (10 μ M) by measuring fluorescence (λ_{ex} = 289 nm and λ_{em} = 488 nm) in lysates (1 mg/mL) of *E. coli* alone or in the presence of various concentrations of NTR
- Figure 3.16. 170

- inhibitor, dicoumarol (DCOM; 100, 250 or 500 μ M) and heat-inactivated lysates.
- Sequence alignment of NfsB from *E. coli* and NfnB from *M. smegmatis*. Alignments were performed using T-coffee and visualized with Jalview. The consensus symbols: “*” and “.” under the amino acids indicate identical and semi-conserved residues that are highlighted in red and blue color, respectively. The FMN binding region shown in bold shared 35% sequence identity.
- Figure 3.17. 171
- Predicted binding mode of **38** to FMN cofactor bound *M. smegmatis* NfnB (A) Ribbon model showing the docked pose of **38** to FMN bound chain A of NfnB (PDB: 2WZW). (B and C) Close-up view of the catalytic site of *M. smegmatis* NfnB showing top-ranked docked poses of (B) bound FMN and (C) **38** in the presence of bound FMN (cyan) resulting from docking simulations. The residues presenting interactions with FMN and **38** are labelled by a one-letter code and shown as a stick model. The red and black dashed lines represent polar and hydrophobic contacts, respectively, and the lengths are indicated.
- Figure 3.18. 172
- Simulation model showing the binding interaction of **38** with *E. coli* NTR. The average distance between the nitro group of **38** and FMN is displayed. Data was provided by Dr. SharathChandra M. (Prof. Jennifer Hirschi Lab, University of Binghamton, USA).
- Figure 3.19. 172
- In vitro* determination of the generation of MXF by measuring the increase in fluorescence ($\lambda_{ex} = 289$ nm and $\lambda_{em} = 488$ nm) after incubation of prodrugs (10 μ M) in lysates of (A) wild-type (WT) and (B) MshA deficient (Δ mshA) *M. smegmatis* (1 mg/mL).
- Figure 3.20. 173
- Monitoring the release of MXF from **38** (10 μ M) by measuring enhancement in fluorescence in lysates (1 mg/mL) of wild-type (WT) and MshA deficient (Δ mshA) *M. smegmatis* alone or in the presence of various
- Figure 3.21. 174

| | | |
|--------------|--|-----|
| | concentrations of NTR inhibitor, dicoumarol (DCOM; 100 and 250 μ M) and heat-inactivated lysates. | |
| Figure 3.22. | Monitoring the release of MXF from 38 (25 μ M) by measuring enhancement of fluorescence (λ_{ex} = 289 nm and λ_{em} = 488 nm) in lysates of replicating (normoxic) and non-replicating (hypoxic) cultures of <i>Mtb</i> . Data was provided by Dr. Piyali Mukherjee (Prof. Amit Singh Lab, IISc Bangalore). | 175 |
| Figure 3.23. | Evaluation of the stability of 38 in lysates (1 mg/mL) of mammalian cell line (A) A549 (lung-cancer cell line) after 2 h and (B) MEF (mouse embryonic fibroblast) after 4 h by measuring fluorescence (λ_{ex} = 289 nm and λ_{em} = 488 nm) corresponding to MXF. | 175 |
| Figure 3.24. | Calibration curve for MXF in pH 7.4 phosphate buffer (10 mM) at 37 °C. | 178 |
| Figure 4.1. | <i>In vivo</i> efficacy of 38 (10 mg/kg) against <i>E.coli</i> ATCC 25922 in a neutropenic murine thigh infection model. MXF (10 mg/kg) was used as a reference compound while Ctrl is untreated mice. Statistical significance was established with respect to Ctrl (** <i>p</i> < 0.001). Data was provided by Dr. Sidharth Chopra Lab, CSIR-CDRI, Lucknow. | 195 |
| Figure 4.2. | Minimum inhibitory concentrations (MIC) of 38 and MXF against <i>Mycobacterium smegmatis</i> (mc ² 155; <i>Msm</i>) determined by Resazurin reduction microplate assay (REMA) | 197 |
| Figure 4.3. | Minimum inhibitory concentrations (MIC) of prodrugs (A) 33 and 34 , (B) 35 and 37 , and (C) 36 and 46 against <i>Mycobacterium smegmatis</i> (mc ² 155; <i>Msm</i>) determined by Resazurin reduction microplate assay (REMA) | 197 |
| Figure 4.4. | Bacterial survival kinetics after treatment of THP-1 macrophages infected with <i>Mtb</i> H37Rv at 5x MIC of 38 and MXF. Data was provided by Prof. Amit Singh, IISc Bangalore. | 201 |
| Figure 4.5. | Bactericidal activity of 38 against non-replicating <i>Mtb</i> . (A) Mycobactericidal effect of MXF and 38 at indicated concentrations (10x MIC) on hypoxia-adapted <i>Mtb</i> bacilli based on visual hypoxia resazurin reduction assay (HyRRA). Isoniazid | 201 |

(INH, 10 μ M) and Metronidazole (MZ, 10 mM) served as a negative and positive control respectively. The pink colour in the tube indicates cell viability under hypoxia while blue colour indicates no growth. (B) Survival of *Mtb* under hypoxia was measured as log₁₀ of colony-forming units (CFU) after treatment with 10x MIC of MFX and **38** for 5 days. Data represent at least three independent experiments performed in triplicate. Error bars represent standard deviation from the mean. Statistical significance was established relative to untreated bacteria control (Ctrl) using unpaired *t*-test with welch's correction student's (** $p \leq 0.01$, *** $p \leq 0.001$ and ns indicate not significant).

| | | |
|--------------|---|-----|
| Figure 4.6. | Emission spectra of MXF (excited at 289 nm) in (A) periplasmic, (B) cytosolic fractions and (C) whole-cell fractions lysates of <i>E.coli</i> ATCC 25922 | 204 |
| Figure 4.7. | Calibration curve for MXF ($\lambda_{ex} = 289$ nm and $\lambda_{em} = 488$ nm) in periplasmic, cytoplasmic fractions and whole cell lysate in pH 3.0 glycine-HCl buffer (0.1 M) | 205 |
| Figure 4.8. | Schematic workflow for LC-MS/MS based accumulation assay in <i>E.coli</i> | 206 |
| Figure 4.9. | Optimization of the concentration of MXF at (A) 50 μ M and (B) 5 μ M with <i>E. coli</i> ATCC 25922 to ensure bacterial cell viability during incubation | 207 |
| Figure 4.10. | Structures of parent and fragment ions of (A) CIP and (B) MXF | 208 |
| Figure 4.11. | (A) Structures of analytes (CIP, MXF and 38) used in the accumulation assay. Optimization of LC-MS/MS conditions for the detection of CIP, MXF and 38 in pH 7.4 PBS (1x). The (B, E, and H) MS1 and (C, F, and I) MS2 signals for CIP, MXF and 38 are shown, respectively. The calibration curve was constructed by monitoring the transition of (D) CIP (m/z 332.14 \rightarrow 314.13), (G) MXF (m/z 402.18 \rightarrow 384.17) and (J) 38 (m/z 544.17 \rightarrow m/z 384.17). | 209 |
| Figure 4.12. | Whole cell intracellular accumulation of drug in <i>E. coli</i> | 210 |

| | | |
|---------------|---|-----|
| Figure 4.13. | Schematic workflow for LC-MS based accumulation assay in replicating and non-replicating <i>Mtb</i> | 211 |
| Figure 4.14. | Suppressive effect of <i>Mtb</i> lysate on MXF signal | 212 |
| Figure 4.15. | (A) Representative extracted ion chromatograms (EIC) and (B) standard calibration curve obtained with different concentrations of MXF (m/z 402.18) | 212 |
| Figure 4.16. | (A) Representative extracted ion chromatograms (EIC) and (B) standard calibration curve obtained with different concentrations of 38 (m/z 544.17) | 213 |
| Figure 4.17. | LC-MS analysis of intracellular concentration of MXF (m/z 402.18) in replicating and non-replicating cultures of <i>Mtb</i> following incubation with MXF (5 μ M) for 30 min. | 214 |
| Figure 4.18. | LC-MS analysis of intracellular concentration of MXF (m/z 402.18) in (A) replicating and (B) non-replicating cultures of <i>Mtb</i> following incubation for 30 min with a fixed concentration (5 μ M) of MXF and 38 . Statistical significance was established relative to MXF treated sample using an unpaired <i>t</i> -test (***) $p \leq 0.001$ and ns indicate not significant). | 214 |
| Figure 5.1.1. | Scope and utility of 2-nitrothiazolyl moiety as NTR-sensitive bioreductive trigger | 222 |
| Figure 5.1.2. | Proposed strategy for the release of CIP from ester prodrug | 223 |
| Figure 5.1.3. | Monitoring the <i>E. coli</i> NTR mediated bioreductive activation of prodrugs by fluorescence ($\lambda_{ex} = 281$ nm and $\lambda_{em} = 445$ nm) after 1 h of incubation with <i>E. coli</i> NTR (15 nM) and NADH (100 μ M) in pH 7.4 phosphate buffer (10 mM) at 37 $^{\circ}$ C. | 224 |
| Figure 5.1.4. | Bioreductive activation of prodrugs (10 μ M) after incubation in lysates (1 mg/mL) of (A) <i>E. coli</i> ATCC 25922 for 2 h and (B) <i>M. smegmatis</i> mc ² 155 in 1 h. | 225 |
| Figure 5.1.5. | Monitoring the release of CIP from prodrugs (10 μ M) after incubation in lysates (1 mg/mL) of (A) <i>E. coli</i> ATCC 25922 for 2 h and (B) <i>M. smegmatis</i> mc ² 155 in 1 h alone or in the presence of NTR inhibitor, dicoumarol (DCOM; 250 μ M). | 225 |

| | | |
|---------------|--|-----|
| Figure 5.2.1. | Proposed mechanism of NTR mediated activation of dual colorimetric fluorescence turn OFF-ON probe | 242 |
| Figure 5.2.2. | (A) Colorimetric response and (B) Emission spectra ($\lambda_{\text{ex}} = 530$ nm) of probes (50 μM) recorded in pH 7.4 phosphate buffer (10 mM) | 245 |
| Figure 5.2.3. | Monitoring the fluorescence response ($\lambda_{\text{ex}} = 530$ nm and $\lambda_{\text{em}} = 605$ nm) of probes after 30 min of incubation with <i>E. coli</i> NTR (15 nM) and NADH (100 μM) in pH 7.4 phosphate buffer (10 mM) at 37 °C. <i>p</i> values were determined using the student's two-tailed unpaired parametric <i>t</i> -test relative to the NTR untreated control. (***) $p \leq 0.001$. | 245 |
| Figure 5.2.4. | Monitoring the visual colorimetric response "turn OFF-ON" response of probe 61 (10 μM) by (A) recording a photographic image and (B) absorption spectra after 5 min of incubation with <i>E. coli</i> NTR (15 nM) and NADH (100 μM) in pH 7.4 phosphate buffer (10 mM) at 37 °C. A distinct colorimetric change (yellow to pink) corresponding to the formation of TCF-OH was observed after incubation of the probe with NTR. (C) Fluorescence spectra ($\lambda_{\text{ex}} = 579$ nm and $\lambda_{\text{em}} = 603$ nm) upon incubation of 61 (10 μM) with NTR (15 nM) and NADH (100 μM) in pH 7.4 phosphate buffer (10 mM). | 246 |
| Figure 5.2.5. | HPLC traces of (A) stability of the probe 61 and (B) enzyme dependent reductive activation of probe 61 (12.5 μM) in the presence of <i>E. coli</i> NTR (15 nM) and NADH (100 μM) in pH 7.4 phosphate buffer. TCF-OH (12.5 μM) was used as a positive control. The signal was detected using the UV detector set at 440 nm. (C) Decomposition of 61 and formation of TCF-OH upon incubation with NTR (15 nM) and NADH (100 μM) in pH 7.4 phosphate buffer at 37 °C as monitored by HPLC. | 247 |
| Figure 5.2.6. | (A) Comparative visual colorimetric response of 61 at different concentrations (10, 25, 50 and 100 μM) before (<i>top panel</i>) and after (<i>middle panel</i>) incubation (5 min) with <i>E. coli</i> NTR relative to TCF-OH (<i>bottom panel</i>). (B-C) Changes in (B) absorbance | 248 |

- signal and (C) fluorescence intensity with different concentrations (0.07 μM to 25 μM) of probe **61** in the presence of NADH (100 μM) and NTR (15 nM) after 5 min of incubation in pH 7.4 phosphate buffer at 37 $^{\circ}\text{C}$.
- (A) Photometric images of visual colour change of probe **61** upon addition of different concentration of NTR (0-15 nM) in the presence of NADH (100 μM) in pH 7.4 phosphate buffer at 37 $^{\circ}\text{C}$. (B-C) Changes in (B) absorbance signal and (C) fluorescence intensity of probe **61** with increasing concentrations of NTR (0-15 nM) in the presence of NADH (100 μM) in pH 7.4 phosphate buffer. (D-E) Linear correlation between enhancement in (D) absorbance and (E) fluorescence intensity of **61** with concentrations of NTR.
- Fluorescence response (and *inset*: absorbance intensity) of **61** (10 μM) in the presence of various biological analytes (100 μM) after 5 min incubation at 37 $^{\circ}\text{C}$. Gal = galactose; Glu = glucose; Ara = arabinose; Vit-C = ascorbic acid; Cys = cysteine; GSH = glutathione; NAC = *N*-acetyl cysteine; H_2O_2 = hydrogen peroxide; Es = esterase 1 U/mL; BSA = bovine serum albumin 1mg/mL; NADH = reduced nicotinamide adenine dinucleotide (100 μM); NTR = *E. coli* nitroreductase (15 nM); NTR (15 nM) + NADH (100 μM) reaction.
- (A) Photometric images of visual colour change of probe **61** upon addition of NTR (15 nM) and NADH (100 μM) in different pH (7.0-10.0) at 37 $^{\circ}\text{C}$. Changes in (B) absorbance signal and (C) fluorescence intensity of probe **61** with NTR (15 nM) and NADH (100 μM) in different pH 7.0-10.0 at 37 $^{\circ}\text{C}$.
- (A) Photometric images of visual colour change of probe **61** upon addition of NTR (15 nM) and NADH (100 μM) in various bacterial media at 37 $^{\circ}\text{C}$. Changes in (B) absorbance signal and (C) fluorescence intensity of probe **61** with NTR (15 nM) and NADH (100 μM) in different bacterial media at 37 $^{\circ}\text{C}$. Media: LB = Luria Bertoni broth for *E. coli*; MHB = Mueller Hinton
- Figure 5.2.7. 249
- Figure 5.2.8. 250
- Figure 5.2.9. 250
- Figure 5.2.10. 251

| | | |
|----------------|---|-----|
| | Broth cation 2 adjusted for <i>S. aureus</i> ; 7H9 = Middlebrook 7H9 broth for <i>Mycobacterium</i> species. | |
| Figure 5.2.11. | Cell Viability assay for cytotoxicity of 61 and TCF-OH in MEF cells | 252 |
| Figure 5.2.12. | Confocal microscope images in <i>E. coli</i> bacterial cells preincubated with (a-d) 61 (5 μ M) or (e-h) TCF-OH (5 μ M) for 2 h. The cells were imaged on the red channel (Alexa fluor 568 for detection of TCF-OH (a and e)), DAPI channel (b and f), merged image of red and DAPI channel (c and g) and DIC image (d and h). | 253 |
| Figure 5.2.13. | HPLC trace of 61 | 257 |

List of Schemes

| | | |
|---------------|---|-----|
| Scheme 1.1. | UV-light mediated selective photoactivation | 14 |
| Scheme 2.1. | Synthesis of 1b | 46 |
| Scheme 2.2. | Synthesis of 1c | 47 |
| Scheme 2.3. | Synthesis of 4(5)-nitroimidazole | 47 |
| Scheme 2.4. | Regioselective <i>N</i> -methylation of 5 with CH ₃ I and (CH ₃) ₂ SO ₄ | 47 |
| Scheme 2.5. | Plausible mechanism for regioselective <i>N</i> -alkylation of 5 | 48 |
| Scheme 2.6. | Synthesis of 1d | 48 |
| Scheme 2.7. | Original and optimized synthetic routes for 2-aminoimidazole ester 9 | 49 |
| Scheme 2.8. | Attempted synthesis of 15 | 49 |
| Scheme 2.9. | Synthesis of 1e | 50 |
| Scheme 2.10. | Synthesis of 1f | 50 |
| Scheme 2.11. | Synthetic approaches to generate ester and carbamate prodrugs of MXF | 51 |
| Scheme 2.12. | Synthesis of 27 | 51 |
| Scheme 2.13. | Synthesis of 28-32 | 52 |
| Scheme 2.14. | Synthesis of 33-38 | 53 |
| Scheme 2.15. | Synthesis of negative control compounds | 55 |
| Scheme 2.16. | Synthesis of 4-nitrophenyl mixed carbonates | 56 |
| Scheme 2.17. | Synthesis of carbamate derivatives of MXF | 56 |
| Scheme 2.18. | Mechanism of Zn-dependent chemoreduction of 33 to release MXF | 65 |
| Scheme 3.1. | Proposed strategy for NTR-dependent bioactivation of prodrugs | 148 |
| Scheme 3.2. | Plausible mechanism for bioreductive activation of 38 | 159 |
| Scheme 3.3. | Plausible mechanism for bioreductive activation of 46 | 160 |
| Scheme 3.4. | Plausible mechanistic scenarios for the reduction of nitro group by NTR | 167 |
| Scheme 4.1. | Reduction of Resazurin | 195 |
| Scheme 5.1.1. | Synthesis of 50 and 51 | 223 |
| Scheme 5.1.2. | Proposed strategy for NTR-mediated bioactivation of prodrugs | 224 |
| Scheme 5.2.1. | Synthesis of 53 | 243 |

Appendix-III: List of Schemes

| | | |
|---------------|--|-----|
| Scheme 5.2.2. | Synthesis of 57 | 243 |
| Scheme 5.2.3. | Synthesis of 58 and 59 | 243 |
| Scheme 5.2.4. | Synthesis of 60 and 61 | 244 |
| Scheme 5.2.5. | Synthesis of TCF-OH | 244 |
| Scheme 5.2.6. | Proposed mechanism of NTR dependent colorimetric and fluorescent turn-on response of 61 | 247 |

List of Tables

| | | |
|--------------|--|-----|
| Table 2.1. | Synthesis of <i>N</i> -boc protected nitroheterocyclic esters of MXF | 52 |
| Table 2.2. | Synthesis of negative control compounds | 55 |
| Table 2.3. | Synthesis of nitro(hetero)cyclic carbamates of MXF | 56 |
| Table 2.4. | HPLC analysis | 57 |
| Table 2.5. | Physicochemical descriptors of NTR-MXF prodrugs | 58 |
| Table 2.6. | Experimentally and computationally derived reduction potentials of prodrugs | 60 |
| Table 3.1. | Estimation of linearity from the reaction progress curves of NTR-MXF prodrugs | 149 |
| Table 3.2. | Comparative analysis of kinetic parameters of NTR-MXF prodrugs | 150 |
| Table 3.3. | Comparative analysis of the docking results of NTR-MXF prodrugs against <i>E. coli</i> NTR (PDB: 1DS7) | 163 |
| Table 3.4. | Comparative analysis of electron transfer barriers with the rate and amount of MXF generated from prodrugs | 168 |
| Table 4.1. | Antibacterial activity of MXF prodrugs against <i>E. coli</i> , <i>S. aureus</i> and <i>M. smegmatis</i> | 196 |
| Table 4.2. | Antimycobacterial activity of prodrugs against <i>Mtb</i> | 198 |
| Table 4.3. | Antimycobacterial activity of <i>N</i> -boc protected MXF derivatives against <i>Mtb</i> | 199 |
| Table 4.4. | Selective indices of MXF prodrugs | 200 |
| Table 4.5. | MIC of MXF and 38 against drug resistant clinical isolates of <i>Mtb</i> | 200 |
| Table 4.6. | MIC of MXF and 38 against FQ-sensitive and resistant strains of <i>E. coli</i> | 202 |
| Table 4.7. | MRM transitions for the compounds used in the accumulation assay | 208 |
| Table 5.1.1. | Synthesis of nitro(hetero)aryl esters of CIP | 224 |
| Table 5.1.2. | Antibacterial activity of CIP prodrugs against <i>E. coli</i> , and <i>S. aureus</i> | 226 |

Targeted Antibacterial Activity Guided by Bacteria-Specific Nitroreductase Catalytic Activation to Produce Ciprofloxacin



Author: Kundansingh A. Pardeshi, T. Anand Kumar, Govindan Ravikumar, et al

Publication: Bioconjugate Chemistry

Publisher: American Chemical Society

Date: Mar 1, 2019

Copyright © 2019, American Chemical Society

PERMISSION/LICENSE IS GRANTED FOR YOUR ORDER AT NO CHARGE

This type of permission/license, instead of the standard Terms and Conditions, is sent to you because no fee is being charged for your order. Please note the following:

- Permission is granted for your request in both print and electronic formats, and translations.
- If figures and/or tables were requested, they may be adapted or used in part.
- Please print this page for your records and send a copy of it to your publisher/graduate school.
- Appropriate credit for the requested material should be given as follows: "Reprinted (adapted) with permission from {COMPLETE REFERENCE CITATION}. Copyright {YEAR} American Chemical Society." Insert appropriate information in place of the capitalized words.
- One-time permission is granted only for the use specified in your RightsLink request. No additional uses are granted (such as derivative works or other editions). For any uses, please submit a new request.

If credit is given to another source for the material you requested from RightsLink, permission must be obtained from that source.

BACK

CLOSE WINDOW

List of Patents

Kumar, T. A., Chakrapani, H., Singh, A. Fluoroquinolone derivatives for treatment of active and latent tuberculosis. Indian Patent 202221069131, November 30, **2022**.

List of Publications

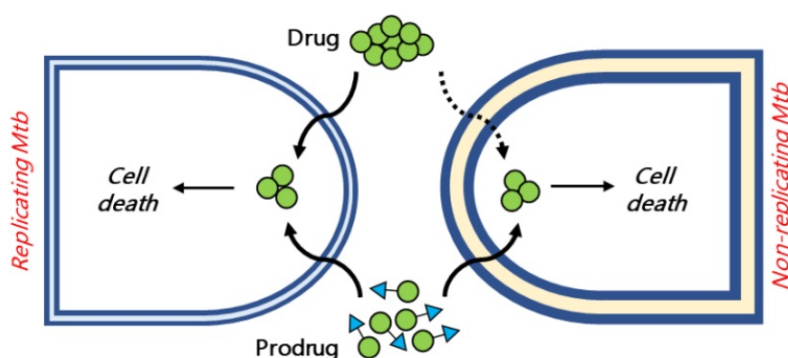
- (a) **Kumar, T. A.**; Mukherjee, P.; Sharath Chandra, M.; Birua, S.; Kaul, G.; Akhir, A.; Chopra, S.; Hirschi, J.; Singh, A.; Chakrapani, H. Intracellular Accumulation-Driven Potentiation of Moxifloxacin Against non-replicating drug-tolerant Mycobacterium tuberculosis through a Prodrug. *bioRxiv*. **2023**. (<https://doi.org/10.1101/2023.03.23.533925>)
- (b) Shee, S.; Singh, S.; Tripathi, A.; Thakur, C.; **Kumar, T. A.**; Das, M.; Yadav, V.; Kohli, S., Rajmani, R. S.; Chandra, N.; Chakrapani, H. Drlica, K. Singh, A. *Antimicrob. Agents Chemother.* **2022**, *66*, 1-7.
- (c) Pardeshi, K.A.; **Kumar, T. A.**; Ravikumar, G.; Shukla, M.; Kaul, G.; Chopra, S.; Chakrapani, H. Targeted Antibacterial Activity Guided by Bacteria-Specific Nitroreductase Catalytic Activation to Produce Ciprofloxacin. *Bioconjugate Chem.* **2019**, *30*, 751–759.

Intracellular Accumulation-Driven Potentiation of Moxifloxacin Against non-replicating drug-tolerant *Mycobacterium tuberculosis* through a Prodrug

T. Anand Kumar,^a Piyali Mukherjee,^b M. SharathChandra,^c Shalini Birua,^b Grace Kaul,^{d,e} Abdul Akhir,^d Sidharth Chopra,^{d,e} Jennifer Hirschi,^{c*} Amit Singh,^{b*} and Harinath Chakrapani^{a*}

^aDepartment of Chemistry, Indian Institute of Science Education and Research (IISER), Pune, India; ^dDivision of Microbiology and Cell Biology, Indian Institute of Science, Bangalore, India; ^cDepartment of Chemistry, Binghamton University, New York, USA; ^dDivision of Molecular Microbiology and Immunology, CSIR-Central Drug Research Institute, Janakipuram Extension, Sitapur Road, Lucknow-226031, Uttar Pradesh, India; ^eAcademy of Scientific and Innovative Research (AcSIR), Ghaziabad 201002, India

KEYWORDS. Latent tuberculosis, persisters, mycobacteria, fluoroquinolone, permeability, drug accumulation, phenotypic antimicrobial resistance



ABSTRACT

During tuberculosis (TB) infection caused by *Mycobacterium tuberculosis* (*Mtb*), a sub-population of mycobacteria can enter a non-replicating persistent state that is not susceptible to most frontline TB drugs, resulting in phenotypic antimicrobial resistance (AMR), which contributes to an extended duration of TB therapy, frequent non-compliance and disease relapse. Recent clinical trial data indicated that inclusion of the fluoroquinolone Moxifloxacin (MXF) led to a shortening of TB treatment from 6-months to 4-months. MXF, however, has limited efficacy on *Mtb* persisting in a hypoxic environment. Here, we report a prodrug approach significantly enhancing MXF's lethality against non-replicating hypoxic *Mtb* while retaining its effectiveness against replicating *Mtb*. Since hypoxia is associated with a reductive environment and induces the expression of reductive enzymes such as nitroreductases (NTRs) in *Mtb*, we designed and synthesized a library of nitroaryl and nitroheteroaryl conjugates of MXF. After optimization of several factors, including reduction potential, rate, and efficiency of drug release, as well as selectivity, we identified 2-nitrothiazole-derivative as a prodrug that is rapidly and nearly quantitatively converted to MXF in the presence of NTR. Biochemical studies supported by computational data reveal a rate-limiting influence of electron transfer in the mechanistic pathway for activation of the nitroaryl group, a key step in prodrug activation leading to drug release. The lead prodrug's potency against replicating bacteria in both cellular and animal model studies, and mode of action is nearly identical to MXF with significantly higher lethality against non-replicating *Mtb* than MXF. The prodrug showed improved accumulation of MXF inside non-replicating *Mtb* when compared with MXF alone, likely due to the prodrug's ability to enhance accumulation of MXF within non-replicating *Mtb*. Hence, together, the newly developed 2-nitrothiazole-prodrug is rapidly, efficiently, and selectively cleaved under reductive conditions to produce the active drug and had superior permeability and accumulation in non-replicating *Mtb*, which likely contributes to its increased efficacy.

This proof-of-concept study supports prodrug approaches with a focus on improving accumulation of the active drug within non-replicating pathogens as a strategy to address phenotypic AMR.

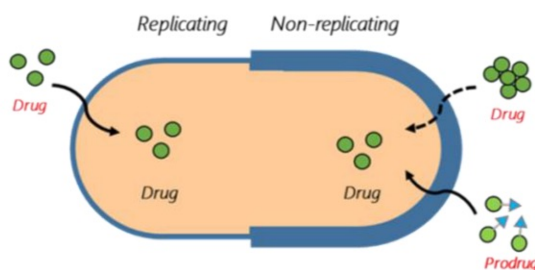
INTRODUCTION

Tuberculosis, a deadly infectious disease caused by *Mycobacterium tuberculosis* (*Mtb*), is among the leading causes of death globally.^{1,2} Although curable through a chemotherapeutic regimen of 6 months, efforts are on to reduce the treatment time, compliance, and relapse while addressing the growing incidences of drug resistance.^{1,3} One important feature about *Mtb* is that a fraction of mycobacteria goes into a non-replicating state wherein bacterial cells are tolerant to clinically-relevant anti-TB drugs.⁴ These cells are genetically identical to the rest of the population but are phenotypically slow growing and enter a metabolically quiescent state in response to immune pressures (e.g., IFN- γ).^{5,6} This phenotypic form of antimicrobial resistance (AMR) is associated with a reduced metabolic rate, activated stress response, altered cell-wall permeability, and heightened drug-efflux activity as compared to drug-susceptible mycobacteria and contribute to the protracted anti-TB regimen and play a significant role in relapse (Figure 1a).⁷⁻¹² Hence, strategies that can eliminate phenotypic AMR are in urgent need.

In a recent clinical trial, reduction of therapy duration from 6 months to 4 months was achieved by the use of Rifapentine and Moxifloxacin (MXF).¹³ However, MXF's lethality against non-replicating *Mtb* is diminished when compared with replicating *Mtb*.^{14,15} Since MXF's target, DNA gyrase, which controls bacterial DNA topology by breaking DNA, passing duplex DNA through the break, and then resealing the gap, is expressed in the non-replicating phase, reduced drug-target engagement contributes to diminished potency in non-replicating *Mtb*.¹⁶⁻¹⁸ One characteristic feature of non-replicating *Mtb* is the increase in thickening of cell wall and

negative zeta potential as a result of an accumulation of polysaccharide and lipid content.^{12,19} Reduced intracellular accumulation has been reported for several drugs, including MXF, and this contributes to decreased potency against non-replicating *Mtb*¹⁴. MXF is relatively hydrophilic (clogP, -0.49) and also exists in pH 7.4 as a carboxylate (pKa of the acid is 6.25)²⁰ and these together likely diminish intracellular accumulation. We considered a prodrug approach to enhance MXF's efficacy by improving permeability and intracellular drug accumulation in non-replicating *Mtb*.

(a) Reduced intracellular accumulation of drugs in non-replicating *Mtb*



(b) MXF and MXF Prodrug design, mechanism of activation and release

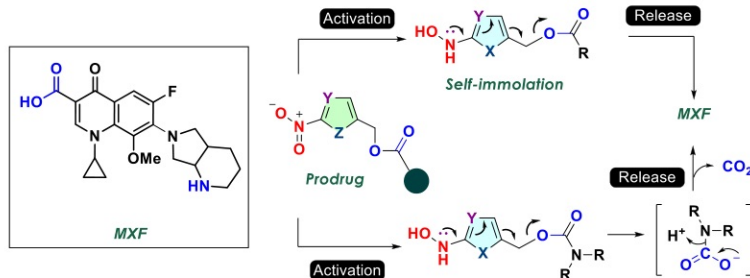


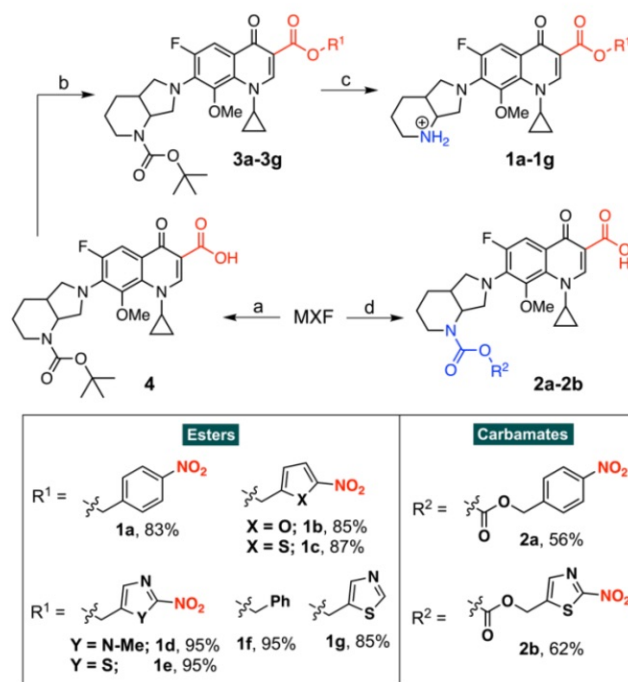
Figure 1. (a) Proposed prodrug strategy to enhance the accumulation of a drug in non-replicating *Mtb*. Non-replicating *Mtb* display a distinctive phenotypic heterogeneity through enhanced cell wall thickness, which may reduce drug uptake. (b) Structures of MXF and its prodrugs (ester and carbamate). (c) Proposed strategy for the generation of MXF following bioreductive activation of nitroheteroaryl ester and carbamate prodrugs. Reduction of prodrug results in the formation of hydroxylamine intermediate, which upon subsequent self-immolation releases MXF.

Within caseating/necrotic TB lesions, non-replicating *Mtb* persists in areas of low oxygen tension, and as a consequence, grows in a bioreductive environment.^{21,22} Comparative gene-expression analysis between replicating and non-replicating *Mtb* reveals the over-expression

of reductive enzymes such as nitroreductases.^{23,24} These enzymes become good pharmacological targets in bacteria-specific drug delivery and imaging. We therefore considered a MXF prodrug that can be cleaved by nitroreductases to generate the active drug for counteracting phenotypic AMR in *Mtb*. A suitably connected nitro(hetero)aryl group allows for the release of MXF, only after reduction of the nitro group to an electron rich hydroxylamino or amino group (Figure 1b). Since bacterial nitroreductases are also prevalent in replicating bacteria, such compounds are expected to generate MXF in actively replicating bacteria as well and hence, the prodrugs should retain their potency. Here, we designed and developed a prodrug of MXF that undergoes rapid and efficient cleavage under bioreductive conditions to produce MXF, provide chemical and biochemical insights into the prodrug activation and release mechanism, and identify a lead compound that had superior efficacy against non-replicating *Mtb* while retaining activity against actively replicating *Mtb*.

RESULTS

Synthesis, physicochemical properties and reduction potential. The *t*-Boc protected MXF derivative **4** was prepared using a reported procedure.²⁵ Esterification of this compound using the corresponding nitroaryl or nitroheteroaryl alcohol afforded analogues **3a-3e** (**Scheme 1**). Deprotection of the *t*-Boc group gave the desired compounds **1a-1e** (**Scheme 1**). As an alternative strategy, we considered carbamates as potential prodrugs (Figure 1b). Fragmentation of the carbamate linkage initiated by the nitro group reduction results in the formation of MXF with the loss of CO₂. As a model substrate, the 4-nitrophenyl based carbamate derivative, **2a** was synthesized from MXF (Scheme 1).



Scheme 1. General procedure for the Synthesis of prodrugs: (a) $(Boc)_2O$, NaOH, H_2O :dioxane (1:1 v/v); (b) R^1OH , HBTU, DMAP, DIPEA, DCM; (c) TFA, DCM; (d) pNO_2PhOR^2 , Et_3N , DMF.

The $clogP$ for derivatives **1a-1e**, and **2a** was determined by ChemDraw 19.1 and as expected, these derivatives had a higher $clogP$ than MXF (Table 1). Next, guided by a recent and comprehensive study on the effect of physicochemical properties on drug accumulation determined that, in addition to $clogP$, molar refractivity (MR) and topological polar surface area (TPSA) were important predictors of drug accumulation in bacteria.²⁶ Using SwissADME,²⁷ we calculated the molar refractivity (MR) and topological polar surface area (TPSA). For compounds **1a-1e** and **2a**, both MR and TPSA were significantly higher (Table 1) when compared with MXF suggesting improved permeability and accumulation of these compounds.

The reduction of the nitro aryl group triggers the release of MXF, which is expected to depend on the reduction potential of the nitroaryl functional group. Cyclic voltametric analysis revealed that the nitroaryl derivative showed a well-defined cathodic peak, that is consistent

with an irreversible nitro group reduction (Figure S1). The reduction potentials (E°_{red} , Exptl) for compounds **1a-1e** and **2a** were found to be -1.21 V to -0.63 V (Table 1).

Table 1. Physicochemical properties and reduction potentials of compounds prepared in this study

| Cpd | clogP ^a | MR ^b | TPSA ^c | E°_{red} (V) | |
|-----------|--------------------|-----------------|-------------------|------------------------------|---------------------|
| | | | | Exptl ^d | Theory ^e |
| 1a | 3.0 | 164.3 | 163.3 | -0.96 | -0.88 |
| 1b | 2.0 | 156.6 | 176.4 | -0.81 | -0.92 |
| 1c | 2.5 | 162.2 | 191.5 | -0.88 | -0.96 |
| 1d | 0.7 | 161.4 | 181.1 | -0.95 | -1.01 |
| 1e | 1.0 | 160.0 | 204.4 | -0.63 | -0.55 |
| 2a | 4.4 | 158.7 | 147.1 | -1.21 | -1.24 |
| 2b | 2.6 | 154.4 | 188.2 | -0.83 | -1.03 |
| MXF | -0.49 | 120.8 | 88.3 | - | - |

^aclogP values were obtained using ChemDraw 19.1 for prodrugs/drug; ^bMR = molar refractivity (represents the molar volume of the molecule); ^cTPSA = topological polar surface area (represents the surface sum over all polar atoms or molecules); ^dexperimentally determined onset reduction potentials using cyclic voltammetry and ^ecomputed reduction potentials are reported in volts (V).

We also computed the reduction potentials of our target molecules using wB97XD/aug-cc-pVDZ//B3LYP/6-31G(d)²⁸⁻³⁰ (Table 1), which were in excellent agreement with the E°_{red} , Exptl for compounds **1a-1e** and **2a** (Figure S2). The 2-nitrothiazole derivative, **1e** has the lowest reduction potential of -0.63 V (-0.55 V theoretical) indicating that the reduction of this compound is thermodynamically the most feasible in the series (Table 1 and Figure S1-S2). Based on this observation, compound **2b**, with the 2-nitrothioazole functional group was synthesized (Scheme 1). This compound had similarly favorable physicochemical properties and was also among the compounds with a lower reduction potential (-0.83 V, exptl; -1.03 V,

theory). Overall, our analysis predicts the 2-nitrothiazolyl group to undergo facile reduction. As a control, two compounds **1f** and **1g** without the nitro group were prepared and hence are not expected to get activated through bioreduction to produce MXF (Scheme 1).

MXF release from prodrugs under chemoreductive and bioreductive conditions. We next assessed the ability of these derivatives to undergo cleavage under chemoreductive and bioreductive conditions to produce MXF. Previous reports show that MXF in pH 7.4 buffer is fluorescent ($\lambda_{\text{ex}} = 289$ nm and $\lambda_{\text{em}} = 488$ nm, $\phi_{\text{F}} = 0.21$, Figure S3).³¹ We found that the MXF derivatives **1** and **2** were themselves only mildly fluorescent and hence enhancement in fluorescence in the presence of the reducing agent would be a good estimate for MXF yield. First, with sodium dithionite ($\text{Na}_2\text{S}_2\text{O}_4$),³² which mimics bioreductive conditions prevalent in hypoxic areas, an enhancement in fluorescence attributable to MXF formation was observed supporting that all nitroaryl compounds generated MXF (Table 2 and Figure S4A). Similarly, with zinc (Zn) and ammonium formate (HCOONH_4 ; AF),³³ which has also been used to simulate bioreductive conditions, the formation of MXF was observed (Table 2 and Figure S4B). The yields of MXF in both experiments were in the range 24-78%, as determined by fluorescence standard curve with authentic MXF. The time course of MXF release following dithionite induced reduction showed that **1e** rapidly (< 5 min, Figure S5A) and in a dose-dependent manner (Figure S5B) underwent reduction to produce MXF when compared to other compounds tested. Under Zn/AF conditions, a similar profile for **1e** was recorded (Figure S5C). In order to assess the correlation between chemoreduction and enzymatic bioreduction, the formation of MXF in the presence of commercially available *E. coli* nitroreductase (NTR) was recorded. Under these conditions, yields ranging from 3-86% were noted with **1e** and **2b** being the most efficient generators of MXF (Table 2 and Figure S6A). Lastly, in order to estimate MXF yields under mycobacterial enzymatic reductive environment, we used whole cell lysate of *Mycobacterium smegmatis* (*Msm*) (Table 2 and Figure S6B): MXF yields ranged from 6-

61%. Together, these data demonstrate a high degree of variability in the yields of MXF under chemo- and bio-reductive conditions and hence a comprehensive evaluation is necessary. For instance, 1-methyl-2-nitroimidazole functional group has been previously shown to be the most efficient substrate for reductive activation of prodrugs.³⁴⁻³⁶ However, our data shows that 1-methyl-2-nitroimidazole prodrug **1d** gave higher yields of MXF under chemoreductive conditions but diminished yields under bioreductive conditions (Table 2). On the other hand, the yields of MXF from 2-nitrothiazole prodrug **1e** and **2b** was uniformly higher (Table 2), suggesting the superiority of the newly developed 2-nitrothiazole caging group for use in bacteria. A recent study shows the utility of 2-nitrothiazole for prodrug activation under hypoxic conditions.³⁷ As expected, the negative control compounds **1f** and **1g** did not produce MXF under any of the aforementioned reductive conditions highlighting the importance of the nitroaryl group in activation and MXF release (Figures S4 and S6).

Table 2. Yields of MXF under reductive conditions monitored by MXF fluorescence enhancement

| Cpd | Chemoreduction | | Bioreduction | |
|-----------|--|-----------------|------------------|-------------------------|
| | Na ₂ S ₂ O ₄ ^a | Zn ^b | NTR ^c | <i>Msm</i> ^d |
| 1a | 55 | 68 | 13 | 6 |
| 1b | 48 | 53 | 8 | 27 |
| 1c | 57 | 56 | 64 | 25 |
| 1d | 32 | 78 | 7 | 18 |
| 1e | 53 | 78 | 86 | 61 |
| 2a | 24 | 29 | 3 | 9 |
| 2b | 39 | 71 | 49 | 53 |

^{a-b}Reductive activation of prodrugs was evaluated by fluorescent measurement of MXF (λ_{ex} = 289 nm and λ_{em} = 488 nm) generated during incubation of **1a-1e** and **2a-2b** (10 μ M) under chemoreductive conditions (^asodium dithionite and ^bZn/AF) and ^{c-d}bioreductive conditions (^cwith *E. coli* NTR (15 nM) and NADH (100 μ M) in pH 7.4 phosphate buffer; and ^dwith whole cell lysates of *Mycobacterium smegmatis* (*Msm*) for 1 h.

To gain a better understanding of the differences in the rate of NTR catalyzed nitroreduction of prodrugs, the kinetics of MXF release was studied. While previous studies with similar nitroaryl compounds used a concentration of 41.6-100 nM NTR,³⁴⁻³⁶ we chose a lower concentration of NTR of 15 nM that provides a more accurate estimate of sensitivity of the substrate towards catalysis by NTR. Initial reaction rates were obtained from the linear portion of the experimental progress curves and these data were fitted into the Michaelis-Menten equation. A significant difference in rates among these compounds was recorded, with **1e** and **2b** being the best substrates for NTR (Figure 2 and Table 3).

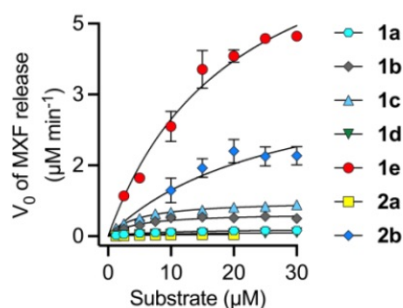


Figure 2. Michaelis-Menten plots of enzyme kinetics using prodrugs **1a-1e**, **2a** and **2b** with *E. coli* NTR. Values are averages ($n = 3$, mean \pm SD)

Table 3. Kinetic parameters for NTR-catalyzed reactions

| Entry | Cpd | k_{cat}^a | K_m^b | k_{cat}/K_m^c | Driving force ^d |
|-------|-----------|-------------|---------|-----------------|----------------------------|
| 1 | 1a | 10 | 7.28 | 1.4 | -1.8 |
| 2 | 1b | 37 | 5.98 | 6 | -5.3 |
| 3 | 1c | 52 | 5.08 | 10 | -3.7 |
| 4 | 1d | 6 | 9.59 | 0.6 | -2.1 |
| 5 | 1e | 494 | 19.81 | 25 | -9.5 |
| 6 | 2a | 3 | 6.66 | 4 | 3.9 |
| 7 | 2b | 219 | 22.5 | 9.7 | -4.8 |

^amin⁻¹; ^bµM (data with estimates of error are available in the SI, Table S1); ^cµM⁻¹ min⁻¹; ^dkcal/mol.

Lineweaver-Burk plots gave k_{cat} and K_m (Figure S7 for individual data plots; Table 3), and analysis of kinetic parameter k_{cat}/K_m showed the superiority of 2-nitrothiazole prodrugs over other compounds tested (Figure S7, S8 and Table 3, entries 5 and 7). Contrary to previous work and in line with data from our bioreductive experiments, we found that 2-nitroimidazole MXF prodrug **1d** had diminished efficiency of reduction and lower yields of the payload when compared with other prodrugs tested.^{34–36} Lastly, molecular dynamics simulations with NTR and FMN cofactor along with the docked substrates in the active site were carried out and the driving force for electron transfer from FMN to the nitro group was determined (Table 3). A moderate correlation (R^2 value of 0.75; Figure S9) between the computed driving force and catalytic efficiency (k_{cat}/K_m) supports the importance of electron transfer in prodrug activation.

Bioreductive activation of 1e. Based on a threshold of 50% yield in all reductive assays and rates of above $0.5 \mu\text{M min}^{-1}$, the prodrug **1e** was identified as the lead molecule for further evaluation. Fluorescence analysis with NTR showed rapid activation and nearly complete conversion to MXF in less than 30 s (Figure 3A and Figure S10). LC/MS analysis of a reaction mixture showed nearly quantitative conversion of **1e** to MXF (Figure 3B and S11).

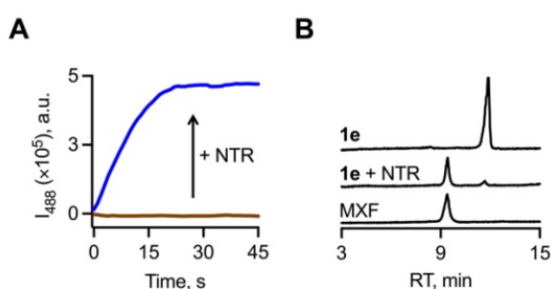


Figure 3. NTR mediated nitro-reduction of **1e** resulted in the release of MXF. (A) Time course of reaction of **1e** at 25 °C without (-) or with (+) NTR (15 nM) and NADH (100 μM) in PB. (B) LC/MS analysis showing the representative total ion chromatograms (TICs) corresponding to the generation of MXF ($[\text{M}+\text{H}]^+$: expected = m/z 402.1824; observed = m/z 402.1826; eluted at 11.8 min) upon reacting **1e** (expected, $[\text{M}+\text{H}]^+$: expected = m/z 544.1661; observed = m/z 544.1664; eluted at 9.4 min) with NTR (15 nM) and NADH (100 μM) in PB (pH 7.4, 10 mM).

The derivative **1e** displayed no significant enhancement in fluorescence attributable to the formation of MXF in the presence of biologically relevant analytes such as thiols (Cys, GSH), reductants (Vit-C), amino acids (His), oxidizing agents (H₂O₂), esterase enzyme (Es), NADH or NTR alone supporting the selectivity of cleavage of **1e** under bioreductive conditions (Figure S12). Due to the poor expression of NTR under normal oxygen saturation, NTR-activated prodrugs have been used in delivering drugs to hypoxic cancer cells.³⁷⁻⁴⁰ We tested if **1e** was cleaved in MEF (mouse embryonic fibroblast cells) under normoxic conditions and found that nearly all **1e** remained intact in 2 h and about 16% of MXF was produced in 4 h (Figure S13). On the contrary, when **1e** was exposed to lysates derived from NTR-expressing *E. coli*, a quantitative yield of MXF was recorded (Figure S14) and diminished MXF yields with heat-inactivated lysate and NTR-inhibitor (dicoumarol).⁴¹ Together these data demonstrated that **1e** was rapidly and selectively activated under bioreductive conditions to give MXF in an excellent yield.

Computational studies. To further understand the mechanism of action, we performed docking studies followed by molecular dynamic simulations. We conceived three possible mechanistic scenarios as illustrated in Figure 4A viz. (1) proton transfer (PT) followed by a formal hydride transfer (2) a formal hydride transfer followed by a proton transfer and (3) two consecutive electron transfer (ET)–proton transfer sequences for the reduction of the nitro groups by NTR, the latter is consistent with the literature precedence observed for CB1954.⁴² The prodrugs (**1a-1e**, **2a**, **2b**) were docked into the homodimer of an FMN-dependent NTR enzyme from *Escherichia coli* (PDB: 1DS7) (SwissDock)⁴³ (Figure S15). In addition, compounds were docked into the FMN-dependent NTR from *Mycobacterium smegmatis* (PDB: 2WZV) that shares a 35% sequence similarity with *E. coli* NTR⁴⁴ (Figure S16). Models with the best docking score were then simulated for further analysis. Molecular dynamic (MD) simulations were performed utilizing the Amber program⁴⁵ with the general amber force field

(GAFF). An 8 nm water box solvated using TIP3P water models and minimized without restraints was used for production runs. Simulated annealing was carried out with 2ns equilibration and a 1fs time step to take the system to 300K. SHAKE algorithm constraints were applied to the waters and LINCS hydrogen bond constraints were applied to the entire system. The equilibrated structures were then subjected to 5ns production runs using a Nosé-Hoover thermostat under NVT conditions with a 2fs time step. This process was performed on three independently docked structures for each prodrug-enzyme complex obtained from Swissdock.⁴³ An average structure from the last 50fs of each production run was utilized to determine the average distance between the FMN cofactor and the nitrogen atom of the nitro moiety. The distances between the cofactor and the nitro group of the prodrugs ranged from 6.4 – 8.2 Å with an average of 7.4 Å (Figure 4B). Based on the distances obtained from the MD simulations described above, a direct hydride transfer from FMN is unlikely. Furthermore, the abundance of water in the active site supports an electron transfer followed by protonation via water as a possible mechanistic scenario. Furthermore, the computed driving force for electron transfer from FMN to each of the prodrugs can be used to indirectly infer the electron transfer barriers. This was done to circumvent complex computations needed to identify the outer sphere reorganization energy inside the enzyme active site. As demonstrated above, the computed driving forces summarized in Table 3 exhibit a positive correlation with the catalytic efficiency (k_{cat}/K_m) measured for *E. coli* NTR suggesting a rate-limiting influence of electron transfer, further validating our mechanistic hypothesis. These results are in agreement with the observations made by Wilke and coworkers⁴² in similar NTR activated prodrugs.

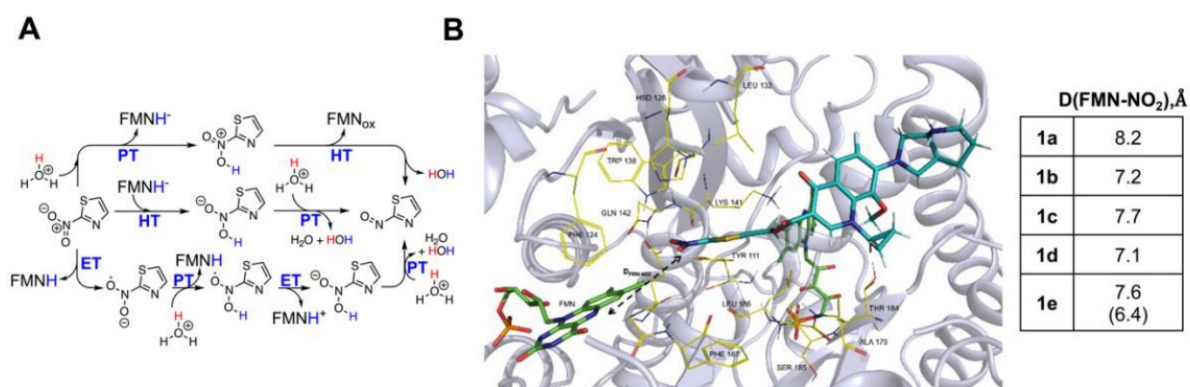


Figure 4. (A) Possible mechanistic scenarios for the reduction of 2-nitrothiazole functionality by *E. coli* NTR: (a) Hydride transfer (HT) from reduced flavin and subsequent proton transfer (PT) from solvent or (b) Electron transfer (ET) from reduced flavin accompanied with PT. (B) MD simulation model of **1e** in *E. coli* NTR (PDB: 1DS7). The key residues in the active site are shown in yellow. The distance [D(FMN-NO₂)] between the FMN residue and **1e** was 7.6 Å in *E. coli* NTR [PDB: 1DS7] and 6.4 Å in *Msm* NTR [PDB: 1DS7] respectively.

Comparison of **1e and MXF in replicating bacteria.** The prodrug was next compared with MXF in laboratory strain *Mtb* H37Rv, and patient-derived multi-drug resistant (MDR), and extensively drug resistant (XDR) strains using an Alamar blue (AB) assay. The minimum inhibitory concentration (MIC) of prodrug **1e** and MXF was identical in all the aforementioned strains (Figure 5A). Next, MXF and the prodrug were compared in a phorbol myristate acetate (PMA)-differentiated THP-1 macrophages infection model, and again, the bactericidal activity of **1e** and MXF were similar suggesting that the prodrug was effective in reducing mycobacterial burden inside macrophages (Figure 5B).

We have recently reported that MXF induces reactive oxygen species (ROS) and suppresses respiration in *Mtb*.¹⁵ Therefore, we compared redox and respiratory changes in *Mtb* upon exposure to **1e** and MFX. We used a *Mtb* strain that expresses the redox biosensor Mrx1-roGFP2 from a plasmid (strain *Mtb*-roGFP2). Mrx1-roGFP2 is a ratiometric fluorescent biosensor that reports the redox potential of the mycothiol redox couple (reduced mycothiol [MSH]/oxidized mycothiol [MSSM]) in the cytoplasm of *Mtb*.⁴⁶ An increase in

biosensor ratio indicates oxidative stress, whereas reductive stress decreases the biosensor ratio.⁴⁶

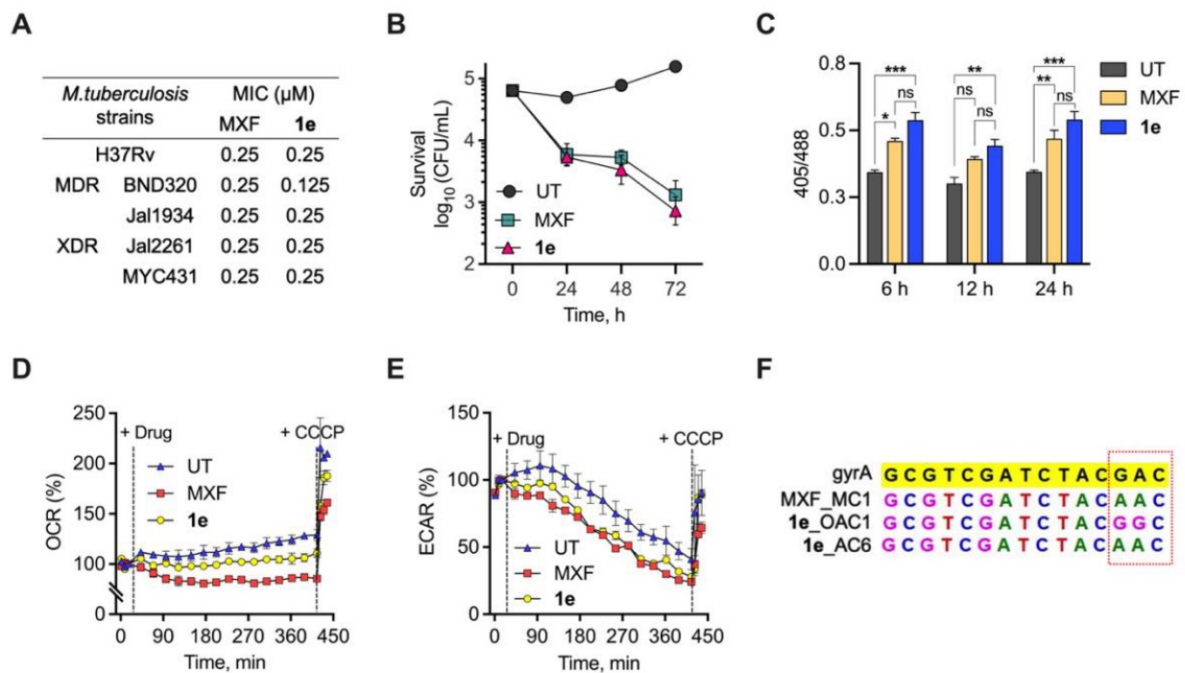


Figure 5. Bactericidal activity of **1e** against replicating *Mtb*. (A) Antimycobacterial activity of MXF and **1e** against drug-susceptible and patient-derived resistant strains of *Mtb*. (B) Bacterial survival kinetics after treatment of THP-1 macrophages infected with *Mtb* H37Rv at 5x MIC of **1e** and MXF. Results are expressed as mean \pm SD from three independent experiments done in triplicate. (C) Ratiometric response of the biosensor following exposure of *Mtb*-roGFP2 to 10x MICs of MXF and **1e** at different intervals (6 h, 12 h and 24 h). Statistical significance was established relative to untreated bacteria control (UT) and MXF using Two-way ANOVA (* $p < 0.05$, ** $p \leq 0.01$, and *** $p \leq 0.001$). Determination of (D) OCR (pmol/min) indicated oxygen consumption rate and (E) ECAR (mpH/min) indicated H^+ production or extracellular acidification due to glycolytic and TCA flux by Seahorse XFP Analyzer. Exponentially growing *Mtb* cultures were either left untreated (UT) or treated with 10x MIC of MXF or **1e** for the indicated times; black dotted lines indicate when drug (MXF or **1e**, 10x MIC) or CCCP (10 μM) were added. The data was represented as percentage of baseline value. (F) Sequences of PCR amplified quinolone resistance determinant region (QRDR) using genomic DNA in *gyrA* of WT and resistant isolates from MXF (MC1) and **1e** (OAC1 and AC6) mutant prevention concentration (MPC) plate. The dotted box highlights the mutation from GAC (aspartic acid) to AAC (asparagine) in resistant colonies of MXF (MC1) and **1e** (OAC1) and to GGC (glycine) in resistant colony of **1e** (AC6).

Exposure to MXF or **1e** (2.5 μ M; 10x MIC) induces comparable increase in the biosensor ratio over-time, indicating elevated oxidative stress (Figure 5C). For bioenergetics, we measured changes in the extracellular acidification rate (ECAR) and oxygen consumption rate (OCR) for MXF- or **1e**-treated *Mtb* as readouts for carbon metabolism (glycolysis and tricarboxylic acid [TCA] cycle) and for oxidative phosphorylation (OXPHOS), respectively, using a Seahorse XFp analyzer.^{47,48} As expected for a normally growing *Mtb*, OCR showed a gradual increase over the duration of the experiment (400 min); OCR increased further upon uncoupling by carbonyl cyanide *m*-chlorophenylhydrazone (CCCP; addition of CCCP stimulates respiration to the maximal level) (Figure 5D). In contrast, addition of MXF or **1e** (2.5 μ M; 10x MIC) inhibited the time-dependent increase in basal OCR.¹⁵ Furthermore, the level of OCR upon uncoupling by CCCP was significantly lower in MXF or **1e**-treated *Mtb* than drug-free *Mtb*. A similar decrease in ECAR was observed upon treatment with MXF or **1e** (Figure 5E). Both MXF and **1e** suppressed OCR and ECAR to a similar degree. We earlier reported that *Mtb* maintains 100% survival in response to 10x MIC for ~ 10 h, confirming that diminished bioenergetics of *Mtb* by MXF or **1e** is not due to dead cells.¹⁵ Lastly, we generated laboratory evolved mutants of *Mtb* in response to MXF and **1e** (Table S2) and confirmed that in both the cases mutations were mapped to the quinolone resistance determinant region (QRDR) of DNA gyrase A (*gyrA*)⁴⁹ (Figure 5F and S17).

In addition to the treatment of TB infections, MXF is widely used as a broad-spectrum antibiotic. The potency of **1e** against ESKAPE pathogens and NTMs was next evaluated using standard assays. Prodrug **1e** had nearly identical inhibitory profile as MXF in these pathogens as well as clinically derived drug-resistant pathogens (Figure S18A and S18B; Table S3, S4 and S5). We also found a similar reduction in bacterial burden in a neutropenic murine *E. coli* ATCC 25922 infected thigh model at comparable doses (Figure S19). Additionally, when **1e** was evaluated in fluoroquinolone-resistant *E. coli* mutants, we found a significantly higher

MIC value (MIC = 80 μ M), which was comparable to MXF (MIC >100 μ M) (Table S6). Hence, it appears that in both *Mtb* as well as *E. coli*, the prodrug **1e** and MXF have similar efficacy as well as mechanism of action.

Comparison of **1e and MXF in non-replicating *Mycobacterium tuberculosis*.** The prodrug was next compared with MXF in non-replicating *Mtb*. A hypoxia resazurin reduction assay (HyRRA) was used to study growth inhibition in non-replicating *Mtb*. Isoniazid (INH) and Metronidazole (MZ) were used as controls. Under these conditions, consistent with literature reports, INH showed no significant growth inhibition while MZ inhibited growth at 10 mM concentrations. MXF had some effect on growth but the compound **1e** was found to have a significantly higher potency when compared with MXF (Figure 6A). Colonies generated from the aforementioned assay were plated and growth was measured and **1e** was significantly better than both MZ and MXF (Figure 6B).

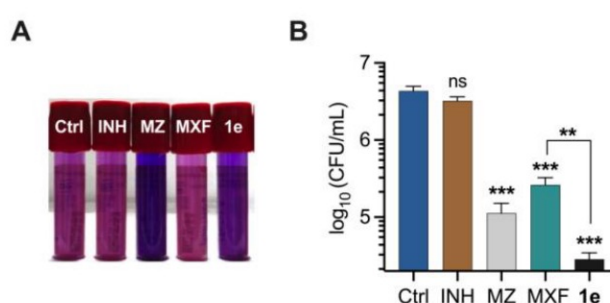


Figure 6. Bactericidal activity of **1e** against non-replicating *Mtb*. (A) Mycobactericidal effect of MXF and **1e** at indicated concentration (10x MIC, 2.5 μ M) on hypoxia-adapted *Mtb* bacilli based on visual hypoxia resazurin reduction assay (HyRRA). Isoniazid (INH, 10 μ M) and Metronidazole (MZ, 10 mM) served as a negative and positive control respectively. The pink colour in the tube indicates cell viability under hypoxia while blue colour indicates no growth. (B) Survival of *Mtb* under hypoxia was measured as log₁₀ of colony-forming units (CFU) after treatment with 10x MIC (2.5 μ M) of MFX and **1e** for 5 days. Results are expressed as mean \pm SD from three independent experiments performed in triplicate. Statistical significance was established relative to untreated bacteria control (Ctrl) using unpaired *t*-test with Welch's correction student's (ns indicate not significant, ** $p \leq 0.01$, and *** $p \leq 0.001$).

Intracellular accumulation of MXF and 1e. Mechanistic studies with replicating *Mtb* demonstrate that the action of **1e** is quite similar to MXF. In order to understand the intracellular accumulation of the drug when treated with MXF alone or prodrug **1e**, an LC/MS assay based on reported methods was developed (Figure 7A and S20).^{14,50} Briefly, exponentially growing *Mtb* were incubated at 37 °C in PBS (1x, pH 7.4) with either MXF or **1e** at a final concentration of 5 μM. After incubation with the test compound for 30 min, replicating bacilli were pelleted by centrifugation through silicone oil mix and then lysed through bead beating. The compounds were extracted from the resultant lysate using PBS-MeOH and filtered through a 3 kDa Amicon® centrifugal filter. The intracellular concentrations were determined using a standard calibration curve (Figure S21 and S22), converted into accumulation values, then normalized with the bacterial count and were finally represented as MXF accumulation (nmol/10⁸ CFUs). We find that in replicating *Mtb*, the accumulation of MXF in cells treated with **1e** was nearly identical to those treated with free MXF (Figure 7B). The intact prodrug **1e** could not be detected under these conditions. This result is consistent with our observation that **1e** was rapidly cleaved under bioreductive conditions (half-life < 1 min) to produce MXF in a nearly quantitative yield (Figure 3A and S10). Hence, our data suggests that **1e** and MXF have similar permeability and accumulation profiles in replicating *Mtb*.

Next, in non-replicating *Mtb*, a similar workflow was used to determine intracellular drug accumulation and whether this contributed to enhanced efficacy of **1e** over MXF. Under these conditions, we find a significant reduction in the amount of MXF in cells that were treated with the free drug. This observation is consistent with previous reports which show the free MXF was poorly accumulated in non-replicating *Mtb*. Under similar conditions when **1e** was used, we find a substantially higher intracellular accumulation of MXF (Figure 7C). Again, the intact prodrug **1e** could not be detected under these conditions.

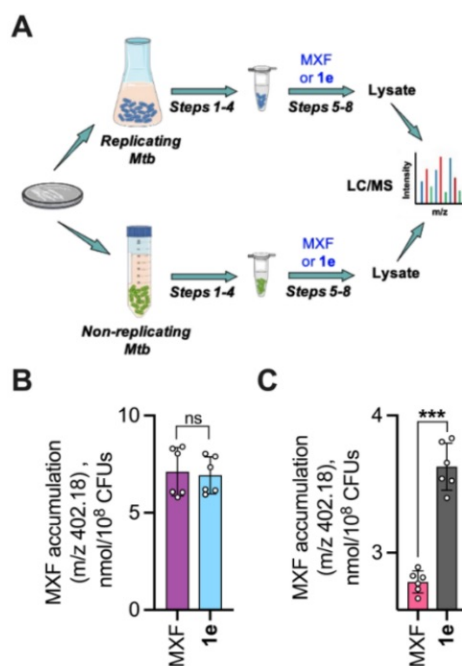


Figure 7. (A) Workflow for Accumulation assay. (B-C) LC-MS analysis of intracellular concentrations of MXF (m/z 402.18) in (B) exponentially growing and (C) hypoxic cultures of *Mtb* following incubation for 30 min with a fixed concentration of MXF and **1e** of 5 μ M. The drug content is expressed as the amount of drug (nmol) per CFU. Statistical significance was established relative to MXF treated sample using unpaired t -test (ns indicate not significant and *** $p \leq 0.001$).

DISCUSSION

Mtb possesses a remarkable ability to evade host immune pressures and enter a quiescent state where most frontline antibiotics are ineffective.^{51,51} The prevalence of non-replicating mycobacterial persisters are a major impediment to effective TB treatment. New regimens incorporating MXF and Rifapentine are promising but the lack of activity of MXF against non-replicating *Mtb* is yet a major concern and needs new interventional strategies.¹³ The equilibrium between non-replicating and replicating bacilli serves as a defining characteristic between latent and active infection.^{51,52} A recent study suggested that *Mtb* exists in a replicating state during the early latency and later transitions into a non-replicating state during prolonged latency.⁵³ The occurrences of latent tuberculosis, where the patient does not present symptoms

of TB is also attributed to non-replicating *Mtb* contributing to phenotypic AMR.⁵⁴ Hence, the need to eliminate both replicating and non-replicating *Mtb* is urgent. The adaptation into a drug-tolerant non-replicating persistent state is often associated with metabolic downshift and increased thickening of lipid-rich cell wall.^{10,11,19} Metabolomic and lipidomic analysis demonstrated that non-replicating bacteria accumulate mycolate wax esters and long-chain triacylglycerol esters along with an increase in the ratio of lipoarabinomannan to lipomannan.^{55,56} This distinct phenotype contributes to reduced penetration and intracellular accumulation of many antibiotics.¹² Our drug of choice was MXF, whose target gyrase is expressed in non-replicating *Mtb*.^{17,18} Mass spectrometric studies revealed that the intracellular accumulation of MXF is diminished to a significant extent in nutrient starved non-replicating *Mtb*, which probably contributes to the marked reduction in bactericidal efficacy of MXF by more than 100-fold.¹⁴ MXF was also found to be less effective against hypoxic non-replicating *Mtb*.¹⁵ In this study, a prodrug approach that increased lipophilicity was exploited to enhance the permeation resulting in increased drug accumulation; the activation mechanism of the prodrug to generate MXF appears selective to bacteria. Here, we provide evidence that enhancing the amount of MXF using a prodrug within non-replicating *Mtb* has a tremendous impact on eliminating persisters. Non-replicating *Mtb* that reside in the hypoxic regions of granulomas strongly induce DevR regulon-controlled genes encoding several nitroreductases (NTRs) by several fold.^{23,24,57} These NTRs probably contribute to combat nitrosative and oxidative stress encountered inside host macrophage to survive and establish infection.^{58,59} Prodrug activation is achieved by nitroreductases that are expressed in non-replicating as well as in replicating *Mtb*, albeit at somewhat lower levels in the latter. Despite the nitro group being somewhat less favored in traditional medicinal chemistry, many clinically used TB drugs (Pretomanid,^{60,61} Delamanid,^{62,63} TB-354,⁶⁴ nitrofuranylcalonolides, and TP-053⁶⁵) contain an essential nitro functional group. To identify a suitable prodrug, preliminary investigation was

conducted with commercially available *E. coli* NTR. The prodrug was rapidly activated under bioreductive conditions to provide MXF in quantitative yield. Detailed computational analysis was ascertained to determine the driving force for electron transfer from FMN to the nitro group, which supported the likelihood of electron transfer in prodrug activation. Notably, this prodrug was equipotent to MXF in its inhibitory activity in both cellular models and animal models. The newly developed prodrug demonstrated superior inhibitory activity against non-replicating *Mtb* when compared with MXF likely due to enhanced accumulation of drug. Our study demonstrates that enhancing permeability and accumulation of a clinical drug can have positive outcomes in inhibiting bacterial growth. The drug concentration within cells leading to adequate drug-target engagement that is necessary to induce lethality will vary from drug to drug. But since drug accumulation in non-replicating *Mtb* is uniformly low for all TB drugs, strategies that enhance bactericidal drug accumulation are expected to address a major clinical problem.⁶⁶

CONCLUSION

We provide evidence for a prodrug approach against phenotypic AMR in *Mtb* by focusing on improving cell-permeability and drug accumulation, while optimizing for rapid, selective and efficient conversion within bacteria. This innovative strategy can, in principle, be extended to other clinical TB drugs and will complement approaches that either target and kill non-replicating bacilli or resuscitate/resensitize them to a drug-susceptible state. Although the development of new molecules with novel targets is important, the discovery and subsequent introduction of new antibiotics into the global market has been a slow, expensive and cumbersome process. Hence, the methodology developed herein provides a sound framework for future prodrug design that can optimize for enhancing accumulation of the active drug to eliminate persisters and potentially improve treatment outcomes.

Corresponding Authors

* jhirschi@binghamton.edu; asingh@iisc.ac.in; harinath@iiserpune.ac.in

ACKNOWLEDGMENT

Financial support for this project was from IISER Pune, Department of Science and Technology (DST) Fund for Improvement of S&T Infrastructure (grant number SR/FST/LSII-043/2016) to the IISER Pune Biology Department for setting up the Biological Mass Spectrometry Facility and Ignite Life Sciences for LC/MS studies. Research fellowship for TAK and GK (DST-INSPIRE), AA thanks UGC. The authors thank Mr. Arnab Chakraborty (Dr. Siddhesh S. Kamat Lab, IISER Pune) and Mrs. Sunita (LC/MS facility incharge, IISc, Bangalore).

ABBREVIATIONS

AB, alamar blue; AMR, Antimicrobial resistance; CCCP, carbonyl cyanide *m*-chlorophenylhydrazone, CFU, colony forming unit; ET, electron transfer; *E. coli*, *Escherichia coli*; ECAR, extracellular acidification rate; FMN, flavin mononucleotide; HyRRA, hypoxia resazurin reduction assay; INH, isoniazid; *Mtb*, *Mycobacterium tuberculosis*; MXF, Moxifloxacin; MR, Molar refractivity; *Msm*, *Mycobacterium smegmatis*; MDR, multi-drug resistant; MD, molecular dynamics; MIC, minimum inhibitory concentration; MZ, metronidazole; NTR, Nitroreductase; NTM, non-tuberculosis mycobacteria; OCR, oxygen consumption rate; OXPHOS, oxidative phosphorylation; PT, proton transfer; QRDR, quinolone resistance determinant region; ROS, reactive oxygen species; TPSA, topological polar surface area; TIC, total ion chromatograms; TCA, tricarboxylic acid cycle; TB, Tuberculosis; XDR, extensively drug-resistant.

REFERENCES

- (1) World Health Organization, *Global Tuberculosis Report 2021*; WHO: Geneva, **2021**, 1-27.
- (2) Paulson, T. Epidemiology: A Mortal Foe. *Nature* **2013**, 502 (7470), S2–S3. <https://doi.org/10.1038/502S2a>.

- (3) Zumla, A.; Nahid, P.; Cole, S. T. Advances in the Development of New Tuberculosis Drugs and Treatment Regimens. *Nat. Rev. Drug Discov.* **2013**, *12*, 388–404. <https://doi.org/10.1038/nrd4001>.
- (4) Horsburgh, C. R.; Barry, C. E.; Lange, C. Treatment of Tuberculosis. *New Eng. J. Med.* **2015**, *373* (22), 2149–2160. <https://doi.org/10.1056/NEJMra1413919>.
- (5) Manina, G.; Dhar, N.; McKinney, J. D. Stress and Host Immunity Amplify Mycobacterium Tuberculosis Phenotypic Heterogeneity and Induce Nongrowing Metabolically Active Forms. *Cell Host Microbe* **2015**, *17* (1), 32–46. <https://doi.org/10.1016/j.chom.2014.11.016>.
- (6) Ahmed, M.; Mackenzie, J.; Tezera, L.; Krause, R.; Truebody, B.; Garay-Baquero, D.; Vallejo, A.; Govender, K.; Adamson, J.; Fisher, H.; Essex, J. W.; Mansour, S.; Elkington, P.; Steyn, A. J. C.; Leslie, A. Mycobacterium Tuberculosis Senses Host Interferon- γ via the Membrane Protein MmpL10. *Commun. Biol.* **2022**, *5* (1), 1317. <https://doi.org/10.1038/s42003-022-04265-0>.
- (7) Cohen, N. R.; Lobritz, M. A.; Collins, J. J. Microbial Persistence and the Road to Drug Resistance. *Cell Host Microbe* **2013**, 632–642. <https://doi.org/10.1016/j.chom.2013.05.009>.
- (8) Sebastian, J.; Swaminath, S.; Nair, R. R.; Jakkala, K.; Pradhan, A.; Ajitkumar, P. De Novo Emergence of Genetically Resistant Mutants of Mycobacterium Tuberculosis from the Persistence Phase Cells Formed against Antituberculosis Drugs in Vitro. *Antimicrob. Agents Chemother.* **2017**, *61* (2). <https://doi.org/10.1128/AAC.01343-16>.
- (9) Zhang, Y. Persisters, Persistent Infections and the Yin-Yang Model. *Emerg. Microbes Infect.* **2014**, *3* (1), e3. <https://doi.org/10.1038/emi.2014.3>.
- (10) Vilchèze, C.; Yan, B.; Casey, R.; Hingley-Wilson, S.; Ettwiller, L.; Jacobs, W. R. Commonalities of Mycobacterium Tuberculosis Transcriptomes in Response to Defined Persisting Macrophage Stresses. *Front. Immunol.* **2022**, *13* (909904), 1-18. <https://doi.org/10.3389/fimmu.2022.909904>.
- (11) Stokas, H.; Rhodes, H. L.; Purdy, G. E. Modulation of the M. Tuberculosis Cell Envelope between Replicating and Non-Replicating Persistent Bacteria. *Tuberculosis (Edinb).* **2020**, *125*, 102007. <https://doi.org/10.1016/j.tube.2020.102007>.
- (12) Cunningham, A. F.; Spreadbury, C. L. Mycobacterial Stationary Phase Induced by Low Oxygen Tension: Cell Wall Thickening and Localization of the 16-Kilodalton-Crystallin Homology. *J. Bacteriol.* **1998**, *180* (4), 801-8. <https://journals.asm.org/journal/jb>.
- (13) Dorman, S. E.; Nahid, P.; Kurbatova, E. V.; Phillips, P. P. J.; Bryant, K.; Dooley, K. E.; Engle, M.; Goldberg, S. V.; Phan, H. T. T.; Hakim, J.; Johnson, J. L.; Lourens, M.; Martinson, N. A.; Muzanyi, G.; Narunsky, K.; Nerette, S.; Nguyen, N. V.; Pham, T. H.; Pierre, S.; Purfield, A. E.; Samaneka, W.; Savic, R. M.; Sanne, I.; Scott, N. A.; Shenje, J.; Sizemore, E.; Vernon, A.; Waja, Z.; Weiner, M.; Swindells, S.; Chaisson, R. E. Four-Month Rifapentine Regimens with or without Moxifloxacin for Tuberculosis. *New Eng. J. Med.* **2021**, *384* (18), 1705–1718. <https://doi.org/10.1056/nejmoa2033400>.

- (14) Sarathy, J.; Dartois, V.; Dick, T.; Gengenbacher, M. Reduced Drug Uptake in Phenotypically Resistant Nutrient-Starved Nonreplicating Mycobacterium Tuberculosis. *Antimicrob. Agents Chemother.* **2013**, *57* (4), 1648–1653. <https://doi.org/10.1128/AAC.02202-12>.
- (15) Somnath, S.; Samsher, S.; Ashutosh, T.; Chandrani, T.; Anand, K. T.; Mayashree, D.; Vikas, Y.; Sakshi, K.; S, R. R.; Nagasuma, C.; Harinath, C.; Karl, D.; Amit, S. Moxifloxacin-Mediated Killing of Mycobacterium Tuberculosis Involves Respiratory Downshift, Reductive Stress, and Accumulation of Reactive Oxygen Species. *Antimicrob. Agents Chemother.* **2022**, *66* (9), e00592-22. <https://doi.org/10.1128/aac.00592-22>.
- (16) Mustaev, A.; Malik, M.; Zhao, X.; Kurepina, N.; Luan, G.; Opegard, L. M.; Hiasa, H.; Marks, K. R.; Kerns, R. J.; Berger, J. M.; Drlica, K. Fluoroquinolone-Gyrase-DNA Complexes. *J. Biol. Chem.* **2014**, *289* (18), 12300–12312. <https://doi.org/10.1074/jbc.M113.529164>.
- (17) Sala, C.; Dhar, N.; Hartkoorn, R. C.; Zhang, M.; Ha, Y. H.; Schneider, P.; Cole, S. T. Simple Model for Testing Drugs against Nonreplicating *Mycobacterium Tuberculosis*. *Antimicrob. Agents Chemother.* **2010**, *54* (10), 4150–4158. <https://doi.org/10.1128/AAC.00821-10>.
- (18) Chopra, S.; Matsuyama, K.; Tran, T.; Malerich, J. P.; Wan, B.; Franzblau, S. G.; Lun, S.; Guo, H.; Maiga, M. C.; Bishai, W. R.; Madrid, P. B. Evaluation of Gyrase B as a Drug Target in Mycobacterium Tuberculosis. *J. Antimicrob. Chemother.* **2012**, *67* (2), 415–421. <https://doi.org/10.1093/jac/dkr449>.
- (19) Jakkala, K.; Ajitkumar, P. Hypoxic Non-Replicating Persistent Mycobacterium Tuberculosis Develops Thickened Outer Layer That Helps in Restricting Rifampicin Entry. *Front. Microbiol.* **2019**, *10*, 2339. <https://doi.org/10.3389/fmicb.2019.02339>.
- (20) Langlois, M.H.; Montagut, M.; Dubost, J.P.; Grellet, J.; Saux, M.C. Protonation Equilibrium and Lipophilicity of Moxifloxacin. *J. Pharm. Biomed. Anal.* **2005**, *37* (2), 389–393. <https://doi.org/10.1016/j.jpba.2004.10.022>.
- (21) Hudock, T. A.; Foreman, T. W.; Bandyopadhyay, N.; Gautam, U. S.; Veatch, A. V.; LoBato, D. N.; Gentry, K. M.; Golden, N. A.; Cavigli, A.; Mueller, M.; Hwang, S.-A.; Hunter, R. L.; Alvarez, X.; Lackner, A. A.; Bader, J. S.; Mehra, S.; Kaushal, D. Hypoxia Sensing and Persistence Genes Are Expressed during the Intragranulomatous Survival of *Mycobacterium Tuberculosis*. *Am. J. Respir. Cell Mol. Biol.* **2017**, *56* (5), 637–647. <https://doi.org/10.1165/rcmb.2016-0239OC>.
- (22) Belton, M.; Brilha, S.; Manavaki, R.; Mauri, F.; Nijran, K.; Hong, Y. T.; Patel, N. H.; Dembek, M.; Tezera, L.; Green, J.; Moores, R.; Aigbirhio, F.; Al-Nahhas, A.; Fryer, T. D.; Elkington, P. T.; Friedland, J. S. Hypoxia and Tissue Destruction in Pulmonary TB. *Thorax* **2016**, *71* (12), 1145–1153. <https://doi.org/10.1136/thoraxjnl-2015-207402>.

- (23) Chauhan, S.; Sharma, D.; Singh, A.; Surolia, A.; Tyagi, J. S. Comprehensive Insights into Mycobacterium Tuberculosis DevR (DosR) Regulon Activation Switch. *Nucleic Acids Res.* **2011**, *39* (17), 7400–7414. <https://doi.org/10.1093/nar/gkr375>.
- (24) Sherman, D. R.; Voskuil, M.; Schnappinger, D.; Liao, R.; Harrell, M. I.; Schoolnik, G. K. Regulation of the Mycobacterium Tuberculosis Hypoxic Response Gene Encoding α -Crystallin. *Proc. Natl. Acad. Sci. U. S. A.* **2001**, *98* (13), 7534-9. <https://doi.org/10.1073/pnas.121172498>.
- (25) Tanaka, K. S. E.; Houghton, T. J.; Kang, T.; Dietrich, E.; Delorme, D.; Ferreira, S. S.; Caron, L.; Viens, F.; Arhin, F. F.; Sarmiento, I.; Lehoux, D.; Fadhil, I.; Laquerre, K.; Liu, J.; Ostiguy, V.; Poirier, H.; Moeck, G.; Parr, T. R.; Rafai Far, A. Bisphosphonated Fluoroquinolone Esters as Osteotropic Prodrugs for the Prevention of Osteomyelitis. *Bioorg. Med. Chem.* **2008**, *16* (20), 9217–9229. <https://doi.org/10.1016/J.BMC.2008.09.010>.
- (26) Machado, D.; Girardini, M.; Viveiros, M.; Pieroni, M. Challenging the Drug-Likeness Dogma for New Drug Discovery in Tuberculosis. *Front. Microbiol.* **2018**, *9* (1367), 1-23. <https://doi.org/10.3389/fmicb.2018.01367>.
- (27) Daina, A.; Michielin, O.; Zoete, V. SwissADME: A Free Web Tool to Evaluate Pharmacokinetics, Drug-Likeness and Medicinal Chemistry Friendliness of Small Molecules. *Sci. Rep.* **2017**, *7* (42717), 1-13.
- (28) Chai, J.-D.; Head-Gordon, M. Long-Range Corrected Hybrid Density Functionals with Damped Atom–Atom Dispersion Corrections. *Phys. Chem. Chem. Phys.* **2008**, *10* (44), 6615. <https://doi.org/10.1039/b810189b>.
- (29) Becke, A. D. Density-functional Thermochemistry. III. The Role of Exact Exchange. *J. Chem. Phys.* **1993**, *98* (7), 5648–5652. <https://doi.org/10.1063/1.464913>.
- (30) Hehre, W. J.; Stewart, R. F.; Pople, J. A. Self-Consistent Molecular-Orbital Methods. I. Use of Gaussian Expansions of Slater-Type Atomic Orbitals. *J. Chem. Phys.* **1969**, *51* (6), 2657–2664. <https://doi.org/10.1063/1.1672392>.
- (31) Viola, G.; Facciolo, L.; Canton, M.; Vedaldi, D.; Dall’Acqua, F.; Aloisi, G. G.; Amelia, M.; Barbafrina, A.; Elisei, F.; Latterini, L. Photophysical and Phototoxic Properties of the Antibacterial Fluoroquinolones Levofloxacin and Moxifloxacin. *Chem. Biodivers.* **2004**, *1* (5), 782–801. <https://doi.org/10.1002/cbdv.200490061>.
- (32) Wang, J.; Liu, J.; Yang, Z. Recent Advances in Peptide-Based Nanomaterials for Targeting Hypoxia. *Nanoscale Adv.* **2021**, *3*, 6027–6039. <https://doi.org/10.1039/d1na00637a>.
- (33) Pardeshi, K. A.; Kumar, T. A.; Ravikumar, G.; Shukla, M.; Kaul, G.; Chopra, S.; Chakrapani, H. Targeted Antibacterial Activity Guided by Bacteria-Specific Nitroreductase Catalytic Activation to Produce Ciprofloxacin. *Bioconjug. Chem.* **2019**, *30* (3), 751–759. <https://doi.org/10.1021/acs.bioconjchem.8b00887>.
- (34) Wang, S.; Wu, X.; Zhang, Y.; Zhang, D.; Xie, B.; Pan, Z.; Ouyang, K.; Peng, T. Discovery of a Highly Efficient Nitroaryl Group for Detection of Nitroreductase and

- Imaging of Hypoxic Tumor Cells. *Org. Biomol. Chem.* **2021**, *19* (15), 3469–3478. <https://doi.org/10.1039/d1ob00356a>.
- (35) Gruber, T. D.; Krishnamurthy, C.; Grimm, J. B.; Tadross, M. R.; Wysocki, L. M.; Gartner, Z. J.; Lavis, L. D. Cell-Specific Chemical Delivery Using a Selective Nitroreductase-Nitroaryl Pair. *ACS Chem. Biol.* **2018**, *13* (10), 2888–2896. <https://doi.org/10.1021/acscchembio.8b00524>.
- (36) Herrlinger, E.-M.; Hau, M.; Melanie Redhaber, D.; Greve, G.; Willmann, D.; Steimle, S.; Müller, M.; Lübbert, M.; Cornelius Miething, C.; Schüle, R.; Jung, M. Nitroreductase-Mediated Release of Inhibitors of Lysine-Specific Demethylase 1 (LSD1) from Prodrugs in Transfected Acute Myeloid Leukaemia Cells. *ChemBioChem.* **2020**, *21* (16), 2329–2347. <https://doi.org/10.26434/chemrxiv.10012937.v1>.
- (37) Sun, Z.; Zhang, H.; Zhang, H.; Wu, J.; Gao, F.; Zhang, C.; Hu, X.; Liu, Q.; Wei, Y.; Wei, Y.; Zhuang, J.; Zhuang, J.; Huang, X. A Novel Model System for Understanding Anticancer Activity of Hypoxia-Activated Prodrugs. *Mol. Pharm.* **2020**, *17* (6), 2072–2082. <https://doi.org/10.1021/acs.molpharmaceut.0c00232>.
- (38) O'Connor, L. J.; Cazares-Körner, C.; Saha, J.; Evans, C. N. G.; Stratford, M. R. L.; Hammond, E. M.; Conway, S. J. Design, Synthesis and Evaluation of Molecularly Targeted Hypoxia-Activated Prodrugs. *Nat. Protoc.* **2016**, *11* (4), 781–794. <https://doi.org/10.1038/nprot.2016.034>.
- (39) Winn, B. A.; Shi, Z.; Carlson, G. J.; Wang, Y.; Nguyen, B. L.; Kelly, E. M.; Ross, R. D.; Hamel, E.; Chaplin, D. J.; Trawick, M. L.; Pinney, K. G. Bioreductively Activatable Prodrug Conjugates of Phenstatin Designed to Target Tumor Hypoxia. *Bioorg. Med. Chem. Lett.* **2017**, *27* (3), 636–641.
- (40) Jin, C.; Zhang, Q.; Lu, W. Synthesis and Biological Evaluation of Hypoxia-Activated Prodrugs of SN-38. *Eur. J. Med. Chem.* **2017**, *132*, 135–141.
- (41) Johansson, E.; Parkinson, G. N.; Denny, W. A.; Neidle, S. Studies on the Nitroreductase Prodrug-Activating System. Crystal Structures of Complexes with the Inhibitor Dicoumarol and Dinitrobenzamide Prodrugs and of the Enzyme Active Form. *J. Med. Chem.* **2003**, *46* (19), 4009–4020. <https://doi.org/10.1021/jm030843b>.
- (42) Christofferson, A.; Wilkie, J. Mechanism of CB1954 Reduction by *Escherichia Coli* Nitroreductase. *Biochem. Soc. Trans.* **2009**, *37* (2), 413–418. <https://doi.org/10.1042/BST0370413>.
- (43) Grosdidier, A.; Zoete, V.; Michielin, O. SwissDock, a Protein-Small Molecule Docking Web Service Based on EADock DSS. *Nucleic Acids Res.* **2011**, *39*, W270–W277. <https://doi.org/10.1093/nar/gkr366>.
- (44) Manina, G.; Bellinzoni, M.; Pasca, M. R.; Neres, J.; Milano, A.; De Jesus Lopes Ribeiro, A. L.; Buroni, S.; Škovierová, H.; Dianišková, P.; Mikušová, K.; Marák, J.; Makarov, V.; Giganti, D.; Haouz, A.; Lucarelli, A. P.; Degiacomi, G.; Piazza, A.; Chiarelli, L. R.; De Rossi, E.; Salina, E.; Cole, S. T.; Alzari, P. M.; Riccardi, G. Biological and Structural Characterization of the Mycobacterium Smegmatis Nitroreductase NfnB, and Its Role

- in Benzothiazinone Resistance. *Mol. Microbiol.* **2010**, *77* (5), 1172–1185. <https://doi.org/10.1111/j.1365-2958.2010.07277.x>.
- (45) Case, D. A.; Cheatham, T. E.; Darden, T.; Gohlke, H.; Luo, R.; Merz, K. M.; Onufriev, A.; Simmerling, C.; Wang, B.; Woods, R. J. The Amber Biomolecular Simulation Programs. *J. Comput. Chem.* **2005**, *26* (16), 1668–1688. <https://doi.org/10.1002/jcc.20290>.
- (46) Bhaskar, A.; Chawla, M.; Mehta, M.; Parikh, P.; Chandra, P.; Bhave, D.; Kumar, D.; Carroll, K. S.; Singh, A. Reengineering Redox Sensitive GFP to Measure Mycothiol Redox Potential of Mycobacterium Tuberculosis during Infection. *PLoS Pathog.* **2014**, *10* (1), e1003902. <https://doi.org/10.1371/journal.ppat.1003902>.
- (47) Lamprecht, D. A.; Finin, P. M.; Rahman, Md. A.; Cumming, B. M.; Russell, S. L.; Jonnala, S. R.; Adamson, J. H.; Steyn, A. J. C. Turning the Respiratory Flexibility of Mycobacterium Tuberculosis against Itself. *Nat. Commun.* **2016**, *7* (1), 12393. <https://doi.org/10.1038/ncomms12393>.
- (48) Mishra, R.; Kohli, S.; Malhotra, N.; Bandyopadhyay, P.; Mehta, M.; Munshi, M.; Adiga, V.; Ahuja, V. K.; Shandil, R. K.; Rajmani, R. S.; Seshasayee, A. S. N.; Singh, A. Targeting Redox Heterogeneity to Counteract Drug Tolerance in Replicating *Mycobacterium Tuberculosis*. *Sci. Transl. Med.* **2019**, *11* (518). <https://doi.org/10.1126/scitranslmed.aaw6635>.
- (49) Sirgel, F. A.; Warren, R. M.; Streicher, E. M.; Victor, T. C.; van Helden, P. D.; Bottger, E. C. GyrA Mutations and Phenotypic Susceptibility Levels to Ofloxacin and Moxifloxacin in Clinical Isolates of Mycobacterium Tuberculosis. *J. Antimicrob. Chemother.* **2012**, *67* (5), 1088–1093. <https://doi.org/10.1093/jac/dks033>.
- (50) Geddes, E. J.; Li, Z.; Hergenrother, P. J. An LC-MS/MS Assay and Complementary Web-Based Tool to Quantify and Predict Compound Accumulation in *E. coli*. *Nat. Protoc.* **2021**, *16* (10), 4833–4854. <https://doi.org/10.1038/s41596-021-00598-y>.
- (51) Dhar, N.; Mckinney, J.; Manina, G. Phenotypic Heterogeneity in Mycobacterium Tuberculosis. *Microbiol. Spectr.* **2016**, *4* (6), 1-27. <https://doi.org/10.1128/microbiolspec.TBTB2-0021>.
- (52) Esmail, H.; Barry, C. E.; Young, D. B.; Wilkinson, R. J. The Ongoing Challenge of Latent Tuberculosis. *Philos. Trans. R. Soc. Lond. B. Biol. Sci.* **2014**, *369* (1645), 20130437. <https://doi.org/10.1098/rstb.2013.0437>.
- (53) Colangeli, R.; Gupta, A.; Vinhas, S. A.; Chippada Venkata, U. D.; Kim, S.; Grady, C.; Jones-López, E. C.; Soteropoulos, P.; Palaci, M.; Marques-Rodrigues, P.; Salgame, P.; Ellner, J. J.; Dietze, R.; Alland, D. Mycobacterium Tuberculosis Progresses through Two Phases of Latent Infection in Humans. *Nat. Commun.* **2020**, *11* (1), 1-10. <https://doi.org/10.1038/s41467-020-18699-9>.
- (54) Zhang, Y.; Yew, W. W.; Barer, M. R. Targeting Persisters for Tuberculosis Control. *Antimicrob. Agents Chemother.* **2012**, *56* (5), 2223-30. <https://doi.org/10.1128/AAC.06288-11>.

- (55) Wright, C. C.; Hsu, F. F.; Arnett, E.; Dunaj, J. L.; Davidson, P. M.; Pacheco, S. A.; Harriff, M. J.; Lewinsohn, D. M.; Schlesinger, L. S.; Purdy, G. E. The Mycobacterium Tuberculosis MmpL11 Cell Wall Lipid Transporter Is Important for Biofilm Formation, Intracellular Growth, and Nonreplicating Persistence. *Infect. Immun.* **2017**, *85* (8), e00131-17. <https://doi.org/10.1128/IAI>.
- (56) Bacon, J.; Alderwick, L. J.; Allnut, J. A.; Gabasova, E.; Watson, R.; Hatch, K. A.; Clark, S. O.; Jeeves, R. E.; Marriott, A.; Rayner, E.; Tolley, H.; Pearson, G.; Hall, G.; Besra, G. S.; Wernisch, L.; Williams, A.; Marsh, P. D. Non-Replicating Mycobacterium Tuberculosis Elicits a Reduced Infectivity Profile with Corresponding Modifications to the Cell Wall and Extracellular Matrix. *PLoS One* **2014**, *9* (2). <https://doi.org/10.1371/journal.pone.0087329>.
- (57) Dong, W.; Shi, J.; Chu, P.; Liu, R.; Wen, S.; Zhang, T.; Pang, Y.; Lu, J. Rv3131, a gene encoding nitroreductase, is essential for Metronidazole Activation in Mycobacterium Tuberculosis under Hypoxic Condition. *Res. Sq.* **2020**, 1–15.
- (58) Peddireddy, V.; Doddam, S. N.; Qureshi, I. A.; Yerra, P.; Ahmed, N. A Putative Nitroreductase from the DosR Regulon of Mycobacterium Tuberculosis Induces Pro-Inflammatory Cytokine Expression via TLR2 Signaling Pathway. *Sci. Rep.* **2016**, *6*, 1–9. <https://doi.org/10.1038/srep24535>.
- (59) Hu, Y.; Coates, A. R. M. Mycobacterium Tuberculosis Acg Gene Is Required for Growth and Virulence in Vivo. *PLoS One.* **2011**, *6* (6), e20958. <https://doi.org/10.1371/journal.pone.0020958>.
- (60) Singh, R.; Manjunatha, U.; Boshoff, H. I. M.; Young, H. H.; Niyomrattanakit, P.; Ledwidge, R.; Dowd, C. S.; Ill, Y. L.; Kim, P.; Zhang, L.; Kang, S.; Keller, T. H.; Jiricek, J.; Barry, C. E. PA-824 Kills Nonreplicating Mycobacterium Tuberculosis by Intracellular NO Release. *Science.* **2008**, *322* (5906), 1392–1395. <https://doi.org/10.1126/science.1164571>.
- (61) Conradie, F.; Bagdasaryan, T. R.; Borisov, S.; Howell, P.; Mikiashvili, L.; Ngubane, N.; Samoilova, A.; Skornykova, S.; Tudor, E.; Variava, E.; Yablonskiy, P.; Everitt, D.; Wills, G. H.; Sun, E.; Olugbosi, M.; Egizi, E.; Li, M.; Holsta, A.; Timm, J.; Bateson, A.; Crook, A. M.; Fabiane, S. M.; Hunt, R.; McHugh, T. D.; Tweed, C. D.; Foraida, S.; Mendel, C. M.; Spigelman, M. Bedaquiline–Pretomanid–Linezolid Regimens for Drug-Resistant Tuberculosis. *New Eng. J. Med.* **2022**, *387* (9), 810–823. <https://doi.org/10.1056/NEJMoa2119430>.
- (62) Matsumoto, M.; Hashizume, H.; Tomishige, T.; Kawasaki, M.; Tsubouchi, H.; Sasaki, H.; Shimokawa, Y.; Komatsu, M. OPC-67683, a Nitro-Dihydro-Imidazooxazole Derivative with Promising Action against Tuberculosis in Vitro and in Mice. *PLoS Med.* **2006**, *3* (11), 2131–2144. <https://doi.org/10.1371/journal.pmed.0030466>.
- (63) Kim, C. T.; Kim, T.-O.; Shin, H.-J.; Ko, Y. C.; Hun Choe, Y.; Kim, H.-R.; Kwon, Y.-S. Bedaquiline and Delamanid for the Treatment of Multidrug-Resistant Tuberculosis: A

- Multicentre Cohort Study in Korea. *Eur. Respir. J.* **2018**, *51* (3), 1702467. <https://doi.org/10.1183/13993003.02467-2017>.
- (64) Upton, A. M.; Cho, S.; Yang, T. J.; Kim, A. Y.; Wang, Y.; Lu, Y.; Wang, B.; Xu, J.; Mdluli, K.; Ma, Z.; Franzblaub, S. G. In Vitro and in Vivo Activities of the Nitroimidazole TBA-354 against Mycobacterium Tuberculosis. *Antimicrob. Agents Chemother.* **2015**, *59* (1), 136–144. <https://doi.org/10.1128/AAC.03823-14>.
- (65) Albesa-Jové, D.; Chiarelli, L. R.; Makarov, V.; Pasca, M. R.; Urresti, S.; Mori, G.; Salina, E.; Vocat, A.; Comino, N.; Mohorko, E.; Ryabova, S.; Pfeiffer, B.; Lopes Ribeiro, A. L. D. J.; Rodrigo-Unzueta, A.; Tersa, M.; Zanoni, G.; Buroni, S.; Altmann, K. H.; Hartkoorn, R. C.; Glockshuber, R.; Cole, S. T.; Riccardi, G.; Guerin, M. E. Rv2466c Mediates the Activation of TP053 to Kill Replicating and Non-Replicating Mycobacterium Tuberculosis. *ACS Chem. Biol.* **2014**, *9* (7), 1567–1575. <https://doi.org/10.1021/cb500149m>.
- (66) Mabhula, A. N. Investigating permeation of anti-mycobacterial agents in *Mycobacterium tuberculosis* and *M. tuberculosis*-infected macrophages in vitro as a model for early stage tuberculosis drug discovery. Ph.D. dissertation, University of Cape Town, South Africa, 2020.



Moxifloxacin-Mediated Killing of *Mycobacterium tuberculosis* Involves Respiratory Downshift, Reductive Stress, and Accumulation of Reactive Oxygen Species

Somnath Shee,^{a,b}  Samsheer Singh,^{a,b*} Ashutosh Tripathi,^{a,b} Chandrani Thakur,^c Anand Kumar T,^d Mayashree Das,^{a,b} Vikas Yadav,^{a,b} Sakshi Kohli,^{a,b} Raju S. Rajmani,^b  Nagasuma Chandra,^c Harinath Chakrapani,^d Karl Drlica,^e  Amit Singh^{a,b}

^aDepartment of Microbiology and Cell Biology, Indian Institute of Science, Bangalore, Karnataka, India

^bCentre for Infectious Disease Research, Indian Institute of Science, Bangalore, Karnataka, India

^cDepartment of Biochemistry, Indian Institute of Science, Bangalore, Karnataka, India

^dDepartment of Chemistry, Indian Institute of Science Education and Research Pune, Pune, Maharashtra, India

^ePublic Health Research Institute and Department of Microbiology, Biochemistry & Molecular Genetics, New Jersey Medical School, Rutgers Biomedical and Health Sciences, Rutgers University, Newark, New Jersey, USA

Somnath Shee and Samsheer Singh contributed equally to this work. Author order was determined by relative contribution to this work.

ABSTRACT Moxifloxacin is central to treatment of multidrug-resistant tuberculosis. Effects of moxifloxacin on the *Mycobacterium tuberculosis* redox state were explored to identify strategies for increasing lethality and reducing the prevalence of extensively resistant tuberculosis. A noninvasive redox biosensor and a reactive oxygen species (ROS)-sensitive dye revealed that moxifloxacin induces oxidative stress correlated with *M. tuberculosis* death. Moxifloxacin lethality was mitigated by supplementing bacterial cultures with an ROS scavenger (thiourea), an iron chelator (bipyridyl), and, after drug removal, an antioxidant enzyme (catalase). Lethality was also reduced by hypoxia and nutrient starvation. Moxifloxacin increased the expression of genes involved in the oxidative stress response, iron-sulfur cluster biogenesis, and DNA repair. Surprisingly, and in contrast with *Escherichia coli* studies, moxifloxacin decreased expression of genes involved in respiration, suppressed oxygen consumption, increased the NADH/NAD⁺ ratio, and increased the labile iron pool in *M. tuberculosis*. Lowering the NADH/NAD⁺ ratio in *M. tuberculosis* revealed that NADH-reductive stress facilitates an iron-mediated ROS surge and moxifloxacin lethality. Treatment with *N*-acetyl cysteine (NAC) accelerated respiration and ROS production, increased moxifloxacin lethality, and lowered the mutant prevention concentration. Moxifloxacin induced redox stress in *M. tuberculosis* inside macrophages, and cotreatment with NAC potentiated the antimycobacterial efficacy of moxifloxacin during nutrient starvation, inside macrophages, and in mice, where NAC restricted the emergence of resistance. Thus, NADH-reductive stress contributes to moxifloxacin-mediated killing of *M. tuberculosis*, and the respiration stimulator (NAC) enhances lethality and suppresses the emergence of drug resistance.

KEYWORDS antimycobacterial, ROS, oxidative stress, moxifloxacin, fluoroquinolone, respiration, *N*-acetyl cysteine, redox biosensor, NADH, reductive stress, resistance

Antimicrobial resistance is a growing problem for the management of tuberculosis (TB). For example, between 2009 and 2016, the number of global cases of multidrug-resistant tuberculosis (MDR-TB), defined as resistance of *Mycobacterium tuberculosis* to at least rifampin and isoniazid, increased annually by over 20% (1). Tuberculosis with additional resistance to a fluoroquinolone and at least one of three injectable agents (kanamycin, amikacin, or capreomycin), termed extensively drug-resistant tuberculosis (XDR-TB), accounted for about 6% of MDR-TB cases in 2018 (2). Alarming, the annual XDR-TB cases reported worldwide increased almost 10-fold between 2011 and 2018 (2, 3). Increased prevalence of XDR-TB is not surprising,

Copyright © 2022 American Society for Microbiology. All Rights Reserved.

Address correspondence to Amit Singh, asingh@iisc.ac.in, or Karl Drlica, drlicaka@njms.rutgers.edu.

*Present address: Samsheer Singh, Lee Kong Chian School of Medicine, Nanyang Technological University Singapore, Singapore. The authors declare no conflict of interest.

Received 26 April 2022

Returned for modification 6 June 2022

Accepted 25 July 2022

Published 17 August 2022

since the fluoroquinolone-containing combination therapies used to halt progression to XDR-TB utilized early quinolones (ciprofloxacin, ofloxacin, and sparfloxacin) that are only modestly effective anti-TB agents (4).

Efforts to find more active fluoroquinolones led to C-8 methoxy derivatives that exhibit improved ability to kill *M. tuberculosis* *in vitro* (5). Two of these compounds, moxifloxacin and gatifloxacin, have been examined as anti-TB agents (6–8). Preclinical studies with moxifloxacin in murine TB models demonstrate effective treatment with reduced relapse frequency as well as treatment-shortening properties (9). Indeed, single-drug clinical studies indicate that the early bactericidal activity of moxifloxacin is similar to that of first-line anti-TB drugs, such as isoniazid and rifampicin. Thus, moxifloxacin could be part of effective multidrug combination treatments to shorten therapy time (10, 11). Shorter treatment could increase treatment compliance, further limiting the progression of MDR- to XDR-TB. However, multiple phase III clinical trials have failed to corroborate the preclinical efficacy data, as moxifloxacin did not shorten treatment time (12–14). One approach for increasing moxifloxacin efficacy is to find ways to increase its lethal action.

The fluoroquinolones have two mechanistically distinct antibacterial effects: (i) they block growth by forming reversible drug-gyrase-DNA complexes that rapidly inhibit DNA synthesis, and (ii) they kill cells (15). Death appears to arise in two ways, one through chromosome fragmentation and the other through accumulation of reactive oxygen species (ROS) (15). The latter appear to dominate when DNA repair is proficient (16, 17). We are particularly interested in fluoroquinolone lethality, because *M. tuberculosis* possesses a remarkable ability to evade host immune pressures (18). In the absence of an effective immune response, bactericidal drugs are essential for clearing infection quickly. If the redox-based mechanisms of fluoroquinolone lethality seen with *Escherichia coli* extend to *M. tuberculosis*, opportunities may exist for increasing ROS and lethality, thereby reducing treatment duration and increasing the cure rate for MDR-TB.

Several methods are available for assessing the contribution of ROS to bactericidal activity. Among these are direct detection of ROS levels using ROS-sensitive dyes, characterization of mutants known to alter ROS levels, and examination of the effects of agents known to suppress ROS accumulation. The present work adds detection of antibiotic-induced changes in redox physiology of *M. tuberculosis* using a noninvasive, genetic biosensor (Mrx1-roGFP2) (19). The sensor measures the redox potential (E_{MSH}) of a major mycobacterial thiol buffer, mycothiol, thereby assessing oxidative effects independently of radical-sensitive fluorescent dye methods whose interpretation has been debated (20, 21). Mrx1-roGFP2 is well suited for this work, as it has been used to measure E_{MSH} of *M. tuberculosis* during *in vitro* growth, infection of macrophages, and exposure to nonquinolone antimicrobials (19, 22–24).

In the present work, we began by asking how well *M. tuberculosis* fits the paradigm for ROS-mediated killing by antimicrobials as developed from studies using *E. coli*. We used moxifloxacin as a lethal stressor, because the fluoroquinolones are among the better-understood agents and because moxifloxacin is potentially important for tuberculosis control. *M. tuberculosis* deviated markedly from *E. coli* by suppressing respiration rather than increasing it during fluoroquinolone-mediated stress. That raised questions about the source of ROS accumulation, since in *E. coli*, ROS levels correlate with increased, not decreased, respiration. We found that an increase in NADH (reductive stress) accounted for the increase in ROS and lethality. When we artificially raised respiration, ROS levels increased, and we observed enhanced moxifloxacin lethality *in vitro*, inside macrophages, and in a murine model of infection. Raising respiration by *N*-acetyl cysteine (NAC) treatment also reduced the emergence of resistance. Thus, the work provides a mechanistic basis for developing respiration enhancers to increase the lethal action of moxifloxacin and perhaps other anti-TB agents.

RESULTS

Moxifloxacin-mediated lethality associated with oxidative stress during aerobic growth. To obtain a reference point for *M. tuberculosis* susceptibility to moxifloxacin, we determined MIC using the resazurin microtiter assay (REMA) (25). The MIC of moxifloxacin ranged from 0.125 μM to 0.5 μM . The MICs were similar for H37Rv and several drug-resistant strains (see Table S1 in the supplemental material; similarity in MICs was also seen for

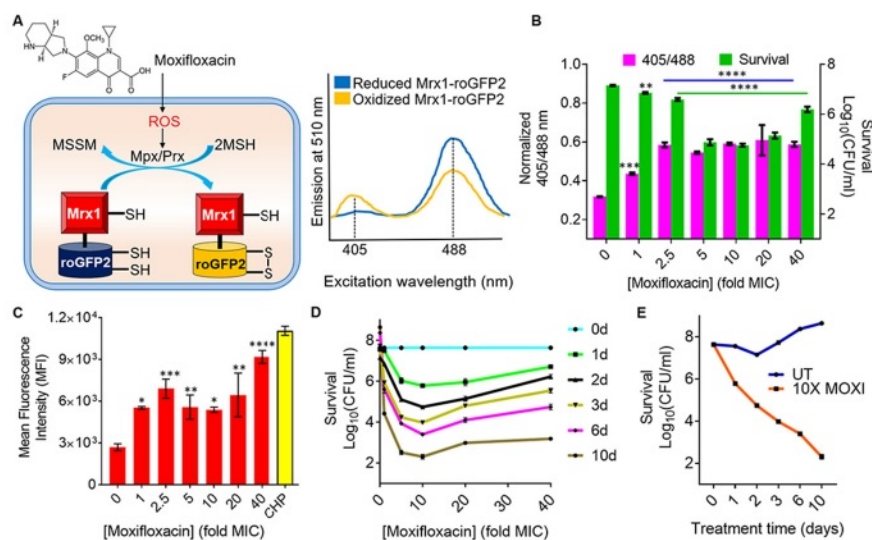


FIG 1 Effect of moxifloxacin on biosensor oxidation, ROS level, and bacterial survival. (A) Moxifloxacin increases oxidative stress, which increases the ratio of oxidized (MSSM) to reduced (MSSH) mycothiol via mycothiol-dependent peroxidoredoxin (Prx) or peroxidase (Mpx). Oxidation of Mrx1-roGFP2 increases fluorescence intensity for excitation at ~ 400 nm and decreases it for excitation at ~ 490 nm. (B) Strain *M. tuberculosis* roGFP2 was exposed to the indicated concentrations of moxifloxacin ($1 \times \text{MIC} = 0.5 \mu\text{M}$) for 48 h, and the ratiometric response of the biosensor and survival following treatment were determined. (C) Cells were treated as for panel B, and ROS were quantified by flow cytometry using CellROX deep red dye. Cumene hydroperoxide (CHP; 10 mM) served as a positive control. Data represent mean fluorescence intensity of the dye. (D) Exponentially growing *M. tuberculosis* H37Rv was treated with moxifloxacin at the indicated concentrations for the indicated times; survival was assessed by determining CFU. (E) Time-kill curves for *M. tuberculosis* treated with $10 \times \text{MIC}$ of moxifloxacin. Error bars represent standard deviations from the mean. Data represent at least two independent experiments performed in at least duplicate. Statistical significance was calculated against the no-treatment control (****, $P < 0.0001$; ***, $P < 0.001$; **, $P < 0.01$; *, $P < 0.05$).

levofloxacin and ciprofloxacin with different *M. tuberculosis* strains). Thus, strain H37Rv appeared to be representative and appropriate for subsequent experiments.

As an initial probe for moxifloxacin-induced oxidative stress, we examined a transformant of *M. tuberculosis* strain H37Rv that expresses the redox biosensor Mrx1-roGFP2 from a plasmid (strain *Mtb-roGFP2*). This biosensor reports the redox state of the mycothiol redox couple (reduced mycothiol [MSSH]/oxidized mycothiol [MSSM]) in the bacterial cytosol (Fig. 1A) (19). Exposure of *Mtb-roGFP2* to hydrogen peroxide (H_2O_2) led to rapid (5 min) oxidation of the biosensor in a concentration-dependent manner (Fig. S1). A 2-fold increase in the biosensor ratio is equivalent to the oxidative stress inside *M. tuberculosis* following treatment with $500 \mu\text{M}$ H_2O_2 (Fig. S1).

Increasing moxifloxacin concentration, up to $2.5 \times \text{MIC}$ ($1 \times \text{MIC} = 0.5 \mu\text{M}$) during a 48-h incubation, increased the biosensor ratiometric signal by almost 2-fold (Fig. 1B; also, see Fig. S2A and C), indicating elevated levels of MSSM. Above $2.5 \times \text{MIC}$, MSSM levels appeared to plateau. Measurement of ROS with CellROX deep red showed a similar increase to $2.5 \times \text{MIC}$ of moxifloxacin, followed by a plateau of mean fluorescence intensity (Fig. 1C). Moxifloxacin treatment damaged DNA and oxidized lipids (Fig. S3), indicating that drug-induced oxidative stress kills *M. tuberculosis* by degrading essential biomolecules.

Maximum bacterial killing was observed at $10 \times \text{MIC}$, a concentration at which survival decreased by $\sim 2 \log_{10}$ -fold at treatment day 1 and by $6 \log_{10}$ -fold at treatment day 10 (Fig. 1D and E). Survival dropped in a concentration-dependent manner, with a minimum being reached at a higher concentration than observed for maximal oxidative stress ($10 \times \text{MIC}$) (Fig. 1B to D). The discordance between the biosensor signal plateauing at $2.5 \times \text{MIC}$ and killing continuing to $10 \times \text{MIC}$ (Fig. 1B) could be explained by the existence of two lethal mechanisms. One mechanism, chromosome fragmentation (8, 26), likely dominates at high quinolone concentrations, with an ROS-based mechanism dominating at lower concentrations. Indeed, for norfloxacin treatment of *E. coli*, oxidative effects on killing are seen only at low to moderate

drug concentrations (27). As expected, oxidative stress was not observed in *M. tuberculosis* treated with subinhibitory concentrations of moxifloxacin (Fig. S2A). The increase in biosensor signal was observed as early as 12 h after initiation of moxifloxacin treatment (half the doubling time of untreated control cells); it then increased significantly at 48 h (Fig. S2A and B). Thus, ROS production precedes and contributes to the death of *M. tuberculosis*. As expected, ROS levels in a moxifloxacin-resistant isolate of *M. tuberculosis* remained low upon treatment with moxifloxacin (Fig. S4A).

We also compared the ability of a weakly effective fluoroquinolone (ciprofloxacin; minimal bactericidal concentration [MBC] = 2 μ M; Table S2), a moderately effective compound (levofloxacin, MBC = 1 μ M), and moxifloxacin (MBC = 0.5 μ M) to oxidize the biosensor, all at 2.5-fold MBC. Moxifloxacin induced biosensor oxidation after treatment for 12 h and 24 h (Fig. S4B). In contrast, ciprofloxacin did not induce biosensor oxidation, and levofloxacin triggered oxidative stress only after a 24-h treatment (Fig. S4B). Thus, ROS levels do not correlate with MBC, a parameter obtained after a long incubation (see Discussion). The more active quinolones are also more bactericidal at the same fold MIC for several bacterial species, including mycobacteria (5, 28, 29). These data corroborate the link between oxidative stress and moxifloxacin lethality.

High-dose chemotherapy is postulated to slow the emergence of drug resistance if the drug concentration is above the mutant prevention concentration (MPC) (30). However, bacterial strains can paradoxically show elevated survival levels at extremely high drug concentrations. In the case of nalidixic acid at very high concentration, *E. coli* survival can be 100% (31). Similarly, *M. tuberculosis* survival increased dramatically at high moxifloxacin concentration (Fig. 1D).

Some aspects of high-concentration survival are discordant when *E. coli* and *M. tuberculosis* are compared. For example, with *E. coli*, this phenotype of high-concentration survival is associated with reduced ROS levels (31); with *M. tuberculosis*, the biosensor and CellROX signals remained high at high levels of moxifloxacin (Fig. 1B and C). This difference between the organisms, which is unexplained, encouraged further comparisons.

Reduction of moxifloxacin-mediated killing of *M. tuberculosis* by ROS-mitigating agents. Work with *E. coli* supports the idea that ROS contribute to quinolone-mediated killing of bacteria (15). For example, superoxide ($O_2^{\cdot-}$) damages Fe-S clusters and increases the free iron (Fe) pool (32), which may then drive the generation of toxic hydroxyl radical ($HO\cdot$) via the Fenton reaction (26, 33). To examine the effects of Fe, we assessed ROS levels in *M. tuberculosis* grown in minimal medium under Fe-deficient and Fe-excess conditions. Fe overload raised ROS levels (Fig. S5). Treatment with thiourea (TU), a thiol-based scavenger of ROS, reversed the Fe-induced ROS increase (Fig. S5). During moxifloxacin treatment of *M. tuberculosis*, a concentration-dependent increase in free Fe occurs (Fig. S6). Pretreatment with thiourea at the nontoxic concentration of 10 mM (34) increased survival of *M. tuberculosis* by almost 10-fold during cotreatment with moxifloxacin ($1\times$ to $10\times$ MIC) (Fig. 2A and B; Fig. S7). These data support the connection between ROS accumulation and moxifloxacin-mediated killing.

Another test involves chelating free ferrous Fe with bipyridyl, a high-affinity Fe^{2+} chelator: with *E. coli*, bipyridyl lowers the lethal action of multiple lethal stressors (33, 35). When we treated *M. tuberculosis* cultures with a noninhibitory concentration (250 μ M) of bipyridyl before moxifloxacin (Fig. 2A), killing was reduced by >100 -fold (Fig. 2C), and ROS accumulation was lowered (Fig. 2D). Treatment with bipyridyl or thiourea also protected cells from moxifloxacin-mediated DNA damage and lipid peroxidation (Fig. S3A and B). Collectively, the data indicate that Fe-mediated ROS production is the underlying oxidative stress associated with moxifloxacin lethality.

Work with *E. coli* also indicates that ROS accumulates even after removal of a lethal stressor (16). When we treated *M. tuberculosis* with moxifloxacin in liquid medium and then plated cells on antibiotic-free 7H11 agar (see the scheme in Fig. 2E), we found that addition of catalase to the agar reduced bacterial killing (Fig. 2F; peroxide diffuses freely across the cell membrane [36], allowing exogenous catalase to reduce endogenous ROS levels). Replacement of catalase with 2.5% bovine serum albumin, which is not expected to degrade peroxide, failed to protect *M. tuberculosis* from moxifloxacin-mediated killing (Fig. S8). Finding that an anti-ROS agent

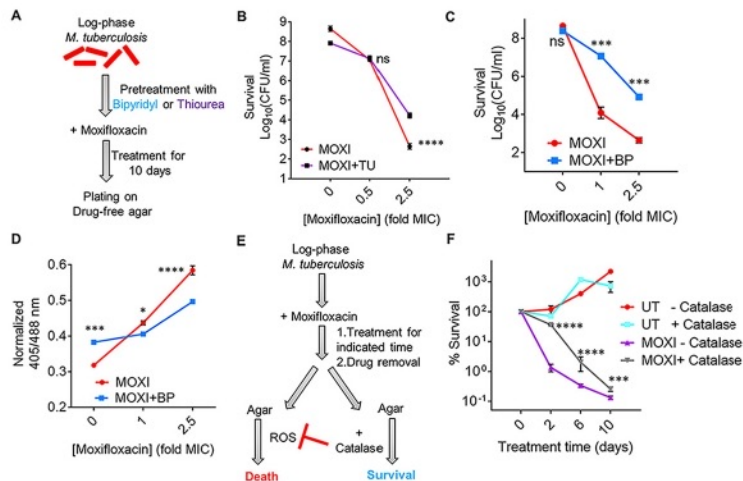


FIG 2 ROS mitigation reduces moxifloxacin-mediated killing of *M. tuberculosis*. (A) Plan for detecting thiourea (TU) and bipyridyl (BP) effects on moxifloxacin lethality. (B) Exponentially growing *M. tuberculosis* H37Rv cultures were either left untreated or treated with 10 mM TU for 1 h before addition of the indicated concentrations of moxifloxacin (MOXI; $1\times$ MIC = $0.5\ \mu\text{M}$) for 10 days followed by determination of CFU. (C) Effect of bipyridyl. *M. tuberculosis* as for panel B was untreated or treated with $250\ \mu\text{M}$ BP for 15 min prior to addition moxifloxacin as for panel B. (D) The Mrx1-roGFP2 biosensor ratiometric response was determined after 48 h treatment of *M. tuberculosis* cultures with the indicated concentrations of MOXI alone or with $250\ \mu\text{M}$ BP. (E) *M. tuberculosis* cultures were treated with moxifloxacin, the drug was removed by washing, and cells were plated on drug-free 7H11 agar with or without catalase followed by CFU determination. (F) *M. tuberculosis* cultures were treated with $1\times$ MIC of moxifloxacin for the indicated times, washed, and plated with or without catalase ($17.5\ \text{U/mL}$ of agar). Percentage survival was calculated relative to CFU of cultures at 0 h. Statistical significance was calculated between the drug-alone group and the drug + catalase group. Statistical considerations were as in Fig. 1.

suppresses killing after the removal of moxifloxacin indicates that the primary damage (rapid formation of fluoroquinolone-gyrase-DNA complexes) can be insufficient to kill *M. tuberculosis*. Thus, the poststressor accumulation of ROS and death demonstrated with *E. coli* occurs with *M. tuberculosis*.

We note that shorter drug treatment times in 7H9 broth (2 days) prior to catalase treatment on drug-free agar resulted in higher survival levels than longer times (6 to 10 days) (Fig. 2F). However, at later time points (6 to 10 days treatment with moxifloxacin), the protective effect of catalase on bacterial survival decreased (Fig. 2F). A similar phenomenon has been observed with *E. coli* (16). These data likely reflect ROS acting rapidly to cause accelerated lethality and then having little effect on long-term killing. Overall, studies with ROS-mitigating agents indicate that ROS contribute causally to quinolone-mediated lethality with both *E. coli* and *M. tuberculosis*.

Reduction of moxifloxacin lethality by nutrient starvation and hypoxia. Our data support previous work (37) in which nutrient starvation blocked the lethal action of moxifloxacin (Loebel-cidal concentration [LCC_{90}] $> 32\ \mu\text{M}$) (Fig. S9A and B; Table S2). This phenomenon has also been reported for older quinolones with *E. coli* (17). With *E. coli*, these effects have been attributed to a metabolic shift that suppresses respiration, which is thought to be a major source of ROS.

Previous work (37, 38) also shows that hypoxic conditions reduce the lethal action of older fluoroquinolones with *M. tuberculosis*. We confirmed this observation by showing that moxifloxacin-mediated killing decreases significantly under hypoxic conditions (Fig. S9A and C; Table S2). With the Wayne-cidal concentration (WCC_{90}) assay (37), the moxifloxacin concentration required to kill 90% of hypoxic bacteria after 5 days of drug treatment was $\sim 10\ \mu\text{M}$ (Table S2). This value corresponds to $20\times$ MIC, or 22-fold higher than the 90% lethal dose (LD_{90}) with *M. tuberculosis* ($0.45\ \mu\text{M}$) cultured under aerobic growth conditions for the same treatment time (Fig. S10).

The hypoxia results are concordant with moxifloxacin lethality being associated with an increase in ROS, an event that should be suppressed by O_2 limitation (intracellular generation

of ROS may depend largely on the transfer of electrons directly to molecular O₂ [39]). However, hypoxic suppression of moxifloxacin lethality could be due to decreased respiration. To test this hypothesis, we stimulated anaerobic respiration by providing nitrate as an alternative electron acceptor (40), since it restores norfloxacin lethality with anaerobic *E. coli* (20). Surprisingly, nitrate lowered residual anaerobic lethality of moxifloxacin by severalfold (Fig. S9D). Nitrate was even more protective with *M. tuberculosis* exposed to metronidazole (Fig. S9D), an antimicrobial known to be lethal in the absence of oxygen (41). The surprising protective effect of nitrate, which is considered in more detail in Discussion, encouraged further comparisons with *E. coli*.

Effect of moxifloxacin on the *M. tuberculosis* transcriptome. When we examined the *M. tuberculosis* transcriptome using published data from a 16-h exposure to 2×, 4×, and 8× MIC of moxifloxacin (42), we found that 359 genes exhibited altered expression (2-fold change across all three treatment conditions). Of these, 219 genes were upregulated, and 140 were downregulated (Data Set S1). Next, we investigated whether deregulated expression of genes after prolonged moxifloxacin exposure (16 h) is largely a secondary effect of induction of other genes. To test this hypothesis, we compared early changes (4-h moxifloxacin exposure) in expression for a set of 28 genes deregulated at 16 h. We saw little difference (Fig. S11A and B). Thus, the patterns we observed at 16 h appear to largely reflect a primary transcription response.

When we classified the differentially expressed genes (DEGs) according to annotated functional categories (43), we found that "Information Pathways and Insertion Sequences and Phages" were 2-fold overrepresented in the moxifloxacin-treated *M. tuberculosis* transcriptome (Table S3). These data suggest that the bacterium responds to the drug mainly by regulating DNA remodeling, transcription, and translational machinery.

Increased expression was also seen with genes involved in redox homeostasis, such as thioredoxin (*trxB1* and *trxC*), thioredoxin reductase (*trxB2*), alkyl hydroperoxide reductase (*ahpC*), the SigH/RshA system, the copper-sensing transcriptional regulator *csoR*, and the *whiB* family (*whiB4* and *whiB7*) (Fig. 3A). Indeed, the transcriptome of moxifloxacin-treated *M. tuberculosis* showed a 67% overlap with the transcriptional signature of H₂O₂-treated cells (Fig. 3B) (44). Statistical analysis showed a significant overlap between the moxifloxacin transcriptome and the response to oxidative stress (H₂O₂; $P = 5.39e-14$) and nitrosative stress (NO; $P = 2.13e-8$) (Fig. S12; Table S4). Induction of oxidant-responsive genes (*sox*, *sod*, and *mar*) is also seen in norfloxacin-treated *E. coli* (26). Other conditions, such as hypoxia and acidic pH, showed nonsignificant overlap with the moxifloxacin transcriptome (Fig. S12; Table S4). Collectively, the data are consistent with our working hypothesis that fluoroquinolones stimulate ROS accumulation.

Several genes involved in repairing DNA (*recA*, *-O*, *-R*, and *-X*, *ruvABC*, *uvrD*, *ung*, *dnaE2*, *xthA*, *radA*, *alkA*, *lexA*, *nei*, and *ligB*), in DNA metabolism (*nrdF2*, *nrdR*, *pyrC*, and *pyrR*), and in Fe-S duster biogenesis (*sufR*) (45, 46) were also upregulated (Fig. 3A). *E. coli* treated with norfloxacin shows similar upregulation of DNA damage responses (*lexA*, *uvr*, and *rec* systems and error-prone DNA polymerases IV and V), nucleotide metabolism, and Fe-S cluster biogenesis (*iscRUSA*) (26). Such results are expected from the known ability of ROS to damage DNA (47, 48).

With *M. tuberculosis*, moxifloxacin suppressed expression of an Fe-responsive repressor (*hupB*) and an iron siderophore (*mbtF*), consistent with drug treatment increasing the intracellular pool of labile Fe (Fig. S6A). Additionally, the microarray data suggest that Fe-S clusters in *M. tuberculosis* are exposed to ROS during treatment with moxifloxacin, resulting in Fe release from damaged clusters and increased expression of Fe-S repair pathways (*sufR*). In contrast, *E. coli* upregulates Fe uptake machinery (26). Thus, *M. tuberculosis* and *E. coli* may generate ROS in different ways.

In *M. tuberculosis*, moxifloxacin repressed the expression of energy-efficient respiratory complexes, such as succinate dehydrogenase (*rv0248c* and *sdhC*), cytochrome *bc₁* (*qcrB*), and type I NADH dehydrogenase (*nuo* operon) (Fig. 3A). In contrast, the level of the energetically inefficient, non-proton-pumping *ndh* was increased. These data indicate that *M. tuberculosis* slows primary respiration and shifts to a lower energy state in response to moxifloxacin.

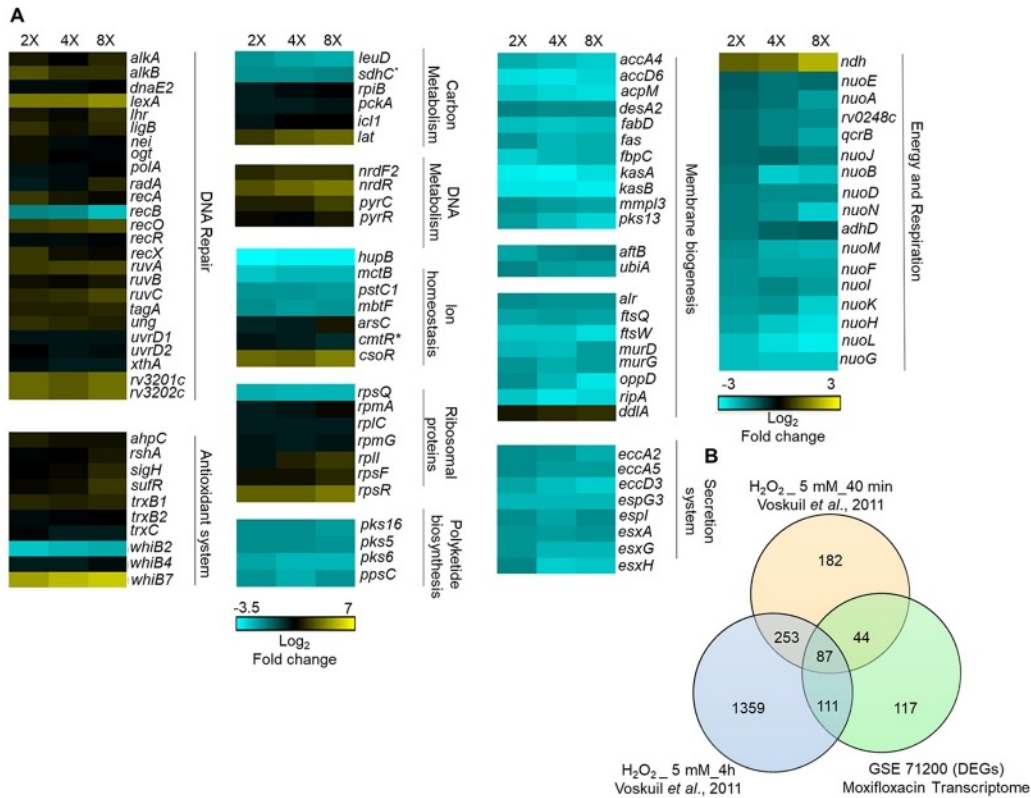


FIG 3 Whole-genome transcriptome profiling of *M. tuberculosis* treated with moxifloxacin. (A) Heat map showing gene expression changes due to 16-h treatment of *M. tuberculosis* with moxifloxacin. DEGs exhibited a 2-fold change across all three treatment conditions (2×, 4×, and 8× MIC of moxifloxacin; 1× MIC = 0.4 μM); the color code for the fold change is at the bottom of the second column (yellow, upregulated genes; turquoise, downregulated genes). Genes are grouped according to function. For genes belonging to bioenergetics processes, the color code for the fold change is at the bottom of the fourth column. *, *sdhC* and *cmrR* are deregulated in two treatment conditions (2× and 4×). (B) Venn diagram showing transcriptome overlap between moxifloxacin-mediated (green circle) and H₂O₂-mediated stress for *M. tuberculosis* (44); DEGs obtained with treatment with 5 mM H₂O₂ for 40 min and 5 mM H₂O₂ for 4 h are shown in beige and blue circles, respectively.

Indeed, several energy-requiring pathways (e.g., cell wall biosynthesis, cofactor biogenesis, cell division, transport, and ESX secretion systems) were downregulated (Fig. 3A and Data Set S1). Moreover, genes coordinating alternate carbon metabolism, such as the gluconeogenesis (*pckA*) and glyoxylate cycle (*icl1*) genes, were upregulated (Fig. 3A). Interestingly, *icl1* protects *M. tuberculosis* from anti-TB drugs (isoniazid, rifampicin, and streptomycin), presumably by counteracting redox imbalance induced by these antibiotics (34). The key idea is that *M. tuberculosis* enters a quasiquiescent metabolic state in response to stress from moxifloxacin, in contrast to fluoroquinolone effects on *E. coli* (20, 26).

Moxifloxacin slows respiration. As a direct test for decelerated respiration, we measured changes in the extracellular acidification rate (ECAR) and oxygen consumption rate (OCR) for moxifloxacin-treated *M. tuberculosis* as readouts for proton-extrusion into the extracellular medium (reflecting glycolysis and tricarboxylic acid [TCA] cycle activity) and for oxidative phosphorylation (OXPHOS), respectively, using a Seahorse XFp analyzer (23, 49). We incubated *M. tuberculosis* in unbuffered 7H9 medium with glucose in an XF microchamber and exposed the culture to 10× MIC of moxifloxacin and later to the uncoupler carbonyl cyanide *m*-chlorophenylhydrazone (CCCP; addition of CCCP stimulates respiration to the maximal level). Changes in OCR and ECAR are reported as percentage of third baseline value. The difference between basal and CCCP-induced OCR estimates the spare (reserve) respiratory capacity (SRC) available to counteract stressful conditions (49, 50).

As expected for a growing, drug-free culture of *M. tuberculosis*, OCR showed a gradual increase over the duration of the experiment (400 min); OCR increased further upon uncoupling by CCCP (Fig. 4A). In contrast, addition of 10× MIC of moxifloxacin inhibited the

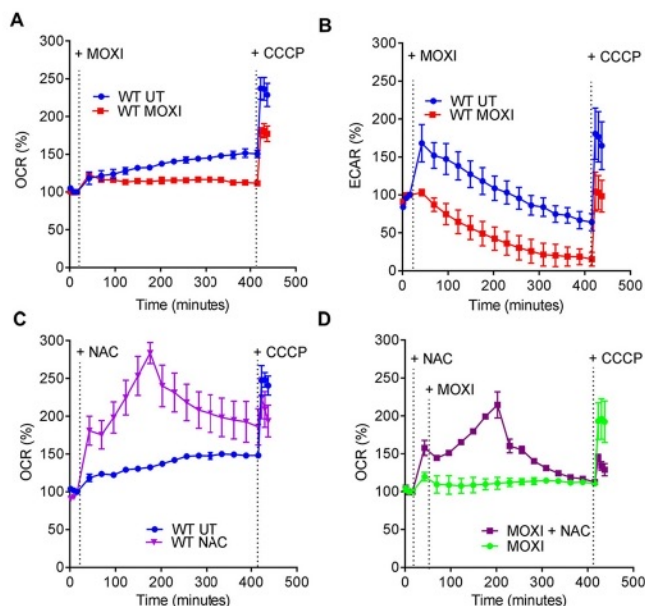


FIG 4 Moxifloxacin-mediated respiration arrest reversed by NAC. (A) OCR (pmol/min). Exponentially growing *M. tuberculosis* cultures were either left untreated (UT) or treated with 10 \times MIC of moxifloxacin (MOXI; 5 μ M) for the indicated times; black dotted lines indicate when MOXI, NAC (1 mM), or CCCP (10 μ M) was added. Determination was done with a Seahorse XFP analyzer. Data are percentages of third baseline values. (B) ECAR (mpH/min) (H^+ production or extracellular acidification due to glycolytic and TCA flux). Determination was as for OCR, with data representing percentages of third baseline values. (C and D) NAC (1 mM) addition enhanced OCR of (C) untreated and (D) MOXI-treated cells. Data are representative of two independent experiments performed in triplicate.

time-dependent increase in basal OCR (Fig. 4A), and the level of OCR upon uncoupling by CCCP was markedly lower than in the absence of moxifloxacin (Fig. 4A). In parallel, we measured viability of *M. tuberculosis* and found that the bacterial culture maintained 100% survival during the entire incubation period and for an additional 4 h (Fig. S13). Thus, the stalled oxygen consumption effect of moxifloxacin cannot be attributed to dead cells.

The ECAR response increased for 60 min and then gradually dropped for untreated bacteria. This transient, early increase in ECAR was absent in cultures of moxifloxacin-treated *M. tuberculosis*, which exhibited a greater reduction of ECAR than untreated cultures at late times (Fig. 4B). At the end of the experiment, moxifloxacin-treated cells were completely exhausted of glycolytic capacity (Fig. 4B). The slowing in OCR and ECAR was also seen with treatment at lower concentrations of moxifloxacin (1 \times and 2.5 \times MIC) (Fig. S14), while an anti-TB drug (ethambutol) that does not generate ROS failed to significantly affect either OCR or ECAR (Fig. S15).

In summary, moxifloxacin decelerates respiration and carbon catabolism in *M. tuberculosis*, which likely renders the bacterium metabolically quiescent and therefore less readily killed by moxifloxacin. In support of this hypothesis, a recent study showed that pretreatment with inhibitors of the electron transport chain (ETC), such as the anti-TB drugs bedaquiline (an ATP synthase inhibitor) and Q203 (a cytochrome *c* oxidase inhibitor), reduces moxifloxacin-mediated killing of *M. tuberculosis* (51).

ROS derive from increased NADH. Since moxifloxacin slows respiratory metabolism (Fig. 4A) while increasing ROS levels (Fig. 1B and C), a source of ROS other than respiration must exist. Slowed respiration during anoxia or chemical hypoxia places the ETC in a reduced state, and NADH accumulates. This phenomenon is known as reductive stress (52). Using a redox cycling assay, we detected accumulation of NADH in *M. tuberculosis* treated with 1 \times , 2.5 \times , and 10 \times MIC of moxifloxacin at 48 h (Fig. 5A). NAD^+ was raised at 1 \times MIC of moxifloxacin, but it showed no significant difference from the untreated control at elevated moxifloxacin concentrations (Fig. 5B); the total NAD/H pool decreased at high drug concentrations (2.5 \times and 10 \times MIC; Fig. S16). Thus, the NADH/ NAD^+ ratio increased as moxifloxacin concentration increased (Fig. 5C), indicating reductive stress.

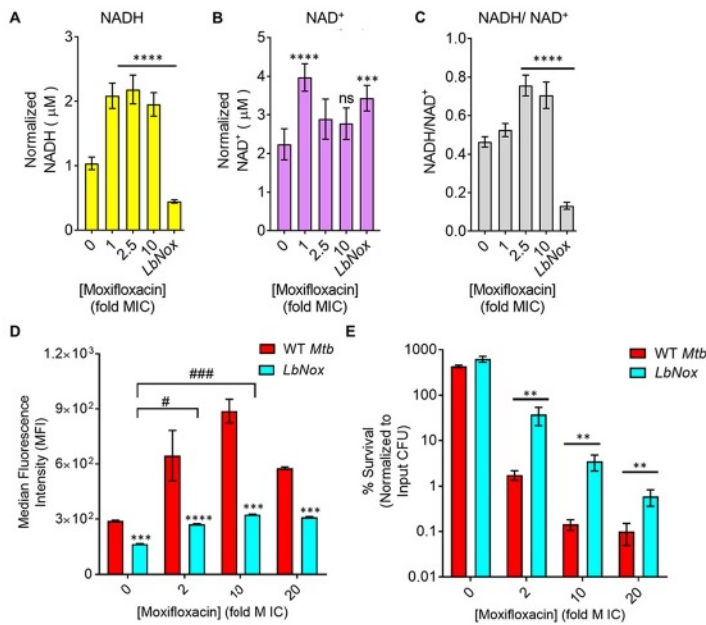


FIG 5 Dissipation of NADH reductive stress diminishes moxifloxacin-induced ROS increase and lethality with *M. tuberculosis*. (A and B) Detection of (A) NADH and (B) NAD⁺ levels. *M. tuberculosis* was treated with moxifloxacin (1× MIC = 0.5 μM) for 2 days, and NADH and NAD⁺ levels were determined by an alcohol dehydrogenase-based redox cycling assay. (C) NADH/NAD⁺ ratio. Untreated *M. tuberculosis* expressing *LbNox* served as a control. *P* was determined by unpaired two-tailed Student's *t* test analyzed relative to the untreated control. (D) ROS response to moxifloxacin. Wild-type *M. tuberculosis* H37Rv (WT *Mtb*) and cells expressing *LbNox* were exposed to the indicated concentrations of moxifloxacin for 48 h, and ROS were quantified by flow cytometry using CellROX deep red. (E) Cultures of exponentially growing wild-type *M. tuberculosis* (WT *Mtb*) and *LbNox* were treated with the indicated concentrations of moxifloxacin for 48 h, and survival was assessed by determining CFU. Statistical considerations were as for Fig. 1 (****, *P* < 0.0001; *** and ###, *P* < 0.001; **, *P* < 0.01; #, *P* < 0.05; ns, not significant).

We also assessed NADH-reductive stress by expressing a genetically encoded, non-invasive biosensor of the NADH/NAD⁺ ratio (Peredox) (53) (Fig. S17). A ratiometric increase in Peredox fluorescence indicated an increase in the NADH/NAD⁺ ratio upon moxifloxacin treatment (1× to 40× MIC) at 48 h. We observed a similar increase in the Peredox ratio upon treatment of *M. tuberculosis* with bedaquiline, a drug known to increase the NADH/NAD⁺ ratio (Fig. S17) (53). As with NADH, NADPH accumulated, and the NADPH/NADP⁺ ratio increased in response to moxifloxacin treatment (Fig. S18). Thus, moxifloxacin triggers NAD(P)H accumulation in *M. tuberculosis*.

In principle, stalled ETC and excessive reducing equivalents (NADH) can stimulate ROS production in two ways. In one, NADH mobilizes bound iron, thereby increasing the labile iron pool (54). As previously mentioned, we found a drug-concentration-dependent increase in the free iron pool in *M. tuberculosis* after moxifloxacin treatment (Fig. S6). Additionally, NADH autooxidation keeps iron in a reduced state (Fe²⁺); thus, NADH can drive the Fenton reaction toward hydroxyl radical generation (54). Second, reduced components of the electron transport chain can directly transfer electrons to molecular oxygen to generate ROS (55, 56). If these ideas are correct, dissipation of the NADH overload, i.e., reductive stress, should lower the labile iron pool, ROS surge, and moxifloxacin lethality.

We lowered the NADH/NAD⁺ ratio with an *M. tuberculosis* strain that constitutively expresses *Lactobacillus brevis* NADH oxidase (*Mtb-LbNox*) (Fig. 5C; Fig. S17) (57). In comparison to wild-type *M. tuberculosis*, *Mtb-LbNox* shows decreased levels of NADH and increased NAD⁺ without affecting the total pool of NAD⁺ + NADH (Fig. 5A to C; Fig. S19). As expected, moxifloxacin-treated *Mtb-LbNox* displayed a significantly reduced free-iron pool (Fig. S6), ROS surge (Fig. 5D), decreased DNA damage (Fig. S6), and a 25- to 30-fold-higher survival rate than wild-type cells (Fig. 5E). Thus, the increased NADH/NAD⁺ ratio occurring during metabolic quiescence caused by moxifloxacin accounts for the increased labile iron pool, which in turn catalyzes Fenton-mediated production of ROS and cell death.

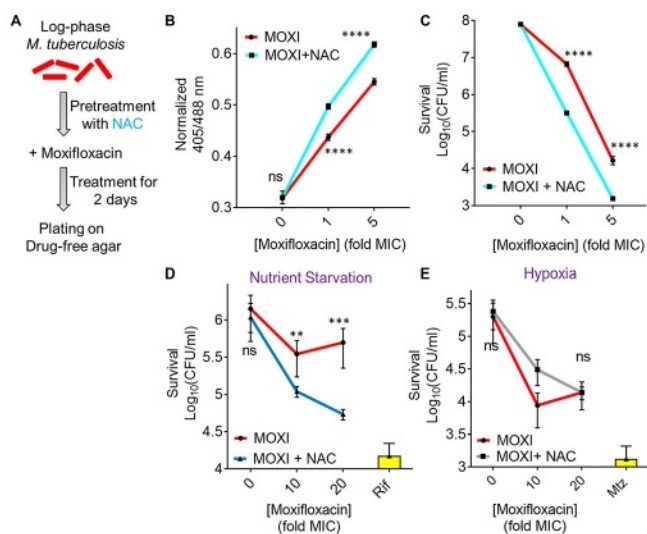


FIG 6 *N*-acetyl cysteine increases oxidative stress and moxifloxacin-mediated killing of *M. tuberculosis*. NAC (1 mM) was administered 1 h before addition of moxifloxacin (MOXI; $1 \times \text{MIC} = 0.5 \mu\text{M}$) at the indicated concentrations followed by 48 h of incubation. (A) Experimental plan. (B) Oxidative stress, measured by the ratiometric response of the Mrx1-roGFP2 biosensor. (C) Bacterial survival, measured by plating on 7H11 agar. (D) Effect of NAC and moxifloxacin combination with dormant bacilli. *M. tuberculosis* cultures were starved of nutrients for 14 days and then treated with moxifloxacin for 5 days in the presence or absence of NAC (1 mM) before determination of survival. Rifampicin (Rif; $25 \mu\text{M}$) served as a positive control. (E) NAC (1 mM) was added when cultures were placed in Vacutainer tubes followed by the treatment conditions indicated in Fig. S2A and D. Metronidazole (Mtz; 10 mM) served as a positive control. Statistical considerations were as for Fig. 1.

The growth, OCR, and ECAR of *Mtb-LbNox* in 7H9 broth were the same as those of wild-type cells (Fig. S20). Furthermore, the MICs of moxifloxacin and other anti-TB drugs (rifampicin, ethambutol, and bedaquiline) for *Mtb-LbNox* were similar to those for wild-type *M. tuberculosis* (Tables S1 and S5), indicating that the interaction between drug and its primary target is unaffected by overexpression of *LbNox*. In contrast, *Mtb-LbNox* exhibited a 2-fold-lower MIC of isoniazid, which is consistent with the interaction of isoniazid and its primary target (enoyl acyl carrier protein [enoyl-ACP] reductase [InhA]) depending on the NADH/NAD⁺ ratio in *M. tuberculosis* (58). Thus, overexpression of *LbNox* appears to have no effect on growth, metabolism, or respiration of *M. tuberculosis* that would complicate our interpretation that NADH dissipation protects from moxifloxacin-mediated killing.

***N*-acetyl cysteine stimulates respiration, oxidative stress, and moxifloxacin lethality.**

Previous work showed that stimulating respiration using cysteine and *N*-acetyl cysteine (NAC) elevates the killing activity of combinations of anti-TB drugs (59, 60). Since *M. tuberculosis* responded to moxifloxacin by dampening OXPHOS, we expected that countering the dampening with NAC would provide a way to increase ROS further and therefore enhance moxifloxacin lethality. We first measured time-dependent changes in OCR of *M. tuberculosis* upon exposure to a nontoxic dose of NAC (1 mM). Addition of NAC alone produced a sharp increase in OCR that reached its maximal level by 200 min (Fig. 4C). At later times, OCR gradually declined; it did not increase upon addition of CCCP (Fig. 4C), indicating that NAC-stimulated respiration exhausted the spare respiratory capacity of *M. tuberculosis*. Pretreatment with NAC reversed moxifloxacin-mediated slowing of respiration (Fig. 4D). As with NAC alone, the OCR of *M. tuberculosis*, treated with NAC plus moxifloxacin, increased for 200 min and then gradually dropped; CCCP remained ineffective at stimulating OCR (Fig. 4D). These data indicate that NAC-stimulated oxygen consumption by *M. tuberculosis* overcomes the dampening effect of moxifloxacin on bacterial respiration.

Respiration, stimulated by NAC, augmented ROS accumulation upon moxifloxacin treatment and increased lethality (Fig. 6A). NAC elevated the Mrx1-roGFP2-dependent redox signal for moxifloxacin-treated *M. tuberculosis*, confirming the increase in oxidative stress (Fig. 6B; Fig. S2C and D). We emphasize that NAC had no effect on moxifloxacin MIC, as

measured by REMA and 7H11 agar plate assay (Fig. S21A and B). Thus, the primary interaction between drug and DNA gyrase (cleaved-complex formation) is unaffected by NAC. Supplementation of moxifloxacin at $1\times$ and $5\times$ MIC with 1 mM NAC reduced survival by 21- and 11-fold, respectively (Fig. 6C), levels that are consistent with published results obtained using drug combinations (60).

As a complement to the suppression of killing by addition of catalase after drug removal (Fig. 2F), we treated *M. tuberculosis* cultures with $1\times$ and $5\times$ MIC of moxifloxacin and then plated the cells on 7H11 agar with 1 mM NAC. Postdrug addition of NAC blocked formation of colonies that would otherwise have been observed (Fig. S22). Extended incubation (>4 weeks) resulted in the appearance of small colonies on the NAC-containing plates, which was likely due to instability/oxidation of NAC (half-life [$t_{1/2}$] \sim 14 h) under aerobic conditions (61–63).

NAC also potentiated moxifloxacin lethality (5- to 7-fold) with nutrient-starved, dormant *M. tuberculosis* (Fig. 6D). These data agree with recent results which showed that activation of oxidative metabolism and respiration, through addition of L-cysteine to nutrient-starved cultures, reduced the fraction of persister subpopulations and enhanced the *in vitro* lethal activity of isoniazid and rifampicin (64). As expected, a similar treatment with NAC failed to enhance moxifloxacin lethality under hypoxic conditions (Fig. 6E), consistent with NAC functioning by inducing oxygen consumption and elevating ROS levels.

To address the effect of NAC on the acquisition of moxifloxacin resistance, we measured the mutant prevention concentration (MPC), i.e., the minimal concentration of moxifloxacin at which no moxifloxacin-resistant clone emerges on moxifloxacin-containing 7H11 agar inoculated with $\sim 2.5 \times 10^9$ bacteria (30, 65). With a clinical MDR isolate of *M. tuberculosis* (NHN1664), moxifloxacin exhibited an MPC of 4 μ M that was reduced to 2 μ M upon cotreatment with either 1 mM or 2 mM NAC (Table S6). For a lower moxifloxacin concentration (1 μ M, $2\times$ MIC), the fraction of cells recovered decreased by 10-fold and 100-fold when coplated with 1 mM and 2 mM NAC, respectively (Table S6). Reduction of MPC is expected when lethal activity is increased (66).

We also addressed the possibility that some effects of NAC derived from adducts formed with moxifloxacin. A series of biochemical tests (thin-layer chromatography, nuclear magnetic resonance [NMR], fluorescence assays, and liquid chromatography-mass spectrometry [LC-MS]) revealed no evidence of adduct formation (Fig. S23).

Moxifloxacin-induced redox imbalance during infection of macrophages. The Mrx1-roGFP2 biosensor previously showed that first-line anti-TB drugs cause an oxidative shift in the E_{MSH} of *M. tuberculosis* residing inside macrophages (19). When we infected macrophages with *M. tuberculosis* H37Rv or an MDR clinical isolate (strain NHN1664), each expressing the biosensor Mrx1-roGFP2, *M. tuberculosis* displayed redox heterogeneity (E_{MSH} -basal, -280 mV; E_{MSH} -oxidized, -240 mV; and E_{MSH} -reduced, -320 mV); the E_{MSH} -reduced subpopulation was predominant (19, 23, 67) (Fig. 7A; Fig. S24). Treatment of *M. tuberculosis*-infected THP-1 macrophages with various concentrations of moxifloxacin significantly increased the E_{MSH} -oxidized subpopulation (Fig. 7A, fuchsia line; Fig. S24).

The shift toward the E_{MSH} -oxidized redox state was seen with moderate concentrations of moxifloxacin ($5\times$ MIC) at an early time point (12 h postinfection), before *M. tuberculosis* survival started to drop (Fig. 7A and B). Thus, moxifloxacin-mediated oxidative stress precedes killing: oxidative stress is not simply a consequence of cell death. Bacterial survival was reduced more by higher moxifloxacin concentrations ($10\times$ and $20\times$ MIC) or longer incubation times (24 h and 48 h) (Fig. 7B).

We also assessed the effect of NAC on E_{MSH} and killing of *M. tuberculosis* inside macrophages. NAC itself is not cytotoxic to macrophages up to at least 5 to 10 mM (59, 68), but at those elevated concentrations, it exhibits antimycobacterial properties (68, 69). Consequently, we selected nontoxic, nonantituberculous concentrations of NAC (1 mM and 2 mM) (68) for our test with moxifloxacin. NAC supplementation induced an oxidative shift in the E_{MSH} of *M. tuberculosis* that exceeded that seen with moxifloxacin alone (Fig. 7C; Fig. S24). NAC alone had no effect on survival of *M. tuberculosis* inside THP-1 macrophages; however, the NAC plus moxifloxacin combination decreased bacterial burden 5 to 10 times more than moxifloxacin

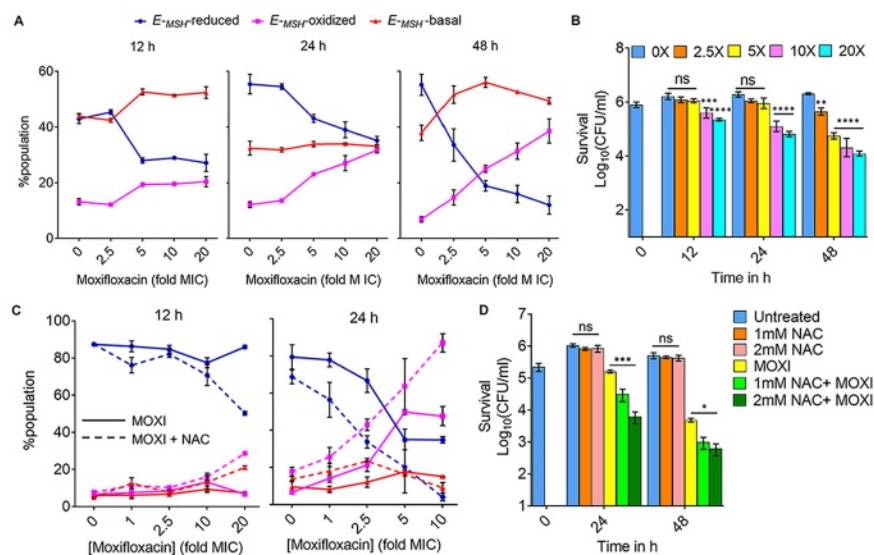


FIG 7 Moxifloxacin-induced oxidative shift in E_{MSH} and killing of *M. tuberculosis* inside macrophages. THP-1 macrophages, infected with *Mtb-roGFP2* (MOI = 1:10), were treated with moxifloxacin (MOXI; $1 \times$ MIC = $0.5 \mu\text{M}$) immediately after infection and incubated for the indicated times. (A) Approximately 10,000 infected macrophages were analyzed by flow cytometry to quantify changes in the E_{MSH} of *M. tuberculosis* subpopulations. (B) Bacterial survival kinetics after MOXI treatment of THP-1 macrophages infected with *Mtb-roGFP2* (CFU determination). (C) *Mtb-roGFP2*-infected THP-1 macrophages were treated with MOXI at the indicated concentrations in the presence or absence of NAC (1 mM) immediately after infection and incubated for the indicated times; analysis was as for panel A. (D) THP1 macrophages, infected by *Mtb-roGFP2*, were treated with NAC (1 mM or 2 mM), MOXI (10 μM), or the combination of NAC plus MOXI at those concentrations. After the indicated incubation times, the bacterial load in the macrophages was determined by plating on drug-free agar. P was determined by two-tailed Student's t test compared to MOXI-alone treatment at each time point. Statistical considerations were as for Fig. 1.

alone in both concentration- and time-dependent manners (Fig. 7D). We note that for either isoniazid or an isoniazid-rifampicin combination, NAC potentiates lethality only at late times (day 6 or 7) (59, 60); NAC acts more rapidly with moxifloxacin, as the killing effect is evident at days 1 and 2 (Fig. 7D). Thus, NAC may not function in the same way with all anti-TB drugs inside macrophages.

Moxifloxacin also lowered the level of an E_{MSH} -reduced subpopulation inside macrophages (Fig. 7A and C, blue line; Fig. S24); this subpopulation was further diminished by NAC supplementation. E_{MSH} -reduced subpopulations are phenotypically tolerant to anti-TB drugs (19, 23) and to moxifloxacin (Fig. S25). Overall, results with infected macrophages demonstrate that accelerating respiration and oxidative metabolism by NAC can enhance moxifloxacin lethality.

Potential of moxifloxacin lethality with NAC lowers *M. tuberculosis* burden in a murine model of infection and restricts the emergence of resistance.

We next asked whether NAC-mediated enhancement of moxifloxacin lethality occurs *in vivo*. Recent work by Vilch ze and Jacobs (60) directed our choice of murine models: they found little enhancement by NAC on the overall lethality of a combination of moxifloxacin and ethionamide when measured after long incubation using an acute model of murine tuberculosis. Since ROS accelerate killing *in vitro* without increasing the extent of killing (70), we shortened the drug treatment time. For this pilot test, we infected BALB/c mice with the clinical MDR strain *M. tuberculosis* NHN1664. Three weeks after aerosol-mediated infection at a low dose (~ 100 bacilli), mice were treated once daily for 10 days with a low dose of moxifloxacin (50 mg/kg body weight), NAC (500 mg/kg body weight), or moxifloxacin plus NAC at the same doses as for monotherapies (Fig. 8A). After 10 days, moxifloxacin monotherapy reduced the bacillary load by 3-fold and 100-fold in lung and spleen, respectively; NAC alone exhibited no antibacterial activity (Fig. 8B and C). The combination of moxifloxacin plus NAC reduced bacterial burden by another 4- and 12-fold beyond that observed for moxifloxacin alone for lung and spleen, respectively (Fig. 8B and C). Thus, this finding indicates that NAC stimulates the lethal action of moxifloxacin *in vivo*.

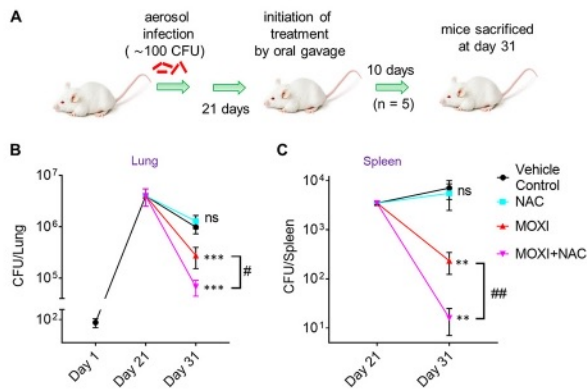


FIG 8 NAC decreases MDR *M. tuberculosis* survival in mice when combined with moxifloxacin. (A) Experimental protocol. (B and C) Bacterial CFU were enumerated from lungs and spleen at the indicated times. *P* was determined by unpaired two-tailed Student's *t* test relative to vehicle control treatment (**, $P \leq 0.01$; ***, $P \leq 0.001$; ns, not significant). Statistical significance between moxifloxacin (MOXI) alone and MOXI + NAC treatment is also shown (#, $P < 0.05$; ##, $P \leq 0.01$). Error bars represent standard deviations from the mean of bacterial burden in 5 mice per group.

As a proof of concept, we also measured the effect of NAC on the selection of moxifloxacin-resistant mutants in mice as described elsewhere (71, 72). We implanted $\sim 4 \times 10^3$ *M. tuberculosis* NHN1664 organisms in the lungs of BALB/c mice, and at day 14 postinfection, when the mean lung \log_{10} CFU reached $\sim 10^7$, mice received moxifloxacin, NAC, or moxifloxacin plus NAC (Table 1). After 14 days of postinfection treatment, 66% of moxifloxacin-treated mice harbored resistant bacteria, compared to 17% when NAC was also present. The combination of moxifloxacin plus NAC brought the number of mutants down to the level seen with untreated animals (Table 1). Enumeration of total resistant colonies confirmed that while moxifloxacin treatment increases emergence of resistance, NAC supplementation reduced the recovery of moxifloxacin-resistant mutants by 8-fold (Table 1).

DISCUSSION

M. tuberculosis responds to moxifloxacin through a lethal stress response characterized by suppressed respiration, elevated NADH levels, and ROS accumulation (shown schematically in Fig. 9). Although ROS accumulation is also observed with *E. coli* during lethal stress, early steps in the *M. tuberculosis* stress response are distinct. *M. tuberculosis* enters a metabolically quiescent state characterized by increased NADH levels and NADH/NAD⁺ ratio plus reduced respiratory and glycolytic rates. This response is opposite to that seen with *E. coli* (20, 33, 73). Decelerated respiration may be an adaptive strategy against ROS-inducing agents produced by the host. Production of ROS likely derives from an increased NADH/NAD⁺ ratio, which increases the labile, reduced form of Fe to fuel the Fenton reaction. Interfering with the NADH/NAD⁺ increase dampened reductive stress and moxifloxacin lethality, suggesting that NADH disposal pathways could be targeted to enhance fluoroquinolone lethality with *M. tuberculosis*.

TABLE 1 N-acetyl cysteine decreases recovery of *M. tuberculosis*-resistant mutants in infected BALB/c mice

| Treatment | No. (%) of mice | | No. of resistant colonies | |
|-------------------|-----------------|------------------------------|---------------------------|------------------------|
| | Total | Harboring resistant colonies | Total/group | Avg/mouse ^a |
| UT ^b | 6 | 1 (17) | 1 | 0.17 |
| NAC ^c | 6 | 2 (33) | 2 | 0.33 |
| MOXI ^d | 6 | 4 (67) | 8 | 1.33 |
| NAC + MOXI | 6 | 1 (17) | 1 | 0.17 |

^aTotal number of resistant colonies in a treatment group divided by total number of mice in that group.

^bUT, untreated (mice were given water [vehicle control]).

^cNAC (500 mg/kg body weight) was given once daily for a period of 2 weeks by oral gavage.

^dMoxifloxacin (MOXI; 50 mg/kg body weight) was given once daily for a period of 2 weeks by oral gavage.

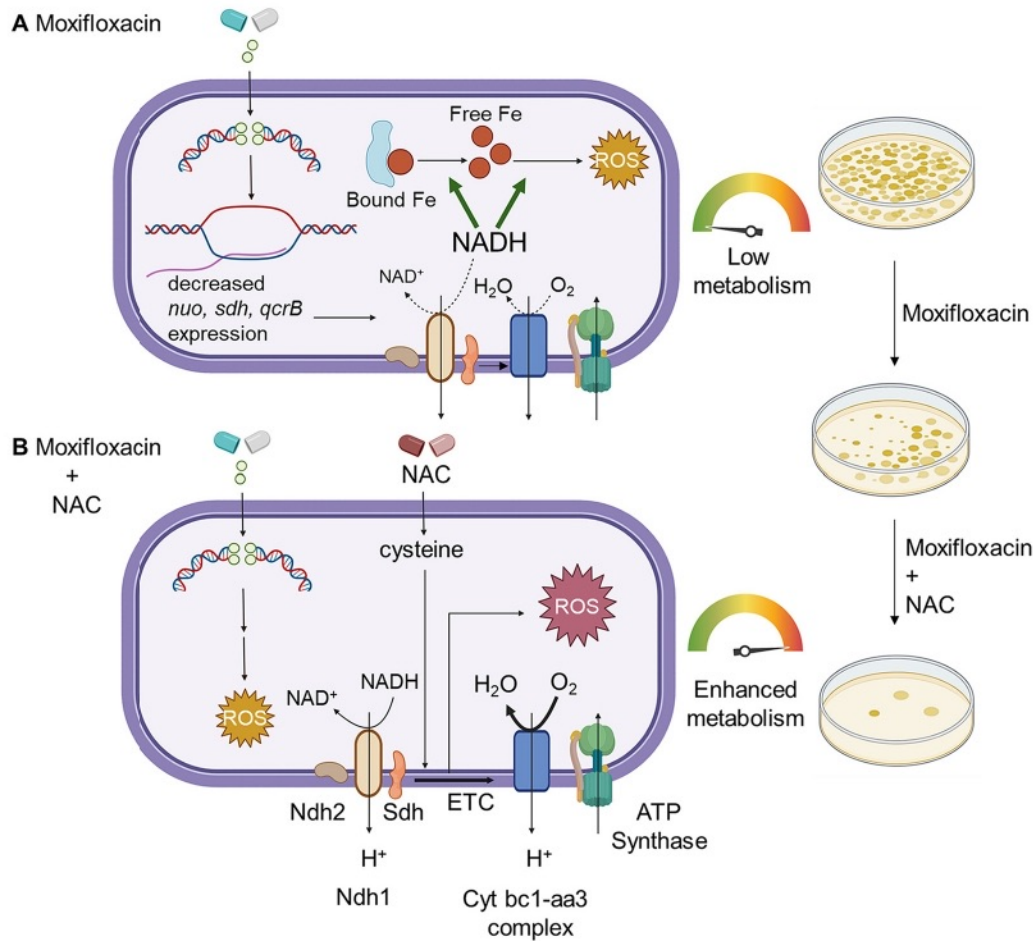


FIG 9 Moxifloxacin-mediated killing of *M. tuberculosis* involves accumulation of NADH-dependent ROS, which is further enhanced by NAC. (A) Moxifloxacin enters *M. tuberculosis* and traps gyrase on DNA as reversible, bacteriostatic drug-enzyme-DNA complexes in which the DNA is broken. The bacterium responds by downregulating the expression of genes involved in respiration. The transcriptional changes result in reduced rate of respiration. NADH levels and the ratio of NADH to NAD⁺ increase. NADH increases the free Fe²⁺ pool by releasing Fe from ferritin-bound forms and keeps it in a reduced state. ROS damage macromolecules in a self-amplifying process, as indicated by exogenous catalase blocking killing when added after removal of moxifloxacin. (B) Addition of *N*-acetyl cysteine to cells stimulates respiration and provides more ROS from moxifloxacin-mediated lesions. NAC alone does not induce ROS or trigger death. The additional ROS increases killing by moxifloxacin. Repair of moxifloxacin-mediated lesions, NADH dissipation, Fe sequestration, and ROS detoxification mechanisms contribute to survival. The image was created using [BioRender.com](https://www.biorender.com).

ROS contribution to lethality. Studies with *E. coli* indicate that ROS kill bacteria by damaging macromolecules, i.e., DNA breakage, protein carbonylation, and lipid peroxidation (15). Our data support the general principle that ROS contribute to stress-mediated death of moxifloxacin-treated *M. tuberculosis*: (i) biosensors show an increase in ROS at lethal drug concentrations; (ii) iron concentrations increase with moxifloxacin treatment; and (iii) two ROS-mitigating agents, thiourea and bipyridyl, reduce oxidative stress and killing. However, the striking increase in survival for *E. coli* at very high quinolone concentrations is associated with a drop in ROS, while this is not the case with *M. tuberculosis*; this difference remains unexplained.

Another difference is the lowering of residual fluoroquinolone lethality by nitrate with hypoxic *M. tuberculosis* (Fig. S9D): the opposite is observed with norfloxacin-treated *E. coli*. Previous *M. tuberculosis* work has shown that nitrate protects hypoxic bacilli from killing caused by exposure to reactive nitrogen intermediates (74), acid stress (74), sudden anaerobiosis (75), or inhibition of type II NADH-dehydrogenase (NDH-2) by thioridazine (75). Two phenomena may contribute to nitrate-mediated protection. (i) *M. tuberculosis* reduces nitrate to nitrite (76), which oxidizes ferrous Fe to the ferric state, thereby displacing Fe from critical Fe-sulfur clusters and inducing bacteriostasis (76). Nitrite also remodels the *M. tuberculosis* transcriptome similar to several host-imposed stresses that suppress antibiotic-mediated

lethality (76) and ensure bacterial survival. (ii) Nitrate, as a terminal electron acceptor, recycles or disposes of excess reducing equivalents that accumulate during anaerobic conditions (77). Discovering strategies or therapeutics to halt such adaptive remodeling (e.g., nitrate reduction during hypoxia) in *M. tuberculosis* could serve as potential adjunct therapy with moxifloxacin against hypoxic bacilli.

Reductive stress as a source of ROS. When we dissipated NADH-reductive stress by overexpression of *LbNox*, the ROS surge was mitigated, and moxifloxacin lethality was lowered. Production of NADH can also be lowered by stimulating the glyoxylate shunt via isocitrate lyase (*icl*)—deletion of *icl* increases the lethal action of isoniazid, rifampicin, and streptomycin (34), suggesting that NADH-mediated ROS accumulation may also contribute to the lethal action of these agents. The observed increase in NADPH/NADP⁺ ratio in response to moxifloxacin exposure could assist *M. tuberculosis* in mitigating oxidative stress by activating NADPH-dependent antioxidant systems, thioredoxins, and mycothiol. As shown by microarray data, the increase in NADPH/NADP⁺ ratio could also be a consequence of downregulation of NADPH-requiring anabolic pathways, such as polyketide/lipid biogenesis, amino acid anabolism, and *de novo* nucleotide synthesis.

In summary, *M. tuberculosis* appears to tolerate lethal stressors of the host immune system by decelerating respiration coupled with dissipation of NADH-reductive stress. The need to dissipate reductive stress may be of general importance, as this type of stress is also generated and amplified by hypoxia, inhibition of aerobic respiration by NO, and catabolism of fatty acids (78, 79). *M. tuberculosis* dissipates reductive stress through WhiB3-mediated anabolism of polyketide lipids (78). Other bacterial species also dispose of excess reductant, which they do by (i) using nitrate as a terminal electron acceptor during hypoxia (74), (ii) fueling fermentation under nitrosative stress (80), and (iii) secreting phenazines (redox-active polyketides) that generate NAD⁺ from NADH (81). Moxifloxacin is the first antimycobacterial agent shown to stimulate NADH-reductive stress.

Lethality enhancement by *N*-acetyl cysteine. Vilchèze and Jacobs (60) reported that NAC boosts the lethality of anti-TB drug combinations *in vitro*. We emphasize that a general, enhancing effect on drug-target interactions by NAC is unlikely, because such effects are usually detected by MIC measurement (15): NAC has no effect on moxifloxacin MIC. This observation reinforces the concept that drug-target interactions are mechanistically distinct from downstream ROS-based killing (protection from killing, which is called tolerance when no change in MIC occurs, is distinct from resistance, which is measured as an increase in MIC).

To simplify interpretation of killing data, we focused on a single drug, moxifloxacin, rather than drug combinations. The previous demonstration that NAC stimulates respiration (60) made it a useful tool for examining killing mechanisms. NAC increased moxifloxacin-mediated ROS accumulation and lethality with cultured *M. tuberculosis*. Increased killing was initially surprising, because NAC has antioxidant properties expected to reduce moxifloxacin lethality (82). It is likely that the effect of NAC depends on the level of stress, since with other bacterial species, genes (*mazF*, *cpx*, and *lepA*) and treatments (chemical generation of superoxide and H₂O₂) are known to be protective at low levels of stress but destructive at high ones (genetic deficiencies are protective) (83–86). Indeed, treatment with a sublethal concentration of H₂O₂ activates the OxyR regulon in *E. coli* and “primes” the bacterium to counteract subsequent oxidative-stress challenge. At higher concentrations, H₂O₂ is bactericidal (87). With the high level of stress produced by moxifloxacin, the respiration-stimulating activity of NAC dominates and adds to ROS derived from NADH-reductive stress.

As expected from *in vitro* studies, NAC increased moxifloxacin-mediated killing of *M. tuberculosis* inside macrophages and in a murine model of infection. The kinetic effects of ROS explain why our short-term treatment model with infected mice showed stimulation by NAC, while the longer treatment used previously with antimicrobial combinations did not (60).

We addressed the potential of NAC to suppress the emergence of resistance by measuring its effect on MPC. Although MPC is a bacteriostatic parameter (MIC of the least susceptible mutant subpopulation), highly lethal agents lower it, presumably by killing mutants (66). Thus, we were not surprised that stimulation of moxifloxacin lethality by NAC lowered MPC. In a murine infection model, NAC reduced the recovery of resistant mutants by 8-fold.

Although the MPC for moxifloxacin is lower than concentrations achieved in serum by approved doses (88), the clinical situation is likely complex: moxifloxacin shows poor penetration into caseous regions of tubercular granulomas in a rabbit model of experimental tuberculosis (89, 90). Low local moxifloxacin concentrations may promote the emergence of fluoroquinolone resistance (91). Thus, NAC supplementation could increase the probability that moxifloxacin concentration is above the MPC *in vivo*, but additional work is required to test this idea.

NAC is a potential candidate as a lethality enhancer, because it is relatively safe for humans (it has been used to alleviate drug-induced toxicity in TB patients [92, 93]). Furthermore, NAC by itself exhibits antimycobacterial activity in macrophages, mice, and guinea pigs (68, 94), and a small clinical trial in which NAC was administered to TB patients showed improved host health, immunological response, and early sputum conversion (95, 96). The present work provides a mechanistic foundation for refining NAC-based enhancement of antituberculosis agents. Assessing the general clinical significance of ROS enhancement is also complex, because ROS accelerate killing without lowering bacterial survival upon long incubations. This phenomenon has been observed with *Staphylococcus aureus* (70), *E. coli* (16), and *M. tuberculosis* (Fig. 2F; Fig. S4B). With *M. tuberculosis*-infected mice, NAC stimulates reduction of bacterial load at short but not long incubation times (60). Thus, an appropriate dosing interval must be determined, initially guided by *in vitro* pharmacodynamic studies (71, 72, 97, 98). Relevant tissue concentrations of NAC and moxifloxacin for various doses over time must also be determined before clinical relevance can be assessed. Therefore, the present report provides a strong foundation for detailed follow-up work to determine the clinical relevance of NAC as an adjunct therapy for moxifloxacin.

MATERIALS AND METHODS

Bacterial strains and culture conditions. *M. tuberculosis* H37Rv and the drug-resistant clinical isolates JAL 1934, JAL 2287, JAL 2261, and BND 320 were kind gifts from Kanury V. S. Rao (International Centre for Genetic Engineering and Biotechnology, Delhi, India). The MDR strain NHN1664, originally isolated in China, was obtained from BEI Resources, NIAID, NIH. Strain *Mtb-roGFP2* was generated by transforming *M. tuberculosis* strain H37Rv with an *E. coli*-mycobacterial shuttle vector, pMV762 (99, 100). Plasmid pMV762 contains the *M. tuberculosis* *hsp60* promoter and a hygromycin resistance gene as a selection marker. Hygromycin (catalog no. 0219417091; MP Biomedical, Santa Ana, CA) was used at a final concentration of 50 $\mu\text{g}/\text{mL}$. A plasmid (pGMCgS-0 \times -Ptb38-LbNOX-FLAG-SD1) containing an *LbNox* construct was a kind gift from Dirk Schnappinger and Sabine Ehrh (Weill Cornell Medicine, New York, NY, USA). Plasmid was electroporated into wild-type *M. tuberculosis* H37Rv to create the *Mtb-LbNox* strain. Streptomycin was used at a final concentration of 25 $\mu\text{g}/\text{mL}$. Plasmid pMV762-Peredox-mchery was a kind gift from Ashwani Kumar (Council of Scientific and Industrial Research, Institute of Microbial Technology, Chandigarh, India).

All strains, including the laboratory *M. tuberculosis* strain H37Rv and *M. tuberculosis* expressing the *Mrx1-roGFP2* redox biosensor, were grown in 7H9 broth supplemented with 0.2% glycerol, 0.05% Tween 80, and ADS (0.5% albumin, 0.2% dextrose, and 0.085% NaCl) with shaking at 180 rpm in a rotary shaker incubator (Lab Therm LT-X; Kuhner, Basel, Switzerland) or on 7H11 agar supplemented with ADS or OADC (ADS plus 0.05% oleic acid and 0.004% catalase) (catalog no. C9322; Sigma-Aldrich, St. Louis, MO) or ADC (ADS plus 0.004% catalase) at 37°C. Bacterial strains expressing *Mrx1-roGFP2* were grown in medium containing hygromycin.

Determination of MIC under aerobic growth conditions. MIC was determined by a resazurin microtiter assay (REMA) using 96-well flat-bottom plates (25). *M. tuberculosis* strains were cultured in 7H9+ADS medium (19) and grown to exponential phase (optical density at 600 nm [OD_{600}] = 0.4 to 0.8). Approximately 1×10^5 bacteria per well were added in a total volume of 200 μL of 7H9+ADS medium. Wells lacking *M. tuberculosis* served as controls. Additional controls consisted of wells containing cells without drug treatment (growth control). After 5 days of incubation at 37°C in the presence of fluoroquinolone (or NAC), 30 μL of 0.02% resazurin (catalog no. R7017; Sigma-Aldrich, St. Louis, MO) was added, and plates were incubated for an additional 24 h. Fluorescence intensity was measured using a SpectraMax M3 plate reader (Molecular Devices, San Jose, CA) in bottom-reading mode with excitation at 530 nm and emission at 590 nm. Percent inhibition was calculated from the relative fluorescence units compared with an untreated control culture; the MIC was taken as the lowest drug concentration that resulted in at least 90% reduction in fluorescence compared to the untreated growth control.

Determination of bacterial survival. To determine the number of viable bacilli, aliquots were removed from cultures, cells were concentrated by centrifugation (4,200 $\times g$, 5 min) to remove drug or treatment compounds, and they were resuspended in an equal volume of medium. Tenfold dilutions were prepared, and 20 μL aliquots were spotted on drug-free 7H11 agar plates containing 10% ADC or ADS. Plates were incubated for 3 to 4 weeks at 37°C for CFU enumeration.

Concentration-kill curves were obtained by treating exponentially growing cultures of *M. tuberculosis* (OD_{600} of 0.3, or $\sim 5 \times 10^7$ cells/mL) with various concentrations of moxifloxacin. Tubes were incubated with

shaking at 180 rpm for 10 days at 37°C. Aliquots were taken at various intervals, serially diluted, and plated on drug-free agar for CFU enumeration.

The LD₉₀ (lethal dose) of moxifloxacin under *in vitro* aerobic-culture conditions was measured by treating 10-mL cultures in 50-mL centrifuge tubes under aerobic conditions (shaking at 180 rpm and 37°C), followed by CFU measurement. The concentration that resulted in a 90% reduction in CFU on treatment day 5, compared with the input control, was defined as the LD₉₀.

To determine the effect of an Fe chelator on moxifloxacin-mediated lethality, 250 μM (a noninhibitory concentration) of bipyridyl (catalog no. D216305; Sigma-Aldrich, St. Louis, MO) was added to bacterial cultures 15 min prior to moxifloxacin addition; bipyridyl was present throughout the experiment (i.e., 10 days).

For experiments with thiourea or *N*-acetyl cysteine (NAC), thiourea (10 mM) or NAC (1 mM) was added 1 h prior to moxifloxacin and was maintained for 2 days or 10 days. Aliquots were taken at indicated times, serially diluted, and plated for CFU enumeration on drug-free agar.

Poststressor bactericidal activity of moxifloxacin. *M. tuberculosis* cultures were treated with moxifloxacin for the indicated durations, the drug was removed by washing, and cells were plated on drug-free 7H11 agar with or without 1 mM NAC or with 2.5% bovine serum albumin (BSA) or catalase (17.5 U/mL of agar), followed by visual CFU determination.

Measurement of E_{MSSH} using the Mrx1-roGFP2 redox biosensor. For intramacrobacterial E_{MSSH} determination during *in vitro* growth or under *ex vivo* macrophage infection conditions, strain *Mtb*-roGFP2 was grown in 7H9 broth or in THP-1 macrophages, respectively. Cultures were then treated with moxifloxacin, and at various times, they were treated with 10 mM *N*-ethylmaleimide (NEM; catalog no. E3876; Sigma-Aldrich, St. Louis, MO) for 5 min at room temperature followed by fixation with 4% paraformaldehyde (PFA; catalog no. GRM3660; Himedia, Mumbai, India) for 1 h at room temperature. Bacilli and infected macrophages were analyzed using a FACSVerse flow cytometer (BD Biosciences, San Jose, CA). Intramacrobacterial E_{MSSH} was determined using the Nernst equation as described previously (19). E_{MSSH} is defined as the standard reduction potential of the MSH/MSSM redox couple (reduced mycothiol to oxidized mycothiol).

The biosensor response was measured by analyzing the fluorescence ratio at a fixed emission (510 nm) after excitation at 405 and 488 nm. Data were analyzed using the BD FACSuite software. These ratiometric data were normalized to measurements with cells treated with 10 mM cumene hydroperoxide (catalog no. 247502; Sigma-Aldrich, St. Louis, MO), which reports maximal oxidation of the biosensor, and 20 mM dithiothreitol (Sigma-Aldrich, catalog no. D9779, St. Louis, MO), which reports maximal reduction. Ten thousand events per sample were analyzed.

ROS measurement using CellROX deep red. Cultures of exponentially growing *M. tuberculosis* at an initial OD₆₀₀ of 0.3 were treated with various concentrations of moxifloxacin for 48 h. Sterile 50-mL polypropylene centrifuge tubes (catalog no. P10404; Abdos, Roorkee, India), containing 10 mL of culture, were incubated in a shaker incubator (180 rpm, 37°C). Then, cells were harvested by centrifugation (4,200 × *g* for 5 min) and resuspended in 100 μL of growth medium. Per the manufacturer's instructions, CellROX deep red (catalog no. C10422; Invitrogen, Waltham, MA) was added to a final concentration of 5 μM, and cells were agitated on a rocker (Biobee Tech, Bangalore, India) for 30 min. After incubation, cells were washed to remove residual dye by centrifugation (4,200 × *g* for 5 min). Cells were resuspended in 300 μL phosphate-buffered saline (pH 7.4) and then fixed by addition of 4% PFA for 1 h at room temperature. Fluorescence was measured at a fixed emission (670 nm) after excitation with a red laser (640 nm) using a BD FACSVerse flow cytometer (BD Biosciences, San Jose, CA) with 10,000 events per sample. No autofluorescence was observed.

Determination of DNA damage by TUNEL assay. DNA damage was measured by using an *in situ* cell death detection kit with tetramethylrhodamine (TMR) red (catalog no. 12156792910; Roche Molecular Biochemicals, Indianapolis, IN), which is based on TUNEL (TdT-mediated dUTP-X nick end labeling) assay (101, 102). Equal numbers of cells (based on OD₆₀₀) were taken at various times of treatment with moxifloxacin, washed once by centrifugation, and fixed in 2% PFA. PFA was removed by washing cells, followed by resuspension in 2% sodium dodecyl sulfate (SDS) and a second wash by centrifugation. DNA double-strand breaks were labeled in 100 μL of TUNEL reaction mix for 3 to 4 h. Cells incubated with label solution only (no terminal transferase) were used as negative controls. Fluorescence was measured at a fixed emission (585 nm) after excitation with green-yellow laser (561 nm) using a BD FACSria flow cytometer (BD Biosciences, San Jose, CA). Ten thousand events were acquired per sample.

Lipid peroxidation assay. Cultures were grown to mid-log phase (OD₆₀₀ = 0.6 to 0.8). Lipid hydroperoxides were quantified from cell pellets after centrifugation (4,000 × *g*, 5 min), using FOX2 reagent (24). Briefly, cell pellets were resuspended in 1:2 chloroform-methanol and mixed by vortexing. Next, chloroform and water were added as a 1:1 mixture. The samples were then centrifuged to separate the water and organic phases. The organic phase was collected and washed twice with water. Two hundred microliters of the organic phase was incubated with 1 mL of FOX2 reagent in the dark for 1 h at 22°C. Lipid hydroperoxides were measured spectrophotometrically at 560 nm and normalized to culture turbidity (OD₆₀₀).

Macrophage preparation and infection by *M. tuberculosis*. The human monocytic cell line THP-1 was grown in RPMI 1640 medium (Cell Clone, Manassas, VA) supplemented with 10% heat-treated (55°C) fetal bovine serum (catalog no. 092916754; MP Biomedical, Santa Ana, CA). A total of 3 × 10⁵ cells/well was seeded into a 24-well cell-culture plate. THP-1 monocytes were stimulated to differentiate into macrophage-like cells by treatment with 20 ng/mL phorbol 12-myristate 13-acetate (PMA; Sigma-Aldrich Co., St. Louis, MO) for 18 to 20 h at 37°C and incubated further for 48 h to allow differentiation (19). The resulting macrophage-like cells were infected with *Mtb*-roGFP2 or MDR *M. tuberculosis* NHN1664 expressing Mrx1-roGFP2 at a multiplicity of infection (MOI) of 10 and incubated for 4 h at 37°C in 5% CO₂. After infection, extracellular bacteria were removed by washing three times (by centrifugation) with phosphate-buffered saline (PBS; 137 mM NaCl, 2.7 mM KCl, 10 mM Na₂HPO₄, and 1.4 mM KH₂PO₄, pH 7.4). Moxifloxacin (catalog no. PHR1542; Sigma-Aldrich, St. Louis, MO), with or without NAC (catalog no. A7250; Sigma-Aldrich, St. Louis, MO), was added to infected cells that were

incubated for various times. For CFU determination, infected cells were lysed in 7H9 medium containing 0.06% SDS; dilutions were prepared using 7H9 medium, and aliquots were plated on 7H11+OADC agar plates (19). Plates were incubated at 37°C for 3 to 4 weeks before colonies were counted.

Nutrient starvation. Starvation was achieved as previously described (37). Briefly, cultures of *M. tuberculosis* H37Rv were grown to exponential phase in roller-culture bottles (catalog no. 430518; Corning, Corning, NY) containing Middlebrook 7H9 medium, supplemented with ADS and 0.05% Tween 80, at 37°C with rolling at 6 rpm in a roller incubator (120 Vac Roll-In incubator; Wheaton, Millville, NJ). Cultures grown to an OD₆₀₀ of ~0.2 were harvested by centrifugation (4,000 × g for 5 min) followed by two washes with PBS (pH 7.4) supplemented with 0.025% Tween 80 (PBST). Bacterial cells were diluted to a final OD₆₀₀ of 0.1 in PBS. Fifty milliliters of this suspension was transferred into a roller culture bottle and incubated for 14 days to achieve starvation conditions.

Hypoxia. For determination of moxifloxacin lethality under hypoxic conditions, bacterial cultures (OD₆₀₀ = 0.1) were placed in Vacutainer tubes (catalog no. 367812; Becton Dickinson, Franklin Lakes, NJ) followed by incubation for 14 to 21 days at 37°C (103). A high cell density (OD₆₀₀ = 0.1) was used for rapid achievement of hypoxia, which was observed as decolorization of methylene blue (final concentration was 1.5 μg/mL) in the culture medium. When hypoxia was established, moxifloxacin was added to cultures anaerobically. Metronidazole at 10 mM and isoniazid at 10 μM were used as positive and negative controls, respectively. Drugs were injected in volumes of 100 μL in phosphate-buffered saline following passage of argon through the drug solution to remove residual oxygen. Hypoxic cultures were treated with drugs for 5 days, similar to the incubation time for MIC determination with aerobically growing cells. After treatment, Vacutainer tubes were unsealed, and endpoint bacterial survival was determined by plating on drug-free agar, incubating for 3 to 4 weeks at 37°C, and visually enumerating colonies.

Effect of nitrate on survival of hypoxic bacteria. Survival during nitrate-dependent respiration was achieved by supplementing *M. tuberculosis* cultures with 5 mM sodium nitrate. Nitrate was added when cultures were placed in Vacutainer tubes before hypoxia. All other conditions were as described above for hypoxia.

Microarray data analysis. Gene expression data from GSE71200 (NCBI Gene Expression Omnibus [GEO]) was used for analyzing the response of *M. tuberculosis* to moxifloxacin (42). The data were expressed as a two-channel microarray with control and drug-exposed *M. tuberculosis* stained with Cy3 and Cy5 dyes, respectively. We used GSM1829746, GSM1829747, and GSM1829748, which consist of published data for *M. tuberculosis* exposed to 2×, 4×, or 8× MIC (1× MIC = 0.4 μM) of moxifloxacin for 16 h. Normalized expression data for GSE71200 were downloaded from GEO (104, 105), and probe IDs were mapped to the respective gene IDs. The expression levels for genes having multiple probes were averaged, and genes lacking data were removed from further analysis. Differentially expressed genes (DEGs) were defined as genes that were upregulated or downregulated by at least 2-fold in all 3 moxifloxacin treatment conditions.

For overlap analysis of differentially expressed genes in moxifloxacin-exposed bacteria compared with other stress-induced conditions (log₂ fold change of >1 or <-1; *P* values of <0.01 are considered to indicate differentially expressed genes in stress conditions), the GeneOverlap (v1.22.0) package from R (v3.6.3) was used (106, 107). It uses Fisher's exact test to find statistical significance by calculating the *P* value and the odds ratio for the overlap (a *P* value of <0.05 and an odds ratio of >1 were taken as the significance thresholds).

OCR and ECAR measurements. To measure basal oxygen consumption rate (OCR) and extracellular acidification rate (ECAR), log-phase *M. tuberculosis* cultures (OD₆₀₀ = 0.6 to 0.8) were briefly (1 day) incubated in 7H9 medium containing the nonmetabolizable detergent tyloxapol (catalog no. 157162; MP Biomedical, Santa Ana, CA) and lacking ADS or a carbon source. These cultures were then passed 10 times through a 26-gauge syringe needle followed by centrifugation at 100 × g for 1 to 2 min to remove clumps of bacterial cells. The resulting single-cell suspensions of bacteria at 2 × 10⁶ cells/well were placed in the bottom of wells of a Cell-Tak (catalog no. 354240; Corning, Corning, NY)-coated XF culture plate (Agilent/Seahorse Biosciences, Santa Clara, CA). Measurements were performed using a Seahorse XFp analyzer (Agilent/Seahorse Biosciences, Santa Clara, CA) with cells in unbuffered 7H9 growth medium (pH 7.35 lacking monopotassium phosphate and disodium phosphate) containing glucose (2 mg/mL) as a carbon source. OCR and ECAR measurements were recorded for ~21 min (3 initial baseline readings) before addition of moxifloxacin (1×, 2.5× or 10× MIC; 1× MIC = 0.5 μM), which was delivered automatically through the drug ports of the sensor cartridge (Wave Software, Agilent Technologies, Santa Clara, CA). NAC or CCCP was similarly added through drug ports at times indicated in the figures. OCR and ECAR were measured for an additional 6 h in the absence or presence of moxifloxacin and/or NAC. Changes in OCR and ECAR readings triggered by moxifloxacin were calculated as a percentage of the third baseline reading for OCR and ECAR taken prior to drug injection.

ROS measurement under Fe depletion conditions. Iron starvation was achieved as described previously (108). Briefly, log-phase *M. tuberculosis* cultures were grown in minimal medium (0.5% [wt/vol] asparagine, 0.5% [wt/vol] KH₂PO₄, 2% glycerol, 0.05% Tween 80, 10% ADS, 0.5 mg/L of sterile ZnCl₂, 0.1 mg/L of MnSO₄, and 40 mg/L of MgSO₄) to early stationary phase (OD₆₀₀ of ~1). To remove metal ions, the minimal medium was treated with 5% Chelex-100 (catalog no. 142-2842; Bio-Rad, Hercules, CA) for 24 h with gentle agitation. This Fe-depleted culture was diluted further to an OD₆₀₀ of 0.1 in the same medium and allowed to grow to early stationary phase to deplete stored Fe. The Fe-depleted cells were further treated with 50 μg/mL of freshly prepared deferoxamine mesylate (catalog no. D9533; Sigma-Aldrich, St. Louis, MO)-containing minimal medium for 6 days. The cells were washed and diluted in minimal medium containing 80 μM FeCl₃ or 80 μM FeCl₃ + 10 mM thiourea for an additional 4 days. ROS was quantified by CellROX deep red dye using flow cytometry as described in the section "ROS measurement using CellROX deep red."

Cellular Fe estimation. Cell-free Fe levels were measured using the ferrozine-based assay as described previously (59, 109). Briefly, *M. tuberculosis* cultures were grown to an OD₆₀₀ of 0.3 to 0.4 followed by treatment with 0×, 1×, 2.5×, or 10× MIC of moxifloxacin. After 48 h of treatment, cells were harvested and washed twice

with ice-cold PBS. The cell pellets were resuspended in 1 mL of 50 mM NaOH and lysed using a bead beater. The cell lysate sample (300 μ L) was mixed with 10 mM HCl (300 μ L) followed by addition of Fe detection reagent (6.5 mM ferrozine, 6.5 mM neocuproine, 1 M ascorbic acid, and 2.5 M ammonium acetate in water) (90 μ L). The reaction mix was incubated at 37°C for 30 min, and then absorbance at 562 nm was measured. The cellular Fe concentration was determined by plotting the absorbance values against a standard curve of FeCl₃ concentration gradient and normalized to protein content. Protein concentration was determined using the Pierce bicinchoninic acid (BCA) protein assay kit (catalog no. 23225; Thermo Scientific, Rockford, IL).

Estimation of NAD⁺, NADP⁺, NADH, and NADPH. *M. tuberculosis* H37Rv was grown to an OD₆₀₀ of ~0.35 and treated with 1 \times , 2.5 \times , or 10 \times MIC of moxifloxacin for 48 h. Pyridine nucleotide levels were determined by a redox-cycling assay (78, 110). Protein concentration of NAD⁺ or NADH extracts was determined using the Pierce BCA protein assay kit (catalog no. 23225; Thermo Scientific, Rockford, IL) to normalize NAD/(P)H and NAD/(P)⁺ concentrations.

Analysis of mixtures containing moxifloxacin with and without NAC by TLC. Thin-layer chromatography (TLC) was performed using silica gel 60 GF₂₅₄ precoated aluminum-backed plates (0.25-mm thickness; Merck, Darmstadt, Germany), and visualization was accomplished by irradiation with UV light at 254 nm. Stock solutions of moxifloxacin (10 mM) and NAC (0.2 M, 2 M, and 20 M) were prepared independently in dimethyl sulfoxide (DMSO) and phosphate buffer (PB; pH 7.4; 10 mM), respectively. In a typical incubation, moxifloxacin (100 μ L at a final concentration of 2 mM) was independently reacted with various concentrations of NAC (5 μ L; final concentration, 2 mM, 20 mM, or 200 mM) in 395 μ L PB (pH 7.4; 10 mM). In a control experiment, moxifloxacin (100 μ L; final concentration, 2 mM) was added to 400 μ L PB (pH 7.4; 10 mM). The mixtures were incubated at 37°C on an Eppendorf ThermoMixer Comfort (800 rpm). The reactions were monitored by spotting aliquots (5 μ L) from the incubation mixtures onto the TLC plate at designated times. The solvent system used was methanol (MeOH) and CHCl₃ (1:9).

Analysis of mixtures containing moxifloxacin plus and minus NAC by NMR. Deuterated PB (10 mM) was prepared by dissolving monobasic potassium phosphate (KH₂PO₄; 4 mg) and dibasic potassium phosphate (K₂HPO₄; 12 mg) in deuterated water (D₂O), and the pH was adjusted to 7.4 using 40% (wt/wt) sodium deuterioxide solution in D₂O (catalog no. 151882; Sigma-Aldrich, St. Louis, MO). Stock solutions of moxifloxacin (10 mM) and NAC (0.2 M) were prepared in DMSO and deuterated PB (pH 7.4; 10 mM), respectively. In a typical reaction, moxifloxacin (200 μ L; 2 mM final concentration) was incubated with NAC (10 μ L; 2 mM final concentration) in 790 μ L deuterated PB (pH 7.4; 10 mM). In a control experiment, moxifloxacin (200 μ L; 2 mM final concentration) was added to 800 μ L deuterated PB (pH 7.4; 10 mM). The mixtures were incubated at 37°C in an Eppendorf ThermoMixer Comfort (800 rpm). An aliquot (0.5 mL) of the incubation mixture was taken after 1 h of incubation, and ¹H NMR and ¹⁹F NMR spectra were recorded. ¹H NMR was acquired with 64 scans on a JEOL 400 MHz spectrometer using D₂O (Sigma-Aldrich) as an internal standard. Chemical shifts (δ) were reported in parts per million downfield from D₂O (δ = 4.79 ppm) for ¹H NMR. ¹⁹F spectra were recorded on a JEOL spectrometer (376 MHz) using an external reference (α, α, α -trifluorotoluene; δ_f = -63.72 ppm).

Fluorescence-based detection of intracellular levels of moxifloxacin in wild-type *M. smegmatis*. Stock solutions of moxifloxacin (0.05 mM) and NAC (200 mM) were prepared in DMSO and phosphate buffer (pH 7.4, 10 mM), respectively. Wild-type *M. smegmatis* cultures were grown in Middlebrook 7H9 broth supplemented with glycerol (0.2%) and Tween 80 (0.1%). Exponential-phase cultures of wild-type *M. smegmatis*, grown to OD₆₀₀ of 0.3 (985 μ L), were transferred to 1.5 mL Eppendorf tubes and either left untreated or treated with NAC (5 μ L, final concentration 1 mM) for 1 h prior to addition of 2 \times MIC of moxifloxacin (10 μ L, final concentration 0.5 μ M). Treated cells were incubated with shaking at 180 rpm in a rotary shaker incubator at 37°C for 48 h. The cell suspension was then centrifuged at 9,391 \times g at 4°C for 15 min, and the pellet was washed twice with 1 \times PBS and resuspended in 1 mL PBS in a microcentrifuge tube. The cells were lysed by sonication using a 130-W ultrasonic processor (Vx 130W) by stepping a microtip with a 4-min pulse-on time (with 3-s on and 3-s off pulse; 60% amplitude; 20-kHz frequency) under ice-cold conditions. An aliquot (100 μ L) of whole-cell lysate was withdrawn from the samples and dispensed into a 96-well microtiter plate. Fluorescence ascribed to moxifloxacin (λ_{ex} = 289 nm and λ_{em} = 488 nm), recovered in NAC-untreated or -pre-treated *M. smegmatis* lysates, was recorded using an EnSight multimode plate reader (PerkinElmer, India). Readings were collected from the top with 25 flashes per well and with a focus height adjusted to 9.5 mm.

Intracellular levels of moxifloxacin in *M. smegmatis* using LC-MS. Stock solutions of moxifloxacin (0.05 mM) and NAC (200 mM) were prepared as described above. Whole-cell lysates of wild-type *M. smegmatis* treated with moxifloxacin (0.5 μ M, 2 \times MIC) with or without NAC (1 mM) were prepared as described for the fluorescence-based method employed for the detection of moxifloxacin. An aliquot (100 μ L) of whole-cell lysate was withdrawn from the incubation mixtures, diluted with methyl alcohol (100 μ L), and centrifuged at 9,390 \times g at 4°C for 15 min. The supernatant fluids (50 μ L) were removed, diluted with methyl alcohol (50 μ L), and analyzed by LC-MS. All measurements were performed using the positive ion mode with high-resolution, multiple-reaction monitoring (MRM-HR) analysis with a Sciex X500R quadrupole time-of-flight (QTOF) mass spectrometer fitted with an Exion ultrahigh-performance LC (UHPLC) system having a Kinetex 2.6-mm hydrophilic interaction liquid chromatography (HILIC) column (100-Å particle size, 150-mm length, and 3-mm internal diameter; Phenomenex, Intek Chromasol Pvt. Ltd., India). Nitrogen was used as the nebulizer gas, with nebulizer pressure set at 50 lb/in². MS was calibrated in the positive mode, and samples were analyzed with the following parameters: mode, electrospray ionization (ESI); ion source gas 1 = 40 lb/in²; ion source gas 2 = 50 lb/in²; curtain gas = 30; CAD (collisionally activated dissociation) gas = 7; spray voltage = 5,500 V; and temperature = 500°C. The MRM-HR mass spectrometry parameters were as follows: moxifloxacin (Q1, M+H⁺) = 402.18, moxifloxacin-NAC adduct (Q2, M+H⁺) = 565.21, declustering potential = 80 V, collision energy = 20 V, collision exit potential = 5 V, and accumulation time = 0.24 s. The LC runs were for 30 min with a gradient of 100% solvent A (0.1% HCOOH in water) for

5 min and a linear gradient of solvent B (acetonitrile, 0% to 100%) for 25 min followed by 100% solvent A for 5 min, all at a flow rate of 0.5 mL/min.

Determination of MPC. MPC of moxifloxacin with *M. tuberculosis* NHN1664 was determined by methods described previously (65, 88). Cultures of MDR strain *M. tuberculosis* NHN1664 were grown to OD_{600} 0.6 to 0.7. Approximately 2.5×10^9 bacilli were plated on 7H11 agar containing either moxifloxacin (2 \times , 4 \times , or 8 \times MIC) alone or in combination with NAC at either 1 mM or 2 mM. Resistant colonies were enumerated after incubation at 37°C for 8 weeks. The drug-resistant phenotype was confirmed by replating on drug-containing 7H11-agar plates. MPC was determined as the lowest concentration of drug that prevented bacterial colony formation when $>2 \times 10^9$ bacteria were plated on drug-containing 7H11 plates. Mutation frequency with moxifloxacin was calculated as the number of mutants appearing on drug-containing plates divided by the viable input bacteria.

Determination of drug-tolerant *M. tuberculosis* population ex vivo. Murine bone marrow-derived macrophages (BMDMs) were infected with Mrx1-roGFP2-expressing *M. tuberculosis* H37Rv at a multiplicity of infection of 10. After extracellular bacteria were washed off, infected macrophages were left untreated for 24 h for the emergence of the drug-tolerant population. At 24 h postinfection, macrophages harboring E_{M5H} -reduced and E_{M5H} -basal *M. tuberculosis* were sorted using a BD FACSAria fusion flow cytometer. The sorted, infected BMDMs were seeded into 96-well plates followed by treatment with 3 \times MIC of moxifloxacin (1 \times MIC = 0.5 μ M) for 48 h. After treatment, cells were lysed with 0.05% sodium dodecyl sulfate (SDS) in 7H9 medium, serially diluted, and plated on 7H11-OADC agar plates. Plates were incubated at 37°C for 3 to 4 weeks before CFU were enumerated.

In vivo drug efficacy. All animal studies were executed as per guidelines prescribed by the Committee for the Purpose of Control and Supervision of Experiments on Animals, Government of India, with approval from the Institutional Animal Ethical Committee and Biosafety Level-3 Committee. Six- to 8-week-old female pathogen-free BALB/c mice were infected via a low-dose aerosol exposure to the *M. tuberculosis* MDR strain NHN1664 using a Madison chamber aerosol generation instrument. The short-course mouse model of infection was performed as described previously (111). At day 1 postinfection, three mice were sacrificed to confirm implantation of ~ 100 CFU of bacteria per mouse. Mice were randomly divided into 4 groups ($n = 5$ per group). Feed and water were given *ad libitum*. Treatment with moxifloxacin and/or NAC started 21 days postinfection and continued for 10 days; untreated control mice received water rather than the two test compounds. Treated mice were administered moxifloxacin (50 mg/kg of body weight), NAC (500 mg/kg of body weight), and a combination of moxifloxacin and NAC at 50 mg/kg and 500 mg/kg of body weight, respectively, by oral gavage, once daily. Five infected mice were sacrificed at the start of treatment as pretreatment controls. After treatment, mice were sacrificed, and the lungs and spleens were harvested for measurement of bacterial burden. CFU were determined by plating appropriate serial dilutions on 7H11 (supplemented with OADC) agar plates and counting visible colonies after 3 to 4 weeks of incubation at 37°C. Data were normalized to whole organs.

Detection of moxifloxacin-resistant mutants in murine model of infection. Six- to 8-week-old female, pathogen-free BALB/c mice were infected via a high-dose aerosol exposure to the *M. tuberculosis* MDR strain NHN1664 using a Madison chamber aerosol generation instrument. At day 1 postinfection, three mice were sacrificed to determine implantation of $>10^3$ CFU of bacteria per mouse. Mice were then randomly divided into 4 treatment groups, with 6 mice each in the vehicle control group, the NAC-only group, and the groups receiving either moxifloxacin or a combination of NAC and moxifloxacin. Feed and water were given *ad libitum*. Treatment with moxifloxacin and/or NAC started 14 days postinfection and continued for 14 days; untreated control mice received water rather than the two test compounds. Treated mice were administered moxifloxacin (50 mg/kg of body weight), NAC (500 mg/kg of body weight), and a combination of moxifloxacin and NAC at 50 mg/kg and 500 mg/kg of body weight, respectively, by oral gavage, once daily. Five infected mice were sacrificed at the start of treatment as pretreatment controls. After treatment, mice were sacrificed, and the lungs and spleens were harvested together. Moxifloxacin-resistant mutants were selected by plating the undiluted homogenates (lung and spleen) on five 7H11 plates containing 0.5 μ M moxifloxacin (4 \times MIC). Plates were incubated for 3 to 4 weeks at 37°C.

Statistical analysis. Statistical analysis was performed using GraphPad Prism version 8.4.3 software (GraphPad, San Diego, CA). Mean and standard deviation values were plotted as indicated in the figure legends. A *P* value of less than 0.05 was considered significant. Statistical significance was determined by unpaired two-tailed Student's *t* test; either one-way or two-way analysis of variance (ANOVA) was performed where comparison of multiple groups was made.

Data availability. Further information, resources, constructs, and reagents are available on request to A.S.

SUPPLEMENTAL MATERIAL

Supplemental material is available online only.

SUPPLEMENTAL FILE 1, PDF file, 1.6 MB.

SUPPLEMENTAL FILE 2, XLSX file, 0.4 MB.

ACKNOWLEDGMENTS

We thank the following for critical comments on the manuscript: Lanbo Shi, Bo Shopsis, and Xilin Zhao.

This work was supported by Wellcome Trust-Department of Biotechnology (DBT) India Alliance grant IA/S/16/2/502700 (A.S.) and in part by DBT grants BT/PR13522/COE/34/27/2015, BT/PR29098/Med/29/1324/2018, and BT/HRD/NBA/39/07/2018-19 (A.S.), DBT-IISc

Partnership Program grant 22-0905-0006-05-987 436, and the Infosys Foundation. A.S. is a senior fellow of Wellcome Trust-DBT India Alliance. S. Singh was supported by a National Postdoctoral Fellowship from the Department of Science and Technology (DST), India vide file number PDF/2018/2941. S. Shee was supported by a fellowship award from Indian Institute of Science (IISc).

The funders had no role in study design, data collection and analysis, decision to publish, or preparation of the manuscript.

We declare that no competing interests exist.

REFERENCES

- Lange C, Chesov D, Heyckendorf J, Leung CC, Udawadia Z, Dheda K. 2018. Drug-resistant tuberculosis: an update on disease burden, diagnosis and treatment. *Respirology* 23:656–673. <https://doi.org/10.1111/resp.13304>.
- WHO. 2019. Global tuberculosis report 2019. World Health Organization, Geneva, Switzerland.
- WHO. 2013. Global tuberculosis report 2013. World Health Organization, Geneva, Switzerland.
- Shandil RK, Jayaram R, Kaur P, Gaonkar S, Suresh BL, Mahesh BN, Jayashree R, Nandi V, Bharath S, Balasubramanian V. 2007. Moxifloxacin, ofloxacin, sparfloxacin, and ciprofloxacin against *Mycobacterium tuberculosis*: evaluation of *in vitro* and pharmacodynamic indices that best predict *in vivo* efficacy. *Antimicrob Agents Chemother* 51:576–582. <https://doi.org/10.1128/AAC.00414-06>.
- Dong Y, Xu C, Zhao X, Domagala J, Drlica K. 1998. Fluoroquinolone action against mycobacteria: effects of C-8 substituents on growth, survival, and resistance. *Antimicrob Agents Chemother* 42:2978–2984. <https://doi.org/10.1128/AAC.42.11.2978>.
- Ruan Q, Liu Q, Sun F, Shao L, Jin J, Yu S, Ai J, Zhang B, Zhang W. 2016. Moxifloxacin and gatifloxacin for initial therapy of tuberculosis: a meta-analysis of randomized clinical trials. *Emerg Microbes Infect* 5:e12. <https://doi.org/10.1038/emi.2016.12>.
- Rodríguez JC, Ruiz M, Climent A, Royo G. 2001. *In vitro* activity of four fluoroquinolones against *Mycobacterium tuberculosis*. *Int J Antimicrob Agents* 17:229–231. [https://doi.org/10.1016/s0924-8579\(00\)00337-x](https://doi.org/10.1016/s0924-8579(00)00337-x).
- Malik M, Zhao X, Drlica K. 2006. Lethal fragmentation of bacterial chromosomes mediated by DNA gyrase and quinolones. *Mol Microbiol* 61: 810–825. <https://doi.org/10.1111/j.1365-2958.2006.05275.x>.
- Nuermberger EL, Yoshimatsu T, Tyagi S, O'Brien RJ, Vernon AN, Chaisson RE, Bishai WR, Grosset JH. 2004. Moxifloxacin-containing regimen greatly reduces time to culture conversion in murine tuberculosis. *Am J Respir Crit Care Med* 169:421–426. <https://doi.org/10.1164/rccm.200310-1380OC>.
- Pletz MWR, De Roux A, Roth A, Neumann K-H, Mauch H, Lode H. 2004. Early bactericidal activity of moxifloxacin in treatment of pulmonary tuberculosis: a prospective, randomized study. *Antimicrob Agents Chemother* 48:780–782. <https://doi.org/10.1128/AAC.48.3.780-782.2004>.
- Dorman SE, Nahid P, Kurbatova EV, Phillips PPJ, Bryant K, Dooley KE, Engle M, Goldberg SV, Phan HT, Hakim J, Johnson JL, Lourens M, Martinson NA, Muzanyi G, Narunsky K, Nerette S, Nguyen NV, Pham TH, Pierre S, Purfield AE, Samaneka W, Savic RM, Sanne I, Scott NA, Shenje J, Sizemore E, Vernon A, Waja Z, Weiner M, Swindells S, Chaisson RE, Tuberculosis Trials Consortium. 2021. Four-month rifapentine regimens with or without moxifloxacin for tuberculosis. *N Engl J Med* 384:1705–1718. <https://doi.org/10.1056/NEJMoa2033400>.
- Gillespie SH, Crook AM, McHugh TD, Mendel CM, Meredith SK, Murray SR, Pappas F, Phillips PPJ, Nunn AJ, REMoxTB Consortium. 2014. Four-month moxifloxacin-based regimens for drug-sensitive tuberculosis. *N Engl J Med* 371:1577–1587. <https://doi.org/10.1056/NEJMoa1407426>.
- Jindani A, Harrison TS, Nunn AJ, Phillips PPJ, Churchyard GJ, Charalambous S, Hatherill M, Geldenhuys H, McIlleron HM, Zvada SP, Mungofa S, Shah NA, Zizhou S, Magweta L, Shepherd J, Nyirenda S, van Dijk JH, Clouting HE, Coleman D, Bateson ALE, McHugh TD, Butcher PD, Mitchison DA, RIFAQUIN Trial Team. 2014. High-dose rifapentine with moxifloxacin for pulmonary tuberculosis. *N Engl J Med* 371:1599–1608. <https://doi.org/10.1056/NEJMoa1314210>.
- Jawahar MS, Banurekha VV, Paramasivan CN, Rahman F, Ramchandran R, Venkatesan P, Balasubramanian R, Selvakumar N, Ponnuraja C, Iliayas AS, Gangadevi NP, Raman B, Baskaran D, Kumar SR, Kumar MM, Mohan V, Ganapathy S, Kumar V, Shanmugam G, Charles N, Sakthivel MR, Jagannath K, Chandrasekar C, Parthasarathy RT, Narayanan PR. 2013. Randomized clinical trial of thrice-weekly 4-month moxifloxacin or gatifloxacin containing regimens in the treatment of new sputum positive pulmonary tuberculosis patients. *PLoS One* 8:e67030. <https://doi.org/10.1371/journal.pone.0067030>.
- Drlica K, Zhao X. 2021. Bacterial death from treatment with fluoroquinolones and other lethal stressors. *Expert Rev Anti Infect Ther* 19:601–618. <https://doi.org/10.1080/14787210.2021.1840353>.
- Hong Y, Zeng J, Wang X, Drlica K, Zhao X. 2019. Post-stress bacterial cell death mediated by reactive oxygen species. *Proc Natl Acad Sci U S A* 116:10064–10071. <https://doi.org/10.1073/pnas.1901730116>.
- Hong Y, Li Q, Gao Q, Xie J, Huang H, Drlica K, Zhao X. 2020. Reactive oxygen species play a dominant role in all pathways of rapid quinolone-mediated killing. *J Antimicrob Chemother* 75:576–585. <https://doi.org/10.1093/jac/dkz485>.
- Ehrt S, Schnappinger D. 2009. Mycobacterial survival strategies in the phagosome: defence against host stresses. *Cell Microbiol* 11:1170–1178. <https://doi.org/10.1111/j.1462-5822.2009.01335.x>.
- Bhaskar A, Chawla M, Mehta M, Parikh P, Chandra P, Bhawe D, Kumar D, Carroll KS, Singh A. 2014. Reengineering redox sensitive GFP to measure mycothiol redox potential of *Mycobacterium tuberculosis* during infection. *PLoS Pathog* 10:e1003902. <https://doi.org/10.1371/journal.ppat.1003902>.
- Dwyer DJ, Belenky PA, Yang JH, MacDonald IC, Martell JD, Takahashi N, Chan CTY, Lobritz MA, Braff D, Schwarz EG, Ye JD, Pati M, Vercruyse M, Ralifo PS, Allison KR, Khalil AS, Ting AY, Walker GC, Collins JJ. 2014. Antibiotics induce redox-related physiological alterations as part of their lethality. *Proc Natl Acad Sci U S A* 111:E2100–E2109.
- Liu Y, Imlay JA. 2013. Cell death from antibiotics without the involvement of reactive oxygen species. *Science* 339:1210–1213. <https://doi.org/10.1126/science.1232751>.
- Mishra S, Shukla P, Bhaskar A, Anand K, Baloni P, Jha RK, Mohan A, Rajmani RS, Nagaraja V, Chandra N, Singh A. 2017. Efficacy of β -lactam/ β -lactamase inhibitor combination is linked to WhiB4-mediated changes in redox physiology of *Mycobacterium tuberculosis*. *Elife* 6:e25624. <https://doi.org/10.7554/eLife.25624>.
- Mishra R, Kohli S, Malhotra N, Bandyopadhyay P, Mehta M, Munshi M, Adiga V, Ahuja VK, Shandil RK, Rajmani RS, Seshasayee ASN, Singh A. 2019. Targeting redox heterogeneity to counteract drug tolerance in replicating *Mycobacterium tuberculosis*. *Sci Transl Med* 11:eaaw6635. <https://doi.org/10.1126/scitranslmed.aaw6635>.
- Nambi S, Long JE, Mishra BB, Baker R, Murphy KC, Olive AJ, Nguyen HP, Shaffer SA, Sassetti CM. 2015. The oxidative stress network of *Mycobacterium tuberculosis* reveals coordination between radical detoxification systems. *Cell Host Microbe* 17:829–837. <https://doi.org/10.1016/j.chom.2015.05.008>.
- Padiadpu J, Baloni P, Anand K, Munshi M, Thakur C, Mohan A, Singh A, Chandra N. 2016. Identifying and tackling emergent vulnerability in drug-resistant mycobacteria. *ACS Infect Dis* 2:592–607. <https://doi.org/10.1021/acinfeddis.6b00004>.
- Dwyer DJ, Kohanski MA, Hayete B, Collins JJ. 2007. Gyrase inhibitors induce an oxidative damage cellular death pathway in *Escherichia coli*. *Mol Syst Biol* 3:91. <https://doi.org/10.1038/msb4100135>.
- Malik M, Hussain S, Drlica K. 2007. Effect of anaerobic growth on quinolone lethality with *Escherichia coli*. *Antimicrob Agents Chemother* 51: 28–34. <https://doi.org/10.1128/AAC.00739-06>.
- Zhao X, Xu C, Domagala J, Drlica K. 1997. DNA topoisomerase targets of the fluoroquinolones: a strategy for avoiding bacterial resistance. *Proc Natl Acad Sci U S A* 94:13991–13996. <https://doi.org/10.1073/pnas.94.25.13991>.
- Zhao X, Wang JY, Xu C, Dong Y, Zhou J, Domagala J, Drlica K. 1998. Killing of *Staphylococcus aureus* by C-8-methoxy fluoroquinolones. *Antimicrob Agents Chemother* 42:956–958. <https://doi.org/10.1128/AAC.42.4.956>.
- Drlica K, Zhao X. 2007. Mutant selection window hypothesis updated. *Clin Infect Dis* 44:681–688. <https://doi.org/10.1086/511642>.

31. Luan G, Hong Y, Drlica K, Zhao X. 2018. Suppression of reactive oxygen species accumulation accounts for paradoxical bacterial survival at high quinolone concentration. *Antimicrob Agents Chemother* 62:e01622-17. <https://doi.org/10.1128/AAC.01622-17>.
32. Keyer K, Imlay JA. 1996. Superoxide accelerates DNA damage by elevating free-iron levels. *Proc Natl Acad Sci U S A* 93:13635–13640. <https://doi.org/10.1073/pnas.93.24.13635>.
33. Kohanski MA, Dwyer DJ, Hayete B, Lawrence CA, Collins JJ. 2007. A common mechanism of cellular death induced by bactericidal antibiotics. *Cell* 130:797–810. <https://doi.org/10.1016/j.cell.2007.06.049>.
34. Nandakumar M, Nathan C, Rhee KY. 2014. Isocitrate lyase mediates broad antibiotic tolerance in *Mycobacterium tuberculosis*. *Nat Comm* 5: 4306. <https://doi.org/10.1038/ncomms5306>.
35. Hong Y, Li L, Luan G, Drlica K, Zhao X. 2017. Contribution of reactive oxygen species to thymineless death in *Escherichia coli*. *Nat Microbiol* 2: 1667–1675. <https://doi.org/10.1038/s41564-017-0037-y>.
36. Seaver LC, Imlay JA. 2001. Hydrogen peroxide fluxes and compartmentalization inside growing *Escherichia coli*. *J Bacteriol* 183:7182–7189. <https://doi.org/10.1128/JB.183.24.7182-7189.2001>.
37. Gengenbacher M, Rao SP, Pethe K, Dick T. 2010. Nutrient-starved, non-replicating *Mycobacterium tuberculosis* requires respiration, ATP synthase and isocitrate lyase for maintenance of ATP homeostasis and viability. *Microbiology (Reading)* 156:81–87. <https://doi.org/10.1099/mic.0.033084-0>.
38. Wayne LG, Hayes LG. 1996. An *in vitro* model for sequential study of shiftdown of *Mycobacterium tuberculosis* through two stages of non-replicating persistence. *Infect Immun* 64:2062–2069. <https://doi.org/10.1128/iai.64.6.2062-2069.1996>.
39. Imlay JA. 2013. The molecular mechanisms and physiological consequences of oxidative stress: lessons from a model bacterium. *Nat Rev Microbiol* 11:443–454. <https://doi.org/10.1038/nrmicro3032>.
40. Wayne LG, Hayes LG. 1998. Nitrate reduction as a marker for hypoxic shiftdown of *Mycobacterium tuberculosis*. *Tuber Lung Dis* 79:127–132. <https://doi.org/10.1054/tuld.1998.0015>.
41. Wayne LG, Sramek HA. 1994. Metronidazole is bactericidal to dormant cells of *Mycobacterium tuberculosis*. *Antimicrob Agents Chemother* 38: 2054–2058. <https://doi.org/10.1128/AAC.38.9.2054>.
42. Ma S, Minch KJ, Rustad TR, Hobbs S, Zhou SL, Sherman DR, Price ND. 2015. Integrated modeling of gene regulatory and metabolic networks in *Mycobacterium tuberculosis*. *PLoS Comput Biol* 11:e1004543. <https://doi.org/10.1371/journal.pcbi.1004543>.
43. Kapopoulou A, Lew JM, Cole ST. 2011. The MycoBrowser portal: a comprehensive and manually annotated resource for mycobacterial genomes. *Tuberculosis (Edinb)* 91:8–13. <https://doi.org/10.1016/j.tube.2010.09.006>.
44. Voskuil M, Bartek I, Visconti K, Schoolnik G. 2011. The response of *Mycobacterium tuberculosis* to reactive oxygen and nitrogen species. *Front Microbiol* 2:105. <https://doi.org/10.3389/fmicb.2011.00105>.
45. Anand K, Tripathi A, Shukla K, Malhotra N, Jamithireddy AK, Jha RK, Chaudhury SN, Rajmani RS, Ramesh A, Nagaraja V, Gopal B, Nagaraju G, Narain Seshayee AS, Singh A. 2021. *Mycobacterium tuberculosis* SufR responds to nitric oxide via its 4Fe–4S cluster and regulates Fe–S cluster biogenesis for persistence in mice. *Redox Biol* 46:102062. <https://doi.org/10.1016/j.redox.2021.102062>.
46. Das M, Dewan A, Shee S, Singh A. 2021. The multifaceted bacterial cysteine desulfurases: from metabolism to pathogenesis. *Antioxidants (Basel)* 10:997. <https://doi.org/10.3390/antiox10070997>.
47. Foti JJ, Devadoss B, Winkler JA, Collins JJ, Walker GC. 2012. Oxidation of the guanine nucleotide pool underlies cell death by bactericidal antibiotics. *Science* 336:315–319. <https://doi.org/10.1126/science.1219192>.
48. Dwyer DJ, Collins JJ, Walker GC. 2015. Unraveling the physiological complexities of antibiotic lethality. *Annu Rev Pharmacol Toxicol* 55:313–332. <https://doi.org/10.1146/annurev-pharmtox-010814-124712>.
49. Lamprecht DA, Finin PM, Rahman MA, Cumming BM, Russell SL, Jonnal SR, Adamson JH, Steyn AJ. 2016. Turning the respiratory flexibility of *Mycobacterium tuberculosis* against itself. *Nat Comm* 7:12393. <https://doi.org/10.1038/ncomms12393>.
50. Saini V, Cumming BM, Guidry L, Lamprecht DA, Adamson JH, Reddy VP, Chinta KC, Mazorodze JH, Glasgow JN, Richard-Greenblatt M, Gomez-Velasco A, Bach H, Av-Gay Y, Eoh H, Rhee K, Steyn AJ. 2016. Ergothioneine maintains redox and bioenergetic homeostasis essential for drug susceptibility and virulence of *Mycobacterium tuberculosis*. *Cell Rep* 14:572–585. <https://doi.org/10.1016/j.celrep.2015.12.056>.
51. Lee BS, Kalia NP, Jin XEF, Hasenoehrl EJ, Berney M, Pethe K. 2019. Inhibitors of energy metabolism interfere with antibiotic-induced death in mycobacteria. *J Biol Chem* 294:1936–1943. <https://doi.org/10.1074/jbc.RA118.005732>.
52. Mavi PS, Singh S, Kumar A. 2020. Reductive stress: new insights in physiology and drug tolerance of mycobacterium. *Antioxid Redox Signal* 32: 1348–1366. <https://doi.org/10.1089/ars.2019.7867>.
53. Bhat SA, Iqbal IK, Kumar A. 2016. Imaging the NADH:NAD⁺ homeostasis for understanding the metabolic response of mycobacterium to physiologically relevant stresses. *Front Cell Infect Microbiol* 6:145. <https://doi.org/10.3389/fcimb.2016.00145>.
54. Jaeschke H, Kleinwaechter C, Wendel A. 1992. NADH-dependent reductive stress and ferritin-bound iron in allyl alcohol-induced lipid peroxidation *in vivo*: the protective effect of vitamin E. *Chem Biol Interact* 81: 57–68. [https://doi.org/10.1016/0009-2797\(92\)90026-h](https://doi.org/10.1016/0009-2797(92)90026-h).
55. Kareyeva AV, Grivennikova VG, Vinogradov AD. 2012. Mitochondrial hydrogen peroxide production as determined by the pyridine nucleotide pool and its redox state. *Biochim Biophys Acta* 1817:1879–1885. <https://doi.org/10.1016/j.bbabi.2012.03.033>.
56. Vinogradov AD, Grivennikova VG. 2016. Oxidation of NADH and ROS production by respiratory complex I. *Biochim Biophys Acta* 1857:863–871. <https://doi.org/10.1016/j.bbabi.2015.11.004>.
57. Titov DV, Cracan V, Goodman RP, Peng J, Grabarek Z, Mootha VK. 2016. Complementation of mitochondrial electron transport chain by manipulation of the NAD⁺/NADH ratio. *Science* 352:231–235. <https://doi.org/10.1126/science.aad4017>.
58. Vilch ze C, Weisbrod TR, Chen B, Kremer L, Hazb n MH, Wang F, Alland D, Sacchetti JC, Jacobs WR, Jr. 2005. Altered NADH/NAD⁺ ratio mediates coreistance to isoniazid and ethionamide in mycobacteria. *Antimicrob Agents Chemother* 49:708–720. <https://doi.org/10.1128/AAC.49.2.708-720.2005>.
59. Vilch ze C, Hartman T, Weinrick B, Jain P, Weisbrod TR, Leung LW, Freundlich JS, Jacobs WR. 2017. Enhanced respiration prevents drug tolerance and drug resistance in *Mycobacterium tuberculosis*. *Proc Natl Acad Sci U S A* 114: 4495–4500. <https://doi.org/10.1073/pnas.1704376114>.
60. Vilch ze C, Jacobs WR. 2021. The promises and limitations of N-acetylcysteine as a potentiator of first-line and second-line tuberculosis drugs. *Antimicrob Agents Chemother* 65:e01703-20. <https://doi.org/10.1128/AAC.01703-20>.
61. Held KD, Biaglow JE. 1994. Mechanisms for the oxygen radical-mediated toxicity of various thiol-containing compounds in cultured mammalian cells. *Radiat Res* 139:15–23. <https://doi.org/10.2307/3578727>.
62. Jaworska M, Szulińska G, Wilk M, Tautt J. 1999. Capillary electrophoretic separation of N-acetylcysteine and its impurities as a method for quality control of pharmaceuticals. *J Chromatogr A* 853:479–485. [https://doi.org/10.1016/s0021-9673\(99\)00727-x](https://doi.org/10.1016/s0021-9673(99)00727-x).
63. Sommer I, Schwebel H, Adamo V, Bonnabry P, Bouchoud L, Sadeghipour F. 2020. Stability of N-acetylcysteine (NAC) in standardized pediatric parenteral nutrition and evaluation of N,N-diacetylcysteine (DAC) formation. *Nutrients* 12:1849. <https://doi.org/10.3390/nu12061849>.
64. Srinivas V, Arrieta-Ortiz ML, Kaur A, Peterson EJR, Baliga NS. 2020. PerSort facilitates characterization and elimination of persister subpopulation in mycobacteria. *mSystems* 5:e01127-20. <https://doi.org/10.1128/mSystems.01127-20>.
65. Singh S, Kalia NP, Joshi P, Kumar A, Sharma PR, Kumar A, Bharate SB, Khan IA. 2017. Boeravinone B, a novel dual inhibitor of NorA bacterial efflux pump of *Staphylococcus aureus* and human p-glycoprotein, reduces the biofilm formation and intracellular invasion of bacteria. *Front Microbiol* 8:1868. <https://doi.org/10.3389/fmicb.2017.01868>.
66. Cui J, Liu Y, Wang R, Tong W, Drlica K, Zhao X. 2006. The mutant selection window in rabbits infected with *Staphylococcus aureus*. *J Infect Dis* 194: 1601–1608. <https://doi.org/10.1086/508752>.
67. Mishra R, Yadav V, Guha M, Singh A. 2021. Heterogeneous host–pathogen encounters coordinate antibiotic resilience in *Mycobacterium tuberculosis*. *Trends Microbiol* 29:606–620. <https://doi.org/10.1016/j.tim.2020.10.013>.
68. Amaral EP, Concei o EL, Costa DL, Rocha MS, Marinho JM, Cordeiro-Santos M, D'Imp rio-Lima MR, Barbosa T, Sher A, Andrade BB. 2016. N-acetyl-cysteine exhibits potent anti-mycobacterial activity in addition to its known anti-oxidative functions. *BMC Microbiol* 16:251. <https://doi.org/10.1186/s12866-016-0872-7>.
69. Cao R, Teskey G, Islamoglu H, Abraham R, Munjal S, Gyrurjian K, Zhong L, Venketaraman V. 2018. Characterizing the effects of glutathione as an immunoadjuvant in the treatment of tuberculosis. *Antimicrob Agents Chemother* 62:e01132-18. <https://doi.org/10.1128/AAC.01132-18>.
70. Liu Y, Liu X, Qu Y, Wang X, Li L, Zhao X. 2012. Inhibitors of reactive oxygen species accumulation delay and/or reduce the lethality of several antistaphylococcal agents. *Antimicrob Agents Chemother* 56:6048–6050. <https://doi.org/10.1128/AAC.00754-12>.
71. Almeida D, Nuernberger E, Tyagi S, Bishai WR, Grosset J. 2007. *In vivo* validation of the mutant selection window hypothesis with moxifloxacin

- in a murine model of tuberculosis. *Antimicrob Agents Chemother* 51: 4261–4266. <https://doi.org/10.1128/AAC.01123-07>.
72. Ginsburg AS, Sun R, Calamita H, Scott CP, Bishai WR, Grosset JH. 2005. Emergence of fluoroquinolone resistance in *Mycobacterium tuberculosis* during continuously dosed moxifloxacin monotherapy in a mouse model. *Antimicrob Agents Chemother* 49:3977–3979. <https://doi.org/10.1128/AAC.49.9.3977-3979.2005>.
 73. Lobritz MA, Belenky P, Porter CBM, Gutierrez A, Yang JH, Schwarz EG, Dwyer DJ, Khalil AS, Collins JJ. 2015. Antibiotic efficacy is linked to bacterial cellular respiration. *Proc Natl Acad Sci U S A* 112:8173–8180. <https://doi.org/10.1073/pnas.1509743112>.
 74. Tan MP, Sequeira P, Lin WW, Phong WY, Cliff P, Ng SH, Lee BH, Camacho L, Schnappinger D, Ehrst S, Dick T, Pethe K, Alonso S. 2010. Nitrate respiration protects hypoxic *Mycobacterium tuberculosis* against acid and reactive nitrogen species stresses. *PLoS One* 5:e13356. <https://doi.org/10.1371/journal.pone.0013356>.
 75. Sohaskey CD. 2008. Nitrate enhances the survival of *Mycobacterium tuberculosis* during inhibition of respiration. *J Bacteriol* 190:2981–2986. <https://doi.org/10.1128/JB.01857-07>.
 76. Cunningham-Bussell A, Zhang T, Nathan CF. 2013. Nitrite produced by *Mycobacterium tuberculosis* in human macrophages in physiologic oxygen impacts bacterial ATP consumption and gene expression. *Proc Natl Acad Sci U S A* 110:E4256–E4265. <https://doi.org/10.1073/pnas.1316894110>.
 77. Shapleigh JP. 2009. Dissimilatory and assimilatory nitrate reduction in the purple photosynthetic bacteria, p 623–642. In Hunter CN, Daldal F, Thurnauer MC, Beatty JT (ed), *The purple phototrophic bacteria*. Advances in photosynthesis and respiration, vol 28. Springer, Dordrecht, The Netherlands.
 78. Singh A, Crossman DK, Mai D, Guidry L, Voskuil MI, Renfrow MB, Steyn AJC. 2009. *Mycobacterium tuberculosis* H37Rv maintains redox homeostasis by regulating virulence lipid anabolism to modulate macrophage response. *PLoS Pathog* 5:e1000545. <https://doi.org/10.1371/journal.ppat.1000545>.
 79. Voskuil MI, Schnappinger D, Visconti KC, Harrell MI, Dolganov GM, Sherman DR, Schoolnik G. 2003. Inhibition of respiration by nitric oxide induces a *Mycobacterium tuberculosis* dormancy program. *J Exp Med* 198:705–713. <https://doi.org/10.1084/jem.20030205>.
 80. Richardson AR, Libby SJ, Fang FC. 2008. A nitric oxide-inducible lactate dehydrogenase enables *Staphylococcus aureus* to resist innate immunity. *Science* 319:1672–1676. <https://doi.org/10.1126/science.1155207>.
 81. Price-Whelan A, Dietrich LEP, Newman DK. 2007. Pyocyanin alters redox homeostasis and carbon flux through central metabolic pathways in *Pseudomonas aeruginosa* PA14. *J Bacteriol* 189:6372–6381. <https://doi.org/10.1128/JB.00505-07>.
 82. Ezerina D, Takano Y, Hanaoka K, Urano Y, Dick TP. 2018. N-acetyl cysteine functions as a fast-acting antioxidant by triggering intracellular H₂S and sulfane sulfur production. *Cell Chem Biol* 25:447–459.E4. <https://doi.org/10.1016/j.chembiol.2018.01.011>.
 83. Rodríguez-Rojas A, Kim JJ, Johnston PR, Makarova O, Eravci M, Weise C, Hengge R, Rolff J. 2020. Non-lethal exposure to H₂O₂ boosts bacterial survival and evolvability against oxidative stress. *PLoS Genet* 16:e1008649. <https://doi.org/10.1371/journal.pgen.1008649>.
 84. Mosel M, Li L, Drlica K, Zhao X. 2013. Superoxide-mediated protection of *Escherichia coli* from antimicrobials. *Antimicrob Agents Chemother* 57: 5755–5759. <https://doi.org/10.1128/AAC.00754-13>.
 85. Li L, Hong Y, Luan G, Mosel M, Malik M, Drlica K, Zhao X. 2014. Ribosomal elongation factor 4 promotes cell death associated with lethal stress. *mBio* 5:e01708-14. <https://doi.org/10.1128/mBio.01708-14>.
 86. Dorsey-Oresto A, Lu T, Mosel M, Wang X, Salz T, Drlica K, Zhao X. 2013. YihE kinase is a central regulator of programmed cell death in bacteria. *Cell Rep* 3:528–537. <https://doi.org/10.1016/j.celrep.2013.01.026>.
 87. Imlay JA, Linn S. 1986. Bimodal pattern of killing of DNA-repair-defective or anoxically grown *Escherichia coli* by hydrogen peroxide. *J Bacteriol* 166:519–527. <https://doi.org/10.1128/jb.166.2.519-527.1986>.
 88. Dong Y, Zhao X, Kreiswirth BN, Drlica K. 2000. Mutant prevention concentration as a measure of antibiotic potency: studies with clinical isolates of *Mycobacterium tuberculosis*. *Antimicrob Agents Chemother* 44: 2581–2584. <https://doi.org/10.1128/AAC.44.9.2581-2584.2000>.
 89. Prideaux B, Via LE, Zimmerman MD, Eum S, Sarathy J, O'Brien P, Chen C, Kaya F, Weiner DM, Chen P-Y, Song T, Lee M, Shim TS, Cho JS, Kim W, Cho SN, Olivier KN, Barry CE, Dartois V. 2015. The association between sterilizing activity and drug distribution into tuberculosis lesions. *Nat Med* 21:1223–1227. <https://doi.org/10.1038/nm.3937>.
 90. Sarathy J, Blanc L, Alvarez-Cabrera N, O'Brien P, Dias-Freedman I, Mina M, Zimmerman M, Kaya F, Ho Liang H-P, Prideaux B, Dietzold J, Salgame P, Savic RM, Linderman J, Kirschner D, Pienaar E, Dartois V. 2019. Fluoroquinolone efficacy against tuberculosis is driven by penetration into lesions and activity against resident bacterial populations. *Antimicrob Agents Chemother* 63:e02516-18. <https://doi.org/10.1128/AAC.02516-18>.
 91. Davies Forsman L, Niward K, Kuhlín J, Zheng X, Zheng R, Ke R, Hong C, Werngren J, Paues J, Simonsson USH, Eliasson E, Hoffner S, Xu B, Alffenaar J-W, Schön T, Hu Y, Bruchfeld J. 2021. Suboptimal moxifloxacin and levofloxacin drug exposure during treatment of patients with multidrug-resistant tuberculosis: results from a prospective study in China. *Eur Respir J* 57:2003463. <https://doi.org/10.1183/13993003.03463-2020>.
 92. Baniyasi S, Eftekhari P, Tabarsi P, Fahimi F, Raoufy MR, Masjedi MR, Velayati AA. 2010. Protective effect of N-acetylcysteine on antituberculosis drug-induced hepatotoxicity. *Eur J Gastroenterol Hepatol* 22: 1235–1238. <https://doi.org/10.1097/MEG.0b013e32833aa11b>.
 93. Kranzer K, Elamin WF, Cox H, Seddon JA, Ford N, Drobniewski F. 2015. A systematic review and meta-analysis of the efficacy and safety of N-acetylcysteine in preventing aminoglycoside-induced ototoxicity: implications for the treatment of multidrug-resistant TB. *Thorax* 70:1070–1077. <https://doi.org/10.1136/thoraxjnl-2015-207245>.
 94. Palanisamy GS, Kirk NM, Ackart DF, Shanley CA, Orme IM, Basaraba RJ. 2011. Evidence for oxidative stress and defective antioxidant response in guinea pigs with tuberculosis. *PLoS One* 6:e26254. <https://doi.org/10.1371/journal.pone.0026254>.
 95. Mahakalkar SM, Nagrale D, Gaur S, Urade C, Murhar B, Turankar A. 2017. N-acetylcysteine as an add-on to Directly Observed Therapy Short-I therapy in fresh pulmonary tuberculosis patients: a randomized, placebo-controlled, double-blinded study. *Perspect Clin Res* 8:132–136.
 96. Nagrale D, Mahakalkar S, Gaur S. 2013. Supplementation of N-acetylcysteine as an adjuvant in treatment of newly diagnosed pulmonary tuberculosis patients: a prospective, randomized double blind, placebo controlled study. *Eur Respir J* 42:P2833.
 97. Firsov AA, Vostrov SN, Lubenko IY, Drlica K, Portnoy YA, Zinner SH. 2003. *In vitro* pharmacodynamic evaluation of the mutant selection window hypothesis using four fluoroquinolones against *Staphylococcus aureus*. *Antimicrob Agents Chemother* 47:1604–1613. <https://doi.org/10.1128/AAC.47.5.1604-1613.2003>.
 98. Gumbo T, Louie A, Deziel MR, Parsons LM, Salfinger M, Drusano GL. 2004. Selection of a moxifloxacin dose that suppresses drug resistance in *Mycobacterium tuberculosis*, by use of an *in vitro* pharmacodynamic infection model and mathematical modeling. *J Infect Dis* 190:1642–1651. <https://doi.org/10.1086/424849>.
 99. Steyn AJC, Joseph J, Bloom BR. 2003. Interaction of the sensor module of *Mycobacterium tuberculosis* H37Rv KdpD with members of the Lpr family. *Mol Microbiol* 47:1075–1089. <https://doi.org/10.1046/j.1365-2958.2003.03356.x>.
 100. Singh A, Mai D, Kumar A, Steyn AJC. 2006. Dissecting virulence pathways of *Mycobacterium tuberculosis* through protein–protein association. *Proc Natl Acad Sci U S A* 103:11346–11351. <https://doi.org/10.1073/pnas.0602817103>.
 101. Fan XY, Tang BK, Xu YY, Han AX, Shi KX, Wu YK, Ye Y, Wei ML, Niu C, Wong KW, Zhao GP, Lyu LD. 2018. Oxidation of dCTP contributes to antibiotic lethality in stationary-phase mycobacteria. *Proc Natl Acad Sci U S A* 115:2210–2215. <https://doi.org/10.1073/pnas.1719627115>.
 102. Vilch e C, Hartman T, Weinrick B, Jacobs WR. 2013. *Mycobacterium tuberculosis* is extraordinarily sensitive to killing by a vitamin C-induced Fenton reaction. *Nat Comm* 4:1881. <https://doi.org/10.1038/ncomms2898>.
 103. Taneja NK, Tyagi JS. 2007. Resazurin reduction assays for screening of anti-tubercular compounds against dormant and actively growing *Mycobacterium tuberculosis*, *Mycobacterium bovis* BCG and *Mycobacterium smegmatis*. *J Antimicrob Chemother* 60:288–293. <https://doi.org/10.1093/jac/dkm207>.
 104. Edgar R, Domrachev M, Lash AE. 2002. Gene Expression Omnibus: NCBI gene expression and hybridization array data repository. *Nucleic Acids Res* 30:207–210. <https://doi.org/10.1093/nar/30.1.207>.
 105. Barrett T, Wilhite SE, Ledoux P, Evangelista C, Kim IF, Tomashevsky M, Marshall KA, Phillippy KH, Sherman PM, Holko M, Yefanov A, Lee H, Zhang N, Robertson CL, Serova N, Davis S, Soboleva A. 2013. NCBI GEO: archive for functional genomics data sets—update. *Nucleic Acids Res* 41: D991–D995. <https://doi.org/10.1093/nar/gks1193>.
 106. Li S, Sinai M. 2019. GeneOverlap: test and visualize gene overlaps. <https://doi.org/10.18129/B9.bioc.GeneOverlap>.
 107. R Core Team. 2018. R: a language and environment for statistical computing. R Foundation for Statistical Computing, Vienna, Austria. <https://www.R-project.org/>.
 108. Kurthkoti K, Amin H, Marakalala MJ, Ghanny S, Subbian S, Sakatos A, Livny J, Fortune SM, Berney M, Rodriguez GM. 2017. The capacity of *Mycobacterium tuberculosis* to survive iron starvation might enable it to

- persist in iron-deprived microenvironments of human granulomas. *mBio* 8:e01092-17. <https://doi.org/10.1128/mBio.01092-17>.
109. Fish WW. 1988. Rapid colorimetric micromethod for the quantitation of complexed iron in biological samples. *Methods Enzymol* 158:357–364. [https://doi.org/10.1016/0076-6879\(88\)58067-9](https://doi.org/10.1016/0076-6879(88)58067-9).
110. Chawla M, Parikh P, Saxena A, Munshi M, Mehta M, Mai D, Srivastava AK, Narasimhulu KV, Redding KE, Vashi N, Kumar D, Steyn AJC, Singh A. 2012. *Mycobacterium tuberculosis* WhiB4 regulates oxidative stress response to modulate survival and dissemination *in vivo*. *Mol Microbiol* 85:1148–1165. <https://doi.org/10.1111/j.1365-2958.2012.08165.x>.
111. Lenaerts AJ, Gruppo V, Brooks JV, Orme IM. 2003. Rapid *in vivo* screening of experimental drugs for tuberculosis using gamma interferon gene-disrupted mice. *Antimicrob Agents Chemother* 47:783–785. <https://doi.org/10.1128/AAC.47.2.783-785.2003>.

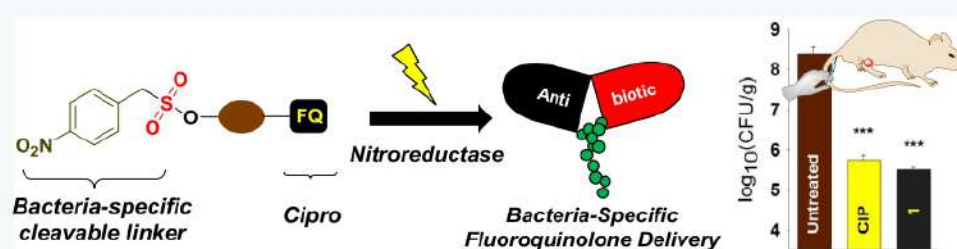
Targeted Antibacterial Activity Guided by Bacteria-Specific Nitroreductase Catalytic Activation to Produce Ciprofloxacin

Kundansingh A. Pardeshi,[†] T. Anand Kumar,[†] Govindan Ravikumar,[†] Manjulika Shukla,^{‡,‡} Grace Kaul,^{‡,‡} Sidharth Chopra,^{*,‡} and Harinath Chakrapani^{*,†,‡}

[†]Department of Chemistry, Indian Institute of Science Education and Research Pune, Dr. Homi Bhabha Road, Pune-411 008, Maharashtra, India

[‡]Division of Microbiology, CSIR-Central Drug Research Institute, Lucknow-226031, Uttar Pradesh, India

Supporting Information



ABSTRACT: Fluoroquinolones (FQs) are among the front-line antibiotics used to treat severe infections caused by Gram-negative bacteria. However, recently, due to toxicity concerns, their use has been severely restricted. Hence, efforts to direct delivery of this antibiotic specifically to bacteria/site of infection are underway. Here, we report a strategy that uses a bacterial enzyme for activation of a prodrug to generate the active antibiotic. The ciprofloxacin-latent fluorophore conjugate **1**, which is designed as a substrate for nitroreductase (NTR), a bacterial enzyme, was synthesized. Upon activation by NTR, release of Ciprofloxacin (CIP) as well as a fluorescence reporter was observed. We provide evidence for the prodrug permeating bacteria to generate a fluorescent signal and we found no evidence for activation in mammalian cells supporting selectivity of activation within bacteria. As a testament to its efficacy, **1** was found to have potent bactericidal activity nearly identical to CIP and significantly reduced the bacterial burden in a neutropenic mouse thigh infection model, again, at comparable potency with CIP, a clinically used FQ. Thus, together, we have developed a small molecule that facilitates bacteria-specific fluoroquinolone delivery.

INTRODUCTION

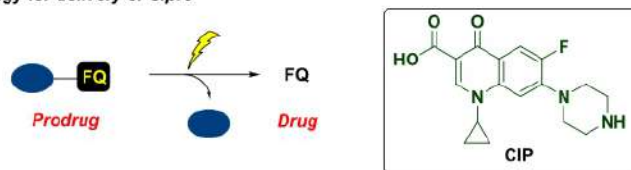
The advent of antibiotics in the past century has revolutionized health care globally and has tremendously improved survival rates. Among the major classes of these drugs, fluoroquinolones (FQs) are widely used to treat a number of serious bacterial infections.¹ However, the side effects associated with this class of antibiotics have recently emerged as a major concern.^{2–4} Therefore, methodologies for activation of the active FQ antibiotic specifically within bacteria are highly desirable. These strategies typically involve appending FQ with a group that renders the antibiotic less active. Upon cleavage of this group, the active antibiotic is released (Figure 1a). Activation methodologies based on a bioreductive enzyme,⁵ esterase,⁶ alkaline phosphatase,⁷ thiol-induced disulfide cleavage,^{8,9} and light^{10–13} have been reported. Miller and co-workers recently reported a bioreductive enzyme activated CIP derivative with excellent antibacterial properties.⁵ However, due to the wide prevalence of bioreductive enzymes, the specificity, if any, of the conjugate toward bacteria remains unclear. Similarly, esterases are found in nearly all cells, and unless other groups for localization are attached, there is little

scope for selectivity. The alkaline phosphatase-strategy has been used to improve aqueous solubility rather than selectivity. The cleavage of a disulfide linker has been used to generate FQ.⁹ Due to the ubiquitous nature of thiols, again, selectivity toward bacteria is not clear. A large number of light-activated methods are in development; at present, the *in vivo* applicability of these technologies is yet unclear.^{10–13} We hypothesized that a prodrug approach involving an enzyme that is expressed in bacteria but not in humans would be ideal. We considered *Escherichia coli* (*E. coli*) nitroreductase (NTR), which is a class of enzymes that is predominantly present in bacteria as the bacterial enzyme. This enzyme has been exploited in developing diagnostics by appending a latent fluorophore with a nitroaryl group.^{14–19} Upon metabolism by NTR, an electron withdrawing nitro group is converted to an electron-rich hydroxylamino or an amino group (Figure 1b).^{20,21} This can lead to a movement of electrons to release a fluorophore. Since electron-deficient aryl groups can quench

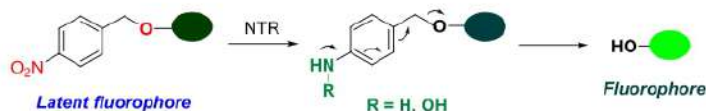
Received: December 12, 2018

Published: January 7, 2019

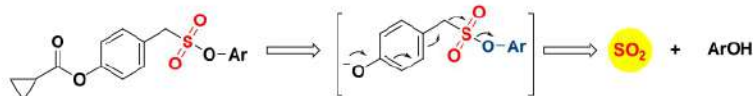
(a) Prodrug strategy for delivery of Cipro



(b) Nitroreductase-activated fluorescent probe for imaging



(c) Sulfonate-based enzyme-triggered release of an aryl alcohol



(d) Proposed prodrug strategy for release of a fluorophore coupled with an antibiotic



Figure 1. (a) Prodrug strategy for delivery of fluoroquinolones (FQs) such as Ciprofloxacin (CIP). (b) Strategies toward activation of latent fluorophores by reduction of the nitroaryl group via nitroreductase. (c) Sulfonate-based prodrug strategy that generates an aryl alcohol and sulfur dioxide: this scaffold has been found to be more stable than the corresponding carbonate linker. (d) Proposed nitroarylsulfonate that is expected to be activated by NTR to produce a FQ as well as a fluorescence reporter.

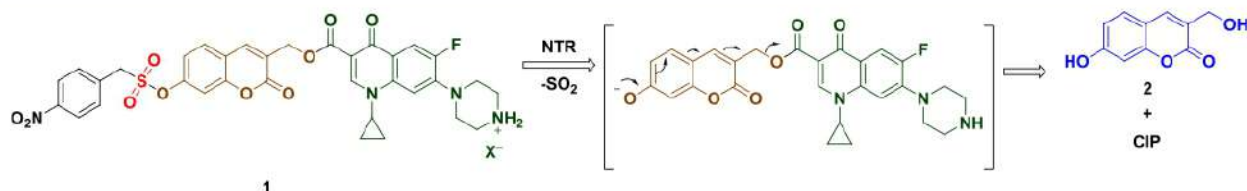
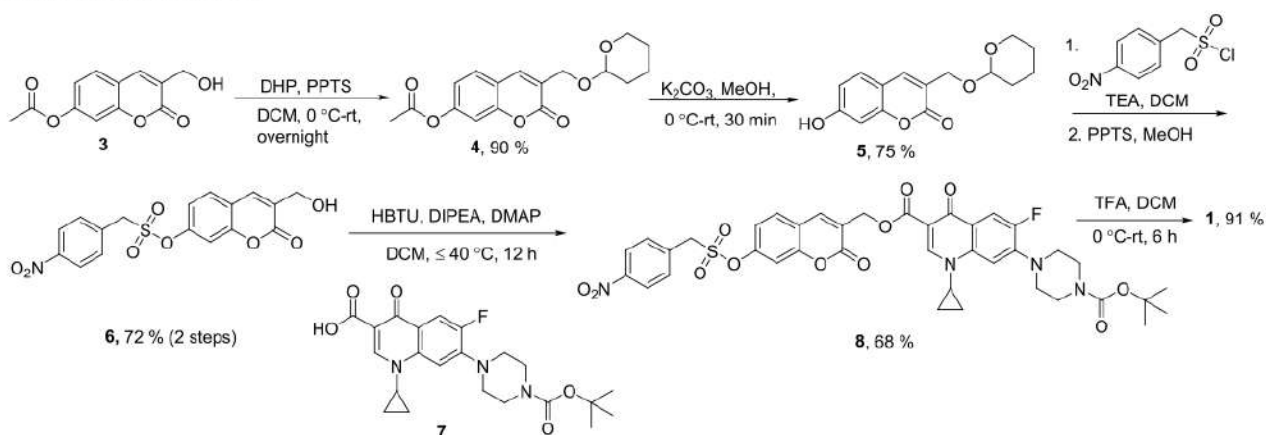


Figure 2. Design of the conjugate **1**: this compound is expected to be activated by nitroreductase to generate a fluorophore **2**, CIP, and sulfur dioxide. $X^- = \text{CF}_3\text{COO}^-$.

Scheme 1. Synthesis of **1**

fluorescence, when this group is detached, a strong fluorescence signal is seen. Thus, we hypothesized that

attaching a nitroaryl linker to FQ will help deliver FQ to bacteria.

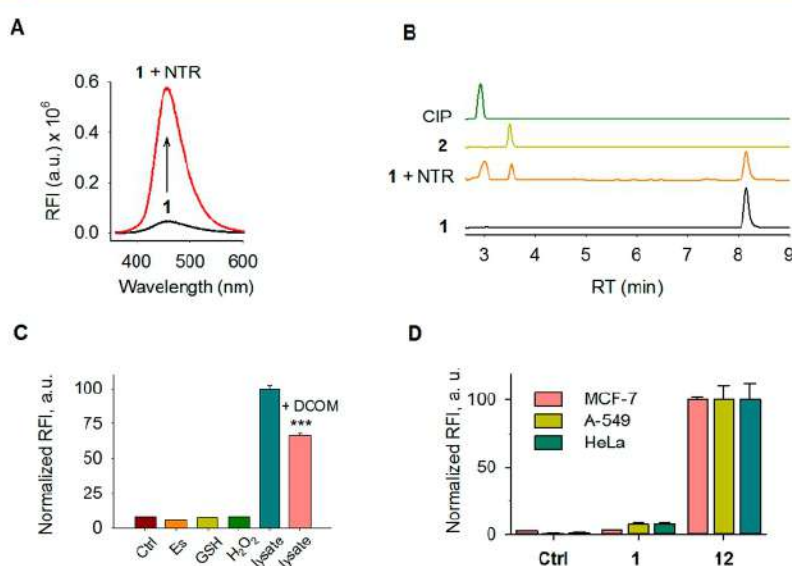


Figure 3. (A) Fluorescence spectra ($\lambda_{\text{ex}} = 350 \text{ nm}$; $\lambda_{\text{em}} = 450 \text{ nm}$) upon incubation of **1** ($10 \mu\text{M}$) in the presence of NTR ($10 \mu\text{g/mL}$) and NADH ($30 \mu\text{M}$) in PBS (pH 7.4, 10 mM). Significant enhancement in the fluorescent signal attributable to the formation of **2** was observed in the presence of NTR and NADH. (B) Monitoring the release of **1** in the presence of NTR by HPLC. Compound **1** ($25 \mu\text{M}$) was incubated with NTR ($20 \mu\text{g/mL}$) and NADH ($75 \mu\text{M}$) in PBS (pH 7.4). Compound **1** is metabolized by NTR to generate fluorophore **2** and CIP. The absorbance at 320 nm was monitored. (C) Stability of compound **1** was estimated by monitoring enhancement in fluorescence ($\lambda_{\text{ex}} = 350 \text{ nm}$; $\lambda_{\text{em}} = 450 \text{ nm}$). Compound **1** ($25 \mu\text{M}$) was incubated in the presence of esterase (ES; 1 U/mL), hydrogen peroxide (H_2O_2 ; 0.25 mM), glutathione (GSH; 0.25 mM), as well as *E. coli* lysate alone or in the presence of NTR inhibitor; Dicoumarol (DCOM, $100 \mu\text{M}$). *** $p < 0.001$. (D) Monitoring the activation of **1** ($25 \mu\text{M}$) in cell lysates of three cancer cell lines (Breast, MCF-7; Lung, A-549; and Cervix, HeLa) by measuring fluorescence ($\lambda_{\text{ex}} = 350 \text{ nm}$; $\lambda_{\text{em}} = 450 \text{ nm}$). Compound **12** ($25 \mu\text{M}$), a cell-permeable generator of UMB was used as a positive control. No significant enhancement in fluorescence signal from **1** suggests its specificity for bacterial cellular environment.

Although certain FOs are mildly fluorescent,^{22,23} they are not easy to track within cells as the excitation wavelength is in the short ultraviolet range ($<300 \text{ nm}$). Therefore, it is desirable to attach a longer wavelength fluorescence reporter. Here, we used the coumarin-based fluorophore strategy that has been previously used to report delivery of a drug or bioactive molecule.^{24,25} Imaging in the green channel is possible and this fluorophore is also compatible with two-photon imaging.²⁶ The phenol-based fluorophore needs to be attached to the trigger. Among the self-immolative linkers, generation of a thermodynamically stable species such as gaseous CO_2 helps improve efficiency of delivery.^{27,28} However, such carbonate linkers are somewhat labile and have poor stability in biological milieu.^{29,30} We recently reported a sulfonate-based linker that was significantly more stable than the carbonate (Figure 1c).³¹ Since SO_2 in the form of sulfites is widely used in the food industry, this group is expected to be well tolerated.^{32–34} Thus, we designed a nitroreductase-activated conjugate of CIP (Figure 1d). The proposed compound **1** is expected to be activated by bacterial NTR to produce a fluorophore (**2**) and CIP (Figure 2). Since the conjugate has a fluorescence reporter, this strategy allows for real-time monitoring of release of the antibiotic at the site of infection (Figure 1d).

RESULTS AND DISCUSSION

Starting from the coumarin derivative **3**, using orthogonal protection and deprotection strategies, compound **6** was synthesized (Scheme 1). This alcohol was coupled with *t*-Boc protected CIP, **7**, to produce **8** in 68% yield. Next, the desired compound **1** was obtained by deprotection of the *t*-Boc group by trifluoroacetic acid (Scheme 1).

Compound **1** was reacted with *E. coli* NTR and a distinct increase in fluorescence corresponding to the formation of **2** (Figure 3a) was observed. In the absence of NTR, a weak fluorescence signal was observed. The difference in intensity between **1** and **1** + NTR was nearly 12-fold suggesting the suitability of this activation method to monitor release of the fluorophore (see SI, Figure S1 for controls). CIP alone showed a mild fluorescence signal ($\lambda_{\text{ex}} = 350 \text{ nm}$; $\lambda_{\text{em}} = 450 \text{ nm}$) under these conditions (see SI, Figure S1). Next, HPLC analysis of this reaction mixture revealed the formation of **2** as well as CIP supporting the capability of **1** to produce the active antibiotic (Figure 3b; for time course, see SI, Figure S2). Together, these results are consistent with the proposed mechanism of activation, which is reduction of the nitro group to produce the electron-rich amine/hydroxylamine, which then collapses to produce **2** and CIP (Scheme S1).

Using *E. coli* cell lysate, we next tested if **1** was metabolized to produce a fluorescent signal attributable to **2**. When this assay was conducted with bacterial cell lysate, a distinct increase in fluorescence signal during incubation for 2 h was recorded (Figure 3c). In the presence of dicoumarol (DCOM), a known NTR inhibitor, a decrease in a fluorescence signal was observed suggesting specificity of activation by NTR (Figure 3c). Next, in order to further confirm whether **1** was cell-permeable, *E. coli* cells were incubated with **1** and the subsequent lysis of cells followed by HPLC analysis revealed that **1** was able to permeate into the *E. coli* cells along with the generation of CIP and **2** (see SI, Figure S5a).

Confocal microscopy of **1** treated *E. coli* cells showed evidence for increase in fluorescence in green channel (see SI, Figure S6). Furthermore, we found evidence for stress induced

Table 1. Calculated Partition Coefficients and Minimum Inhibitory Concentrations (MICs)

| Entry | Compd | clogP ^a | MIC ($\mu\text{g/mL}$) ^b | | | |
|-------|--------------|--------------------|---------------------------------------|----------|----------|----------|
| | | | ATCC 25922 | NR 17663 | NR 17666 | NR 17661 |
| 1 | 1 | 3.21 | 0.03 | 0.125 | 0.125 | >64 |
| 2 | 7 | 3.53 | >64 | - | - | - |
| 3 | 8 | 4.88 | >64 | - | - | - |
| 4 | 9 | 3.52 | 2 | - | - | - |
| 5 | 10 | 3.47 | 8 | - | - | - |
| 6 | 11 | 3.46 | 4 | - | - | - |
| 7 | 17 | 2.64 | 2 | - | - | - |
| 8 | CIP | 1.86 | 0.000725 | 0.0075 | 0.015 | 32 |
| 9 | Norfloxacin | 1.81 | <0.03 | - | - | - |
| 10 | Levofloxacin | -0.51 | 0.015 | 0.03 | 0.03 | 32 |
| 11 | Moxifloxacin | 2.53 | 0.015 | 0.015 | 0.03 | 32 |

^aCalculated using ChemBioDraw Ultra 13.0. ^b*E. coli* strains.

in cells, likely due to the generation of CIP (see SI, Figure S6). Next, the ability of **1** to inhibit growth of *E. coli* (ATCC 25922) was tested by determining its minimum inhibitory concentration (MIC) using the standard broth dilution assay. The MIC was determined to be 0.03 $\mu\text{g/mL}$ (Table 1, entry 1). This value is comparable with the MIC of other FQs tested (Table 1, entries 8–11). Compound **1** retained its potency against NR17663 and NR17666, which are both clinically derived pathogenic strains of *E. coli* (Table 1). However, with Cipro-resistant strain NR-17661 (MIC of CIP, 32 $\mu\text{g/mL}$; Table 1, entry 8), no detectable inhibitory activity was observed, supporting the generation of CIP as the active antibiotic.

In order to study if **1** was active against other bacteria, this compound was next tested for its inhibitory potency against *Staphylococcus aureus* ATCC 29213, *Klebsiella pneumonia* BAA-1705, *Acinetobacter baumannii* ATCC 1605, and *Pseudomonas aeruginosa* ATCC 27853. We found moderate inhibitory activity against these pathogens (Table 2, entries 1–4). A

Table 2. Minimum Inhibitory Concentrations (MICs) of **1** against Various Bacteria

| Entry | Bacterial species | MIC ($\mu\text{g/mL}$) | |
|-------|-----------------------------------|--------------------------|------------------------------|
| | | 1 | reference value ^a |
| 1 | <i>Staphylococcus aureus</i> | 4 | 0.125 ^a |
| 2 | <i>Klebsiella pneumonia</i> | >64 | 64 ^a |
| 3 | <i>Acinetobacter baumannii</i> | >64 | 8 ^a |
| 4 | <i>Pseudomonas aeruginosa</i> | 2 | 0.5 ^a |
| 5 | <i>Mycobacterium abscessus</i> | >64 | 2 ^b |
| 6 | <i>Mycobacterium chelonae</i> | 16 | 2 ^b |
| 7 | <i>Mycobacterium fortuitum</i> | 32 | 0.125 ^b |
| 8 | <i>Mycobacterium tuberculosis</i> | >64 | 0.03 ^c |

^aCiprofloxacin was used as the reference. ^bLevofloxacin was used as the reference. ^cIsoniazid was used as the reference.

variation in the reduction efficiency of the aryl nitro group in various bacteria has been previously reported, which could contribute to differences in activity.^{16,35,36} The superfamily of nitroreductases have been recently studied by Babbitt and co-workers and their study provides a framework for understanding the functional diversity in this enzyme class and will help design better substrates to address the species-specific differences.³⁷ Furthermore, the permeability of the compound may also play a role in the low inhibitory potency. When tested against mycobacteria, we found that the compound has

uniformly low potency including against *Mycobacterium tuberculosis* (Table 2, entries 5–8). In order to test if this is due to diminished permeability or metabolism of the nitroaryl group, we treated lysate obtained from *Mycobacterium smegmatis* with **1**. An increased fluorescence signal for the coumarin fluorophore supported the capability of mycobacteria to metabolize **1** (see SI, Figure S7). Hence, it is possibly the poor cell permeability of **1** that contributes to diminished activity. However, further studies will need to be carried out to better characterize these differences.

Again, this data may be reflective of diminished cell permeability or differences in metabolism of the nitroaryl group to release the active drug; this aspect will need further investigation. Together, our observations support the selectivity of **1** in inhibiting *E. coli* when compared with other Gram-positive and Gram-negative bacteria. The *t*-Boc derivative **8** was found to be a poor inhibitor of *E. coli* growth, as the active component of this derivative is compound **7** which is a modified analogue of CIP (MIC = > 64 $\mu\text{g/mL}$, Table 1, entries 2 and 3).⁵ In addition, when **8** was incubated with NTR, we found diminished signal attributable to the formation of **2** when compared with a similar assay carried out with **1** (see SI, Figure S8). This result suggests that **8** is a poor substrate for NTR. Hence, it is likely that **8** is poorly metabolized in *E. coli*, and since it produces an inactive compound **7** upon activation, the conjugate is not a good inhibitor of bacterial growth.

In order to test if the sulfonate-linker was compatible with other FQs, **9**, **10**, and **11** were prepared (Figure 4; see SI for synthesis). These compounds were found to undergo decomposition in the presence of Zn/ammonium formate to generate the respective FQ (SI, Figure S4). The MIC for these compounds was determined and the Cipro derivative was most potent in inhibiting *E. coli* (Table 1, entries 4–6). Furthermore, **1** was significantly higher in its inhibitory potency when compared with **9** suggesting that the coumarin-based scaffold enhanced bacterial cell-permeability (Table 1, entries 1 and 4). Furthermore, the adducts **9**–**11** all had a free amine, supporting the need for this functional group in the bacterial growth inhibition.

Next, we investigated the stability and selectivity profile of **1**. In order to test if the carboxylester linkage of **1** was labile, we investigated the stability of **1** for toward esterases by HPLC analysis and the compound **1** was recovered in an excellent yield (>95%, 30 min incubation; see SI, Figure S9). This data was further corroborated by fluorescence measurements to

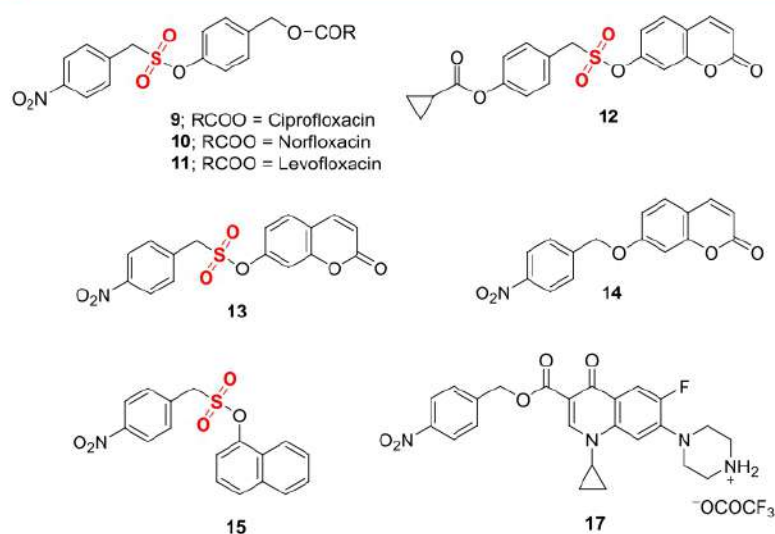


Figure 4. Structures of key compounds used in this study.

monitor the formation of **2** (Figure 3c). Here, we find no significant increase in fluorescence suggesting that the compound was stable during incubation with esterase. A similar result was recorded for **1** in the presence of glutathione (0.25 mM) and hydrogen peroxide (0.25 mM) (Figure 3c).

In order to test the selectivity of activation of **1** in bacteria versus host cells, we studied the stability of sulfonate-linker in the mammalian cell lysate. In this experiment, three cancer cell lines were independently treated with **1**, we found no evidence for increased fluorescence attributable to the formation of **2** (Figure 3d). Here, we used **12** (Figure 4), an esterase triggered generator of umbelliferone (UMB), as the positive control (Figure 3d). In addition, we independently tested **9** in mammalian cell lysate and found no evidence for the generation of CIP as determined by measuring fluorescence ($\lambda_{\text{ex}} = 272 \text{ nm}$; $\lambda_{\text{em}} = 424 \text{ nm}$) during incubation for 1 h (see SI, Figure S10). This results were further corroborated by an independent HPLC experiment with A549 cell lysate, and compound **1** was recovered in an excellent yield (>80%) (see SI, Figure S11). Thus, it appears that carboxylester of **1** was not labile and the nitroaryl sulfonate-linker is stable in cellular milieu that lacks NTR to activate the compound **1**. Together, these data support bacteria-selective activation of the conjugate **1** to produce the antibiotic along with a fluorescence reporter.

We next compared the newly developed sulfonate linker with the alternative, 4-nitrobenzyl linker. In order to study, head-to-head, the nitro group metabolism efficiency, we synthesized **13** and **14**, which each had a fluorescence reporter (Figure 4). In the presence of NTR, we find that sulfonate **13** was more efficient in generating UMB when compared with **14** (see SI, Figure S3). This is likely due to the formation of thermodynamically stable gaseous SO_2 . The formation of SO_2 was verified by synthesizing the naphthol adduct **15**; using the fluorophore **16** (see SI, Figure S12) that is sensitive to sulfite (see SI, Scheme S2).³⁸ Using this fluorophore, the formation of sulfite when **15** was incubated with NTR was observed (see SI, Figure S12). Again, this finding is consistent with the proposed mechanism of fragmentation of **1** to generate **2**, CIP, and SO_2 (see SI, Scheme S1).

Finally, we synthesized **17**, the 4-nitrobenzyl ester of CIP (see SI). The MIC for this compound was determined (Table

1, entry 7) and **17** was found to be a potent inhibitor of *E. coli*. However, **1** was better than **17** in inhibiting bacterial growth. Finally, when **17** was incubated in mammalian cell lysate, we found no evidence for formation of CIP (see SI, Figure S10). This result is a testament to the bacteria-selectivity of the nitroaryl functional group, which has been previously characterized.³⁹

Having established that **1** was a potent inhibitor of *E. coli* growth in culture, we proceeded to further evaluate this compound for its bactericidal effects. Time-kill analysis showed significant concentration-dependent bactericidal activity that is comparable with CIP (Figure 5a). Two concentrations of MIC and 10× MIC were used and a significant reduction in viable bacteria was observed. Finally, using a neutropenic mouse thigh infection model, **1** significantly diminished the bacterial burden in infected animals (Figure 5b). The bactericidal activity of **1** was comparable with that of Ciprofloxacin (Figure 5b). Thus, newly developed conjugate **1** had potent *in vivo* bactericidal activity.

Taken together, we have developed a new strategy to selectively generate a FQ within bacteria. The sulfonate group afforded excellent stability in the biological milieu and the byproduct SO_2 does not appear to have an adverse effect at the tested concentrations, suggesting that the sulfonate linker developed herein is promising as a replacement for a carbonate linker. Due to its potential side effects, the Food and Drug Administration (FDA) has issued an advisory on FQ use citing mental health concerns,⁴⁰ adverse reactions associated with blood sugar,⁴¹ cardiotoxicity,^{42,43} neurotoxicity,^{44,45} and tendinitis.⁴⁶ Selective activation of FQ within bacteria may significantly reduce these deleterious effects. Furthermore, another major concern is the lack of selectivity between pathogenic and nonpathogenic *E. coli*. Recently, a siderophore-conjugated CIP was reported by Nolan and co-workers.⁶ This elegant strategy spares nonpathogenic bacteria and kills pathogenic bacteria and, in principle, can be adapted to our prodrug approach as well. Previously, hybrid-drugs containing a cephalosporin as well as a fluoroquinolone have been reported.^{47–49} These compounds are sensitive to β -lactamases and produce a fluoroquinolone in the proximity of bacteria and the results are highly encouraging for further development of

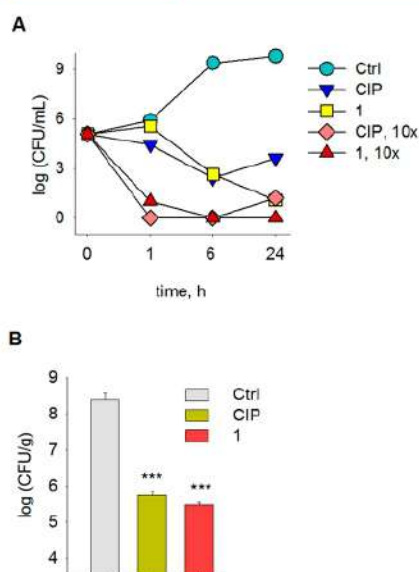


Figure 5. (A) Time-kill analysis conducted on *E. coli* ATCC 29213 by counting CFU at 1 \times and 10 \times MIC. (B) Neutropenic mouse thigh infection model was used to study the efficacy of **1** (10 mg/kg) with Ciprofloxacin (10 mg/kg) as controls. The drug/compound was dosed through the intraperitoneal route, 3 and 6 h post-infection to a group of five mice. Ciprofloxacin was used as a reference compound while Ctrl is untreated mice.*** $p < 0.001$ and are determined with respect to Ctrl.

these compounds.^{47–50} A number of nanoparticle-based theranostics approaches for bacteria are in development.^{51–57} For example, CIP has been conjugated with a pentafluoroaryl group to produce a nanoparticle that facilitates localization of drug.⁵⁸ These methods along with the complementary prodrug strategies will help address the major concerns associated with the use of fluoroquinolones.

In summary, we have developed a new conjugate based on a sulfonate linker that fragments to generate a drug, and forms the basis for bacterial enzyme-guided FQ delivery. The use of reduction of the nitro group to deliver anticancer drugs is in development.^{15,59} NTR is used as a metabolic trigger for gene-directed enzyme prodrug therapy (GDEPT) and antibody-directed enzyme prodrug therapy (ADEPT).²⁷ This enzyme is introduced either by transfection methodologies (for GDEPT) or by the use of tumor-specific antigens conjugated to the enzyme (for ADEPT).¹⁵ Upon exposure to the exogenous enzyme, the inactive prodrug, which is a substrate for the enzyme, is metabolized to produce the cytotoxic species either intracellularly or in the proximity of tumors. Since the expression of NTR in normal cells is minimal, this strategy has been widely exploited. Here, we report for the first time a conjugate that is activated by bacterial nitroreductase to deliver an antibiotic. Conjugate **1** was highly potent in inhibiting bacteria and generated a fluorescence signal upon activation by NTR. The fluorescence signal could be detected by confocal imaging, thus laying the foundation for theranostic targeting of bacteria.⁶⁰ The fluorophore will need to be developed further to permit real-time *in vivo* imaging. Our study lays the platform for further development of “seek and kill” approaches, which spare the host of the deleterious effects of these highly potent and life-saving drugs.

MATERIALS AND METHODS

4-(1-Cyclopropyl-6-fluoro-3-(((7-(((4-nitrobenzyl)sulfonyl)oxy)-2-oxo-2H-chromen-3-yl)methoxy)-carbonyl)-4-oxo-1,4-dihydroquinolin-7-yl)piperazin-1-ium, TFA salt (1**).** TFA (2.09 mL, 27.34 mmol) was added dropwise to a solution of **8** (110 mg, 0.14 mmol) dissolved in DCM (20 mL) at 0 °C under a nitrogen atmosphere. The resulting reaction mixture was stirred for 6 h at rt. After complete disappearance of starting material (observed via TLC), the solvent was removed under vacuum at $T < 20$ °C. The product was precipitated from diethyl ether on sonication. The obtained white solid was washed by adding diethyl ether and then its careful decantation, and was finally dried under vacuum. Compound **1** (102 mg, 91%) was isolated as a colorless solid; ¹H NMR (400 MHz, DMSO-*d*₆): δ 8.94 (s, 2H), 8.55 (s, 1H), 8.33–8.29 (m, 3H), 7.87 (d, $J = 4.0$ Hz, 1H), 7.84–7.80 (m, 3H), 7.50 (d, $J = 7.4$ Hz, 1H), 7.46 (d, $J = 2.3$ Hz, 1H), 7.30 (dd, $J = 8.5, 2.4$ Hz, 1H), 5.34 (s, 2H), 5.14 (s, 2H), 3.74–3.68 (m, 1H), 3.47–3.45 (m, 4H), 3.34 (br, 4H), 1.30–1.25 (m, 2H), 1.15–1.11 (m, 2H); ¹³C NMR (100 MHz, DMSO-*d*₆): δ 171.5 (d), 163.9, 158.9, 153.6, 153.2, 151.2, 150.3, 148.8, 147.7, 142.7 (d), 139.4, 137.9, 135.2, 132.4, 129.9, 123.8, 123.7, 122.5 (d), 118.7, 117.7, 111.8 (d), 110.0, 108.4, 106.7, 60.6, 55.3, 46.4, 42.6, 34.9, 7.5; FTIR (ν_{\max} , cm⁻¹): 1176, 1263, 1349, 1512, 1621, 1695; HRMS (ESI) calcd for C₃₄H₃₀FN₄O₁₀S [M]⁺: 705.1661; found [M]⁺: 705.1661.

Nitroreductase Activated Decomposition of **1 for Monitoring the Release of Fluorescent Compound **2** by Fluorimetry.** Stock solutions of compound **1** (1 mM), CIP (1 mM) and **2** (1 mM) were prepared in DMSO independently. A stock solution of *E. coli* nitroreductase, NTR (1 μ g/1 μ L), and NADH (3 mM) was prepared in PBS (pH 7.4, 10 mM). In a reaction, compound **1** (10 μ L, final conc. 10 μ M), NADH (10 μ L, final conc. 30 μ M), and NTR (10 μ L, final conc. 10 μ g/mL) were added to 970 μ L PBS. The reaction mixture was incubated at 37 °C for 30 min on an Eppendorf thermomixer comfort (800 rpm). The reaction mixture was transferred into a quartz fluorescence cell (Hellma, path length 1.0 cm) and fluorescence measurements were carried out using a HORIBA Jobin Yvon Fluorolog fluorescence spectrophotometer. Fluorescence was monitored for **2** ($\lambda_{\text{ex}} = 350$ nm and $\lambda_{\text{em}} = 450$ nm). The emission profile was recorded with an excitation slit width of 1 nm and emission slit width of 1 nm.

Decomposition Studies by HPLC. Stock solutions of compounds **1** (5 mM), **2** (5 mM), **13** (5 mM), **14** (5 mM), and UMB (5 mM) were prepared in DMSO independently. A stock solution of ciprofloxacin (CIP, 5 mM) was prepared in 0.01 N HCl, while those of *E. coli* NTR (1 μ g/1 μ L) and NADH (7.5 mM) were prepared in PBS (pH 7.4, 10 mM). In a typical reaction, the respective compound (5 μ L, final conc. 25 μ M), NADH (10 μ L, final conc. 75 μ M), and NTR (20 μ L, final conc. 20 μ g/mL) were added to 965 μ L PBS. Reaction mixtures were incubated at 37 °C on an Eppendorf thermomixer comfort (800 rpm). Aliquots were taken periodically and injected (25 μ L) in an HPLC instrument attached with a diode-array detector (detection wavelength 320 nm). The stationary phase used was a C-18 reversed phase column (4.6 mm \times 250 mm, 5 μ m). The mobile phase used was 0.1% TFA in H₂O:ACN. HPLC run time was 15 min with a flow rate of 1 mL/min with 60:40 \rightarrow 0–5 min, 50:50 \rightarrow 5–10 min, 30:70 \rightarrow 10–15 min, 60:40, and the reduction of the

test compounds was analyzed using HPLC by monitoring the disappearance of the peak for the test compound.

Antibiotic Susceptibility Test. MIC for a compound is defined as the lowest concentration of it, where there is no visible growth of cells such as bacteria. Antibiotic susceptibility testing of compounds against MSSA, MRSA, *E. coli*, *P. aeruginosa*, and resistant clinical isolates of *E. coli* was carried out according to the CLSI (Clinical and Laboratory Standards Institute) guidelines for broth microdilution assay. 10 mg/mL stock solutions of test compounds were prepared in DMSO. Bacterial cultures were inoculated in Muller Hilton broth II (MHB II) and OD of the cultures was measured at the 600 nm wavelength, followed by dilution to achieve $\sim 10^5$ CFU/mL. The compounds were tested ranging from 64 to 0.03 mg/L in a 2-fold serial diluted fashion, with 2.5 μ L of each concentration added to each well of a 96-well round-bottom microtiter plate. Later, 97.5 μ L of bacterial suspension was added to each well containing the test compound along with appropriate controls. The plates were incubated at 37 °C for 18–24 h, following which, the MIC was identified.⁶¹

Time-Kill Kinetics. Bactericidal activity was assessed by the time-kill method. In brief, *E. coli* ATCC 25922 was diluted to $\sim 10^5$ CFU/mL in MHB II and treated at 1 \times and 10 \times MIC of the compounds, then incubated at 37 °C with shaking for 24 h. From these, 100 μ L samples were collected at time intervals of 0, 1, 6, and 24 h, serially diluted and plated on MHA (mueller Hinton Agar) followed by incubation at 37 °C for 18–20 h. Kill curves were constructed by counting the colonies from plates and plotting the CFU/mL of surviving bacteria at each time point, in the presence and absence of a compound. Each experiment was repeated three times in duplicate and the mean data is plotted.

Neutropenic Mouse Thigh Model of Infection. The use of mice for infectious studies (IAEC/2014/139 dated 03.12.2014) was approved by Institutional Animal Ethics Committee at CSIR-CDRI, Lucknow. Balb/C male mice weighing 24–26 g were housed 2 days prior to the start of the experiment, kept in groups of 4 per cage and given food and water *ad libitum*. To cause neutropenia in mice, cyclophosphamide was injected 4 days before infection, through the intraperitoneal route (150 mg/kg body weight), and 1 day before (100 mg/kg body weight) infection. 100 μ L intramuscular infection of 10^7 log CFU/mL was given in the thigh muscle of each mouse. The drug/compound was dosed through the intraperitoneal route, 3 and 6 h post-infection, to a group of five mice at a concentration of Ciprofloxacin (10 mg/kg body weight) and compound **1** (10 mg/kg body weight). Ciprofloxacin was used as a reference compound, while untreated mice were the controls. Mice were sacrificed 24 h post-infection. The thighs were removed and homogenized, and dilutions were plated aseptically to procure the infection load in each mouse.⁶²

Statistical Methods. For *in vivo* bactericidal activity of **1** and Ciprofloxacin, Kruskal–Wallis test was used to evaluate the significant decrease of bacterial burden in infected animals. Significance level was set at <0.0001 . Graphics and statistical analysis were performed with GraphPad Prism 5.0.

■ ASSOCIATED CONTENT

📄 Supporting Information

The Supporting Information is available free of charge on the ACS Publications website at DOI: 10.1021/acs.bioconjchem.8b00887.

Experimental procedures, protocols, and supporting data (PDF)

■ AUTHOR INFORMATION

Corresponding Authors

*E-mail: skchopra007@gmail.com.

*E-mail: harinath@iiserpune.ac.in.

ORCID

Harinath Chakrapani: 0000-0002-7267-0906

Author Contributions

#M.S. and G.K. contributed equally.

Notes

The authors declare no competing financial interest.

■ ACKNOWLEDGMENTS

The authors thank the Department of Science and Technology (DST, Grant number EMR/2015/000668), Department of Biotechnology, India (BT/PR15848/MED/29/1025/2016) for financial support for our research. Council for Scientific and Industrial Research (CSIR) and the Department of Science and Technology – Innovation in Science Pursuit for Inspired Research (DST-INSPIRE) for fellowships.

■ REFERENCES

- (1) Klein, E. Y., Van Boeckel, T. P., Martinez, E. M., Pant, S., Gandra, S., Levin, S. A., Goossens, H., and Laxminarayan, R. (2018) Global Increase and Geographic Convergence in Antibiotic Consumption between 2000 and 2015. *Proc. Natl. Acad. Sci. U. S. A.* 115, E3463–E3470.
- (2) Stahlmann, R., and Lode, H. M. (2013) Risks Associated with the Therapeutic Use of Fluoroquinolones. *Expert Opin. Drug Saf.* 12, 497–505.
- (3) Sarker, P., Mily, A., Mamun, A., Jalal, S., Bergman, P., Raqib, R., Gudmundsson, G., and Agerberth, B. (2014) Ciprofloxacin Affects Host Cells by Suppressing Expression of the Endogenous Antimicrobial Peptides Cathelicidins and Beta-Defensin-3 in Colon Epithelia. *Antibiotics* 3, 353–374.
- (4) Badal, S., Her, Y. F., and Maher, L. J. (2015) Nonantibiotic Effects of Fluoroquinolones in Mammalian Cells. *J. Biol. Chem.* 290, 22287–22297.
- (5) Ji, C., Miller, P. A., and Miller, M. J. (2015) Syntheses and Antibacterial Activity of N-Acylated Ciprofloxacin Derivatives Based on the Trimethyl Lock. *ACS Med. Chem. Lett.* 6, 707–710.
- (6) Neumann, W., Sassone-Corsi, M., Raffatelli, M., and Nolan, E. M. (2018) Esterase-Catalyzed Siderophore Hydrolysis Activates an Enterobactin-Ciprofloxacin Conjugate and Confers Targeted Antibacterial Activity. *J. Am. Chem. Soc.* 140, 5193–5201.
- (7) Baker, W. R., Cai, S., Dimitroff, M., Fang, L., Huh, K. K., Ryckman, D. R., Shang, X., Shawar, R. M., and Therrien, J. H. (2004) A Prodrug Approach toward the Development of Water Soluble Fluoroquinolones and Structure-Activity Relationships of Quinolone-3-Carboxylic Acids. *J. Med. Chem.* 47, 4693–4709.
- (8) Pal, S., Ramu, V., Taye, N., Mogare, D. G., Yeware, A. M., Sarkar, D., Reddy, D. S., Chattopadhyay, S., and Das, A. (2016) GSH Induced Controlled Release of Levofloxacin from a Purpose-Built Prodrug: Luminescence Response for Probing the Drug Release in Escherichia Coli and Staphylococcus Aureus. *Bioconjugate Chem.* 27, 2062–2070.
- (9) Neumann, W., and Nolan, E. M. (2018) Evaluation of a Reducible Disulfide Linker for Siderophore-Mediated Delivery of Antibiotics. *JBIC, J. Biol. Inorg. Chem.* 23, 1025–1036.
- (10) Velema, W. A., Hansen, M. J., Lerch, M. M., Driessen, A. J. M., Szymanski, W., and Feringa, B. L. (2015) Ciprofloxacin-Photoswitch Conjugates: A Facile Strategy for Photopharmacology. *Bioconjugate Chem.* 26, 2592–2597.

- (11) Wong, P. T., Tang, S., Mukherjee, J., Tang, K., Gam, K., Isham, D., Murat, C., Sun, R., Baker, J. R., and Choi, S. K. (2016) Light-Controlled Active Release of Photocaged Ciprofloxacin for Lipopolysaccharide-Targeted Drug Delivery Using Dendrimer Conjugates. *Chem. Commun.* 52, 10357–10360.
- (12) Kumari, P., Kulkarni, A., Sharma, A. K., and Chakrapani, H. (2018) Visible-Light Controlled Release of a Fluoroquinolone Antibiotic for Antimicrobial Photopharmacology. *ACS Omega* 3, 2155–2160.
- (13) Wegener, M., Hansen, M. J., Driessen, A. J. M., Szymanski, W., and Feringa, B. L. (2017) Photocontrol of Antibacterial Activity: Shifting from UV to Red Light Activation. *J. Am. Chem. Soc.* 139, 17979–17986.
- (14) Roldán, M. D., Pérez-Reinado, E., Castillo, F., and Moreno-Vivián, C. (2008) Reduction of Polynitroaromatic Compounds: The Bacterial Nitroreductases. *FEMS Microbiol. Rev.* 32, 474–500.
- (15) Williams, E. M., Little, R. F., Mowday, A. M., Rich, M. H., Chan-Hyams, J. V. E., Copp, J. N., Smail, J. B., Patterson, A. V., and Ackerley, D. F. (2015) Nitroreductase Gene-Directed Enzyme Prodrug Therapy: Insights and Advances toward Clinical Utility. *Biochem. J.* 471, 131–153.
- (16) Çelik, A., and Yetiş, G. (2012) An Unusually Cold Active Nitroreductase for Prodrug Activations. *Bioorg. Med. Chem.* 20, 3540–3550.
- (17) Pitsawong, W., Hoben, J. P., and Miller, A. F. (2014) Understanding the Broad Substrate Repertoire of Nitroreductase Based on Its Kinetic Mechanism. *J. Biol. Chem.* 289, 15203–15214.
- (18) Wylie, S., Roberts, A. J., Norval, S., Patterson, S., Foth, B. J., Berriman, M., Read, K. D., and Fairlamb, A. H. (2016) Activation of Bicyclic Nitro-Drugs by a Novel Nitroreductase (NTR2) in *Leishmania*. *PLoS Pathog.* 12, 1–22.
- (19) Lee, M. K., Williams, J., Twieg, R. J., Rao, J., and Moerner, W. E. (2013) Enzymatic Activation of Nitro-Aryl Fluorogens in Live Bacterial Cells for Enzymatic Turnover-Activated Localization Microscopy. *Chem. Sci.* 4, 220–225.
- (20) Shukla, P., Khodade, V. S., SharathChandra, M., Chauhan, P., Mishra, S., Siddaramappa, S., Pradeep, B. E., Singh, A., and Chakrapani, H. (2017) On Demand” Redox Buffering by H(2)S Contributes to Antibiotic Resistance Revealed by a Bacteria-Specific H(2)S Donor. *Chem. Sci.* 8, 4967–4972.
- (21) Sharma, K., Sengupta, K., and Chakrapani, H. (2013) Nitroreductase-Activated Nitric Oxide (NO) Prodrugs. *Bioorg. Med. Chem. Lett.* 23, 5964–5967.
- (22) Cuquerella, M. C., Miranda, M. A., and Bosca, F. (2006) Role of Excited State Intramolecular Charge Transfer in the Photophysical Properties of Norfloxacin and Its Derivatives. *J. Phys. Chem. A* 110, 2607–2612.
- (23) Seifrtová, M., Aurfartová, J., Vytlačilová, J., Pena, A., Solich, P., and Nováková, L. (2010) Determination of Fluoroquinolone Antibiotics in Wastewater Using Ultra High-Performance Liquid Chromatography with Mass Spectrometry and Fluorescence Detection. *J. Sep. Sci.* 33, 2094–2108.
- (24) Weinstein, R., Segal, E., Satchi-Fainaro, R., and Shabat, D. (2010) Real-Time Monitoring of Drug Release. *Chem. Commun.* 46, 553–555.
- (25) Ravikumar, G., Bagheri, M., Saini, D. K., and Chakrapani, H. (2017) FLUORO/NO: A Nitric Oxide Donor with a Fluorescence Reporter. *ChemBioChem* 18, 1529–1534.
- (26) Behara, K. K., Rajesh, Y., Venkatesh, Y., Pinninti, B. R., Mandal, M., and Singh, N. D. P. (2017) Cascade Photocaging of Diazeniumdiolate: A Novel Strategy for One and Two Photon Triggered Uncaging with Real Time Reporting. *Chem. Commun.* 53, 9470–9473.
- (27) Rautio, J., Kumpulainen, H., Heimbach, T., Oliyai, R., Oh, D., Järvinen, T., and Savolainen, J. (2008) Prodrugs: Design and Clinical Applications. *Nat. Rev. Drug Discovery* 7, 255–270.
- (28) Sykes, B. M., Hay, M. P., Bohinc-Herceg, D., Helsby, N. A., O’Connor, C. J., and Denny, W. A. (2000) Leaving Group Effects in Reductively Triggered Fragmentation of 4-Nitrobenzyl Carbamates. *J. Chem. Soc. Perkin Trans. 1* 10, 1601–1608.
- (29) Østergaard, J., and Larsen, C. (2007) Bioreversible Derivatives of Phenol. 1. The Role of Human Serum Albumin as Related to the Stability and Binding Properties of Carbonate Esters with Fatty Acid-like Structures in Aqueous Solution and Biological Media. *Molecules* 12, 2380–2395.
- (30) Binderup, E., Bjorkling, F., Hjamaa, P. V., Latini, S., Baltzer, B., Carlsen, M., and Binderup, L. (2005) EB1627: A Soluble Prodrug of the Potent Anticancer Cyanoguanidine CHS828. *Bioorg. Med. Chem. Lett.* 15, 2491–2494.
- (31) Pardeshi, K. A., Ravikumar, G., and Chakrapani, H. (2018) Esterase Sensitive Self-Immolative Sulfur Dioxide Donors. *Org. Lett.* 20, 4–7.
- (32) Ough, C. S., and Crowell, E. A. (1987) Use of Sulfur Dioxide in Winemaking. *J. Food Sci.* 52, 386–388.
- (33) Prabhakar, K., and Mallika, E. N. (2014) Preservatives: Permitted Preservatives - Sulfur Dioxide. In *Encyclopedia of Food Microbiology*: 2nd ed. (Batt, C. A., and Tortorella, M. L., Eds.) pp 108–112, Vol. 3, Elsevier.
- (34) Coşkun, A. L., Türkyilmaz, M., Aksu, Ö. T., Koç, B. E., Yemiş, O., and Özkan, M. (2013) Effects of Various Sulphuring Methods and Storage Temperatures on the Physical and Chemical Quality of Dried Apricots. *Food Chem.* 141, 3670–3680.
- (35) Prosser, G. A., Copp, J. N., Mowday, A. M., Guise, C. P., Syddall, P., Williams, E. M., Horvat, C. N., Swe, P. M., Ashoorzadeh, A., Denny, W. A., et al. (2013) Creation and Screening of a Multi-Family Bacterial Oxidoreductase Library to Discover Novel Nitroreductases That Efficiently Activate the Bioreductive Prodrugs CB1954 and PR-104A. *Biochem. Pharmacol.* 85, 1091–1103.
- (36) Gruber, T. D., Krishnamurthy, C., Grimm, J. B., Tadross, M. R., Wysocki, L. M., Gartner, Z. J., and Lavis, L. D. (2018) Cell-Specific Chemical Delivery Using a Selective Nitroreductase–Nitroaryl Pair. *ACS Chem. Biol.* 13, 2888–2896.
- (37) Akiva, E., Copp, J. N., Tokuriki, N., and Babbitt, P. C. (2017) Evolutionary and Molecular Foundations of Multiple Contemporary Functions of the Nitroreductase Superfamily. *Proc. Natl. Acad. Sci. U. S. A.* 114, E9549–E9558.
- (38) Sun, Y. Q., Liu, J., Zhang, J., Yang, T., and Guo, W. (2013) Fluorescent Probe for Biological Gas SO₂ derivatives Bisulfite and Sulfite. *Chem. Commun.* 49, 2637–2639.
- (39) Xu, S., Wang, Q., Zhang, Q., Zhang, L., Zuo, L., Jiang, J. D., and Hu, H. Y. (2017) Real Time Detection of ESKAPE Pathogens by a Nitroreductase-Triggered Fluorescence Turn-on Probe. *Chem. Commun.* 53, 11177–11180.
- (40) Owens, R. C., and Ambrose, P. G. (2005) Antimicrobial Safety: Focus on Fluoroquinolones. *Clin. Infect. Dis.* 41, S144–S157.
- (41) Ghaly, H., Kriete, C., Sahin, S., Pflöger, A., Holzgrabe, U., Zünder, B. J., and Rustenbeck, I. (2009) The Insulinotropic Effect of Fluoroquinolones. *Biochem. Pharmacol.* 77, 1040–1052.
- (42) Briasoulis, A., Agarwal, V., and Pierce, W. J. (2011) QT Prolongation and Torsade de Pointes Induced by Fluoroquinolones: Infrequent Side Effects from Commonly Used Medications. *Cardiology* 120, 103–110.
- (43) Inghammar, M., Svanström, H., Melbye, M., Pasternak, B., and Hviid, A. (2016) Oral Fluoroquinolone Use and Serious Arrhythmia: Bi-National Cohort Study. *BMJ.* 352, 1–8.
- (44) Samyde, J., Petit, P., Hillaire-Buys, D., and Faillie, J.-L. (2016) Quinolone Antibiotics and Suicidal Behavior: Analysis of the World Health Organization’s Adverse Drug Reactions Database and Discussion of Potential Mechanisms. *Psychopharmacology (Berl)*. 233, 2503–2511.
- (45) Oreagba, I. A., Oshikoya, K. A., Ogar, C., Adefurin, A. O., Ibrahim, A., Awodele, O., and Oni, Y. (2017) Adverse Reactions to Fluoroquinolones in the Nigerian Population: An Audit of Reports Submitted to the National Pharmacovigilance Centre from 2004 to 2016. *Pharmacol. Res. Perspect.* 5, 1–15.
- (46) Arabyat, R. M., Raisch, D. W., McKoy, J. M., and Bennett, C. L. (2015) Fluoroquinolone-Associated Tendon-Rupture: A Summary of

Reports in the Food and Drug Administration's Adverse Event Reporting System. *Expert Opin. Drug Saf.* 14, 1653–1660.

(47) Albrecht, H. A., Beskid, G., Christenson, J. G., Georgopapadakou, N. H., Keith, D. D., Konzelmann, F. M., Pruess, D. L., Rossman, P. L., and Wei, C. C. (1991) Dual-Action Cephalosporins: Cephalosporin 3'-Quinolone Carbamates. *J. Med. Chem.* 34, 2857–2864.

(48) Albrecht, H. A., Beskid, G., Chan, K. K., Christenson, J. G., Cleeland, R., Deitcher, K. H., Georgopapadakou, N. H., Keith, D. D., Pruess, D. L., et al. (1990) Cephalosporin 3'-Quinolone Esters with a Dual Mode of Action. *J. Med. Chem.* 33, 77–86.

(49) Albrecht, H. A., Beskid, G., Christenson, J. G., Durkin, J. W., Fallat, V., Georgopapadakou, N. H., Keith, D. D., Konzelmann, F. M., and Lipschitz, E. R. (1991) Dual-Action Cephalosporins: Cephalosporin 3'-Quaternary Ammonium Quinolones. *J. Med. Chem.* 34, 669–675.

(50) Georgopapadakou, N. H., and Bertasso, A. (1993) Mechanisms of Action of Cephalosporin 3'-Quinolone Esters, Carbamates, and Tertiary Amines in *Escherichia Coli*. *Antimicrob. Agents Chemother.* 37, 559–565.

(51) Zhao, Z., Yan, R., Yi, X., Li, J., Rao, J., Guo, Z., Yang, Y., Li, W., Li, Y. Q., and Chen, C. (2017) Bacteria-Activated Theranostic Nanoprobes against Methicillin-Resistant *Staphylococcus Aureus* Infection. *ACS Nano* 11, 4428–4438.

(52) Gopinath, P. M., Ranjani, A., Dhanasekaran, D., Thajuddin, N., Archunan, G., Akbarsha, M. A., Gulyás, B., and Padmanabhan, P. (2016) Multi-Functional Nano Silver: A Novel Disruptive and Theranostic Agent for Pathogenic Organisms in Real-Time. *Sci. Rep.* 6, 1–16.

(53) Thakur, M., Pandey, S., Mewada, A., Patil, V., Khade, M., Goshi, E., and Sharon, M. (2014) Antibiotic Conjugated Fluorescent Carbon Dots as a Theranostic Agent for Controlled Drug Release, Bioimaging, and Enhanced Antimicrobial Activity. *J. Drug Delivery* 2014, 282193.

(54) Ferreira, K., Hu, H. Y., Fetz, V., Prochnow, H., Rais, B., Müller, P. P., and Brönstrup, M. (2017) Multivalent Siderophore–DOTAM Conjugates as Theranostics for Imaging and Treatment of Bacterial Infections. *Angew. Chem., Int. Ed.* 56, 8272–8276.

(55) Li, Q., Lu, F., Ye, H., Yu, K., Lu, B., Bao, R., Xiao, Y., Dai, F., and Lan, G. (2018) Silver Inlaid with Gold Nanoparticles: Enhanced Antibacterial Ability Coupled with the Ability to Visualize Antibacterial Efficacy. *ACS Sustainable Chem. Eng.* 6, 9813–9821.

(56) Khan, S. A., Singh, A. K., Senapati, D., Fan, Z., and Ray, P. C. (2011) Targeted Highly Sensitive Detection of Multi-Drug Resistant *Salmonella* DT104 Using Gold Nanoparticles. *Chem. Commun.* 47, 9444–9446.

(57) Kim, T., Zhang, Q., Li, J., Zhang, L., and Jokerst, J. V. (2018) A Gold/Silver Hybrid Nanoparticle for Treatment and Photoacoustic Imaging of Bacterial Infection. *ACS Nano* 12, 5615–5625.

(58) Xie, S., Manuguri, S., Proietti, G., Romson, J., Fu, Y., Inge, A. K., Wu, B., Zhang, Y., Häll, D., Ramström, O., et al. (2017) Design and Synthesis of Theranostic Antibiotic Nanodrugs That Display Enhanced Antibacterial Activity and Luminescence. *Proc. Natl. Acad. Sci. U. S. A.* 114, 8464–8469.

(59) O'Connor, L. J., Cazares-Körner, C., Saha, J., Evans, C. N. G., Stratford, M. R. L., Hammond, E. M., and Conway, S. J. (2016) Design, Synthesis and Evaluation of Molecularly Targeted Hypoxia-Activated Prodrugs. *Nat. Protoc.* 11, 781–794.

(60) Guo, T., Cui, L., Shen, J., Zhu, W., Xu, Y., and Qian, X. (2013) A Highly Sensitive Long-Wavelength Fluorescence Probe for Nitroreductase and Hypoxia: Selective Detection and Quantification. *Chem. Commun.* 49, 10820–10822.

(61) Clinical and Laboratory Standards Institute (2012) *Methods for Dilution Antimicrobial Susceptibility Tests for Bacteria That Grow Aerobically. Approved Standard — 9th ed.*, CLSI document M07-A9, Clinical and Laboratory Standards Institute, Wayne, PA.

(62) Shan, Q., Liang, C., Wang, J., Li, J., and Zeng, Z. (2014) In Vivo Activity of Cefquinome against *Escherichia Coli* in the Thighs of Neutropenic Mice. *Antimicrob. Agents Chemother.* 58, 5943–5946.